

OPTUM COMPUTATIONAL ENGINEERING

Optum^{G2}

EXAMPLES



Version 2019

Contents

I INTRODUCTION	9
I.I Drainage and Time Scope	9
I.II Initial conditions	10
I.III Shortcut keys	12
II INTRODUCTORY EXAMPLE	13
II.I Geometry	13
II.II Materials	15
II.III Loads	16
II.IV Analysis	17
II.V Results	19
1 SHALLOW FOUNDATION 1	21
1.1 Limit analysis	21
1.1.1 Mesh adaptivity	23
1.2 Elastoplastic analysis	25
1.3 Multiplier Elastoplastic analysis	27
1.4 Variation of undrained shear strength with depth	29
2 SHALLOW FOUNDATION 2	31
2.1 Limit Analysis	32
2.2 Elastoplastic analysis	34
3 SETTLEMENT OF STRIP FOOTING ON ELASTIC SOIL	36
4 STRIP LOAD ON GIBSON SOIL	38
5 FOOTING ON SOIL WITH USER DEFINED MATERIAL DATA	40
6 SLOPE STABILITY – LONG TERM	42
6.1 Gravity Multiplier	43
6.2 Strength Reduction	43
6.3 Summary	44
7 SLOPE STABILITY – SHORT TERM	45
7.1 Automatic computation of initial stresses	45
7.2 Initial stresses by excavation	46
8 STABILITY OF SLOPE SUBJECTED TO UNCONFINED SEEPAGE	48
9 STABILITY OF SLOPE SUBJECTED TO RAPID DRAWDOWN	50
9.1 Short term stability	51
9.2 Long term stability	52
10 SLOPE WITH PRE-EXISTING FAULT	54

11 STABILITY OF SEISMICALLY LOADED SLOPE	56
11.1 Loukidis et al. example	56
11.2 Short term conditions – total stress analysis	57
11.3 Short term conditions – effective stress analysis	58
12 STABILITY OF RETAINING WALL	59
13 STABILITY OF STEM WALL	61
14 STABILITY OF CANTILEVER SHEET PILE WALL	63
14.1 Strength Reduction – Solids	65
14.2 Strength Reduction – Structs	65
15 STABILITY OF STRUTTED SHEET PILE WALL	67
16 STABILITY OF ANCHORED SHEET PILE WALL	70
17 SHEET PILE WALL SUBJECTED TO SEEPAGE PRESSURES	72
18 ACCRETIONARY WEDGE	74
19 FISSURED MOHR-COULOMB SLOPE	76
20 HOEK-BROWN SLOPE 1	78
20.1 Gravity Multiplier Limit Analysis	79
20.2 Strength Reduction	79
20.3 Summary	80
21 HOEK-BROWN SLOPE 2	82
21.1 Gravity Multiplier Limit Analysis	82
21.2 Strength Reduction analysis	82
22 UNDERGROUND CAVITY IN HOEK-BROWN MATERIAL	84
23 STRIP FOOTING ON MOHR-COULOMB SAND	86
23.1 On mesh adaptivity	89
24 STRIP FOOTING ON GSK SAND	91
25 STRIP FOOTING ON HOEK-BROWN MATERIAL	93
26 COMBINED LOADING OF SHALLOW FOUNDATION	96
26.1 Effect of tension cut-off	98
27 COMBINED LOADING OF PIPELINE	100
28 BEARING CAPACITY OF SKIRTED FOUNDATION	104

29 LOAD-DISPLACEMENT ANALYSIS – INTRODUCTORY EXAMPLE	107
29.1 Multiplier Elastoplastic analysis settings	107
29.2 Data logging	108
29.3 Results	108
30 LOAD-DISPLACEMENT ANALYSIS OF FOUNDATION IN MC CLAY	110
30.1 Short Term analysis	111
30.2 Long Term analysis	113
30.3 Limit Analysis	115
30.3.1 Short Term analysis	115
30.3.2 Long Term analysis	115
30.4 Summary	116
31 LOAD-DISPLACEMENT ANALYSIS OF FOUNDATION IN MC SAND	117
32 LOAD-DISPLACEMENT ANALYSIS OF FOUNDATION IN HMC SAND	120
33 PULL-OUT OF ANCHOR IN SAND	123
34 FAULT RUPTURE PROPAGATION IN SAND	125
35 CONFINED SEEPAGE AROUND IMPERMEABLE SHEET PILE	127
35.1 Alternative modeling	129
35.2 Mesh adaptivity	131
36 UNCONFINED SEEPAGE THROUGH RECTANGULAR DAMS	132
37 FREE SURFACE FLOW THROUGH EARTH DAM	135
38 EXCAVATION MODEL TEST	137
38.1 Soil model	138
38.2 Structural elements	138
38.2.1 Prestress	139
38.3 Strength Reduction analysis	140
38.4 Excavation analysis	140
39 EXCAVATION IN SAND – MOHR-COULOMB VS HMC	143
40 EXCAVATION WITH SEEPAGE	148
41 EXCAVATION IN MOHR-COULOMB CLAY	150
42 PRELOADED FOOTING ON CLAY	153
43 SHALLOW FOUNDATION IN CLAY: EFFECTS OF PRELOADING	155
44 TUNNELING USING CONVERGENCE-CONFINEMENT METHOD	157
45 EXCAVATION WITH UNDERDRAINAGE	161

46 ONE-DIMENSIONAL CONSOLIDATION	163
46.1 'Degree of consolidation'	164
46.2 Analytical solution	165
46.3 Results	166
47 EFFECT OF CONSOLIDATION ON BEARING CAPACITY	167
48 EMBANKMENT CONSTRUCTION – PART 1	169
49 EMBANKMENT CONSTRUCTION – PART 2	172
50 CONSOLIDATION OF EXCAVATION	174
51 TRESCA VS AUS FAILURE ANALYSIS	175
51.1 Problem 1: Circular foundation	176
51.2 Problem 2: Cylindrical excavation	178
51.3 Problem 3: Deep anchor	180
52 AUS – CALIBRATION AND SIMULATION	182
52.1 Simple shear elemental test	185
53 FOUNDATION ON marginally STABLE SLOPE	186
54 DESIGN OF ANCHORED SHEET PILE WALL	189
54.1 Serviceability limit state	197
55 PULL-OUT CAPACITY OF HELICAL ANCHOR IN CLAY	199
55.1 Single-plate anchor	199
55.2 Multi-plate anchor	200
55.3 AUS analysis	202
56 PULL-OUT CAPACITY OF ANNULAR ANCHOR IN SAND	205
57 STOCHASTIC ANALYSIS – INTRODUCTORY EXAMPLE	208
57.1 Variability of material parameters	208
57.2 Random fields	210
57.3 Deterministic analysis	212
57.4 Stochastic analysis	212
57.5 Collapse mechanisms	214
57.6 Analysis type, number of elements and number of runs	215
57.6.1 Analysis type	215
57.7 Number of elements	216
57.8 Number of runs	217
58 STOCHASTIC FACTOR OF SAFETY ANALYSIS OF SLOPE IN CLAY	218
59 STOCHASTIC ANALYSIS OF FOOTING IN CLAY WITH DEPTH DEPENDENT STRENGTH	221

60 STOCHASTIC ANALYSIS OF DEEP EXCAVATION	224
60.1 Deterministic analysis	224
60.2 Stochastic analysis	225
61 EMBANKMENT CONSTRUCTION ON SOFT SOIL PRONE TO CREEP	228
61.1 Without drains	229
61.2 With drains	229
62 ULS DESIGN OF CANTILEVER SHEET PILE WALL TO EUROCODE 7	231
62.1 Partial factors	231
62.2 Loads	232
62.3 Soil-wall interface strengths	233
62.4 Overdig	233
62.5 Analysis	234
62.6 Workshop solutions	234
62.7 Stochastic analysis	236
63 ULS DESIGN OF ANCHORED SHEET PILE WALL TO EUROCODE 7	238
63.1 Partial factors	238
63.2 Loads	239
63.3 Soil-wall interface strengths	239
63.4 Overdig	239
63.5 Analysis	239
63.6 Workshop solutions	240
63.7 Sensitivity analysis	243
64 REINFORCED SOIL RETAINING WALL	245
65 MODELING PLATES AND SHELLS USING SOLIDS	248
66 BEARING CAPACITY OF FOOTING IN UNSATURATED SLOPE	252
67 PILE ROWS – INTRODUCTORY EXAMPLE	254
67.1 Limit analysis	256
67.2 Elastoplastic analysis	257
68 BRACED EXCAVATION	261
68.1 Without preloading	262
68.2 With preloading	263
68.3 Results	264
68.3.1 Factor of safety analysis	264
68.3.2 Displacements	265
69 STABILITY OF EARTH DAM SUBJECTED TO SEEPAGE	267
69.1 Seepage	267
69.2 Factor of safety	269
70 STABILITY OF CRACKED SLOPE	271

This manual introduces the various features of OPTUM G2 through examples and further serves as a validation manual. It only provides a rudimentary introduction to the theory, a full description of which can be found in the Theory Manual.

While we have done our best to avoid errors, some bugs will inevitably persist. Should you wish to report these, or if you have any other questions, comments or suggestions, please contact us at www.optumce.com. We hope you enjoy using OPTUM G2.

Note: This manual cites a range of numerical results for the analyses conducted. As OPTUM G2 is under continual development, the results obtained with the latest version of the program may differ slightly from those cited in this document.

I INTRODUCTION

OPTUM G2 is a finite element package developed specifically for geotechnical applications. The graphical user interface allows for a rapid generation of complex finite element models. The computational core, which is based on concepts of modern numerical optimization, has been developed with particular attention to robustness and efficiency.

The features and analysis types in OPTUM G2 include:

- Limit Analysis to compute rigorous upper and lower bounds on collapse loads.
- Strength Reduction analysis for determination of strength based factors of safety.
- Elastoplastic analysis for serviceability analysis and staged construction.
- Seepage analysis for general partially saturated flow.
- Initial stress analysis for determination of in-situ stress on the basis of the earth pressure coefficient.
- Structural elements for modeling walls, anchors, geotextiles, etc.
- Mesh adaptivity for all analysis types.

In addition, a number of standard materials with parameters representing common geomaterials and structural elements are available.

I.1 Drainage and Time Scope

OPTUM G2 requires that a drainage condition is specified for each Solid material. There are three possible settings: Drained/Undrained, Always Drained, and Non-Porous. Moreover, for each analysis (each stage), a Time Scope must be chosen. There are two possibilities: Short Term or Long Term. These two settings, Drainage Condition and Time Scope, determine whether the material behaves in a drained or undrained manner. The basic idea is that some materials behave in an undrained manner in the short term (e.g. clay) while others always behave as drained (e.g. sand). Finally, Non-Porous materials never involve any excess or other types of pore pressure and therefore effectively behave as dry Always Drained materials.

The rules for whether a given point in the domain behaves in a drained or an undrained manner are summarized in the table below.

	Drained/Undrained	Always Drained	Non-Porous
Short Term	Undrained	Drained	Drained
Long Term	Drained	Drained	Drained

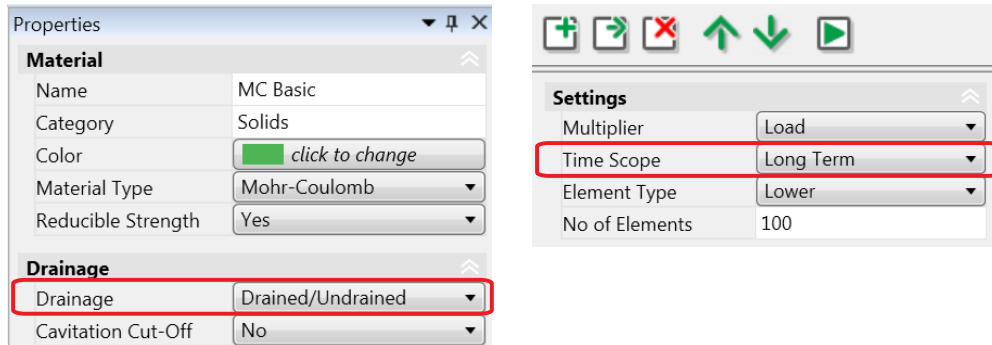


Figure 1: Material behavior as function of Drainage and Time Scope.

I.II Initial conditions

The determination of initial stresses and seepage pressures is an integral part of most geomechanics analyses. These may be calculated in a separate stage that is then linked to the main analysis stage. The linking is achieved by specifying a relevant From stage in the Stage Manager. The state of the From stage will then be used as the initial state of the analysis.

For the purpose of determining the initial state, OPTUM G2 includes a unique analysis type, Initial Stress, that carries out the following two steps:

1. Seepage analysis to determine steady state seepage pressures.
2. Initial stress computation on the basis of the earth pressure coefficient or by gravity loading.

In step 2 drained conditions are assumed. Concerning step 2, there are two possibilities for calculating the stress state. The exact method of calculation depends on the Initial Conditions setting for the material:

1. Compute by Gravity Loading: the selfweight is here applied in an elastoplastic calculation that uses the elastic and plastic material parameters.
2. Compute by K_0 Analysis: this is a specialized calculation that aims to find a stress distribution that satisfies the equilibrium and yield conditions while at the same time aiming to satisfy the initial stress conditions $\sigma'_{x,0} = \sigma'_{z,0} = K_0 \sigma'_{y,0}$ to the greatest possible extent. The earth pressure coefficient, K_0 , must be specified if this method is chosen (it is equal to 0.66 for the Firm Clay material).

In this manual, unless otherwise noted explicitly, the second option is used.

As an alternative to specifying a separate stage in which the initial state is determined, it is possible to have the initial stresses and seepage pressures calculated automatically. This will be done if no From stage is specified. In that case, the two steps of the Initial Stress analysis discussed above will be performed. The exceptions are the analysis types Elastic and Elastoplastic in which only the first

step is performed (the second step is the elastic/elastoplastic analysis itself which is carried out with the Time Scope specified). It is highly recommended that the initial stresses be examined critically as part of the overall result interpretation. And if in doubt about the veracity of the automatically calculated state, it is recommended that it is determined in a separate stage (the additional cost of this is usually negligible and may even save time if the same initial state is used in multiple analyses).

More information about the calculation of initial stresses can be found in the Analysis Manual.

I.III Shortcut keys

The following shortcut keys are available in OPTUM G2:

Ctrl+A	:	Select All
Ctrl+C	:	Copy
Ctrl+V	:	Paste
Ctrl+M	:	Move
Ctrl++	:	Zoom In
Ctrl+-	:	Zoom Out
Ctrl+Q	:	Zoom All
Ctrl+Z	:	Undo
Ctrl+Y	:	Redo
Ctrl+S	:	Save
Ctrl+Shift	:	Move with mouse drag
Tab	:	Redefine reference point for ortho-lines
Exit	:	Cancel drawing tool (point, line, etc).
Del	:	Delete selected object (point, line, etc).

II INTRODUCTORY EXAMPLE

In the following, the steps to setting up and solving a problem of limit analysis are detailed. The problem, shown in Figure 1, concerns a shallow foundation on top of a slope of cohesive-frictional soil. The task is to determine the bearing capacity of the footing, i.e. the maximum load, q_u (kN/m²), that it can be subjected to. A surcharge load of $q_s = 10$ kN/m² acts of the top of the slope. The soil is modeled as a Mohr-Coulomb material with cohesion $c = 10$ kPa, friction angle $\phi = 20^\circ$ and unit weight $\gamma = 20$ kN/m³. The foundation is assumed perfectly rigid with a unit weight of $\gamma = 23$ kN/m³.

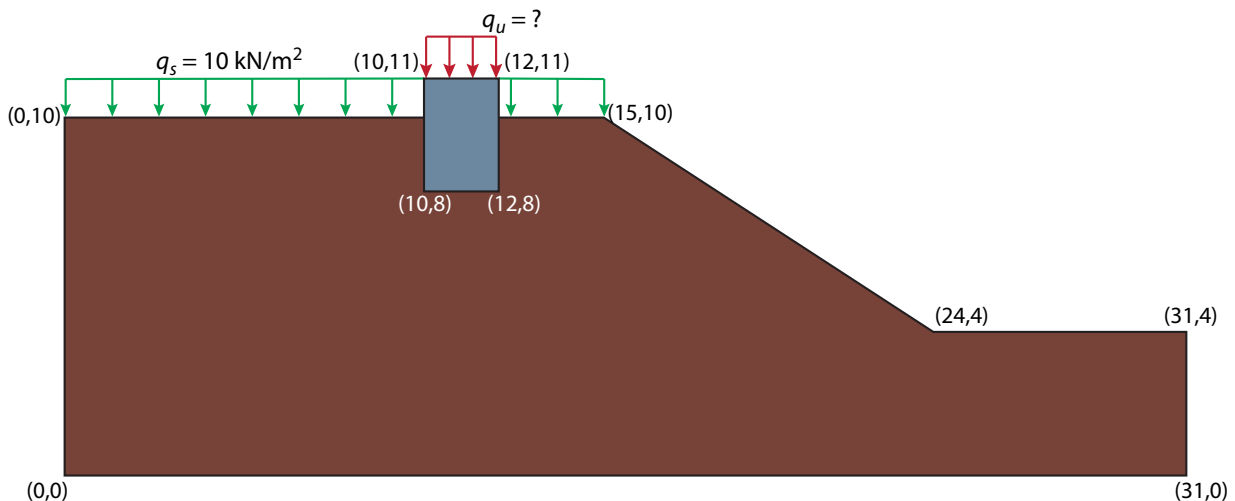


Figure 1: Shallow foundation on top of slope.

With conventional finite element analysis, the bearing capacity of the foundation would be determined by means of an incremental elastoplastic analysis where the foundation load would be increased from zero to a value implying sufficiently large displacements for the system to be deemed at failure. While such analyses also can be carried out by OPTUM G2, the present example deals with the determining the bearing capacity in the most direct way, namely by means of Limit Analysis.

II.1 Geometry

When OPTUM G2 is started up, the Geometry ribbon is the default active one. This contains various tools for defining and manipulating geometry. It is shown in Figure 2.



Figure 2: Geometry ribbon.

The slope geometry is first defined. For this purpose the Line tool is used as follows:

1. Left-click the Lines button in the Geometry ribbon.
2. Place the cursor at (0,0) and left-click. This defines the first point.



Figure 3: Relative (left) and absolute (right) coordinate input modes.

- To define the next point, a choice between input mode must be made. OPTUM G2 offers two modes: relative and absolute coordinate input (see Figure 3).
 For relative coordinate input (the default setting), the x and y coordinates relative to the last defined point are entered. Moving counter-clockwise in Figure 1, the following coordinates should be entered: (31,0), (0,4), (-7,0), (-9,6),... This can be done either via the keyboard by pressing Enter for each entry or via the mouse by left-click.
 To enter the absolute coordinates shown in Figure 1 directly, use the ABS/REL button in the left bottom corner of the program window to toggle the input mode to ABS. The ABS/REL toggling can only be done once the first point has been defined.
 Zoom All (via the button in ribbon or in the upper right corner of the drawing canvas) can be used at any time.
- Next, the foundation is defined. This is most easily done using the Rectangle tool. Click the tool, move the mouse cursor to position (10,8) and left-click to define the lower left point. Move the cursor to position (12,11) and left-click to define the second point. The foundation is then created along with the intersections between the foundation and the soil. The resulting line through the foundation can be deleted (select the line and press Del on the keyboard or right-click the line and select Delete) or left as it is.

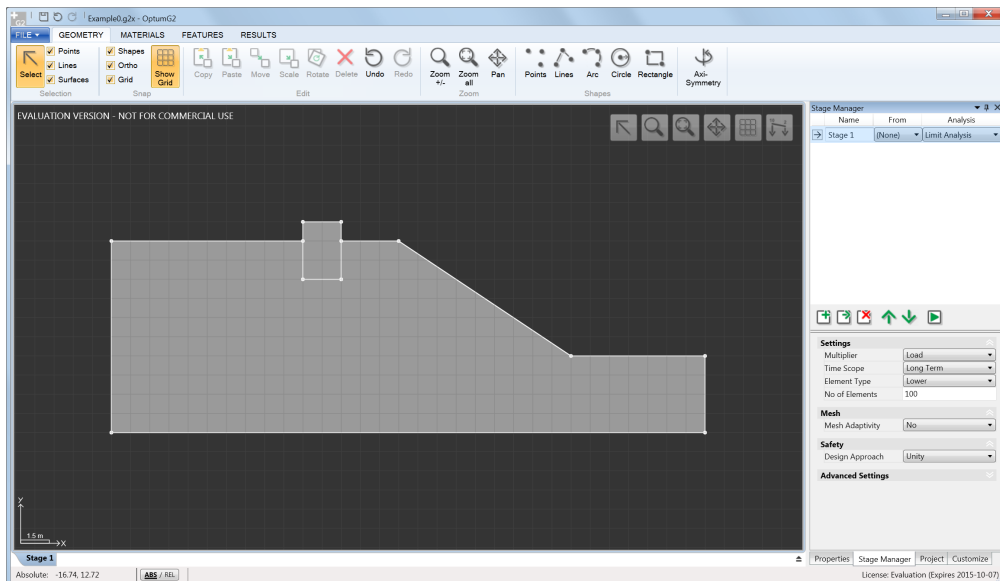


Figure 4: After definition of geometry. The line through the foundation created as a result of the automatic intersection between the slope and the foundation has been deleted.

II.II Materials

To assign materials first switch to the Materials ribbon (see Figure 5).



Figure 5: Materials ribbon (only Solids shown).

For the problem at hand, the material parameters for the soil correspond to the predefined material Firm Clay-MC and the foundation corresponds to the material Rigid.

To assign the soil material, first select the gray surface corresponding to the soil by left-click of the mouse. The color then changes to magenta indicating selection. Next, click the Firm Clay-MC button in the ribbon. Similarly, select the foundation and click the Rigid button in the ribbon. Finish by clicking anywhere on the drawing canvas outside the geometry defined.

The material parameters can be changed either by selecting the material from the ribbon by mouse click or by selecting a surface to which the material has been assigned. The parameters then appear in the property window on the righthand side of the program window and can be edited via the keyboard.

For the present problem, the unit weight of the foundation, i.e. of the Rigid material, must be changed from its default value of 0 to 23 kN/m^3 . To do this select the foundation by mouse click and enter 23 into the appropriate field of the property window (see Figure 6).

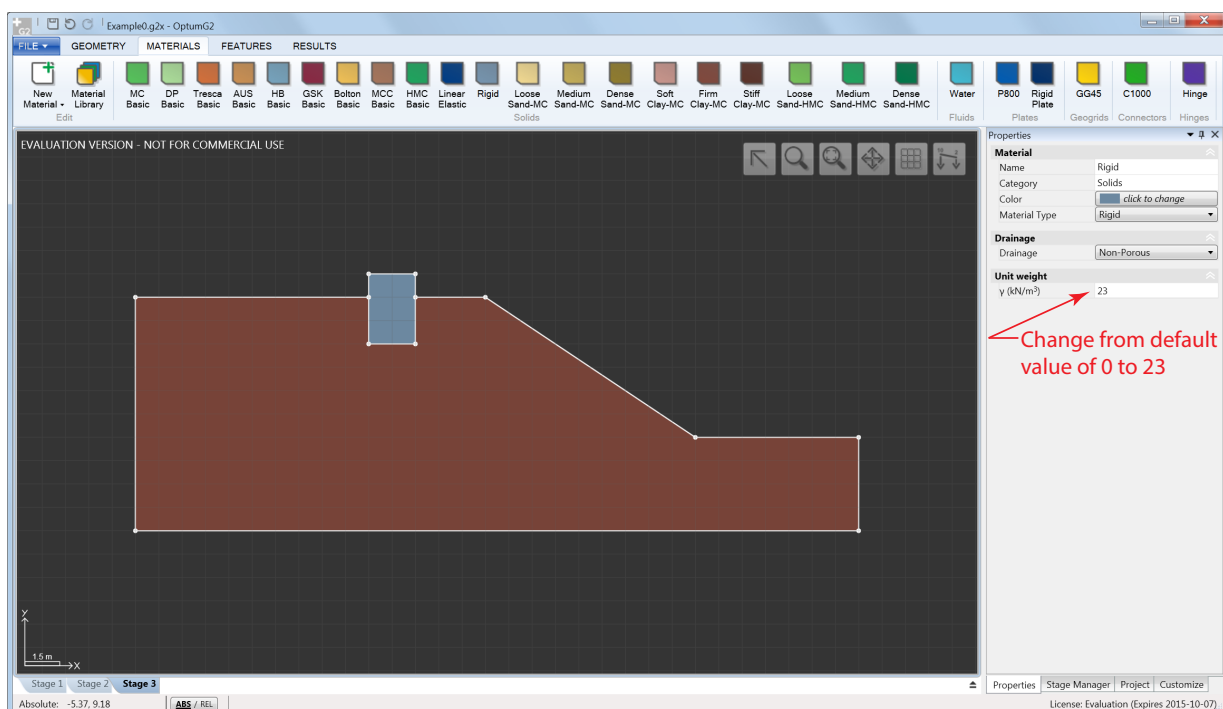


Figure 6: After assignment of materials.

II.III Loads

To assign loads first switch to the Features ribbon (see Figure 7).

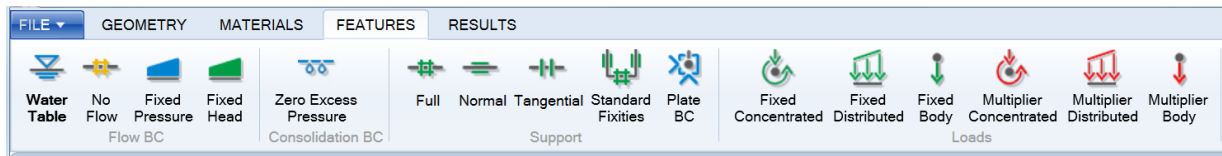


Figure 7: Features ribbon (partial).

Besides gravity which is always included by default, the present problem contains two kinds of loads:

1. The surcharge which is to remain at a value of 10 kN/m^2 .
2. The load acting on the foundation whose ultimate value (corresponding to collapse) is to be determined.

In OPTUM G2, these two types of loads are referred to as Fixed and Multiplier loads respectively (see Figure 7). Fixed loads always remain constant while Multiplier loads are magnified from their reference value to bring about a state of collapse. The factor by which the Multiplier loads should be magnified to bring about a state of collapse is also referred to as the collapse multiplier. Denoting this quantity by α , the ultimate limit load is given by

$$q_u = \alpha q_{\text{mult}} \quad (\text{II.1})$$

where q_{mult} is the multiplier load.

To assign loads, first select the line defining the top of the foundation and then click Multiplier Distributed in the Features ribbon. This assigns a distributed load of magnitude -1 kN/m^2 .

Next, select the line defining the ground surface to the left of the foundation. While pressing Shift, select the ground surface line to the right of foundation. Both lines should now be selected. Next, click Fixed Distributed in the Features ribbon. This assigns the surcharge loads (see Figure 8). Finally, in the property window on the right, change the magnitude of the loads to -10 kN/m^2 . Finish by clicking the drawing canvas anywhere outside the geometry defined.

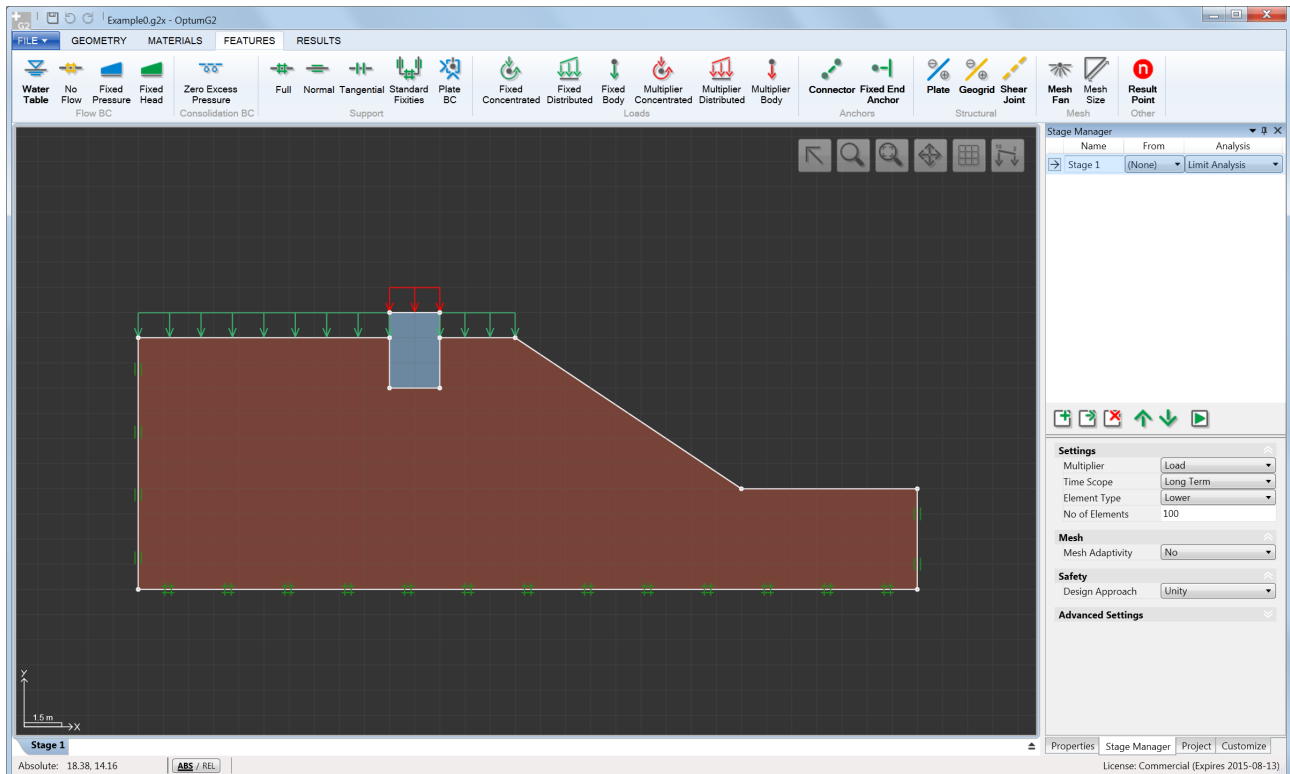


Figure 8: After assignment of loads.

II.IV Analysis

We are now ready to run the analysis. The type of analysis is selected from the Stage Manager window shown on the right in Figure 8. The default analysis type is Limit Analysis which is what is required for this example.

For each analysis type, a number of settings are available. These are shown in the lower half of the Stage Manager window (Figure 8). For the purpose of the present analysis, two settings are of interest:

1. The type of element to be used (Element Type under Settings. Default = Lower).
2. The number of elements to be used (No of Elements under Settings. Default = 100).

Regarding the element type, we will use the default Lower element. This results in a rigorous lower bound on the ultimate limit load.

The number of elements is changed to 1,000.

Next, in order to compute an upper bound on the ultimate limit load (in addition to a lower bound), we will first create a copy of the single stage presently available. This is done via the clone button (second button from the left in the Stage Controls shown in Figure 9).

In the new stage, the Element Type is changed to Upper and the No of Elements is set to 1,000. The situation is thereby as shown in Figure 10.

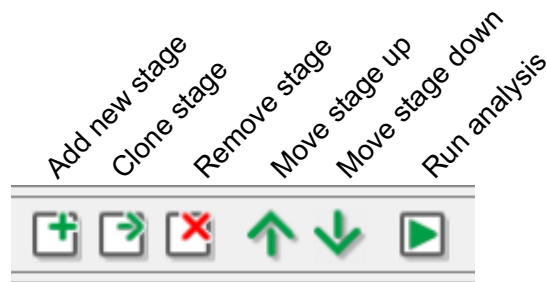


Figure 9: Stage Manager controls.

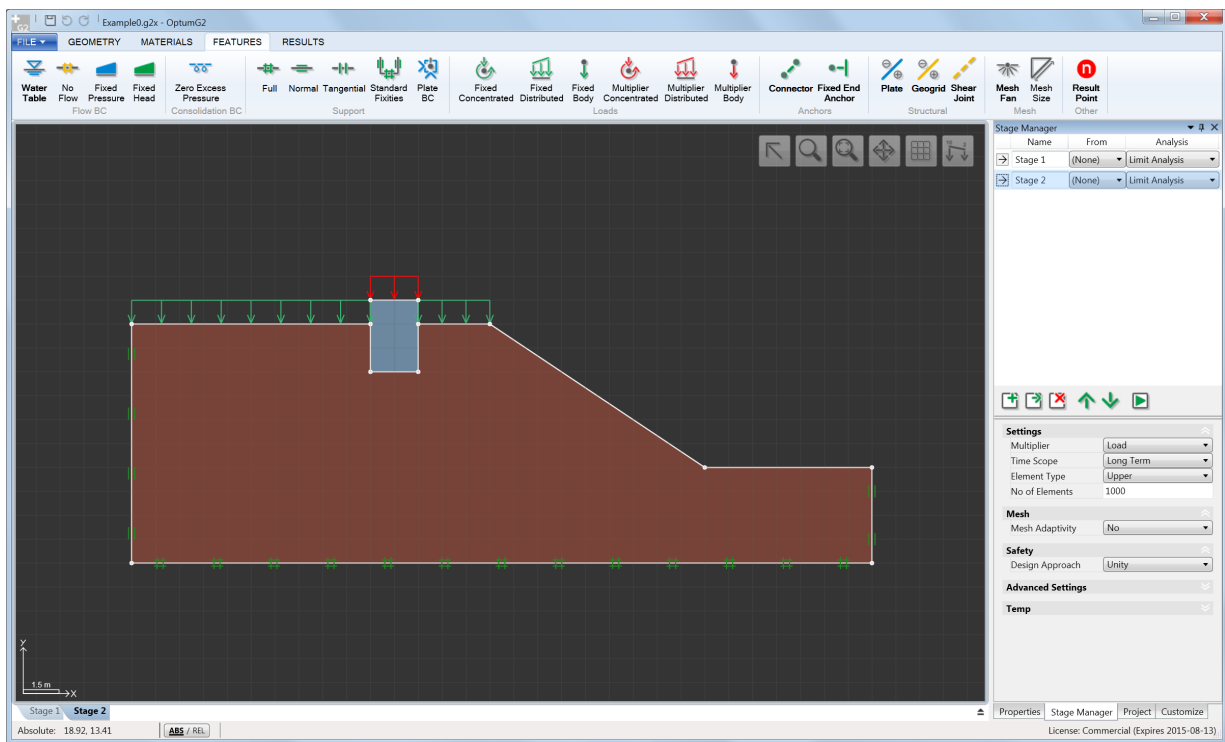


Figure 10: After cloning of Stage 1 and change of Element Type and No of Elements.

The problem, comprising two stages, is processed by clicking the Run Analysis button in the Stage Manager control panel (see Figure 9). The results of the analysis are displayed in the analysis log shown in Figure 11.

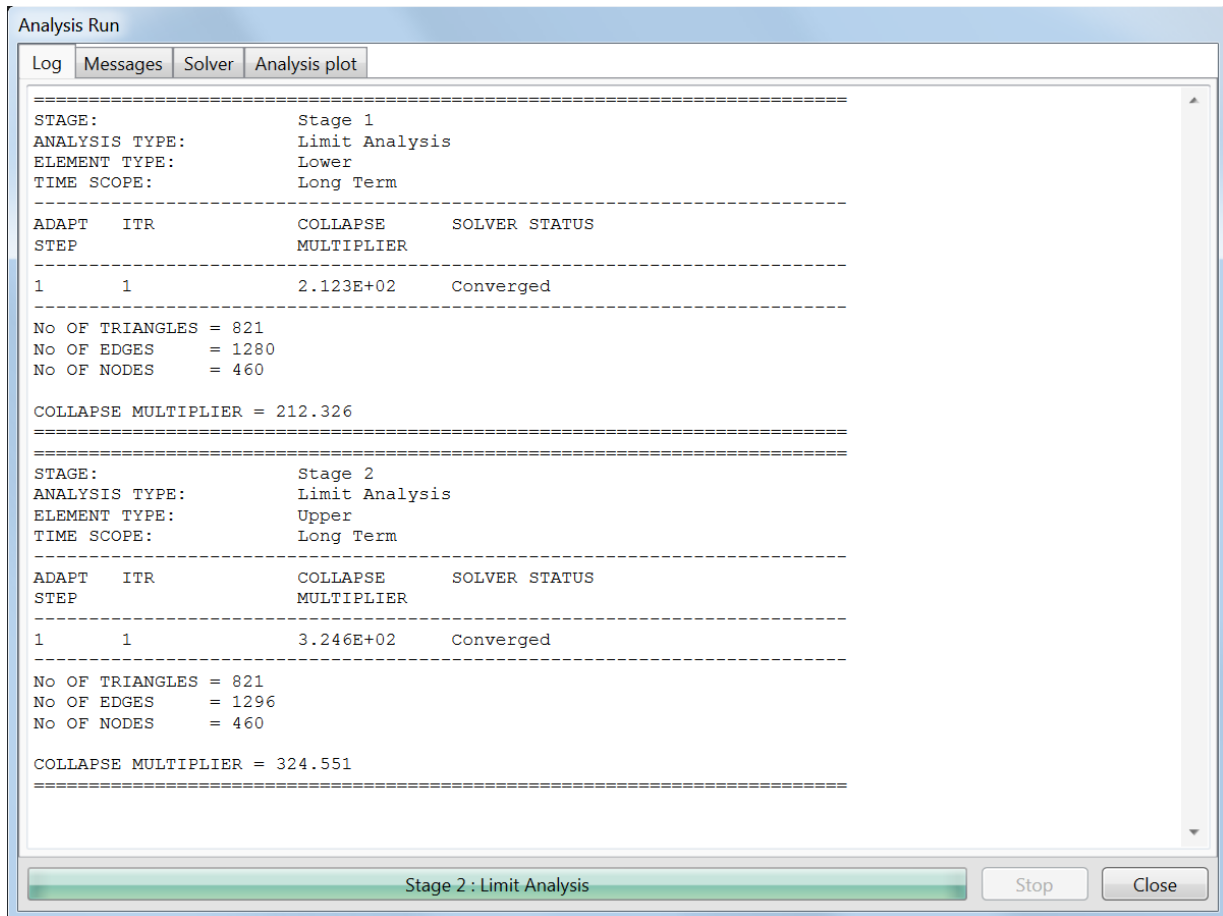


Figure 11: Analysis log.

In summary, the results are:

- A lower bound collapse multiplier of 212.3 and thereby a collapse load of $q_{u,LB} = 212.3 \text{ kN/m}^2$.
- An upper bound collapse multiplier of 324.6 and thereby a collapse load of $q_{u,UB} = 324.6 \text{ kN/m}^2$.

This means the true collapse load is given by

$$q_u = 268.4 \pm 56.2 \text{ kN/m}^2 \quad (\text{II.2})$$

or:

$$q_u = 268.4 \text{ kN/m}^2 \pm 20.9\% \quad (\text{II.3})$$

That is, the estimate of collapse load calculated as the mean value between the upper and lower bounds, $q_u = 268.4 \text{ kN/m}^2$, is in error by at most 20.9%. It may be on the safe side or on the unsafe side, but the error will not be greater than 20.9% either way. This worst case error can be reduced either by increasing the number of elements or by using mesh adaptivity, or by a combination of the two. Many of the examples in this manual make use of these possibilities.

II.V Results

After the analysis log window is closed, the program switches automatically to the Results ribbon and the situation is as shown in Figure 12.

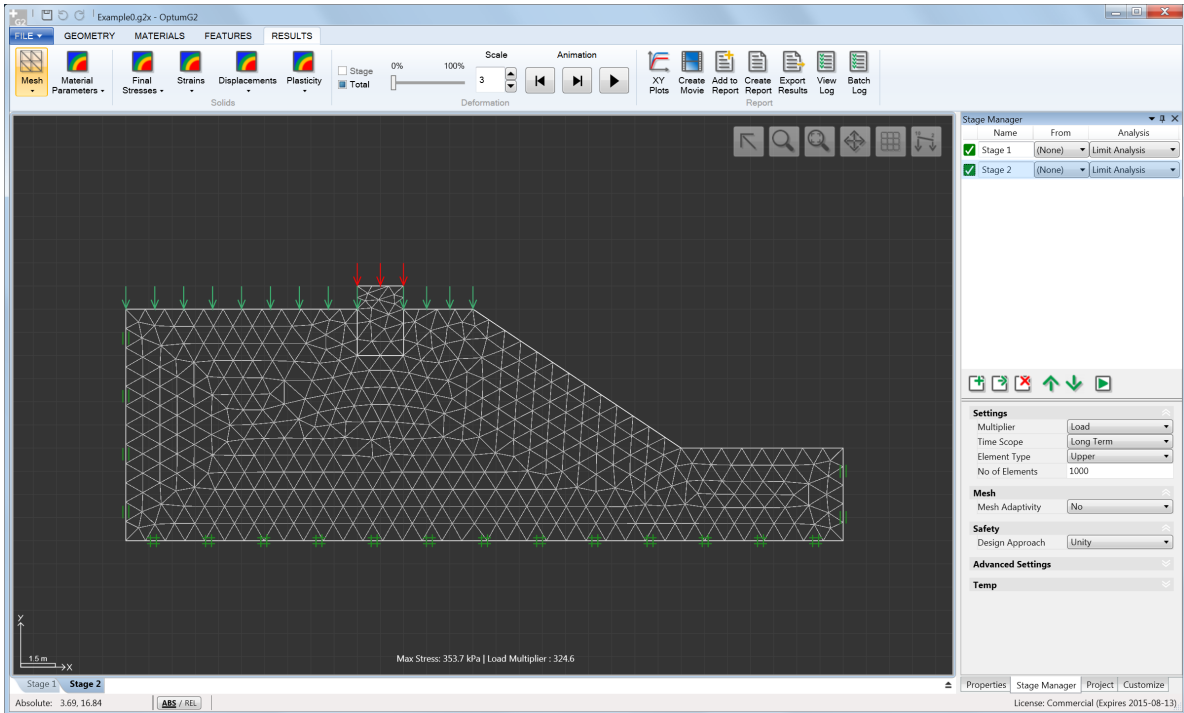


Figure 12: After analysis.

The default results set shown is the mesh. Note that OPTUM G2 does not require a separate mesh generation stage – the mesh is created automatically as part of the analysis. Using the menus and controls in the Results ribbon, various plots can be created. An example is shown in Figure 13 which shows the distribution of deviatoric strain $|\epsilon_1 - \epsilon_3|$ available under Strains.

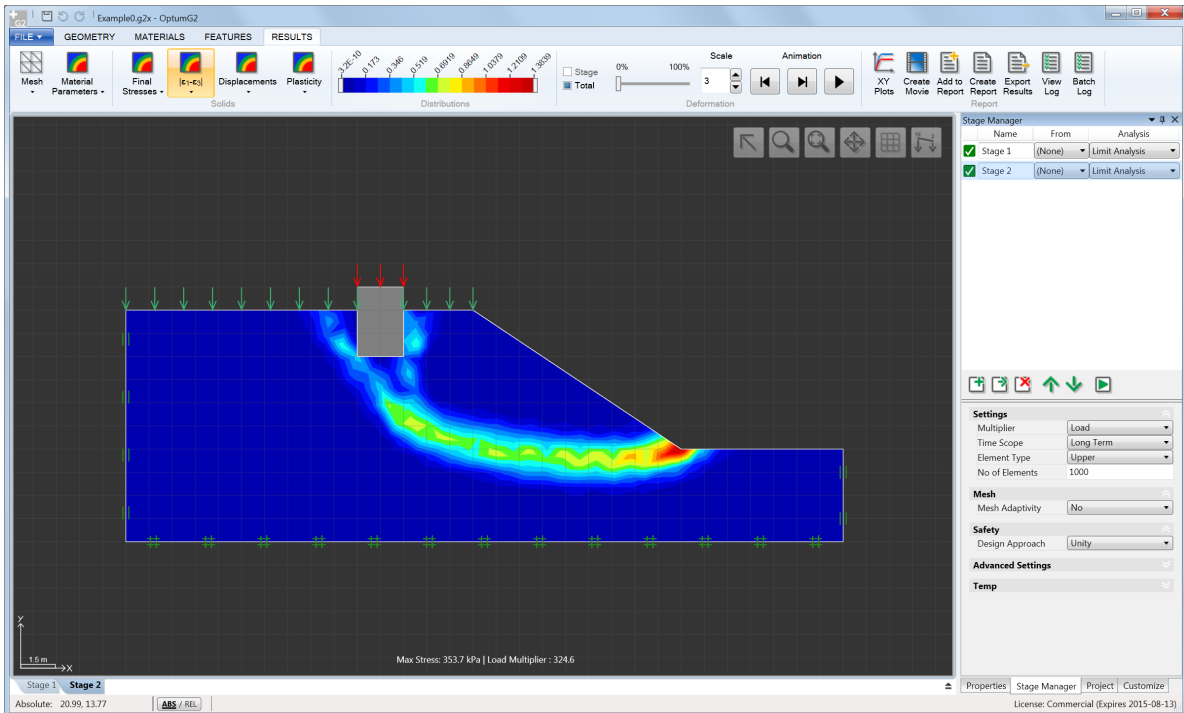


Figure 13: Distribution of deviatoric strain $|\epsilon_1 - \epsilon_3|$ available under Strains.

1 SHALLOW FOUNDATION 1

This example deals with the an eccentrically loaded foundation as shown in Figure 1.1. The soil is saturated clay and the analysis is to be performed assuming undrained conditions. For this purpose a total stress analysis approach is adopted. The soil is modeled by means of the Tresca model with an undrained shear strength $s_u = 30$ kPa and an undrained Young's modulus of $E_u = 40$ MPa. The foundation is modeled as Rigid material with a unit weight of 24 kN/m³. The material properties are shown in the property window on the right in Figure 1.1.

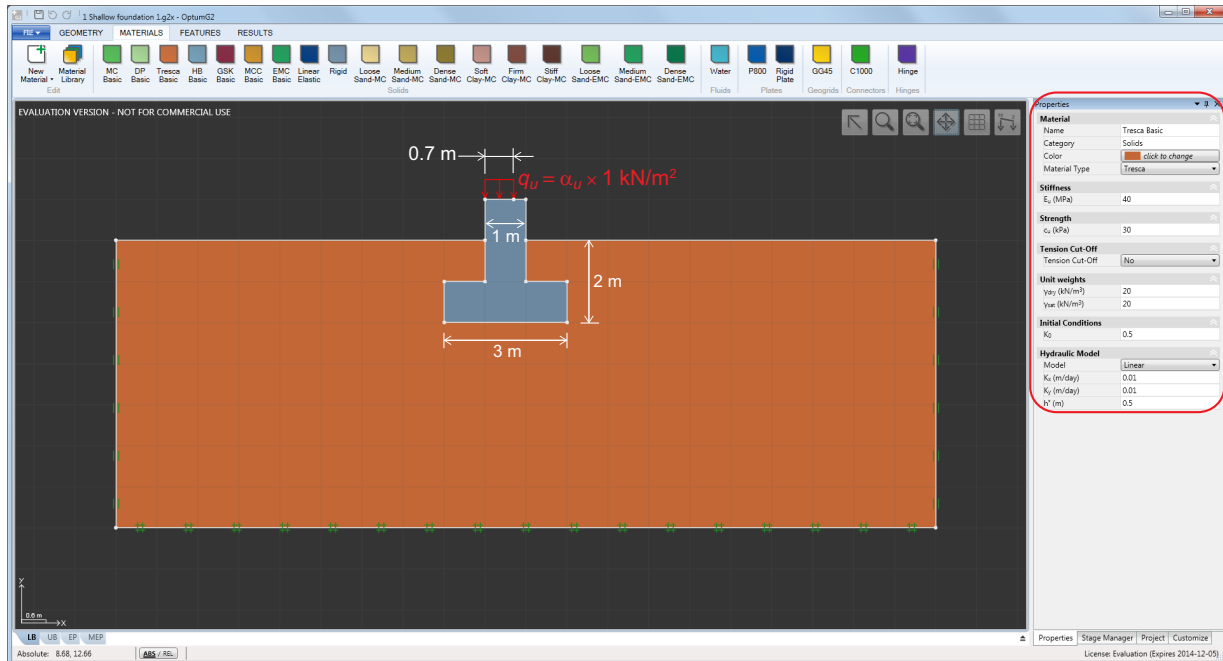


Figure 1.1: Shallow foundation in Tresca USS soil.

The task of setting up the problem proceeds by creating the geometry and then assigning materials and load. The boundary conditions are then applied by the Standard Fixities button in the Features ribbon.

1.1 Limit analysis

The first goal of the the analysis is to determine the ultimate magnitude, α_u , of the vertical reference load of 1 kN/m² working on the foundation. For this purpose Limit Analysis is used. The result of this analysis is the load multiplier α_u , i.e. the factor by which the multiplier load (shown in red) should be magnified in order to induce a state of collapse.

In the Stage Manager, Limit Analysis is chosen as the relevant analysis. Under Settings in the lower half of the Stage Manager window, the particular settings of the stage are specified. For the present analysis Multiplier should be set to Load since the aim is to determine the ultimate magnitude of an external load. The Time Scope is in this case (for the Tresca model) irrelevant and may be set to Long Term.

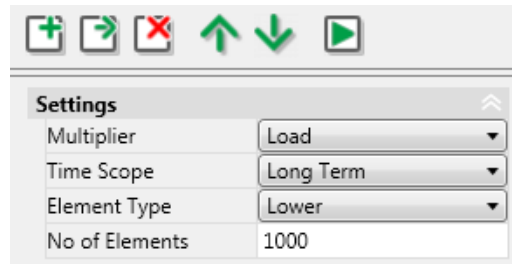


Figure 1.2: Stage settings for lower bound limit analysis. The Time Scope is irrelevant for the Tresca model.

Rather than determine an approximate solution to the problem, upper and lower bounds on the exact bearing capacity will be computed. This requires two separate calculations which may be organized in two stages with Element Type = Lower and Upper respectively. For both analyses, the number of elements (No of Elements in Settings) is set to 1,000.

Running the analyses results in lower and upper bound collapse multipliers of 851.1 and 1017.4 respectively. In other words, the maximum vertical load that can be sustained is:

$$851.1 \times 1 \text{ kN/m}^2 \leq q_u \leq 1017.4 \times 1 \text{ kN/m}^2 \quad (1.1)$$

or, in terms of total force (the load works over 0.8 m):

$$680.9 \text{ kN/m} \leq Q_u \leq 813.9 \text{ kN/m} \quad (1.2)$$

The result may also be stated as

$$q_u = 934.2 \text{ kN/m}^2 \pm 8.9\% \quad (1.3)$$

In other words, the error in the mean value between the upper and lower bounds is $\pm 8.9\%$.

1.1.1 Mesh adaptivity

The gap between the upper and lower bounds can be narrowed either by increasing the number of elements or by using mesh adaptivity. In the following we opt for the latter.

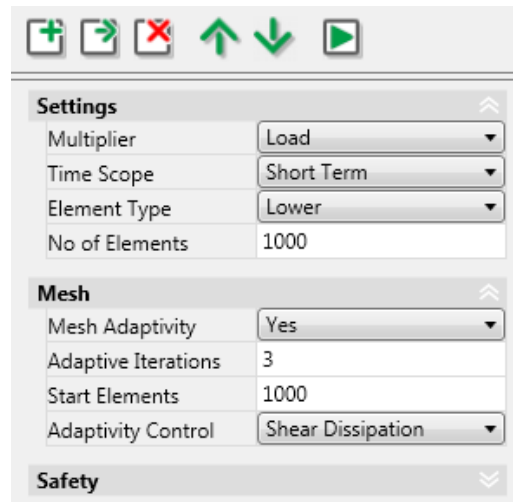


Figure 1.3: Stage settings for lower bound limit analysis mesh adaptivity.

Mesh adaptivity is defined under the category Mesh in the Stage Manager (see Figure 1.3). In the following, we will use 3 adaptivity steps together with the default option of Shear Dissipation as adaptivity control. This means that a total of 3 calculations will be carried out, each with a mesh adapted according to the previous distribution of the shear dissipation and such that the number of elements in the final mesh is equal to the number of elements specified in Settings (1,000 as before).

The results of the analyses are:

$$860.0 \text{ kN/m}^2 \leq q_u \leq 930.0 \text{ kN/m}^2 \quad (1.4)$$

or:

$$q_u = 895.0 \text{ kN/m}^2 \pm 3.9\% \quad (1.5)$$

which is a substantial improvement on the previous solution. Further improvements – at the expense of computational cost – can be achieved by increasing the number of elements.

The initial and adapted meshes for 1,000 elements are shown in Figure 1.4 along with the collapse solution.

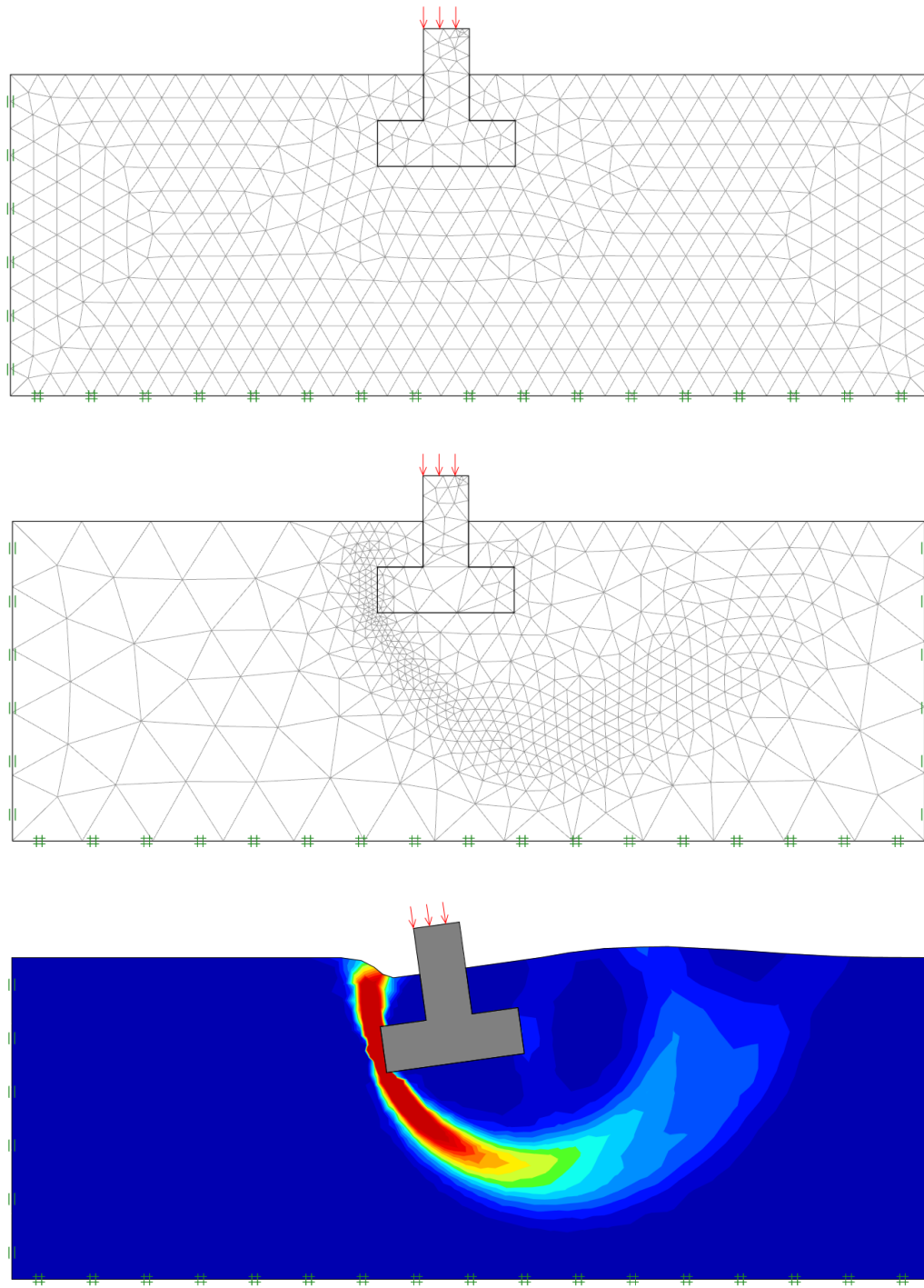


Figure 1.4: Initial and adapted meshes and collapse solution with intensity of dissipation (Upper element).

1.2 Elastoplastic analysis

Next, with the information that the collapse load is approximately 895 kN/m^2 , the deformations for a fixed load of 600 kN/m^2 are to be determined. For this purpose an Elastoplastic analysis is carried out. It is most convenient to clone the last stage and specify Elastoplastic in the Analysis column in the upper half of the Stage Manager window. In the lower half, the stage settings then appear. The Time Scope is again irrelevant. The Element Type is selected as 6-node Gauss which is well suited for deformation analysis. The No of Elements is set to 1,000. The number of Load Steps is set to 1. This means that the whole load is applied in a single step. For loads relatively far from collapse such as the present one (600 kN/m^2 vs a collapse load of 895 kN/m^2), this is usually adequate. Note: in contrast to the previous Limit Analysis, the loads of the current analysis are Fixed (shown in green).

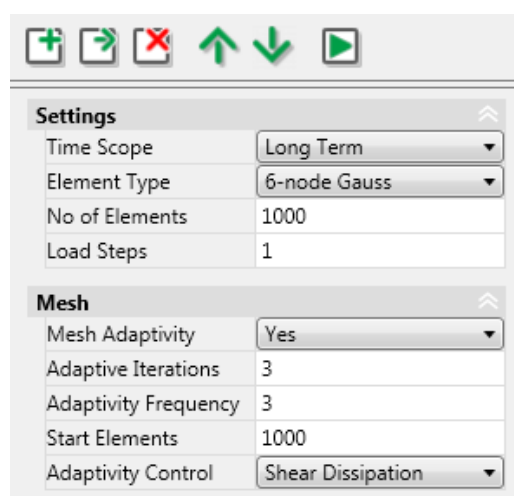


Figure 1.5: Stage settings Elastoplastic analysis with mesh adaptivity. The Time Scope is irrelevant for the Tresca model.

As for Limit Analysis, mesh adaptivity can be used. Again, this feature is activated by setting Mesh Adaptivity = Yes. A number of fields then appears. Adaptivity Iterations has the same meaning as before and is set to 3. Adaptivity Frequency is relevant only if more than one load step is used and is left at the default value of 3. And as before, the Adaptivity Control is set to Shear Dissipation. In the case of Elastoplastic analysis, the control variable incorporates both shear dissipation and elastic energy.

Any elastoplastic analysis requires an initial state of stress. In the present example, no From stage is specified, and consequently, the initial stresses are calculated automatically (see Section I.II).

The deformed configuration is shown in Figure 1.6 along with the distributions of shear dissipation and elastic energy. As expected, the plastic zones are less developed than at full collapse (compare to Figure 1.4).

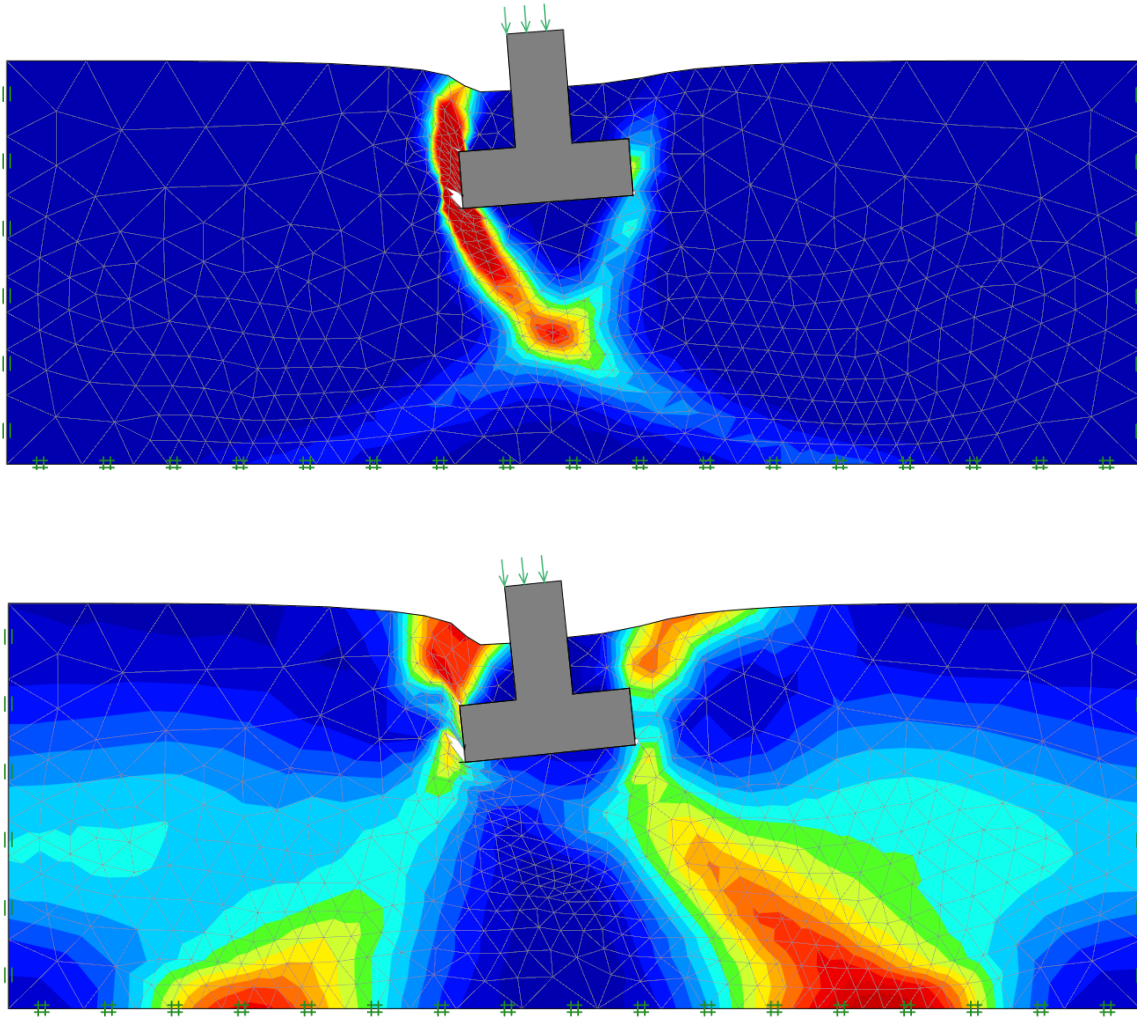


Figure 1.6: Deformations and distribution of shear dissipation (top) and elastic energy (bottom) from Elastoplastic analysis (displacements scaled by a factor of 30).

The displacements at selected points can be accessed by mouse click. In this way, the displacements at the upper left edge of the foundation are found as:

$$\begin{aligned} u_x &= -6.0 \text{ mm} \\ u_y &= -13.8 \text{ mm} \end{aligned} \tag{1.6}$$

These results may be improved slightly by increasing the number of elements and the number of load steps.

1.3 Multiplier Elastoplastic analysis

Besides determining the ultimate bearing capacity and the deformations under serviceability conditions in a direct and rapid manner, OPTUM G2 also allows for the full load-displacement response to be traced. Such analyses are carried out using the Multiplier Elastoplastic analysis type. This analysis type may be thought of as combining the two previous analysis types. As in Limit Analysis, a set of Multiplier Loads (shown in red) are incremented in a sequence of steps until collapse. And as in Elastoplastic analysis, the deformations are determined for each load step.

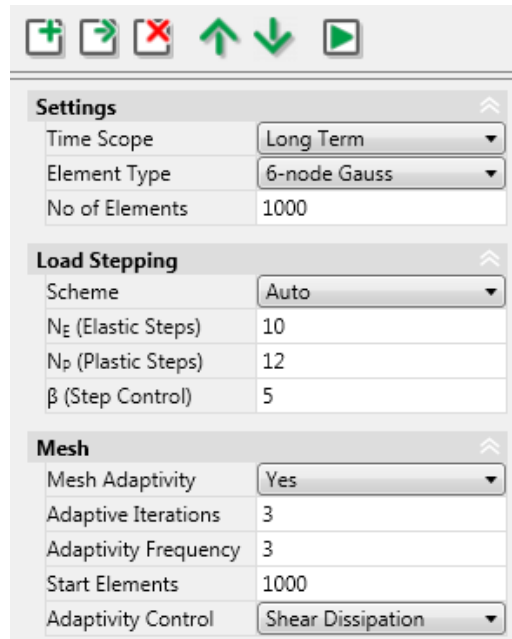


Figure 1.7: Stage settings for Multiplier Elastoplastic analysis with mesh adaptivity. The Time Scope is irrelevant for the Tresca model.

In the following, we apply a multiplier load of 600 kN/m^2 (such that a multiplier $\alpha = 1$ corresponds to the state arrived at in the previous analysis). All other parameters are left at their default values except that the No of Elements is set to 1,000 and Mesh Adaptivity is used, again with default values. The Adaptivity Frequency (= 3) here indicates that the mesh is adapted in load steps 1, 4, 7, etc. The specification of initial stresses follows that of the previous Elastoplastic analysis. No From stage is specified, implying that the initial stresses will be calculated automatically. For further details on Multiplier Elastoplastic analysis, please refer to the Analysis Manual.

The results of the analysis in terms of the displacement, stress, etc versus load multiplier can be plotted using the XY Plots tool located in the Results ribbon. In order to specify a point at which to collect such data during the analysis, the Result Point tool located in the Features ribbon can be used. In this case, a Result Point is defined (prior to running the analysis) at the top left corner of the foundation (see Figure 1.8).

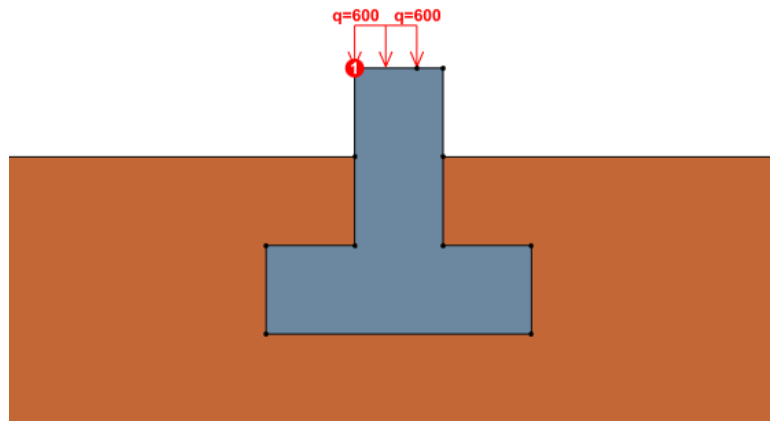


Figure 1.8: Setup for Multiplier Elastoplastic analysis: Multiplier Distributed Load of 600 kN/m² and Result Point located at the top left corner of the foundation (only a section of the full problem domain is shown).

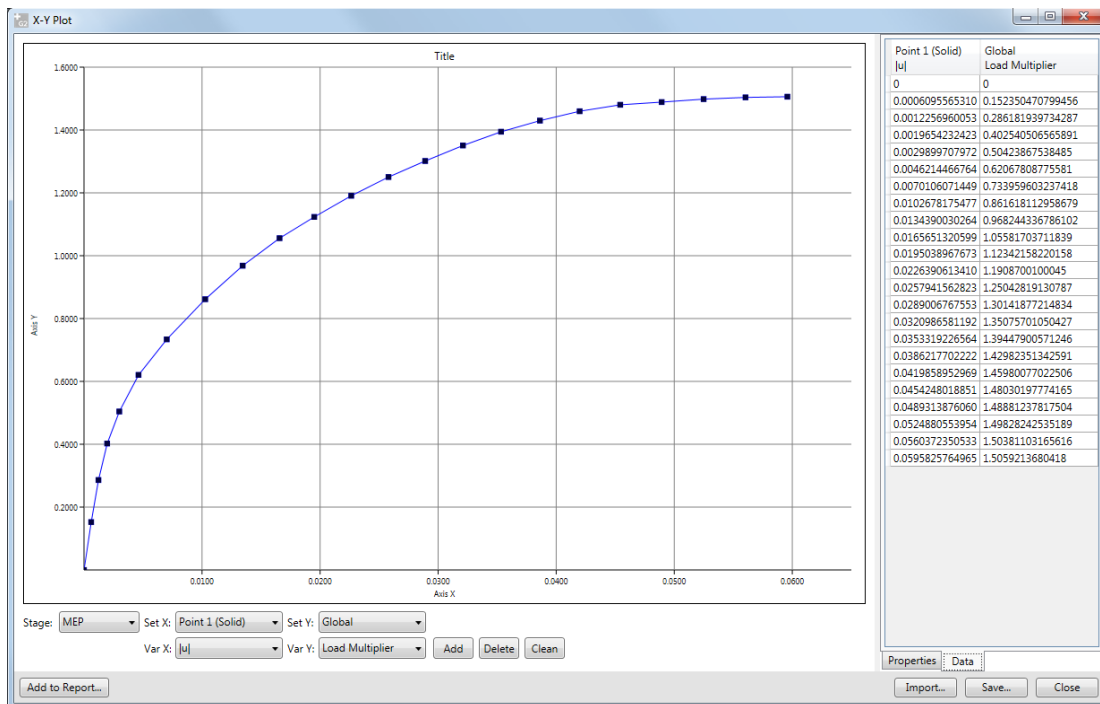


Figure 1.9: Load-displacement curve created by the XY Plots tool. The actual data can be accessed via the Data tab that appears in the right bottom corner when the curve is selected.

Using the XY Plots tool, the displacement $|u| = \sqrt{u_x^2 + u_y^2}$ is plotted as function of the load multiplier as shown in Figure 1.9. We note that the result previously found by means of Elastoplastic analysis (using a single load step), $|u| = \sqrt{0.006^2 + 0.0138^2} = 0.01477$ is in good agreement with the result of the Multiplier Elastoplastic analysis (which uses 8 load steps to reach a load multiplier of 1 versus only a single step in the previous analysis).

Similarly, the final load multiplier of around 1.5, corresponding to a total load of $1.5 \times 600 = 900$ kN/m², is in good agreement with the results of the Limit Analyses ($q_u = 895$ kN/m² \pm 3.9%).

1.4 Variation of undrained shear strength with depth

The use of a constant undrained shear strength is often a rather crude approximation to reality where one will usually observe an increase of shear strength with depth. In OPTUM G2, linear variations of all parameters can be specified via the righthand side icon that appears when any parameter field is selected (see Figure 1.10).

In the following, a shear strength varying from $s_u = 15$ kPa at the top surface (at level of $y = 16$ m) and increasing by 5 kPa/m with depth is used. Such a variation is can be defined using the Material Parameter dialog shown in Figure (1.10).

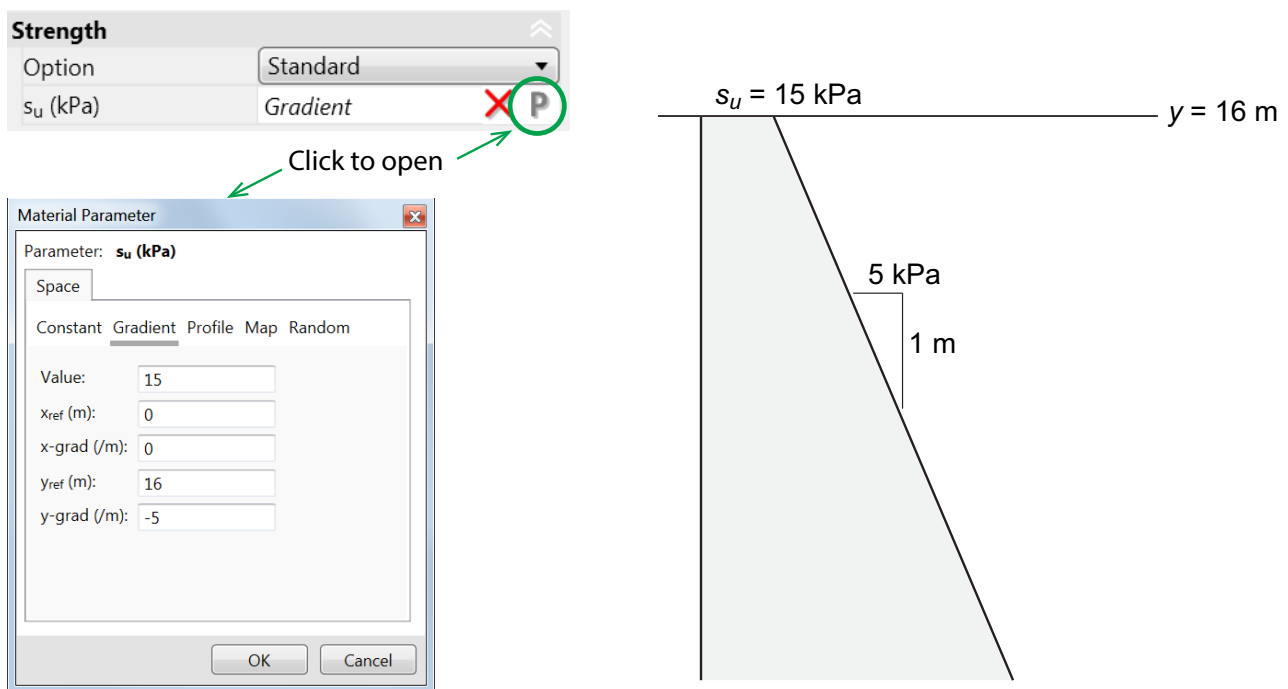


Figure 1.10: Specification of linear distribution of s_u .

Running upper and lower bound limit analysis for this problem gives:

$$q_u = 833.5 \pm 3.5\% \text{ kN/m}^2 \quad (1.7)$$

as compared to the value of $q_u = 895.0 \text{ kN/m}^2$ for a constant $s_u = 30$ kPa.

Finally, as a check that the correct distribution of s_u has been specified, the distribution of all material parameters can be visualized under Results (see Figure 1.11).

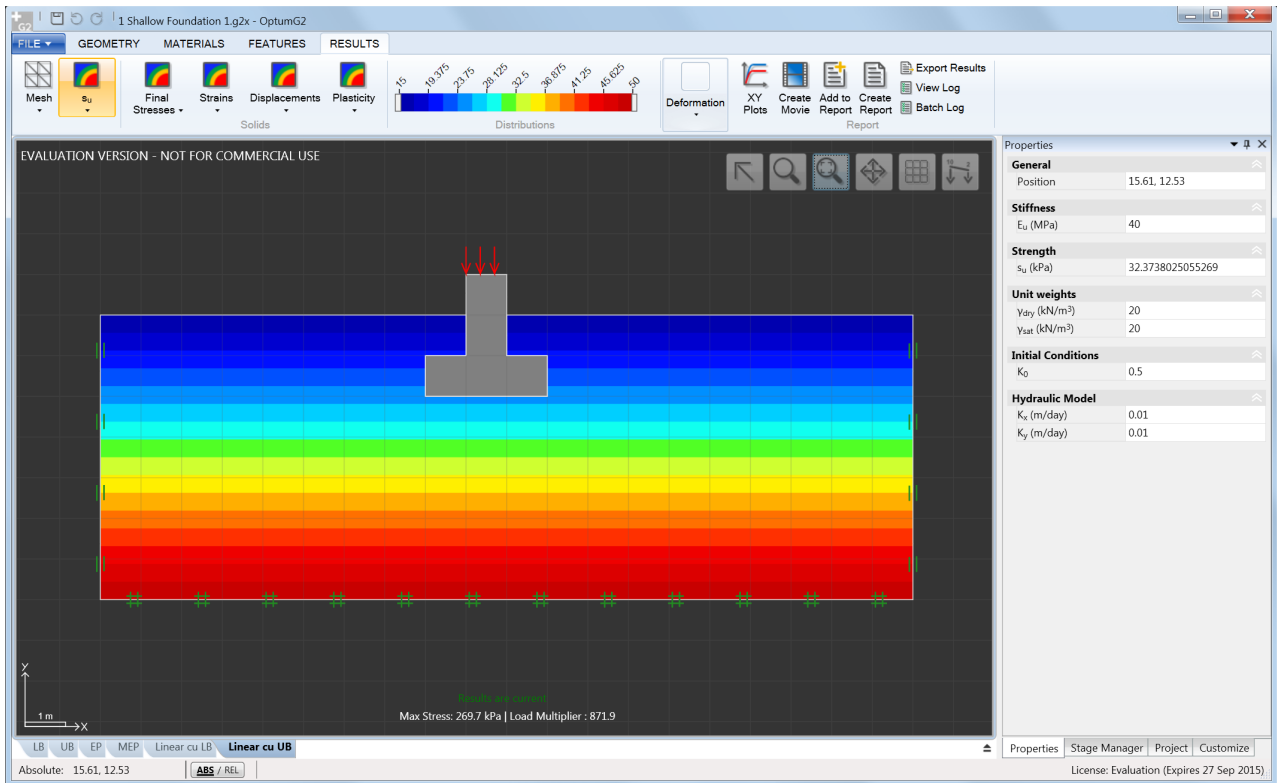


Figure 1.11: Variation of s_u .

2 SHALLOW FOUNDATION 2

The previous example demonstrates the analysis of a shallow foundation in clay under undrained conditions using a total stress Tresca analysis. While convenient and also theoretically well founded, the effective stress approach is in many ways more satisfying. The material parameters used in this type of analysis are those measured under drained conditions while the excess pore pressures that develop in the short term are calculated explicitly as part of the analysis. This, among other things, means that both the conditions in the short term and in the long term can be assessed – something that is not possible using the total stress approach of the previous example.

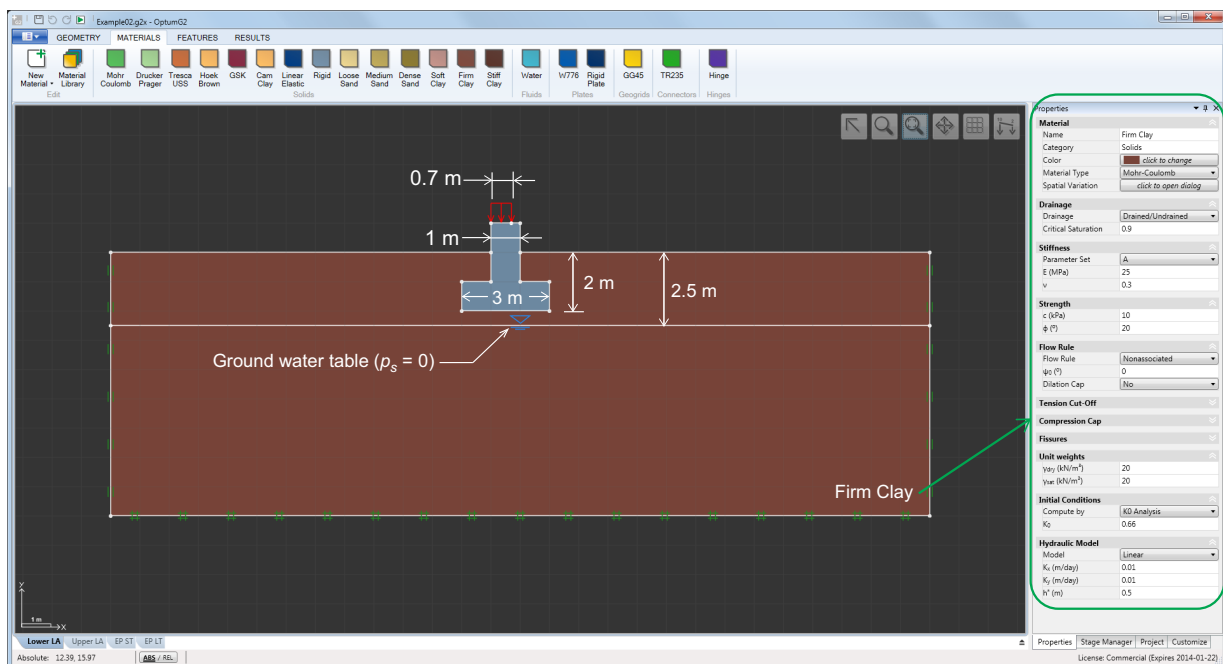


Figure 2.1: Shallow foundation in Firm Clay-MC.

The material used in this example is the default material Firm Clay-MC (Mohr-Coulomb material with $E = 25$ MPa, $\nu = 0.3$, $c = 10$ kPa, $\phi = 20^\circ$). The overall geometry, shown in Figure 2.1, is the same as that of the previous example. Again, the aim of the example is to conduct Limit Analyses to determine the bearing capacity and Elastoplastic analyses to determine settlements.

In contrast to the previous analysis, however, a static water table is defined 2.5 m below the ground surface. This can be done by using the Water Table tool in the Features ribbon.

Also, in contrast to the previous example, it is important to distinguish between Long Term and Short Term conditions. That is, the Drainage Conditions of the Firm Clay material are Drained/Undrained, meaning that excess pore pressures are generated in the short term but not in the long term. The appropriate selection of long/short term conditions is made for each stage in the lower half of the Stage Manager under Time Scope (see Figure 2.2).

For all analyses involving hydraulic boundary conditions or Fluid materials, the hydraulic model needs to be considered. In OPTUM G2, all seepage calculations are carried out as general variably

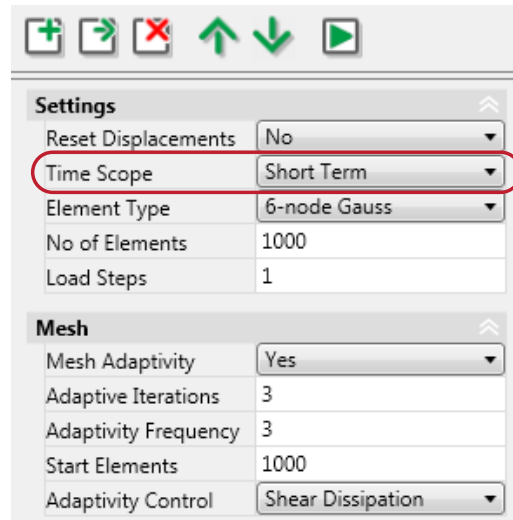


Figure 2.2: Stage settings for a Short Term analysis with Mesh Adaptivity.

saturated analyses. As such, both the saturated hydraulic conductivities and the hydraulic model need to be considered. In the following, we use the default Linear hydraulic model (see the Materials manual) with default settings as indicated in Figure 2.1.

Finally, for any Short Term analysis, the initial stress state needs to be calculated. As described in the previous example, this may be done via a separate stage or, if no From stage is specified, it is done automatically using either the specialized K_0 Analysis or an Elastoplastic Analysis as specified for the given material. In both cases, the pore pressures are calculated as part of the analysis. In the present example, the K_0 Analysis is used with an earth pressure coefficient of $K_0 = 0.66$ (see Figure 2.1).

2.1 Limit Analysis

Upper and lower bound limit analyses are conducted as described in the previous example, except that the Time Scope is Short Term. A total of 1,000 elements are used along with 3 adaptivity iterations (these settings are shown in Figure 2.2).

This results in the following bounds on the limit load:

$$667.2 \text{ kN/m}^2 \leq q_u \leq 727.7 \text{ kN/m}^2 \quad (2.1)$$

or:

$$q_u = 697.4 \text{ kN/m}^2 \pm 4.3\% \quad (2.2)$$

Increasing the number of elements to 2,000 gives:

$$q_u = 695.8 \text{ kN/m}^2 \pm 2.5\% \quad (2.3)$$

and to 4,000:

$$q_u = 696.8 \text{ kN/m}^2 \pm 1.6\% \quad (2.4)$$

at which point the solution is deemed sufficiently accurate. Note that while the error reduces three-fold by increasing the number of elements from 1,000 to 4,000, the calculated mean value increases

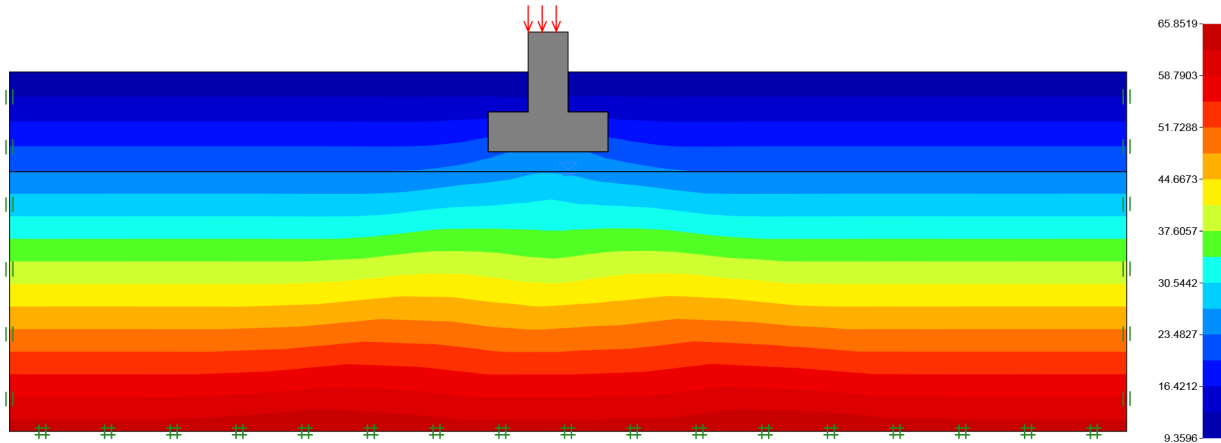


Figure 2.3: Distribution of undrained shear strength s_u .

by only slightly over 1%. This trend, that the mean value is rather more accurate than suggested by the error between the upper and lower bounds, is quite typical. It is a consequence of the fact that the errors made in the upper and lower bound calculations tend to be of a similar magnitude and thus cancel each other out in the mean value.

The distribution of undrained shear strength is shown in Figure 2.3. For the Mohr-Coulomb model used in this example it is given by (see Materials Manual):

$$s_u = c \cos \phi + \frac{1}{2}(1 + K_0) \sin \phi \sigma'_{v,0} \quad (2.5)$$

where $\sigma'_{v,0}$ is the initial vertical effective stress (positive in compression).

The collapse mechanism and distribution of shear dissipation is shown in Figure 2.4. It follows that of the previous example quite closely.

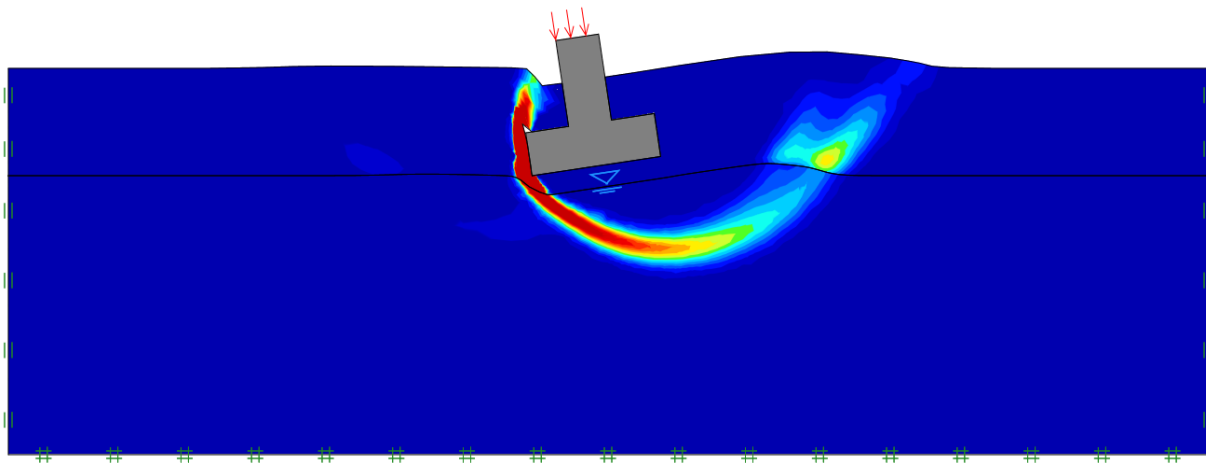
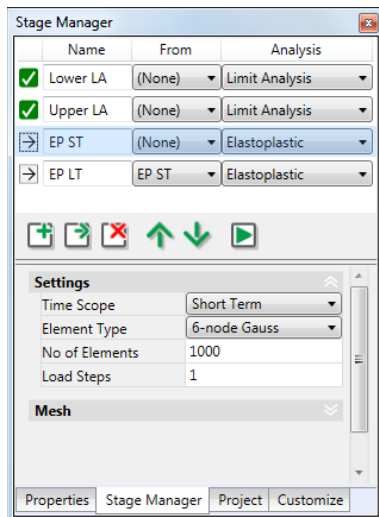
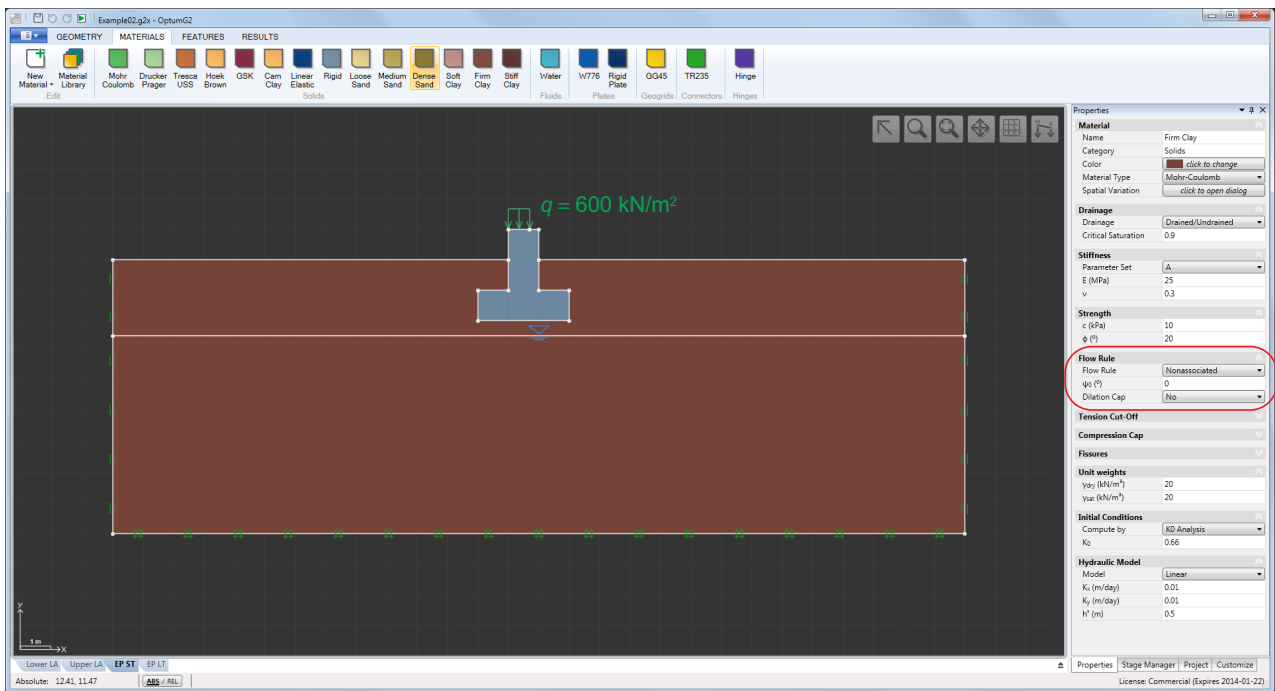


Figure 2.4: Collapse solution with intensity of shear dissipation.

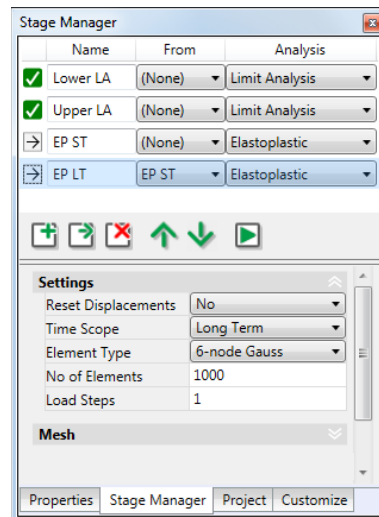
2.2 Elastoplastic analysis

Next, we aim to determine the deformations for a fixed load of 600 kN/m^2 as shown in Figure 2.5. The load is assumed to be applied sufficiently rapidly for undrained conditions to be considered. It then remains on the foundation until all excess pore pressures have dissipated. The complete analysis must therefore consider both Short and Long Term Time Scopes.

This is done via two separate stages. First an Elastoplastic analysis stage with Time Scope = Short Term is defined. This stage is then cloned and the Time Scope changed to Long Term. In addition,



Short Term Elastoplastic analysis



Long Term Elastoplastic analysis using Short Term stage as From stage

Figure 2.5: Geometry, loads and material (top) and appearance of Stage Manager for Short Term (EP ST) and Long Term (EP LT) Elastoplastic analysis stages.

the From stage is chosen as the preceding Short Term stage. This means that the result of the first stage is used as input when processing the second stage. The Stage Manager for the two stages is shown in Figure 2.5. We note that it is possible to reset the displacements at the beginning of the Long Term stage that follows on from the Short Term stage. Since we are interested in the final total displacements, this option is not utilized and the default option of not resetting the displacements is used.

Generally speaking, for Elastoplastic analysis of Drained/Undrained materials under Short Term conditions, a nonassociated flow rule with a dilation angle of zero should be used in order to obtain reasonable results (see the Theory Manual). This setting is invoked via the material property window as indicated in Figure 2.5.

Running the two stages, both with 1,000 6-node Gauss elements and 3 adaptivity iterations, results in terms of the deformed configurations are shown in Figure 2.6. It is noted that the majority of the deformation occurs in the short term, i.e. in this case the effects of consolidation are relatively minor compared to the instantaneous deformations.

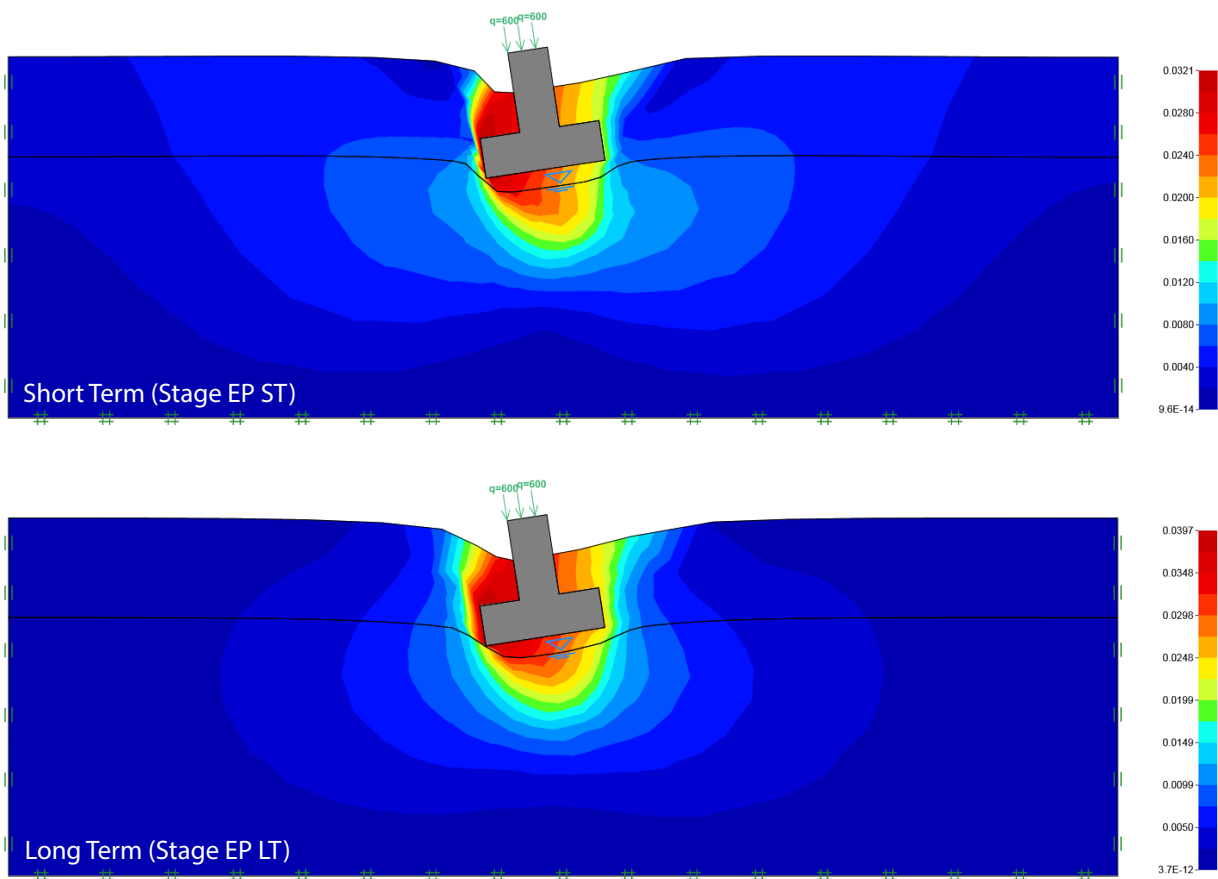


Figure 2.6: Deformations and distributions of $|u| = (u_x^2 + u_y^2)^{\frac{1}{2}}$ (displacements scaled by a factor of 30).

3 SETTLEMENT OF STRIP FOOTING ON ELASTIC SOIL

The following example demonstrates the capabilities of OPTUM G2 in computing upper and lower bounds not only on the ultimate limit load, but also the elastic energy and, in turn, on the deformations. The example under consideration is shown in Figure 3.1. It involves a centrally loaded weightless rigid strip footing on an elastic soil. The footing and the soil are modeled using the default materials Rigid and Linear Elastic respectively.

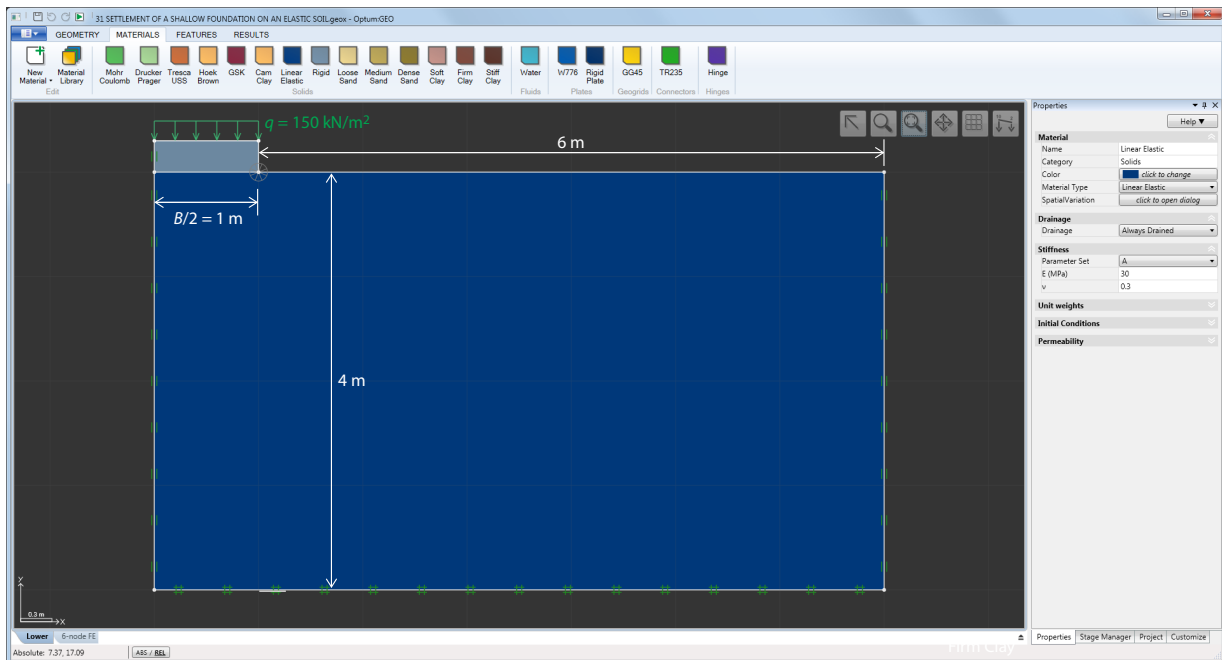


Figure 3.1: Shallow foundation on an elastic soil.

Using dimensional analysis arguments, it may be shown that the vertical displacement of the footing can be expressed as:

$$u_v = \beta \frac{qB}{E} \quad (3.1)$$

where q is the footing pressure, B is the footing width, E is Young's modulus and β is a parameter that, for fixed geometric dimensions, depends only on Poisson's ratio.

As is discussed in detail in the Theory Manual, the elements Lower and 6-node FE provide bounds on the elastic energy. The elastic energy is equal to the external energy which in this case is given simply by the footing pressure times the vertical displacement which is constant along the footing. As such, the Lower element will provide an overestimate of the vertical displacement while the 6-node FE will provide an underestimate.

In the following, the default Young's modulus of $E = 30$ MPa is used and the load applied is $q = 150$ kN/m². With the vertical displacement calculated, (3.1) is used to determine β . For both types of elements, a total of 10,000 elements are used. The analysis can either be carried out using the Elastoplastic or the Elastic analysis types.

The results are shown in Table 3.1.

ν	Lower bound (6-node FE)	Upper bound (Lower)	Mean	Error ($\pm\%$)
0.00	1.022	1.035	1.029	0.68
0.05	1.025	1.038	1.032	0.68
0.10	1.020	1.033	1.027	0.68
0.15	1.007	1.019	1.013	0.59
0.20	0.984	0.995	0.990	0.61
0.25	0.950	0.960	0.955	0.52
0.30	0.903	0.912	0.908	0.55
0.35	0.840	0.848	0.844	0.47
0.40	0.758	0.765	0.762	0.52
0.45	0.653	0.659	0.656	0.46
0.50	0.516	0.523	0.520	0.77

Table 3.1: Upper and lower bounds on parameter β (Eqn. 3.1) for elastic settlement of shallow foundation in an elastic soil using 10,000 elements.

To give an indication of the error in typical analyses, the problem is re-analyzed using 100 elements. The results are shown in Figure 3.2 and indicate that the 6-node FE is somewhat more accurate than the Lower bound element. This observation is quite general and holds for most problems.

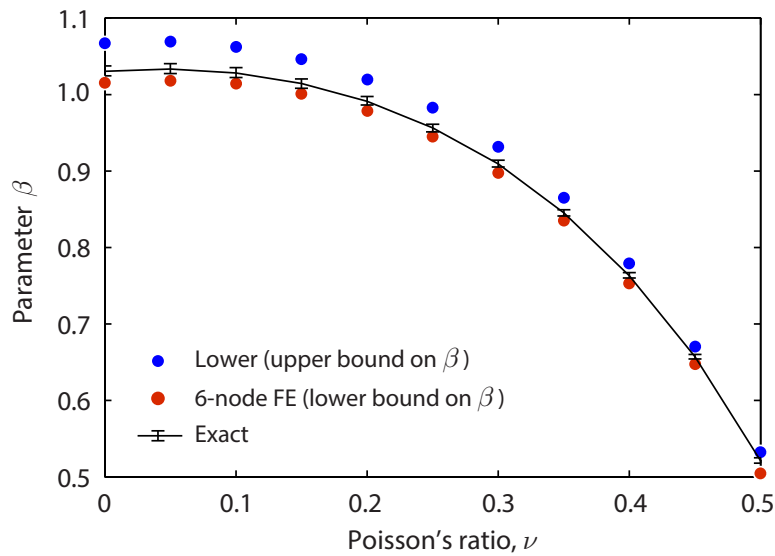


Figure 3.2: Parameter β using 100 Lower and 6-node FE.

4 STRIP LOAD ON GIBSON SOIL

The following example concerns the problem of a strip load on a semi-infinite domain of a Gibson soil, i.e. an elastic material with a Young's modulus that increases linearly with depth from a value of zero at the top surface. In the following, rather than using an actual semi-infinite domain, a sufficiently large one is used (see Figure 4.1). We note that the effect of the domain size decreases rather rapidly as the stiffness increases with depth (as opposed to the case where Young's modulus is constant and the deformation at the top surface is a function of the domain depth).

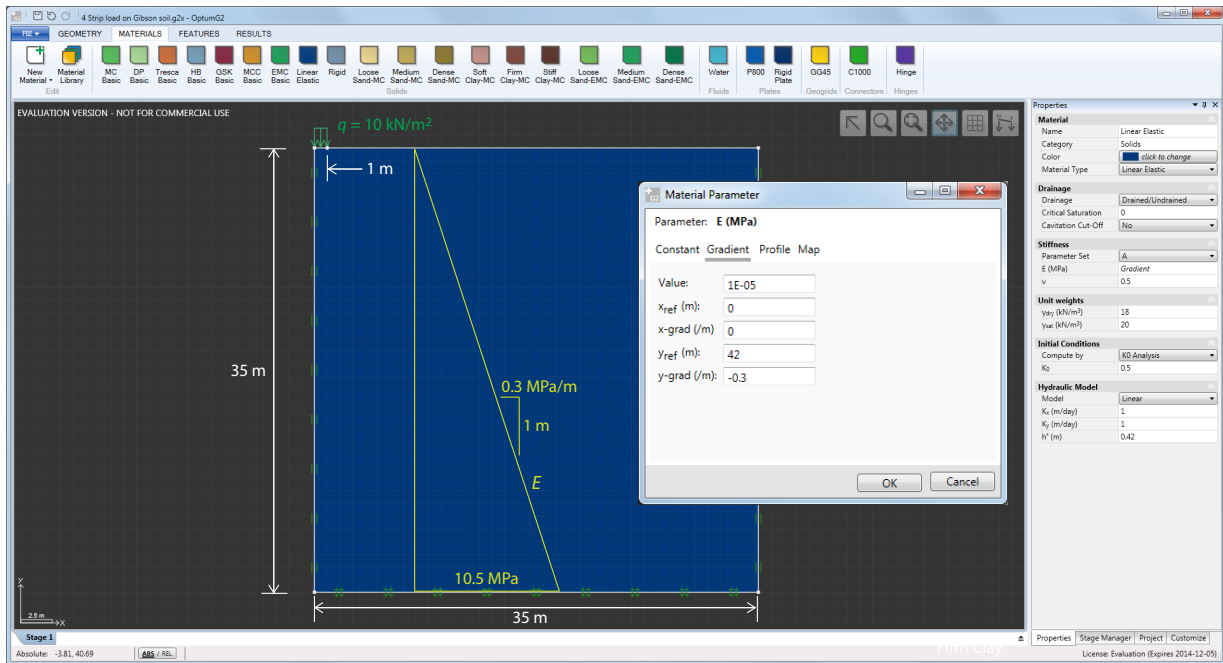


Figure 4.1: Strip load on Gibson soil.

For $q = 10 \text{ kN/m}^2$, $\nu = 0.5$ and an increase in Young's modulus of 0.3 MPa/m , Gibson (1967) gives the exact solution of a uniform displacement of $u = 0.05 \text{ m}$ underneath the load. With 10,000 6-node FE, we obtain a maximum displacement of 0.0494 m which is in error by about 1%. The vertical deformation field is shown in Figure 4.2.

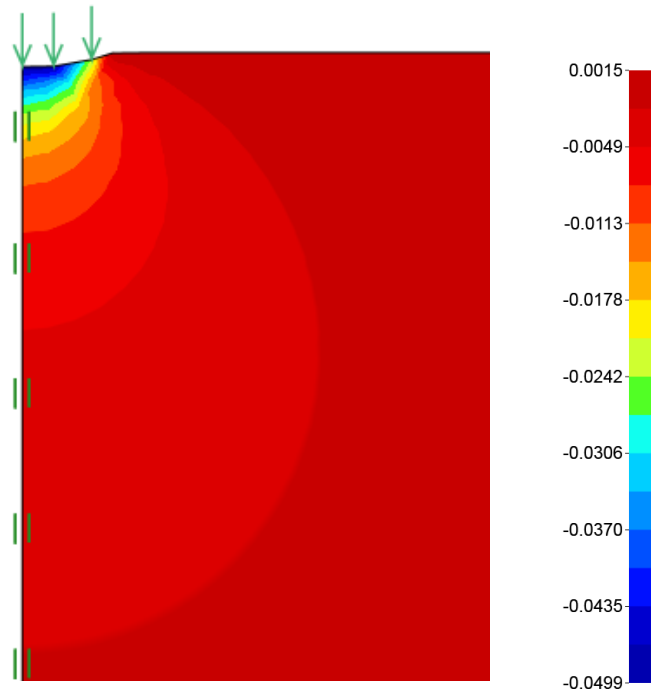


Figure 4.2: Strip load on Gibson soil: vertical deformation field.

5 FOOTING ON SOIL WITH USER DEFINED MATERIAL DATA

In some cases, it may be necessary to use a spatial variation of certain material parameters that cannot easily be described by simple analytical expressions. OPTUM G2 caters for this scenario by allowing for arbitrary distributions of all material parameters to be used as demonstrated in the following. The problem setup is shown in Figure 5.1. The limit load of the footing is to be determined with the undrained shear strength, s_u , being imported from a data set external to OPTUM G2.

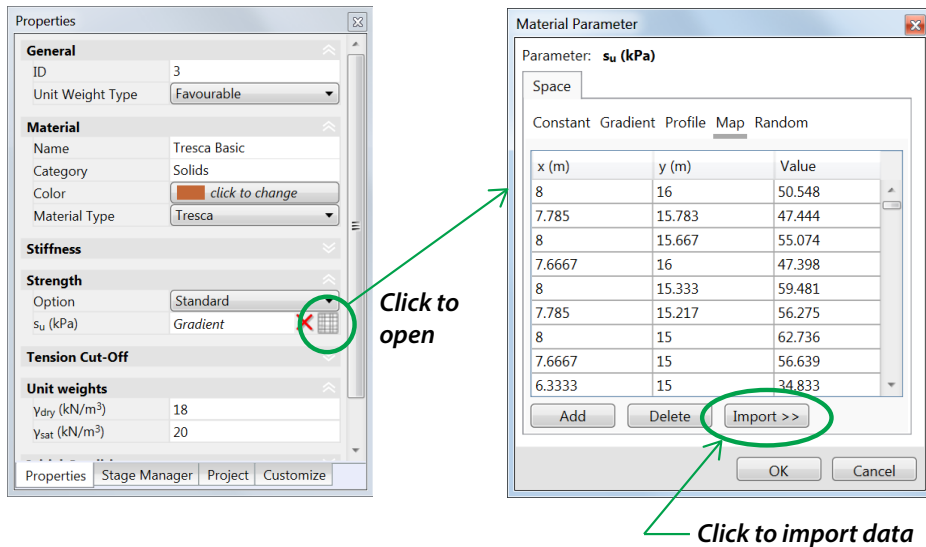
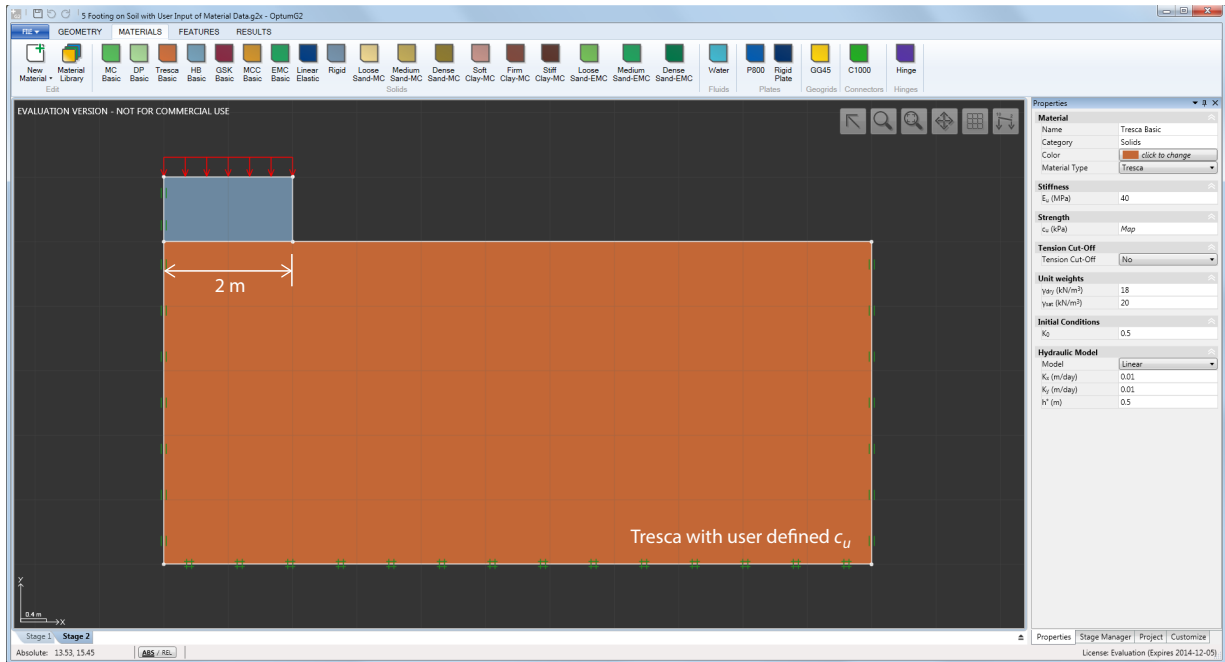


Figure 5.1: Footing on soil with user defined material data (top) and specification of input data (bottom).

The steps needed to import an arbitrary distribution of s_u are illustrated in the figure above. The button on the right hand side of the s_u field in the property window opens the dialog shown on the right in the figure. Using the Import button, a file with the material data can be loaded into the project. The input file must contain three columns with the x and y coordinates and the parameter value

respectively. No particular ordering of the coordinates is needed, but the data are expected to cover the whole domain for which they are specified. The data can be unloaded via the red cross next to the button that opens the Material Parameter window.

With the input defined, upper and lower bound Limit Analyses are conducted using 5,000 elements and 3 adaptivity iterations. The results are a bearing capacity of

$$q_u = 241.1 \text{ kN/m}^2 \pm 0.6\% \quad (5.1)$$

The parameter map can be visualized under Results via the Material Parameters drop-down. The distribution of s_u is shown in Figure 5.2. The collapse mechanism (lower bound) is shown in Figure 5.3.

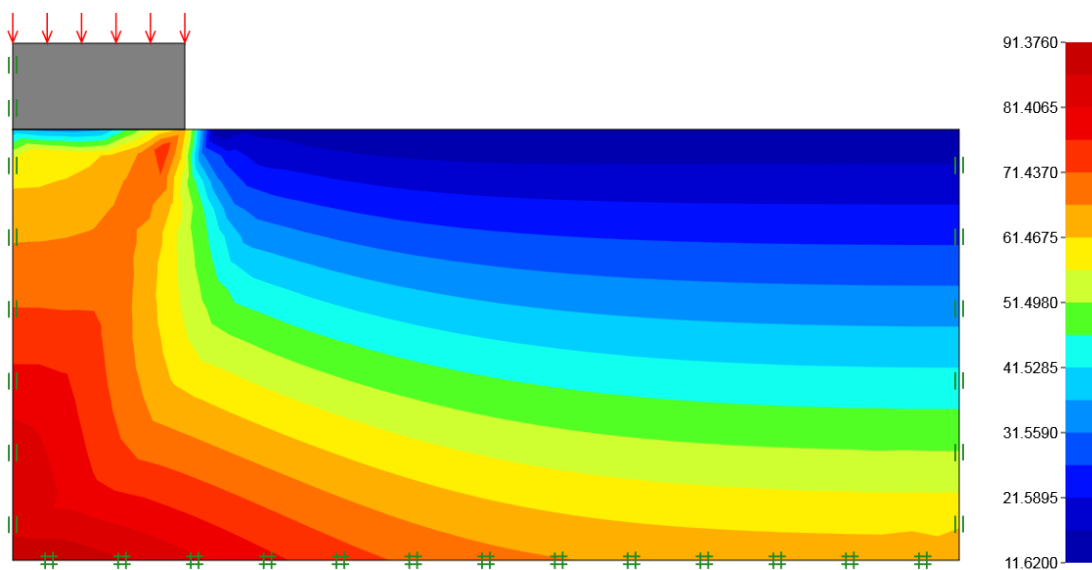


Figure 5.2: Variation of s_u from user defined input data.

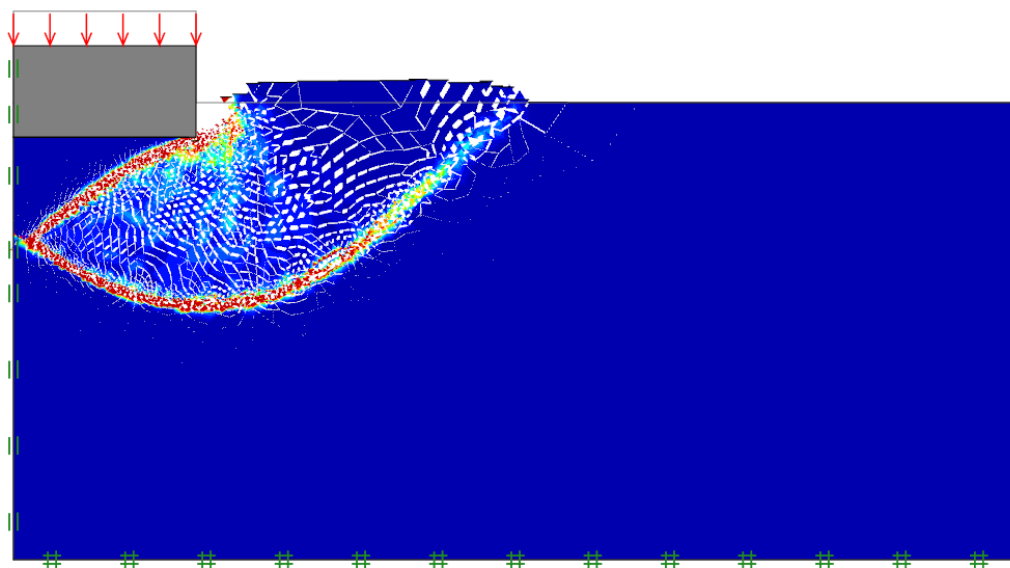


Figure 5.3: Collapse mechanism and distribution of shear dissipation (Element Type = Lower).

6 SLOPE STABILITY – LONG TERM

In this example we consider the stability of a layered slope as shown in Figure 6.1. The layers comprise the default materials Firm Clay and Stiff Clay. In the following, only long term analysis is considered. The ground water table is assumed to be located well beneath the toe of the slope.

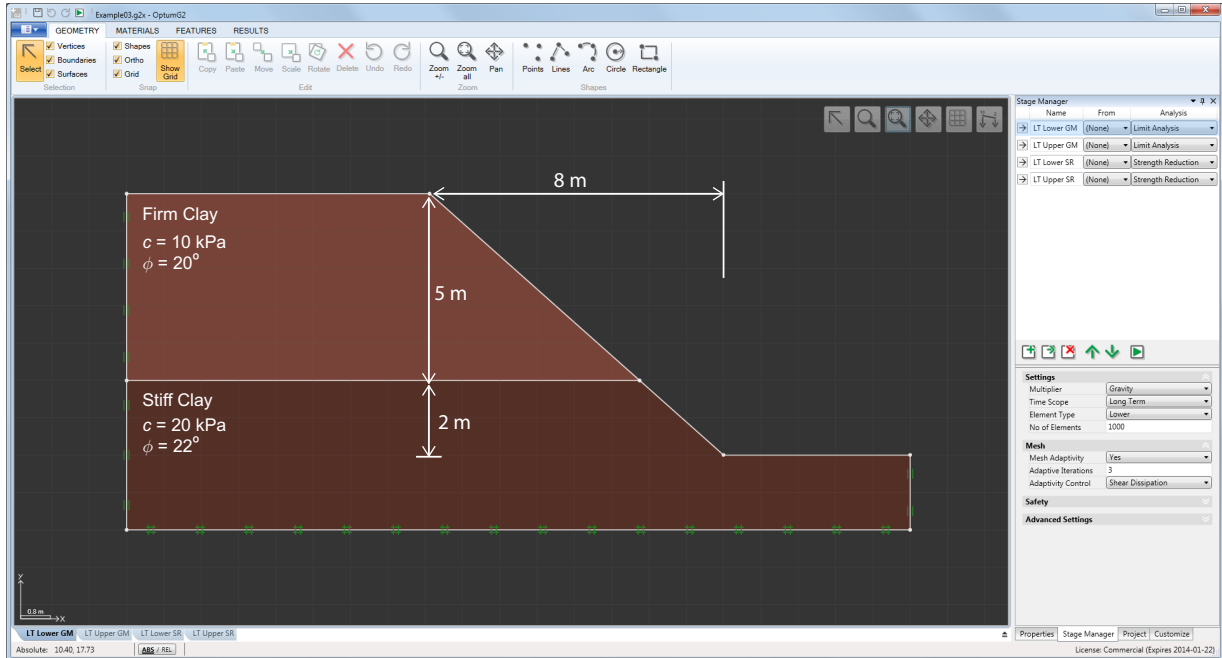


Figure 6.1: Layered slope.

The central quantity in slope stability analysis is the Factor of Safety (FS). All common definitions of the factor of safety operate with $FS > 1$ indicating stability and $FS < 1$ indicating instability. However, how much above or below unity the factor of safety is in a given case depends very much on its exact definition.

A common definition involves the actual unit weight in relation to the unit weight that will lead to incipient collapse:

$$FS_{\gamma} = \frac{\gamma_{cr}}{\gamma} \quad (6.1)$$

where γ is the actual unit weight and γ_{cr} is the unit weight that will lead to incipient collapse. Alternatively, this factor of safety may be defined in terms of gravitational accelerations:

$$FS_g = \frac{g_{cr}}{g} \quad (6.2)$$

where g is the actual gravitation acceleration ($=9.8 \text{ m/s}^2$ by default) and g_{cr} is the gravitational acceleration that will lead to incipient collapse.

Another common definition involves the material strengths in relation to the strengths that will lead to incipient collapse. In particular, for Mohr-Coulomb materials the factor of safety may be defined as

$$FS_s = \frac{c}{c_{cr}} = \frac{\tan \phi}{\tan \phi_{cr}} \quad (6.3)$$

where c and ϕ are the actual material strengths and c_{cr} and ϕ_{cr} are those that will lead to incipient collapse.

Both definitions have pros and cons. Generally, the strength based definition is more conservative, i.e. leads to lower values of FS, than the gravity based definition. Indeed, for some, not unrealistic problems, FS_g will tend to infinity while FS_s may be finite and not much greater than unity. Also, it may be argued that since the real uncertainty is in the strength of the materials rather than their weight, the strength based definition is the more reasonable one.

OPTUM G2 allows for the calculation of both gravity and strength based factors of safety. The former is realized via Limit Analysis using the Gravity Multiplier option while the latter type of calculation can be carried out using Strength Reduction analysis.

6.1 Gravity Multiplier

The assessment of the gravity based factor of safety using Limit Analysis is realized by setting Multiplier = Gravity under Settings in the lower half of the Stage Manager window (see Figure 6.1). This type of limit analysis ignores all multiplier loads and magnifies the gravitational acceleration (and thereby the unit weight) until a state of failure is attained. The resulting collapse multiplier is the sought Factor of Safety FS_g .

Long Term analysis is specified by the Time Scope field in the lower half of the Stage Manager window. For this and subsequent calculations we will use 1,000 elements and Mesh Adaptivity with 3 Adaptivity Iterations and Shear Dissipation as the Adaptivity Control. Lower and upper bound calculations are defined in separate stages by setting Element Type to Lower and Upper respectively. These settings are all shown in Figure 6.1.

The results of the analyses are:

$$1.87 \leq FS_g \leq 1.94 \quad (6.4)$$

or:

$$FS_g = 1.90 \pm 0.04 \quad (6.5)$$

from which we can conclude that the slope is stable in the long term. The collapse solution is shown in Figure 6.2.

6.2 Strength Reduction

The objective of Strength Reduction analysis is to determine a set of reduced parameters that lead to incipient collapse, i.e. that imply a gravity multiplier equal to 1. For the Mohr-Coulomb model, the strengths are reduced according to Eqn. (6.3). The calculations are carried out as a series of limit analyses. Hence, Strength Reduction analysis is usually significantly more expensive than a single Gravity Multiplier Limit Analysis.

Strength Reduction analysis is carried out by choosing this analysis in the Stage Manager window. Using 1,000 elements and 3 adaptivity steps as in the previous analysis, we obtain:

$$1.34 \leq FS_s \leq 1.37 \quad (6.6)$$

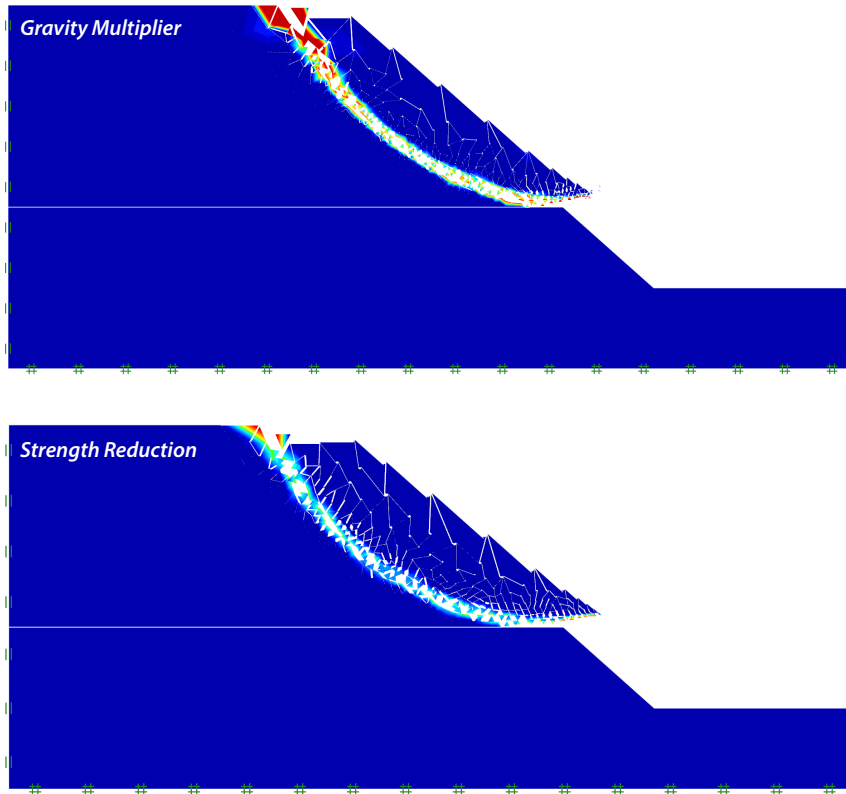


Figure 6.2: Gravity Multiplier Limit Analysis and Strength Reduction collapse solutions for layered slope (lower bound) with intensity of total dissipation.

or:

$$FS_s = 1.35 \pm 0.02 \quad (6.7)$$

from which we again conclude that the slope is stable in the long term, though with a numerically smaller factor safety than in the previous analysis.

The lower bound collapse solutions for the two analyses are shown in Figure 6.2. We note that the displacements (or velocities) are discontinuous which is a particular feature of the Lower bound element. The two collapse mechanisms are quite similar, with the differences stemming from the fact that the Strength Reduction analysis implies failure under a friction angle of $\phi_{cr} = \arctan[\tan(20^\circ)/1.35] \simeq 15^\circ$ while the gravity multiplier mechanism corresponds to failure with the original value of $\phi = 20^\circ$.

6.3 Summary

This example demonstrates some of the basic features of slope stability, in particular the difference between the gravity and strength based factors of safety. More advanced examples, considering short term analysis, the effect of the initial stresses, and slopes subjected to seismic loads are given in the following sections.

7 SLOPE STABILITY – SHORT TERM

This example concerns the slope previously introduced in the previous section (shown again in Figure 7.1). While the long term stability was considered in the previous section, the aim of the present example is to determine the short term stability. Again, the ground water table is assumed to be located well beneath the toe of the slope. At the same time, it is assumed that the degree of saturation throughout the slope is sufficient for excess pore pressures to develop, i.e. for the material to respond in an undrained manner under short term conditions everywhere.

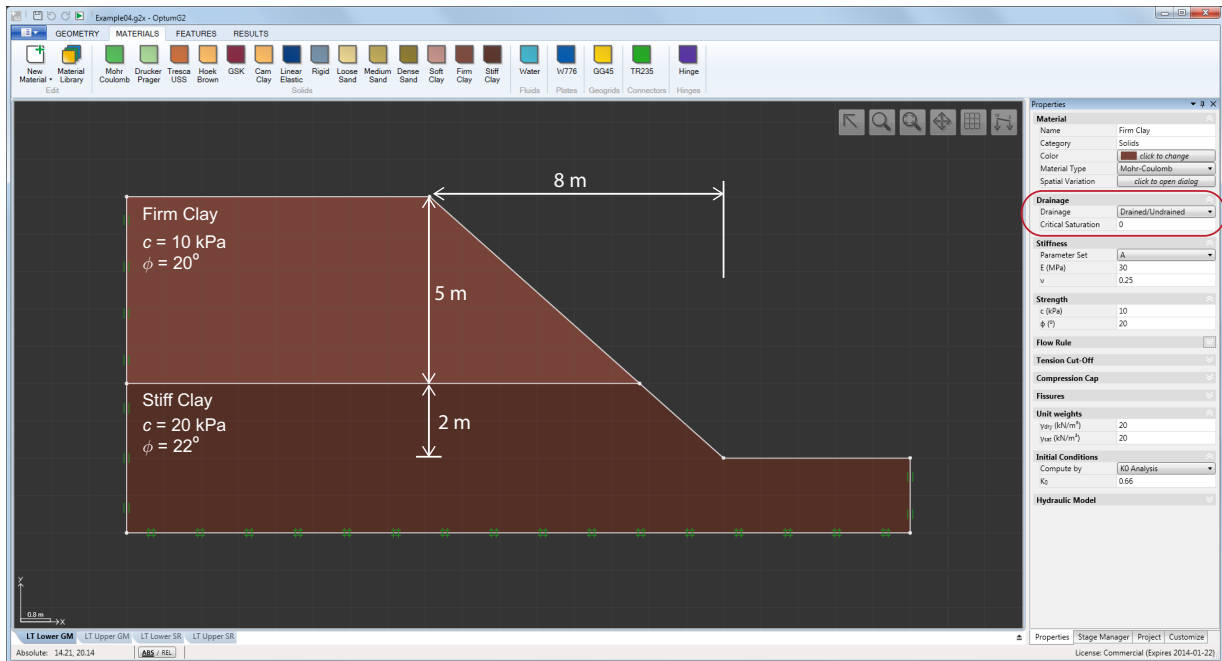


Figure 7.1: Layered slope.

As usual for analyses with Drained/Undrained materials under Short Term conditions, the initial stresses in the slope are an essential component in evaluating its stability. OPTUM G2 offers a number of approaches for determining the initial stress of the present kind of scenario. The most direct and convenient one is to let the initial stresses be computed automatically to yield a state of stress that satisfies $\sigma'_x = \sigma'_z = K_0 \sigma'_y$ to the greatest possible extent.

Secondly, since the initial stresses are a function of history of the slope, one might take the approach of beginning with an initially rectangular domain where $\sigma'_x = \sigma'_z = K_0 \sigma'_y$ is satisfied and then excavate the necessary parts to form the slope. In the following, both approaches will be considered.

7.1 Automatic computation of initial stresses

This approach is the most direct and convenient. The initial stresses are here determined automatically using the approach described in detail in the previous section. Using Strength Reduction analysis with 1,000 elements and 3 adaptivity iterations leads to the following estimate of the strength based factor of safety:

$$1.47 \leq FS_s \leq 1.49 \quad (7.1)$$

or:

$$FS_s = 1.48 \pm 0.01 \quad (7.2)$$

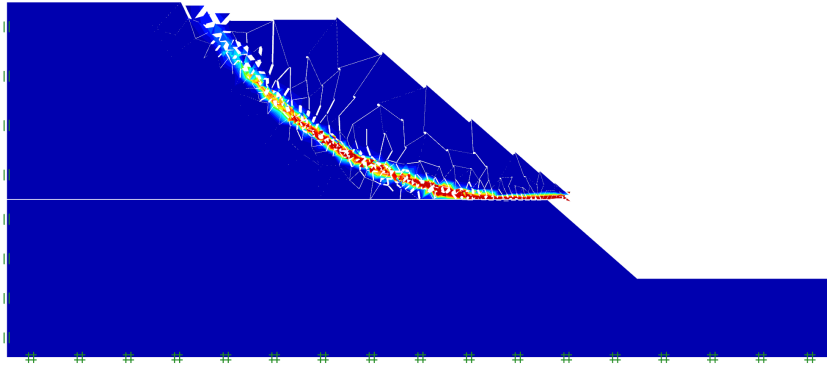


Figure 7.2: Collapse mechanism (short term Strength Reduction analysis).

This can be compared to the long term factor of approximately 1.34 in the previous section. In conclusion, the slope is slightly more stable in the short term than in the long term. The collapse mechanism is shown in Figure 7.2.

7.2 Initial stresses by excavation

An alternative approach to the determination of the initial stresses is to begin with an initially rectangular domain and then excavate the necessary material to create the slope. OPTUM G2 is particularly suited for this type of task. The different stages involved and the task of linking these to each other is explained in Figure 7.4.

The resulting factor of safety is given by

$$1.39 \leq FS_s \leq 1.41 \quad (7.3)$$

or:

$$FS_s = 1.40 \pm 0.01 \quad (7.4)$$

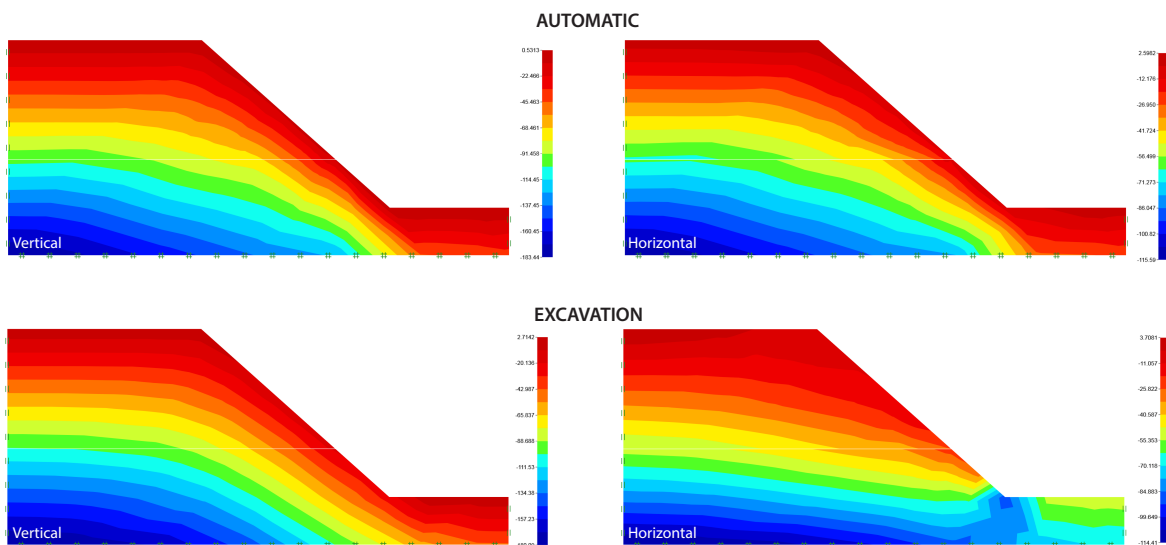
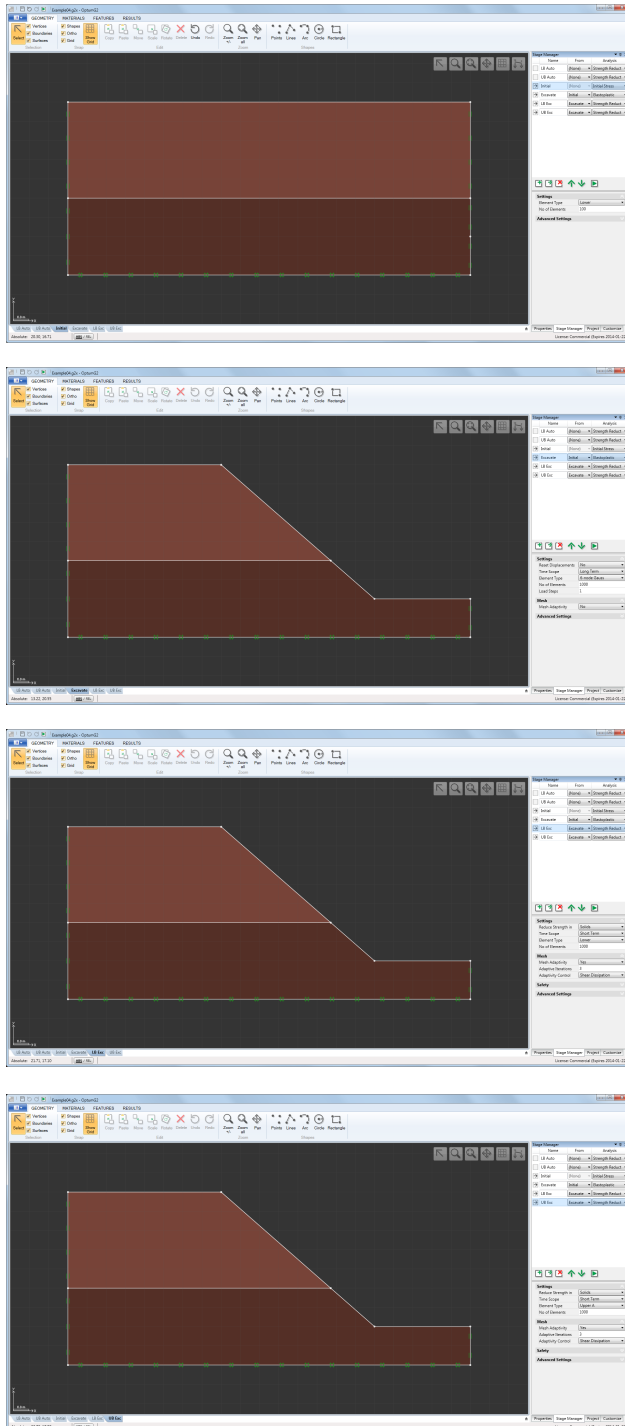


Figure 7.3: Initial vertical and horizontal stresses.

which is slightly lower than was obtained using the automatic approach. The initial stress distributions resulting from each of the approaches are shown in Figure 7.3. The differences here are ultimately reflected in the corresponding factors of safety. It should be noted that there is no general rule that one approach will imply a higher strength than the other. Indeed, in most cases the result will, as in this case, be fairly similar.



Initial: Compute the initial stresses for a rectangular domain using Initial Stress analysis. The vertical and horizontal stresses are here related by $\sigma_h = K_0 \sigma_v$ where $K_0 = 0.66$ for the upper layer and $K_0 = 0.63$ for the lower layer.

A total of 100 elements of type Lower are used which in this case is enough to provide the exact solution.

Excavate: Using Elastoplastic analysis and using the **Initial** stage as the From stage, the necessary material is removed to create the slope.

For this analysis, a total of 1,000 elements of the type 6-node FE are used. The Time Scope is Long Term implying that the slope is first excavated after which a sufficient amount time passes for the pore pressures to dissipate.

LB Exc: Using Strength Reduction analysis and using the **Excavate** stage as From stage, a lower bound estimate of the strength based factor of safety is determined.

A total of 1,000 Lower elements with 3 adaptivity iterations are used and the Time Scope is Short Term.

UB Exc: Using Strength Reduction analysis and using the **Excavate** stage as From stage, an upper bound estimate of the strength based factor of safety is determined.

A total of 1,000 Upper A elements with 3 adaptivity iterations are used and the Time Scope is Short Term.

Figure 7.4: Stages in lower and upper bound short term strength reduction using elastoplastic analysis to excavate the slope.

8 STABILITY OF SLOPE SUBJECTED TO UNCONFINED SEEPAGE

The following example considers the stability of the slope shown in Figure 8.1. The seepage pressure distribution and the location of the phreatic surface are not known a priori except that the groundwater table is located at the foot of the slope and the conditions at a distance of 15 m from the crest of the slope correspond to hydrostatic conditions. These boundary conditions are imposed using the Water Table tool available in the Features ribbon. In particular, by clicking any point on a vertical line, a constant head with value equal to the position is imposed.

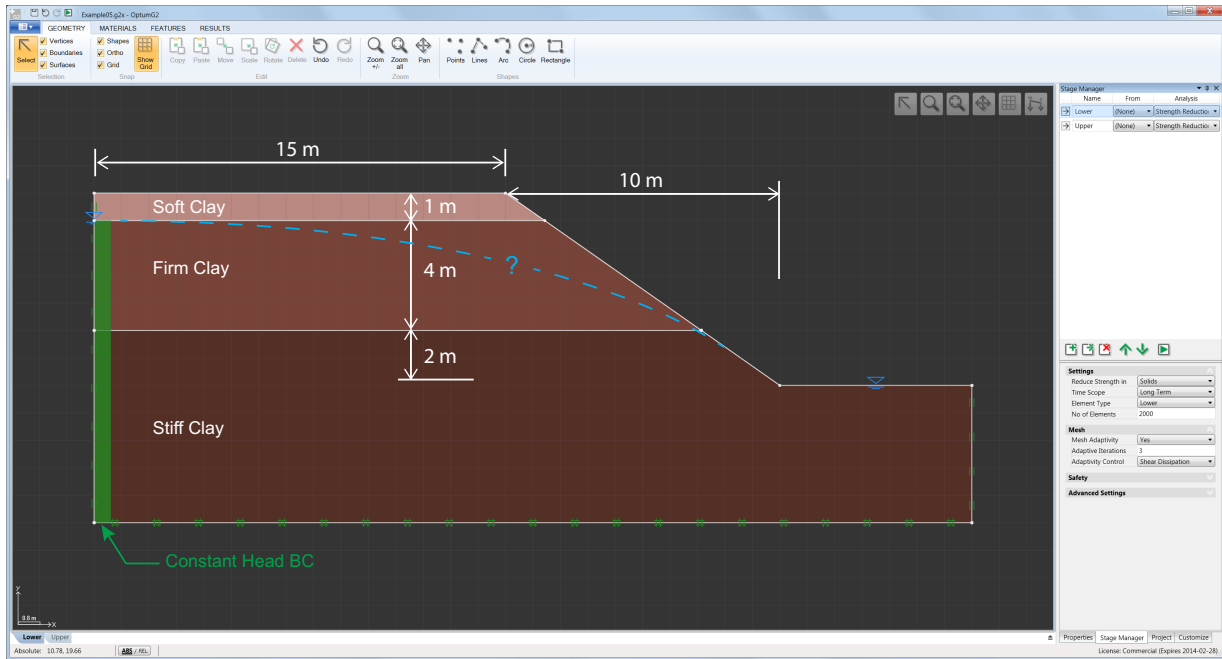


Figure 8.1: Slope subjected to unconfined seepage.

In the following, upper and lower bound Strength Reduction analyses are conducted considering the stability in the long term. All materials involved have Drainage = Drained/Undrained. With Time Scope = Long Term, the conditions are thus drained throughout the slope.

The analyses proceed as in the the previous examples by defining two stages with Element Type being Lower and Upper respectively. A total of 2,000 elements are used with 3 adaptivity iterations. As part of these analyses, the seepage pressures are calculated automatically. Moreover, where seepage is involved, the Adaptivity Control called Shear Dissipation includes a component related to the flow field.

The results of the analyses are a strength based factor of safety bracketed by:

$$1.48 \leq FS_s \leq 1.51 \tag{8.1}$$

or:

$$FS_s = 1.49 \pm 0.02 \tag{8.2}$$

The saturation distribution is shown in Figure 8.2. The collapse solution is shown in Figure 8.3. It is interesting to note the mechanism which comprises two independent slip lines.

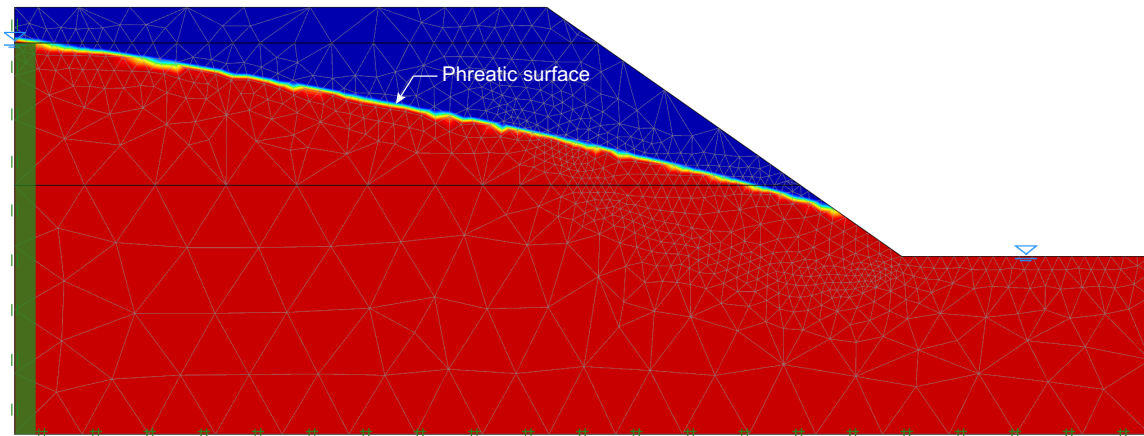


Figure 8.2: Degree of saturation (red corresponds to $S = 1$ and blue to $S = 0$).

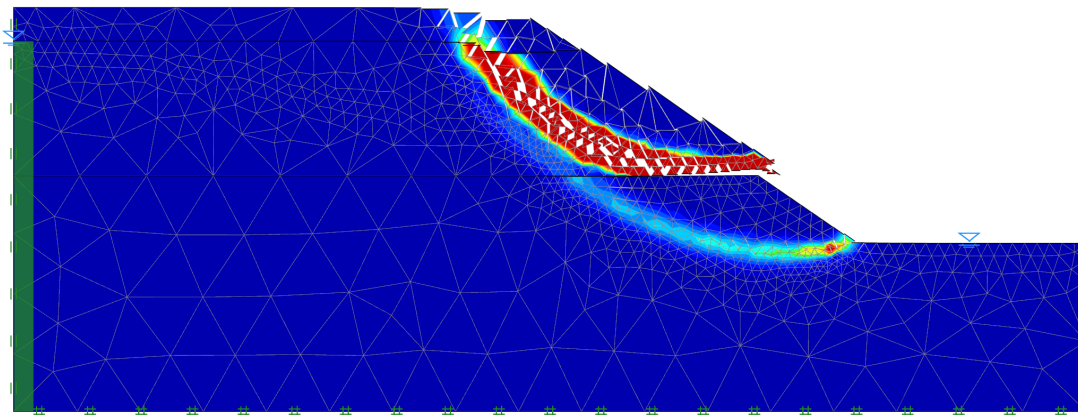
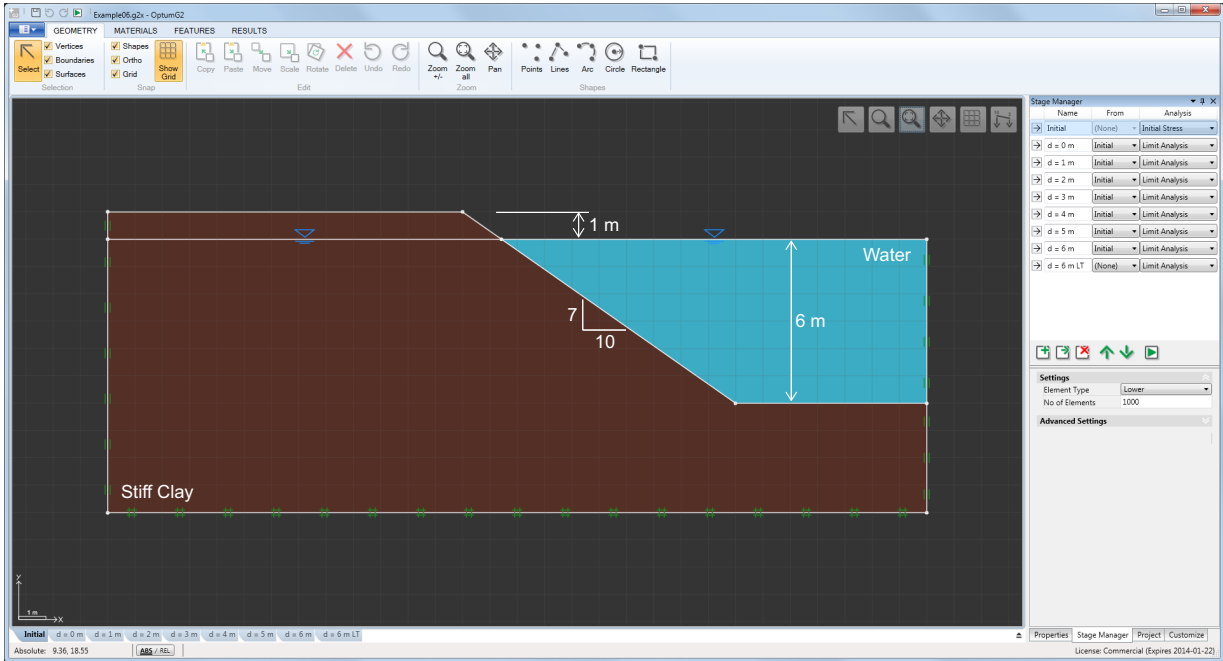


Figure 8.3: Collapse solution (Lower).

9 STABILITY OF SLOPE SUBJECTED TO RAPID DRAWDOWN

This example examines the effects of rapid drawdown on slope stability. The problem setup is sketched in Figure 9.1. From the initial state shown in the figure, the water level is lowered suddenly. Due to the loss of the stabilizing effect of the water, the factor of safety will decrease.

Initial state



Limit Analysis at drawdown level of $d = 2$ m

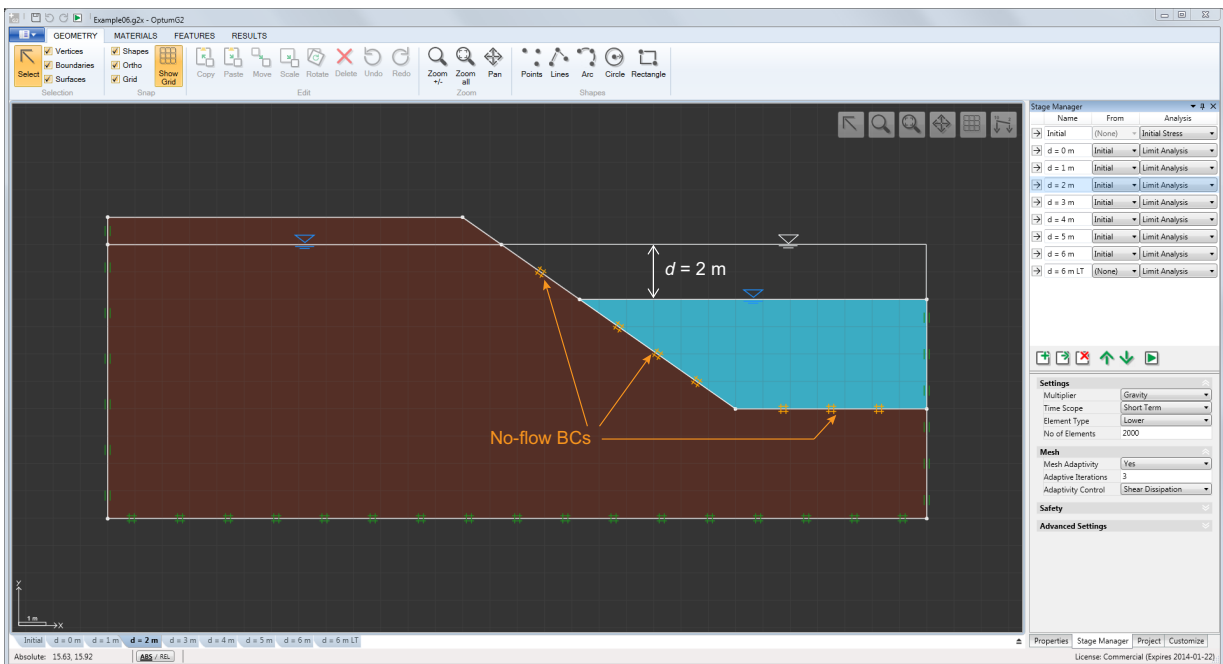


Figure 9.1: Slope subjected to rapid drawdown.

As a result of the drawdown, the seepage pressure will change to comply with the new boundary

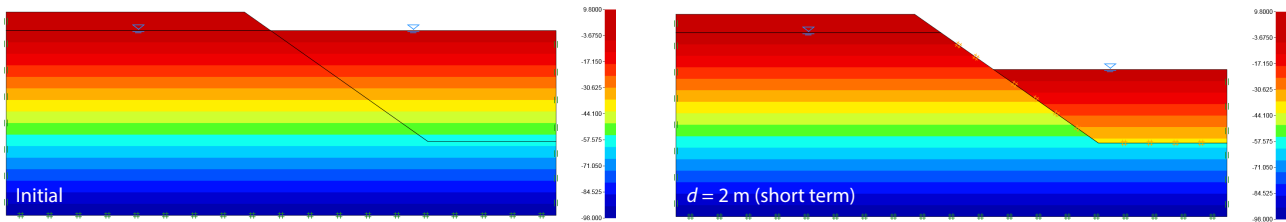


Figure 9.2: Seepage pressures (kPa) before (left) and after rapid drawdown to $d = 2$ m.

conditions. At the same time, as a result of the altered state of stress, excess pore pressures will be generated.

9.1 Short term stability

The stability of the slope in the short time is first evaluated. In doing so, it is assumed that the seepage pressures in the slope do no change at all from the initial state. In the water, on the other hand, a hydrostatic distribution is assumed at all times. Provided that the permeability of the material is sufficiently low, this is a reasonable assumption. As with any other analysis, excess pore pressures are generated automatically as a consequence of the Time Scope being Short Term and the Drainage Conditions of the materials being Drained/Undrained.

In evaluating the short term stability of the slope, the following strategy is used. First, stage is defined to compute the initial stresses using Initial Stress analysis (see Figure 9.2). Then a limit analysis stage, with a specific lowering of the dam water level, is defined. This stage uses the initial stage as From stage and has Time Scope = Short Term. Moreover, no-flow boundary conditions are imposed on the face of the slope to achieve a hydrostatic state of seepage pressure both in the slope and in the water (see Figure 9.2).

In the following, Limit Analysis with Multiplier = Gravity is used to evaluate the factor of safety. Using 2,000 Lower and Upper elements with 3 adaptivity iterations, the result, in terms of the gravity based factor of safety versus drawdown level, are shown in Figure 9.3. We see that the stability decreases as the drawdown level increases. The collapse solutions corresponding to $d = 0$ m and $d = 5$ m are shown in Figure 9.4.

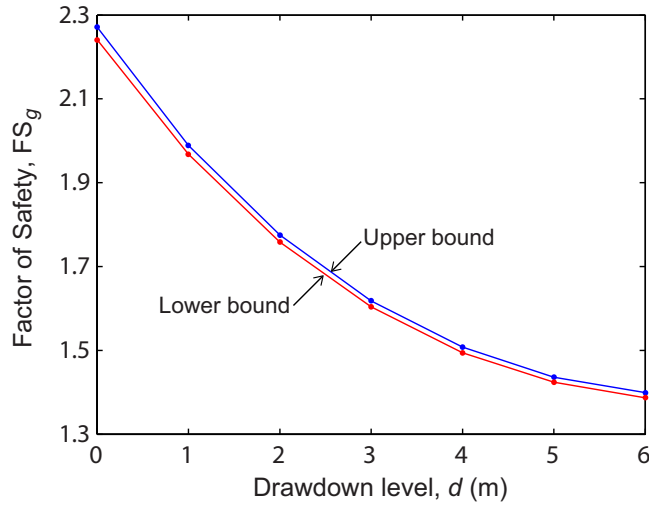


Figure 9.3: Upper and lower bound Gravity based Factors of Safety, FS_g .

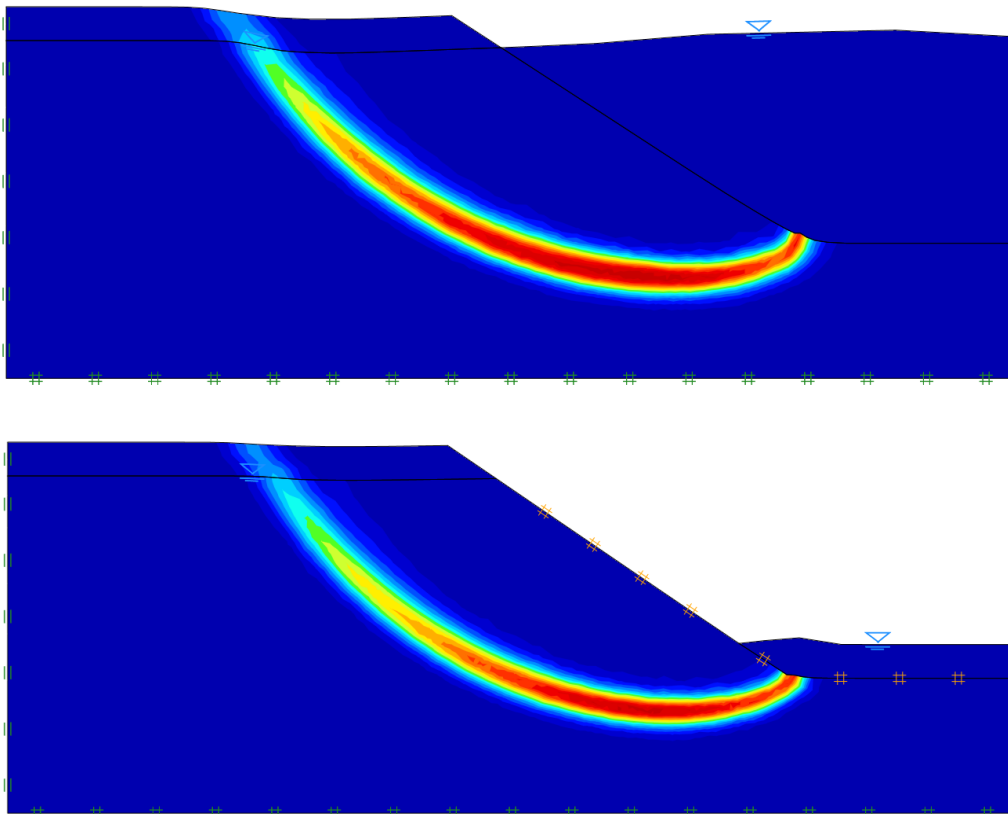


Figure 9.4: Collapse mechanisms resulting from Gravity Multiplier Limit Analysis before (top) and after (bottom) drawdown by 5 m.

9.2 Long term stability

Finally, the stability of the slope in the long term is investigated with respect to the maximum draw-down level, $d = 6$ m. The no-flow boundary conditions on the face of the slope at the bottom of the reservoir are here removed and the long term steady state pore pressures are calculated as part of

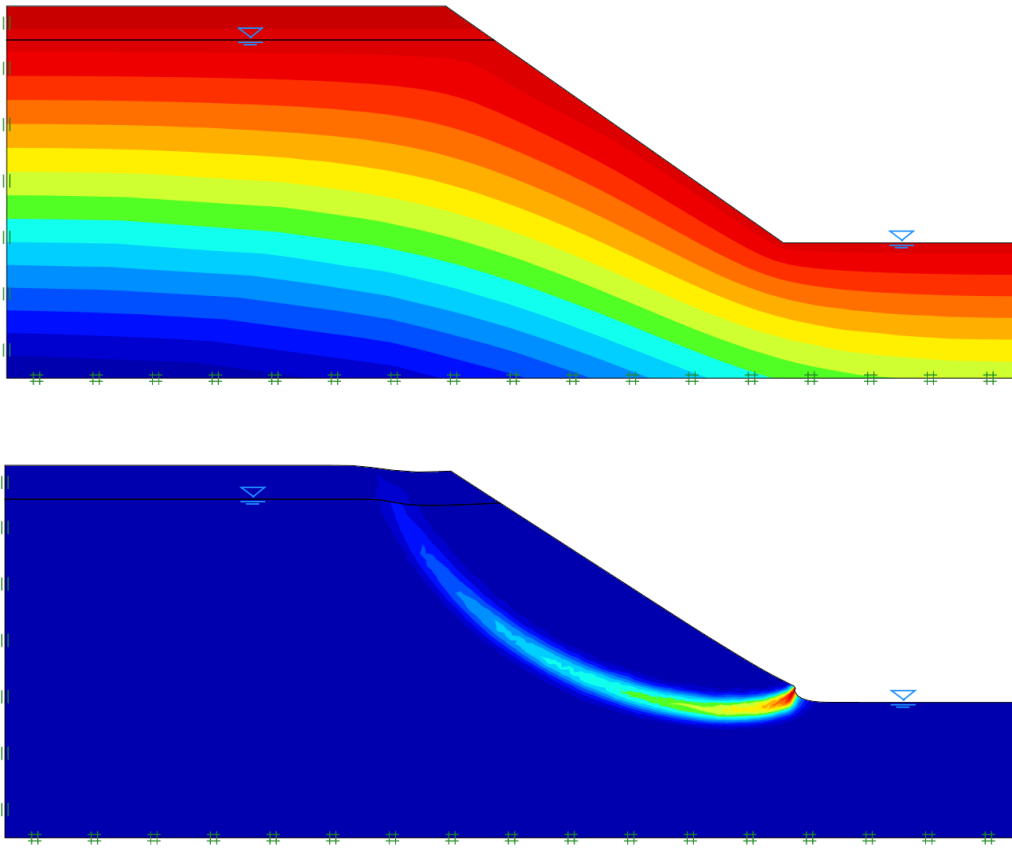


Figure 9.5: Long term pore pressure (top) and collapse (bottom) solutions for $d = 6$ m.

the Limit Analysis. Using the same element and adaptivity settings as above, we obtain:

$$FS_g = 2.07 \pm 0.06 \quad (9.1)$$

The pore pressure and collapse solutions are shown in Figure 9.5.

10 SLOPE WITH PRE-EXISTING FAULT

This example considers the stability of a slope with a pre-existing fault as shown in Figure 10.1. In OPTUM G2, this scenario may be modeled by the use of Shear Joints. These are essentially infinitely thin patches of material sandwiched between the surrounding material. As such, Shear Joints can be assigned any of the properties that apply to solid domains of a finite extent, including materials, drainage conditions, etc.

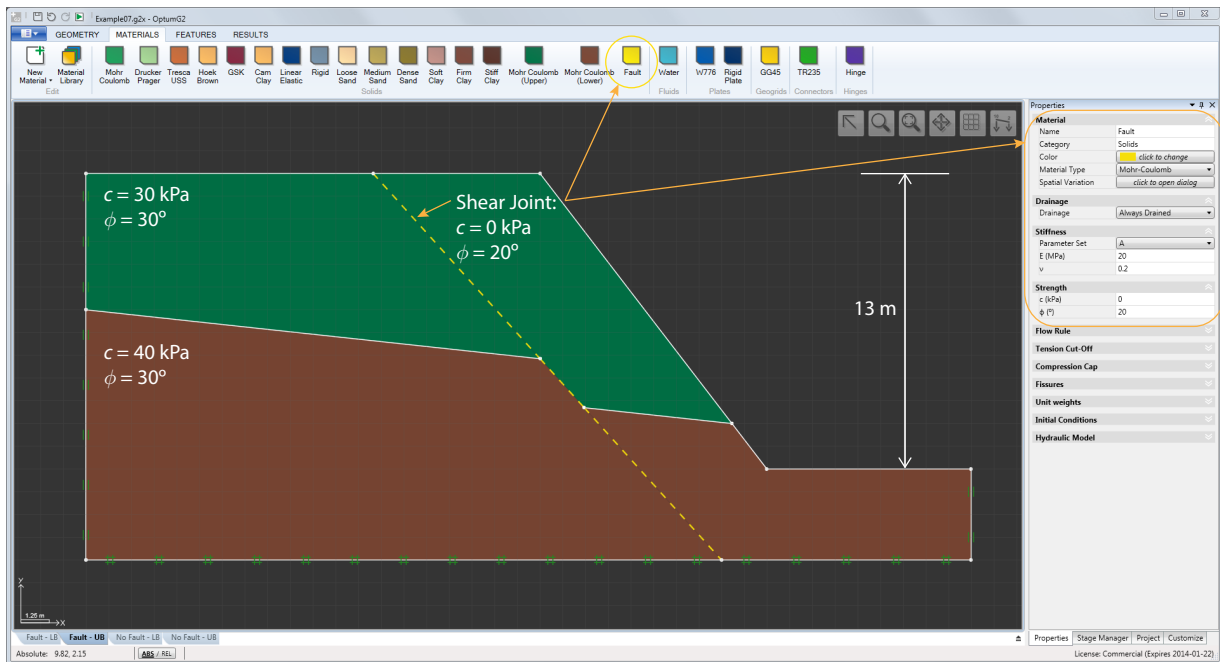


Figure 10.1: Slope with pre-existing fault.

Running Long Term Gravity Multiplier Limit Analysis using 5,000 elements (Lower and Upper) and 3 adaptivity iterations results in the following gravity based factors of safety:

$$\begin{aligned} \text{Without fault : } & FS_g = 2.38 \pm 0.04 \\ \text{With fault : } & FS_g = 1.57 \pm 0.04 \end{aligned} \tag{10.1}$$

The collapse solutions are shown in Figure 10.2 and reflect the significant reduction in strength resulting from the presence of the fault.

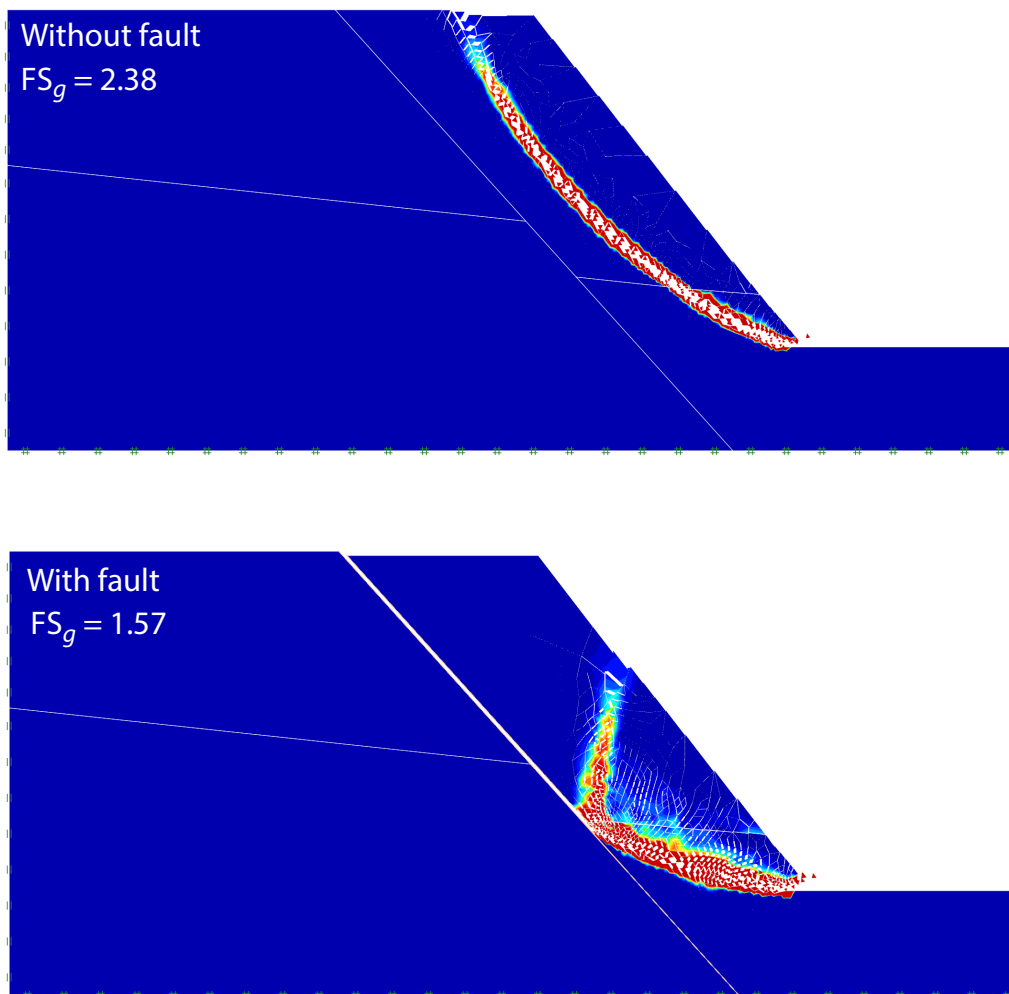


Figure 10.2: Collapse solutions and total dissipation field for slopes with and without fault.

11 STABILITY OF SEISMICALLY LOADED SLOPE

The stability of geotechnical structures under seismic loading is often assessed via so-called pseudo-static analysis. The earthquake induced forces are here represented by body accelerations that are applied statically. Usually, one considers a situation where the vertical acceleration is kept fixed at $g_v = 9.8 \text{ m/s}^2$ while the horizontal acceleration is increased until failure. The resulting ratio between the vertical and horizontal accelerations, $k_c = g_h/g_v$, is referred to as the critical seismic coefficient. In the following, a slope with the geometry shown in Figure 11.1 is considered.

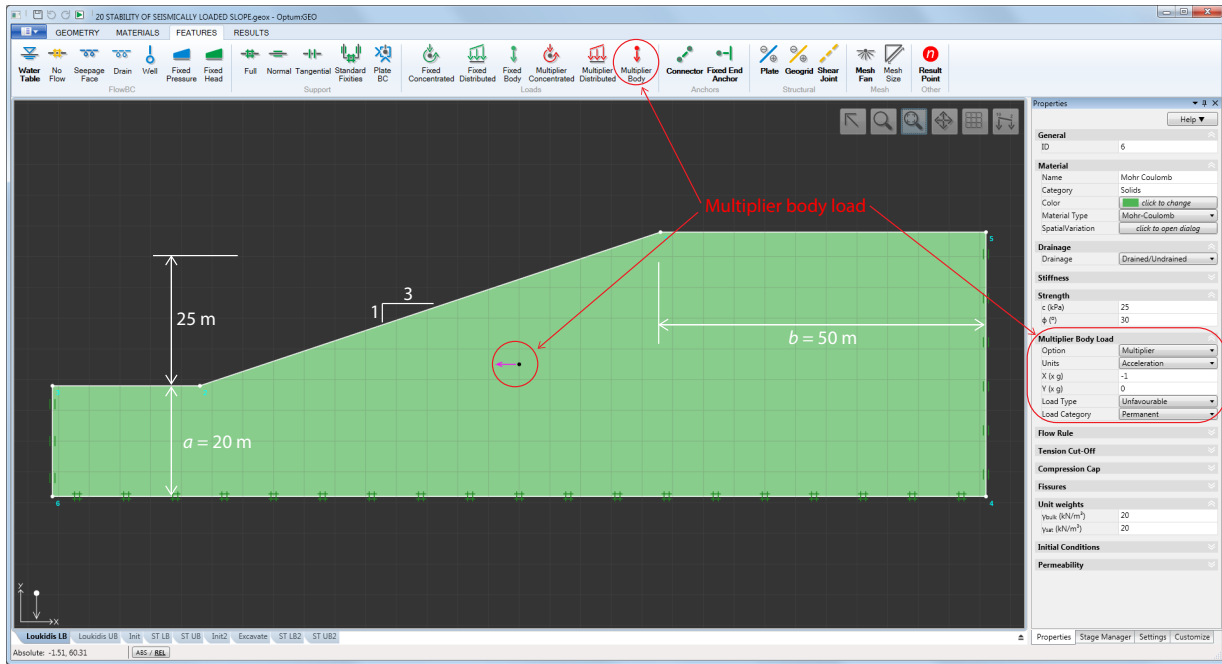


Figure 11.1: Seismically loaded slope.

The pseudo-static seismic load is accounted for by a Multiplier Body Load. This type of load applies to solids and structural elements only and is applied by selecting the solid or structural element and clicking the Multiplier Body icon in the Features ribbon. Body loads can be applied in terms of two different sets of units: force (kN/m^3) or acceleration which is taken as a fraction of the default downward gravitational acceleration of $g = 9.8 \text{ m/s}^2$. In the present case the latter approach is used. Using Limit Analysis with Multiplier = Load, the collapse multiplier is thus the critical seismic coefficient, $k_c = g_v/g_h$.

11.1 Loukidis et al. example

We begin by analyzing a problem previously analyzed by Loukidis et al. (2003). The material is of the Mohr-Coulomb type with $c = 20 \text{ kPa}$, $\phi = 30^\circ$ and has a unit weight of 20 kN/m^3 . Limit Analysis with 1,000 elements and 3 adaptivity steps is used. No excess pore pressures are generated so Time Scope is set to Long Term (although seismic forces of course work in the short term). For these settings we find:

$$0.427 \leq k_c \leq 0.439 \quad (11.1)$$

These results are in very good agreement with those of Loukidis et al. (2003) who for a total of four different hand calculation methods (Spencer's, Bishop's simplified, Sarma's, and log-spiral upper

bound) found values of k_c ranging from 0.426 to 0.432. In addition, a conventional finite element analysis performed by Loukidis et al. resulted in $k_c = 0.433$ while upper and lower bound limit analyses of the kind used in OPTUM G2 gave bounds similar to the ones found in the present analysis.

11.2 Short term conditions – total stress analysis

Next, we consider seismic excitation in the short term. As for other problems (footings, slopes, etc), a common approach is to use a total stress analysis where the original Mohr-Coulomb criterion is replaced by a Tresca criterion with the undrained shear strength as the single parameter. If limited data is available, it is tempting to use a constant undrained shear strength that, by some reasonable estimate, would represent the average undrained shear strength encountered in the slope. However, as will be demonstrated in the following, this approach is not appropriate and will lead to unrealistic results.

The overall geometry is the same as above, except that the geometric parameters a and b are varied. The material is Tresca with an undrained shear strength of $s_u = 150$ kPa. In the first example, the critical seismic coefficient is independent of a and b provided they are sufficiently large. However, assuming a purely cohesive material alters this in such a way that the critical seismic coefficient comes to depend directly on a and b . In the following this is illustrated by increasing a and b proportionally, i.e b is increased while the ratio $a/b = 2.5$ is maintained. The effect is as shown in Figure 11.2: the collapse mechanism extends to the right boundary and bottom of the domain regardless of its dimensions and the critical seismic coefficient gradually decreases to zero.

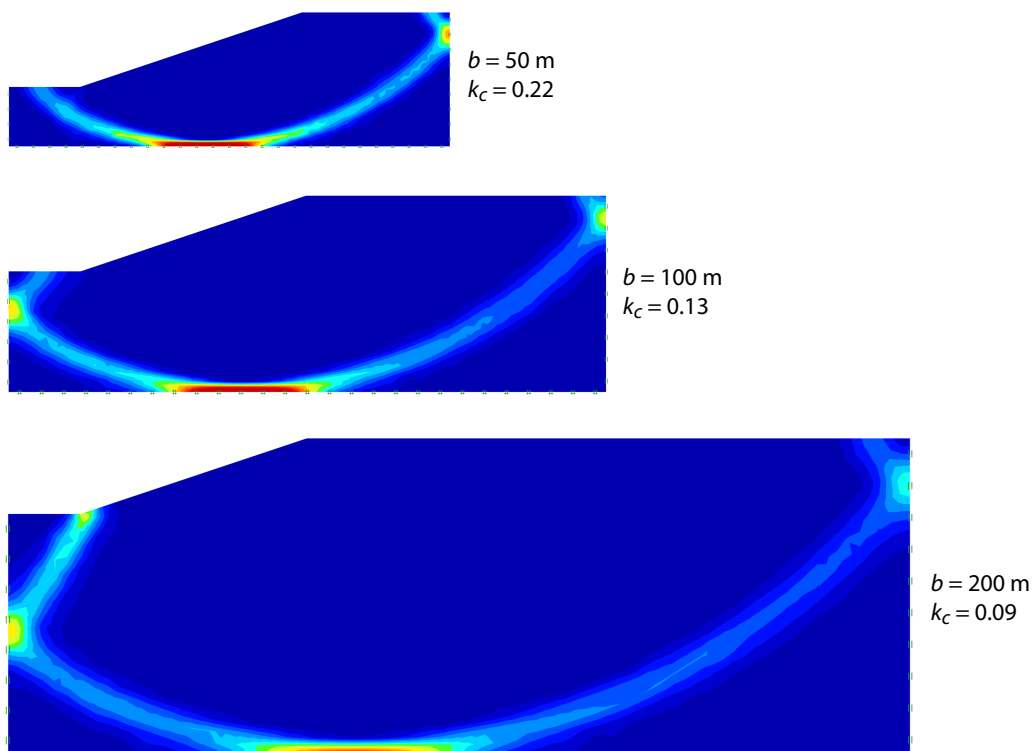


Figure 11.2: Effect of extending domain for a slope with constant undrained shear strength.

11.3 Short term conditions – effective stress analysis

A more reasonable result can be obtained either by assuming some increase of undrained shear strength with depth or by using an effective stress analysis, i.e. by using Time Scope = Short Term for a relevant material with Drainage = Drained/Undrained. If no From stage is specified, the initial stresses will be calculated automatically to comply with the initial stress conditions defined via the earth pressure coefficient K_0 .

Using these settings and assuming the soil is the default Stiff Clay-MC material, we obtain

$$0.183 \leq k_c \leq 0.188 \quad (11.2)$$

The collapse solution is shown in Figure 11.3.

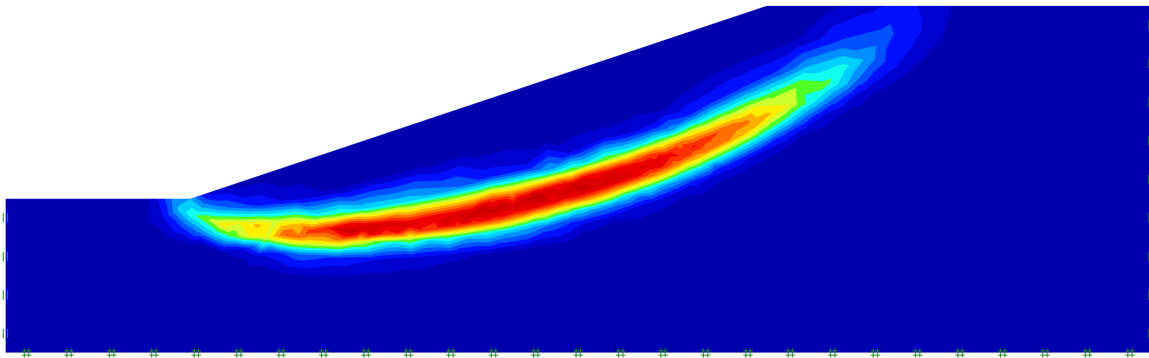


Figure 11.3: Short term collapse mechanism for slope of Stiff Clay-MC material.

12 STABILITY OF RETAINING WALL

This example concerns the stability of a retaining wall as shown in Figure 12.1. The soil is modeled using the default material Medium Sand-MC (a purely frictional Mohr-Coulomb material with a friction angle of 35° and a bulk unit weight of 16 kN/m^3). The retaining wall is modeled as a Rigid material with a unit weight of 22 kN/m^3 .

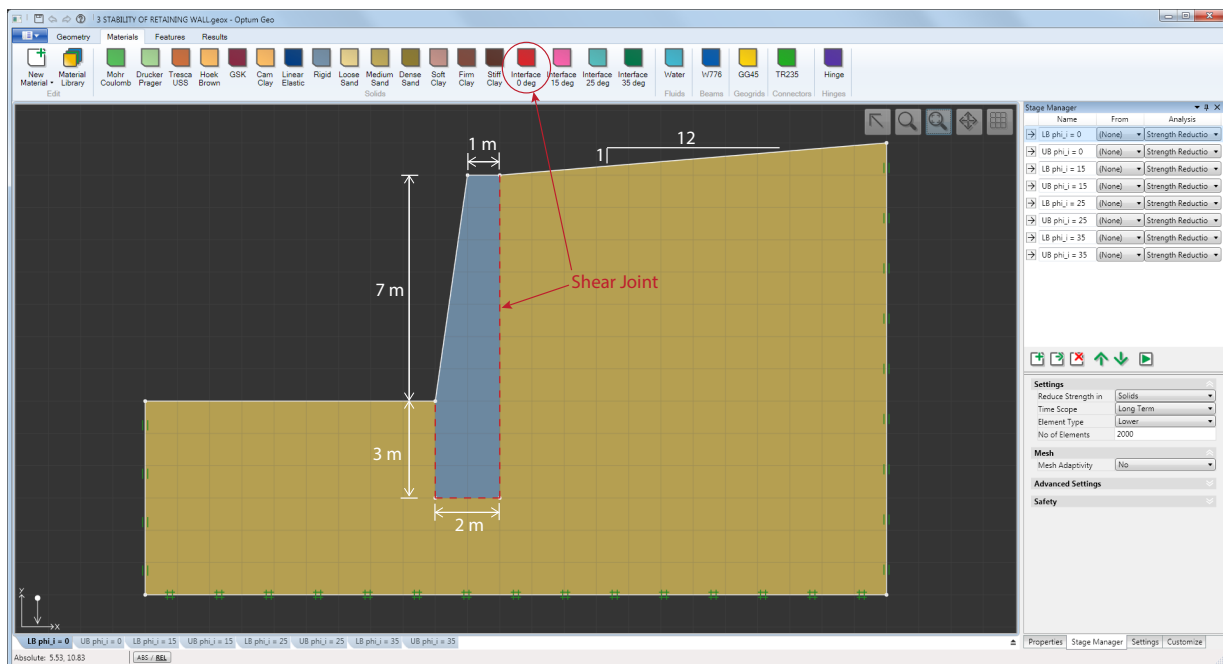


Figure 12.1: Retaining wall.

The interface between the soil and the wall is modeled by means of Shear Joints. These elements may be specified by using the Shear Joint tool under Features. Once a Shear Joint has been applied to an edge, its material may be changed either by drag-and-drop or by select-and-assign in the same way as for solid materials applied to surfaces. It should be borne in mind that materials are *global* in the sense that any modifications made in one stage affects all stages. In the following example where we wish to investigate the influence of the soil-wall friction coefficient, we thus need a number of independent materials. In Figure 12.1 these materials appear as 'Interface 0 deg', ..., 'Interface 35 deg'. These materials are of the same type as the soil, i.e. Solids of Material Type Mohr-Coulomb. Physically, a Shear Joint may be thought of as an infinitely thin layer of solid material. In OPTUM G2, they are modeled as such and all the parameters that are relevant to usual solids are thus relevant to Shear Joints (although some of them, unit weight for example, will have no influence on their physical behaviour).

As in the previous example the stability can be gauged either via Limit Analysis with Multiplier set to Gravity or via Strength Reduction analysis. Regarding the former option it is often observed for purely frictional materials that the gravity collapse multiplier is either zero (unstable) or infinite (stable). As such, little quantitative information is obtained. We therefore opt to use Strength Reduction analysis for this example.

Strength Reduction analysis essentially consists of a sequence of limit analyses with the strength being reduced or increased according to the last determined state until a reduction factor implying a collapse multiplier close to unity is obtained.

Since the Drainage condition of the Medium Sand is Always Drained, only Long Term analysis is relevant. In the following we compute upper and lower bounds on the strength reduction factor (the factor of safety, FS_s , introduced in the previous examples) using 2,000 elements without mesh adaptivity. Four different soil-wall interface angles are used: $\phi_i = 0, 15^\circ, 25^\circ$ and 35° . The results are shown in Table 12.1.

ϕ_i ($^\circ$)	Lower	Upper	Mean	Err ($\pm\%$)	Stability
35	1.29	1.48	1.38	6.9	Stable
25	1.22	1.35	1.28	5.1	Stable
15	1.09	1.22	1.15	5.6	Stable
0	0.83	0.95	0.89	6.7	Unstable

Table 12.1: Strength reduction factors (FS_s) for retaining wall as function of soil-wall interface friction angle using 2,000 elements.

We see that the soil-wall interface friction angle has a rather marked effect on the stability of the wall. Also, despite the relatively low number of elements, the gaps between the upper and lower bound solutions are quite moderate.

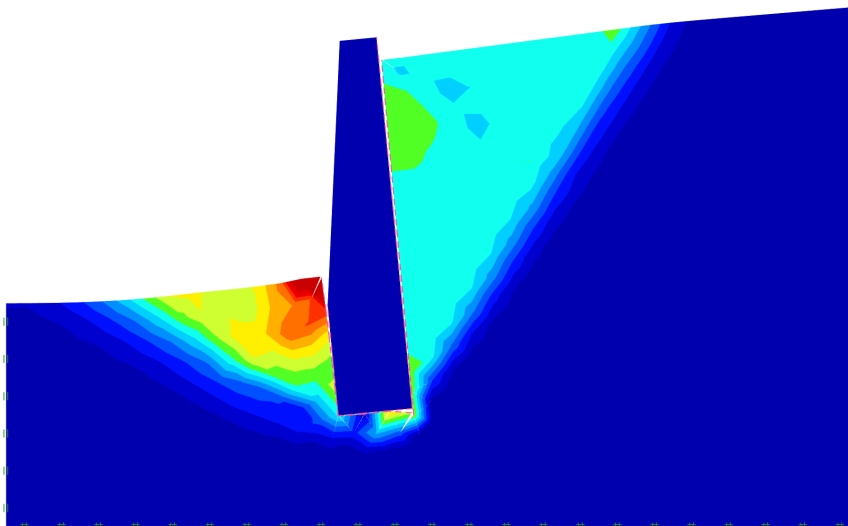


Figure 12.2: Collapse solution for retaining wall with $\phi_i = 15^\circ$ (upper bound) with intensity of plastic multiplier.

13 STABILITY OF STEM WALL

The next example is, on the surface, relatively uncomplicated and can be handled in much the same way as the previous example. It concerns the stability of a stem wall as shown in Figure 13.1. The soil consists of the default Medium Sand-MC material (a purely frictional Mohr-Coulomb material with $\phi = 35^\circ$) and the wall is modeled as Rigid material with a unit weight of 20 kN/m^3 .

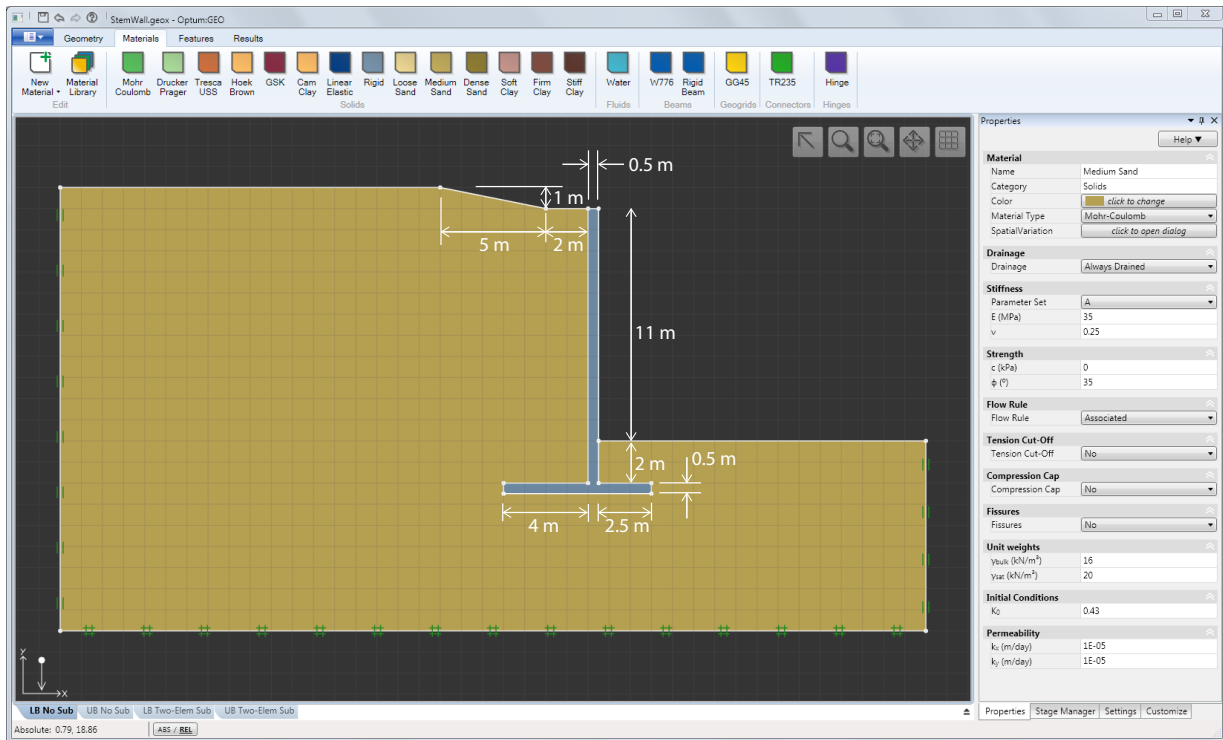


Figure 13.1: Stem wall.

As in the previous example, Strength Reduction analysis is used to determine the strength based factor of safety, FS_s . We begin by calculating upper and lower bounds for a fixed number of elements without using mesh adaptivity.

No Elem	No subdivision			Two-element subdivision		
	Lower	Upper	Mean±Err	Lower	Upper	Mean±Err
1,000	0.071	1.63	0.85 ± 0.78	1.45	1.63	1.54 ± 0.09
2,000	0.073	1.61	0.84 ± 0.77	1.45	1.59	1.52 ± 0.07
4,000	0.095	1.59	0.84 ± 0.75	1.45	1.57	1.51 ± 0.06
8,000	0.097	1.55	0.83 ± 0.73	1.46	1.55	1.51 ± 0.04
16,000	1.46	1.53	1.49 ± 0.04	1.46	1.53	1.49 ± 0.04

Table 13.1: Strength reduction factors for stem wall with and without subdivision.

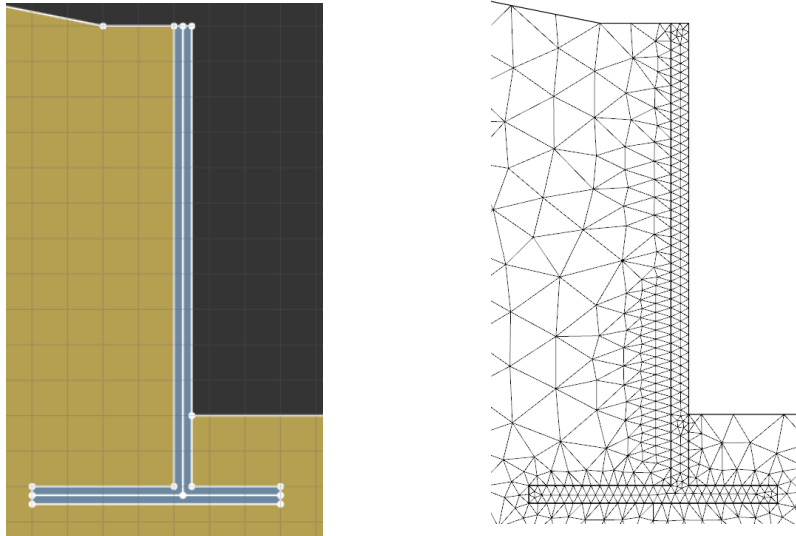


Figure 13.2: Manual subdivision of wall (left) and mesh resulting from specifying a minimum element size of 0.25 m for the wall (right).

The results, shown in left half of Table 13.1, reveal a very significant gap between the upper and lower bound solutions up to 16,000 elements where the gap suddenly reduces to an acceptable magnitude. More precisely, the lower bounds up to the largest number of elements considered are very poor and in all cases predict that the structure is far from being stable. The upper bounds, on the other hand, display a less erratic convergence behaviour.

On closer examination of the meshes produced in the various runs, it is observed that only a single layer of elements across the width of the wall is produced for the 1,000 to 8,000 element runs. When the number of elements reaches 16,000, two layers of elements are present in most of the wall. This phenomenon, that rigid domains may affect lower bound solutions adversely if they are not resolved properly, is well-known. Indeed, since the lower bound method requires that the stress fields satisfy the strong form of the equilibrium equations, all parts of the domain – rigid and well as deformable – must necessarily be represented with enough elements to accommodate the exact stress distribution to within a reasonable degree of accuracy. The upper bound method, on the other hand, balances the internal and external work rates and since no work is dissipated in rigid parts, their resolution is of less importance as clearly seen from the results.

In this case – and in general – the only remedy to improving the lower bound solutions is to use more elements to discretize the wall. With OPTUM G2, this is most easily done by subdividing the wall as shown in Figure 13.2. This subdivision guarantees at least two elements across the width of the wall and improves the results dramatically as summarized in Table 13.1. It should also be noted that mesh adaptivity will be of little utility unless the wall is subdivided so that a reasonable initial solution, on the basis of which the subsequent mesh is adapted, is available.

As an alternative to manual subdivision, the Mesh Size tool available under Features can be used to specify a minimum element length. As a general rule, the minimum element length should be one third to one half of the wall thickness. For the present example, a minimum element size of 0.25 m (half the wall thickness) leads to the desired layer of two elements across the wall thickness (see Figure 13.2) and thereby to satisfactory results.

14 STABILITY OF CANTILEVER SHEET PILE WALL

This example deals with a cantilever sheet pile wall supporting a wide excavation as shown in Figure 14.1. The soil is modeled using the default material Medium Sand (a purely frictional Mohr-Coulomb material with a friction angle of 35°). The sheet pile wall is modeled using Plate elements. These elements couple with the solid elements used in the soil domain. In the following example, we use the default P800 plate.

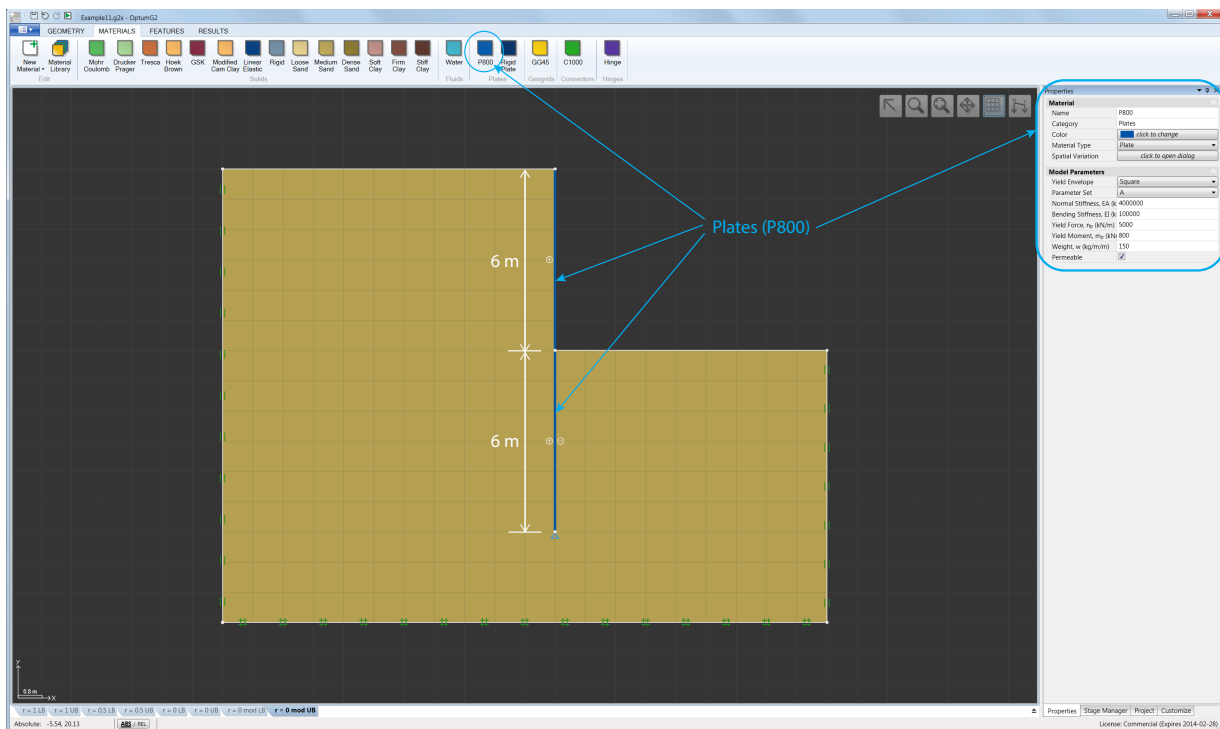


Figure 14.1: Cantilever sheet pile wall.

Plate elements may be specified in three different ways:

1. By selecting a segment and then selecting the relevant Plate material from the Materials ribbon.
2. By drag-and-drop of a Plates material from the Materials ribbon onto a segment.
3. By using the Plate tool available in the Features ribbon. In that case, the material assigned is the first material from the left in the Beams category under the Materials ribbon ('P800' by default).

When Plates are assigned to segments that are part of domains to which solid materials have already been assigned, Plate interfaces are automatically generated. These appear as \oplus or \ominus and can be modified by selecting a given Plate through the property window (see Figure 14.1). Besides assigning arbitrary Solid materials to the interfaces, it is possible to specify a Reduction Factor such that the interface strengths are reduced as compared to those of the parent material. For the Mohr-Coulomb model, the reduced interface strengths, c_i and ϕ_i , are given by

$$c_i = rc, \quad \phi_i = r\phi \quad (14.1)$$

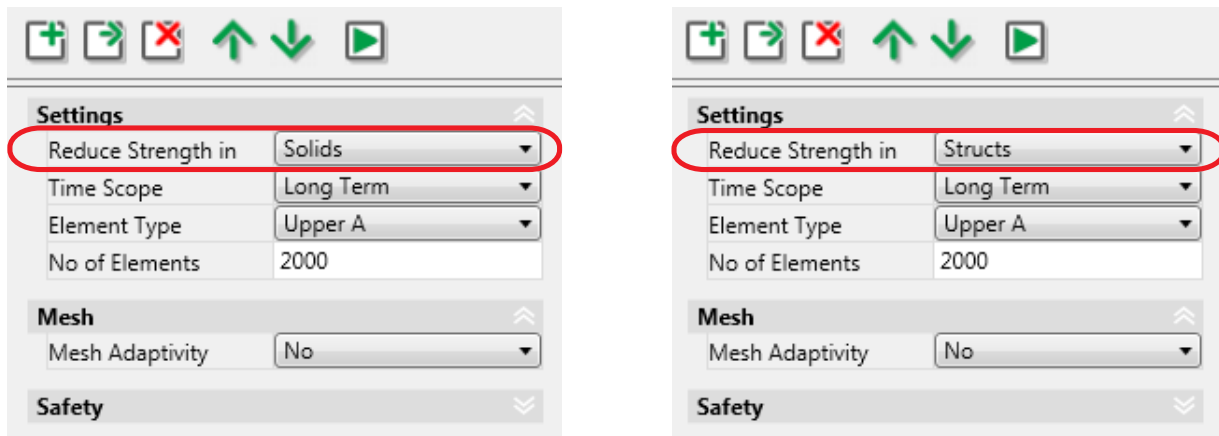


Figure 14.2: Stage settings for Strength Reduction with respect to solids (left) and structural elements (right).

where c and ϕ are the strengths of the parent Solid material and r is the Reduction Factor. Alternatively, the interface strength reduction can be applied to c and $\tan \phi$ by changing the setting under Project/Physical Parameters.

Since the Drainage condition of the Loose Sand is Always Drained, only Long Term analysis is relevant. In the following we compute upper and lower bounds on the strength reduction factor (the factor of safety, FS_s , introduced previously) using 2,000 elements without mesh adaptivity. Three different soil-wall strength Reduction Factors are used: $r = 1$ (no reduction, perfectly rough wall), $r = 0.5$, and $r = 0$ (no strength, perfectly smooth wall).

As in the previous example, the stability of the structure is best evaluated by means of Strength Reduction analysis. That is, while Limit Analysis in principle is applicable, for purely frictional materials there is a tendency for the collapse multipliers to either attain very small values (often zero) for structures that are unstable and very large values (often infinity) for structures that are stable. As such, little quantitative information about the proximity to failure is obtained.

Concerning the stage settings, Strength Reduction analysis offers two different approaches:

1. Either the strengths of the solid domains (the soil in this example) are reduced until the structure is at a state of incipient collapse. All other strengths are kept constant.
2. Or the strengths of the structural elements (Plates in this example) are reduced until the structure is at a state of incipient collapse. All other strengths are kept constant.

Either of the two options can be specified via the Settings category in the lower half of the Stage Manager windows (see Figure 14.2).

14.1 Strength Reduction – Solids

We first use the Reduce Strength in Solids approach. The results are shown in Table 14.1.

r	Lower	Upper	Mean	Err \pm
1.00	1.58	1.72	1.65	0.07
0.50	1.51	1.58	1.54	0.03
0.00	0.00	0.00	0.00	0.00
0.00 ^{*)}	1.24	1.29	1.26	0.02

Table 14.1: Strength reduction factors (Solids) for cantilever sheet pile wall as function of soil-wall interface Reduction Factor, $r = \tan \phi_i / \tan \phi$, using 2,000 elements. ^{*)}Sheet pile wall supported vertically.

We see that the soil-wall interface strength has some influence on the overall Factor of Safety. Moreover, the error in the estimated Factor of Safety (mean value between the upper and lower bounds) is in all cases below 5%.

The case of $r = 0$ (perfectly smooth wall) is somewhat pathological. In this case there is no strength available to sustain the weight of the wall vertically. As such, the Factor of Safety is zero. However, assuming that some vertical resistance is available even for a perfectly smooth wall – and accounting for this via a vertical support at the bottom of the wall – gives a finite Factor of Safety indicating stability.

Some collapse solutions are shown in Figure (14.3) where the effects of interface friction are clearly seen.

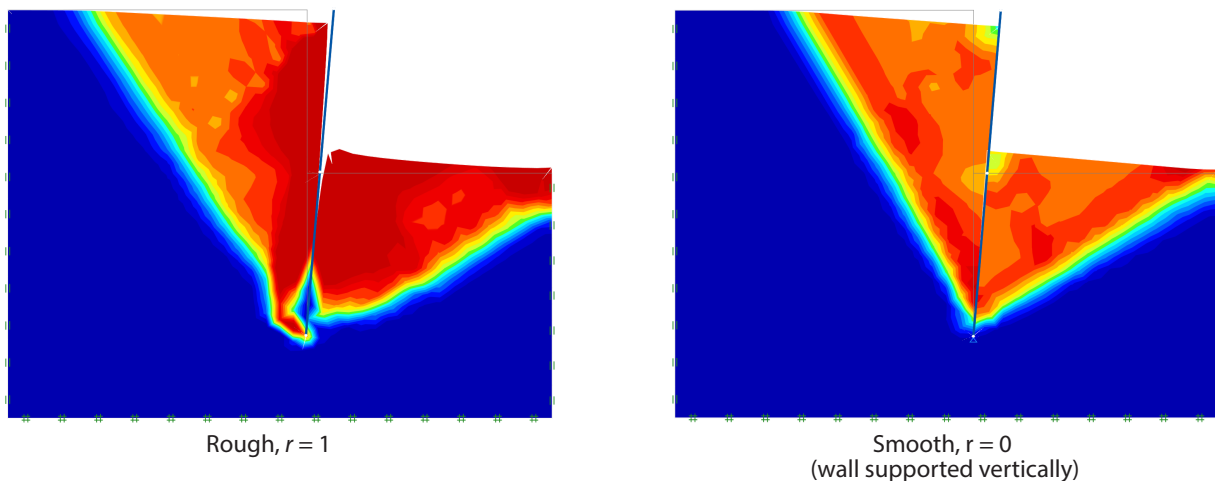


Figure 14.3: Collapse solutions for sheet pile wall (upper bound) with intensity of plastic multiplier.

14.2 Strength Reduction – Structs

Next, we use the Reduce Strength in Structs approach. The results are shown in Table 14.2. We see that the strength reduction factors (or factors of safety) follow the same trend as in for the Reduce

Strength in Solids approach though the factors are rather larger. These results indicate that the wall strength is not fully utilized and that the wall dimensions could be reduced substantially without affecting the overall stability of the system.

r	Lower	Upper	Mean	Err \pm
1.00	3.91	4.95	4.43	0.52
0.50	3.63	4.07	3.85	0.22
0.00	0.00	0.00	0.00	0.00
0.00 ^{*)}	2.72	2.82	2.77	0.05

Table 14.2: Strength reduction factors (Structs) for cantilever sheet pile wall as function of soil-wall interface Reduction Factor, $r = \tan \phi_i / \tan \phi$, using 2,000 elements. ^{*)}Sheet pile wall supported vertically.

In summary, the system may fail in two different ways: either due to failure of the soil or due to failure of the wall. The Reduce Strength in Solids option picks up the former type of failure while Reduced Strength in Structs picks up the latter. In general, it is recommended that both types of failure are considered. In particular, it may be quite unsafe to rely only on the Reduce Strength in Structs option.

15 STABILITY OF STRUTTED SHEET PILE WALL

This example deals with a sheet pile wall as shown in Figure 15.1. The soil is modeled using the default material Loose Sand-MC (a purely frictional Mohr-Coulomb material with a friction angle of 30°). The wall is supported by a strut modeled as a Fixed End Anchor. These elements are equivalent one-dimensional bar elements and are assigned using the Fixed End Anchor tool from the Features ribbon. The materials that can be assigned to Fixed End Anchors are those of the Connector type. In the present case the default Connector materials C1000 (yield force $n_0 = 1,000 \text{ kN/m}$) is used.

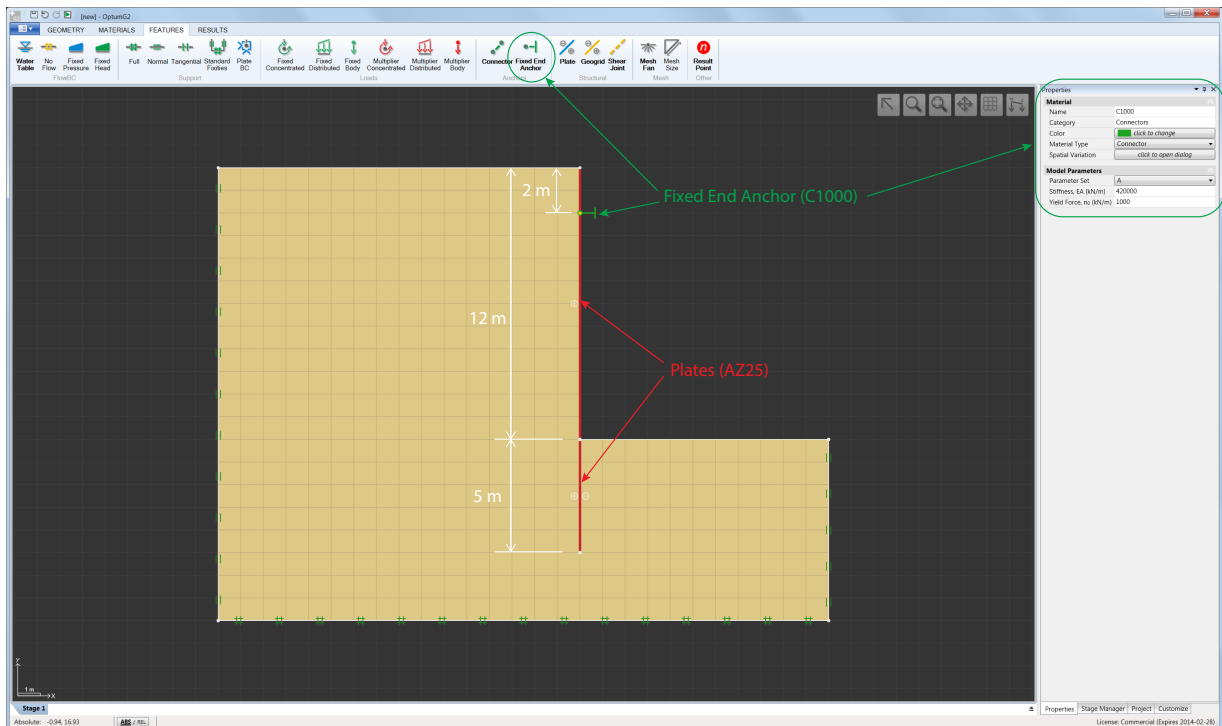


Figure 15.1: Strutted sheet pile wall. The upper strut (Fixed End Anchor) is selected and its properties are shown in the window on the right.

The sheet pile wall is modeled using the AZ25 beam from the Sheet Piles materials library (see Figure 15.2). This profile has a yield moment of 775.71 kNm/m . The soil-wall interface strength reduction factor is $r = 0.67$ [meaning that the interface friction angle is $\phi_i = \arctan(0.67 \times \tan \phi) = 21.1^\circ$].

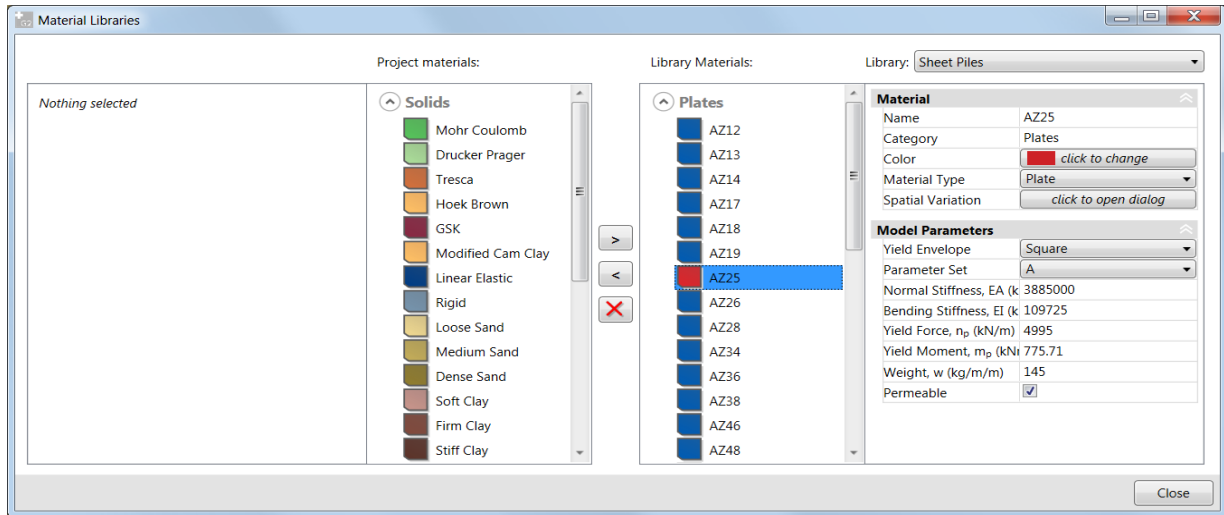


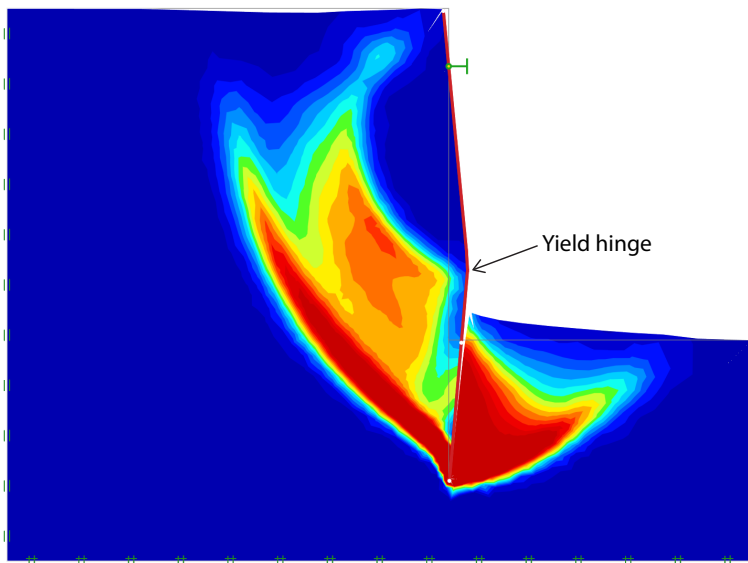
Figure 15.2: Sheet Piles material library with AZ25 selected.

The analyses are carried out using Strength Reduction analysis, first with the Reduce Strength in Solids approach and then with the Reduce Strength in Struts approach. In the latter case, both the strength of the wall and of the struts are reduced (see the previous example for details). Upper and lower bounds are computed using 2,000 elements with 3 adaptivity iterations. The results of the analyses are:

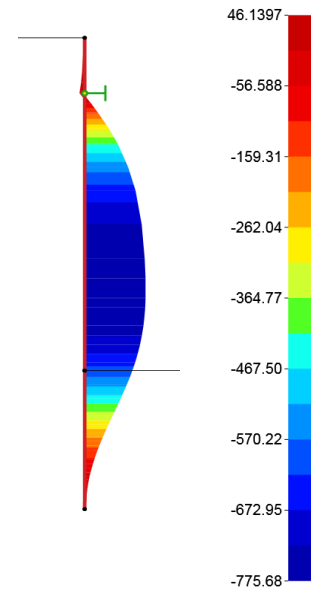
$$\begin{aligned}
 \text{Reduce Strength in Solids:} & \quad FS = 1.39 \pm 0.01 \\
 \text{Reduce Strength in Struts:} & \quad FS = 3.15 \pm 0.07
 \end{aligned}
 \tag{15.1}$$

As in the previous example, the Reduce Strength in Struts approach gives a rather more flattering assessment of the safety of the structure. This differences in factors of safety between the two approaches also manifest themselves in the associated collapse solutions as shown in Figure 15.3. We here see that while the Solids approach implies that a single yield hinge is formed, the Struts approach gives rise to a rather different collapse mechanism involving two yield hinges. The moment distributions confirm these observations: in the Solids case the maximum moment is approximately 775 kNm/m corresponding to full utilization of the wall strength. Conversely, in the Struts approach the moment at collapse is about 241 kNm/m such that with a strength reduction factor of about 3.15, the wall is at the point of yielding ($775/3.15 \simeq 241$).

Reduce Strength in Solids

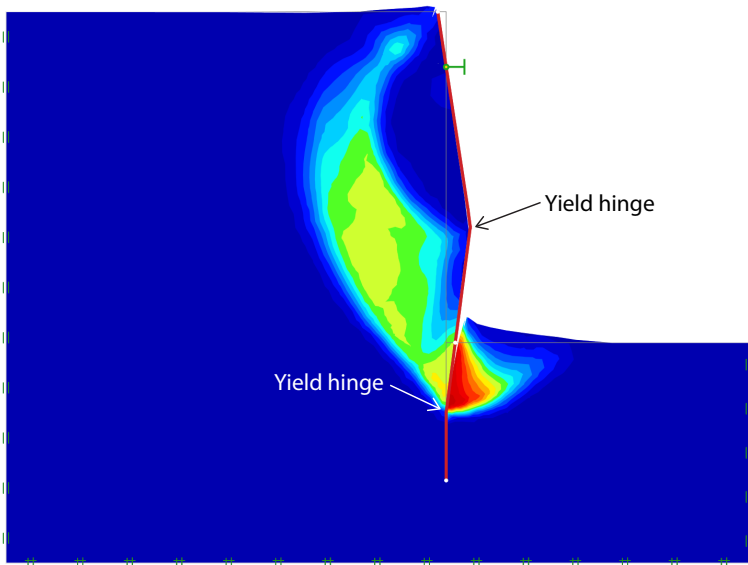


Collapse mechanism and shear dissipation field

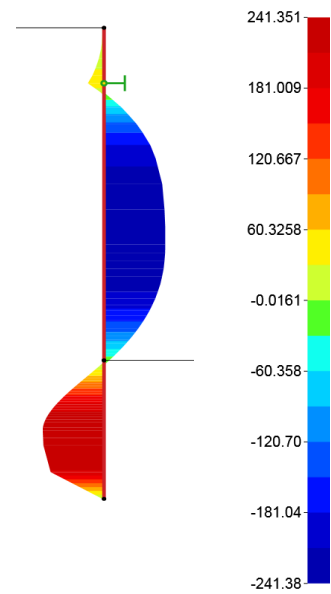


Moment distribution

Reduce Strength in Struts



Collapse mechanism and shear dissipation field



Moment distribution

Figure 15.3: Collapse solutions and moment distributions (Upper).

16 STABILITY OF ANCHORED SHEET PILE WALL

This example deals with a sheet pile wall as shown in Figure 16.1. The soil is modeled using the default material Medium Sand-MC (a purely frictional Mohr-Coulomb material with a friction angle of 35°). The wall is modeled using Plate elements with the default P800 profile. The anchoring system is modeled by a combination of Connectors (which do not interact with the soil) and Geogrids (which do interact with the soil and are used to account for grouting). It is important, especially when using elements of type Lower, that the Geogrid and Connector elements are perfectly aligned. Any misalignment will lead to inferior results (though still rigorously bounded if the elements Lower and Upper/B are used).

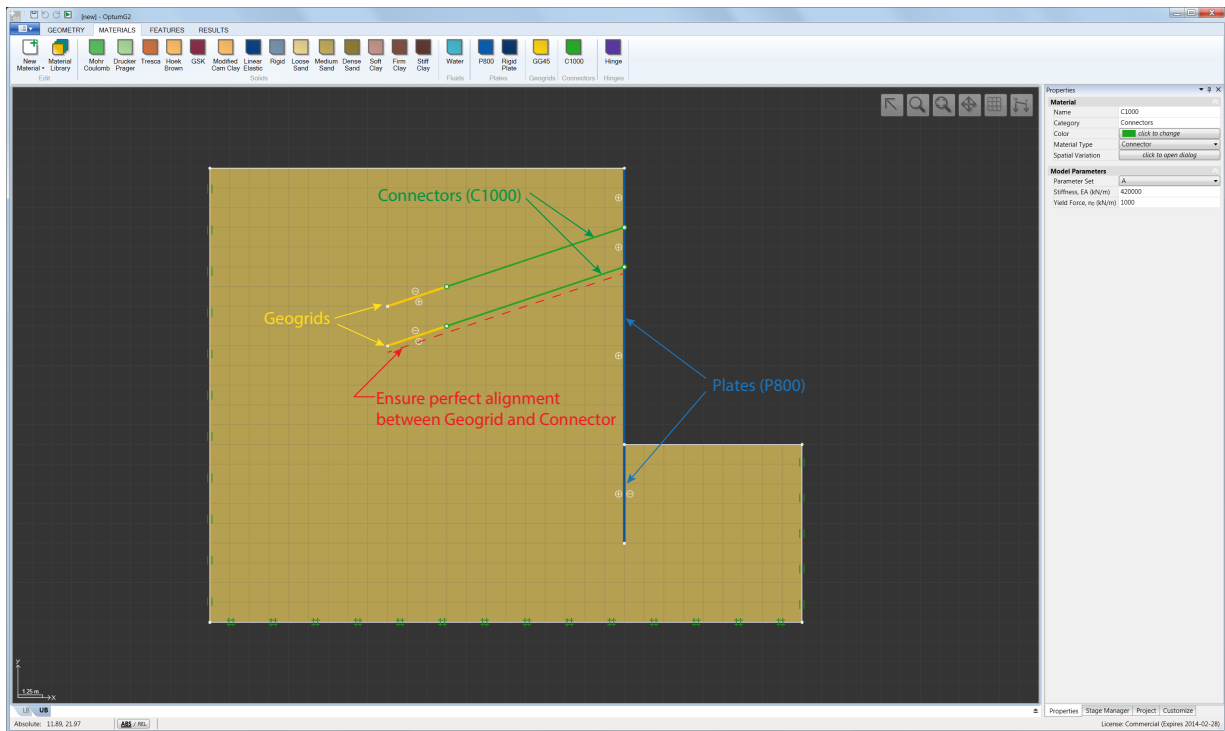


Figure 16.1: Anchored sheet pile wall.

As in the previous examples, the stability of the structure is gauged via Strength Reduction analysis using the Reduce Strength in Solids approach. Upper and lower bounds are calculated using 2,000 elements without mesh adaptivity to obtain an estimate of the factor of safety given by

$$FS = 1.32 \pm 0.05 \quad (16.1)$$

The upper bound collapse mechanism is shown in Figure 16.2. As seen, the system fails by a combination of wall yielding and the Geogrids being pulled out.

In the above analysis, the Square yield criterion is used. This means that the moments and normal forces in the wall are limited independently according to:

$$\left| \frac{m}{m_p} \right| \leq 1, \quad \left| \frac{n}{n_p} \right| \leq 1 \quad (16.2)$$

where m_p and n_p are the yield moments and forces respectively.

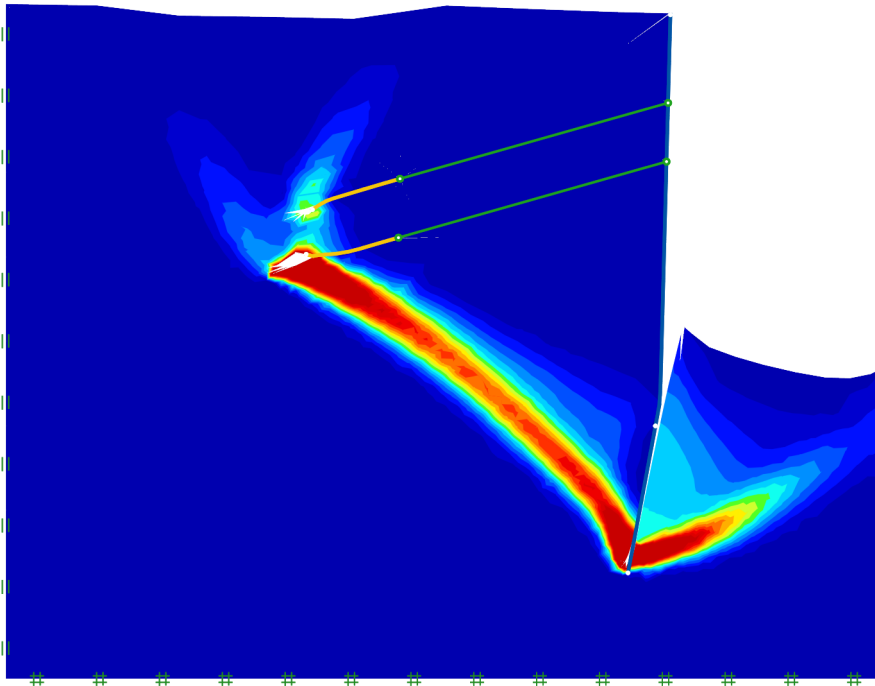


Figure 16.2: Collapse solution (Upper).

A more conservative estimate of the strength of the wall may be realized by use of the Diamond yield criterion:

$$\left| \frac{m}{m_p} \right| + \left| \frac{n}{n_p} \right| \leq 1 \quad (16.3)$$

The two yield criteria are shown in Figure 16.3.

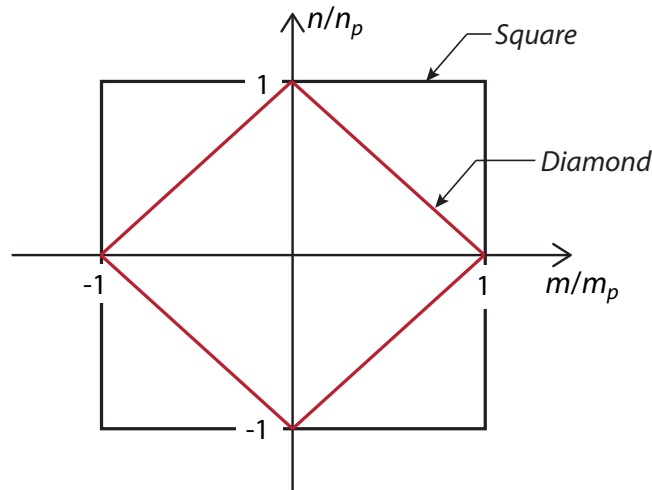


Figure 16.3: Square and Diamond yield criteria.

However, in this case, the difference in results between the two yield criteria is very minor:

$$\begin{aligned} \text{Square:} & \quad 1.274 \leq \text{FS} \leq 1.377 \\ \text{Diamond:} & \quad 1.271 \leq \text{FS} \leq 1.377 \end{aligned} \quad (16.4)$$

17 SHEET PILE WALL SUBJECTED TO SEEPAGE PRESSURES

This example considers the effects of seepage pressures on a sheet pile wall as shown in Figure 17.1. The wall, which is impermeable, supports a 10 m excavation with a variable water depth, d_w . Due to the difference in head between the left and right hand sides of the wall (for $d_w < 10$ m), a flow will occur around the tip of the wall and into the excavation (see Figure 17.2).

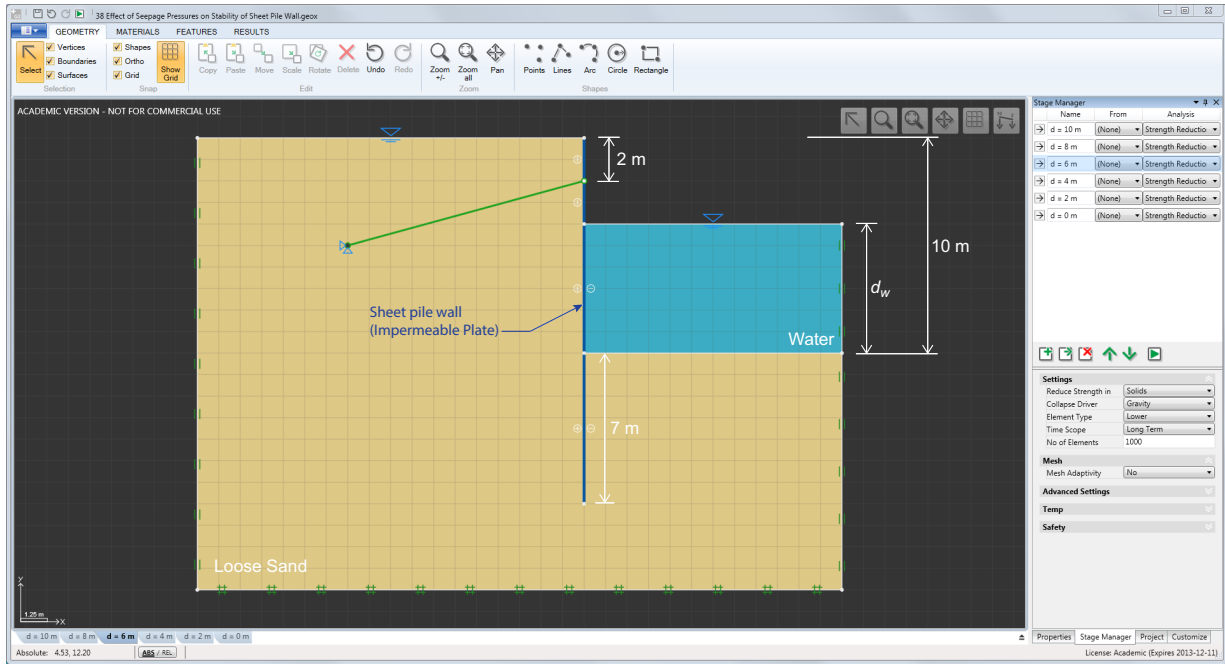


Figure 17.1: Sheet pile wall subjected to seepage pressures.

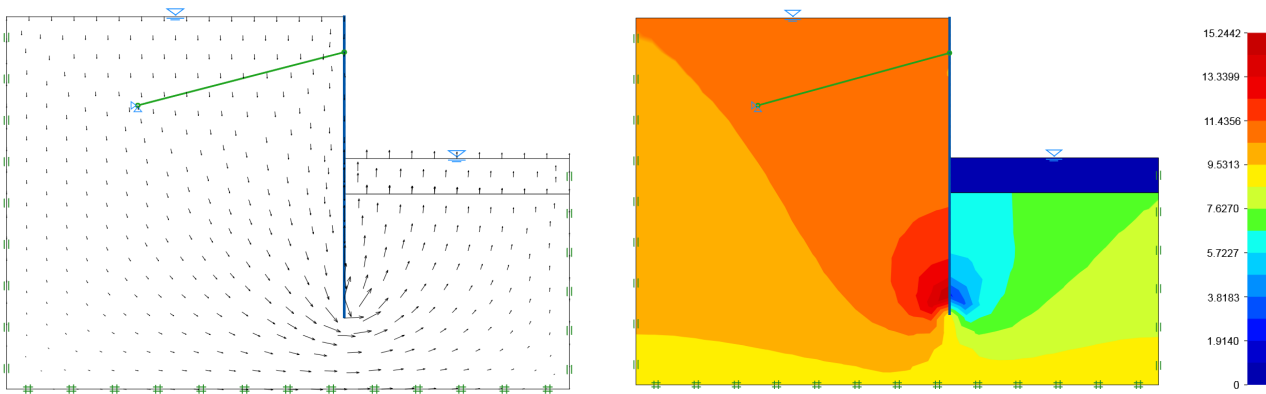


Figure 17.2: Flow vectors and effective vertical unit weight, γ'_y (kN/m³), for $d_w = 2$ m.

A key quantity of interest are the effective unit weights: (available under Pore Pressures in the Results ribbon):

$$\gamma'_x = -\frac{\partial p_s}{\partial x}, \quad \gamma'_y = \gamma_{sat} - \frac{\partial p_s}{\partial y} \tag{17.1}$$

For the present problem, the vertical component is of particular interest. With a saturated unit weight of 19 kN/m³, the effective unit weight corresponding to a hydrostatic pore pressure distribution is $\gamma'_y = 9.2$ kN/m³. From Figure (17.2), we see an increase of effective unit weight from about

11 kN/m³ on the upper half of the wall to a maximum of about 15 kN/m³ close to the tip. Conversely, the effective unit weight decreases on the right hand side of the wall to a minimum value of about 3 kN/m³. At the bottom of the excavation, the effective unit weight is about 6 kN/m³ meaning that there is no immediate danger of piping as would be implied by $\gamma'_y \leq 0$.

The stability evaluation proceeds by running Strength Reduction analyses for different water depths, d_w . In this example, we have used fairly coarse meshes comprising 1,000 elements (Lower or Upper). The results are shown in Table 17.1. As expected, we see a gradual decrease in the factor of safety as the water level in the excavation decreases. For $d_w = 0$, the system is very close to the limit of stability. Indeed, the lower bound analysis suggests instability while the upper bound analysis suggests the opposite. Whether or not the system is stable or unstable can be settled by increasing the number of elements and possibly using mesh adaptivity.

d_w (m)	Lower	Upper	Mean	Error (\pm)
10	2.02	2.23	2.12	0.11
8	1.66	1.83	1.75	0.09
6	1.42	1.57	1.50	0.08
4	1.24	1.37	1.30	0.07
2	1.07	1.17	1.12	0.05
0	0.96	1.05	1.00	0.05

Table 17.1: Strength reduction factors, FS, for different water levels, d_w .

It is interesting to note that the mode of failure changes fundamentally at a water level of around 5 m. For higher water levels, the moments in the wall are very limited and the mode of failure involves a rigid rotation of the wall about the connector point. As the water level decreases, the wall strength becomes fully utilized and a yield hinge forms approximately halfway down the wall. Some examples are shown in Figure 17.3.

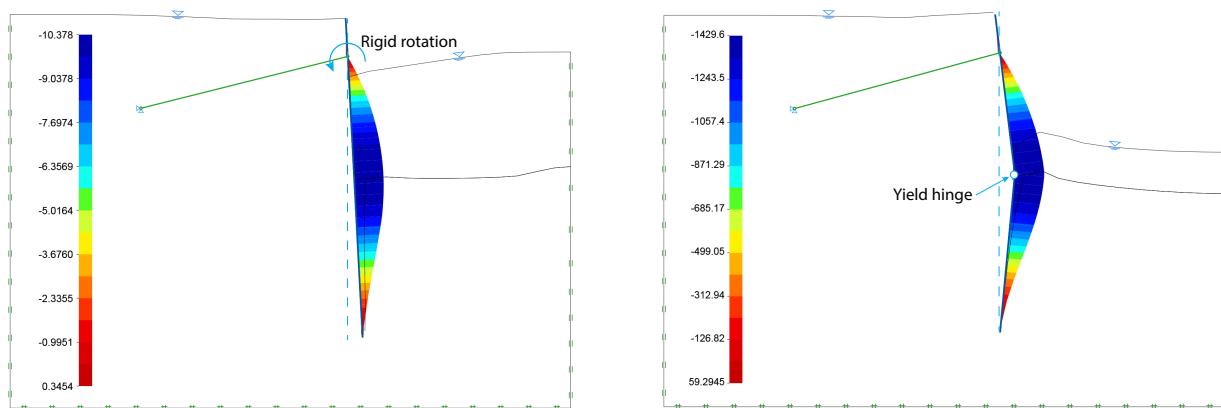


Figure 17.3: Bending moments (kNm/m) and modes of failure for high (left) and low (right) water levels.

18 ACCRETIONARY WEDGE

This example is concerned with the maximum force that can be exerted on a wedge as shown in Figure 18.1. This is a classical problem in structural geology where it has been studied quite extensively – analytically, numerically and experimentally (see Souloumiac et al. 2010, and references therein).

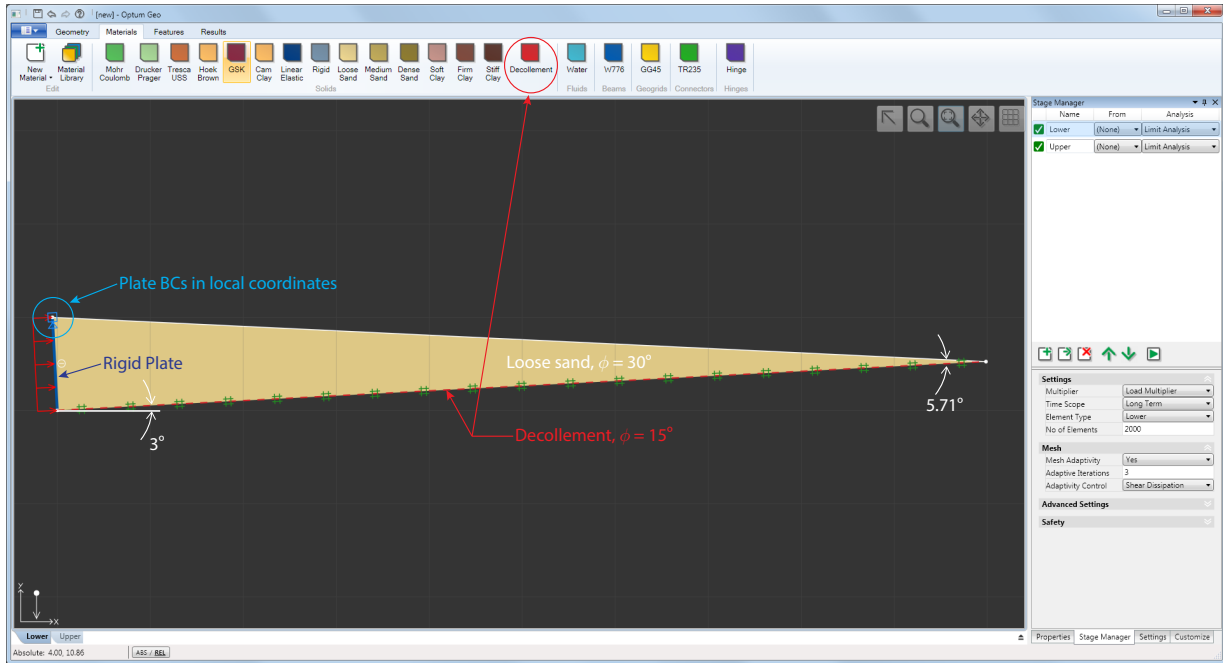


Figure 18.1: Accretionary wedge.

Upper and lower bounds on the maximum tectonic force are computed using the 2,000 elements and 3 adaptivity steps. The result in terms of the collapse multiplier is:

$$24.44 \leq \alpha \leq 24.57 \tag{18.1}$$

Even though the exact value of the maximum force usually is of minor interest in structural geology applications, the very tight bounds obtained do indicate that the calculated solutions are close to the

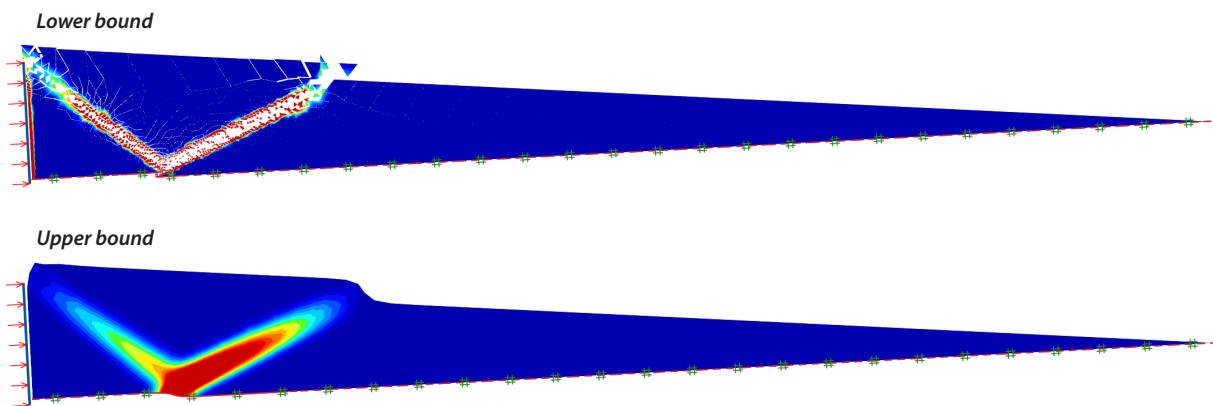


Figure 18.2: Lower and upper bound collapse solutions with intensity of shear dissipation.

exact one, both in terms of the force and in terms of the collapse kinematics.

The collapse solutions are shown in Figure 18.2. Both the upper and lower bound calculations reveal the characteristic V-shaped failure mechanism observed by many others in both calculations and experiments. We note that the lower bound solution tends to be somewhat more localized which is quite common.

Also shown in the figures is the intensity of plastic shear dissipation. This quantity is defined as:

$$D_s = \boldsymbol{\sigma}_s^T \dot{\boldsymbol{\epsilon}}_s^p \quad (18.2)$$

where

$$\boldsymbol{\sigma}_s = \boldsymbol{\sigma} - \mathbf{m}p, \quad \dot{\boldsymbol{\epsilon}}_s^p = \boldsymbol{\epsilon} - \frac{1}{3}\mathbf{m}\dot{\epsilon}_v^p \quad (18.3)$$

with $p = \frac{1}{3}\mathbf{m}^T\boldsymbol{\sigma}$ and $\dot{\epsilon}_v^p = \mathbf{m}^T\dot{\boldsymbol{\epsilon}}^p$ being the mean stress and volumetric plastic strain rates respectively and $\mathbf{m} = (1, 1, 1, 0, 0, 0)^T$. The shear dissipation is particularly relevant for purely frictional materials where the total dissipation, $D = \boldsymbol{\sigma}^T\dot{\boldsymbol{\epsilon}}_v^p$, is zero and where the plastic multiplier field may be somewhat unreliable, especially in lower bound calculations. Hence, the shear dissipation is also the preferred control variable for mesh adaptivity.

19 FISSURED MOHR-COULOMB SLOPE

This example concerns the stability of a slope of fissured Mohr-Coulomb material as shown in Figure 19.1. We here use the default material Stiff Clay-MC ($c = 20 \text{ kPa}$, $\phi = 22^\circ$) as the base material. A single fissure plane is then added via the property window on the right at an angle of $\alpha = 45^\circ$ (see Figure 19.1). The fissure plane has Mohr-Coulomb parameters $c = 0$ and $\phi = 22^\circ$.

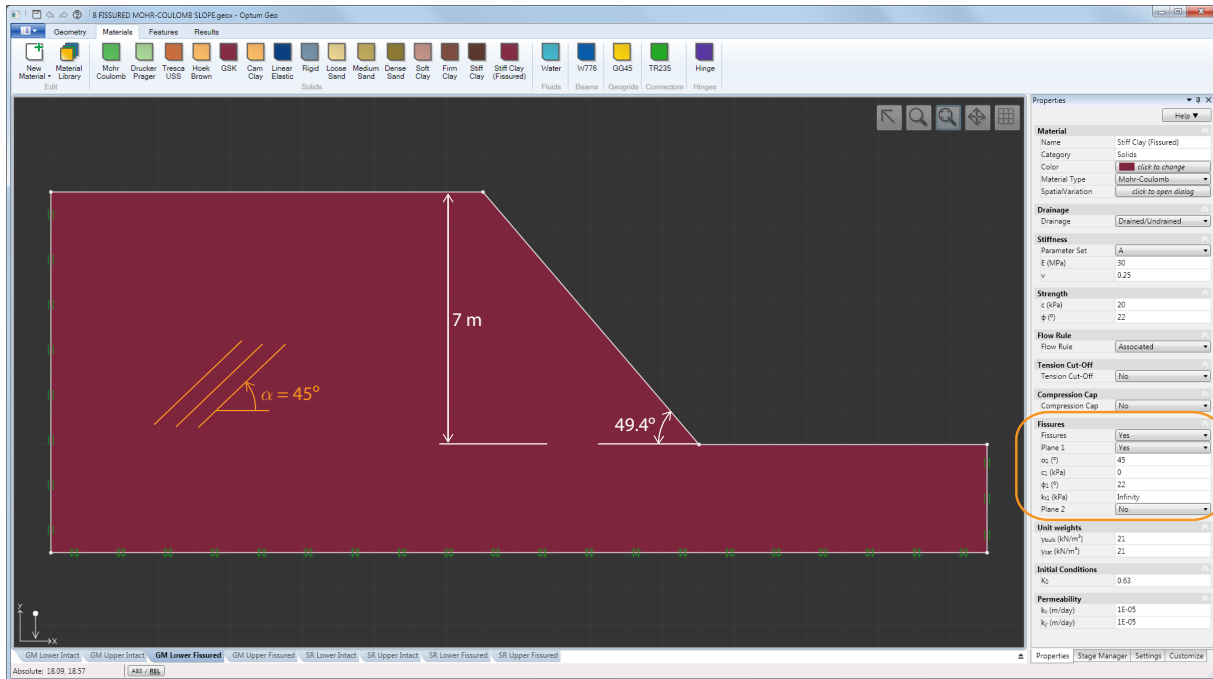


Figure 19.1: Slope of fissured Mohr-Coulomb material.

To investigate the effect of the fissure plane, we conduct both Gravity Multiplier Limit Analysis and Strength Reduction for the intact Stiff Clay material and for the material with the fissures included. Only Long Term analysis is considered. Using 2,000 elements and 3 adaptivity iterations, the gravity based factor of safety is determined as:

$$\begin{aligned} \text{Intact:} \quad & 2.07 \leq FS_g \leq 2.13 \quad \text{or:} \quad FS_g = 2.10 \pm 0.03 \\ \text{Fissured:} \quad & 1.52 \leq FS_g \leq 1.64 \quad \text{or:} \quad FS_g = 1.58 \pm 0.06 \end{aligned} \tag{19.1}$$

The corresponding collapse solutions are shown in Figure 19.2 where the effects of the fissures are quite evident, especially on the upper half of the slope.

Next, strength based factors of safety are calculated using Strength Reduction analysis. In this analysis, the strength parameters of both the parent material and of the fissures are reduced to obtain a state of incipient collapse. The results are:

$$\begin{aligned} \text{Intact:} \quad & 1.46 \leq FS_s \leq 1.50 \quad \text{or:} \quad FS_s = 1.48 \pm 0.02 \\ \text{Fissured:} \quad & 1.17 \leq FS_s \leq 1.21 \quad \text{or:} \quad FS_s = 1.19 \pm 0.02 \end{aligned} \tag{19.2}$$

Again, we see a drop in strength for the fissured material and, as is usually the case, the strength based factors of safety are somewhat lower than the gravity based factors of safety.

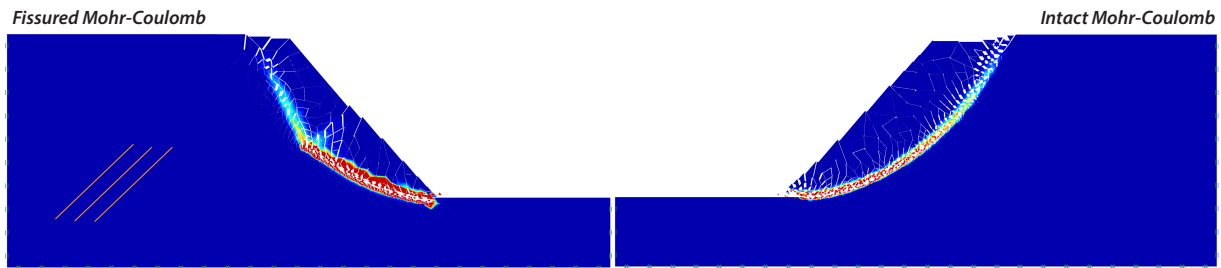


Figure 19.2: Collapse solutions and intensity of shear dissipation.

Finally, we vary the angle of the failure plane and calculate strength based factors of safety. The results of this analysis are shown in Figure 19.3. We conclude that the slope is stable in the range $-15^\circ \leq \alpha \leq 55^\circ$.

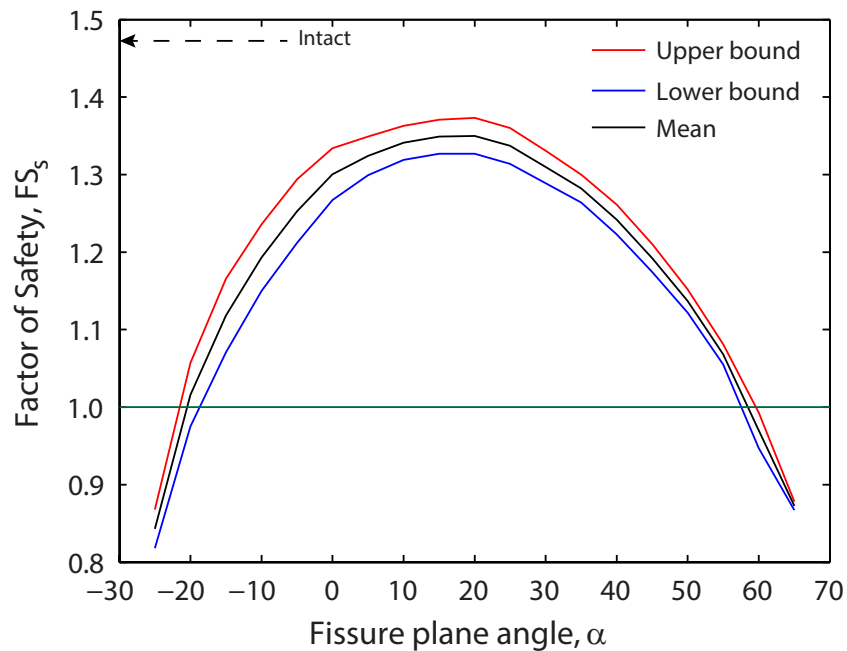


Figure 19.3: Variation of strength based factor of safety with fissure plane angle.

20 HOEK-BROWN SLOPE 1

The Hoek-Brown failure criterion is commonly used to assess the strength and stability of fractured rock masses. In this example, we consider the stability of a slope of Hoek-Brown material as shown in Figure 20.1. To validate the results, two procedures for approximating the Hoek-Brown criterion by an equivalent Mohr-Coulomb criterion are discussed.

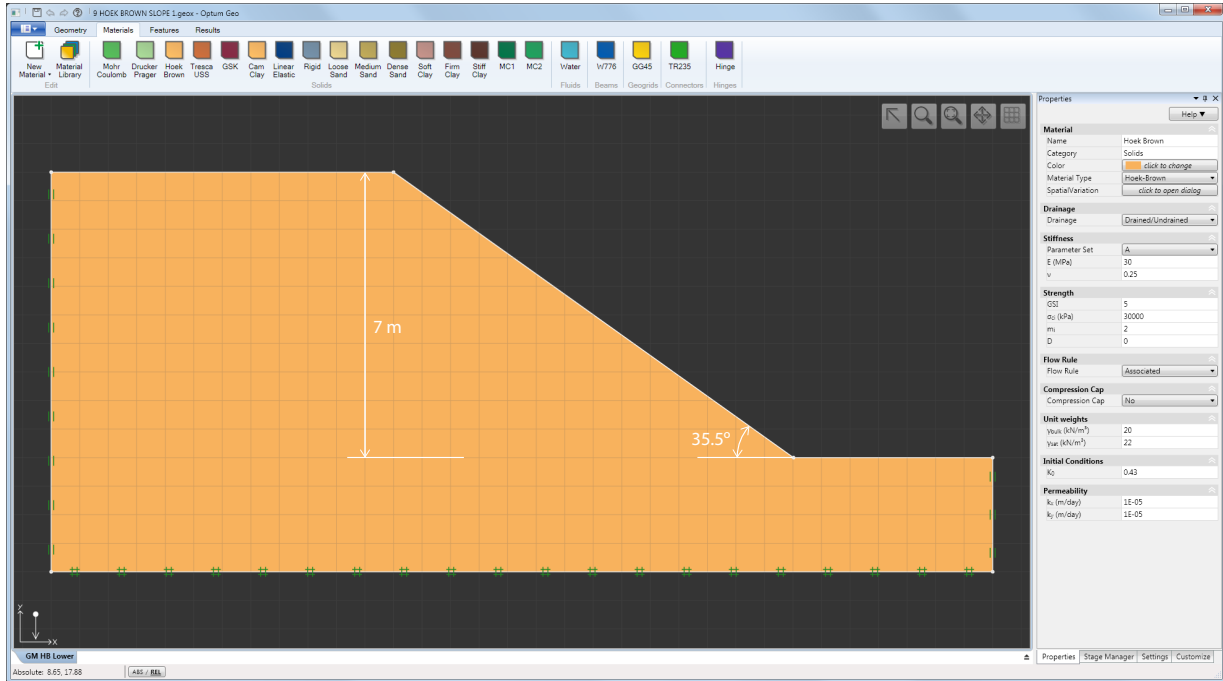


Figure 20.1: Slope of Hoek-Brown material.

The curved Hoek-Brown yield envelope may be approximated by the Mohr-Coulomb model using the standard Mohr-Coulomb cone augmented with a tension-cutoff following the approach described by Hoek (2007).

Firstly, with reference to the Mohr-Coulomb model implemented in OPTUM G2, the tension cut-off parameters are given by

- $k_t = \frac{5\sigma_{ci}}{m_b}$ [kPa]
- $\phi_t = 90^\circ$

Secondly, a best-fit Mohr-Coulomb line in the interval between $-\sigma_t \leq -\sigma_3 \leq \sigma_{3,max}$, leads to the following Mohr-Coulomb parameters:

- $\phi = \arcsin \left[\frac{6am_b(s + m_b\sigma_{3n})^{a-1}}{2(1+a)(2+a) + 6am_b(s + m_b\sigma_{3n})^{a-1}} \right] [^\circ]$
- $c = \frac{\sigma_{ci}[(1+2a)s + (1-a)m_b\sigma_{3n}](s + m_b\sigma_{3n})^{a-1}}{(1+a)(2+a)\sqrt{1 + \frac{6am_b(s + m_b\sigma_{3n})^{a-1}}{(1+a)(2+a)}}}$ [kPa]

where $\sigma_{3n} = \sigma_{3,\max}/\sigma_{ci}$ with $\sigma_{3,\max}$ being positive in compression. In these approximations, the key question is how $\sigma_{3,\max}$ should be chosen. In the following, this question is addressed with respect to two different types of analysis: Gravity Multiplier Limit Analysis and Strength Reduction analysis.

20.1 Gravity Multiplier Limit Analysis

First, the stability of the slope is assessed by means of Limit Analysis with Multiplier = Gravity (Settings in the lower half of the Stage Manager window). We use 2,000 elements and 3 adaptivity iterations to calculate upper and lower bounds of the gravity based factor of safety. The results are:

$$3.05 \leq FS_g \leq 3.14 \quad \text{or:} \quad FS_g = 3.09 \pm 0.05 \quad (20.1)$$

The collapse solution is shown in Figure 20.2. We see that the collapse mechanism is given in terms of a rather well defined curved slip line extending from the toe of the slope to the upper surface.

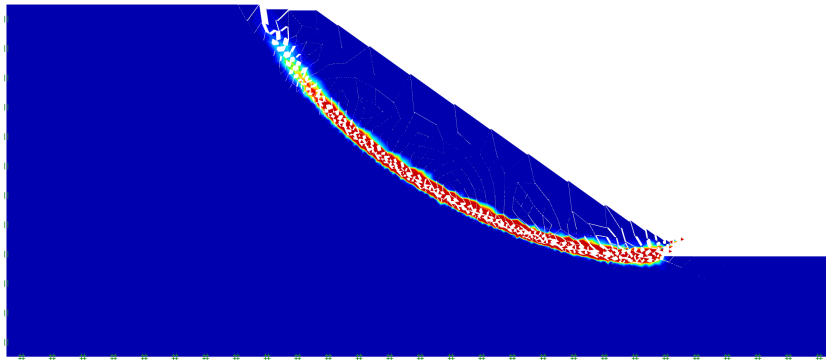


Figure 20.2: Collapse mechanism and intensity of shear dissipation (Lower).

Since it is the stresses in the slip line that are determining for the overall strength of the slope, it is reasonable to estimate the value of $\sigma_{3,\max}$ on the basis of the stresses in the slip line. In the present example, this is done in an approximate manner by mouse click under Results. The corresponding stresses are displayed in the window on the right. In this way, the maximum value of the minor principal stress in the slip line is determined as approximately 110 kPa. This value is used as $\sigma_{3,\max}$ which together with the Hoek-Brown material data gives the following Mohr-Coulomb parameters:

$$c = 16.0 \text{ kPa}, \quad \phi = 23.7^\circ, \quad k_t = 11.6 \text{ kPa} \quad (20.2)$$

The corresponding gravity based factor of safety using equivalent Mohr-Coulomb parameters is determined as:

$$2.92 \leq FS_g \leq 3.07 \quad \text{or:} \quad FS_g = 3.00 \pm 0.08 \quad (20.3)$$

which is in good agreement with the previously determined native Hoek-Brown factor of 3.09 ± 0.05 .

20.2 Strength Reduction

For the Hoek-Brown model, Strength Reduction is carried out by reducing the parameters σ_{ci} and m_i proportionally until incipient collapse, i.e. until a gravity multiplier of 1 is attained. We again use

2,000 elements and 3 adaptivity iterations to calculate the following estimate of the strength based factor of safety:

$$1.77 \leq FS_s \leq 1.80 \quad \text{or:} \quad FS_s = 1.78 \pm 0.02 \quad (20.4)$$

The collapse solution is shown in Figure 20.3.

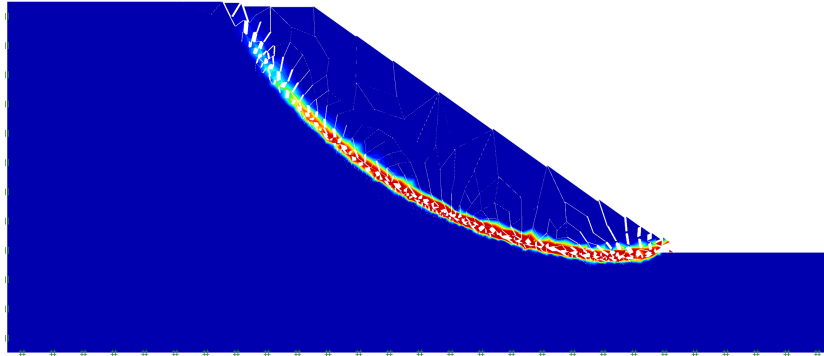


Figure 20.3: Collapse mechanism and intensity of shear dissipation (Lower).

This solution corresponds to a gravity multiplier of 1 which is attained by reducing σ_{ci} and m_i by a factor of approximately 1.78. A verification may thus be carried out by determining equivalent Mohr-Coulomb parameters for this state and checking that the resulting strength based factor of safety is in reasonable proximity of unity. Using the same procedure as above, we estimate $\sigma_{3,\max}$ as approximately 40 kPa. Using this value in conjunction with the reduced Hoek-Brown parameters of $\sigma_{ci} = 30,000/1.78 = 16,854$ kPa, $m_i = 2.0/1.78 = 1.12$ gives the following equivalent Mohr-Coulomb parameters:

$$c = 7.8 \text{ kPa}, \quad \phi = 21.2^\circ, \quad k_t = 11.6 \text{ kPa} \quad (20.5)$$

The corresponding strength based factor of safety is determined as:

$$1.02 \leq FS_s \leq 1.04 \quad \text{or:} \quad FS_s = 1.03 \pm 0.01 \quad (20.6)$$

which is reasonable close to the expected value of 1.0.

20.3 Summary

OPTUM G2 allows for direct computation of the both gravity and strength based factors of safety for the Hoek-Brown model. The resulting factors may be verified by the use of equivalent Mohr-Coulomb parameters using the following approaches.

Gravity Multiplier Limit Analysis:

1. Determine the gravity based factor of safety for the native Hoek-Brown model.
2. Using the resulting solution, estimate $\sigma_{3,\max}$ as the maximum value of σ_3 in the slip line or the parts of the body undergoing failure.
3. Compute equivalent Mohr-Coulomb parameters and verify that the resulting gravity based factor of safety is in reasonable agreement with the factor determined in Step 1.

Strength Reduction analysis:

1. Determine the strength based factor of safety for the native Hoek-Brown model.
2. Using the resulting solution, estimate $\sigma_{3,\max}$ as the maximum value of σ_3 in the slip line or the parts of the body undergoing failure.
3. On the basis of reduced Hoek-Brown parameters σ_{ci} and m_i , compute equivalent Mohr-Coulomb parameters and verify that the resulting strength based factor of safety is in reasonable proximity of unity.

21 HOEK-BROWN SLOPE 2

To further verify the Hoek-Brown model, we now consider a higher and steeper slope with a set of Hoek-Brown parameters that implies a significantly higher strength than in the previous example. The problem is shown in Figure 21.1.

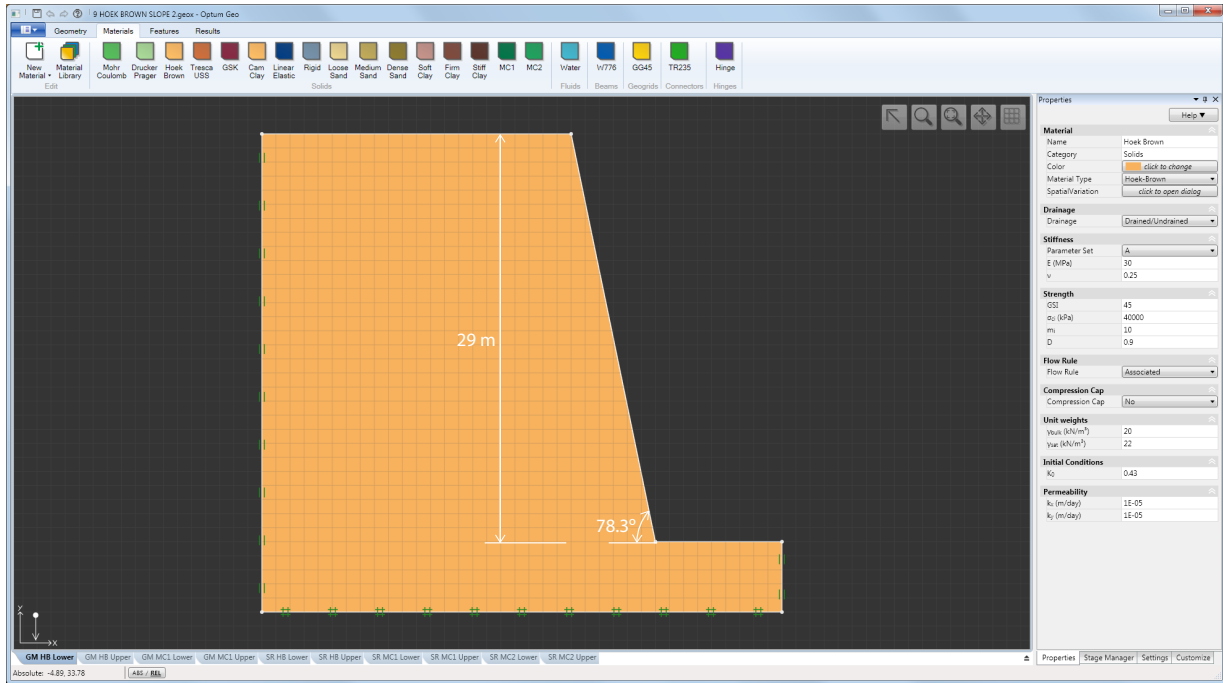


Figure 21.1: Slope of Hoek-Brown material.

21.1 Gravity Multiplier Limit Analysis

Using 2,000 elements and 3 adaptivity iterations we first calculate the following upper and lower bounds of the gravity based factor of safety:

$$2.75 \leq FS_g \leq 2.97 \quad \text{or:} \quad FS_g = 2.86 \pm 0.11 \quad (21.1)$$

Next, using the same procedure as in the previous example, we estimate a value of $\sigma_{3,max} = 40$ kPa and calculate the following equivalent Mohr-Coulomb parameters:

$$c = 65.7 \text{ kPa}, \quad \phi = 56.6^\circ, \quad k_t = 23.0 \text{ kPa} \quad (21.2)$$

The corresponding gravity based factor of safety determined as:

$$2.66 \leq FS_g \leq 2.93 \quad \text{or:} \quad FS_g = 2.80 \pm 0.14 \quad (21.3)$$

which is in good agreement with that of the native Hoek-Brown model.

21.2 Strength Reduction analysis

Using Strength Reduction analysis with 2,000 elements and 3 adaptivity iterations, the following estimate of the factor of safety for the native Hoek-Brown model is determined:

$$2.27 \leq FS_s \leq 2.39 \quad \text{or:} \quad FS_s = 2.33 \pm 0.06 \quad (21.4)$$

Next, estimating $\sigma_{3,\max}$ at 30 kPa and using the reduced Hoek-Brown parameters $\sigma_{ci} = 40,000/2.32 = 17,241$ kPa and $m_i = 10/2.32 = 4.31$ gives the following equivalent Mohr-Coulomb parameters:

$$c = 39.7 \text{ kPa}, \quad \phi = 44.7^\circ, \quad k_t = 23.0 \text{ kPa} \quad (21.5)$$

Using these parameters, the strength based factor of safety is determined as:

$$0.97 \leq FS_s \leq 0.99 \quad \text{or:} \quad FS_s = 0.98 \pm 0.01 \quad (21.6)$$

which is sufficiently close to 1.0 that the verification may be considered successful.

The collapse solutions for the Hoek-Brown models for the two analyses – Gravity Multiplier Limit Analysis and Strength Reduction – are shown in Figure 21.2. We here see that the former solution corresponds to a higher equivalent friction angle than the latter.

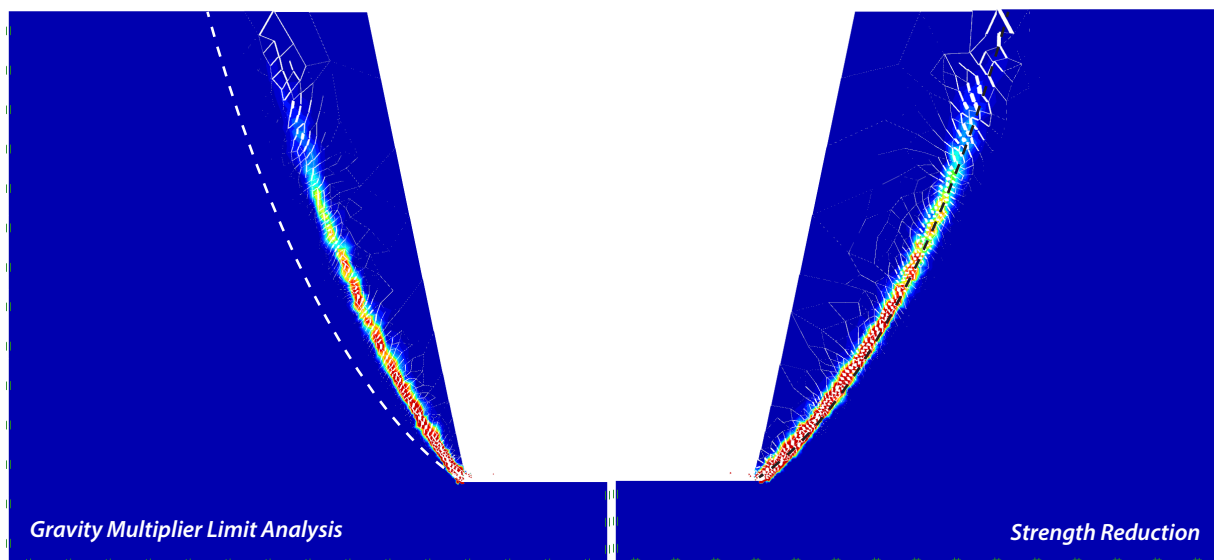


Figure 21.2: Collapse solutions and intensity of shear dissipation (Lower). The dashed lines indicate the Strength Reduction slip line.

22 UNDERGROUND CAVITY IN HOEK-BROWN MATERIAL

This example deals with a rectangular underground cavity in a Hoek-Brown material as shown in Figure 22.1. Note that the boundary conditions imply symmetry about the left vertical edge. The Hoek-Brown parameters are: $GSI = 50$, $\sigma_{ci} = 10,000$ kPa, $m_i = 10$, $D = 0$.

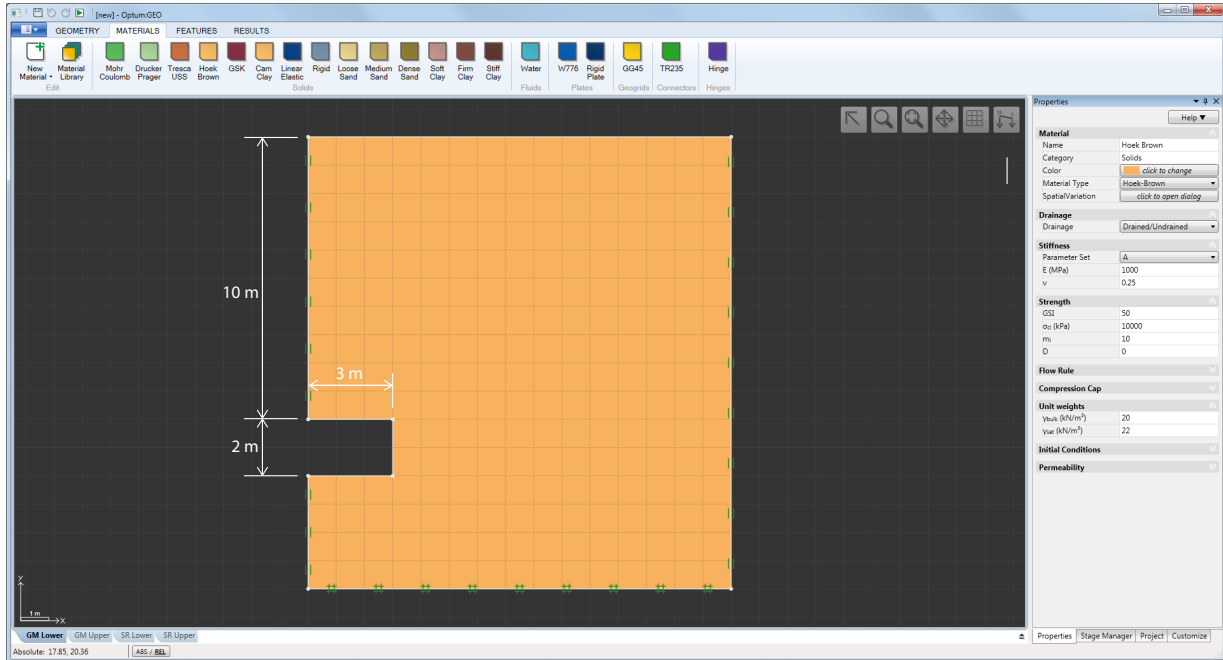


Figure 22.1: Rectangular cavity in Hoek-Brown material (symmetry utilized to model half the problem).

As in the previous examples, both Strength Reduction and Limit Analyses (with Multiplier = Gravity Multiplier) are conducted. In both cases, 2,000 Lower and Upper elements are used with 3 adaptivity iterations. The results are as follows:

$$\begin{aligned}
 \text{Limit Analysis (Gravity Multiplier):} & \quad FS_g = 2.25 \pm 0.14 \\
 \text{Strength Reduction:} & \quad FS_s = 4.20 \pm 0.14
 \end{aligned}
 \tag{22.1}$$

In contrast to the previous examples, the Strength Reduction analysis here implies a greater level of safety than the Gravity Multiplier Limit Analysis. This is due to the fact that the failure (see Figure 22.2) is primarily of the tensile type with the roof collapsing into the cavity. The tensile strength implied by the Hoek-Brown criterion is given by $\sigma_t = s\sigma_{ci}/m_b$ where m_b and s are related to GSI and D and m_b is proportional to m_i (see the Materials Manual). In the Strength Reduction analysis used in OPTUM G2, σ_{ci} and m_i are reduced proportionally, meaning that the tensile strength remains unaltered. This situation is analogous to that of the Mohr-Coulomb criterion where the tensile strength is $\sigma_t = c/\tan \phi$ and thus is unaffected by an equal and simultaneous reduction of c and $\tan \phi$.

In conclusion: while the strength based factor of safety, FS_s , in most cases is smaller than the gravity based factor of safety, FS_g , exceptions do exist and can be expected to be most pronounced for problems dominated by tensile failure.

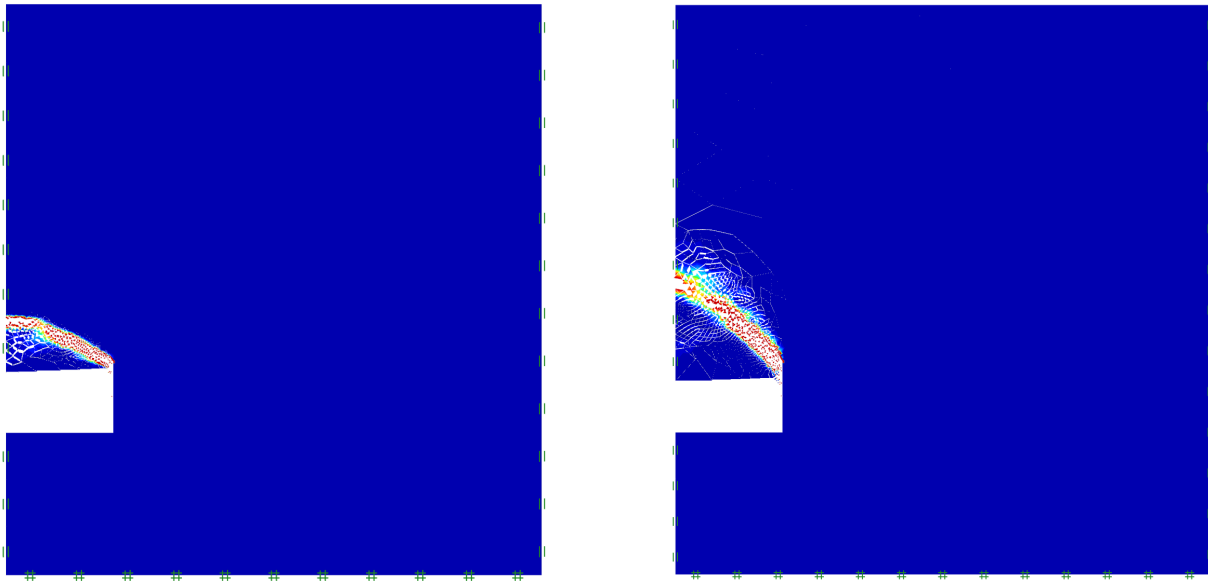


Figure 22.2: Failure mechanism for underground cavity in Hoek-Brown material showing roof collapse into the cavity using Limit Analysis (left) and Strength Reduction analysis (right).

23 STRIP FOOTING ON MOHR-COULOMB SAND

This example concerns the classic problem of the bearing capacity of a strip footing on a deep layer of sand as shown in Figure 23.1. Despite its apparent simplicity, this problem, also referred to as the N_γ problem, is widely recognized as being problematic to deal with. Firstly, the combination of a free surface and a purely frictional material causes problems for most conventional Newton-Raphson based finite element schemes. Consequently, it is often necessary to introduce some not insignificant cohesion. Secondly, the point at the edge of the footing is a singular point and failure to address this fact may lead to quite erroneous results. Thirdly, the problem is extremely sensitive to the friction angle. For example, the bearing capacity is more than doubled between $\phi = 30^\circ$ and $\phi = 35^\circ$ and tripled between $\phi = 35^\circ$ and $\phi = 41^\circ$. Finally, it should be noted that the problem does not have a closed form solution and that some of the formulas cited in the literature come with not insignificant errors. In the following, we will use the solutions provided by Martin (2005) resulting from direct numerical integration of the ODE derived by von Karman (1926). These solutions are for all practical purposes exact.

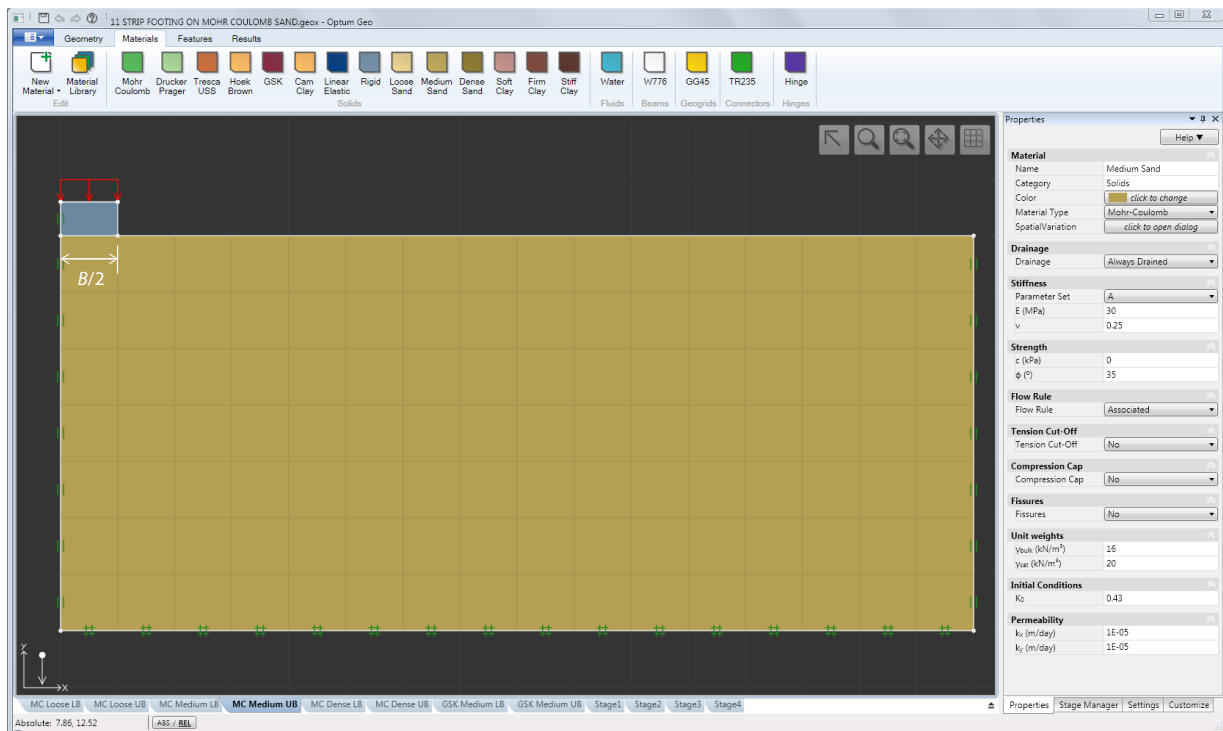


Figure 23.1: Strip footing on Mohr-Coulomb sand (symmetry utilized to model half the problem).

The procedures implemented in OPTUM G2 differ fundamentally from those of other finite element programs. For the problem at hand, this means that:

- A cohesion identically equal to zero can be used. Note that the Shear Dissipation, rather than the Total Dissipation, is the quantity of interest, both for mesh adaptivity and in terms of visualizing the results.
- Upper and lower bounds may be calculated as for all other problems. This gives a direct measure of the error in the numerical solution. Furthermore, it is often observed that the mean between the upper and lower bounds furnish a good estimate of the exact solution – even if the gap between the bounds is significant.

- The singularity at the footing edge may be handled using the Mesh Fan tool available under Features. This feature constructs a fan of elements around the singularity which often leads to improved solutions, especially for lower bound elements. An example is shown in Figure 23.2.

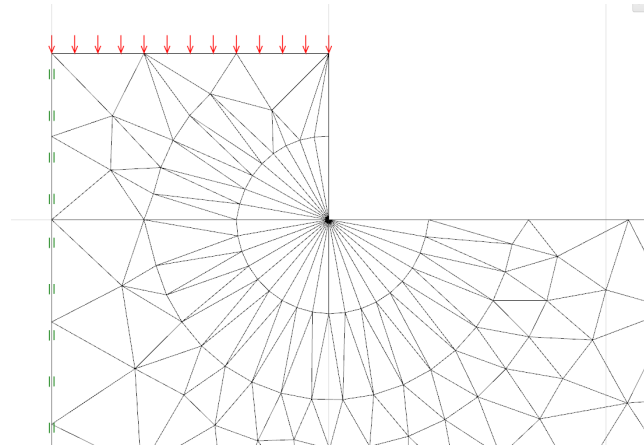


Figure 23.2: Mesh fan (10°) at footing edge.

The bearing capacity of a centrally loaded strip footing on sand as shown in Figure 23.1, can be expressed as

$$q_u = \frac{1}{2} B \gamma N_\gamma \quad (23.1)$$

where N_γ is the bearing capacity factor which depends on the friction angle. For the Loose Sand-MC, Medium Sand-MC, and Dense Sand-MC default materials these are:

Loose Sand	$(\phi = 30^\circ)$:	$N_\gamma = 14.7543$	
Medium Sand	$(\phi = 35^\circ)$:	$N_\gamma = 34.4761$	(23.2)
Dense Sand	$(\phi = 40^\circ)$:	$N_\gamma = 85.5656$	

To investigate the relative effects of using mesh adaptivity and a mesh fan at the singularity, four different scenarios are considered:

- a) No adaptivity, no mesh fan.
- b) No adaptivity, mesh fan.
- c) Adaptivity, no mesh fan.
- d) Adaptivity, mesh fan.

The mesh adaptivity calculations are carried out using 4 adaptivity iterations starting with 1,000 elements (see Section 23.1). The mesh fan is 10° in all cases.

The results are shown in Tables 23.1-4. We here see that while the introduction of a mesh fan does improve the solutions, its benefit is relatively greater for coarser meshes. Mesh adaptivity, on the other hand, is very effective (and also more expensive), with or without mesh fan. Furthermore, the mean value between the upper and lower bound solutions offer a very good estimate of the exact solution. Indeed, the error is rarely greater than 5%, even when the respective bounds are rather poor. Moreover, they are generally on the safe side, indicating that the lower bound solutions usually

are slightly less accurate than the upper bound solutions. The finest mesh and the collapse solution for the dense sand in case c) are shown in Figure 23.3. The concentration of deformation at the singularity is here quite apparent.

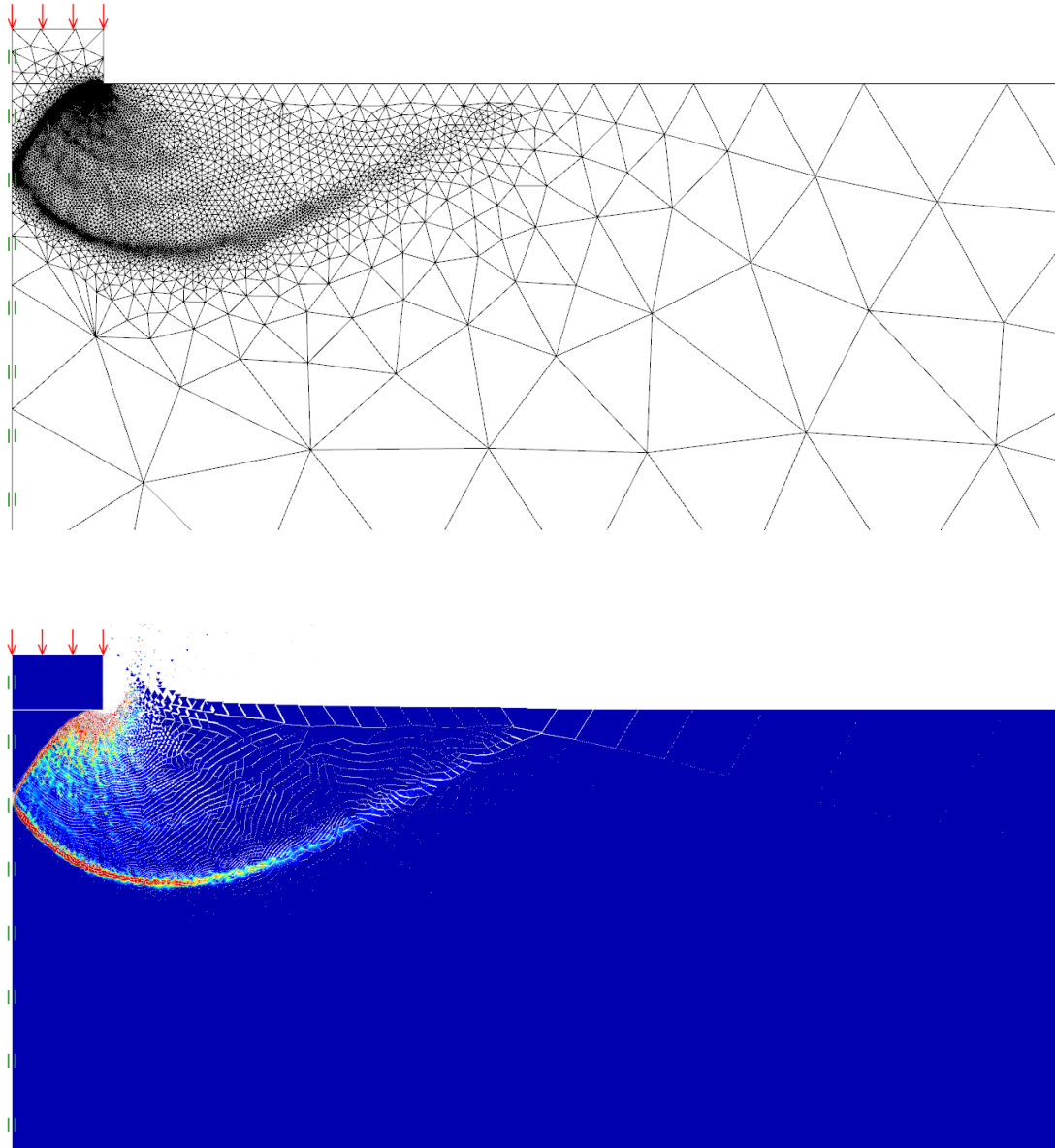


Figure 23.3: Mesh and collapse solution with intensity of shear dissipation for Medium Sand (lower bound).

No Elem	Loose				Medium				Dense			
	Lower	Upper	Mean	Err (%)	Lower	Upper	Mean	Err (%)	Lower	Upper	Mean	Err (%)
1,000	0.374	1.767	1.071	+7.1	0.360	1.798	1.079	+7.9	0.302	1.818	1.060	+6.0
2,000	0.424	1.561	0.993	-0.7	0.420	1.550	0.985	-1.5	0.404	1.571	0.988	-1.3
4,000	0.497	1.397	0.947	-5.3	0.506	1.410	0.958	-4.2	0.475	1.432	0.954	-4.6
8,000	0.568	1.281	0.925	-7.5	0.581	1.289	0.935	-6.5	0.576	1.301	0.939	-6.1
16,000	0.661	1.201	0.931	-6.9	0.670	1.204	0.937	-6.3	0.656	1.214	0.935	-6.5

Table 23.1: Limit loads, q_u/q_{exact} , for footing on Mohr-Coulomb sand. a) No adaptivity, no mesh fan.

No Elem	Loose				Medium				Dense			
	Lower	Upper	Mean	Err (%)	Lower	Upper	Mean	Err (%)	Lower	Upper	Mean	Err (%)
1,000	0.575	1.554	1.065	+6.5	0.515	1.582	1.049	+4.9	0.446	1.622	1.049	+4.9
2,000	0.538	1.442	0.990	-0.1	0.503	1.457	0.980	-0.2	0.449	1.475	0.980	-2.0
4,000	0.682	1.285	0.984	-1.6	0.620	1.295	0.958	-4.2	0.555	1.323	0.958	-4.3
8,000	0.738	1.216	0.977	-2.3	0.701	1.225	0.963	-3.7	0.652	1.231	0.963	-3.7
16,000	0.784	1.154	0.969	-3.1	0.753	1.150	0.952	-4.8	0.708	1.159	0.952	-4.9

Table 23.2: Limit loads, q_u/q_{exact} , for footing on Mohr-Coulomb sand. b) No adaptivity, mesh fan.

No Elem	Loose				Medium				Dense			
	Lower	Upper	Mean	Err (%)	Lower	Upper	Mean	Err (%)	Lower	Upper	Mean	Err (%)
1,000	0.829	1.074	0.952	-4.8	0.804	1.094	0.949	-5.1	0.757	1.126	0.942	-5.8
2,000	0.890	1.043	0.967	-3.3	0.883	1.053	0.968	-3.2	0.846	1.066	0.956	-4.4
4,000	0.932	1.024	0.978	-2.2	0.919	1.029	0.974	-2.6	0.902	1.041	0.972	-2.8
8,000	0.952	1.015	0.984	-1.6	0.946	1.018	0.982	-1.8	0.939	1.023	0.981	-1.9
16,000	0.965	1.011	0.988	-1.2	0.962	1.012	0.987	-1.2	0.958	1.014	0.986	-1.4

Table 23.3: Limit loads, q_u/q_{exact} , for footing on Mohr-Coulomb sand. c) Adaptivity, no mesh fan.

No Elem	Loose				Medium				Dense			
	Lower	Upper	Mean	Err (%)	Lower	Upper	Mean	Err (%)	Lower	Upper	Mean	Err (%)
1,000	0.877	1.069	0.973	-2.7	0.841	1.087	0.964	-3.6	0.779	1.108	0.944	-5.6
2,000	0.917	1.036	0.977	-2.3	0.892	1.044	0.968	-3.2	0.860	1.063	0.962	-3.8
4,000	0.941	1.021	0.981	-1.9	0.928	1.026	0.977	-2.3	0.907	1.035	0.971	-2.9
8,000	0.964	1.013	0.989	-1.1	0.955	1.016	0.986	-1.4	0.941	1.020	0.981	-1.9
16,000	0.974	1.009	0.992	-0.8	0.968	1.010	0.989	-1.1	0.961	1.013	0.987	-1.3

Table 23.4: Limit loads, q_u/q_{exact} , for footing on Mohr-Coulomb sand. d) Adaptivity, mesh fan.

23.1 On mesh adaptivity

In this example, we have deviated from the default mesh adaptivity settings by using 4 adaptivity steps instead of the default 3. This and other settings related to mesh adaptivity may be modified via the Mesh categories under Stage Manager and Project (see Figure 23.4).

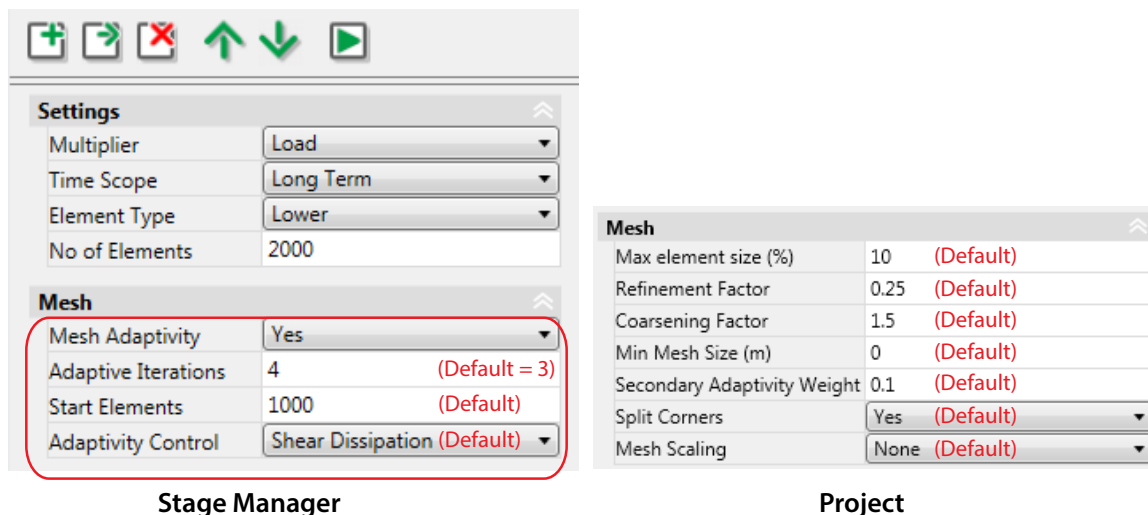


Figure 23.4: Settings related to mesh adaptivity. The settings under Stage Manager (left) are stage specific whereas the settings under Project (right) global and apply to all stages.

Using mesh adaptivity, the aim is to increase the number of elements from Start Elements (1,000 in the above case) to No of Elements (8,000 in the above case) in the course of a given number of Adaptivity Iterations (4 in the above case). This is done subject to the constraints that the maximum element size cannot increase by more than a given factor between two iterations. Similarly, the minimum element size is constrained to not decrease by more than a predefined factor. These two factors are referred to as the Coarsening Factor and the Refinement Factor, respectively, in the Mesh category under Project. Their default values are 1.5 and 0.25 respectively. In general, these settings, together with the other default settings, lead to reasonable meshes and moderate gaps between the resulting upper and lower bounds. However, in some cases a more careful strategy is required. Thus, restricting the increase/decrease of element sizes between iterations generally leads to a more reliable behaviour, though of course at the expense of more adaptivity iterations to reach the final number of elements. Conversely, a more aggressive strategy than that implied by the default coarsening and refinement factors may also be successful (for example reducing the refinement factor to 0.1). Finally, starting with too few elements (as given by Start Elements) may lead to a rather poor solution on the basis of which it is difficult to construct a better mesh. In conclusion, if the default settings fail to produce results with the desired accuracy for No of Elements = 10,000 or above, the settings to change, in order of priority, are:

1. Increase Adaptivity Iterations (typical value = 4).
2. Increase Start Elements (typical value = 2,000).
3. Decrease Refinement Factor (typical value = 0.15).
4. Increase Coarsening Factor (typical value = 2.0).

Finally, when tension cut-off with $k_t = 0$ is used in the Mohr-Coulomb, Drucker-Prager or Tresca models, Total Dissipation is often more appropriate as Adaptivity Control than the default Shear Dissipation, especially when using lower bound elements.

24 STRIP FOOTING ON GSK SAND

This example follows on from the previous one, now using the GSK model with the parameters shown in Figure 24.1

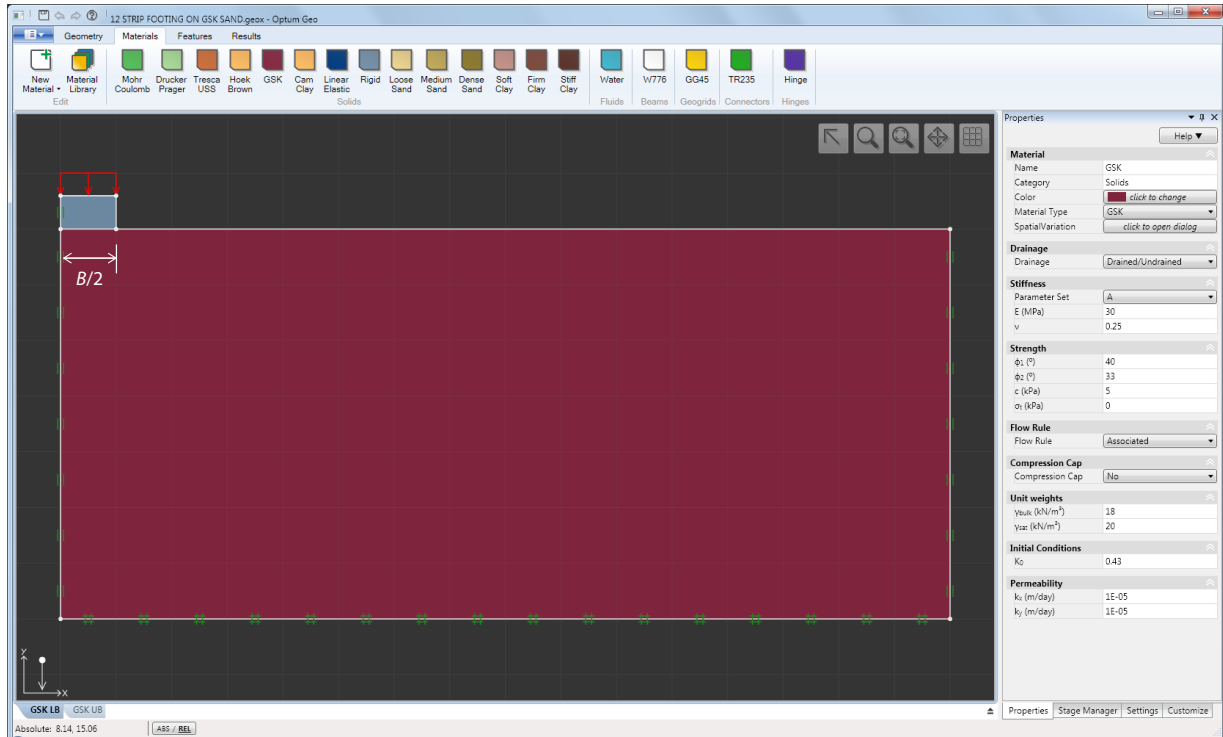


Figure 24.1: Strip footing on GSK sand (symmetry utilized to model half the problem).

The GSK model involves a curved Mohr-Coulomb envelope (see Figure 24.2) and is particularly relevant at low stress levels where the apparent friction angle may be significantly higher than at higher stress levels. The nonlinearity of the GSK failure envelope means that the effective friction angle is stress dependent. This in turn means that the bearing capacity of the footing no longer scales linearly with footing width as predicted by the Mohr-Coulomb model. In the following, we investigate

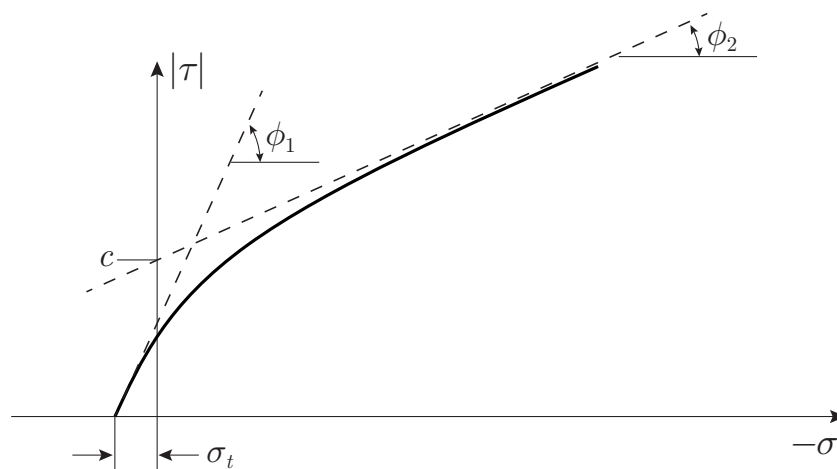


Figure 24.2: GSK failure envelope.

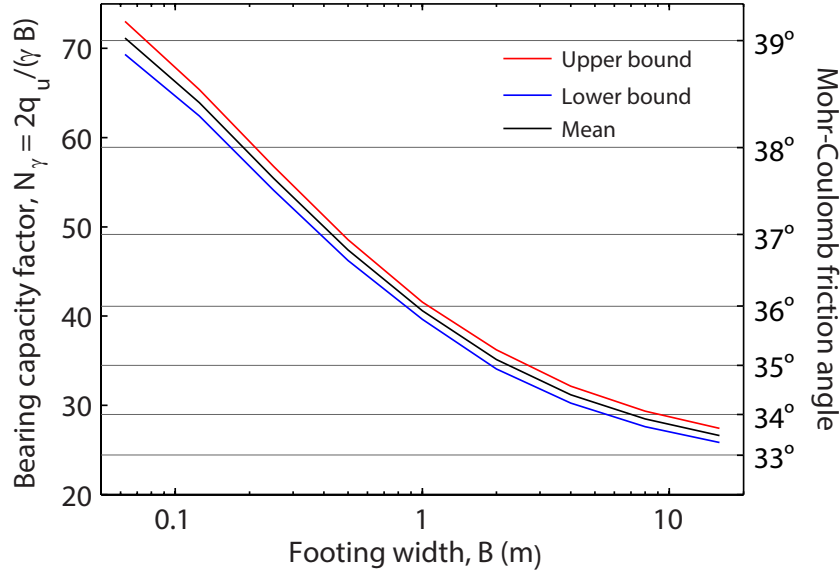


Figure 24.3: Effective bearing capacity factor for medium GSK sand as function of footing width.

the effective footing width dependence for a GSK sand with $\phi_1 = 40^\circ$ and $\phi_2 = 33^\circ$ corresponding to a medium sand (see the Material Manual). Upper and lower bounds are calculated using 8,000 elements and 4 adaptivity iterations.

For each footing width, we express the bearing capacity as

$$q_u(B) = \frac{1}{2} B \gamma N_\gamma(B) \tag{24.1}$$

The results are shown in Figure 24.3. We see that the effective bearing capacity factor ranges between the Mohr-Coulomb factors corresponding to $\phi_1 = 40^\circ$ and $\phi_2 = 33^\circ$. The former limit is approached for $B \rightarrow 0$ while the latter limit is approached as the footing width tends to infinity.

The collapse mechanisms are in all cases similar to the one shown in Figure 23.3.

25 STRIP FOOTING ON HOEK-BROWN MATERIAL

In this example, a strip footing on a Hoek-Brown material is considered. The setup, shown in Figure 25.1, is similar to the previous two examples.

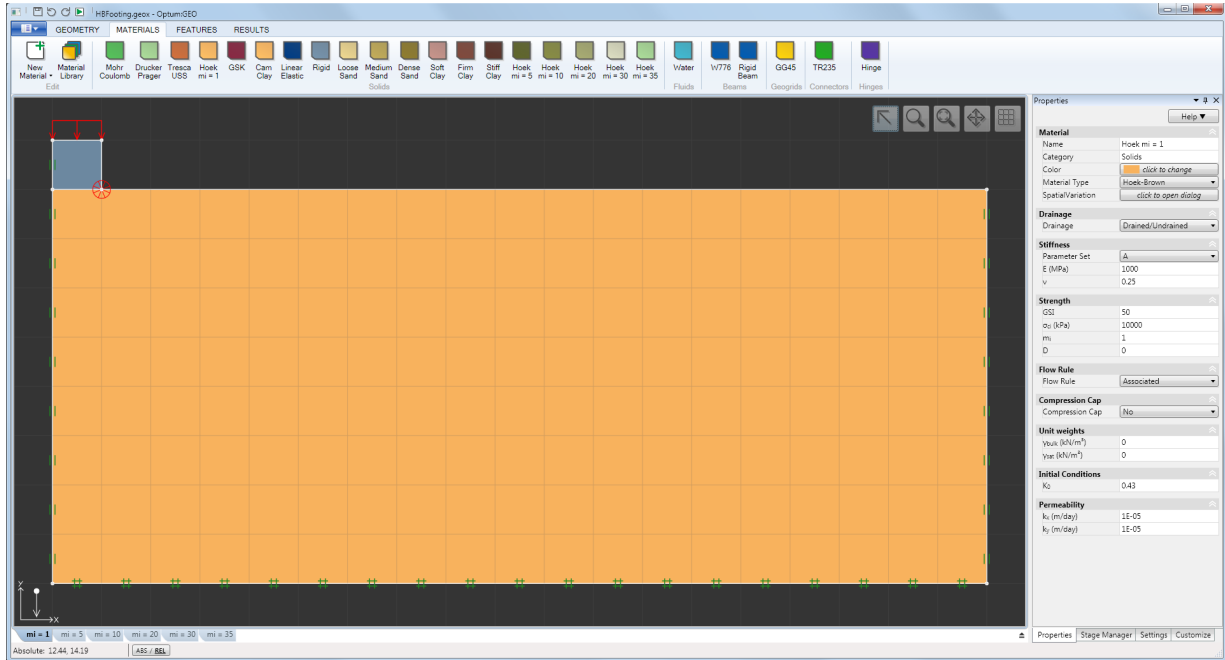


Figure 25.1: Strip footing on Hoek-Brown material.

Assuming a weightless material, the bearing capacity can be expressed as

$$q_u = N_\sigma \sigma_{ci} \tag{25.1}$$

where N_σ is the bearing capacity factor which depends on the material data (GSI, m_i and D) and σ_{ci} is the compressive strength of the intact rock. We recall that the Hoek-Brown criterion implies an

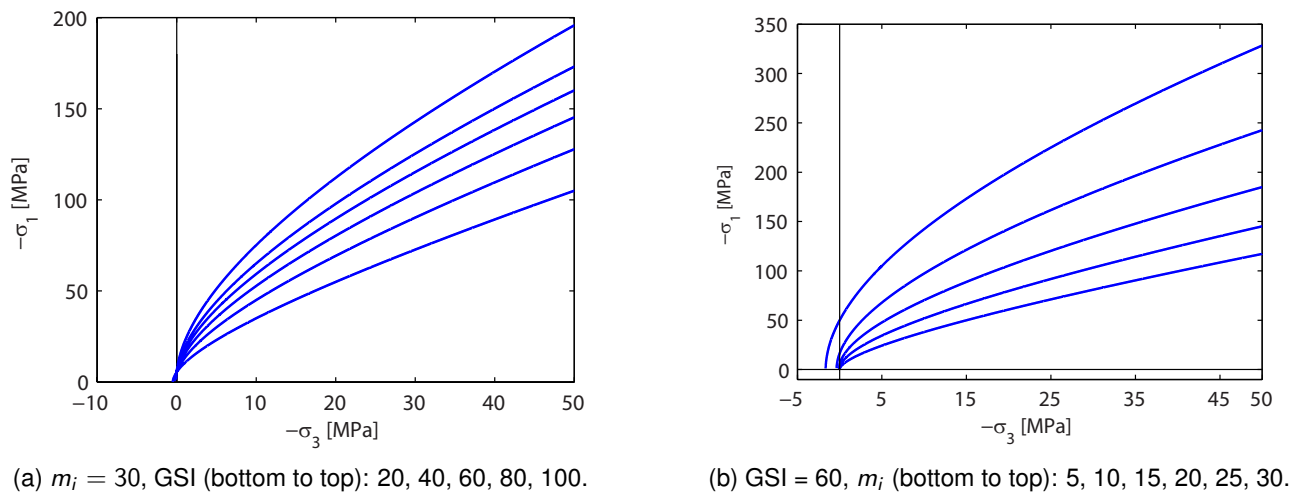


Figure 25.2: Hoek-Brown failure envelopes for different GSI (left) and m_i (right).

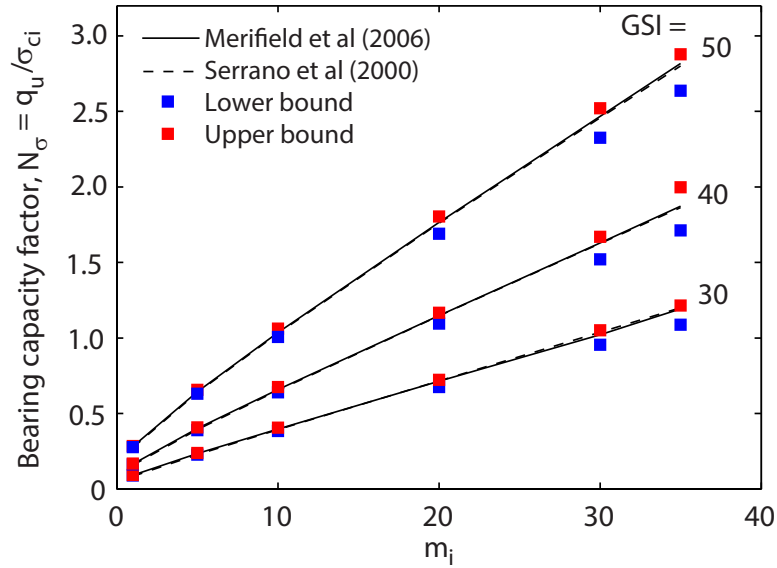


Figure 25.3: Bearing capacity factors for strip footing on weightless Hoek-Brown material.

increase of strength with increasing GSI and m_i (see Figure 25.2).

Upper and lower bounds on the footing pressure (and thereby on the bearing capacity factor) are calculated using Limit Analysis for a range of m_i and GSI. In these calculations, 5,000 elements with 3 adaptivity iterations and 1,000 initial elements are used. In addition, a Mesh Fan with a fan angle of 30° is used. The results are shown in Figure 25.3 together with the solutions of Serrano et al. (2000) and Merifield et al. (2006) which have been verified as being within close proximity to the exact solutions. The accuracy of the present results follows that of Section 23 (Mohr-Coulomb footing on sand): the upper bounds tend to be somewhat more accurate than the lower bounds and the accuracy decreases with increasing material strength.

Finally, we consider an example of a ponderable material with a unit weight of $\gamma = 20 \text{ kN/m}^3$. The Hoek-Brown parameters are taken from the book of Hoek (jointed quartz mica schist encountered at the Nathpa Jhakri Hydroelectric project in Himachel Pradesh, India): $\sigma_{ci} = 30 \text{ MPa}$, $m_i = 15$, $\text{GSI} = 65$, $D = 0$. This rock mass is described as being of average quality. With the same mesh settings as used above, we obtain a footing pressure of:

$$81.0 \text{ MPa} \pm 3.2\% \tag{25.2}$$

The collapse solution is shown below.

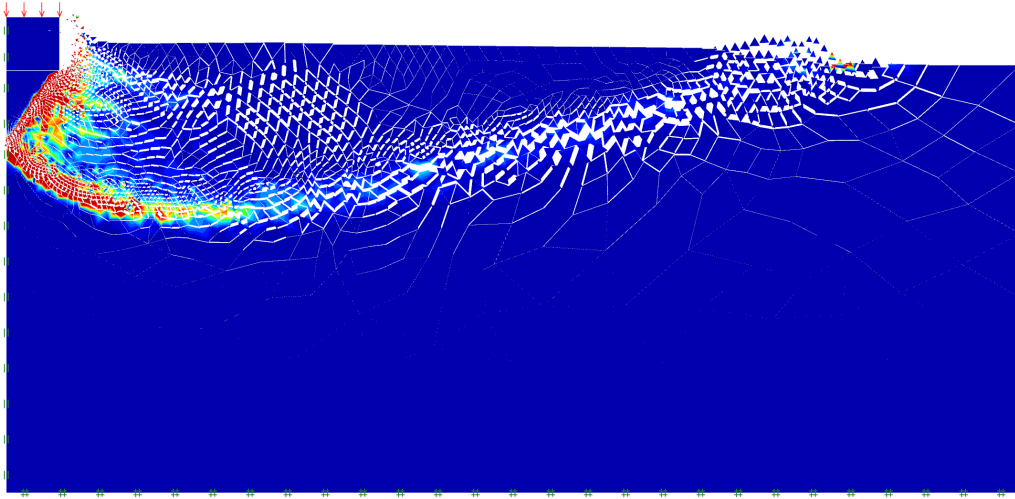


Figure 25.4: Collapse solution for ponderable Hoek-Brown material ($\sigma_{ci} = 30$ MPa, $m_i = 15$, GSI = 65, $D = 0$).

26 COMBINED LOADING OF SHALLOW FOUNDATION

This example considers the combined loading of a shallow foundation as shown in Figure 26.1. The foundation is embedded in a Tresca material, taken to represent undrained conditions using a total stress analysis. The undrained shear strength is $s_u = 35$ kPa.

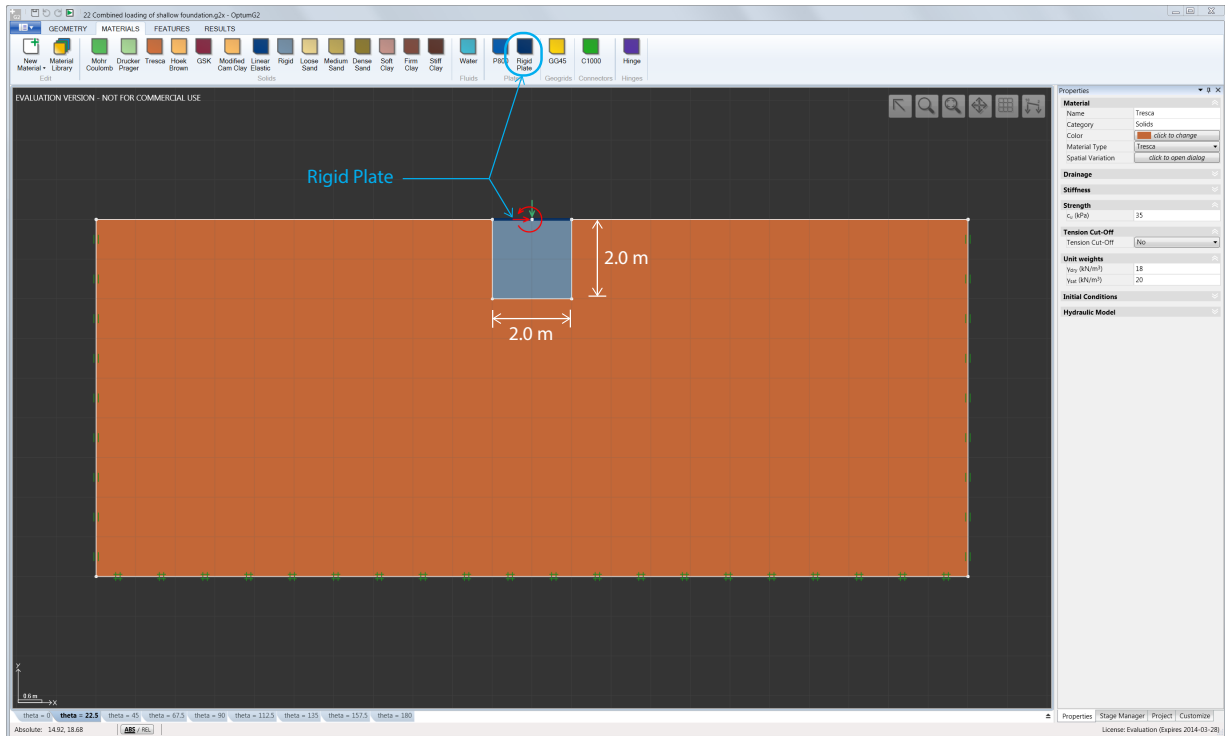


Figure 26.1: Combined loading of shallow foundation.

The strength of a shallow foundation subjected to combined moment (M), vertical (V) and horizontal (H) forces may be represented as a closed surface in the space of the three force components. In the following, the vertical force is kept fixed at $V = 200$ kN/m while ultimate magnitudes of combinations of moment and horizontal force are determined using Limit Analysis. In other words, a two-dimensional $H-M$ slice of the complete three-dimensional $V-H-M$ surface is determined.

In OPTUM G2, moments and concentrated forces may be applied to Plates and Geogrids only. Hence, a weightless Rigid Plate is defined on the top surface of the foundation, which itself is of Rigid material with a unit weight of 20 kN/m³. The horizontal force and moment are specified as a Multiplier Concentrated Load with components:

$$\begin{aligned}
 \text{Force X} &= \cos \theta \\
 \text{Force Y} &= 0 \\
 \text{Moment} &= \sin \theta
 \end{aligned}
 \tag{26.1}$$

where θ is varied from 0 to 180° is a number of steps, each generating a separate analysis. When specifying the concentrated force components the in-built calculator (see Figure 26.2) is useful. This is opened via the calculator icon in the right side of any numerical field.

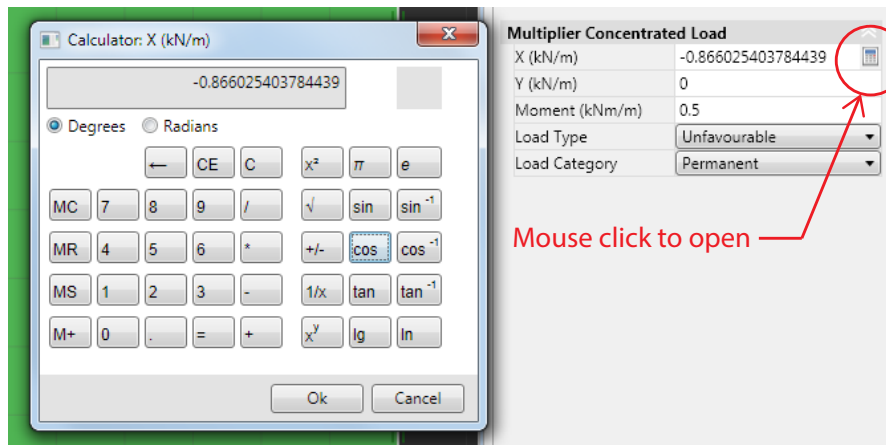


Figure 26.2: Calculator.

As in previous examples, the calculations are organized in a series of independent stages, each corresponding to a particular value of θ . The resulting ultimate horizontal force and moment are given by

$$\begin{aligned} H &= \alpha_u \cos \theta \\ M &= \alpha_u \sin \theta \end{aligned} \tag{26.2}$$

where α_u is the collapse multiplier generated by the analysis.

Using 2,000 elements with 3 adaptivity iterations and using both upper and lower bound elements, the H - M surface shown in Figure 26.3 may be generated (the actual plotting is done externally on the basis of the computed results).

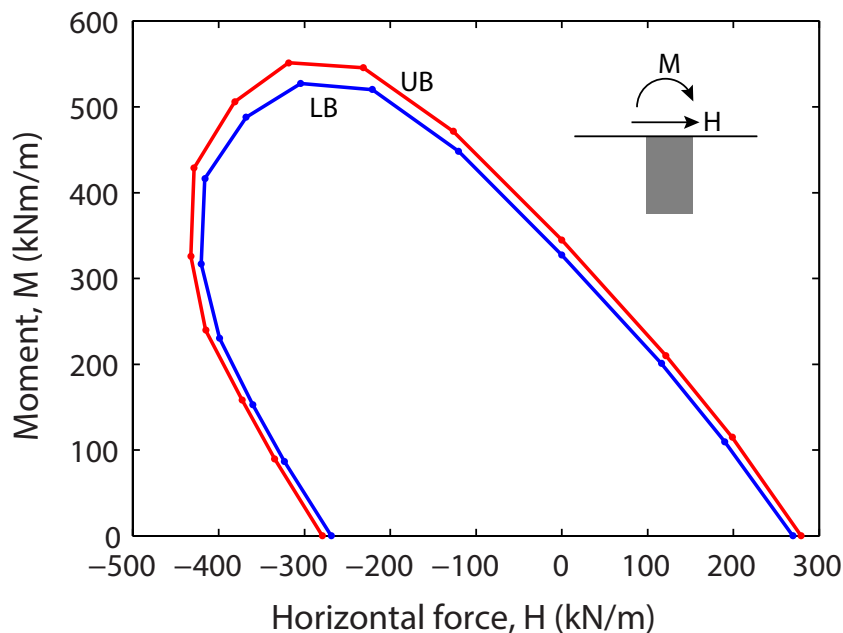


Figure 26.3: Upper and lower bound H - M envelopes for $V = 200$ kN/m.

Although the gap between the upper and lower bound envelopes in some regions appears to be

sizeable, the corresponding collapse multipliers are in fact nowhere in error by more than 3%.

26.1 Effect of tension cut-off

The type of analysis conducted above allows for tensile total stresses. If the material is not able to sustain tension under drained conditions, this implies that tensile total stresses can be realized only as a consequence of excess pore pressure corresponding to suction. To see this, recall the principle of effective stress:

$$\sigma' = \sigma - p_e \tag{26.3}$$

where both the stresses and the excess pore pressure are positive corresponding to tension. If no tensile stresses are allowed under drained conditions, the failure criterion must necessarily be such that $\sigma' \leq 0$. As such, $\sigma > 0$ implies $p_e > 0$ corresponding to suction. Whether or not this suction can reasonably be expected to be established or the material is able to sustain some tension under drained conditions depends on the particular circumstances, but it is clearly on the safe side to take neither into account. This scenario is accounted for by including a tension cut-off with $\phi_t = 90^\circ$ and $k_t = 0$.

In the following we rerun the previous analyses with a tension cut-off included. All settings are the same except that the Adaptivity Control is changed to Total Dissipation which is often more appropriate when a tension cut-off is applied. The modified settings are shown in Figure 26.4.

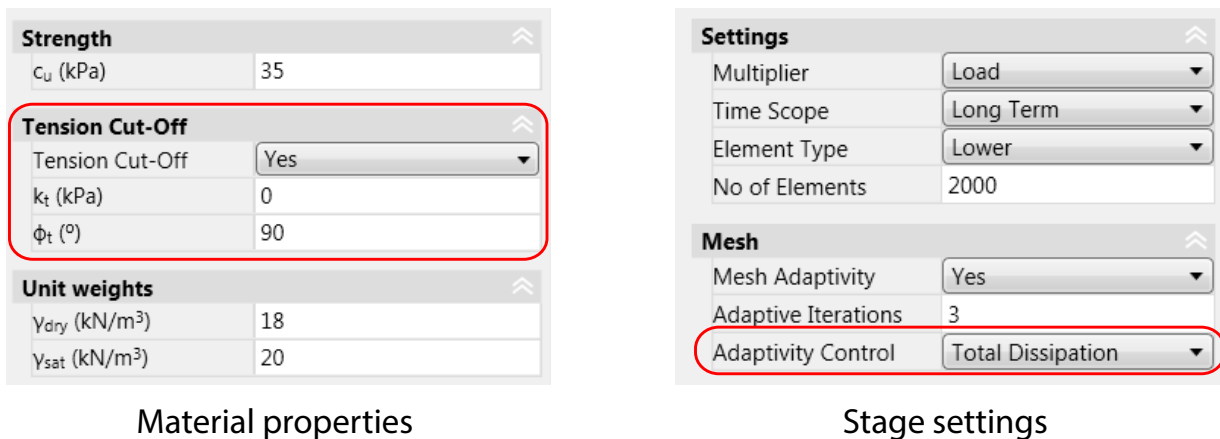


Figure 26.4: Modified settings for analysis with tension cut-off.

The modified H - M envelopes are shown in Figure 26.5. We see that the new envelopes imply somewhat of a decrease in strength with the exact magnitude depending to the particular H/M ratio.

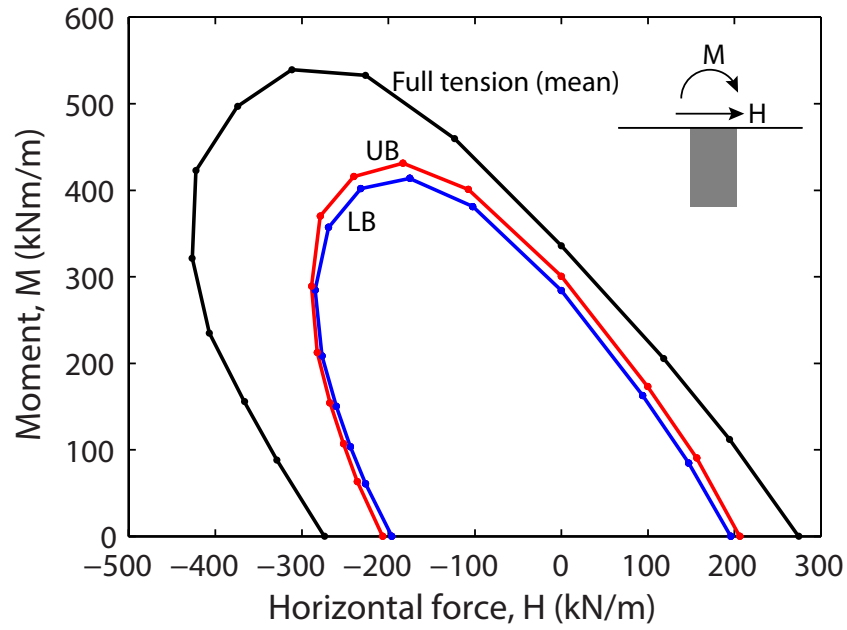


Figure 26.5: Upper and lower bound H - M envelopes for $V = 200$ kN/m with tension cut-off.

27 COMBINED LOADING OF PIPELINE

This example deals with the combined loading of a pipeline idealized as a plane strain cylinder (see Figure 27.1). The pipeline is partially embedded in a Tresca soil with an undrained shear strength of $s_u = 30 \text{ kPa}$. The pipeline is situated on the seabed and in the total stress analysis that follows we assume an effective soil unit weight of $\gamma' = 10 \text{ kN/m}^3$ whereas the effective unit weight of the pipeline is 2 kN/m^3 . The loading consists of a combination of horizontal load (H) and vertical load (V). As in the previous example, the application of concentrated loads is facilitated by including weightless Plate elements as shown in Figure 27.1.

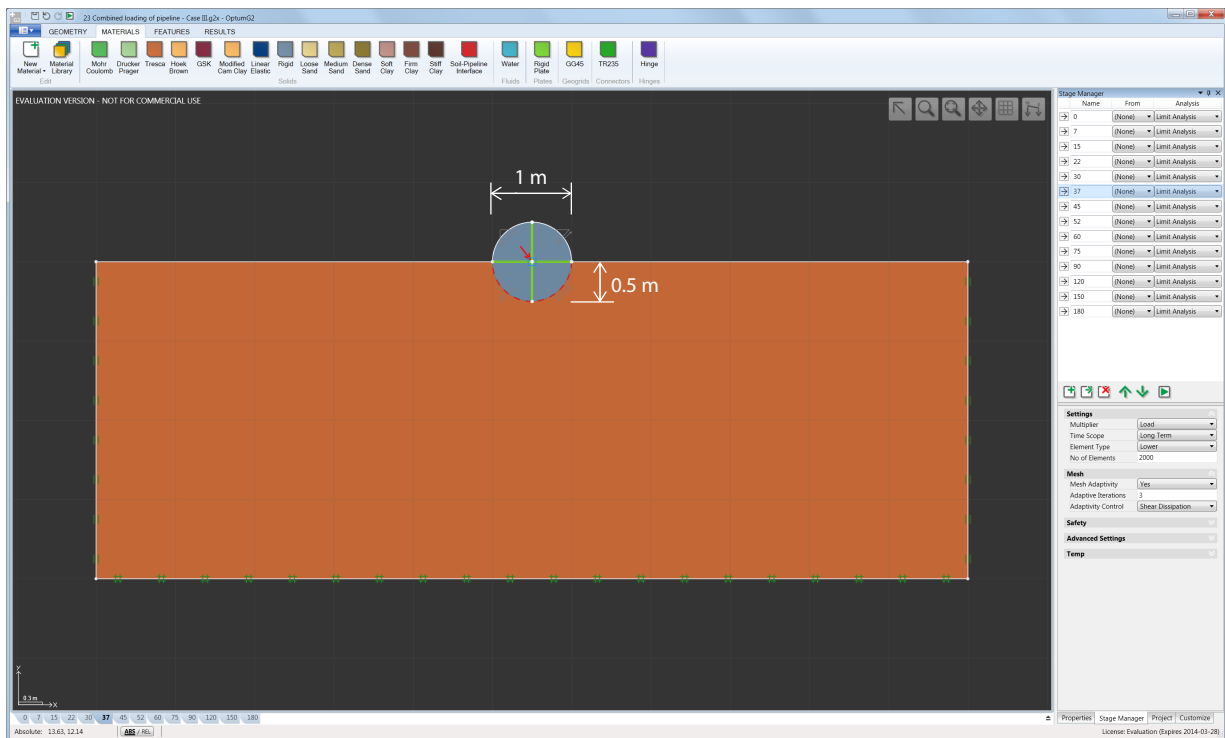


Figure 27.1: Pipeline subjected to combined vertical and horizontal loading.

As in the previous example, we aim to determine the full V - H failure envelope. This is done by means of Limit Analysis using multiplier loads

$$\begin{aligned} \text{Force } X &= \sin \theta \\ \text{Force } Y &= -\cos \theta \\ \text{Moment} &= 0 \end{aligned} \quad (27.1)$$

for a range of θ in interval 0 to 180° . The resulting vertical and horizontal forces are then given by:

$$\begin{aligned} V &= \alpha_u \cos \theta \\ H &= \alpha_u \sin \theta \end{aligned} \quad (27.2)$$

where α_u is the collapse multiplier and V is positive downwards.

For the present problem, three issues are of particular importance:

1. To what extent is the pipeline constrained against rotation?
2. To what extent can the soil-pipeline interface sustain tension?
3. What is the magnitude of shear stress that can be sustained at the soil-pipeline interface?

These questions may be partly answered by considering the two extremes of the range of possibilities:

1. Pipeline rotation: either free to rotate or fully constrained against rotation.
2. Tensile stress at the interface: either zero or unlimited.
3. Maximum shear stress at the interface: either zero or equal to that of the surrounding soil.

Regarding the first point, the rigid plates connecting to the rigid cylinder may be constrained against rotation (as indicated in Figure 27.1) by applying a Plate BC to the center of the cross.

Regarding the two latter points, there are number of possibilities for modeling the soil-pipeline interface, some of which are summarized in Figure 27.2, namely:

- i) Rough/full tension: this model assumes that the interface properties are identical to those of the surrounding soil. In that case, no provisions need to be taken. However, one may include a shear joint of the same material as the soil. For some elements, this may improve the results slightly.
- ii) Smooth/full tension: this option assumes a zero shear stress at the interface while no constraints are imposed on the normal stresses which therefore may be tensile. This model is realized via a shear joint of the same material type as the surrounding but with $s_u = 0$.
- iii) Rough/no tension: this model assumes that the maximum shear stress at the interface is equal to that of the soil. At the same time, normal stresses are constrained to be strictly compressive. This model is realized via a shear joint of the same material as the surrounding soil with a tension cut-off defined by $k_t = 0$, $\phi_t = 90^\circ$. As for all other materials, the tension cut-off is activated via the material property window.
- iv) Smooth/no tension: as above except the shear strength of the interface is zero. This model is the most conservative in the sense that it leads to the smallest failure load among all the possible interface models.
- v) Generalized: the above models may all be seen as special cases of a more general model that involves a interface shear strength equal to some fraction α of the soil shear strength and a tension cut-off with a finite tensile strength k_t and an inclination with the horizontal different from 90° .

Finally, it should be mentioned that a 'rough no-tension' interface sometimes is taken to mean that the normal stress remains compressive while no conditions are placed on the shear stress. Such interfaces, which may lead to significantly higher limit loads than in the case where the shear stress is limited to the soil shear strength, will not be considered any further but can quite easily be accounted for in OPTUM G2, for example by using a shear joint of Mohr-Coulomb material with $c = 0$ and $\phi = 90^\circ$.

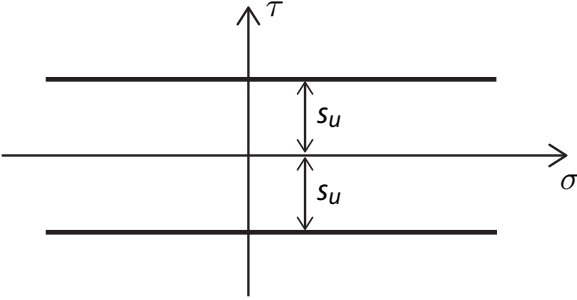
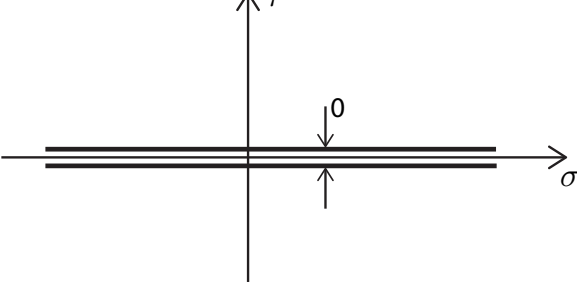
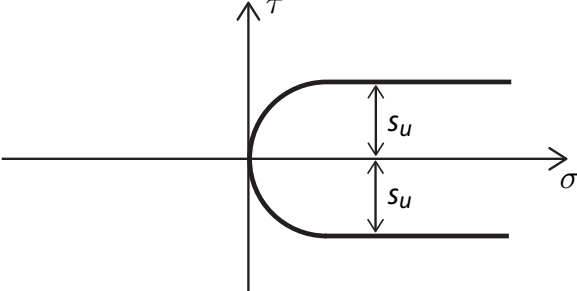
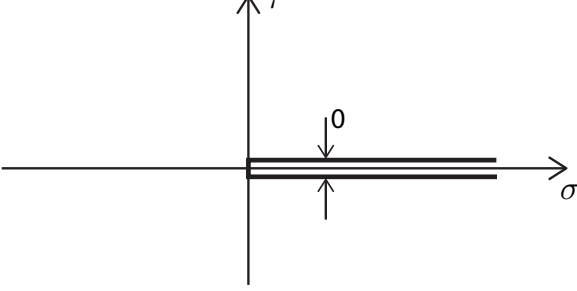
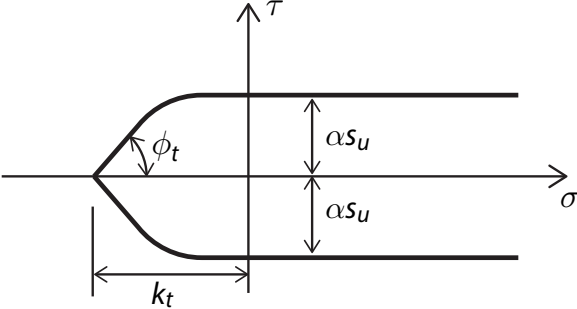
	<p>Rough/full tension</p> <p>Modeling: Shear joint of Tresca material. Note: a joint with the same properties as the surrounding solid is applied by default.</p>
	<p>Smooth/full tension</p> <p>Modeling: Shear joint of Tresca material with $s_u = 0$. Note: alternatively, the Reduction Factor r for the relevant Plate-soil interfaces may be set to zero.</p>
	<p>Rough/no tension</p> <p>Modeling: Shear joint of Tresca material plus tension cut-off with $k_t = 0$ and $\phi_t = 90^\circ$.</p>
	<p>Smooth/no tension</p> <p>Modeling: Shear joint of Tresca material with $c_u = 0$ plus tension cut-off with $k_t = 0$ and $\phi_t = 90^\circ$.</p>
	<p>Generalized</p> <p>Modeling: Shear joint of Tresca with strength αc_u plus tension cut-off with $k_t \geq 0$ and $0 \leq \phi_t \leq 90^\circ$.</p>

Figure 27.2: Soil-structure interface models.

The V - H diagrams for each of these interface models are shown in Figure 27.3 (mean values between upper and lower bounds using 2,000 elements and 3 adaptivity iterations). While it is obvious that the rough/full tension and smooth/no tension cases constitute upper and lower bounds, respectively, on the strength, the intermediate options are more complex to categorize. Thus, in some regions, the smooth/full tension interface is more favorable than the rough/no tension interface and vice versa.

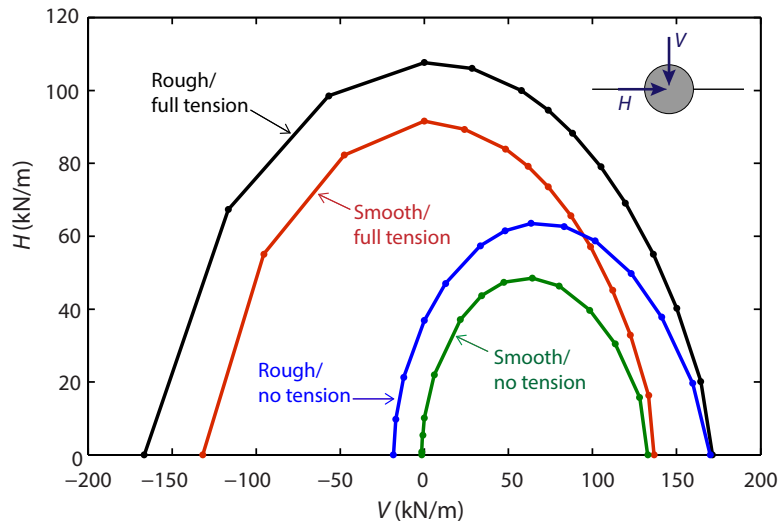


Figure 27.3: V - H diagrams for four different soil-pipeline interface models.

Finally, it should be noted that while the V - H diagrams give the critical pair of (V, H) for any direction of loading, they also contain information about the failure modes for a given pair of (V, H) leading to failure. This is illustrated in Figure 27.4. Considering a critical (V, H) , the associated mode of deformation follows from the normality rule in the sense that the vector of incremental displacement (u_V, u_H) at failure is normal to the (V, H) curve.

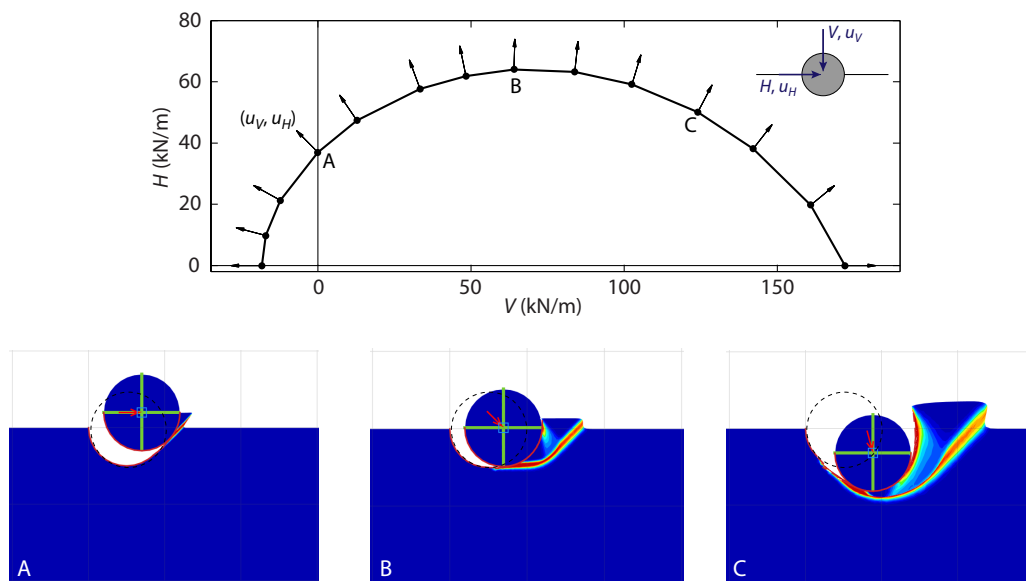


Figure 27.4: V - H diagram for the rough/no tension case and failure modes for selected ultimate (V, H) .

28 BEARING CAPACITY OF SKIRTED FOUNDATION

This example concerns the bearing capacity of a skirted foundation as shown in Figure 28.1. The foundation is subjected to a central point load inclined at 15° with the vertical. The foundation is modeled as a Rigid material with a unit weight of 24 kN/m^3 while the skirts are modeled as plates with a yield moment of 800 kNm/m (corresponding to the default P800 Plate material). As in the previous examples, the concentrated vertical force and moment are transferred to the foundation via a rigid weightless plate. A plate of this type is also used at the bottom of the foundation to connect the skirts. In the following, we consider two types of connections between the skirts and the bottom foundation plate: a standard rigid connection and a hinged connection as shown in Figure 28.1. The soil is modeled as a Tresca material with an undrained shear strength of $s_u = 30 \text{ kPa}$. Finally, a soil-skirt interface strength reduction factor of $r = 0.5$ is assumed.

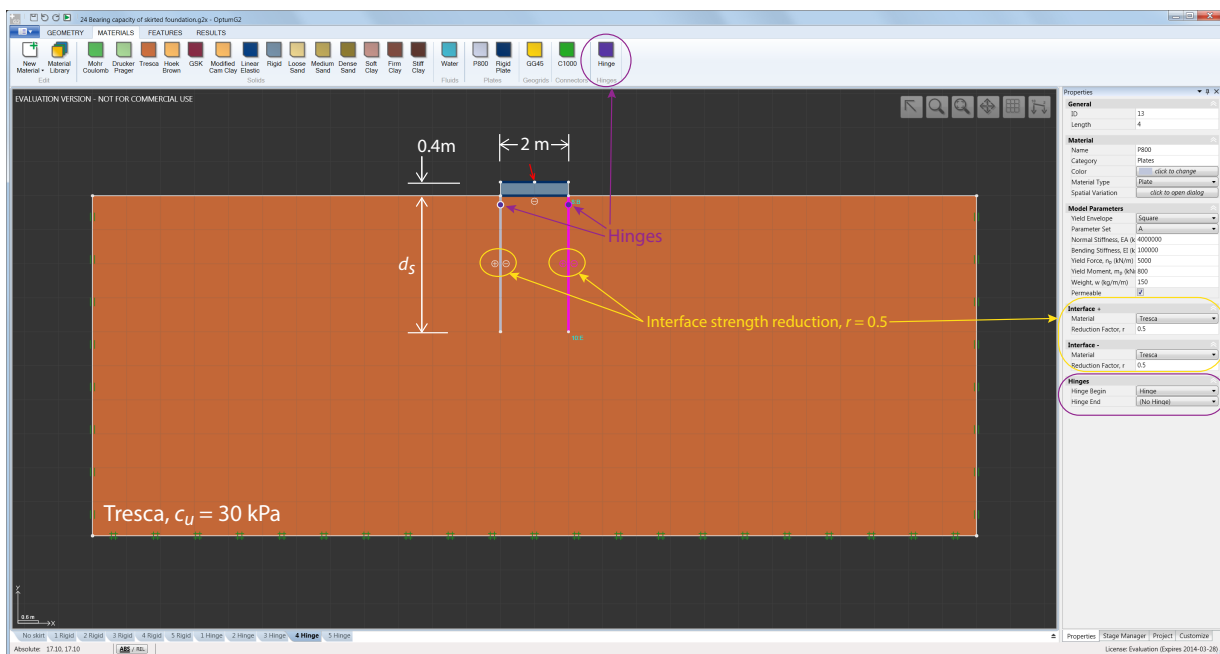


Figure 28.1: Skirted foundation (the right skirt is selected and its properties shown in the window on the right).

Regarding the connection between the skirts and the foundation, some care must be exercised. Firstly, it should be recognized the plates connect to solids only along segments and not at points. In order to establish a connection between the skirts and the foundation, a weightless and rigid plate is placed at the bottom of the foundation. This plate connects to the skirts at its end points and thus establishes the necessary connection between the skirts and the foundation (see Figure 28.2).

Secondly, regarding the mechanics of the connection. It may be impractical to construct a perfectly rigid connection that transmits the full moment between the skirt and the bottom foundation plate. In OPTUM G2, the flexibility of the connection may be taken into account by adding a hinge to the end of the skirts. Hinges are defined through the property window that appears when a plate element is selected (see Figure 28.1). The properties of the hinge are given in terms of special Hinge materials that can be modified via the Materials ribbon. In the present example, we will use the default Hinge material which comes with a yield moment of 0, meaning that no moment is transmitted between the

lower foundation plate and the skirts.

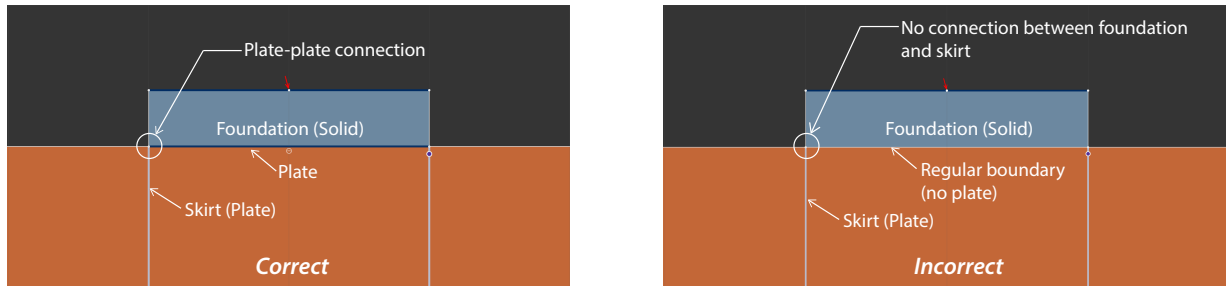


Figure 28.2: Plate-plate connection. The skirt on the left is connected rigidly to the bottom foundation plate while the right skirt is hinged.

In the following, Limit Analysis is used to assess the bearing capacity of the foundation for different skirt depths. A total of 5,000 Lower and Upper elements are used along with 3 adaptivity iterations. The results of the analyses are shown in Figure 28.3. While the rigid foundation-skirt connection leads to a higher strength than the hinged connection, the latter still increases the bearing capacity substantially as compared to the case of a standard foundation without skirts. Selected collapse solutions are shown in Figure 28.4.

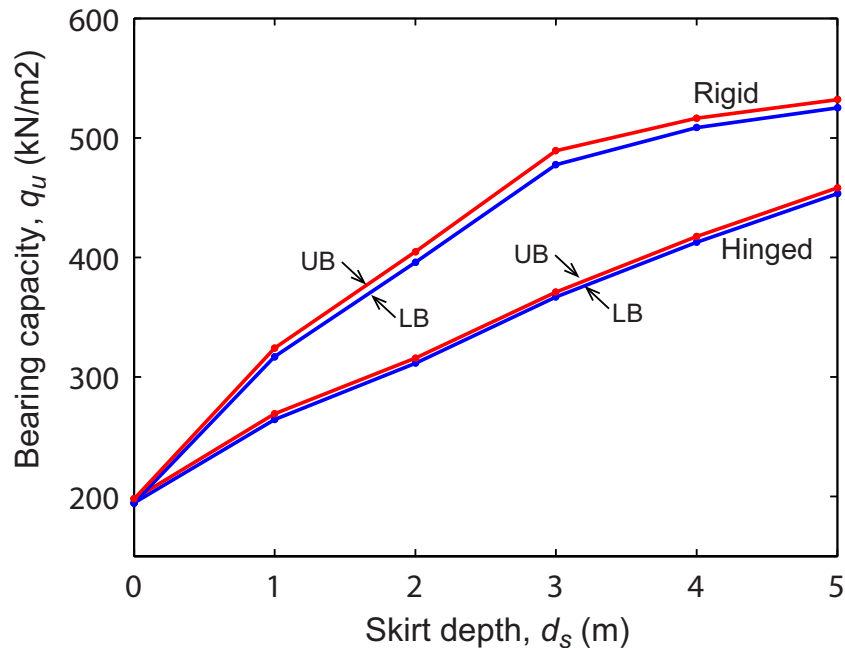


Figure 28.3: Bearing capacity of skirted foundation as function of skirt depth.

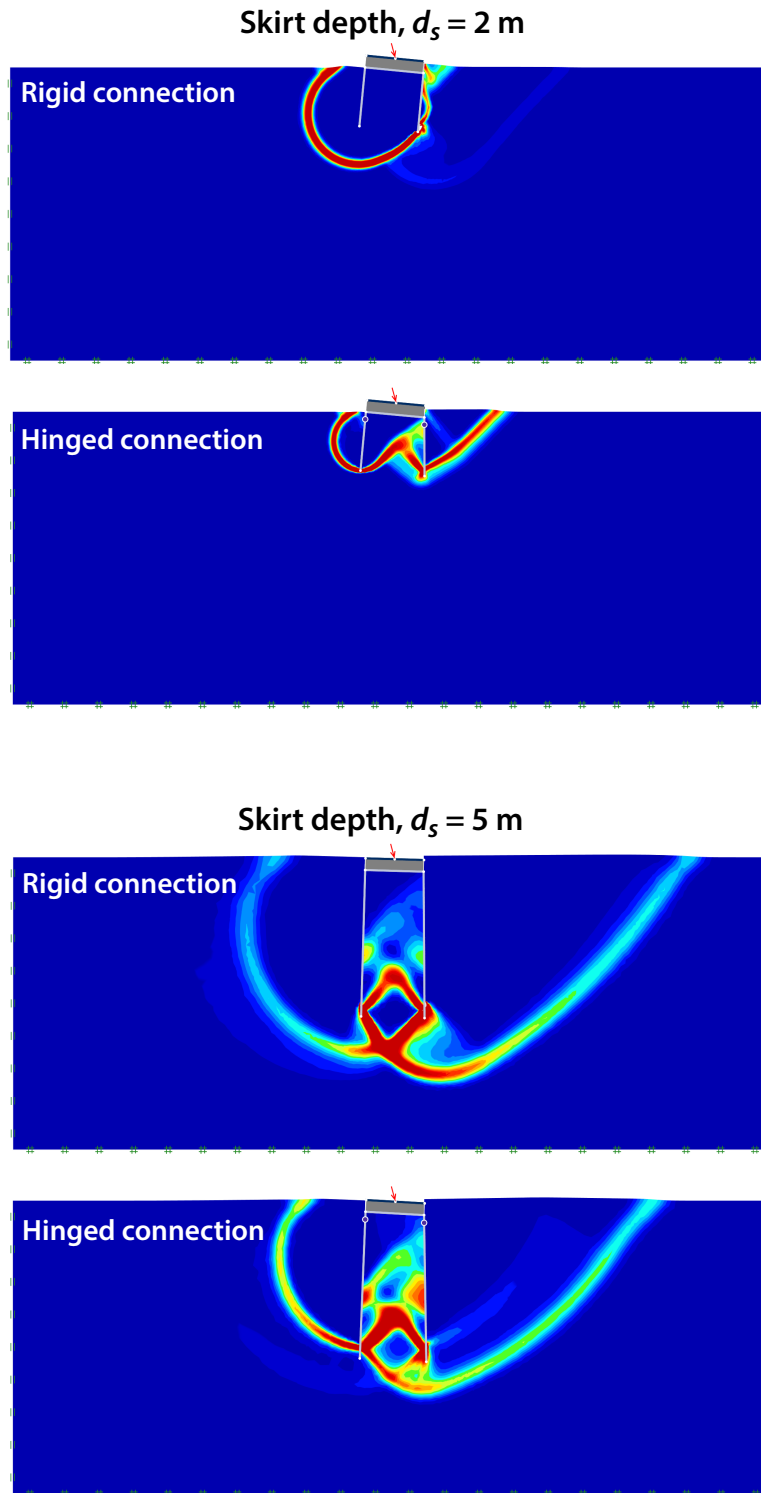


Figure 28.4: Failure modes for skirted foundations.

29 LOAD-DISPLACEMENT ANALYSIS – INTRODUCTORY EXAMPLE

The following example introduces load-displacement analysis using the Multiplier Elastoplastic analysis type. This analysis type is based on an algorithm that is unique to OPTUM G2. In the following it is verified on the basis of previous results of Sloan et al. (2000) using a traditional algorithm. The verification example is shown in Figure 29.1. Two cases are considered: associated flow with $\phi = 30^\circ$ and nonassociated flow where the dilation angle is reduced to $\psi = 20^\circ$. In both cases, the soil of type Mohr-Coulomb with $c = 1$ kPa, $E = 1.04$ MPa and $\nu = 0.3$. Both the soil and the footing are weightless.

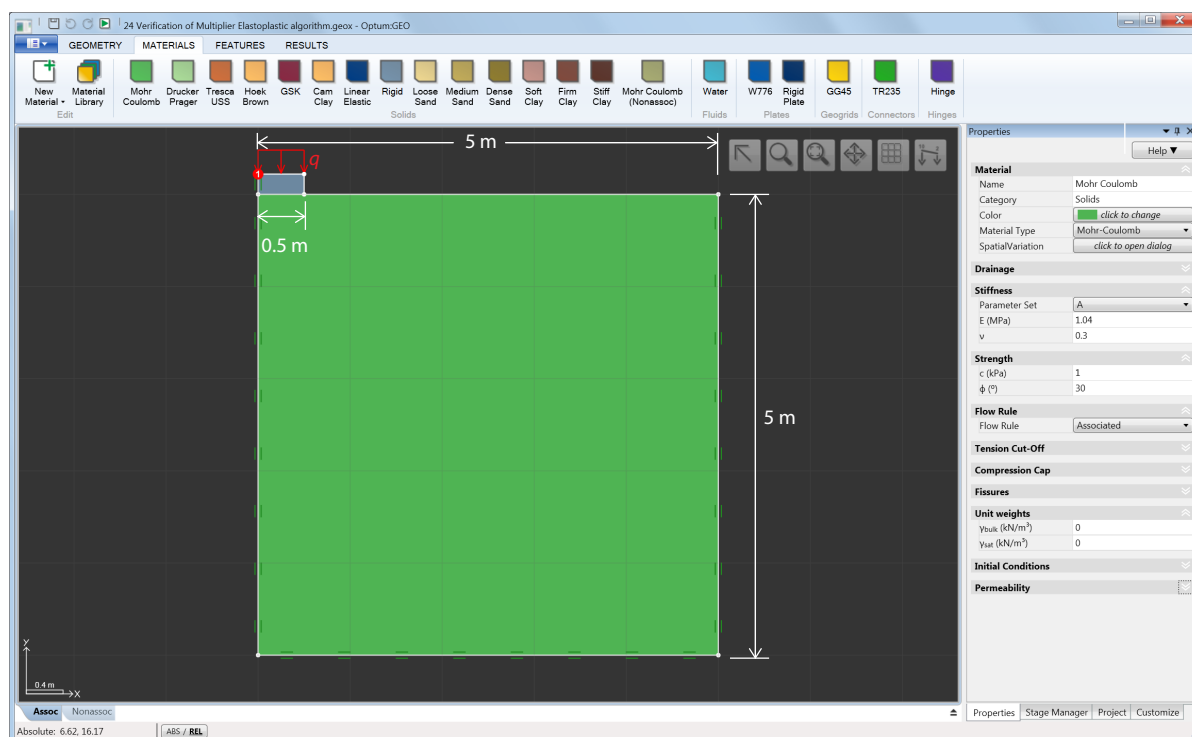


Figure 29.1: Centrally loaded strip footing on a weightless Mohr-Coulomb soil.

29.1 Multiplier Elastoplastic analysis settings

Multiplier Elastoplastic analysis requires that one or more Multiplier Loads (Concentrated, Distributed, or Body) are defined. The magnitude of these loads will then be increased until the bearing capacity is exhausted or else, by appropriate settings, until a predefined level of loading or displacement has been reached. The relevant settings for this purpose are available under the Advanced Settings in the Stage Manager. Fixed Loads, on the other hand, will remain at their specified value throughout the analysis.

The load stepping is controlled via three parameters accessible under Settings in the Stage Manager: N_E , N_P , and β . Considering a typical load-displacement curve as shown in Figure 29.2, the response will initially be approximately linear elastic and then gradually become more and more plastic. N_E and N_P specifies the approximate number of steps in these two regions. The parameter β is used for automatic adjustment of the load step from step to step. For $\beta = 1$, the step size (measured in terms of work) will not vary while higher values of β implies a more aggressive strategy with

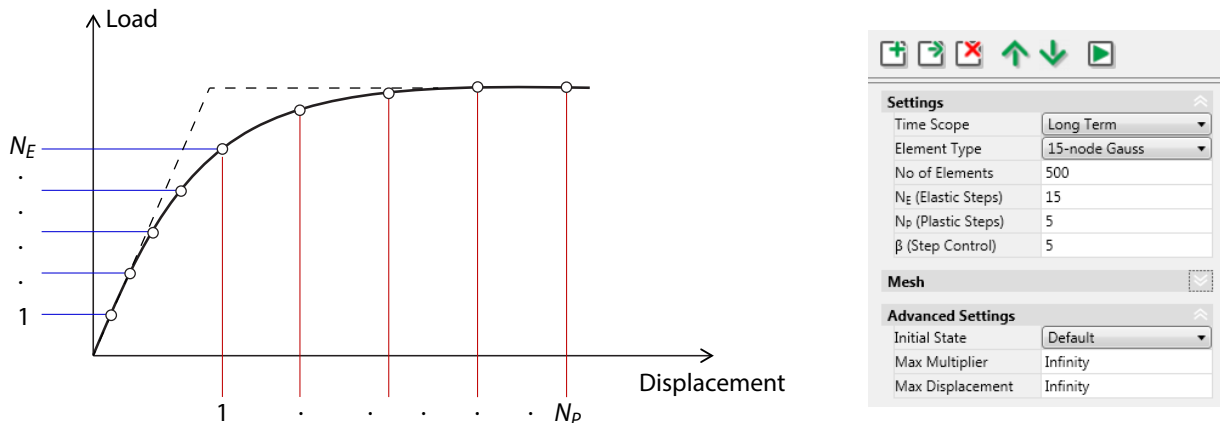


Figure 29.2: Typical load-displacement curve (left) and Settings (Stage Manager).

the step size being increased for parts of the curve where there is little change. For most problems, the default parameters, $N_E = 10$, $N_P = 10$, and $\beta = 5$, are a good starting point and often little improvement is observed as a result of increasing the number of steps, i.e. increasing N_E and N_P .

The initial stresses may be computed in a separated stage which is then linked to the Multiplier Elastoplastic stage by specifying it as From stage. Alternatively, if no From stage is specified, the option Initial State under Advanced provides a number of options for computing the initial stresses. The three options are:

1. Default. The initial stresses are calculated automatically using an Initial Stress analysis (see Section I.II). All Multiplier Loads are ignored in this phase.
2. Auto. This setting is relevant for problems that initially are unstable unless the Multiplier Loads are different from zero. On the basis of an elastoplastic calculation, both a stress field and a minimum load multiplier leading to a stable state are computed.
3. User. This setting is equivalent to Auto except that the initial value of the load multiplier is user specified.

If a From stage is specified, the initial stresses are simply the final stresses of the From stage.

In the following, no From stage is specified and the Default option is used.

29.2 Data logging

It is usually of interest to log various data during the load stepping procedure, for example the displacement at certain points. In OPTUM G2, the load multiplier is automatically logged while a Result Point (Features ribbon) may be defined at any point to log displacements, stresses and various other quantities at that point. These results may then be plotted using the XY Plots tool in the Results ribbon.

29.3 Results

Using 500 15-node Gauss elements, $N_E = 15$ and $N_P = 5$, the load-displacement response shown in Figure 29.3 is computed. As seen, the agreement between the computed solution and that of

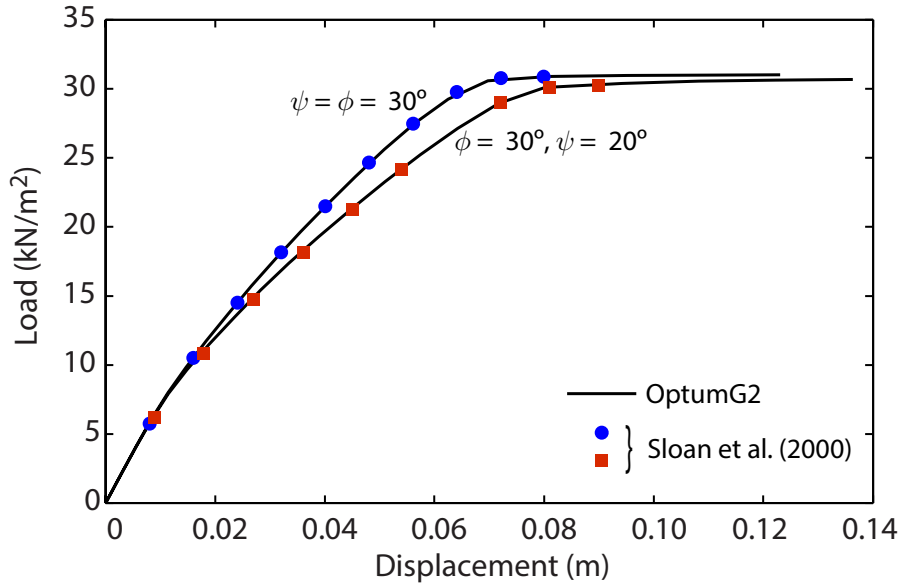


Figure 29.3: Computed load-displacement response of strip footing and comparison to Sloan et al. (2000).

Sloan et al. (2000) is excellent.

The deformations at the end of the analyses and the patterns of shear dissipation are shown in 29.4. We note that the size of the domain used by Sloan et al. (2000) in the associated case is somewhat too small to be considered semi-infinite although this is irrelevant to the conclusions of the present analysis.

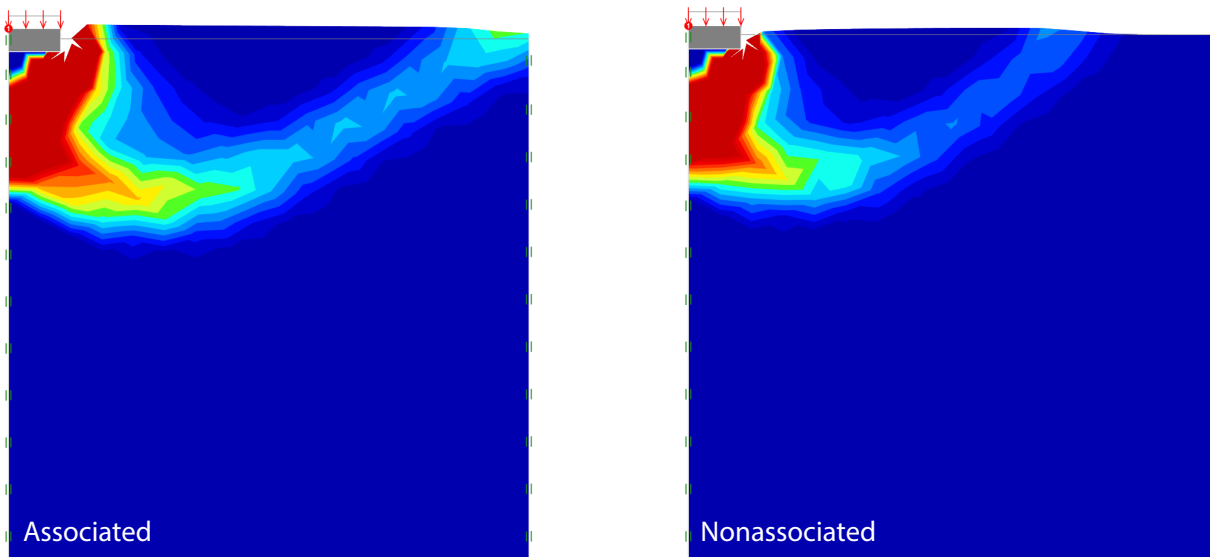


Figure 29.4: Deformations and distributions of shear dissipation.

30 LOAD-DISPLACEMENT ANALYSIS OF FOUNDATION IN MC CLAY

This example concerns the load-displacement analysis of a shallow foundation as shown in Figure (30.1). The soil is the default Firm Clay material and the foundation is modeled as a Rigid material with a unit weight of 22 kN/m^3 . The analyses are carried out as a Multiplier Elastoplastic analysis where all Multipliers are incremented until the bearing capacity is exhausted or the process terminated due to a specified load level or displacement having been reached (see the previous section for details). The soil-foundation interface is modeled using a Shear Joint. The material is of the same type as the Firm Clay material used to model the soil but the strengths have been reduced to $c_{\text{interface}} = 0.5 \times c_{\text{soil}} = 5 \text{ kPa}$ and $\phi_{\text{interface}} = \arctan[0.5 \tan(\phi_{\text{soil}})] = 10.3^\circ$.

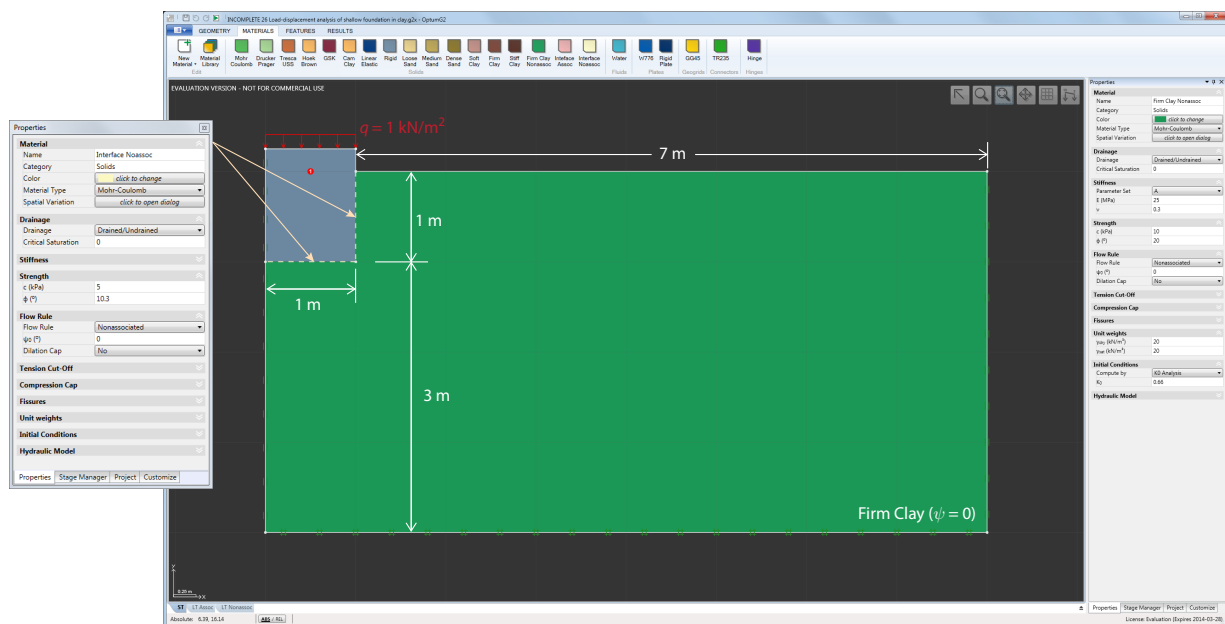


Figure 30.1: Shallow foundation in Firm Clay.

Elastic parameters

For this analysis, and in contrast to the most of the problems discussed so far, both elastic and plastic parameters must be considered. The former can be defined in two ways: either via Parameter Set A which requires specification of Young's modulus E and Poisson's ratio ν , or via Parameter Set B which requires specification of the bulk modulus K and the shear modulus G . The relation between the two sets of parameters is given in the Materials Manual. Parameter Set A is the default. It should be noted that the two sets are not linked, i.e. a change to one set will not affect the parameters in the other set.

Flow rule

In the previous examples involving Limit Analysis and Strength Reduction analysis, the flow rule has been assumed associated. Indeed, the framework of limit analysis hinges crucially on this type of flow rule. However, as is well known, the associated flow rule tends to overestimate the dilation actually observed experimentally for typical geomaterials. In contrast to Limit Analysis, Multiplier Elastoplastic analysis opens the possibility of using any flow rule. For the Mohr-Coulomb criterion,

the flow rule is specified via the dilation angle, ψ , as described in the Materials Manual. In summary, $\psi = \phi$ implies associated flow (and thus, for most materials, excessive dilation) while $\psi = 0$ implies zero volumetric plastic strains. Under undrained conditions, the associated flow rule is particularly problematic as it leads to an infinite limit load, as will any dilation angle greater than zero.

Multiplier Elastoplastic analysis settings

The Multiplier Elastoplastic settings are the default ones. Since no From stage is specified, the initial stresses will be computed automatically using an Initial Stress analysis. This analysis aims to find a stress state that satisfies yield and equilibrium while satisfying the initial stress conditions $\sigma'_x = \sigma'_z = K_0 \sigma'_y$ to the greatest possible extent (see the Analysis Manual for details). In this example, the earth pressure coefficient is $K_0 = 0.66$.

30.1 Short Term analysis

We begin by a Short Term analysis using default settings for all parameters related to load stepping. The default element for Multiplier Elastoplastic analysis is the 6-node Gauss element. 2,000 of such elements are used.

Upon solving, distributions of stresses, strains, displacements, etc corresponding to the final state can be plotted in the same way as for the previous analysis types.

In addition, various data at the location of the Result Point are stored and can subsequently be plotted via the XY Plots tool under Report in the Results ribbon (see Figure 30.2).

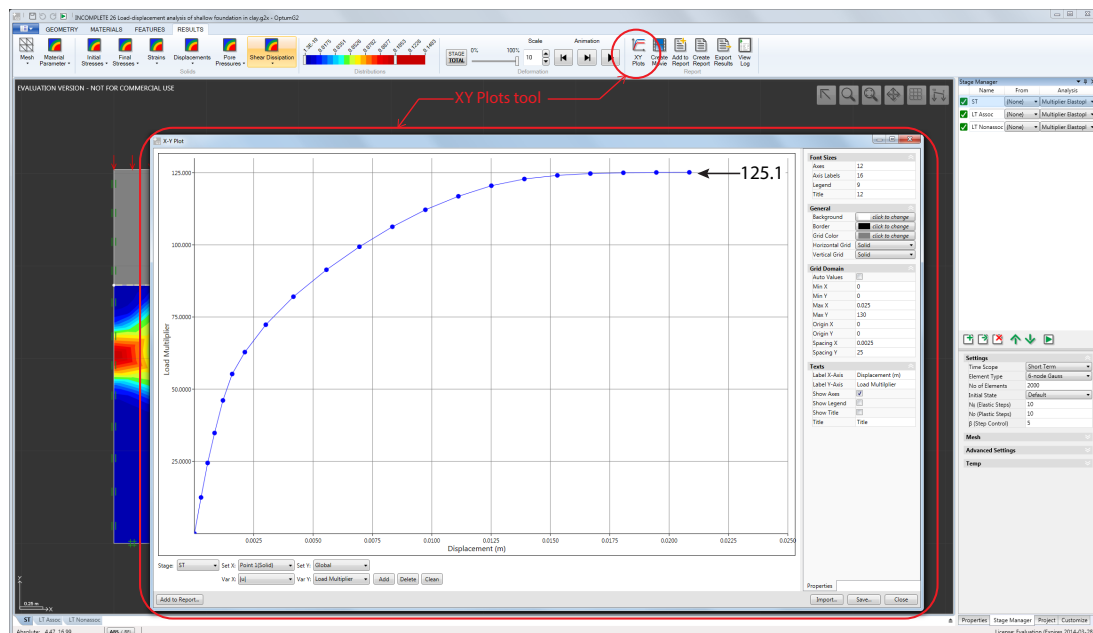


Figure 30.2: Load-displacement curves for Short Term analysis using the XY Plots tool.

Upon entering the XY Plots window, the stage for which results should be plotted is first selected. Then one of a number of results sets are selected and finally variables from these result sets are

plotted using Add button. For the X axis, we choose the variable set Point 1 (Solid), corresponding to the previously defined Result point, and from this set choose the variable $|u|$ (the length of the displacement vector, $|u| = \sqrt{u_x^2 + u_y^2}$) which in this case is the absolute value of the vertical displacement. For the Y axis, the set General is chosen and from this set Load Multiplier is chosen. The resulting curve thus shows the foundation displacement (positive downwards) versus the load multiplier which, with a reference Multiplier Distributed load of 1, is equal to the load q (kN/m²).

Finally, the deformations and shear dissipation distribution for the nonassociated material at the final state are shown in Figure (30.3). We see that the collapse field is consistent with a dilation angle of $\psi = 0$.

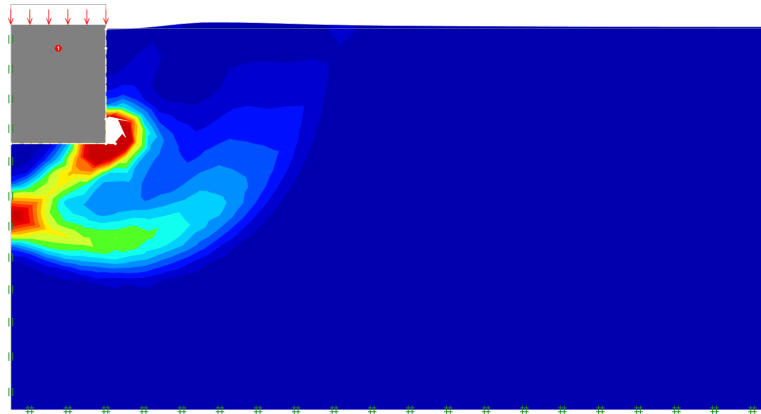


Figure 30.3: Deformed geometry (scaled by a factor of 10) and shear dissipation distribution for the final state of the analysis.

The final collapse load arrived at in the above analysis could also have been computed using Limit Analysis. Moreover, upper and lower bounds bracketing the true solution could have been computed using the Upper and Lower elements respectively. Alternatively, these elements may be used in a Multiplier Elastoplastic analysis to not only bracket the ultimate strength but also the stiffness of the system. An example is shown in Figure 30.4 where 2,000 elements have been used in all the analyses.

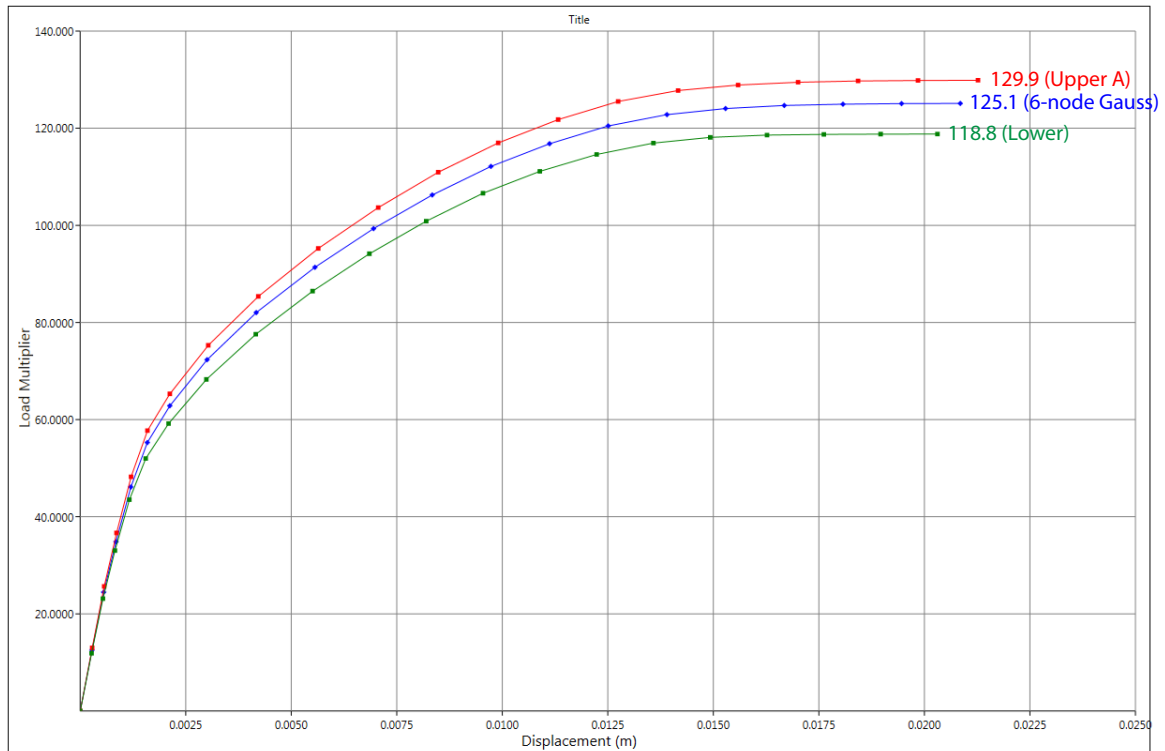


Figure 30.4: Short Term Multiplier Elastoplastic analysis using 6-node Gauss, Lower and Upper elements.

30.2 Long Term analysis

Next, the two cases, $\psi = \phi$ and $\psi = 0$, are considered in the long term. The necessary switch is easily achieved by changing the Time Scope to Long Term (Settings in the Stage Manager).

Regarding the calculations, it should be noted that while calculations with associated material requires only a single solution in each load step, nonassociated analyses require a number of iterations in each load step, each of which is approximately equal to a single associated calculation. As such, analyses with nonassociated materials are usually somewhat more expensive than the equivalent associated calculation. In the present example, the nonassociated analysis requires on average 3 solutions per load step in comparison to the single solution per load step of the associated analysis.

The resulting load-displacement curves are shown in Figure 30.5. In this case, the difference in bearing capacity is rather moderate while the difference in displacement at certain load levels is more pronounced. In both regards, the nonassociated material is the more conservative, i.e. it is both less stiff and has less strength than the equivalent associated material. While it can be shown that the strength of an associated material is always greater than or equal to that of the nonassociated material, the same cannot be said about the deformations: for some problems (such as the present one), the associated flow rule will imply smaller displacements while for other problems the trend is the opposite. It is also noted that the load-displacement curve in the nonassociated case displays an apparent softening. This is a consequence of the flow rule alone and not of numerical artifacts or material softening (see the Theory Manual).

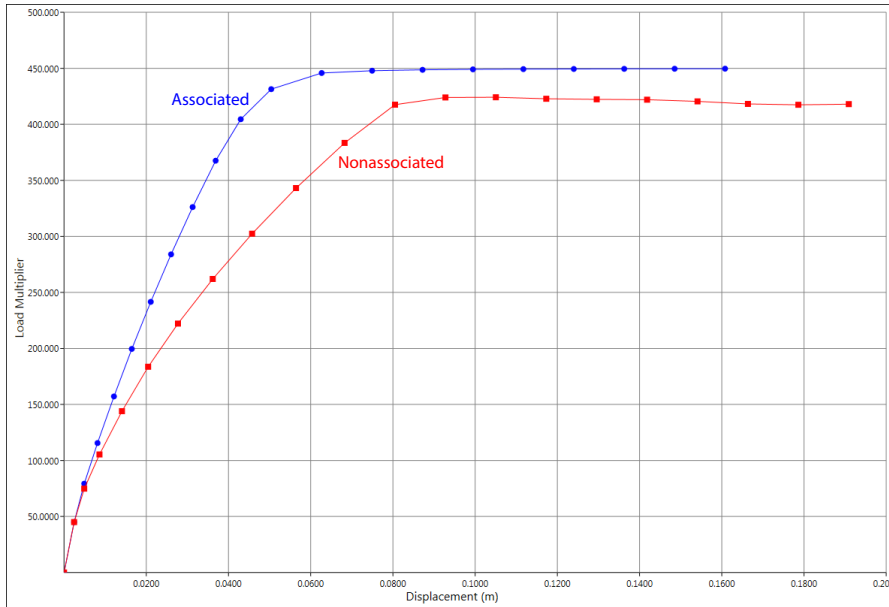


Figure 30.5: Load-displacement curves for Long Term analysis.

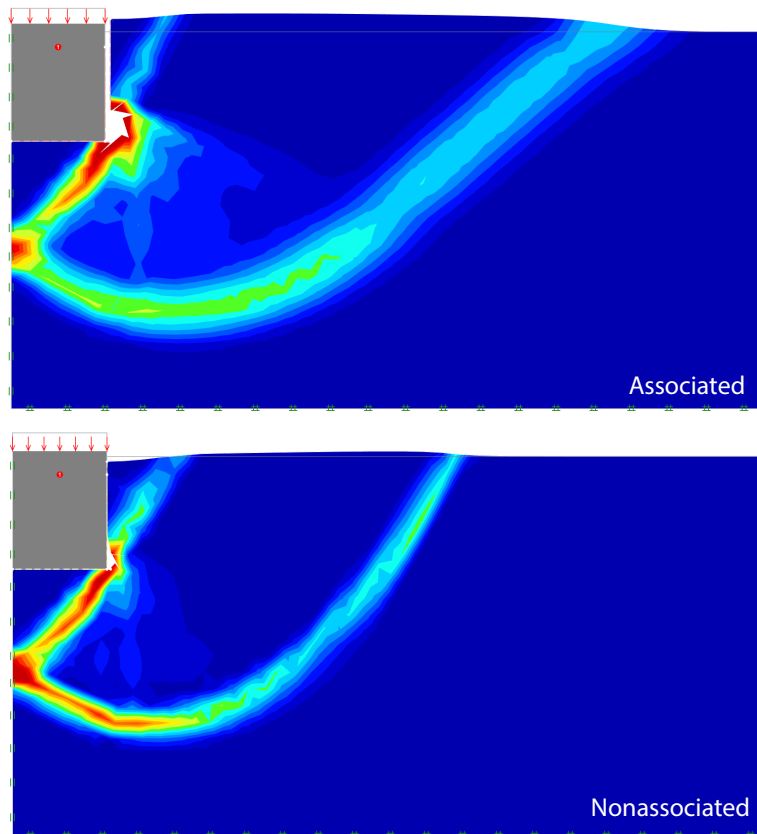


Figure 30.6: Deformed geometry (to scale) and plastic multiplier field for final state of analyses.

The deformations and plastic multiplier fields for the two cases are shown in Figure 30.6. These reveal somewhat different modes of collapse and degrees of dilation (for example at the vertical soil-foundation interface for the associated material). It is also noted that the plastic strains (as gauged by the plastic multiplier field) are somewhat more localized than for the associated material.

30.3 Limit Analysis

The key advantage of limit analysis over elastoplastic analysis of the type discussed above is that only a single calculation is necessary to determine the ultimate limit load. The drawback is that no information about the displacements (other than the collapse mechanism) is obtained. Furthermore, a key feature of limit analysis is that the flow rule is associated. In the short term analysis this would essentially imply that the limit load is infinite. However, in OPTUM G2 a more specialized form of limit analysis able to operate with a zero dilation angle in the case of undrained conditions has been implemented. As such, depending on the type of element used in the limit analysis, a result similar or identical to the one found above will be obtained. Under drained conditions, however, the flow rule of limit analysis is always associated. These features are illustrated below.

30.3.1 Short Term analysis

Provided that identical material models, meshes, element types, etc are used in Multiplier Elastoplastic analysis and Limit Analysis, the final result in terms of the ultimate limit load will be the same in the two types of analysis. This point is illustrated by the results summarized in Table 30.1.

In the above Multiplier Elastoplastic analysis, 2,000 elements of types 6-node Gauss, Lower, and Upper are used. Rerunning the problem using Limit Analysis a practically identical result is obtained, the slight difference being due to the fact that displacements in the Multiplier Elastoplastic analysis (about 0.2 cm, see Figure 30.2) still are such that a state of total collapse, in principle, has not been attained. However, by continuing the loading, the value obtained from Limit Analysis will eventually be replicated exactly.

Mesh and Elements	Analysis Type	Limit Load
2,000 6-node Gauss	Multiplier Elastoplastic	125.1
2,000 6-node Gauss	Limit Analysis	125.2
2,000 Lower	Multiplier Elastoplastic	118.8
2,000 Lower	Limit Analysis	118.8
2,000 Upper	Multiplier Elastoplastic	129.9
2,000 Upper	Limit Analysis	130.0

Table 30.1: Short Term limit loads using different elements and analysis types.

From the results of Table 30.1, we see that the original results computed using the 6-node Gauss element fall approximately in between the results of the Lower and Upper elements. As such, they can be regarded as being fairly accurate.

30.3.2 Long Term analysis

We now consider the case of long term analysis. As discussed above, the flow rule has an influence on both the failure load and the displacements prior to failure. For drained analysis, Limit Analysis and Multiplier Elastoplastic analysis will generally only be in agreement if the flow rule is associated. However, it is possible to determine effective, or Davis, parameters that when used in a limit analysis setting lead to a reasonable, and usually conservative, estimate of the ultimate limit load observed

in a nonassociated Multiplier Elastoplastic analysis (see the Theory Manual). For $\phi = 20^\circ$, $\psi = 0$ and $c = 10$ kPa, the Davis parameters are (see the Materials Manual):

$$c_D = 9.40 \text{ kPa}; \quad \phi_D = 18.88^\circ \quad (30.1)$$

Table 30.2 summarizes a variety of results obtained using these parameters as well as the original ones. These first of all confirm the fact that Limit Analysis and Multiplier Elastoplastic analysis provide identical bearing capacities in the case where the flow rule is associated. Secondly, in the case where the flow rule is nonassociated, Limit Analysis using Davis parameters furnish a reasonable, and in this case conservative, estimate of the bearing capacity.

Mesh and Elements	Flow Rule	Analysis Type	Limit Load
2,000 6-node Gauss	Associated	Multiplier Elastoplastic	459.6
2,000 6-node Gauss	Associated	Limit Analysis	460.4
2,000 6-node Gauss	Nonassociated	Multiplier Elastoplastic	424.9
2,000 6-node Gauss	Associated, Davis	Limit Analysis	400.6

Table 30.2: Short Term limit loads using different elements and analysis types.

30.4 Summary

The influence of the flow rule for the Mohr-Coulomb material can be summarized as follows:

- Provided the same material parameters and finite element model are used, the ultimate limit loads obtained from Limit Analysis and Multiplier Elastoplastic analysis are identical.
- For Short Term analysis of Drained/Undrained materials, the ultimate limit loads obtained from Limit Analysis and Multiplier Elastoplastic analysis are identical.
- For Long Term analysis, both the bearing capacity and the displacements prior to the ultimate limit state are affected by the flow rule. The effect of the flow rule on the bearing capacity can be estimated by using Davis parameters in a standard Limit Analysis calculation.
- All the finite elements available in OPTUM G2 are applicable to all analysis types. Using Lower and Upper elements in Multiplier Elastoplastic analysis, it is possible to compute solutions that provide bounds on both the strength and the stiffness of the system.

31 LOAD-DISPLACEMENT ANALYSIS OF FOUNDATION IN MC SAND

This example (Figure 31.1) is similar to the previous one. Again, Multiplier Elastoplastic analysis is used to trace the load-displacement curve from the initial unloaded state to incipient collapse. The default strength parameters of the Medium Sand material are $c = 0$, $\phi = 35^\circ$ and, in the case of nonassociated flow, $\psi = 5^\circ$. In contrast to the previous example where the soil-foundation interface was modeled by means of a Shear Joint with reduced material parameters, we use Rigid Plate elements as shown in Figure 31.1. The interface strength reduction factor can then be applied directly without having to specify a separate material. In the following, we use a reduction factor of $r = 0.5$ throughout. The Drainage Conditions are Always Drained so the Time Scope (Long Term or Short Term) is immaterial.

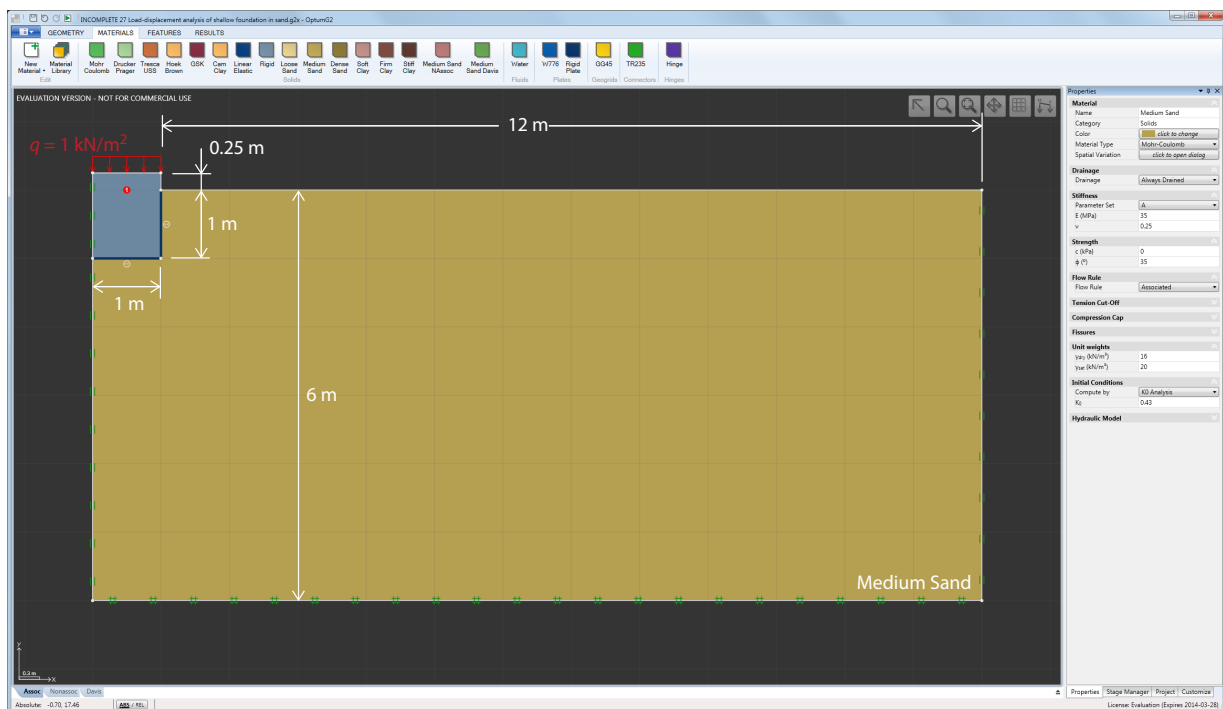


Figure 31.1: Shallow foundation in Medium Sand.

We proceed by solving the problem for both the associated ($\psi = \phi$) and nonassociated ($\psi = 5^\circ$) cases using 2,000 of 6-node Gauss elements. Mesh adaptivity with default settings is used. The initial stresses are computed automatically (Initial State = Default under Settings in the Stage Manager). In addition, to estimate the effects of nonassociativity without performing a full Multiplier Elastoplastic analysis, a Limit Analyses using Davis parameters is carried out, also with 2,000 6-node FE. In the case of $c = 0$, $\phi = 35^\circ$, $\psi = 5^\circ$ the Davis parameters are: $c_D = 0$, $\phi_D = 31.03^\circ$.

The resulting load-displacement curves are shown in Figure 31.2 while the collapse solutions in the two cases are shown in Figure 31.3. The key features are:

- The load-displacement response in the two cases differs in several ways: the apparent stiffness in the nonassociated case is smaller, as is the strength. Moreover, the load-displacement curve for the nonassociated case displays a peak followed by an apparent softening to a residual level. Note, that no explicit material softening is included in the model; the apparent softening is a consequence of the flow rule alone.

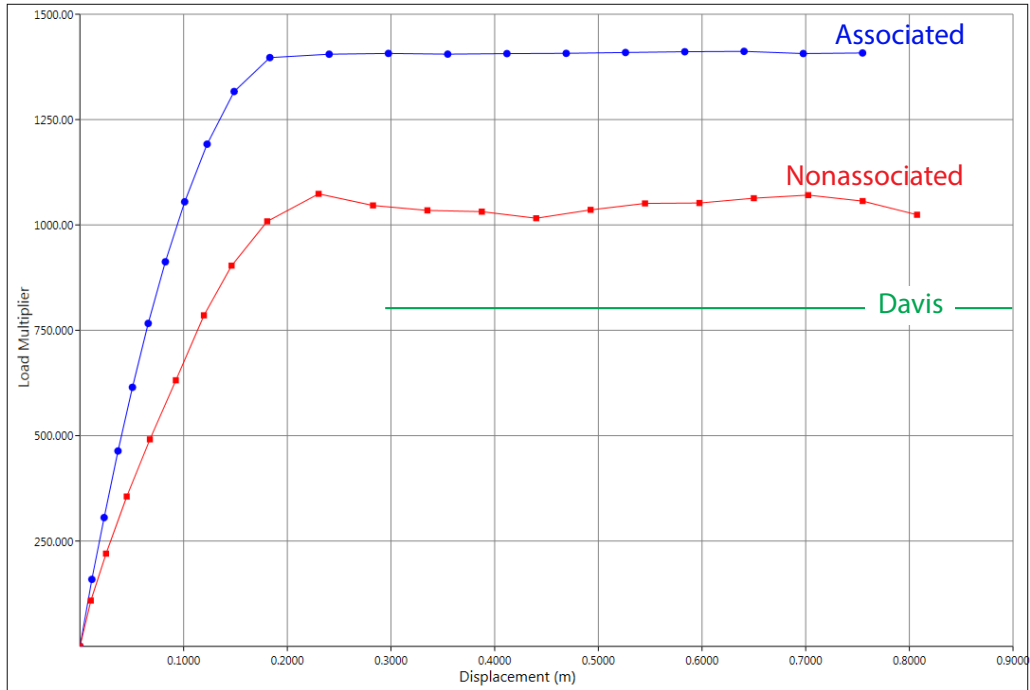


Figure 31.2: Load-displacement curves for shallow foundation in Medium Sand.

- The Davis solution provides a somewhat conservative estimate of the actual bearing capacity in the nonassociated case.
- The final collapse solutions differ significantly in the two cases and reflect the very different dilation angles ($\phi = 35^\circ$ in the associated case versus $\psi = 5^\circ$ in the nonassociated case). Also, as noted in the previous example, the plasticity in the nonassociated case is somewhat more localized than in the associated case.

These key features and differences between associated and nonassociated flow rules are discussed in more detail in the Theory Manual.

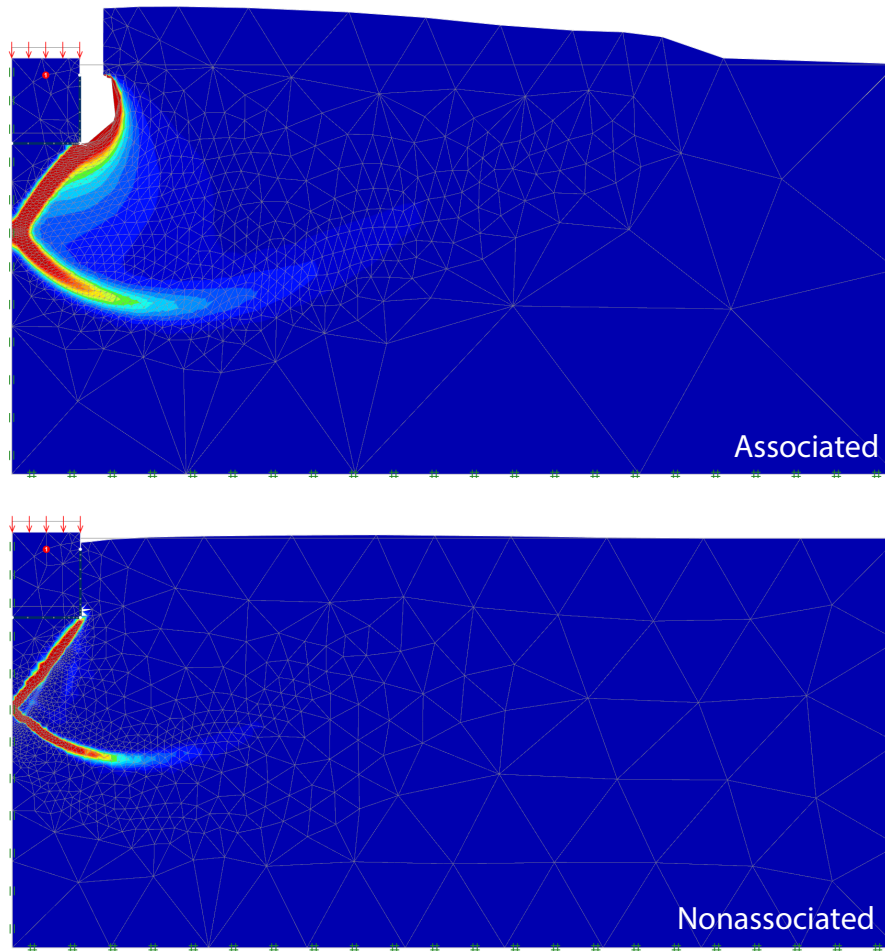
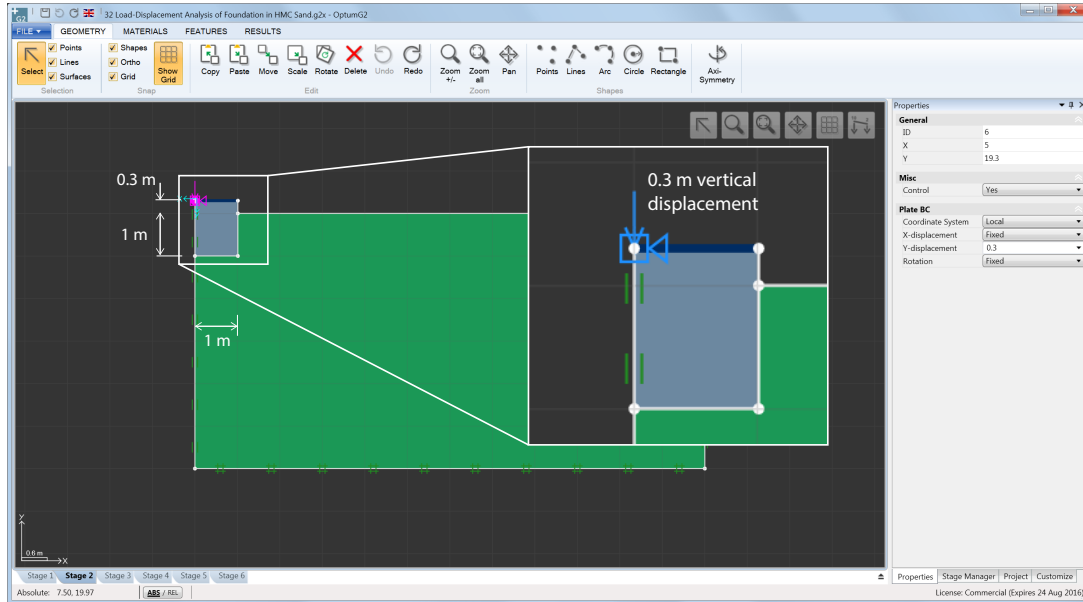


Figure 31.3: Shear dissipation and collapse mechanism for associated and nonassociated materials.

32 LOAD-DISPLACEMENT ANALYSIS OF FOUNDATION IN HMC SAND

The following example considers the load-displacement analysis of a shallow foundation as shown in Figure 32.1. Three different analyses with three different materials are considered: Loose Sand-HMC, Medium Sand-HMC and Dense Sand-HMC. These are default materials available in OPTUM G2 and represent, approximately, a loose, medium and dense sand parameterized by the HMC model. The material parameters are as shown in Figure 32.1.



Material	Medium Sand/EMC	Dense Sand/EMC
Material	Medium Sand/EMC	Dense Sand/EMC
Name	Medium Sand/EMC	Dense Sand/EMC
Category	Solids	Solids
Color	Green	Green
Material Type	EMC	EMC
Spatial Variation	click to open dialog	click to open dialog
Drainage	Always Drained	Always Drained
Stiffness	Parameter Set: A Eur, ref (MPa): 75 ν: 0.25 E50, ref (MPa): 25	Parameter Set: A Eur, ref (MPa): 150 ν: 0.3 E50, ref (MPa): 50
Strength	c (kPa): 0 φ (°): 35	c (kPa): 0 φ (°): 40
Flow Rule	Flow Rule: Taylor ψ (°): 5	Flow Rule: Taylor ψ (°): 10
Pressure Dependence	pref (kPa): 100 m: 0.5	pref (kPa): 100 m: 0.5
Unit weights	γdry (kN/m³): 16 γsat (kN/m³): 20	γdry (kN/m³): 18 γsat (kN/m³): 21
Initial Conditions	K0: 0.426423563648954	K0: 0.357212390313461

Figure 32.1: Shallow foundation in HMC sand (top) and parameters for default materials Loose Sand-HMC, Medium Sand-HMC and Dense Sand-HMC (bottom).

The HMC model is described in detail in the Materials Manual. Compared to the standard Mohr-

Coulomb model, the main distinguishing features are:

- Use of two stiffness moduli: a secant modulus $E_{50,ref}$ characterizing initial loading and a modulus $E_{ur,ref}$ characterizing unloading/reloading. Both moduli refer to a standard triaxial compression test at a confining pressure of p_{ref} ($= 100$ kPa for the default HMC materials). Both moduli are pressure dependent to capture the behavior for pressures different from p_{ref} .
- Use of Taylor's stress-dilatancy relation instead of the constant dilation in the Mohr-Coulomb model (the latter relation is an option in the HMC model). Whatever the flow rule chosen, the dilation angle at the ultimate limit state is given by ψ .

In the following, displacement controlled Elastoplastic analyses are conducted using 2,000 6-node Gauss elements with 20 steps. The final vertical displacement is 0.3 m and is specified as part of the Plate BC associated with the Rigid plate on top of the foundation (see Figure 32.1). The resulting load-displacement curves are shown in Figure 32.2. As for the standard Mohr-Coulomb model with a nonassociated flow rule, some apparent softening is observed, especially for the dense sand. The ultimate limit loads follow a similar pattern: they fall in between those obtained with Limit Analysis using the original friction angle and the Davis angle respectively and are closer to the former. Note, however, that since the problems considered are prone to localization, significantly lower bearing capacities could be obtained as a result of increasing the number of elements or using mesh adaptivity.

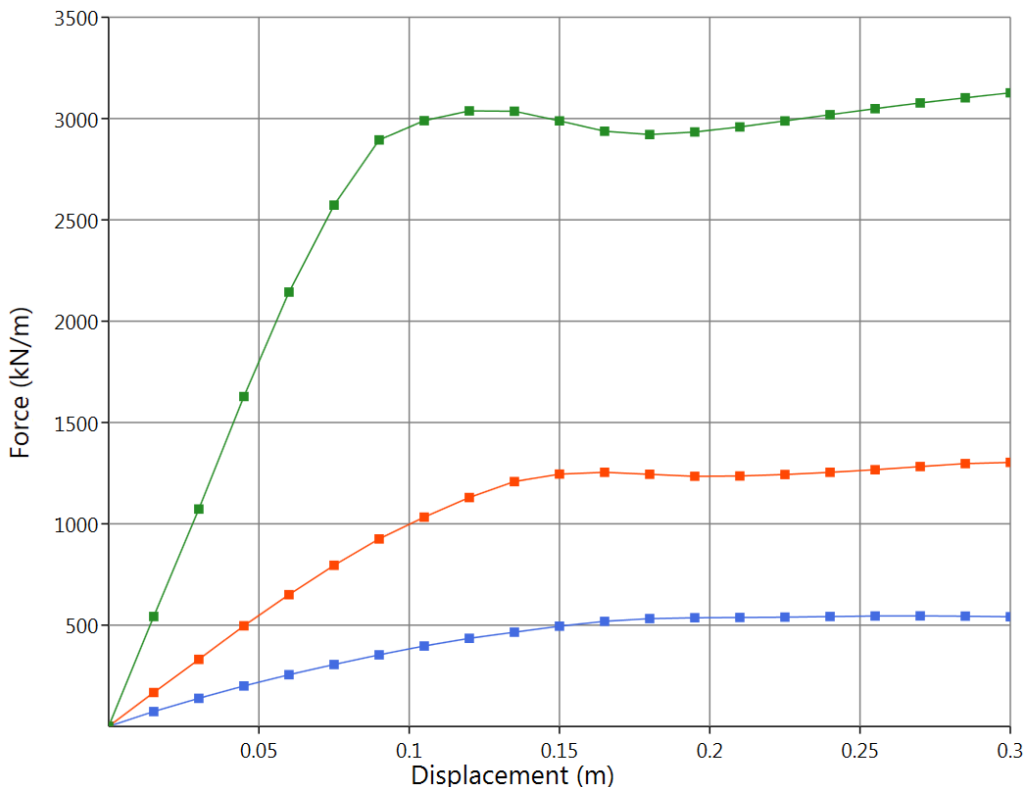


Figure 32.2: Load-displacement curves for shallow foundation on HMC sand.

	EP	LA-Original	LA-Davis
Loose Sand-HMC	540	630	360
Medium Sand-HMC	1,250	1,480	800
Dense Sand-HMC	3,000	3,560	1,720

Table 32.1: Approximate limit loads computed by means of Multiplier Elastoplastic analysis (MEP), Limit Analysis using the original friction angles (LA-Original), and Limit Analysis using the Davis angles (LA-Davis). The Davis angles are $\phi_D = 26.6^\circ$, 31.0° and 35.5° for the loose, medium and dense sands respectively.

Finally, the deformations and plastic multiplier field for the Medium case are shown in Figure 32.3. The overall picture is here again similar to that of the standard Mohr-Coulomb model.

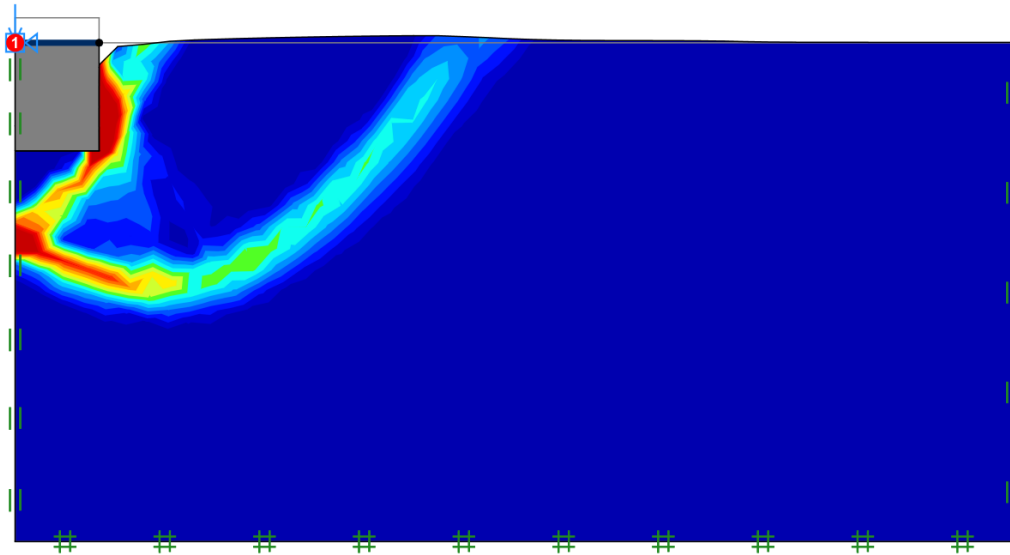


Figure 32.3: Deformations and plastic multiplier field for Medium Sand-HMC.

33 PULL-OUT OF ANCHOR IN SAND

This example concerns the pull-out of an anchor as shown in Figure 33.1. The soil is the default Loose Sand material and the anchor is modeled as a weightless Rigid Plate with rough interfaces. The boundary conditions used imply symmetry about the left vertical boundary. We again examine the effects of the flow rule using Multiplier Elastoplastic analysis for two cases: associated ($\psi = \phi$) and nonassociated with $\psi = 0$. In both cases the cohesion is zero.

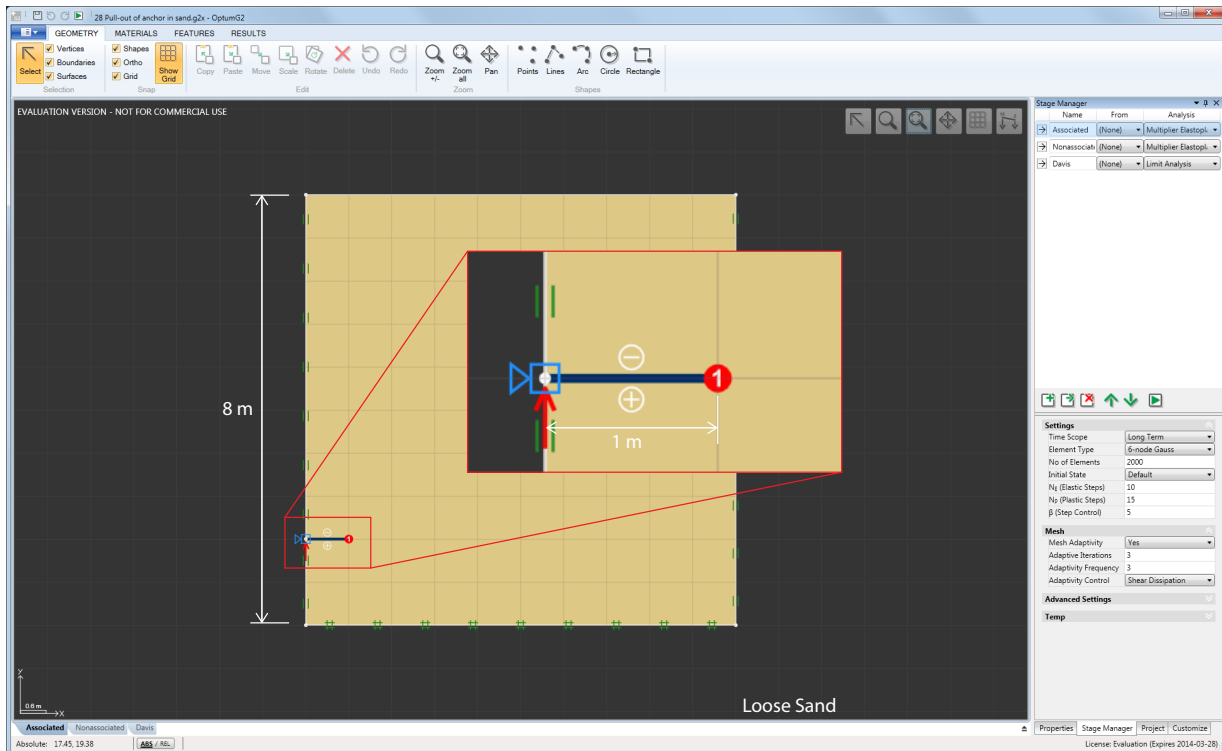


Figure 33.1: Pull-out of anchor in Loose Sand.

The Settings for both the associated and the nonassociated analysis are as shown in Figure 33.1. In contrast to the previous example, we use slightly more ‘plastic’ steps ($N_P = 15$) than ‘elastic’ steps ($N_E = 10$). Also, mesh adaptivity with default settings (Adaptive Iterations = 3 and Adaptivity Frequency = 3 is used).

The resulting load-displacement curves are shown in Figure 33.2. As in the previous example, nonassociativity implies a reduction in both strength and stiffness. However, in contrast to the previous examples, the Davis friction angle, $\phi_D = 26.5651^\circ$ in this case, leads to an overestimate of the strength in the nonassociated case. This has previously been noted and discussed by Krabbenhoft et al. (2012) and the current results thus confirm that while the Davis parameters usually lead to a good estimate of the strength of nonassociated materials, it is not necessarily conservative.

Finally, the deformations and plastic multiplier fields at the end of the analyses are shown in Figure 33.3. As in the previous examples, the effects of dilation are apparent.

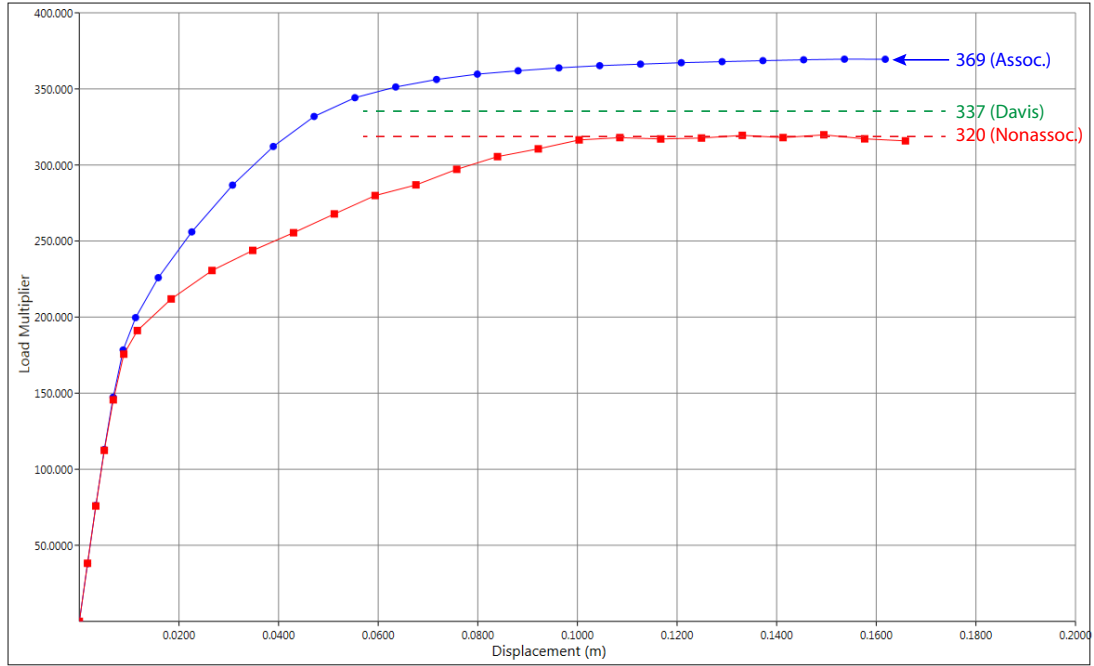


Figure 33.2: Load-displacement curves for anchor pull-out in Loose Sand.

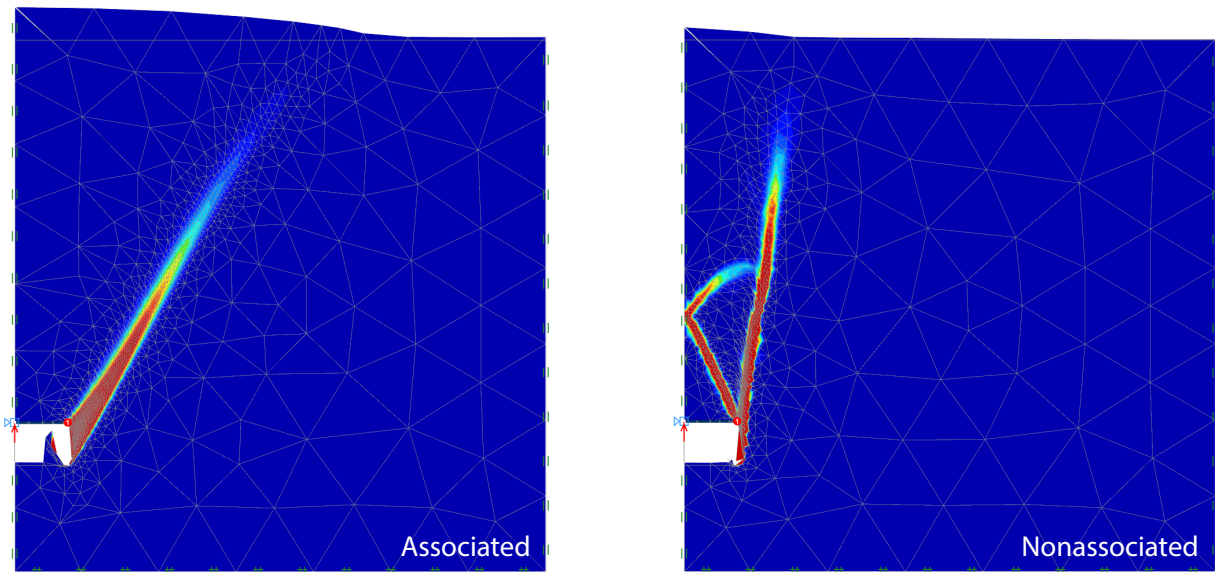


Figure 33.3: Deformations (scaled by a factor of 5) and plastic multiplier fields.

34 FAULT RUPTURE PROPAGATION IN SAND

This example demonstrates the application of non-standard boundary conditions as well as the influence of the flow rule on the failure kinematics of frictional materials such as sands. The problem under consideration is inspired by the study of Anastasopoulos et al. (2007). The setup is as sketched in Figure 34.1. In the normal faulting configuration, the right and bottom walls are gradually moved downwards at a given inclination α_N until a failure occurs. In the reverse faulting configuration, the walls are instead moved upwards at an inclination α_R with the horizontal.

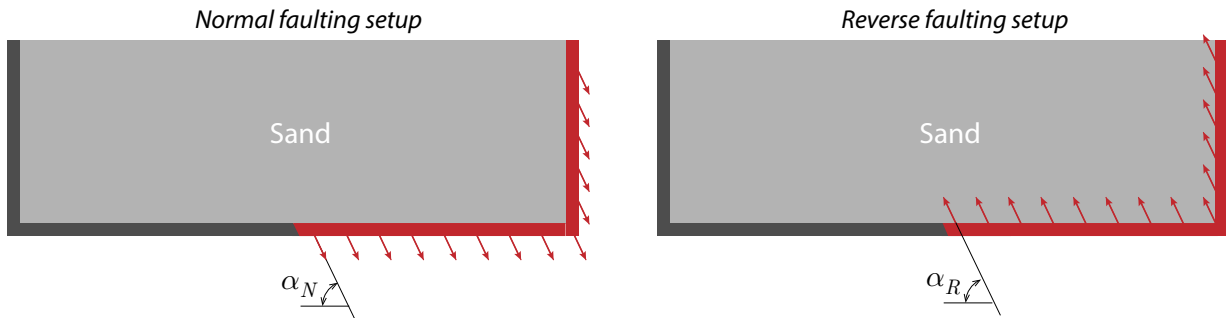


Figure 34.1: Normal and reverse faulting setups. The gray walls are immovable while displacements are prescribed on the red walls. All walls are assumed rigid.

In OPTUM G2, displacement boundary conditions can be imposed with respect to structural elements only. For the present problem, the moveable walls are modeled as Rigid Plates as shown in Figure 34.2 while regular Supports are used for the immovable walls. Next, from the lower right

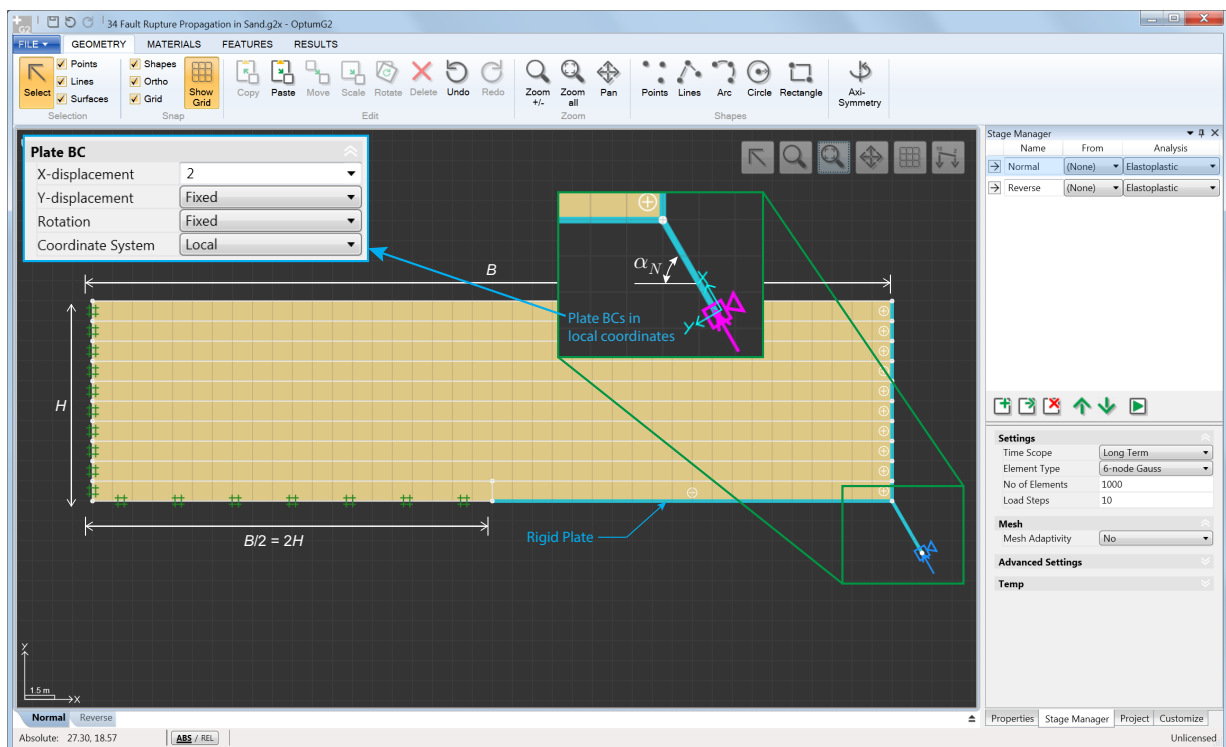


Figure 34.2: Fault propagation problem (reverse faulting). The horizontal divisions are included for visualization purposes only.

corner, another Rigid Plate is extended downwards at a direction corresponding to the direction of faulting (α_N or α_R). At the end of this plate, displacement boundary conditions can be imposed in a local coordinate system to allow the whole Rigid Plate system to move only along the direction given by the extension plate.

In the following, the normal and reverse fault configurations for $\alpha_N = \alpha_R = 60^\circ$ are considered. The material is the default material Loose Sand with a nonassociated flow rule ($\phi = 30^\circ, \psi = 0^\circ$). The problems are analyzed by Multiplier Elastoplastic analysis using a total of 10,000 6-node Gauss elements.

The deformations and plastic multiplier fields at the final state of the analyses are shown in Figure 34.3. The solutions are in good agreement with those observed experimentally by Anastasopoulos et al. (2007).

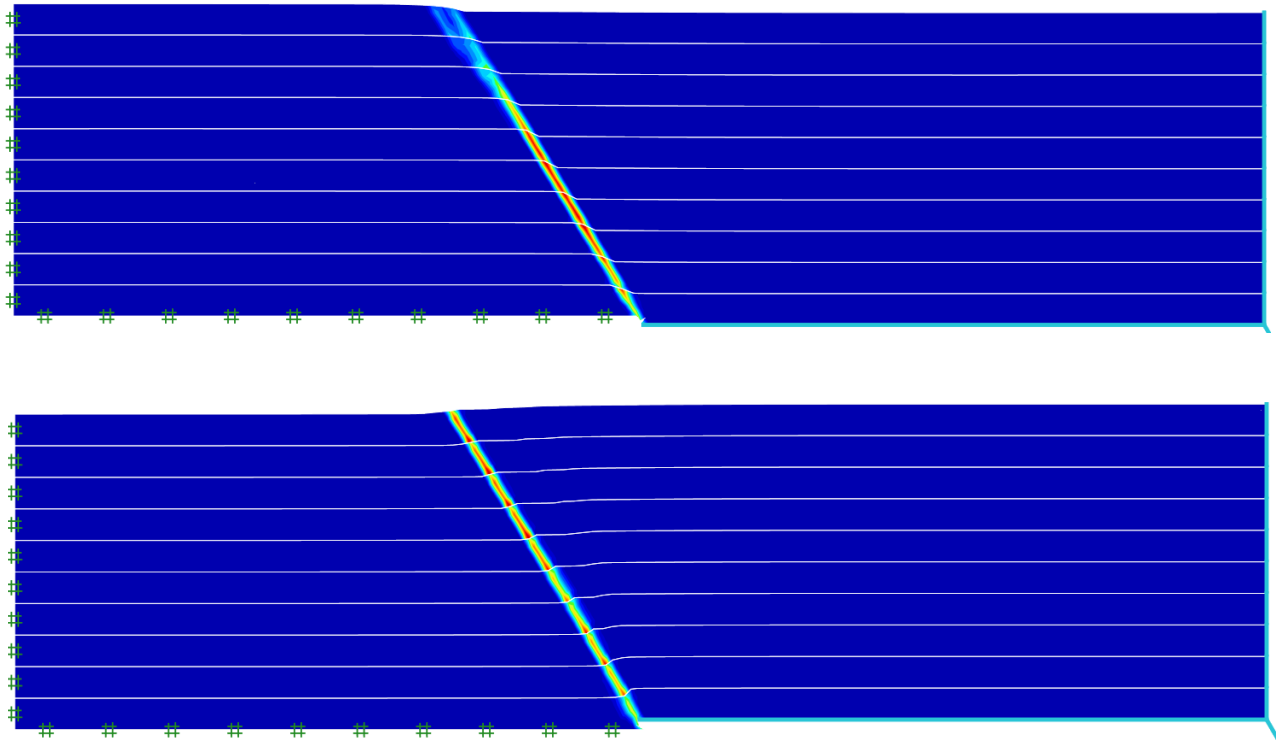


Figure 34.3: Normal (top) and reverse (bottom) fault configurations close to failure.

35 CONFINED SEEPAGE AROUND IMPERMEABLE SHEET PILE

In this example, we consider the confined seepage around a sheet pile wall as shown in Figure 35.1. It is assumed that the sheet pile wall is positioned under an 8 m wide impermeable dam. Rather than modeling the dam, the base of the dam is considered impermeable. Similarly, rather than explicitly modeling the water on the upstream side of the dam, equivalent fixed head boundary conditions are imposed. On the downstream side of the dam, the water table is maintained at ground level. The sheet pile wall is modeled as a Rigid Plate. In OPTUM G2, such elements may be either permeable or impermeable as indicated in Figure 35.1. In this example, the sheet pile is considered impermeable. The hydraulic model is taken as the Linear model with default settings and $k_x = k_y = 1 \text{ m/day}$.

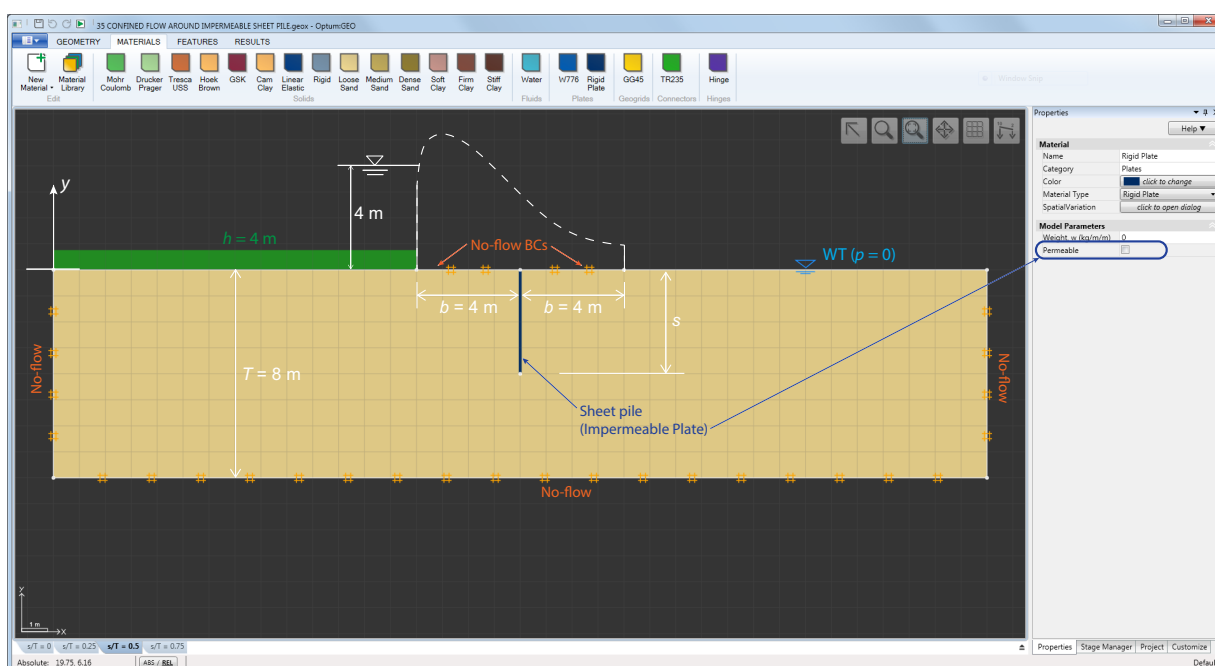


Figure 35.1: Confined seepage around sheet pile.

This problem has been solved analytically by Polubarinova-Kochina (1962) for a range of geometries. The total flux, Q , from one side of the dam to the other can be determined from the charts in Figure 35.2. Comparisons between analytical and computed solutions for selected wall depths, s , are shown in Table 35.1. We see that the numerical and analytical solutions are in very good agreement already for the coarsest meshes comprising 1,000 elements. The pressure head distributions (for 16,000 elements) are shown in Figure 35.3.

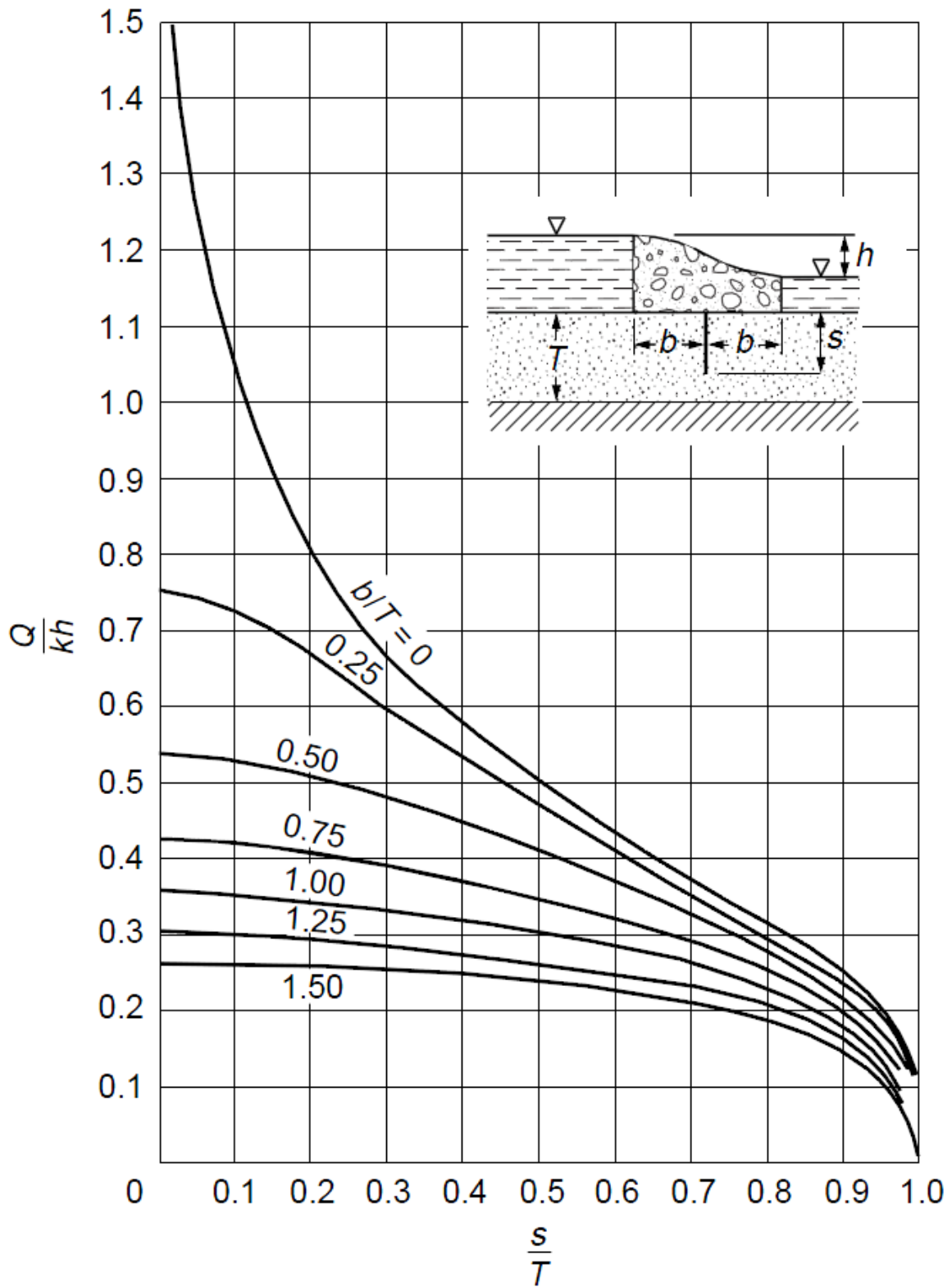


Figure 35.2: Polubarinova-Kochina (1962) solution for confined seepage around sheet pile.

s (m)	OPTUM G2					Analytical
	1,000	2,000	4,000	8,000	16,000	
0.0	2.19	2.17	2.16	2.15	2.14	2.14
2.0	2.05	2.03	2.01	2.00	1.99	1.98
4.0	1.69	1.67	1.66	1.65	1.64	1.64
6.0	1.27	1.25	1.24	1.23	1.22	1.21

Table 35.1: Comparison between analytical (Polubarinova-Kochina 1962) and computed fluxes Q ($m^3/day/m$) using 1,000 to 16,000 elements.

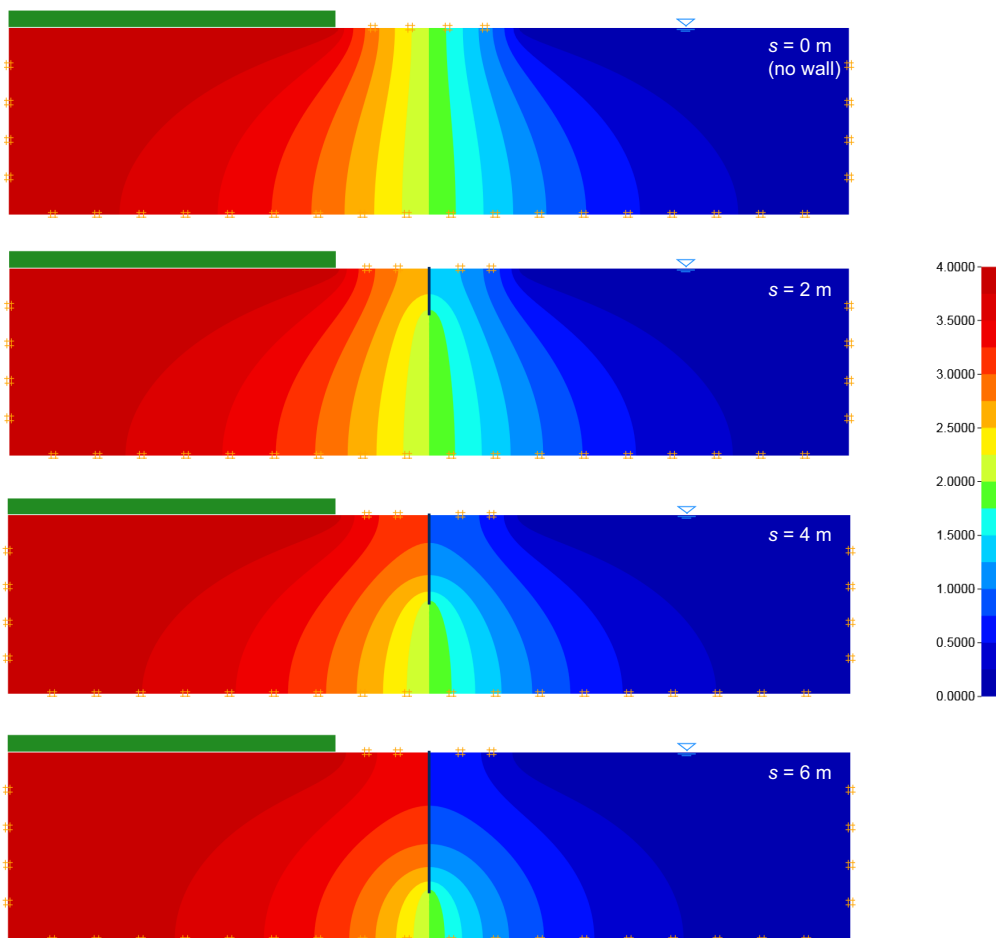


Figure 35.3: Pressure head distributions (m).

35.1 Alternative modeling

Instead of modeling the problem by imposing relevant fixed head and no-flow boundary conditions to account for the reservoir and the dam, both may be modeled using the Water material from the Fluids category and a solid with Drainage = Non-Porous from the Solids category. This alternative problem setup is shown in Figure 35.4. The reservoir may here be defined as usual, by defining the geometry and assigning the relevant material, or it may be defined using the Water Table tool available in the Features ribbon. Whichever approach is used it is important to note that the top of the water domain must be defined as a zero pressure line (indicated by a blue triangle). The geom-

CONFINED SEEPAGE AROUND IMPERMEABLE SHEET PILE

etry of the dam is defined in the usual way and the Rigid material assigned. The default drainage condition for this material is Impermeable and placing the dam on top of the soil domain as shown will thus have the same effect as imposing a no-flow boundary condition as was done originally.

Using this alternative modeling strategy, all domains including the reservoir and the dam are discretized by finite elements as shown below.

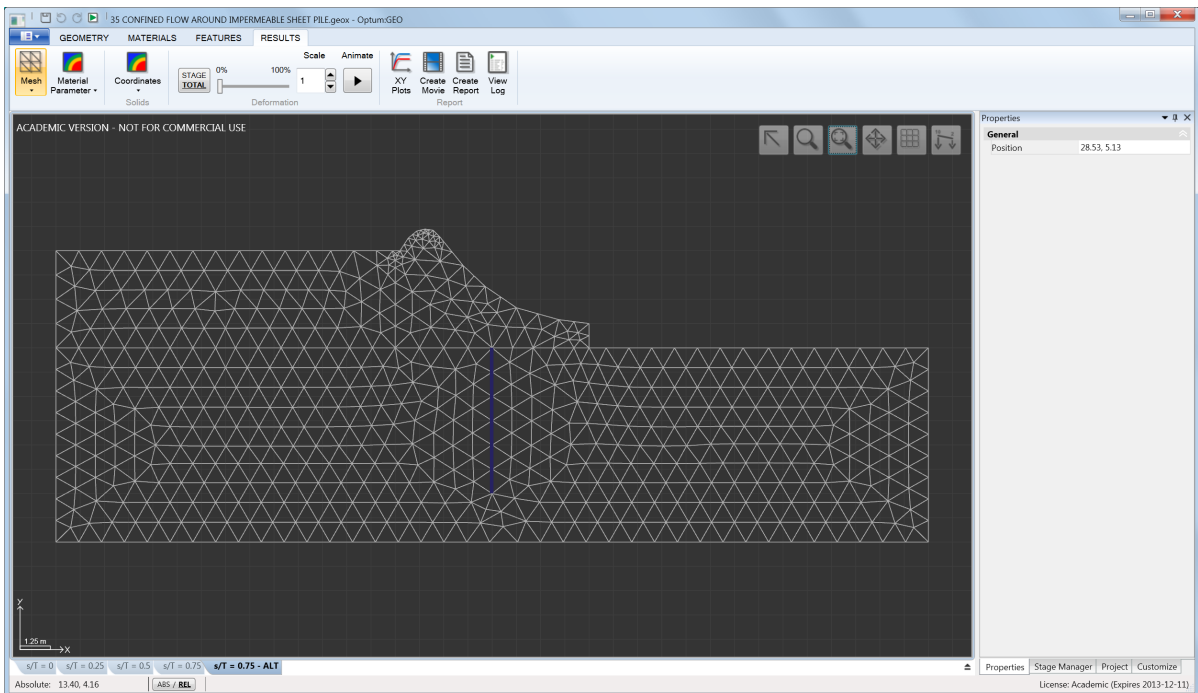
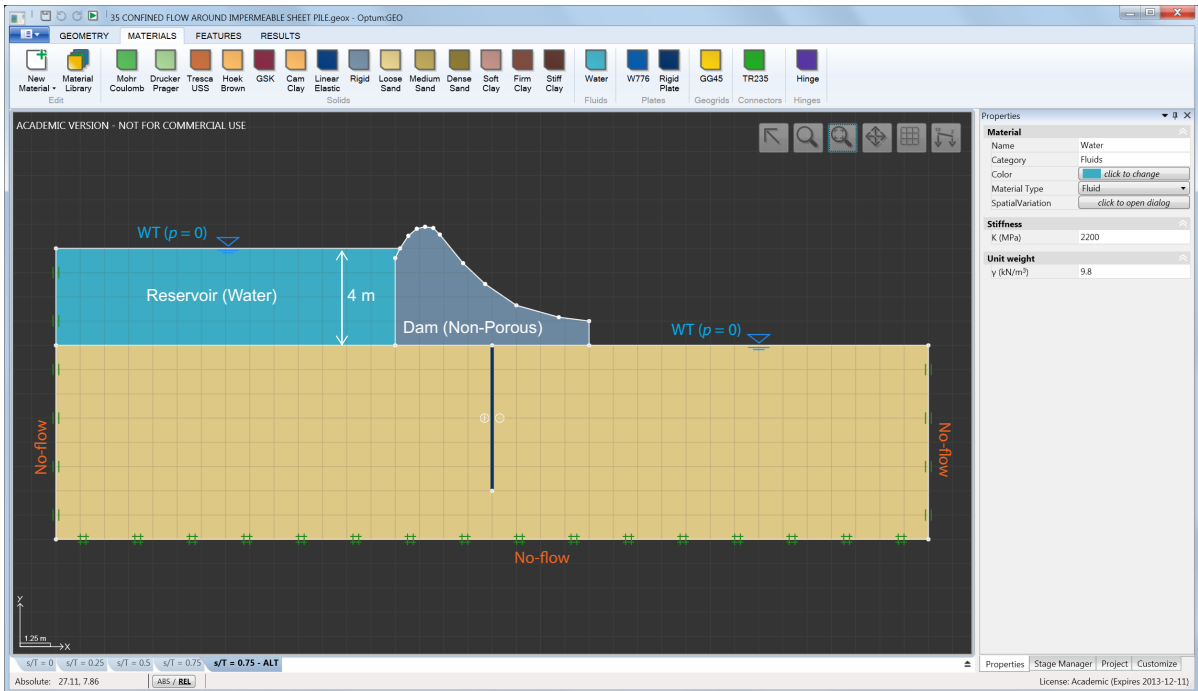


Figure 35.4: Confined seepage around sheet pile: alternative modeling and resulting mesh.

35.2 Mesh adaptivity

As with all other analysis types, it is for Seepage analysis possible to adapt the mesh in a series of adaptivity iterations. In this case, the relevant Adaptivity Control variable is Flow. This ensures that the mesh is adapted on the basis of a combination of the 'flow energy', $\frac{1}{2} \mathbf{q}^T \mathbf{K} \mathbf{q}$, and a measure ensuring a reasonable concentration of elements around free surfaces (not relevant in the present problem).

The results of the analyses using 1,000 elements and 3 adaptivity iterations are shown in Figure 35.5. As seen, the critical regions are the edges of the dam and the bottom of the sheet pile. Also, note that the results in terms of the total flow are of an accuracy similar to or better than those obtained with 16,000 elements without adaptivity.

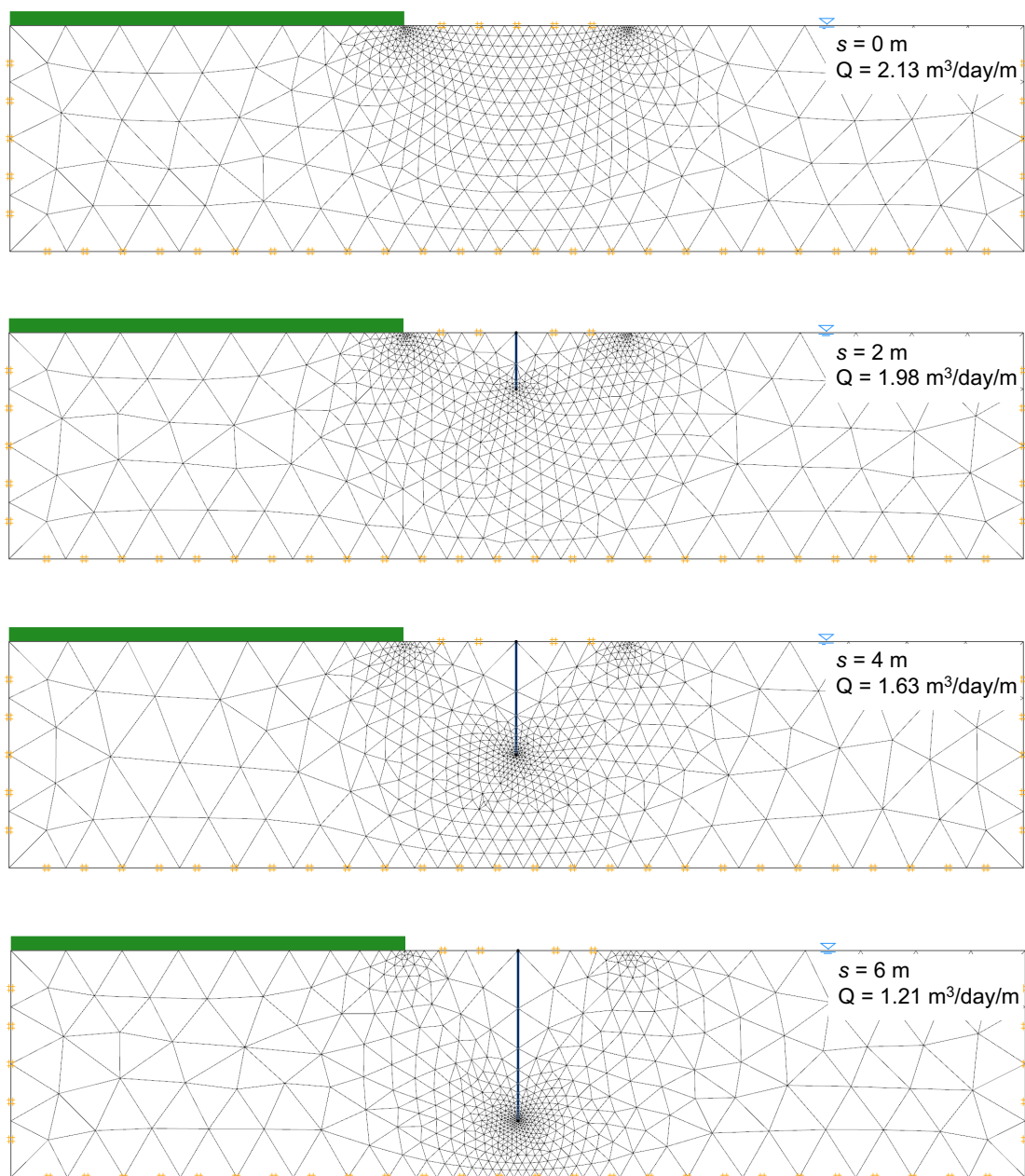


Figure 35.5: Adapted meshes (1,000 elements) and resulting fluxes.

36 UNCONFINED SEEPAGE THROUGH RECTANGULAR DAMS

In this example the classical problem of unconfined seepage through a rectangular dam is considered. The problem setup is shown in Figure 36.1. A dam of height $H_A = 10$ m and length $L = 5$ m is considered. On the left side, the water level is at $H_A = 10$ m while on the right side it is at $H_B = 4$ m. To account for these conditions, pressure boundary conditions are imposed with the pressures varying linearly from the top to $H_A\gamma_w = -980$ kPa and $H_B\gamma_w = -39.2$ kPa, respectively, on the left and right sides (note the sign of the boundary pressures). Finally, at the bottom, a no-flow boundary condition is imposed. The remaining boundaries for which no conditions have been imposed will be treated as seepage faces, i.e. boundaries at which a discharge at zero pressure can take place.

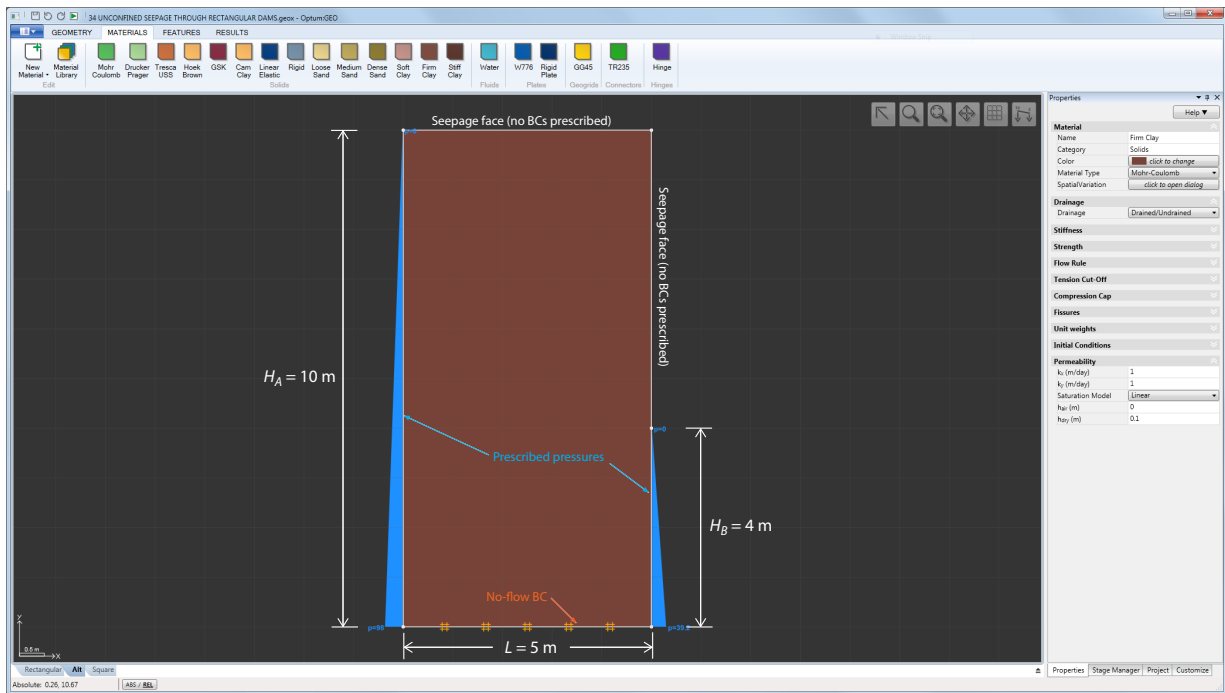


Figure 36.1: Unconfined seepage through rectangular dam (pressure boundary conditions).

Alternatively, instead of fixed pressure boundary conditions, fixed head boundary conditions may be used. Recall that the pressure head is defined as:

$$h = y - \frac{p}{\gamma_w} \tag{36.1}$$

where y is the vertical coordinate and p is the pressure (negative in the fully saturated range consistent with the sign convention used for stresses). Thus, with the pressures at left boundary varying as

$$p_A = -\gamma_w(H_A + y_0 - y), \tag{36.2}$$

where y_0 is the vertical coordinate at the base of the dam, the equivalent boundary head is:

$$h_A = H_A + y_0 \tag{36.3}$$

The equivalent problem with these conditions imposed is shown in Figure (36.2). The vertical coordinate at the base of the dam is here $y_0 = 0$ m.

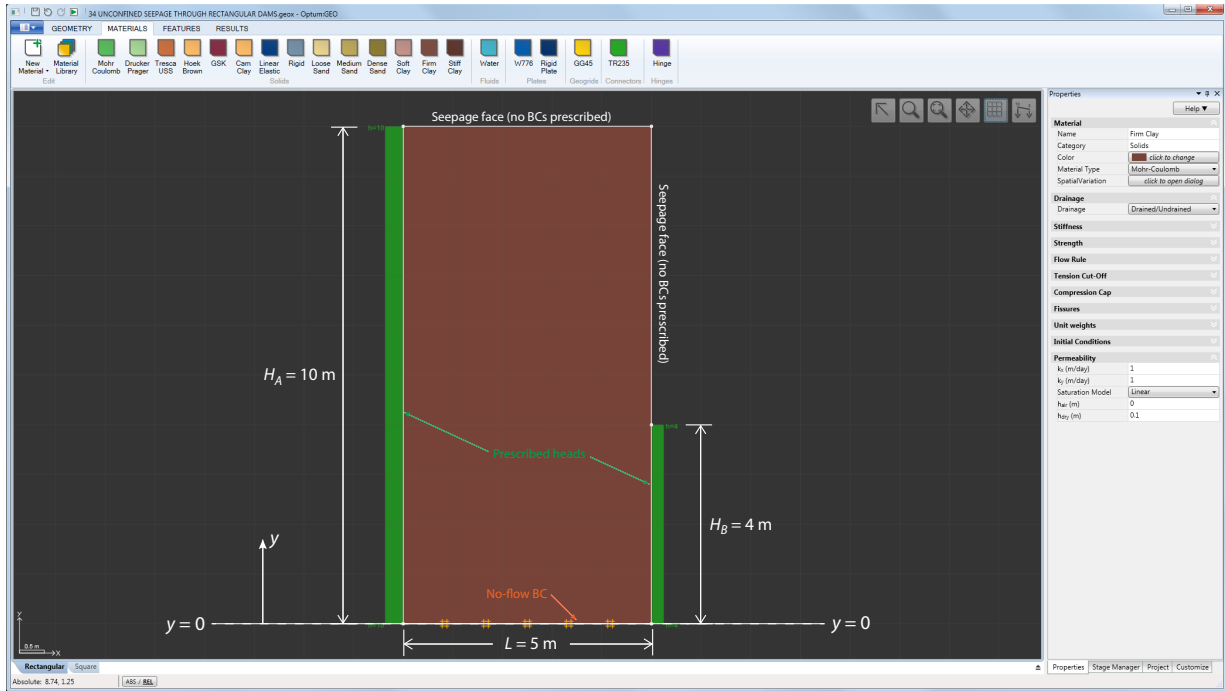


Figure 36.2: Unconfined seepage through rectangular dam (head boundary conditions).

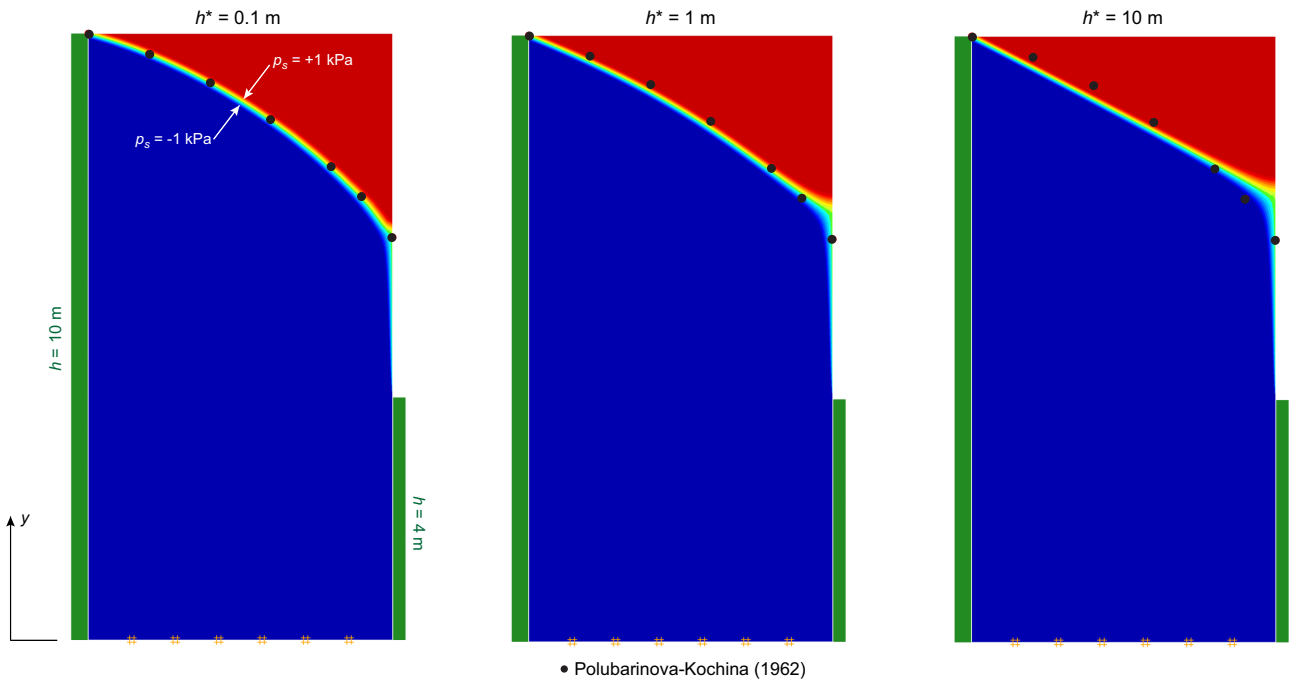


Figure 36.3: Flow through rectangular dam: location of phreatic surface for different h^* compared with the solution of Polubarinova-Kochina (1962).

The calculations are carried out with the Seepage analysis type using 10,000. The hydraulic model is the Linear model. The influence of the parameter h^* indicating the range of the unsaturated zone (see the Materials Manual) is shown in Figure (36.3). We see that the results obtained for $h^* = 0.1$ m and $h^* = 1$ m are quite similar and in good agreement with the analytical solution of Polubarinova-Kochina (1962) which assumes $h^* = 0$. On the other hand, a value of $h^* = 10$ m appears to be too

high in this case although the basic features of the solution are still captured.

Finally, the same analysis is repeated for a square dam with $L = 10$ m, $H_A = 10$ m and $H_B = 0$ m. Again, the solutions for the smaller values of h^* are in good agreement with the analytical solution of Polubarinova-Kochina (1962).

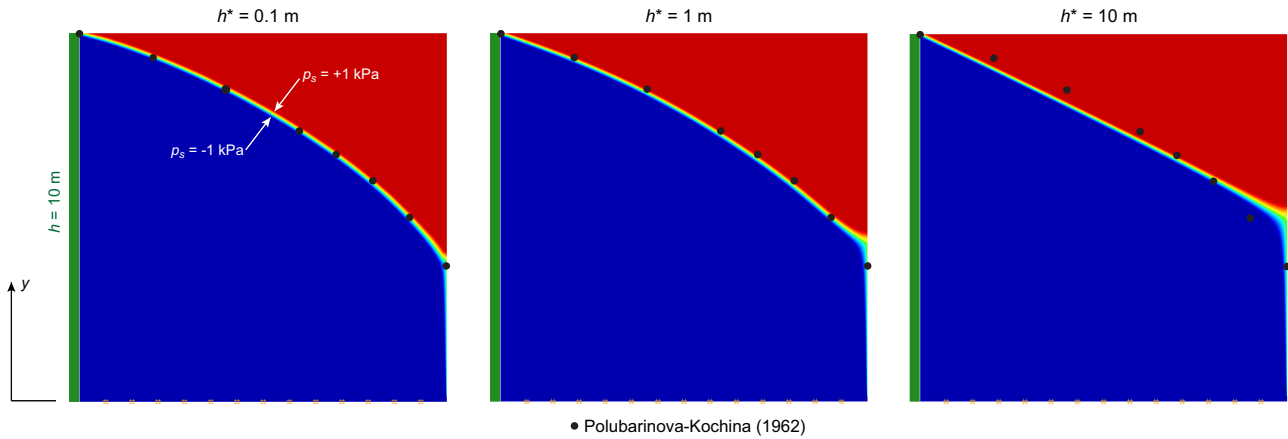


Figure 36.4: Flow through square dam: location of phreatic surface for different h^* compared with the solution of Polubarinova-Kochina (1962).

37 FREE SURFACE FLOW THROUGH EARTH DAM

This example considers the flow through a trapezoidal dam as shown in Figure 37.1. The hydraulic conductivity of the core of the dam (Zone 2) is different from that in the other parts of the dam (Zone 1). A drain is situated at the bottom right part of the dam. This example has been considered by Kazemzadeh-Parsi and Daneshmand (2012) for a range of conductivities in the two zones as summarized in Table 37.1. We note that cases 5-9 involve an anisotropic hydraulic conductivity with $K_x > K_y$ in all cases.

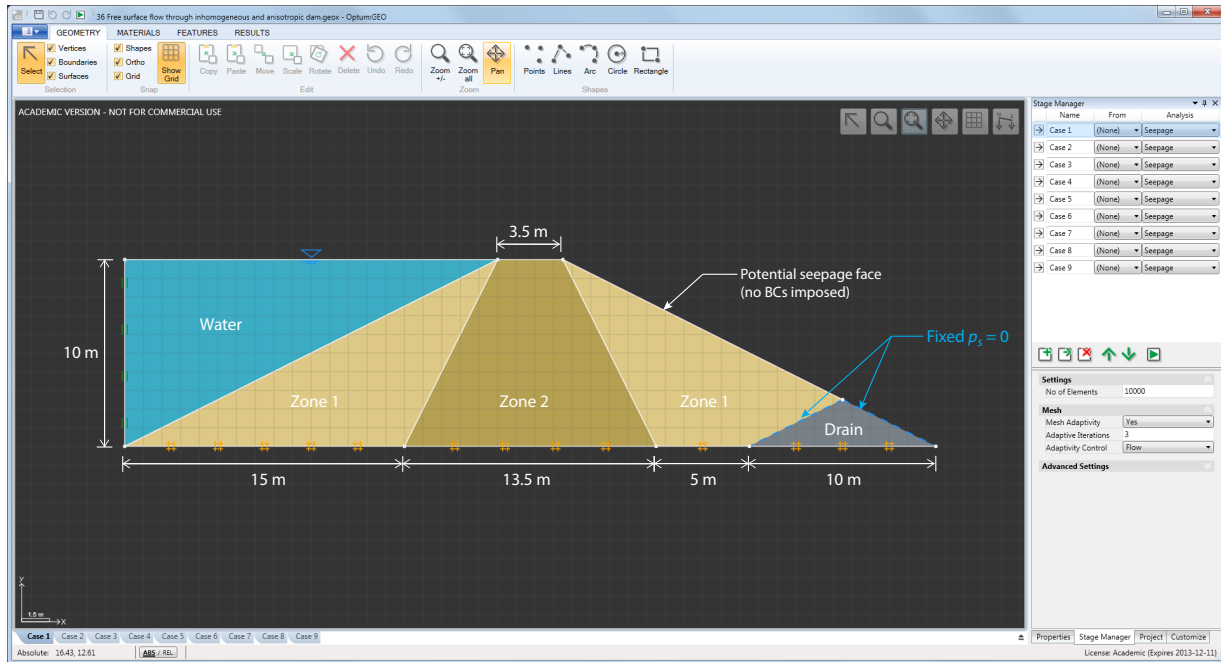


Figure 37.1: Inhomogeneous and anisotropic dam.

The hydraulic model used by Kazemzadeh-Parsi and Daneshmand (2012) corresponds to the Linear model with $h^* = 0$, i.e. step saturation versus pressure and pressure versus conductivity functions.

Case	Conductivity Zone 1 (m/day)		Conductivity Zone 2 (m/day)		Flux (m ³ /day/m)	
	K_x	K_y	K_x	K_y	K-P & D	OPTUM G2
1	1	1	1	1	2.68	2.82
2	1	1	0.1	0.1	0.52	0.51
3	1	1	0.01	0.01	0.08	0.06
4	1	1	0.25	0.25	1.12	1.13
5	2	1	0.5	0.25	2.09	2.17
6	4	1	1	0.25	3.96	4.16
7	8	1	2	0.25	7.62	8.03
8	16	1	4	0.25	15.02	15.19
9	32	1	8	0.25	30.03	30.08

Table 37.1: Conductivities in Zones 1 and 2 and resulting fluxes at the water table compared to those obtained by Kazemzadeh-Parsi and Daneshmand (2012).

In the following, we approximate this situation by using $h^* = 0.1$ m. The drain at the bottom right of the dam is modeled by imposing a Fixed Pressure boundary condition with $p_s = 0$ as shown in Figure 37.1. Other boundary conditions are Tangential Supports on the left vertical boundary, which act as no-flow BCs, and actual no-flow BCs at the bottom boundary (any Supports could have been used here). On the remaining inclined boundary on the right side of the dam, no boundary conditions are imposed. This implies that these boundaries act as seepage faces allowing for an outward discharge at zero pressure.

As with other analysis types, Seepage Analysis gives the possibility to adapt the mesh in a number of successive iterations. The relevant Adaptivity Control setting is Flow (see Figure 37.1). With this setting, the mesh is adapted on the basis of a combination of the ‘flow energy’, $\frac{1}{2} \mathbf{q}^T \mathbf{K} \mathbf{q}$, and a measure ensuring a reasonable concentration of elements around free surfaces.

The results of the nine analyses in terms of the total rate of flow through the dam are shown in Table 37.1. These are seen to compare well with the results obtained by Kazemzadeh-Parsi and Daneshmand (2012).

The distributions of saturation are shown in Figure 37.1 for selected cases. The effects of inhomogeneity (Case 1 vs. Case 4) and anisotropy (Case 4 vs. Case 7) are apparent.

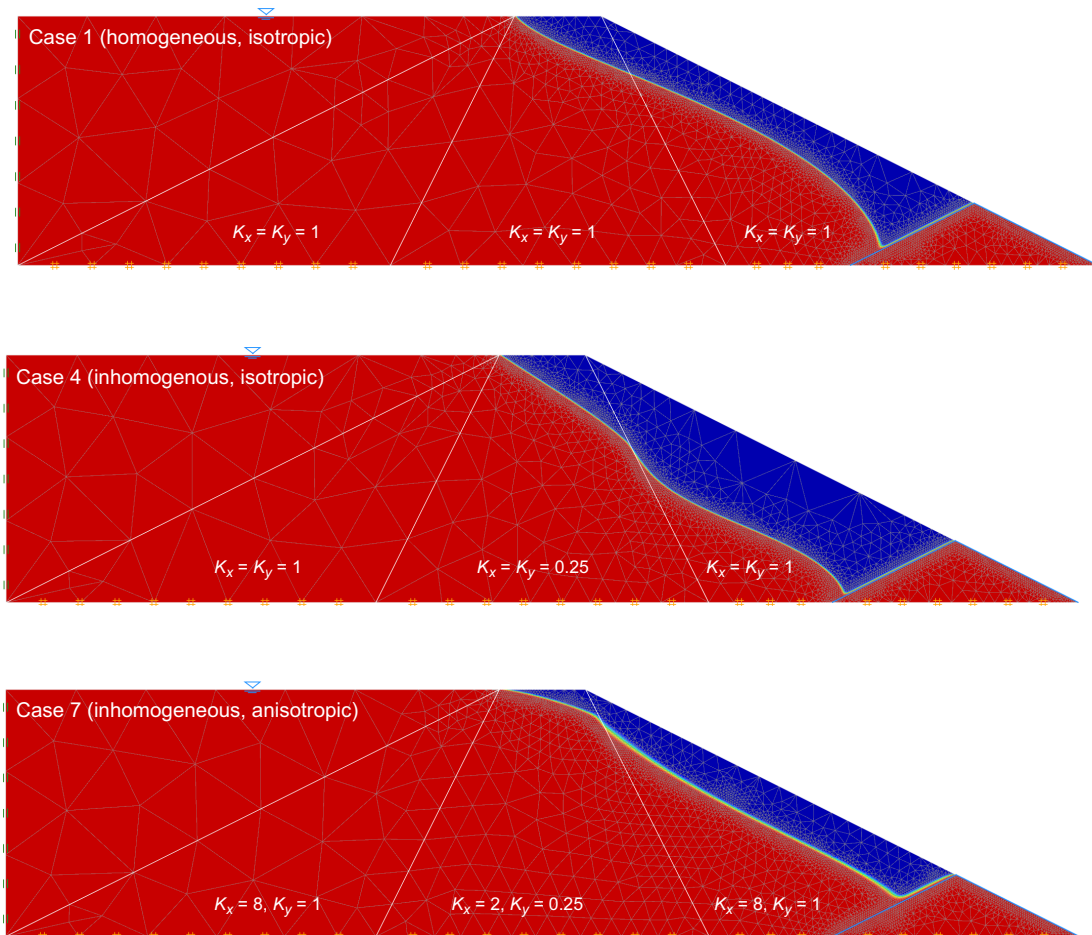


Figure 37.2: Saturation distributions for selected cases (red corresponds to $S = 1$ and blue to $S = 0$).

38 EXCAVATION MODEL TEST

The following problem concerns the simulation of a model excavation test carried out by Tefera et al. (2006) at NTNU in Trondheim, Norway. The model is shown schematically in Figure 38.1. It comprises a 3×4 m box filled with sand. At 1 m from the vertical boundary a 2.5 m wall has been installed. The soil in front of the wall is then excavated in a number of stages. In the course of the excavation, at a level of 0.91 m, a strut is inserted and prestressed to 5 kN/m.

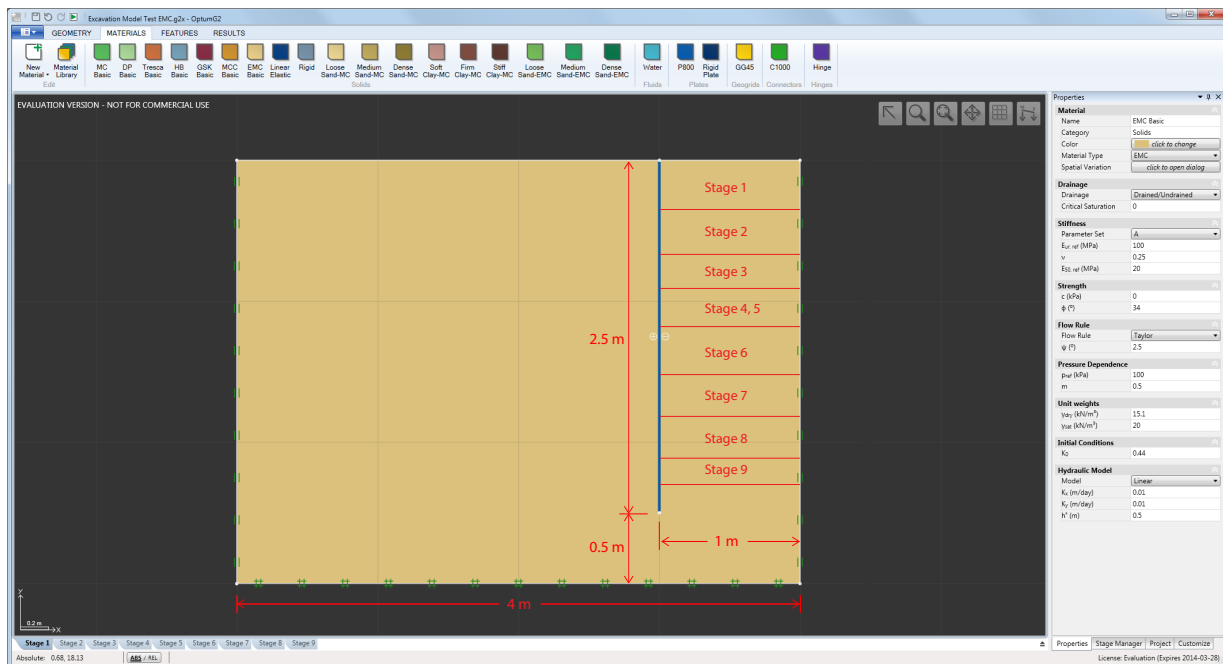


Figure 38.1: Excavation model test setup with indication of the material excavated in each stage.

The sequence of stages is shown in Table 38.1. With the exception of the first stage, which computes the initial stresses, these are all of type Elastoplastic and each stage uses the preceding stage as From stage.

Stage	Excavation depth (m)	Analysis Type	Apply Prestress?	Prestress (kN/m)
0	0.00	Initial Stress	—	—
1	0.35	Elastoplastic	—	—
2	0.67	Elastoplastic	—	—
3	0.91	Elastoplastic	—	—
4	0.91	Elastoplastic	Yes	5.0
5	1.18	Elastoplastic	No	—
6	1.52	Elastoplastic	No	—
7	1.82	Elastoplastic	No	—
8	2.11	Elastoplastic	No	—
9	2.30	Not processed*)	No	—

Table 38.1: Stages in excavation model test. *)Initial Strength Reduction analysis reveals an upper bound strength reduction factor of 0.95.

38.1 Soil model

Excavation analysis is an example of a problem type where the behaviour of the soil in loading and unloading may be important. As the excavation proceeds, the soil behind the wall will unload (active pressure) whereas the soil in front of the wall below the current excavation level will experience loading (passive pressure). The HMC model, which allows for the specification of separate loading and unloading moduli, is well suited to capture this behaviour. In the following, this model is used with the parameters reported by Tefera et al. (2006), see Table 38.2.

Sand (HMC)		
Unloading/reloading modulus	$E_{ur,ref}$	100 MPa
Poisson's ratio	$\nu_{ur,ref}$	0.2
Secant modulus	$E_{50,ref}$	20 MPa
Cohesion	c	0 kPa
Friction angle	ϕ	34°
Flow rule		Taylor
Dilation angle	ψ	2.5°
Reference pressure	p_{ref}	100 kPa
Power	m	0.5
Earth pressure coefficient	K_0	0.44

Table 38.2: Sand properties (after Tefera et al. 2006).

While the HMC model is more advanced than the standard Mohr-Coulomb model, the latter model is in fact in many cases able to capture the key features of excavation analyses quite adequately. Indeed, the overall behaviour is governed mainly by the failing soil mass behind the wall and the stiffness of the wall rather than by the elastic properties of the soil. Therefore, in the absence of detailed information about the soil properties, use of the standard Mohr-Coulomb model – with reasonable estimates of the parameters – is generally quite reasonable. The following example explores the differences between the two models in more detail.

38.2 Structural elements

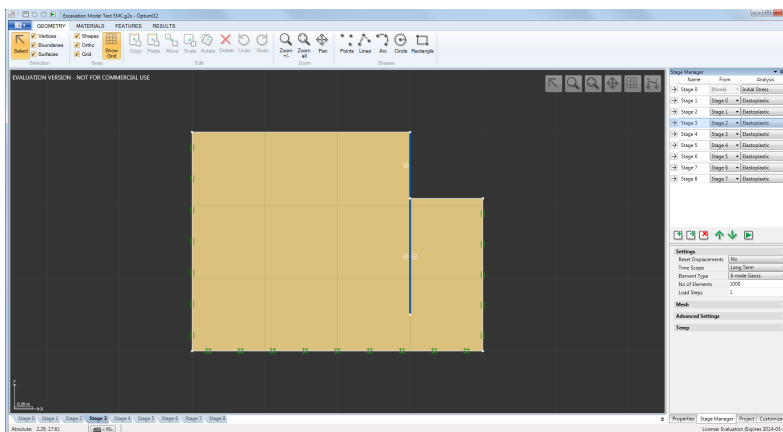
The wall and strut are modeled using Plate and Connector elements respectively. The parameters are given in Table 38.3.

Wall (Plate)		
Normal Stiffness	EA	320,000 kN/m
Bending Stiffness	EI	23.4 kNm ² /m
Weight	w	14.9 kg/m/m
Interface Reduction Factor	r	0.6
Strut (Connector)		
Normal Stiffness	EA	9500 kN/m
Length		1 m

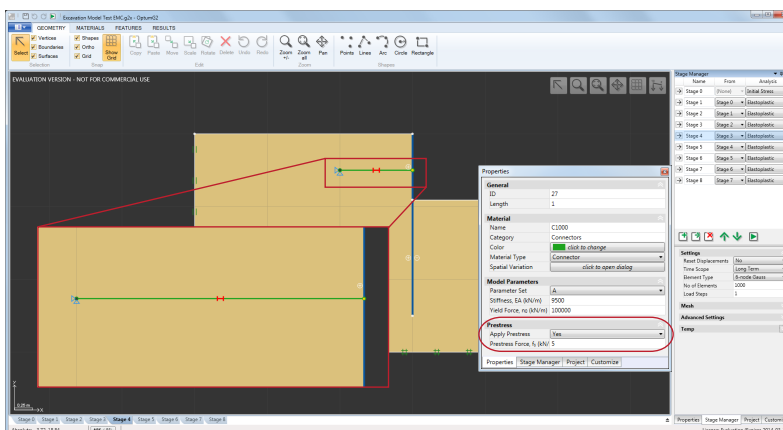
Table 38.3: Wall and strut properties (after Tefera et al. 2006).

38.2.1 Prestress

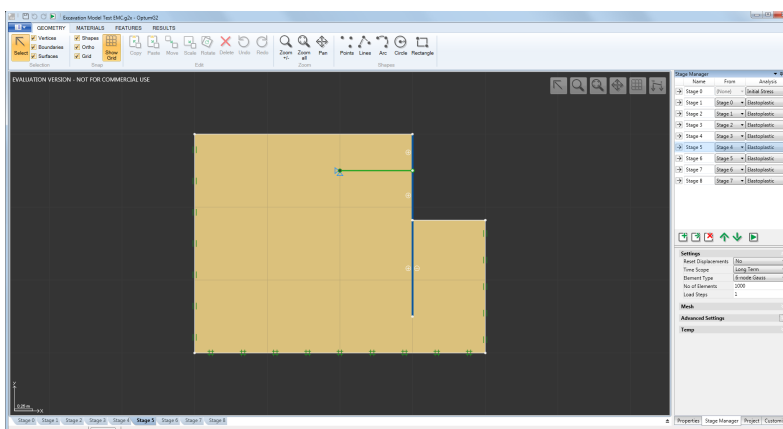
As indicated in Table 38.1, the simulation proceeds by first excavating to a depth of 0.91 m in three stages. At this point, the Connector is inserted 0.5 m below the top level. By selecting the Connector its properties appear in the property window. Under Prestress, Apply Prestress is set to Yes and a Prestress Force of 5 kN/m is entered. This applies the specified prestress at the current stage in a single step. In the subsequent stages, the Connector is still present but with Apply Prestress set to No. An overview of the prestressing functionality is given in Figure 38.2.



Excavation level = 0.91 m before definition of Connector.



Excavation level = 0.91 m. Connector is defined and a prestress of 5 kN/m is applied. Prestress is applied via the property window (see inset) by selecting the connector. Application of prestress is indicated by a **H** superposed on the Connector.



In subsequent stages no prestress is applied.

Figure 38.2: Prestressing of Connector.

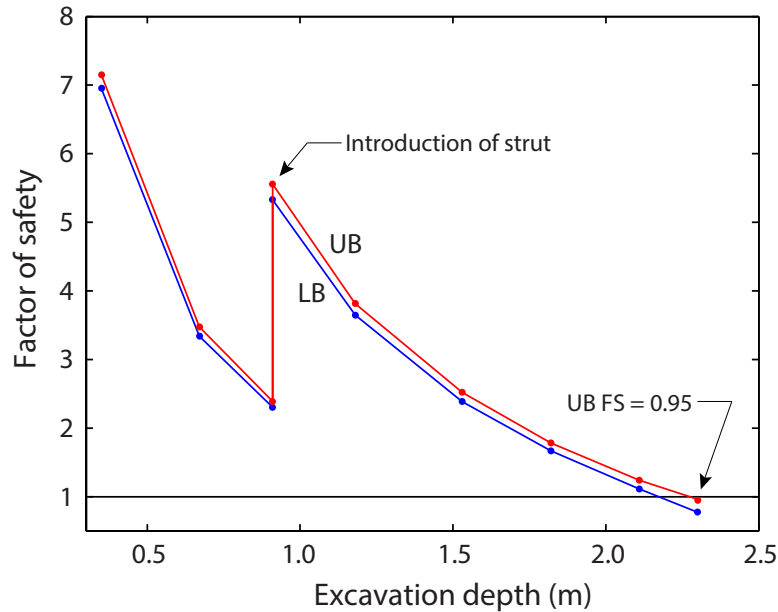


Figure 38.3: Upper and lower bound strength based factors of safety as function of excavation depth.

38.3 Strength Reduction analysis

Before the actual excavation simulation gets under way, it is useful to run Strength Reduction analyses for all stages to gauge the proximity to failure of each stage. The results of upper and lower bound analyses of this type are shown in Figure 38.3. Of particular note are the results for an excavation depth of 2.3 m. Both the lower, and more importantly the upper, bound analyses here reveal that the factor of safety is below unity. In other words, the system is not stable at this level and for the material parameters assumed. This is in contrast to the experiment. The present result is confirmed by the numerical analyses of Tefera et al. (2006) who reported ‘convergence problems’ for this level of excavation.

38.4 Excavation analysis

The analysis proceeds by running the 9 stages indicated in Table 38.1. For all stages, 1,000 6-node Gauss elements are used with three adaptivity iterations. The results in terms of the horizontal displacement of the top of the wall are shown in Figure 38.4. Also shown are the experimental results as well as the results of numerical analysis of Tefera et al. (2006) using the so-called Hardening Soil (HS), a detailed description of which has been given by Benz (2007).

The results shown in Figure 38.4 show a very good agreement between the HS and HMC models. As already discussed at length by Tefera et al. (2006), there are several points of discrepancy between the experiments and the results, the most noticeable of which are the underestimate of wall displacement at the beginning of the excavation and as a result of the application of prestress at a level of 0.91 m.

Tefera et al. (2006) also monitored the force in the strut, from the initial application of the prestress to the end of the excavation. Again, there is some quantitative discrepancy between the experimental data and the predictions, especially towards the end of the excavation. However, the HMC model

appears to make somewhat better predictions than the HS model used by Tefera et al. (2006). For example, at the first stage after the application of the prestress, the former predicts a decrease in force, consistent with the experimental data, while the latter predicts an increase.

Finally, the deformations and the intensity of plastic dissipation at various stages of the excavation are shown in Figure 38.5. We see that the distribution of plasticity varies quite significantly with excavation depth. The adaptive mesh procedure used ensures a high degree of accuracy while maintaining a moderate number of elements in each stage.

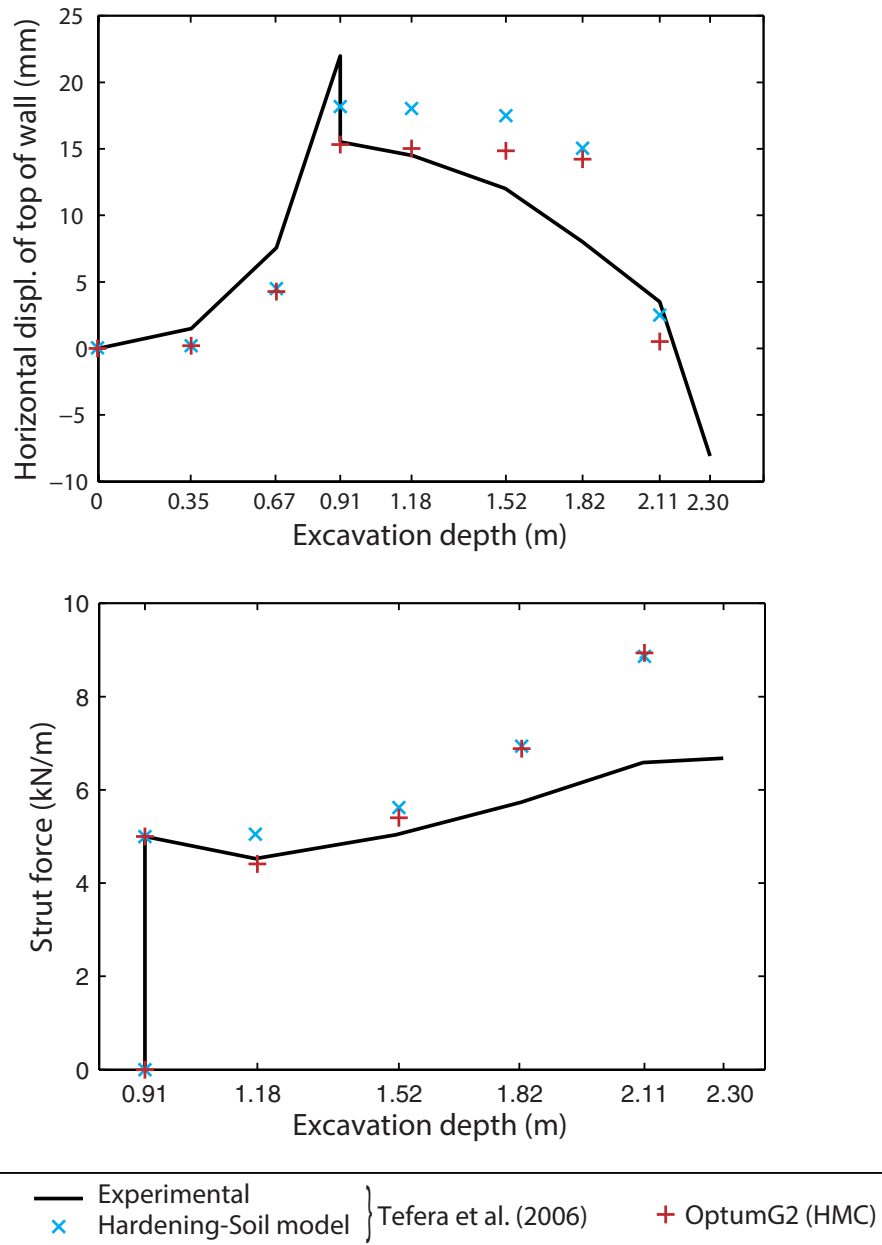


Figure 38.4: Horizontal displacement of top of wall as function of excavation depth (top) and strut force as function of excavation depth (bottom).

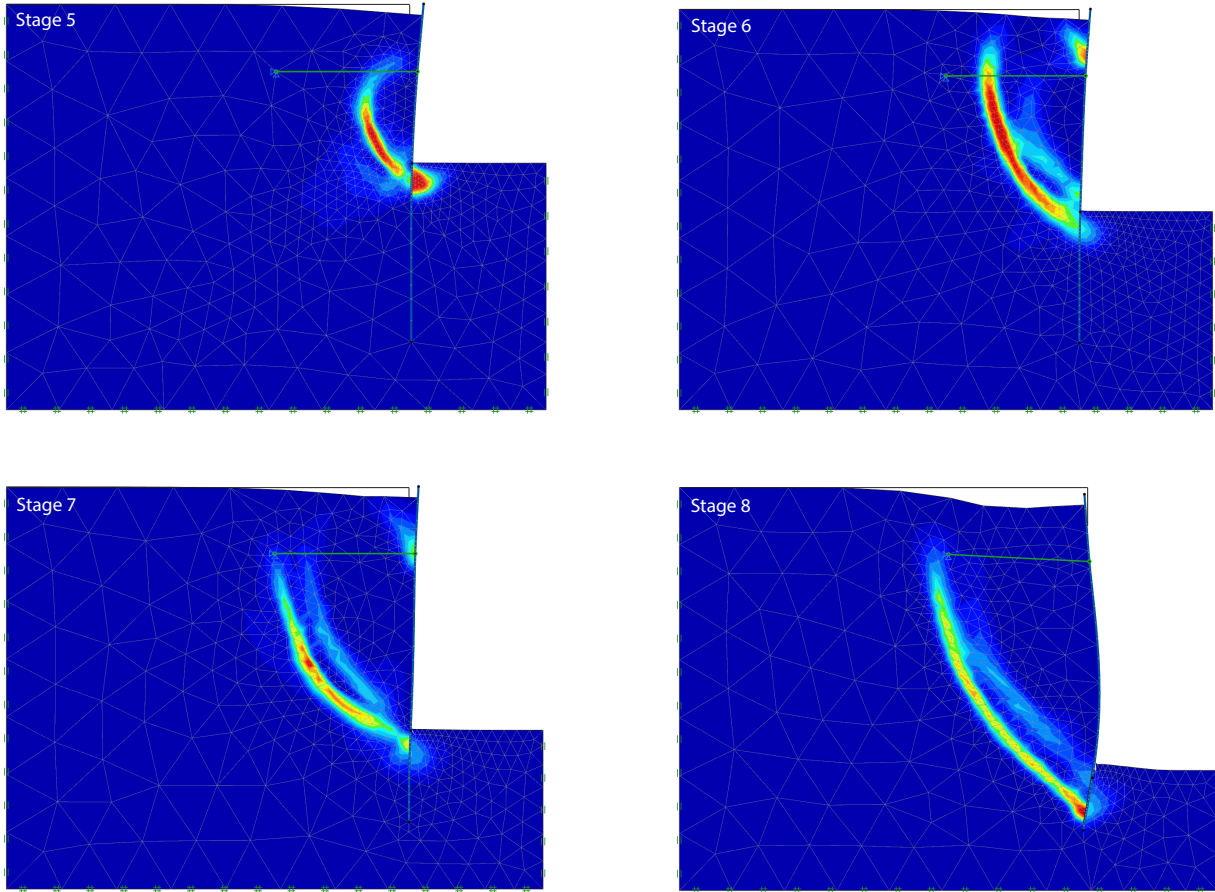


Figure 38.5: Deformations (scaled by a factor of 5) and plastic dissipation for the last four excavation stages.

39 EXCAVATION IN SAND – MOHR-COULOMB VS HMC

The following problem is similar to the previous one. An excavation in sand, supported by a sheet pile wall, is to be conducted. The problem is sketched in Figure 39.1. The analysis begins by determining the geostatic stresses (with the sheet pile ‘wished in place’). 4 m of soil is then excavated in front of the wall in the first stage followed by another 4 m in the second stage. In the third stage, a strut is inserted 2 m below ground level and another 4 m excavated bringing the total excavation depth to 12 m. In the fourth stage, the strut is prestressed to a force of 500 kN/m. Finally, in the fifth stage, another 4 m of soil is excavated bringing the final excavation depth to 16 m.

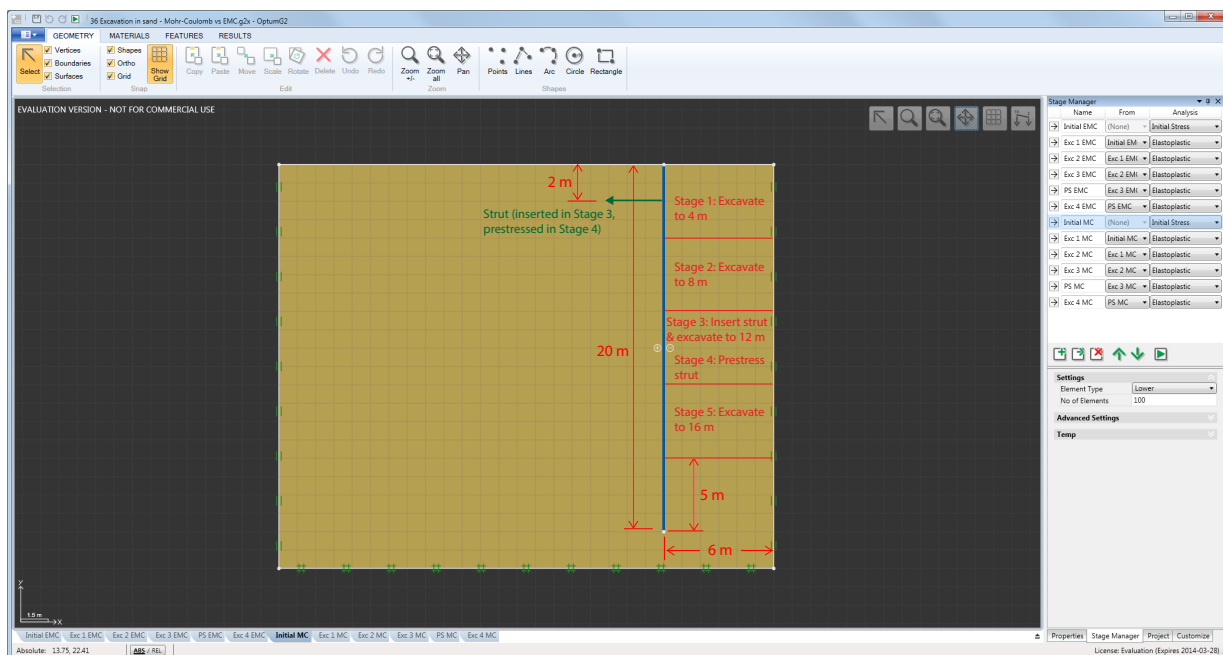


Figure 39.1: Excavation in sand: problem setup.

As discussed in the previous example, excavation analyses are a class of problems where both loading (in front of the wall) and unloading (behind the wall) takes place and may be important to capture correctly. As such, the HMC model appears well suited in that it operates with separate stiffness moduli for initial elastoplastic loading and subsequent elastic unloading/reloading. However, successful application of the HMC model to any problem hinges crucially on relevant experimental data being available. In the absence of such data, one could argue that the standard Mohr-Coulomb model – with a reasonable estimate of the parameters – might be more appropriate. The purpose of the following analyses is to gauge the sensitivity of the overall behaviour to the constitutive model and in particular the choice of stiffness moduli. For this purpose, the HMC and Mohr-Coulomb models are used with the parameters shown in Table 39.1. While the reference stiffness moduli used in the HMC model are $E_{50,ref} = 25$ MPa and $E_{ur,ref} = 125$ MPa, two runs are performed with the Mohr-Coulomb model using fixed Young's moduli of $E = 25$ MPa and $E = 125$ MPa. It should be noted that these do not represent actual bounds on the HMC moduli as the latter are pressure dependent.

All calculations are performed on a mesh with 1,000 6-node Gauss elements. While this spatial discretization is somewhat coarse, it does not affect the main conclusions of the analysis.

HMC			Mohr-Coulomb		
Unload./reload. modulus	$E_{ur,ref}$	125 MPa	Young's modulus	E	25 or 125 MPa
Poisson's ratio	$\nu_{ur,ref}$	0.2	Poisson's ratio	ν	0.2
Secant modulus	$E_{50,ref}$	25 MPa			
Cohesion	c	0 kPa	Cohesion	c	0 kPa
Friction angle	ϕ	35°	Friction angle	ϕ	35°
Flow rule		Taylor	Flow rule		Nonassociated
Dilation angle	ψ	5°	Dilation angle	ψ	5°
Reference pressure	p_{ref}	100 kPa			
Power	m	0.5			
Earth pressure coeff.	K_0	0.43	Earth pressure coeff.	K_0	0.43

Table 39.1: HMC and Mohr-Coulomb parameters for the soil considered

The results of the three calculations are shown in Figures 39.2–39.4. Generally, there is good agreement between all three calculations with the Mohr-Coulomb calculation using $E = 125$ MPa agreeing particularly well with the HMC calculation. All in all, it appears that the discrepancy between the different models is of a magnitude not larger than that resulting from uncertainty in the material parameters, geometry, exact method of excavation, etc.

In conclusion: while the choice of stiffness moduli does have some effect on the overall behavior, it is, for this example, relatively moderate. This conclusion is consistent with the assertion that what mainly governs the behavior are the earth pressures behind and in front of the wall. And with these being a function of the friction angle, it is in fact the strength of the soil rather than its stiffness that governs the overall behavior of the problem. Note, however, that for problems where the extent of soil failure is limited and elasticity dominates, the elastic law and/or the exact value of the elastic parameters is of paramount importance. For the present example, this is observed in the first excavation stage where the Mohr-Coulomb model with $E = 25$ MPa predicts an excessive heave behind the wall.

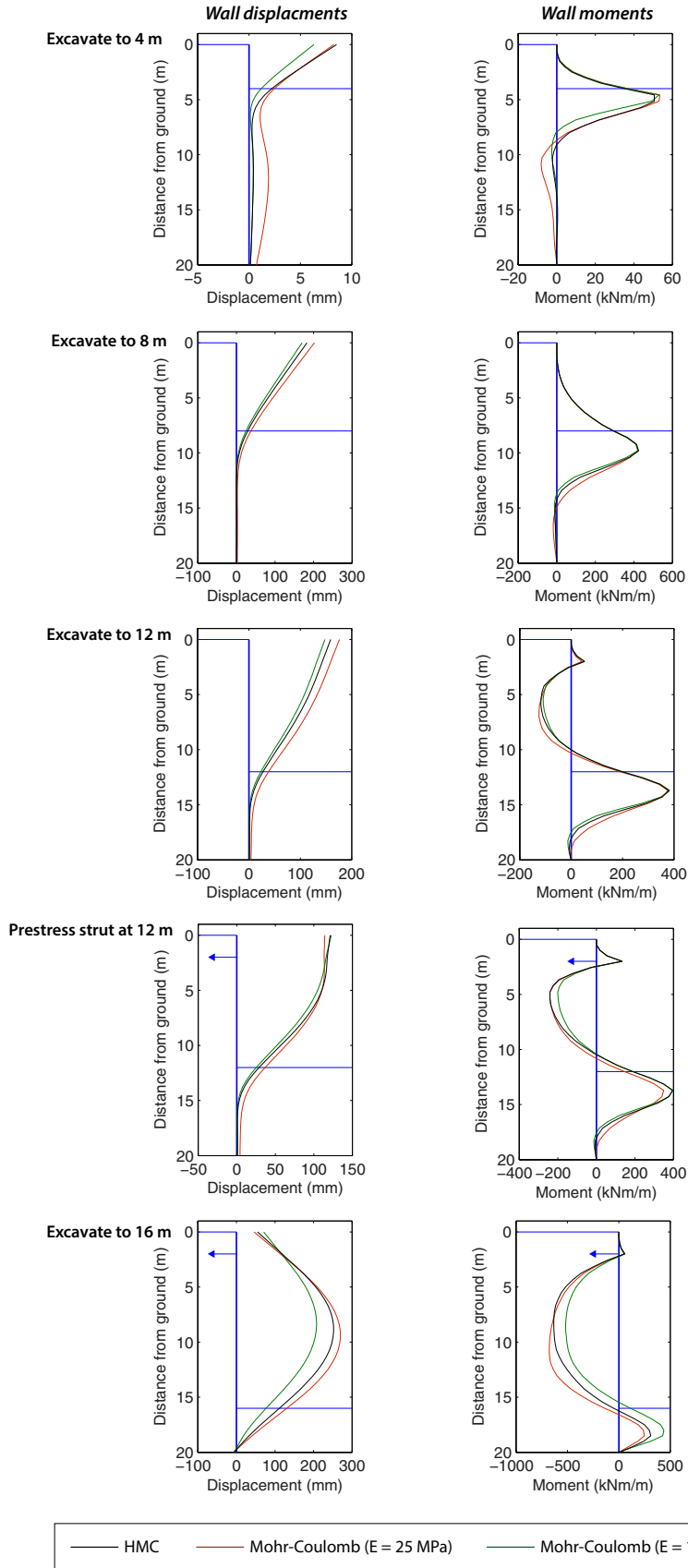


Figure 39.2: Wall displacements (left column) and moments (right column).

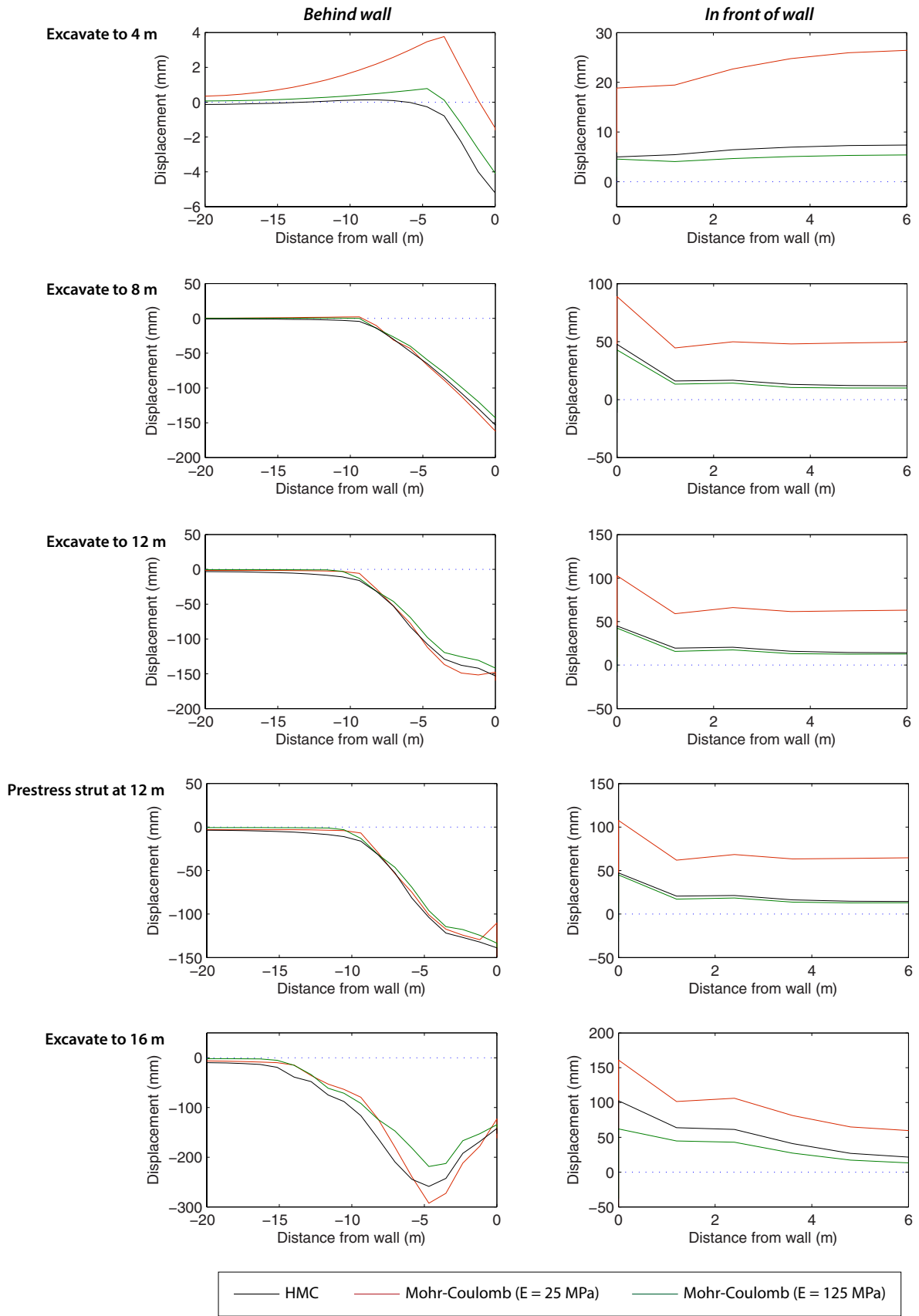


Figure 39.3: Ground displacements behind wall (left column) and in front of wall (right column).

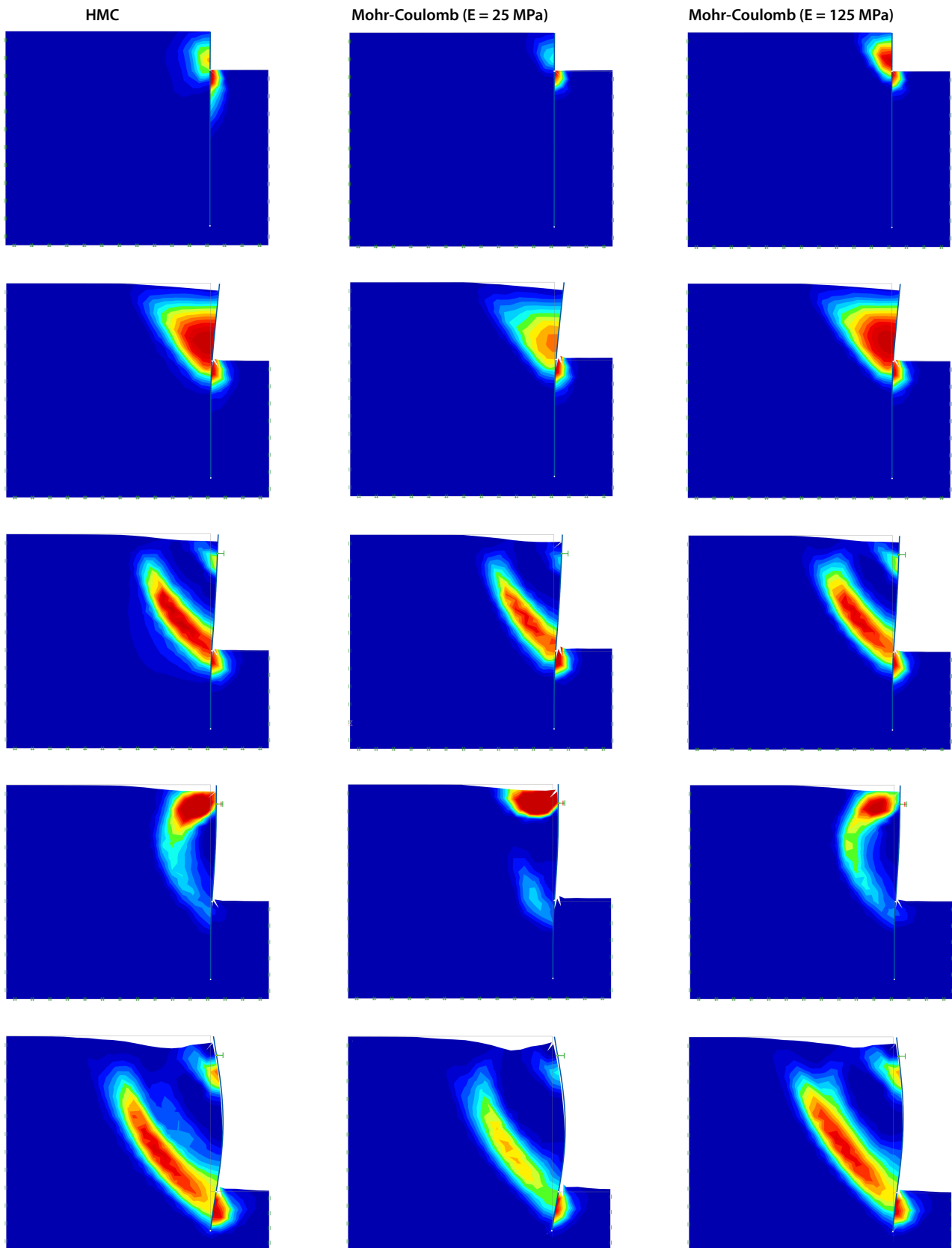


Figure 39.4: Deformations and shear dissipation for HMC and Mohr-Coulomb models.

40 EXCAVATION WITH SEEPAGE

The following example demonstrates the process of excavation with a gradual lowering of the ground-water table within the excavation. The problem setup is shown in Figure 40.1. The material is the default Medium Sand-MC, though with a Young’s modulus set to $E = 120 \text{ MPa}$.

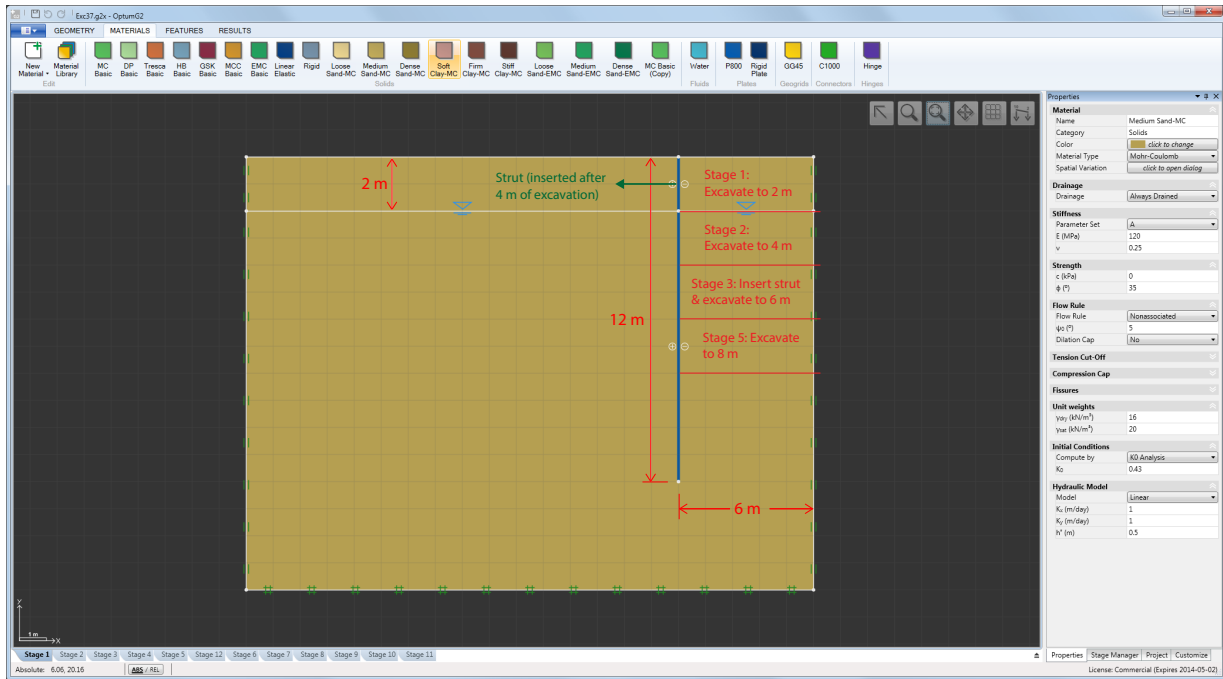


Figure 40.1: Dry excavation in sand: problem setup.

The excavation is to be performed in four stages. First to a level of 2 m, coinciding with the ground water table. Then a second stage of 2 m where the ground water table within the excavation is lowered to the bottom of the excavation, i.e. 4 m below ground level. In the third stage, a Fixed End Anchor is inserted before another 2 m is excavated, again with a 2 m lowering of the groundwater table within the excavation. Finally, in the fourth stage, the excavation is taken to the final depth of 8 m and the ground water table lowered accordingly.

In OPTUM G2, seepage is automatically included as part of any analysis and is performed before any mechanical analysis. As such, the lowering of the groundwater table does not need to be considered in anymore detail than simply prescribing the groundwater table at the bottom of the excavation in each stage. This is most easily done using the Water Table Tool located under Flow BCs in Features, but may also be done using the Fixed Pressure or Fixed Head boundary conditions.

All stages are run using 2,000 6-node Gauss elements with 3 Adaptivity iterations. The results in terms of pressure heads and deformations are shown in Figure 40.2.

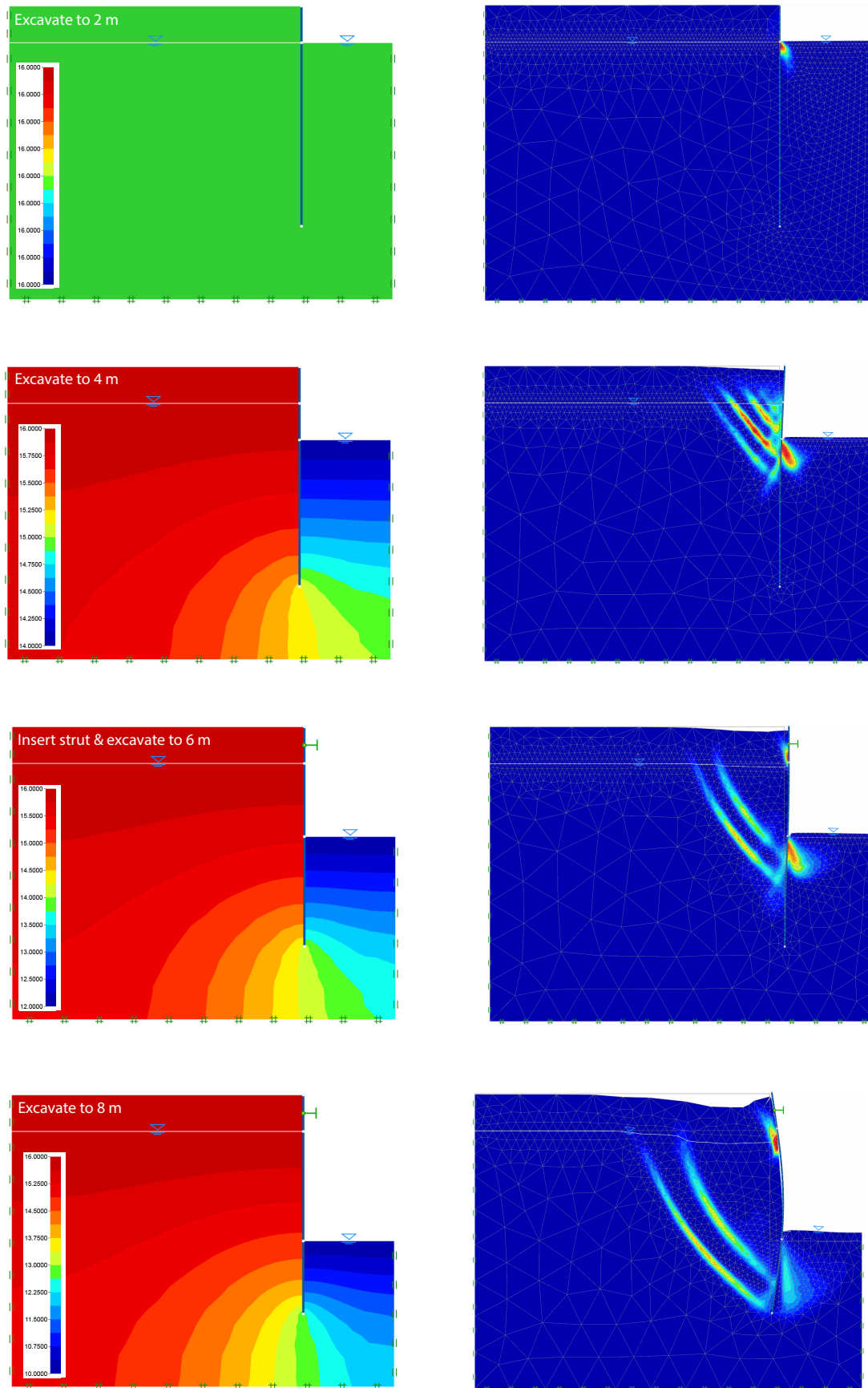


Figure 40.2: Pressure heads (m) and deformations (scaled by a factor of 10) with shear dissipation.

41 EXCAVATION IN MOHR-COULOMB CLAY

The following example concerns an excavation in clay as sketched in Figure 41.1. The three layers consist of the default materials Soft Clay-MC, Firm Clay-MC, and Stiff Clay-MC. The groundwater table is located 1 m below ground level.

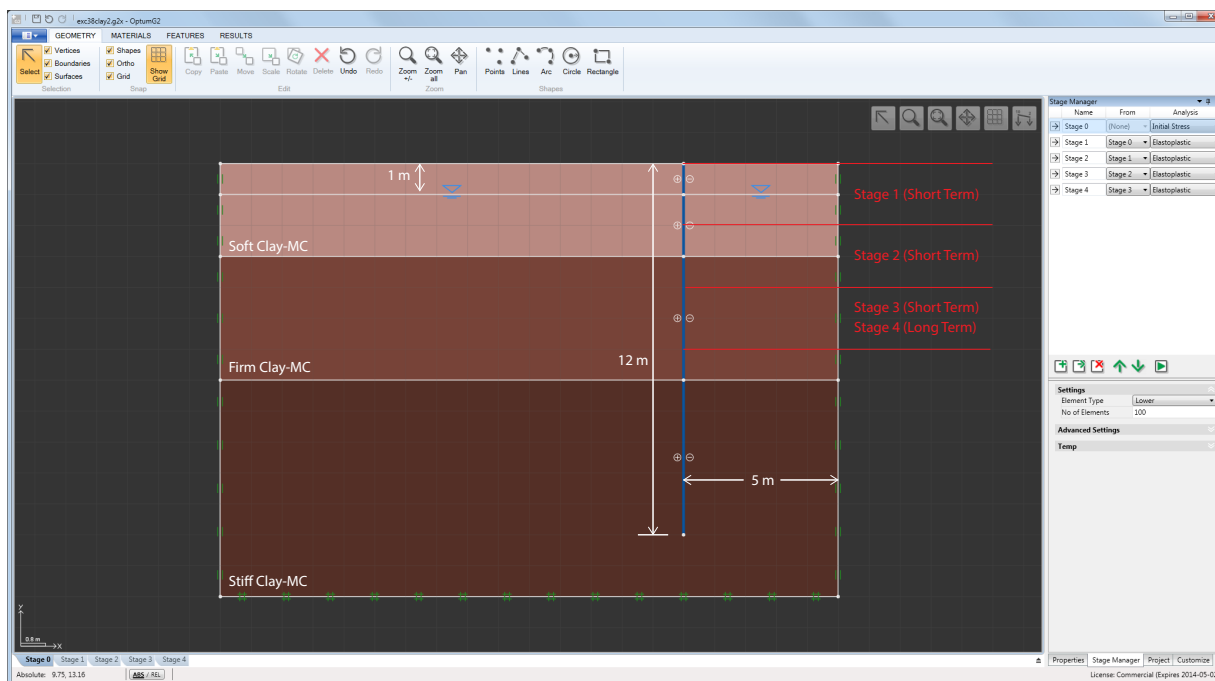


Figure 41.1: Excavation in Mohr-Coulomb clay: problem setup.

Besides the initial stage where the geostatic stress field is computed, the problem comprises three stages, each involving 2 m of excavation. The material is here assumed to behave in an undrained manner, i.e. the Time Scope is set to Short Term. Additionally, the seepage pressures must be considered. For a fine grained material, it is reasonable to assume that the initial hydrostatic seepage pressure does not change in the short term. Appropriate boundary conditions must therefore be imposed to ensure that the initial seepage pressure distribution remains unchanged. In the present example, where the wall is considered impermeable, this is done by imposing no-flow boundary conditions at the bottom of the excavation in each stage.

Finally, at a depth of 6 m, the excavation is left to consolidate with the groundwater table being maintained at the bottom of the excavation. In other words, the transition from short term conditions to long term conditions must be accounted for. This is done via a final stage where Time Scope is set to Long Term. The evolution of seepage pressures and the different boundary conditions imposed at the bottom of the excavation are shown in Figure 41.2.

The deformations at various stages of the excavation are shown in Figure 41.3. We see that the deformations increase dramatically in the long term. Furthermore, the factor of safety against collapse decreases markedly (see Figure 41.4) and the excavation is in fact barely stable in the long term.

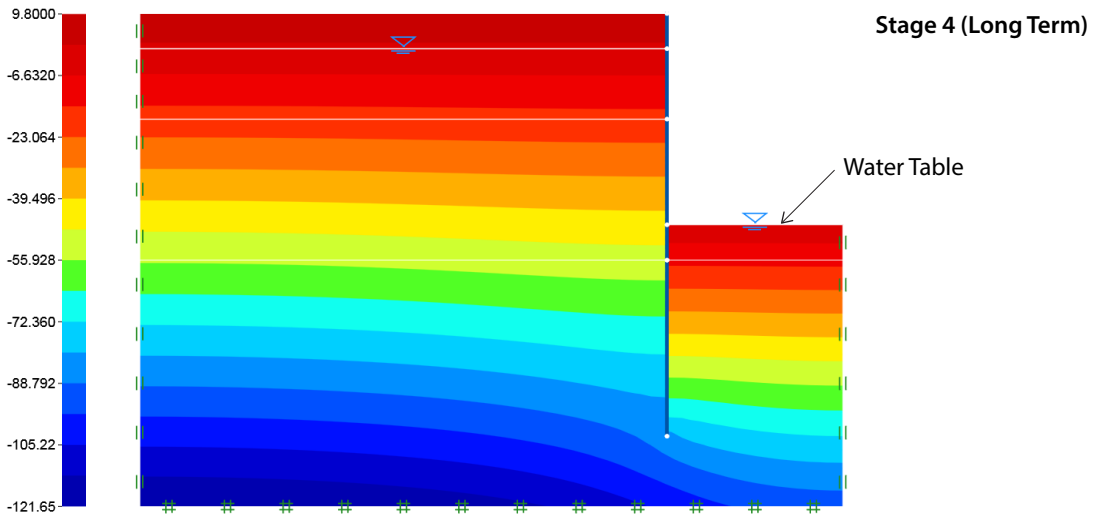
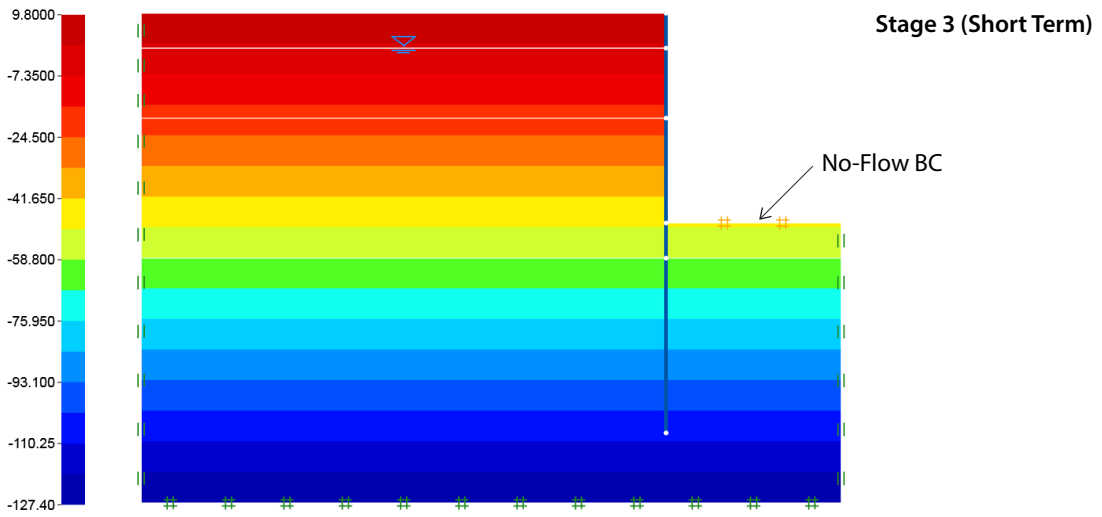
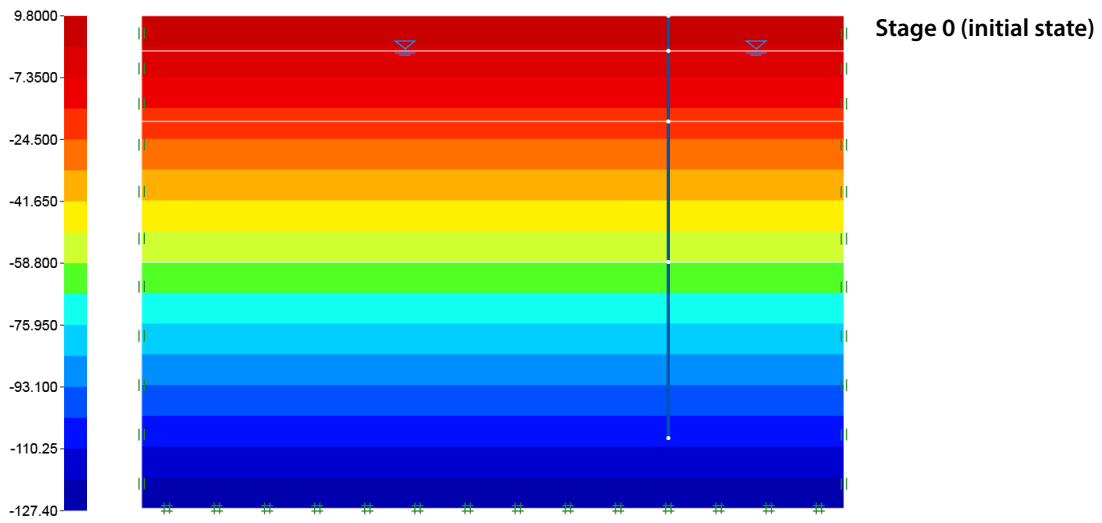


Figure 41.2: Pore pressure distributions.

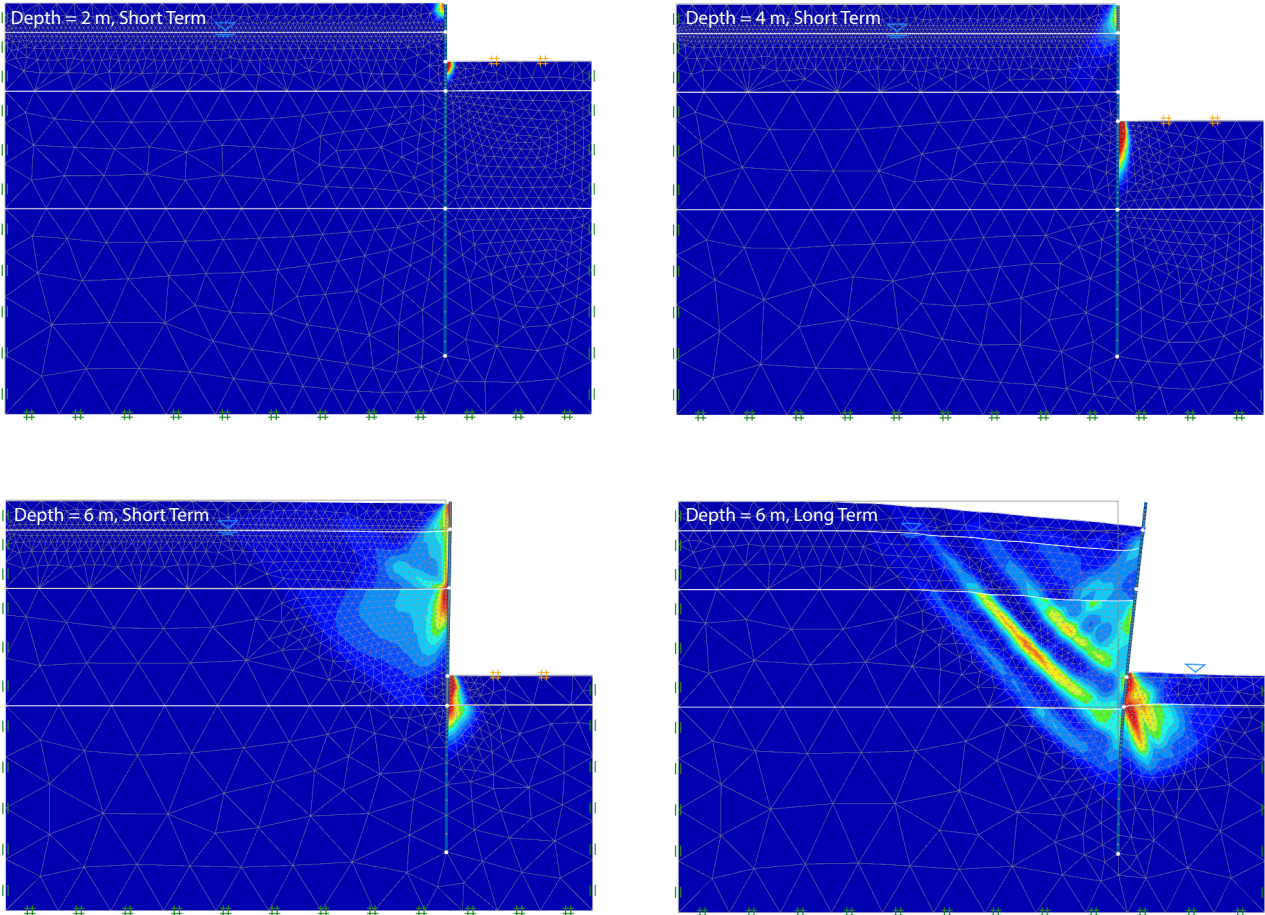


Figure 41.3: Deformations (scaled by a factor of 5) and distribution of shear dissipation.

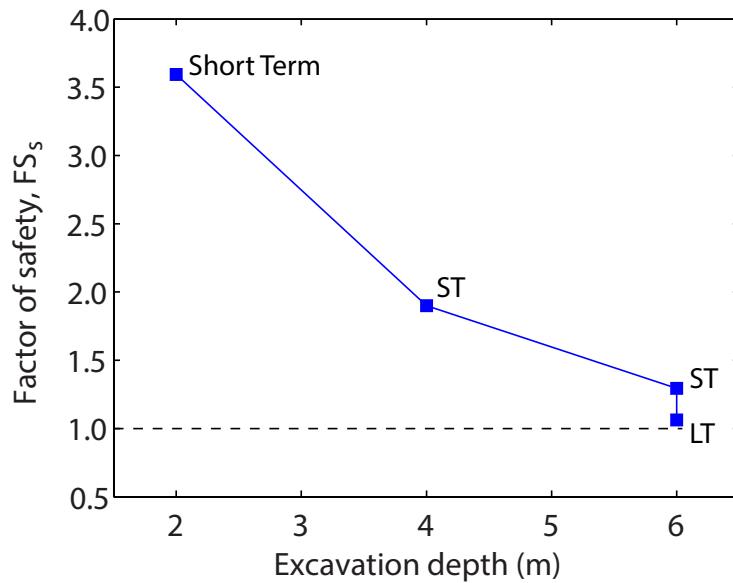


Figure 41.4: Strength based factor of safety versus excavation depth. At a depth of 6 m the factor of safety decreases from about 1.3 in the short term to about 1.06 in the long term.

42 PRELOADED FOOTING ON CLAY

This problem considers the following scenario. A building was originally erected on strip footings such as the one shown in Figure 42.1. The soil was of the kind that could be described reasonably well by the default Firm Clay-MC material. The building was erected sufficiently rapidly for its loading of the foundations to be considered undrained. At the end construction, the building exerted a load of $q = 45 \text{ kN/m}^2$ on the foundations. This corresponds to approximately 70% of the short term bearing capacity. Many years then pass until one day it is decided to extend the building by another storey. The question is: can this be done?

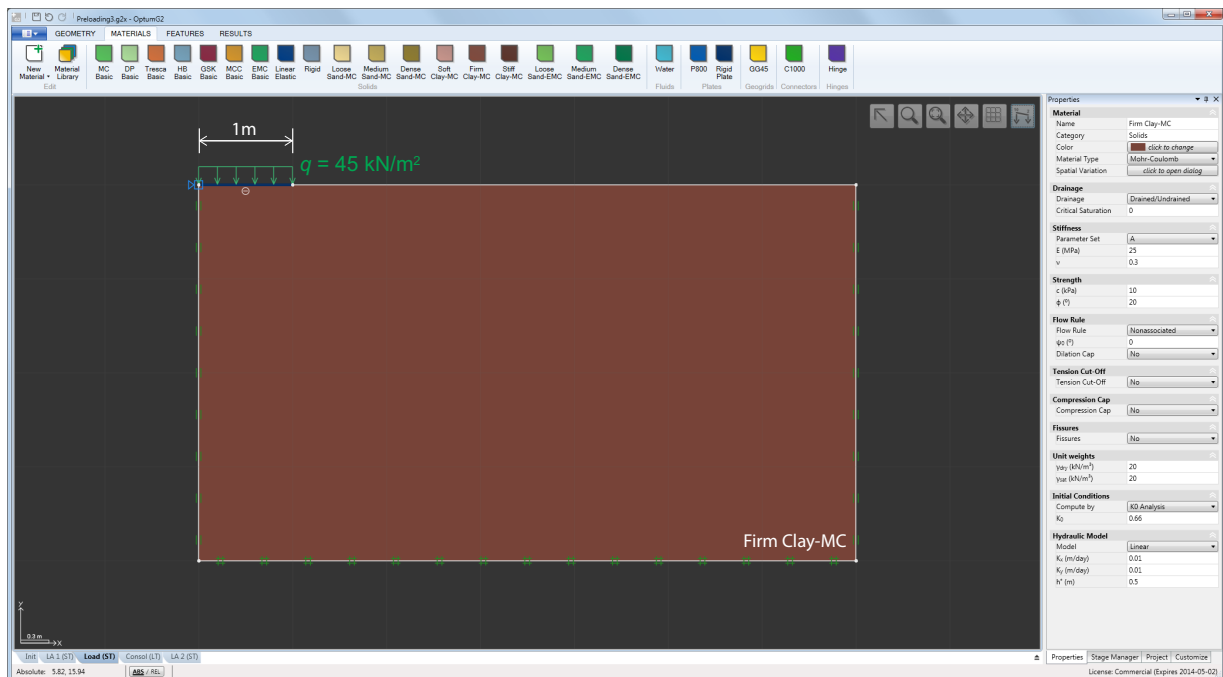


Figure 42.1: Problem setup (initial short term loading).

To answer this question it should first be clarified that by 'many years having passed', is meant a sufficient amount of time for all the excess pore pressures that were generated in response the initial loading to have dissipated. Assuming that to be the case, the effective stresses in the ground will most likely have increased and it is likely that the new short term bearing capacity in effect has been increased. To see this, recall that the undrained shear strength implied by the Mohr-Coulomb model is given by

$$s_u = c \cos \phi - \frac{1}{2}(\sigma'_{x,0} + \sigma'_{y,0}) \sin \phi \quad (42.1)$$

where $-(\sigma'_{x,0} + \sigma'_{y,0})$ is the initial effective pressure in the ground, i.e. the pressure in the ground prior to the (possible) extension of the building. With this quantity undoubtedly having increased, especially underneath the foundation, the undrained shear strength and thereby the overall bearing capacity must necessarily also have increased. The distributions of undrained shear strength prior to the original construction and prior to the planned construction are shown in Figure 42.2 (the undrained shear strength distribution is available under Initial Stresses in Results).

The entire analysis is carried out using three stages. First a stage where the original 45 kN/m^2 is applied in the short term. Then a stage where the original loading is maintained but where Time Scope = Long Term. This stage uses the first stage as From stage. Finally, a Limit Analysis stage that

uses the previous stage as From stage and has Time Scope = Short Term. The result is an additional bearing capacity of 52 kN/m². In other words, the original bearing capacity ($q_u \approx 64 \text{ kN/m}^2$) has increased by some 50% (to $45 + 52 = 97 \text{ kN/m}^2$). This increase corresponds very well to that reported by Lehane and Jardine (2002) for a field study concerning a scenario similar to the one described in this example.

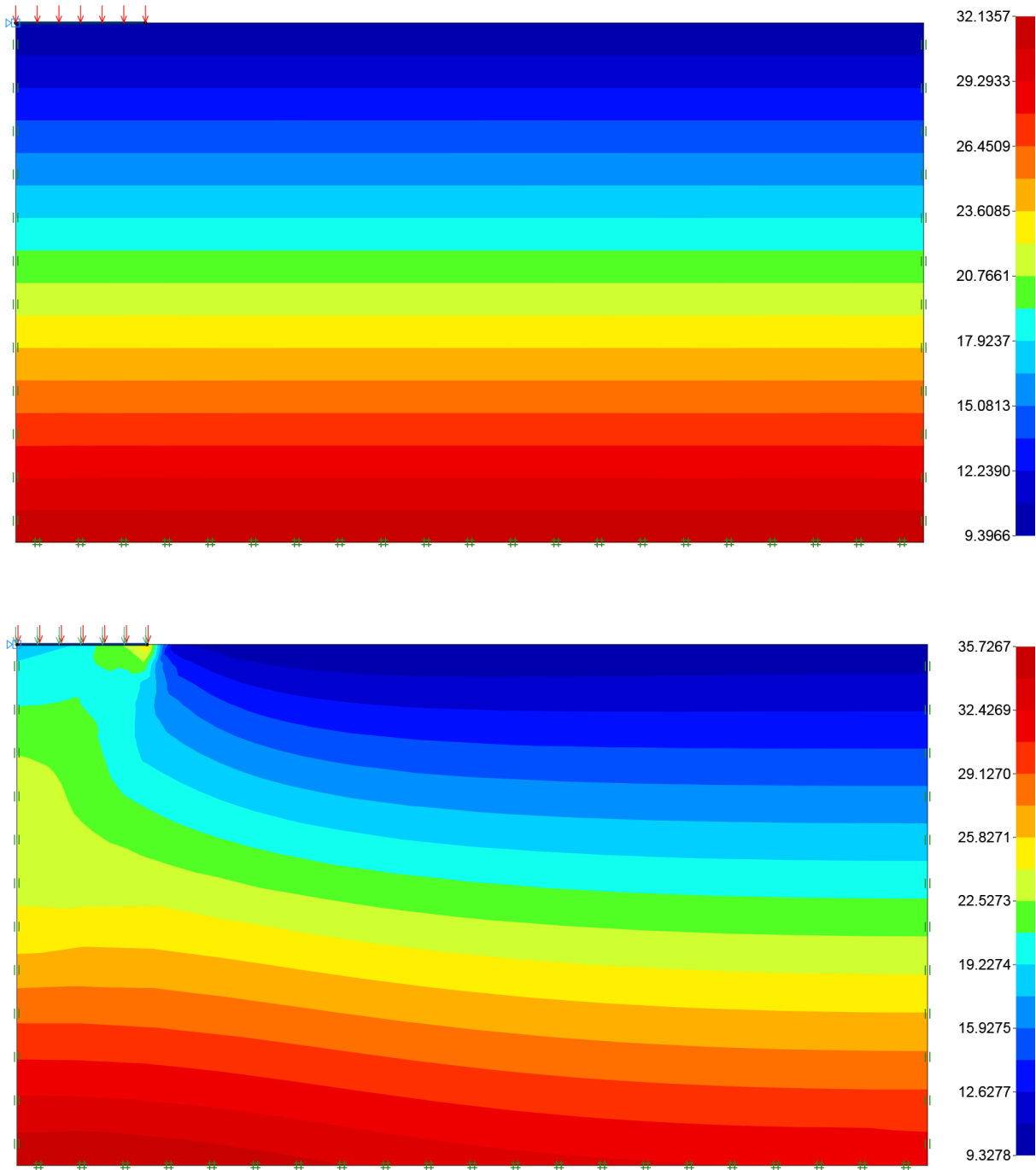


Figure 42.2: Undrained shear strength (kPa) before original construction (top) and prior to new construction (bottom).

43 SHALLOW FOUNDATION IN CLAY: EFFECTS OF PRELOADING

The following example is similar to the previous one and is inspired by the work of Gourvenec et al. (2014). It considers the effect of preloading on the bearing capacity of a shallow foundation as shown in Figure 43.1. The material is Modified Cam Clay with $\phi = 30^\circ$, $e_0 = 1.2$, $\kappa = 0.044$, $\lambda = 0.205$, $\nu = 0.25$ and $\gamma = 18 \text{ kN/m}^2$. The foundation is of Rigid material with a unit weight of $\gamma = 20 \text{ kN/m}^2$.

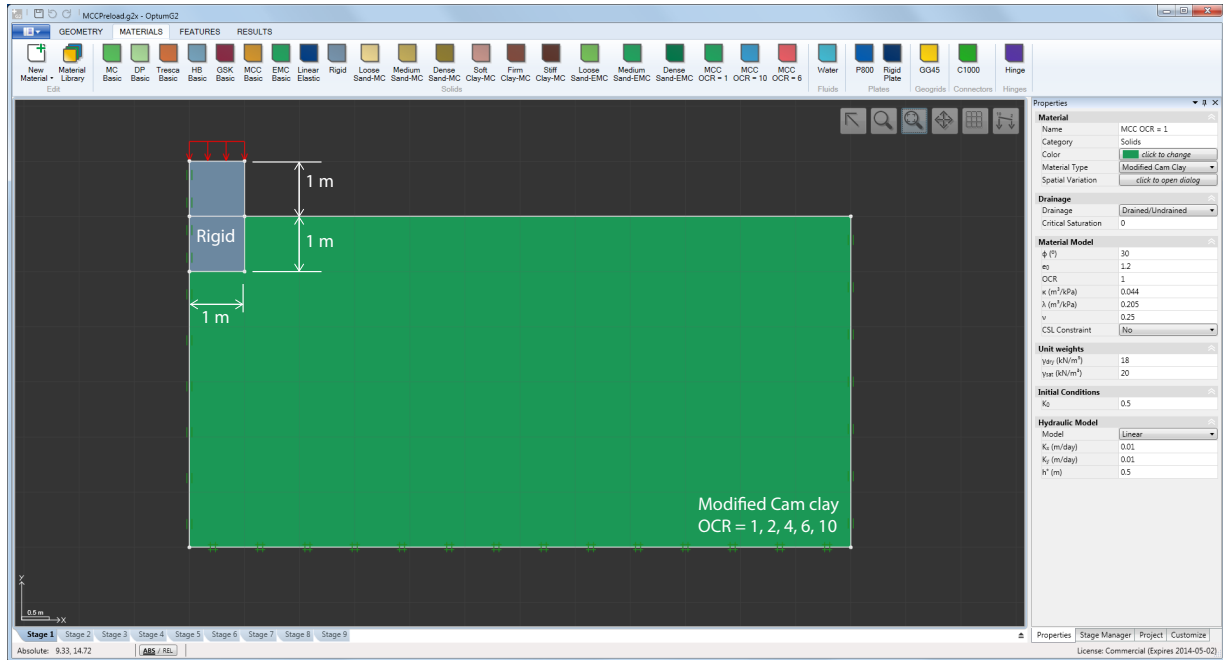


Figure 43.1: Shallow foundation in a Modified Cam Clay soil.

The aim of the analysis is to determine the bearing capacity, Q_α , for different magnitudes of preloading for different overconsolidation ratios. Following Gourvenec et al. (2014), the short term bearing capacity, Q_0 , assuming no preloading is first determined for OCR = 1, 2, 4, 6 and 10 (note: CLS Constraint under Strength is set to No, see the Materials Manual for details). For each OCR, the foundation is then subjected to preloading of a magnitude $P = \alpha Q_0$ where $\alpha = 0.1, 0.2, \dots, 0.9$ before a final short term Limit Analysis is conducted to determine the bearing capacity.

In all analyses, the earth pressure coefficient is taken as:

$$K_0 = (1 - \sin \phi) \text{OCR}^{\sin \phi} \quad (43.1)$$

Besides the initial Limit Analysis to determine the bearing capacity without preloading, each analysis comprises two stages:

- An Elastoplastic analysis with Time Scope = Long Term and a fixed load $P = \alpha Q_0$. This stage is run without a From stage meaning that the initial stresses in the ground are determined automatically on the basis of the earth pressure coefficient K_0 .
- A Limit Analysis with Time Scope = Short Term. The From stage is here the Elastoplastic stage in which the preload is applied.

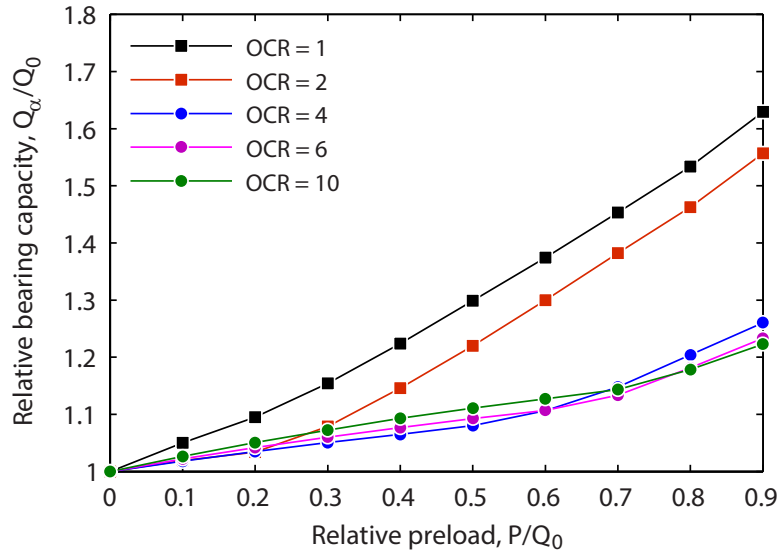


Figure 43.2: Relative preload versus relative bearing capacity for different OCR.

Both stages are run using 2,000 6-node Gauss elements with three Adaptivity Iterations used for the Limit Analysis stage.

The results of the analyses are shown in Figure 43.2. As seen, the relative gain in bearing capacity decreases for increasing OCR. This result, which is in agreement with Gourvenec et al. (2014), is not surprising. While preloading will tend to increase the bearing capacity by virtue of the stresses in the ground increasing, the gain is greater when the OCR is also increased, i.e. when the yield surface hardens, and thereby expands, as a result of the preloading.

44 TUNNELING USING CONVERGENCE-CONFINEMENT METHOD

The following example considers the construction of a circular lined tunnel in weathered rock as shown in Figure 44.1. The rock is modeled as a Mohr-Coulomb material and the lining is modeled using Plate elements. Both sets of material parameters are shown in the figure below.

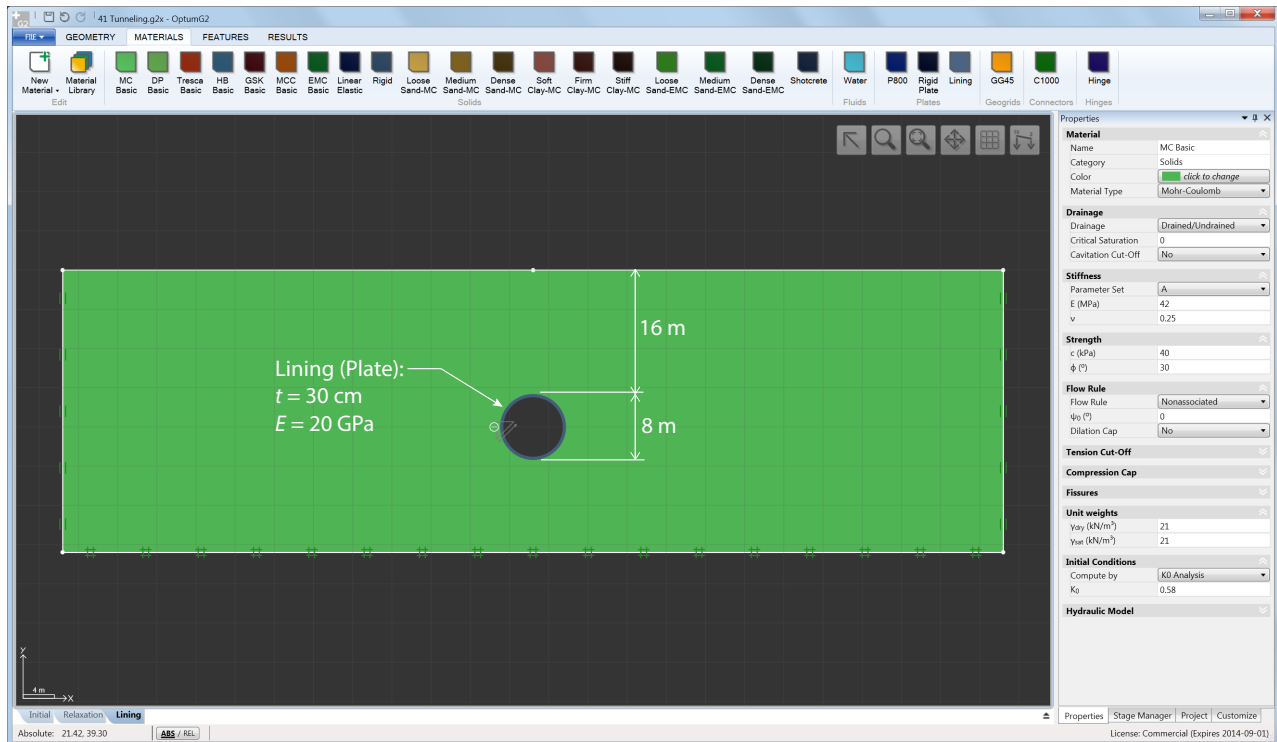


Figure 44.1: Circular tunnel.

Tunneling is an inherently three-dimensional problem and should ideally be modeled as such. However, a number of plane strain approaches have been developed and remain widely used in practice. These include the convergence-confinement, the progressive softening method, and volume loss control method. A thorough review of these methods is given by Potts and Zdravkovic (2001).

The approximate plane strain methods all consider a cross section of the tunnel perpendicular to the direction of excavation. The critical issue is what cross section should be considered. One extreme would be to first excavate the tunnel and then, once a new stress state has been obtained, to insert the lining. Another extreme would be to have the lining wished in place from the outset and then excavate the soil inside the tunnel. In the former case, the ground settlements would be overestimated and in the latter the sectional forces in the lining would be overestimated. It is noted that both models effectively neglect 3D effects – the former by assuming an infinitely long unsupported tunnel and the latter by assuming an infinitely long tunnel supported at all cross sections. The approximate plane strain mentioned above methods all seek to account for 3D effects by establishing a reasonable compromise between these extremes.

In the following, the convergence-confinement method is used. The basic principles are as follows (see Figure 44.2). From an initial state, the tunnel is excavated while keeping the perimeter of the tunnel fully supported. This induces no changes to the stress state and hence no deformations.

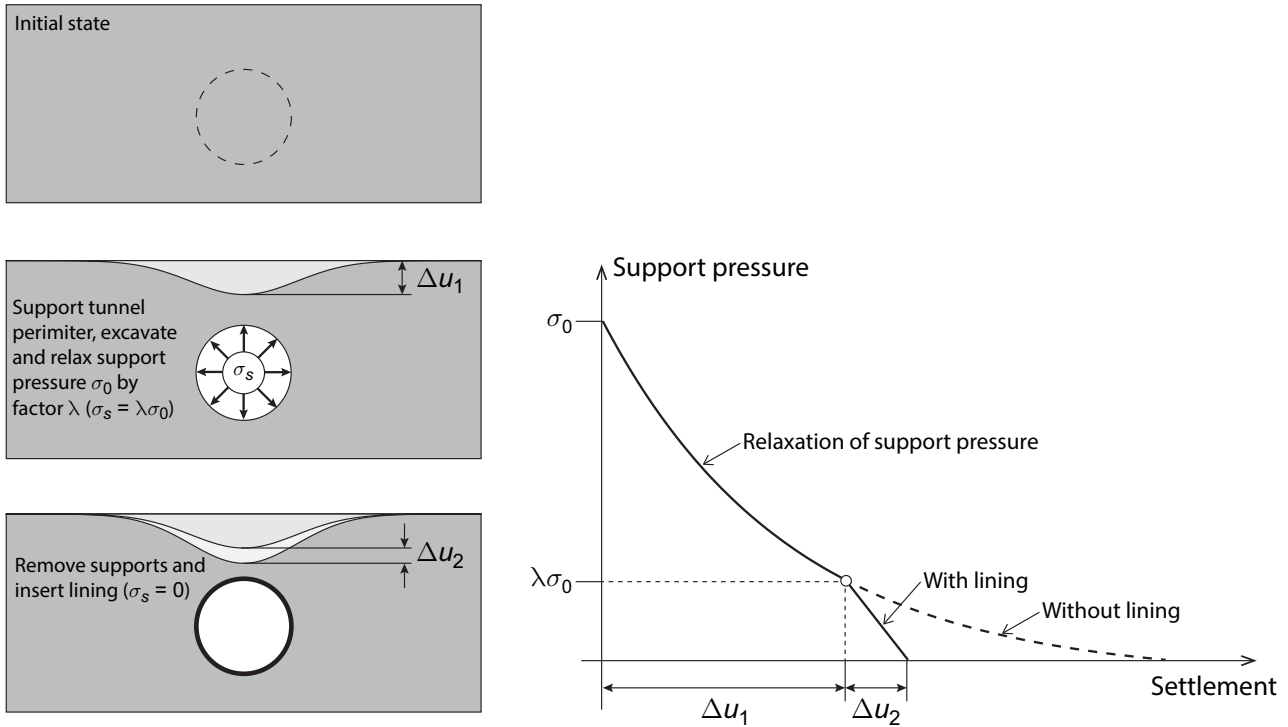


Figure 44.2: Schematics of the convergence-confinement method (after Vermeer et al. 2003).

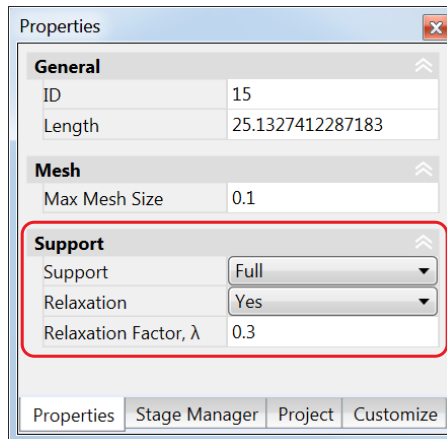


Figure 44.3: Support relaxation in OPTUM G2.

Next, the reactions on the tunnel perimeter are relaxed, i.e. reduced by a factor λ where $0 \leq \lambda \leq 1$. Finally, the lining is inserted and all supports around the tunnel perimeter are removed. This induces further settlements.

In OPTUM G2, the convergence-confinement method may be set up using three stages following Figure 44.2:

1. An initial stage where the initial stresses are calculated using an Initial Stress analysis.
2. A second stage where the tunnel is excavated. The tunnel perimeter is here fully supported and a Relaxation Factor, λ , is specified (see Figure 44.3).

3. A final stage where the perimeter supports are replaced by a Plate to model the lining.

The crucial issue in the convergence-confinement method is the selection of the relaxation factor λ . In practice it is either selected on the basis of experience and/or field calibration or by considering two values at either end of the spectrum, for example $\lambda = 0.3$ and $\lambda = 0.7$, the idea being that the smaller value tends to overestimate the ground settlements while the larger value tends to overestimate the sectional forces in the lining. More generally, to aid in establishing the appropriate value of the relaxation factor, various quantities of interest can be examined as function of λ . Some examples are shown in Figures 44.4-5 where the ground settlement above the center of the tunnel and the maximum bending moment in the lining are plotted as function of λ .

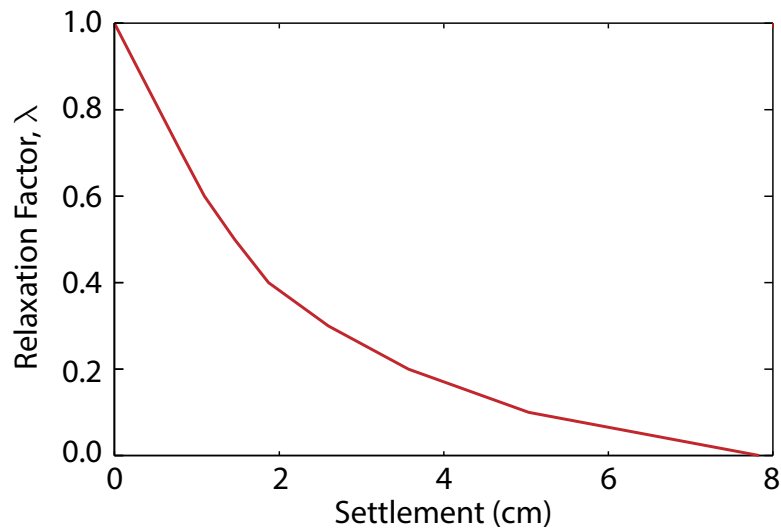


Figure 44.4: Ground settlement (Δu_1) as function of support relaxation factor.

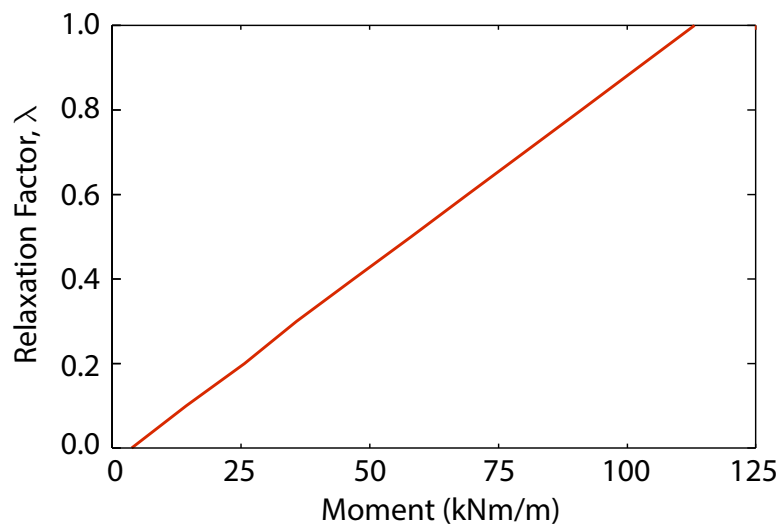


Figure 44.5: Bending moment as function of support relaxation factor.

The final vertical displacements (after introduction of the lining) for a value of $\lambda = 0.3$ are shown in Figure 44.6 while the normal forces and bending moments are shown in Figure 44.7.

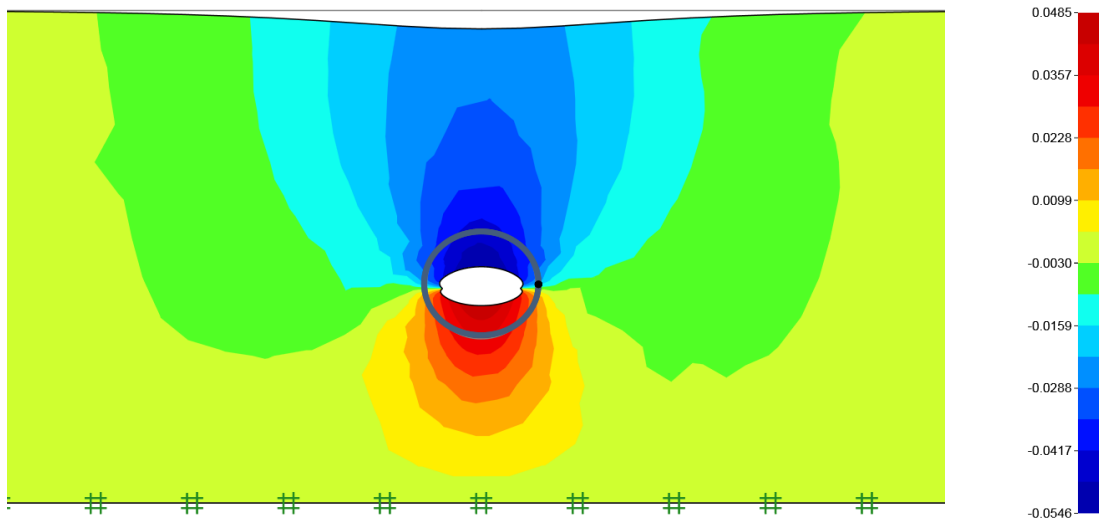


Figure 44.6: Final vertical displacements for $\lambda = 0.3$ (deformations scaled by a factor of 50).

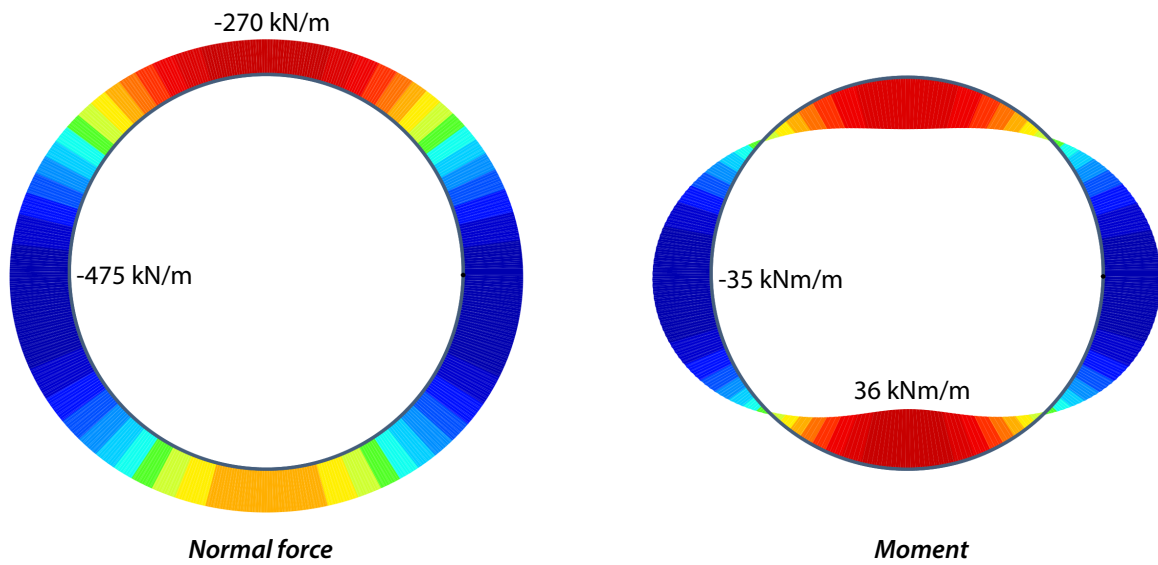


Figure 44.7: Normal forces and bending moments in lining for $\lambda = 0.3$.

45 EXCAVATION WITH UNDERDRAINAGE

The following example considers the excavation in a soil where the steady state seepage pressures deviate from the usual hydrostatic distribution. In particular, an under-drained pressure profile as indicated in Figure 45.1 is considered. This type of profile is commonly observed in the London area (see Potts and Zdravkovic 2001, and references therein)

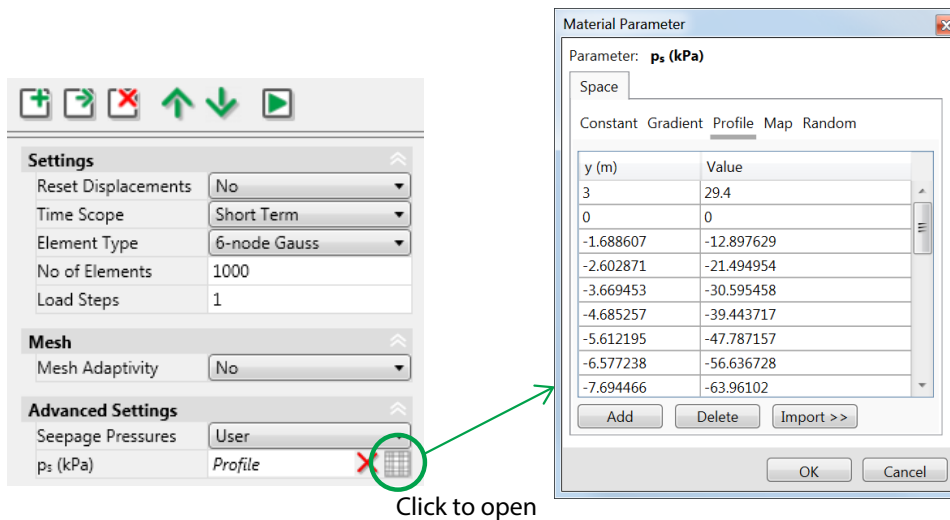
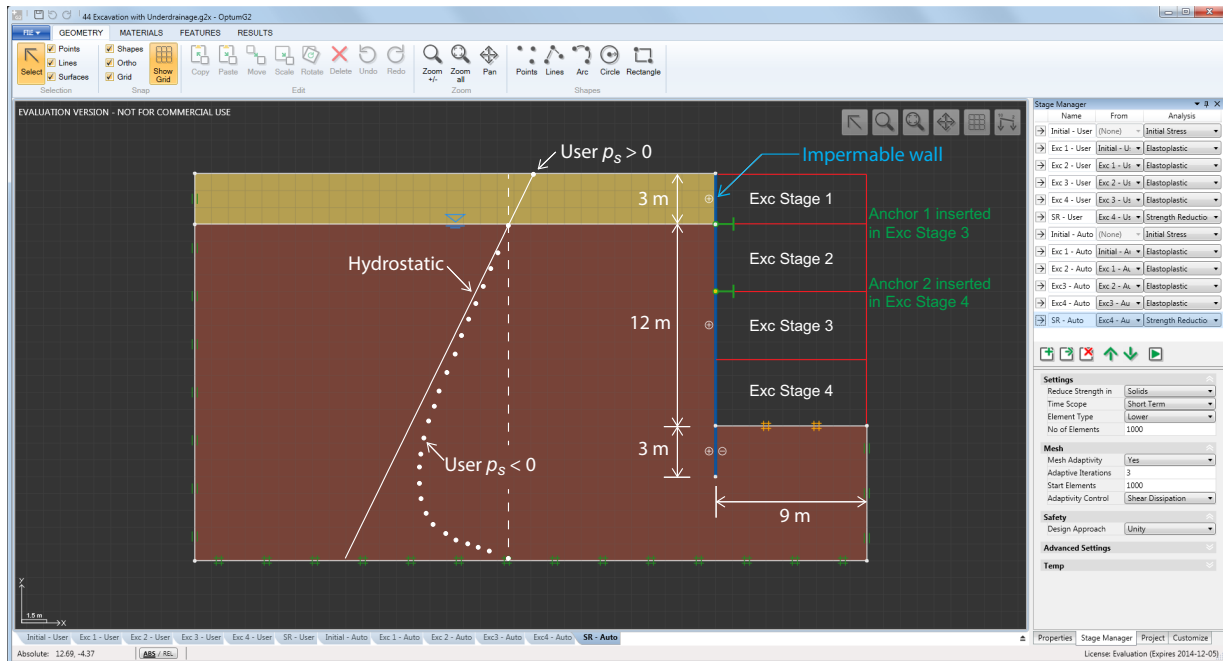


Figure 45.1: Problem setup (top) and specification of user defined seepage pressure profile. The Flow BCs (Water Table and No-Flow conditions) are ignored when a user defined seepage pressure profile is specified.

The profile indicated in Figure 45.1 is defined by a set of points giving the pressure as function of depth, i.e. the y coordinate. The steps needed to import an arbitrary distribution of seepage pressure are illustrated in the figure above. In the lower half of stage manager under Advanced, Seepage Pressure = User is selected. The button on the right hand side of the field below opens the dialog shown on the right in the figure. Using the Import button, a file with the data can be loaded into

the project. The input file must contain two columns with the y coordinate and the pressure value. No particular ordering of the coordinates is needed, but the data are expected to cover the entire problem domain. Hence, a point at the very top of the problem domain is needed to specify that p_s in the upper sand layer. It is important that $p_s < 0$ be specified in areas that are deemed to be above the ground water table – a pore pressure of $p_s = 0$ will be interpreted a degree of saturation $S = 1$. The data can be unloaded via the red cross next to the button that opens the Material Parameter window.

The problem is analyzed as indicated in Figure 45.1 with an Initial Stress stage followed by four excavation stages of type Elastoplastic. Anchors are inserted in the third and fourth excavation stages. Finally, after the last excavation stage, a short term Strength Reduction analysis is carried out.

In addition to the user defined profile, the problem is also run for a standard hydrostatic seepage pressure distribution, i.e. by selecting Seepage Pressures = Auto under Advanced in the stage manager. The results of the analyses in terms of the maximum horizontal displacement of the wall are shown in Figure 45.2. We see that the displacements are somewhat larger for the hydrostatic distribution.

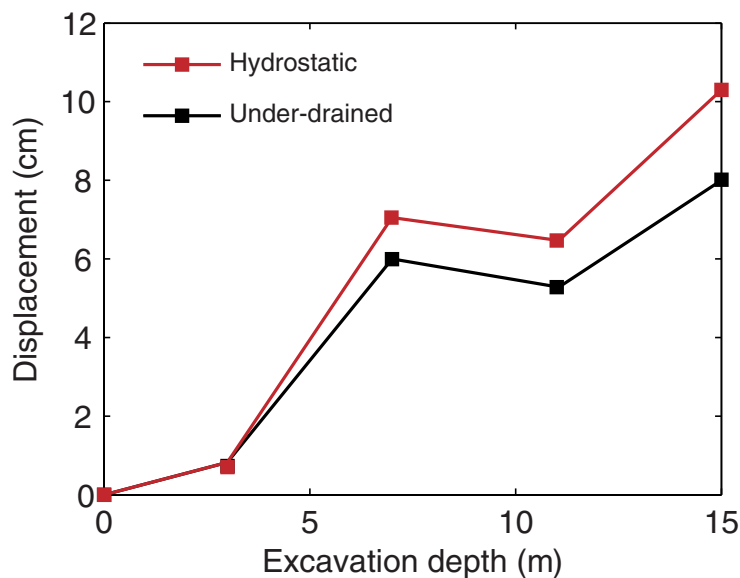


Figure 45.2: Maximum displacement of wall versus excavation depth.

The Strength Reduction analysis give the following results:

$$\begin{aligned}
 \text{Hydrostatic:} & \quad FS_s = 1.03 \pm 0.02 \\
 \text{Under-drained:} & \quad FS_s = 1.16 \pm 0.03
 \end{aligned}
 \tag{45.1}$$

The differences between the results of the two seepage pressure distributions are mainly due to two factors: 1) larger effective stresses in the under-drained case lead to greater undrained shear strength (see Initial Stresses/Undrained Shear under Results) and 2) smaller pore pressures behind the wall in the under-drained case increase the overall stability.

46 ONE-DIMENSIONAL CONSOLIDATION

The following example introduces the various possibilities of the Consolidation analysis implemented in OPTUM G2. The problem is shown in Figure 46.1 and involves a 1 m by 1 m block of elastic material. The Young's modulus is 30 MPa and the Poisson's ratio has been set to $\nu = 0$ to facilitate a direct comparison with known analytical solutions. The block consolidates under a load of $q = 100 \text{ kN/m}^2$.

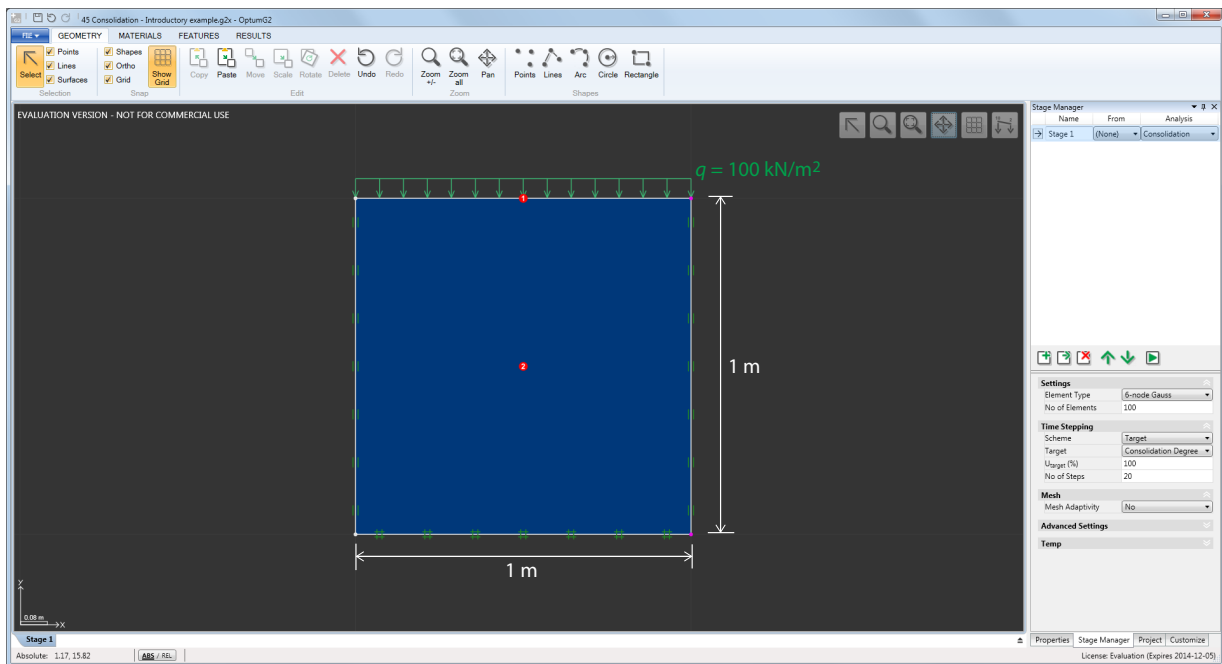


Figure 46.1: One-dimensional consolidation problem.

The analysis proceeds by selecting Consolidation in the Analysis column of the stage manager. The stage settings then appear in the lower half of the window. As for all other analysis types, the Element Type and No of Elements must be selected. For this problem, 100 6-node Gauss elements are used, but any of the available elements are in principle applicable.

The second category of the stage settings, Time Stepping, contains various options and parameters to control the time stepping. Three different time stepping schemes are available: Auto, Target/Time, Target/Degree (see Figure 46.2).

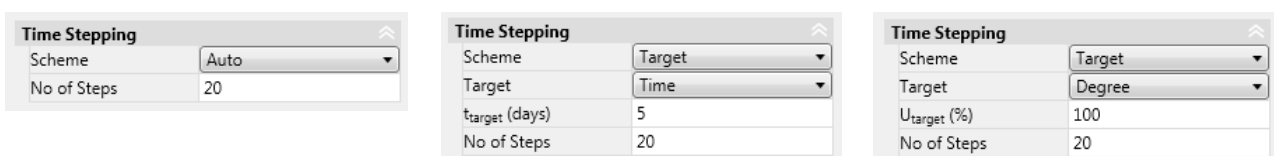


Figure 46.2: Time stepping settings: Auto (left), Target/Time (center), and Target/Degree (right).

The Auto scheme steps with automatic adjustment of the time step to reach a state near full consolidation in the specified number of steps.

For the Target scheme, two targets are possible: Time and Degree. The former involves the specification of the time at which the analysis is terminated and a number of steps to reach that time. The latter requires specification of the degree of consolidation and the number of steps to reach this target. In this case, the time step is adjusted automatically as in the Auto scheme.

In OPTUM G2, Consolidation analysis without specification of a From stage proceeds via the following steps:

1. An Initial Stress analysis to compute the initial stresses and steady state seepage pressures. The analysis is identical to that used in Elastoplastic analysis, i.e. Fixed loads are not included in the K_0 procedure.
2. A short term analysis to compute the state just before the actual consolidation commences, i.e. after application of loads but before dissipation of excess pore pressures. This analysis is equivalent to an Elastoplastic analysis with Time Scope = Short Term.
3. A long term analysis, starting from the short term state, to compute an estimate of the state after a very long time. This analysis is equivalent to an Elastoplastic analysis with Time Scope = Long Term.
4. The actual consolidation analysis.

46.1 ‘Degree of consolidation’

The degree of consolidation is problematic to define for general boundary value problems and various measures of the proximity to the short and long term states are used in OPTUM G2.

Firstly, with the short and long term states available from Steps 2 and 3, a work based degree of consolidation can be defined as

$$U_W(t) = \frac{W(t) - W_{ST}}{W_{LT} - W_{ST}} \times 100\% \quad (46.1)$$

where $W(t)$ is the work at time t and W_{ST} and W_{LT} are the short and long term work respectively. This is perhaps the best general measure of the degree of consolidation. However, a complication is that W_{LT} is computed using a single step while the actual W_{LT} will depend on the exact time dependent process to reach the long term state. As such, the computed single step estimate may be somewhat inaccurate and values of U_W slightly above or below 100% at full consolidation may be encountered.

For cases where the loading is applied to a rigid footing, the work based degree of consolidation is identical to that based on settlements:

$$U_u(t) = \frac{u(t) - u_{ST}}{u_{LT} - u_{ST}} \times 100\% \quad (46.2)$$

where $u(t)$ is the vertical settlement of the foundation and u_{ST} and u_{LT} are the short and long term settlements respectively. Again, the problem with this measure, as well as other displacement based measures, is that the final state is not readily estimated a priori.

Another quantity of interest is the average normalized excess pore pressure:

$$\frac{P_e(t)}{P_{e,0}} = \frac{\int_V p_e(x, y, t) dV}{\int_V p_{e,0}(x, y) dV} \quad (46.3)$$

where $p_{e,0}(x, y)$ is the pore pressure distribution at $t = 0$ (computed in Step 2 of the above) and $p_e(x, y, t)$ is the excess pore pressure distribution at time t . On the basis of this quantity, the degree of consolidation may be defined as:

$$U_P(t) = \left(1 - \frac{P_e(t)}{P_{e,0}}\right) \times 100\% \quad (46.4)$$

This definition of the degree of consolidation tends to differ slightly from the work based degree of consolidation, U_W .

For the purpose of time load stepping in OPTUM G2, a combination of U_W and U_P , denoted U , is used. This measure of the degree of consolidation tends to be closer to U_P than U_W .

In conclusion: the degree of consolidation is somewhat ambiguous and it is recommended to scrutinize the actual state for a computed value of U , U_W or U_P .

46.2 Analytical solution

The problem of one-dimensional consolidation can be described in terms of a diffusion type equation involving the excess pore pressures as variables:

$$\frac{\partial p_e}{\partial t} = \left(C_v \frac{\partial^2 p_e}{\partial y^2}\right) \quad (46.5)$$

where the coefficient of consolidation, C_v , is given by

$$C_v = \frac{KE}{\gamma_w} \quad (46.6)$$

with K being the permeability and γ_w ($= 9.8 \text{ kN/m}^3$) the unit weight of water.

The solution to this equation, for constant C_v , is given by

$$\frac{p_e(y, t)}{p_{e,0}} = \frac{p_e(y, t)}{q} = \frac{4}{\pi} \sum_{i=1}^{\infty} \frac{(-1)^{i-1}}{2i-1} \cos\left(\left(2i-1\right)\frac{\pi y}{2H}\right) \exp\left(-\left(2i-1\right)^2 \frac{\pi^2 C_v}{4H^2} t\right) \quad (46.7)$$

with H being the height of the block ($H = 1 \text{ m}$ in the present case).

With the excess pore pressures determined, the effective vertical stress and thereby the vertical settlement can be determined as:

$$\frac{u_y(y, t)}{H} = \frac{q}{E} \left[1 - \frac{8}{\pi^2} \sum_{i=1}^{\infty} \frac{(-1)^{i-1}}{(2i-1)^2} \sin\left(\left(2i-1\right)\frac{\pi y}{2H}\right) \exp\left(-\left(2i-1\right)^2 \frac{\pi^2 C_v}{4H^2} t\right)\right] \quad (46.8)$$

46.3 Results

The results of the analysis using the Auto scheme with 20 steps are shown in Figure 46.3. The agreement between numerical and analytical solution is very good and can be improved further by increasing the number of steps in the analysis.

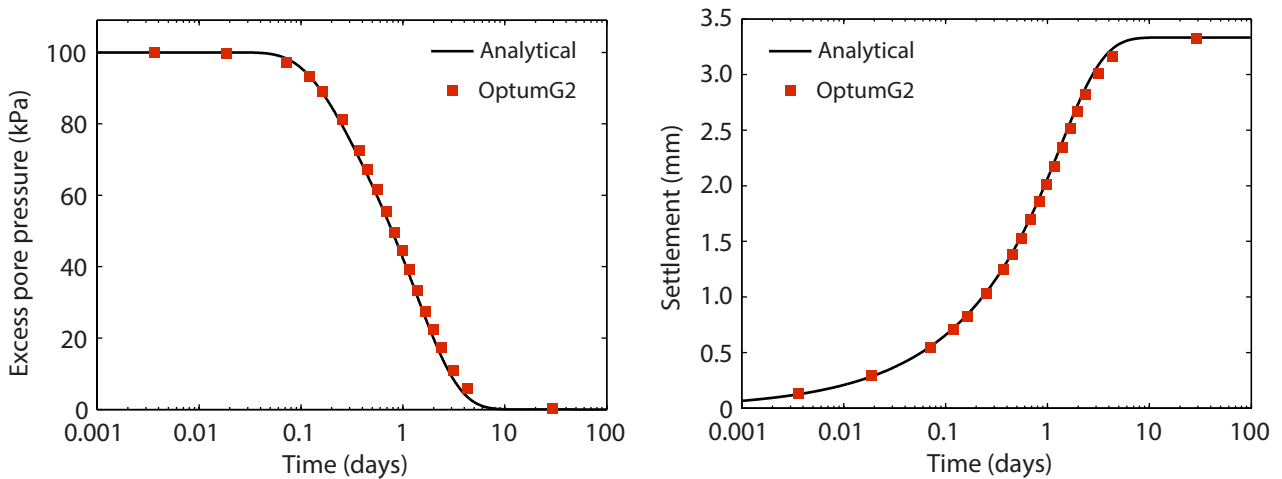


Figure 46.3: Evolution of excess pore pressure at the center of the block with time (left) and evolution of settlement of top surface with time (right).

47 EFFECT OF CONSOLIDATION ON BEARING CAPACITY

The following example is similar to that of Section 42. A shallow foundation in a Firm Clay-MC material (Figure 47.1) is loaded rapidly and then left to consolidated. After a period of time, the load is removed and the short term bearing capacity is determined. Following Example 42, we expect a short term bearing capacity that increases with consolidation time as a result of an increase in effective stresses, and hence an increase in the undrained shear strength, beneath the foundation.

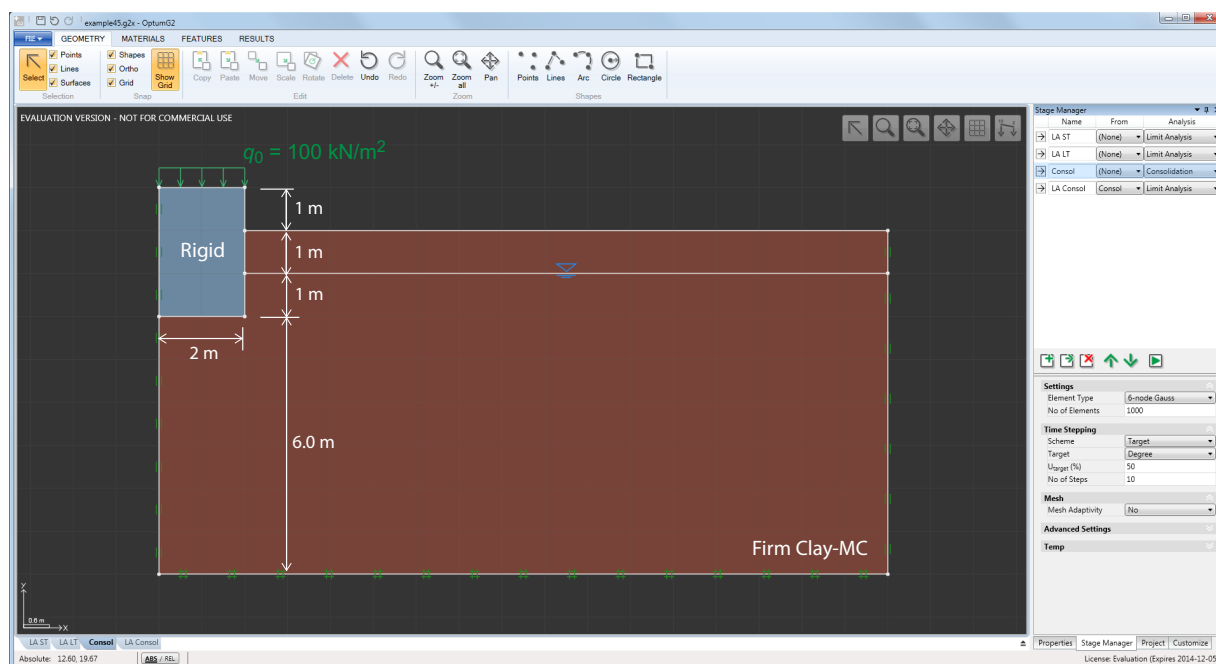


Figure 47.1: Problem setup (consolidation stage).

The example commences by determining the short term bearing capacity from a standard Limit Analysis. The result is a limit load of approximately $Q_0 = 280$ kN/m. Next, a Consolidation analysis with a fixed load of $P = 200$ kN/m, representing about 70% of the short term bearing capacity, is carried out. The Target time stepping scheme is used with Target = Degree and a specified target degree of consolidation, U_1 , corresponding to a time t_1 . Finally, a Limit Analysis stage, linked to the Consolidation stage, is used to determine the new short term bearing capacity, $Q(t_1)$.

The results of the analyses are shown in Figures 47.2-3. Figure 47.2 shows the evolution of bearing capacity with time while Figure 47.3 shows the relative gain as function of the degree of consolidation. It is observed that the gain increases approximately linearly with the work based degree of consolidation:

$$\frac{Q(t)}{Q_0} \simeq 1 + \left(\frac{Q_\infty}{Q_0} - 1 \right) \frac{U_w(t)}{100\%} \quad (47.1)$$

where Q_∞ is the short term bearing capacity after full consolidation. Finally, we note that the gain for $U = 100\%$, $Q(t)/Q_0 = Q_\infty/Q_0 = 1.45$, corresponds approximately to that found in Example 42 for $OCR = 1$. Similar gains for the applied level of preloading have been observed in full scale field experiments by Lehane and Jardine (2002) for a scenario similar to the one considered in this example.

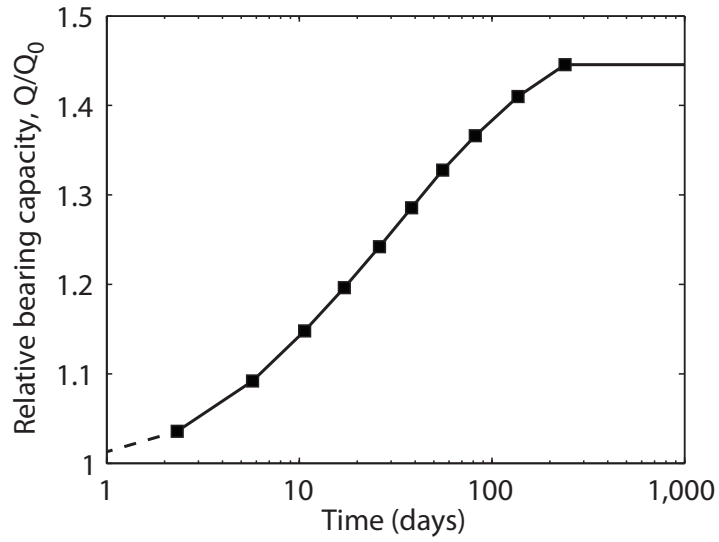


Figure 47.2: Relative bearing capacity gain, Q/Q_0 , as function of time.

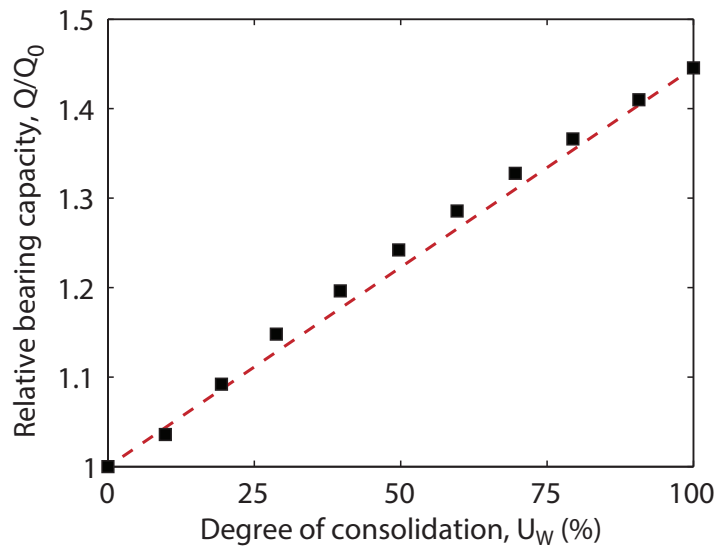


Figure 47.3: Relative bearing capacity gain, Q/Q_0 , as function of degree of consolidation.

48 EMBANKMENT CONSTRUCTION – PART 1

The following two sections describe the analysis of an embankment (see Figure 48.1) to be constructed on a soft soil overlaying a layer of dense sand. The soft soil is modeled by means of the Modified Cam Clay model whereas the embankment fill and the dense sand layer are modeled as Mohr-Coulomb materials. For full details of the material parameters used, please refer to the accompanying input file that can be accessed via the welcome window in OPTUM G2 or via File/Examples.

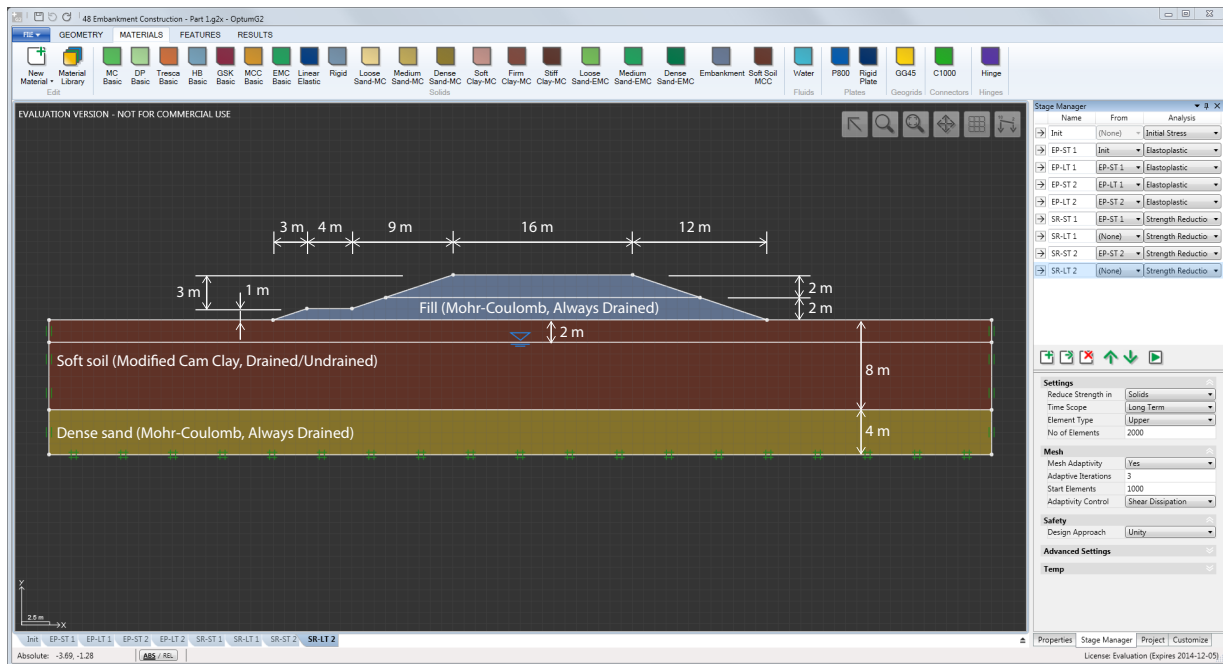


Figure 48.1: Embankment construction: problem setup.

The embankment is constructed in two stages, each 2 m in height as indicated in the figure above. Between each stage, the underlying soft soil is left to consolidate. This type of analysis can be carried out using Consolidation. However, if only the settlements immediately after construction of each stage and the ones induced as a result of full consolidation are of interest, Elastoplastic analysis may be used. That approach is the subject of this section while the time dependent consolidation is covered in the next.

The analysis proceeds by way of five stages:

1. An Initial Stress stage to determine the in-situ stresses and steady state seepage pressures before construction.
2. An Elastoplastic stage, starting from 1 and with Time Scope = Short Term, to simulate the first 2 m of construction.
3. An Elastoplastic stage, starting from 2 and with Time Scope = Long Term, to account for the effects of full consolidation.
4. An Elastoplastic stage, starting from 3 and with Time Scope = Short Term, to simulate the next 2 m of construction.

5. An Elastoplastic stage, starting from 4 and with Time Scope = Long Term, to account for the effects of full consolidation.

In addition, five Strength Reduction stages are used to gauge the factor of safety at various stages of the construction:

- I. A Strength Reduction, starting from 2 and with Time Scope = Short Term, to determine the factor of safety immediately after the first construction stage.
- II. A Strength Reduction with Time Scope = Long Term to determine the factor of safety after consolidation of the first construction stage.
- III. A Strength Reduction, starting from 4 and with Time Scope = Short Term, to determine the factor of safety immediately after the second construction stage.
- IV. A Strength Reduction with Time Scope = Long Term to determine the long term factor of safety after consolidation of the second construction stage.
- V. A Strength Reduction, starting from 5 and with Time Scope = Short Term, to determine the short term factor of safety after consolidation of the second construction stage.

In this example, the majority of the deformations take place in the two long term stages 3 and 5. The stage displacement of these two stages are shown below. The vertical displacement of the center of the embankment is about 17 cm in each of the two stages.

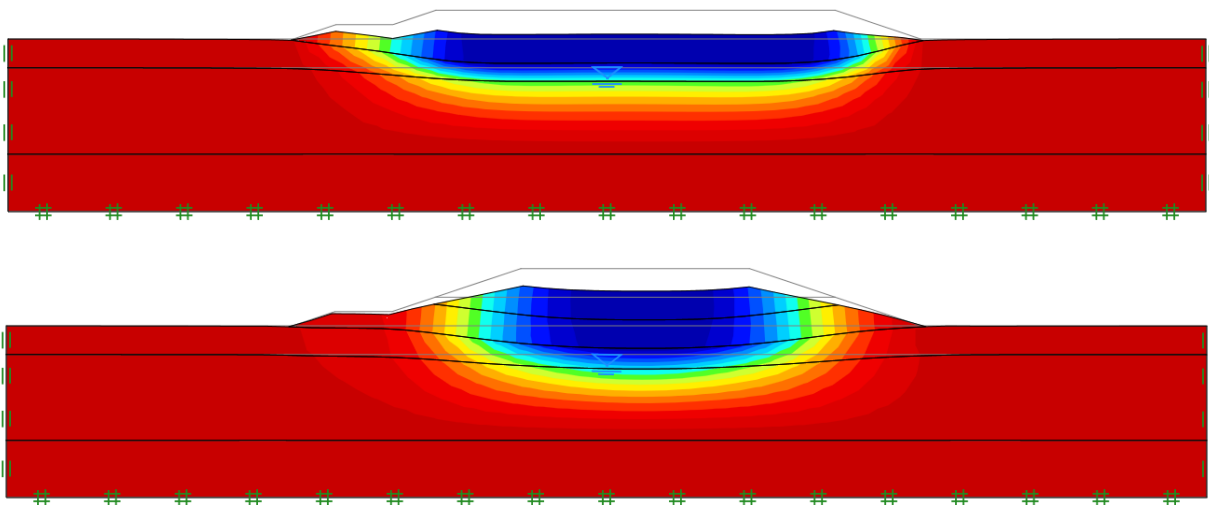


Figure 48.2: Vertical stage displacements for Stages 3 and 5. The deformations are scaled by a factor of 10.

The factors of safety are:

- I. (Short Term): $FS_s = 1.55 \pm 0.02$
 - II. (Long Term): $FS_s = 3.12 \pm 0.03$
 - III. (Short Term): $FS_s = 1.54 \pm 0.01$
 - IV. (Long Term): $FS_s = 2.52 \pm 0.02$
 - V. (Short Term): $FS_s = 1.78 \pm 0.01$
- (48.1)

As expected, the long term stability decreases as the height of the embankment increases. For the short term stability, the increase in embankment height is compensated by the increase in undrained shear strength as a result of consolidation of the soft soil, to an extent that the short term stability at the completion of construction and dissipation of all excess pressure is greater than at any point during construction. The factors of safety and associated distributions of shear dissipation are shown in Figure 48.3.

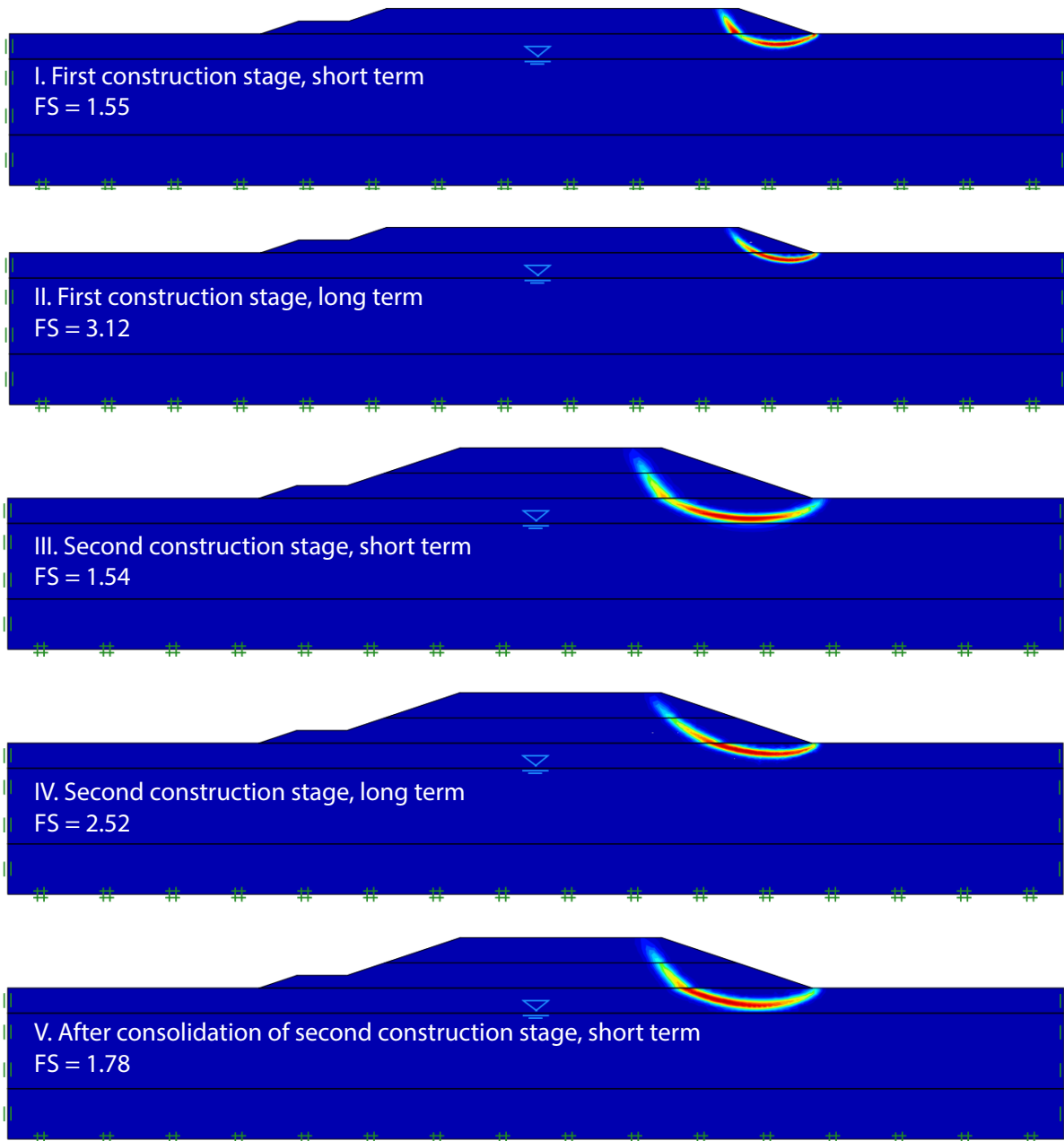


Figure 48.3: Distributions of shear dissipation from Strength Reduction analysis.

In summary, this example demonstrates the capabilities of OPTUM G2 to rapidly carry out analyses that provide the essential information required for the design of the embankment, namely the short and long term deformations and the factors of safety. What is missing is information about the variation of excess pore pressures with time after each construction stage. That analysis is covered in the next example.

49 EMBANKMENT CONSTRUCTION – PART 2

The second part of the example concerns the consolidation of the embankment after each construction stage, i.e. the dissipation of excess pore pressure with time. Two different situations are considered. The first one as sketched in the previous example and the second one with pre-installed drains underneath the embankment is shown in Figure 49.1. In OPTUM G2, drains may be modeled by means of the Zero Excess Pressure BC.

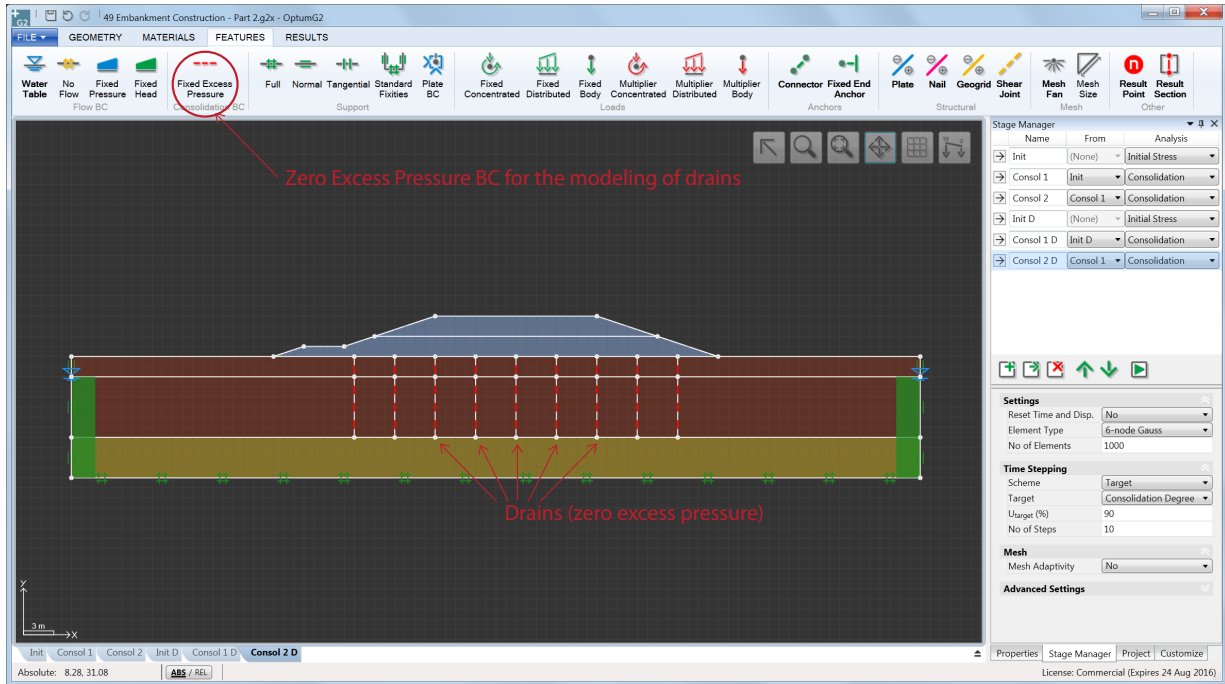


Figure 49.1: Embankment with drains.

In each of the two situations (drains or no drains), the problem is modeled by using an Initial Stress stage. This is linked to a Consolidation stage accounting for the construction of the lower part of the

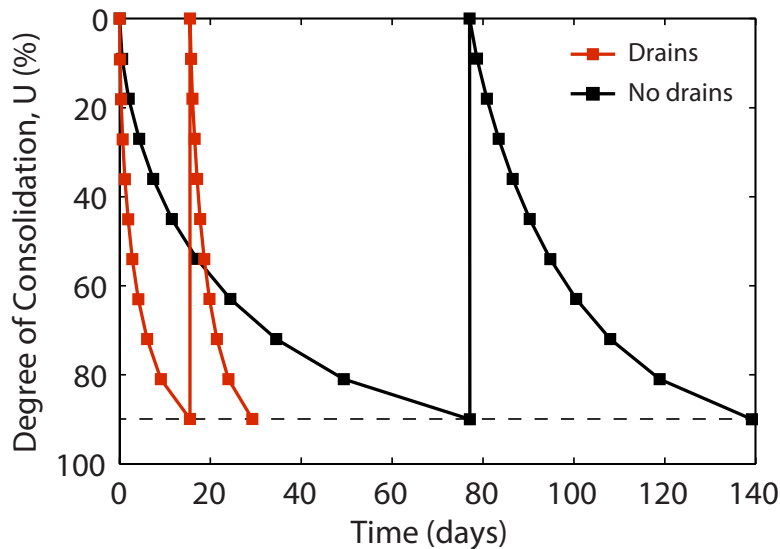


Figure 49.2: Degree of consolidation versus time with and without drains.

embankment. Finally, a second Consolidation stage, accounting for the upper part of the embankment is defined and linked to the previous stage. In both Consolidation stages, the Target scheme with Degree = 90% is used. It should be noted that in the case where drains are used, these are included already in the Initial Stress stage. In other words, it is assumed that the drains have been placed well in advance of the actual construction and that a steady state seepage pressure distribution exists before construction.

The degree of consolidation with time for each of the two situations is shown in Figure 49.2. As expected, the drains facilitate a significantly more rapid consolidation. Note also, the the rate of consolidation increases between the two construction stages. This is a consequence of the stress dependence of the Modified Cam Clay model which implies an increase in Young's modulus with effective mean stress. As such, the coefficient of consolidation, $C_v = KE/\gamma_w$, increases accordingly.

50 CONSOLIDATION OF EXCAVATION

This problem considers an excavation in front of a sheet pile wall as sketched in Figure 50.1. After the excavation – which is assumed to be performed sufficiently rapidly for no significant excess pore pressure dissipation to have taken place – a consolidation analysis to full consolidation is performed. The soil soil profile consists of 2 m of loose sand overlying a deep layer of clay.

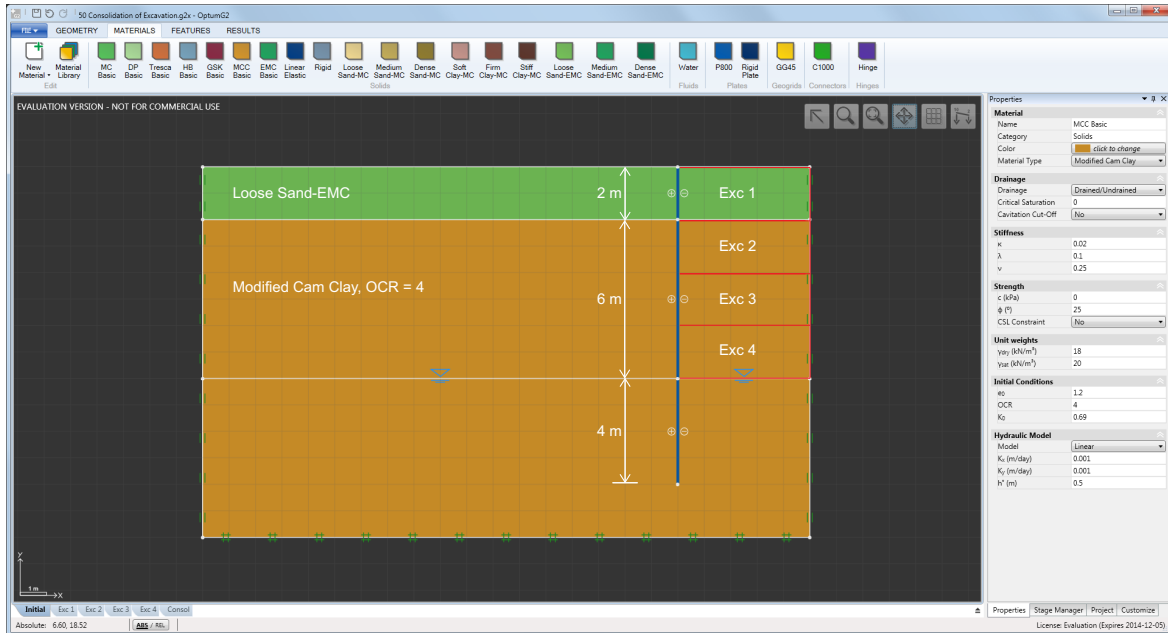


Figure 50.1: Problem setup.

The excavation is carried out in four stages as indicated in Figure 50.1. At the end of the excavation process, a consolidation stage is used to simulate the process of excess pore pressure dissipation to a final time of 200 days. From Figure 50.2 it is seen that the displacements resulting from excess pore pressure dissipation are of a similar magnitude to those induced in the short term as a result of the excavation, approximately 5 cm.

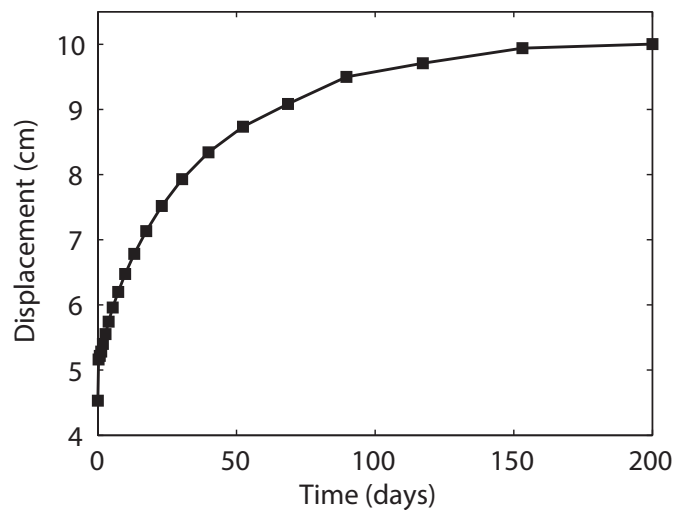


Figure 50.2: Maximum horizontal displacement.

51 TRESCA VS AUS FAILURE ANALYSIS

Under undrained conditions in plane strain, the Mohr-Coulomb model is equivalent to the Tresca model with an undrained shear strength that depends on the initial effective stresses and the Mohr-Coulomb cohesion and friction angle (see the Theory and Materials Manuals of details). Under more general stress states, including those encountered in axisymmetry, this equivalence does not hold. For example, the Mohr-Coulomb model will display different undrained strengths in triaxial compression and extension. More generally, the undrained shear strength depends on the Lode angle. This characteristic cannot be reproduced by the Tresca model which operates with a single, Lode angle independent, undrained shear strength.

In OPTUM G2 offers two models capable of accounting for Lode angle dependent undrained shear strength: the Generalized Tresca model and the AUS model. Both models use the undrained shear strengths in triaxial compression and extension as input parameters. Furthermore, for the Isotropic version of the AUS model, the yield surface is identical to that of the Generalized Tresca model (see Figure 51.1). In terms of plasticity, the key difference between the two model is the flow rule. While the Generalized Tresca model assumes associated flow, the flow rule of AUS model model is non-associated with the plastic potential being that of von Mises (a circle in the deviatoric plane).

In the following, the bearing capacity predictions of the Standard and Generalized Tresca models and the AUS model are examined for three different problems.

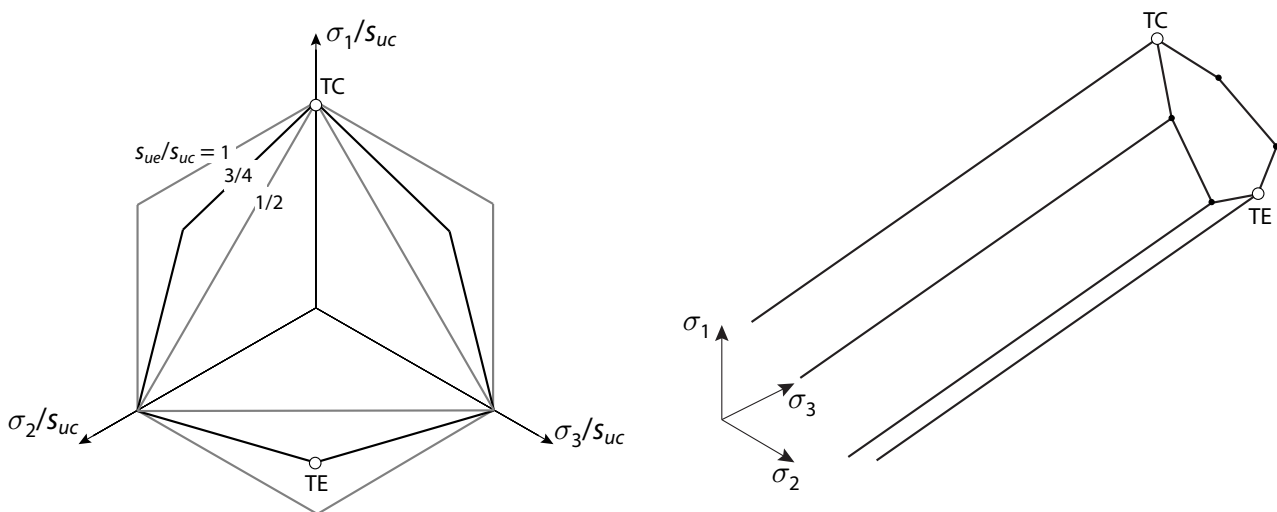


Figure 51.1: Generalized Tresca failure surface in the deviatoric plane (left) and in principal stress space for an intermediate value of s_{ue}/s_{uc} (right). The points indicated correspond to triaxial compression (TC), triaxial extension (TE) and plane strain (PS). No particular ordering of the principal stresses is assumed.

51.1 Problem 1: Circular foundation

The first problem concerns the bearing capacity of a circular foundation as shown in Figure 51.2.

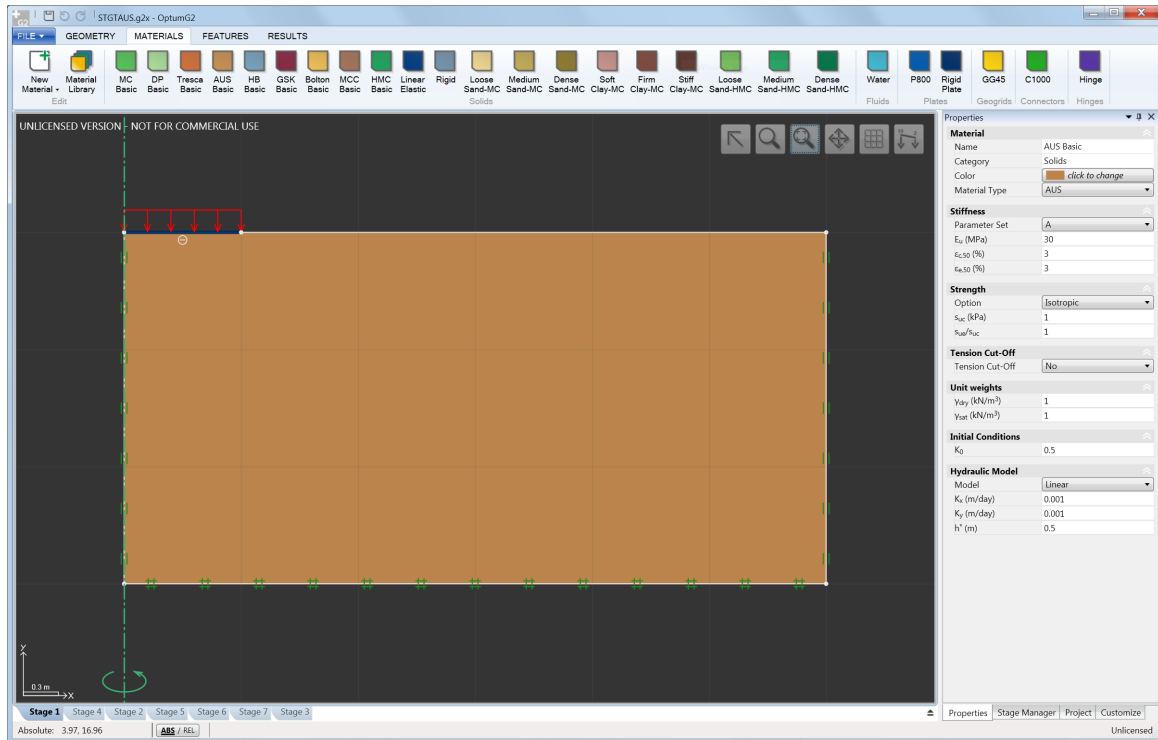


Figure 51.2: Problem 1: circular foundation.

For the Standard Tresca model, the bearing capacity is (Cox et al. 1961):

$$q_{u,ST} = 6.05s_u \tag{51.1}$$

Using 10,000 Lower/Upper elements with 3 adaptivity iterations, this solution is reproduced with negligible error.

For the Generalized Tresca model the result is exactly the same, regardless of the value of s_{ue} in relation to s_{uc} . Inspection of the Lode angle (available under Final Stresses in the Results tab) reveals a value equal to -30° throughout the areas undergoing plasticity. In other words, the stress state corresponds to triaxial compression and the strength in extension has no influence on the results.

For the AUS model on the other hand, the bearing capacity does depend on the s_{uc}/s_{ue} ratio as shown in Figure 51.3. As would be expected the bearing capacity increasing with increasing s_{ue}/s_{uc} . The fact that it does not equal the Tresca value for $s_{ue}/s_{uc} = 1$ is due to the effect of the flow rule (nonassociated von Mises for AUS and associated for Tresca).

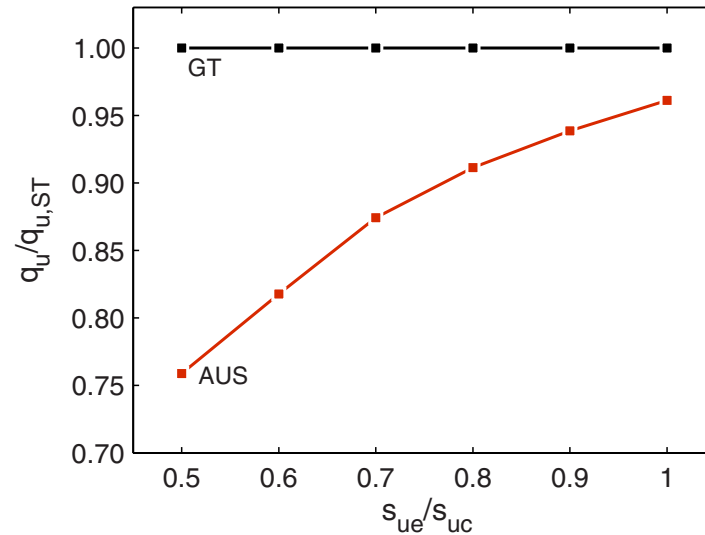


Figure 51.3: Bearing capacity of circular foundation for the Generalized Tresca and AUS model relative to the Standard Tresca Model (mean values between upper and lower bounds).

The failure mechanisms are in all cases similar to the familiar Prandtl mechanisms although some deviation is observed with the AUS model for low values of s_{ue}/s_{uc} (see Figure 51.4).

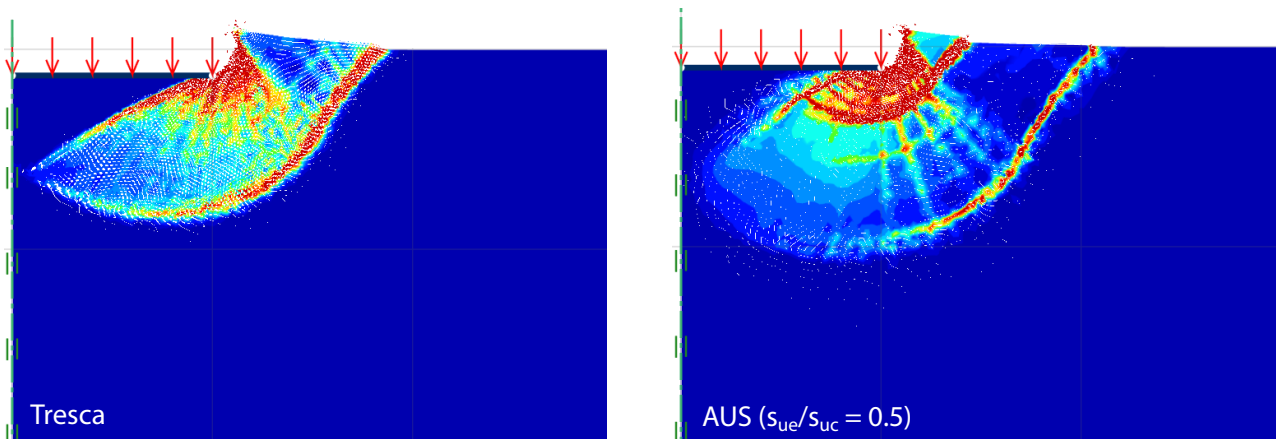


Figure 51.4: Failure mechanisms for the Tresca and AUS models.

51.2 Problem 2: Cylindrical excavation

The next problem concerns a cylindrical excavation as shown in Figure 51.5.

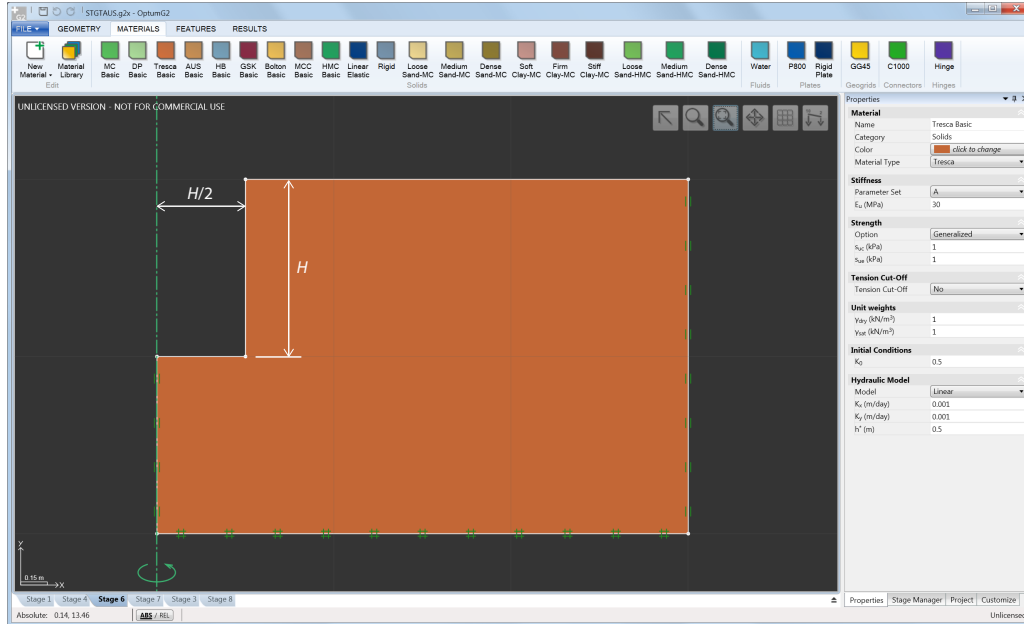


Figure 51.5: Cylindrical excavation.

Using 10,000 Upper/Lower elements with 3 adaptivity iterations, the Standard Tresca model predicts a non-dimensional stability number equal to:

$$N_{ST} = \frac{s_u}{\gamma H} = 5.99 \pm 0.02 \tag{51.2}$$

The predictions of the Generalized Tresca and AUS models are shown in Figure 51.6.

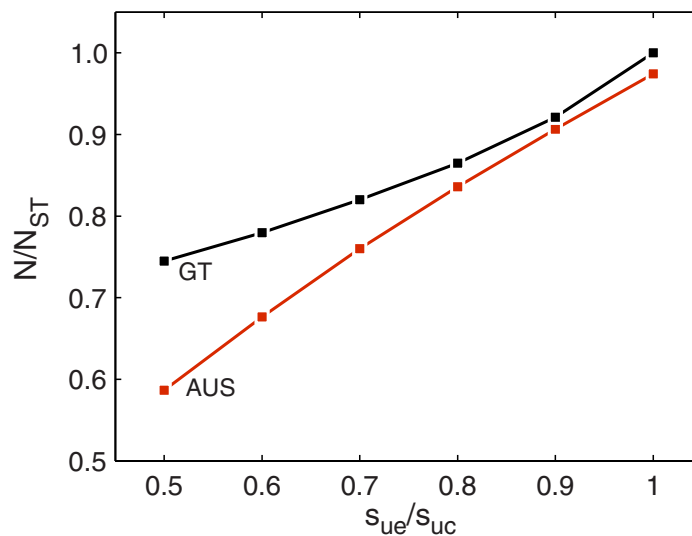


Figure 51.6: Stability number of cylindrical excavation for the Generalized Tresca and AUS models relative to the Standard Tresca Model (mean values between upper and lower bounds).

In contrast to the previous example, there is now a marked dependence of the stability number on the s_{ue}/s_{uc} ratio. A plot (Figure 51.7) of the Lode angle at failure reveals a Lode angle of around zero along the main slip line (corresponding, approximately, to simple shear) and an angle of close to 30° (corresponding to triaxial extension) in large regions within the failing mass. This distribution of Lode angle is consistent with the observed decrease in strength with decreasing s_{ue}/s_{uc} for both the Generalized Tresca and the AUS model.

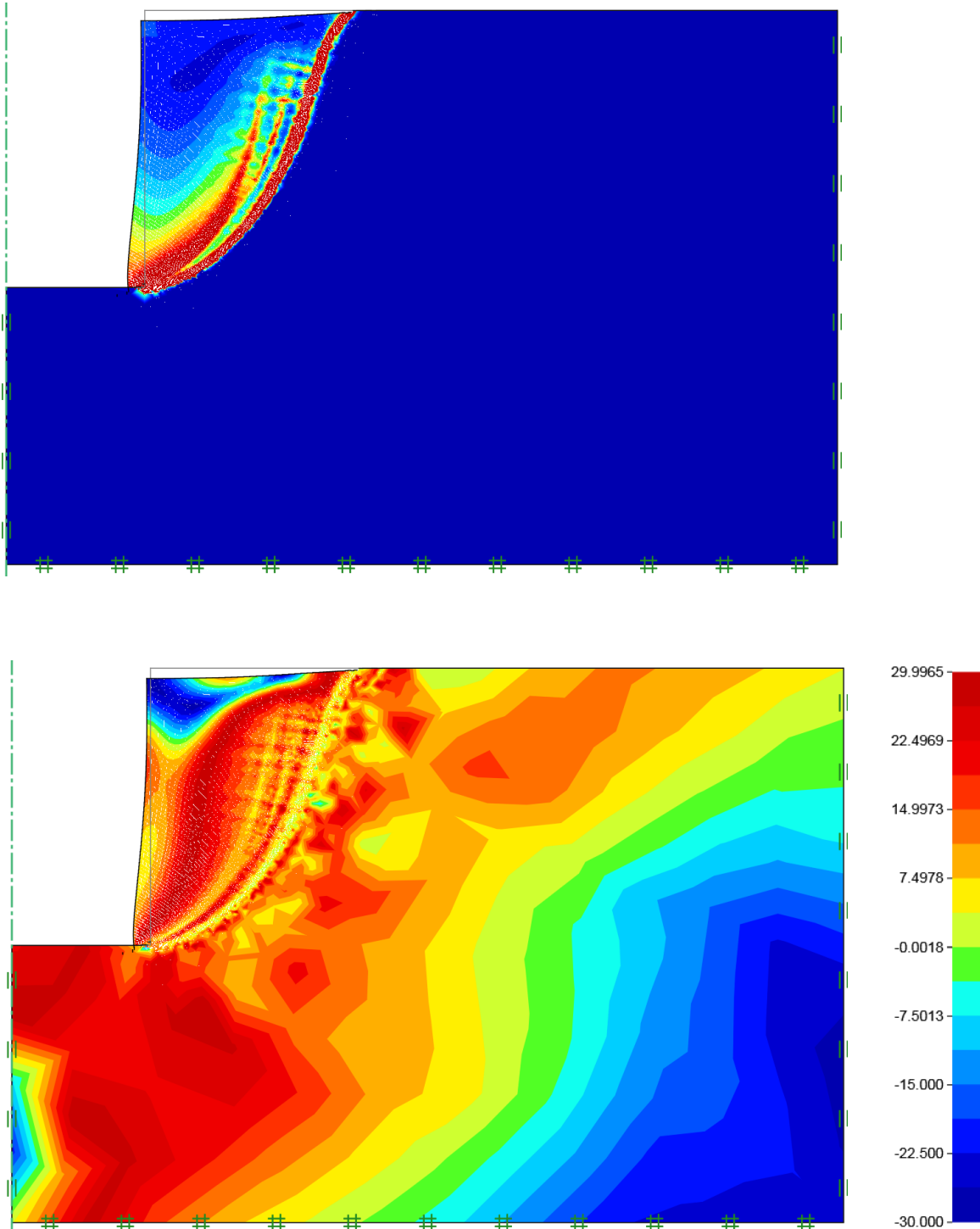


Figure 51.7: Failure mechanism and Lode angle distribution for AUS model with $s_{ue}/s_{uc} = 0.5$.

51.3 Problem 3: Deep anchor

The final problem concerns the pull-out capacity of a deep anchor as shown in Figure 51.8.

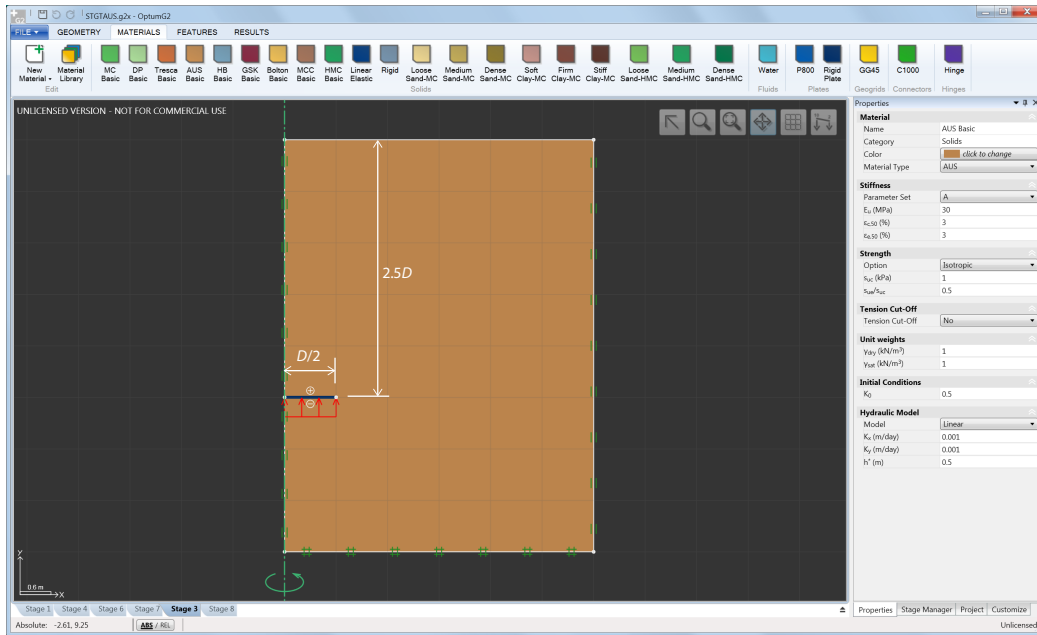


Figure 51.8: Deep anchor.

Assuming rough interfaces between the soil and the anchor plate, the pull-out capacity is computed as (10,000 Upper/Lower elements with 3 adaptivity steps):

$$\frac{q_{u,ST}}{s_u} = \frac{Q_{u,ST}}{\pi(D/2)^2 s_u} = 13.07 \pm 0.12 \quad (51.3)$$

The predictions of the Generalized Tresca and AUS models are shown in Figure 51.9.

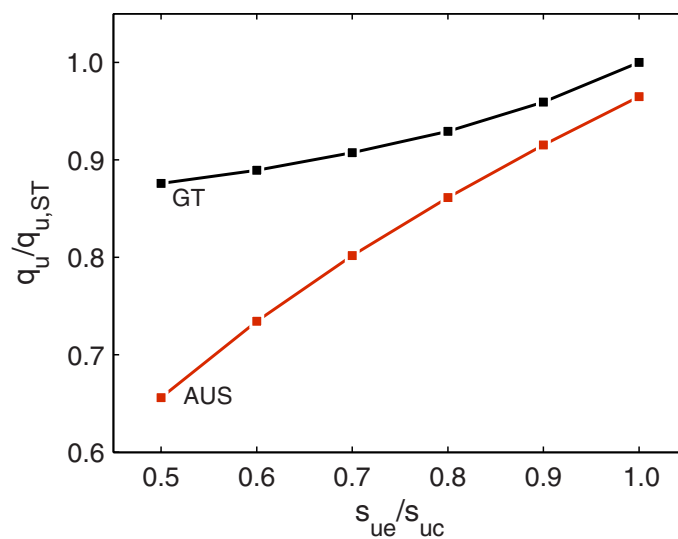


Figure 51.9: Pull-out capacity of deep anchor for the Generalized Tresca and AUS models relative to the Standard Tresca Model (mean values between upper and lower bounds).

The trend is here similar to the previous example with the pull-out capacity decreasing with decreasing s_{UE}/s_{UC} . A plot of the Lode angle (Figure 51.10) reveals that stress state below of the anchor plate anchor plate corresponds to approximately to triaxial extension ($\theta = +30^\circ$) while the stress above corresponds roughly to triaxial compression ($\theta = -30^\circ$). The result is a bearing capacity that depends on the s_{UE}/s_{UC} as shown in Figure 51.9.

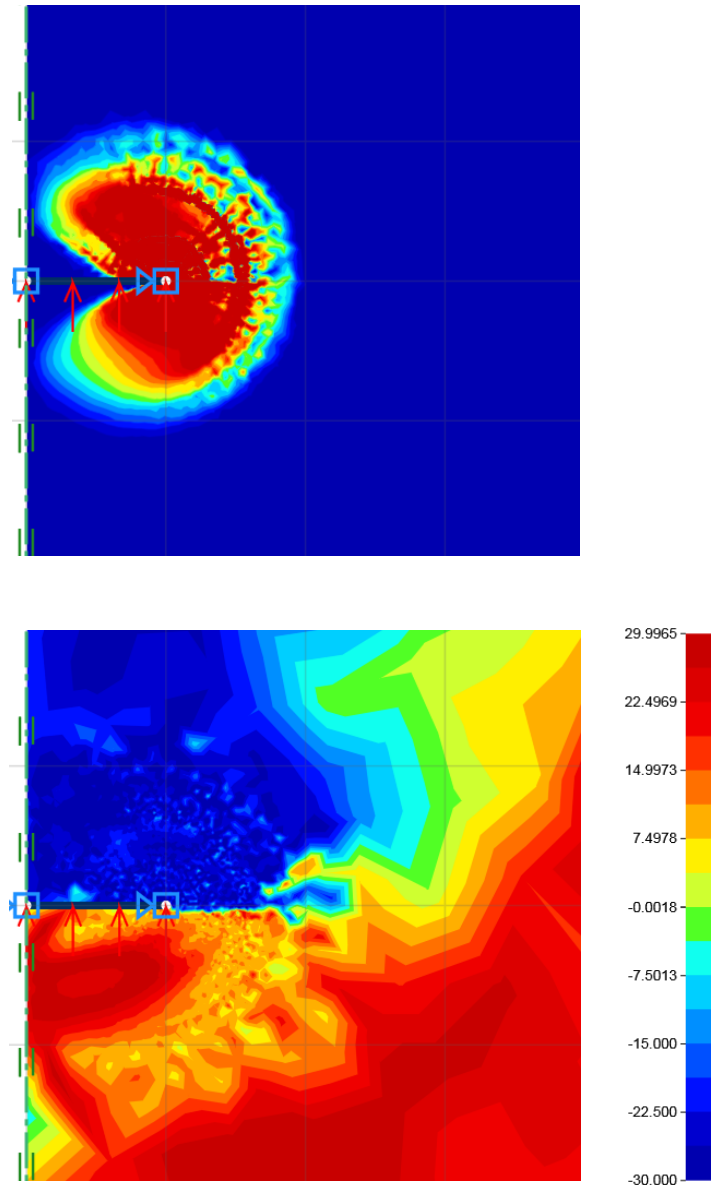


Figure 51.10: Plastic strain (top) and Lode angle (bottom) distributions.

52 AUS – CALIBRATION AND SIMULATION

The following example concerns the AUS model. A set of test data are first fitted and the model is then applied to the simulation of a circular skirted foundation.

The test data used in the example is adapted from Won (2013). It comprises triaxial compression and extension data. In OPTUM G2, these two tests are simulated using Multiplier Elastoplastic analysis under axisymmetric conditions as indicated in Figure 52.1. The Fixed loads here represent the initial axial and radials stresses while the axial Multiplier load is increased in the course of the analysis to reach the ultimate limit state.

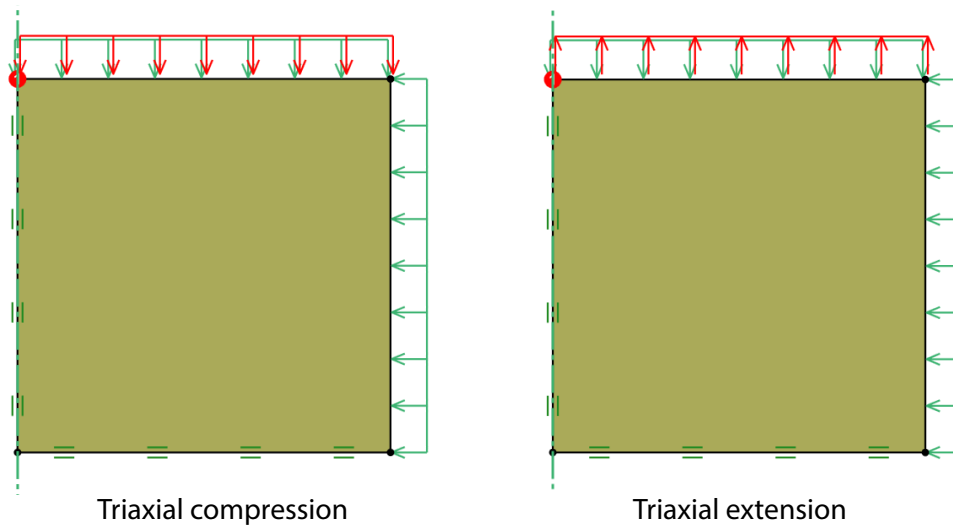


Figure 52.1: Setups for triaxial compression and extension tests.

By a process of trial and error, the fits shown in Figure 52.2 are obtained. For this data set where no information about the behaviour in simple shear is available and $s_{ue}/s_{uc} = 0.81$ is well within the

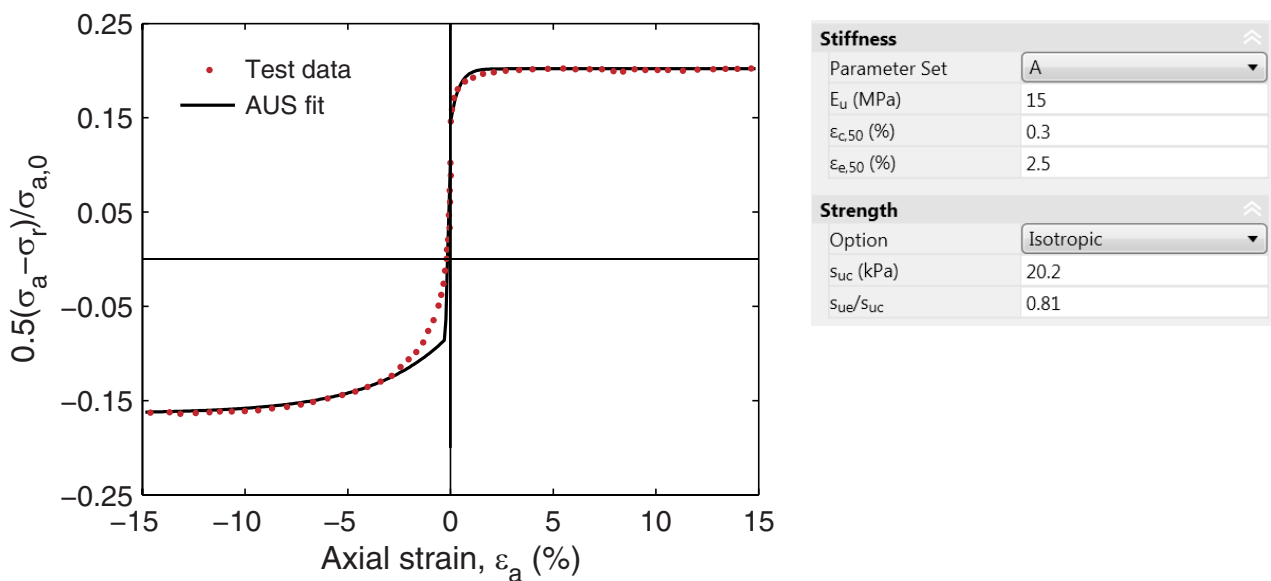


Figure 52.2: AUS fits to triaxial test data.

range that can be accommodated by the Isotropic strength option, there is little reason to assume any anisotropy. We note that the compression secant modulus in compression is only half the extension secant modulus. This is somewhat unusual, but in this case nevertheless what fits the data best.

Having calibrated the model, it is applied to the simulation of the circular skirted foundation shown in Figure 52.3. The compression shear strength is here taken to linearly from the top surface with a gradient of 3 kPa/m.

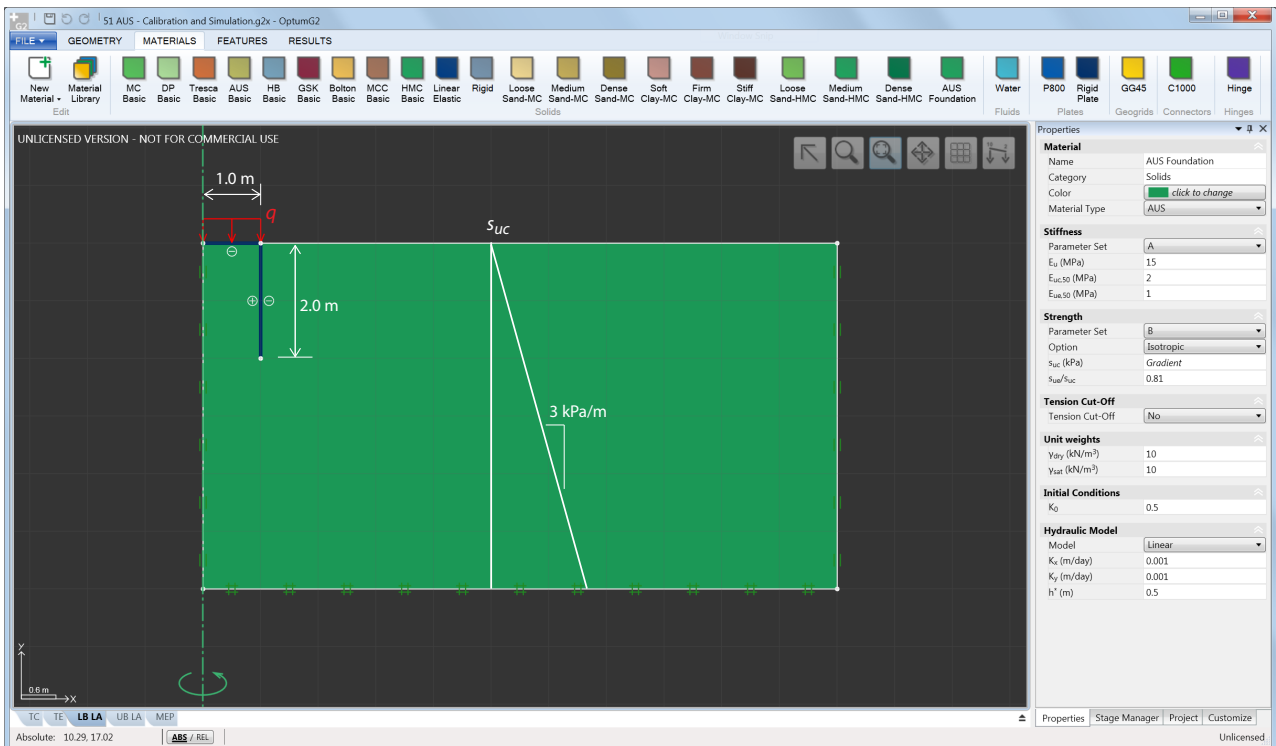


Figure 52.3: Circular skirted foundation on AUS material.

Upper and lower bound limit analysis are first conducted leading to an ultimate limit load of (1,000 elements, 3 adaptivity iterations):

$$q = 66.4 \text{ kN/m}^2 \pm 2.0\% \tag{52.1}$$

The collapse mechanism is shown in Figure 52.4.

In comparison, the Tresca model with an undrained shear equal to the compression strength of the AUS model gives a limit load of:

$$q = 72.7 \text{ kN/m}^2 \pm 2.2\% \tag{52.2}$$

In other words, the reduction in bearing capacity from accounting for an extension strength lower than that compression strength is in this case fairly limited. Furthermore, for the common Tresca approximation:

$$s_u = \frac{1}{3}(s_{uc} + s_{us} + s_{ue}) = \frac{1}{3}[s_{uc} + 2s_{uc}s_{ue}/(s_{uc} + s_{uc}) + s_{ue}], \tag{52.3}$$

the limit load is:

$$q = 65.6 \text{ kN/m}^2 \pm 2.2\% \tag{52.4}$$

in excellent agreement with the prediction of the AUS model.

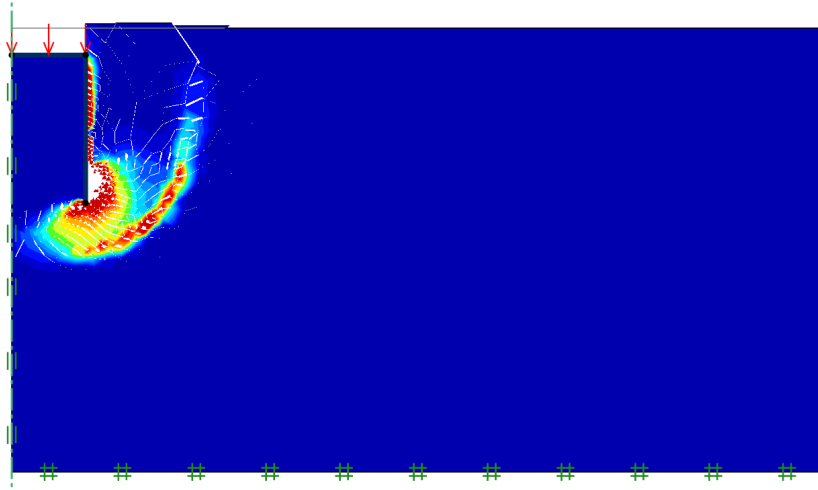


Figure 52.4: Collapse mechanism (Lower).

Finally, the foundation is loaded to failure via a Multiplier Elastoplastic analysis using 1,000 6-node Gauss elements and standard setting for mesh adaptivity. The load-displacement curve is shown in Figure 52.5. The slightly oscillatory behaviour close to failure is due to a combination of mesh adaptivity and nonassociativity.

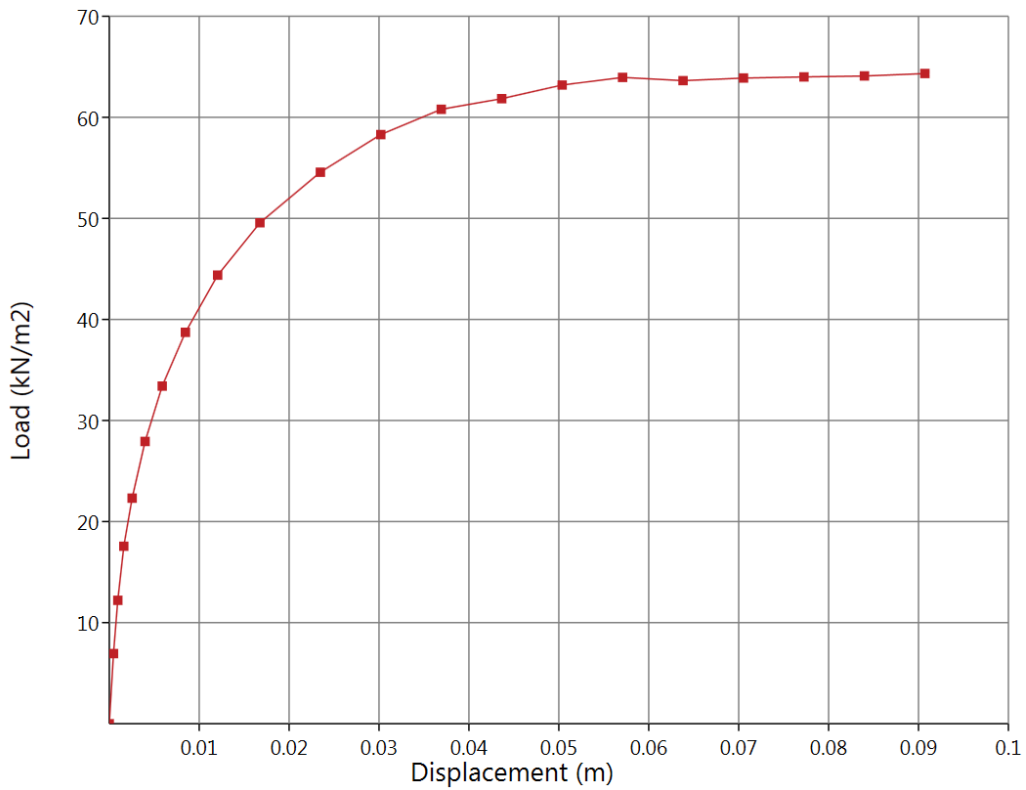


Figure 52.5: Load-displacement response.

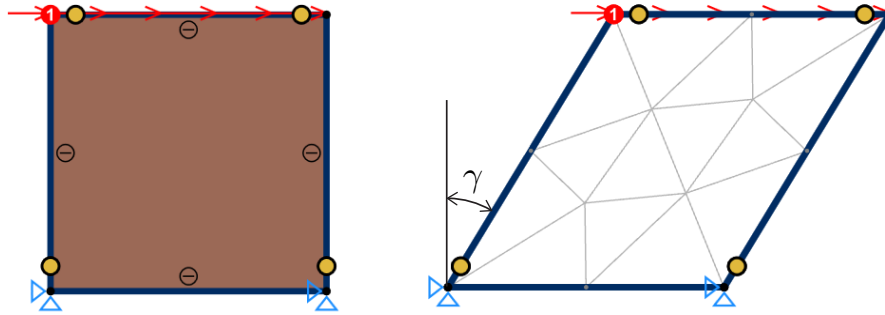


Figure 52.6: Setup of simple shear test using Rigid Plate and Hinges (left) and resulting deformation (right).

52.1 Simple shear elemental test

While the triaxial compression and extension elemental tests are straightforward to setup (see Figure 52.1), the simple shear test requires more care and consideration. One possibility is shown in Figure 52.6. Rigid Plates with appropriately placed Hinges are here used to set up a test that results in a state of simple shear.

The results of all three tests – triaxial compression/extension and simple shear – are shown in Figure 52.7 for an anisotropic AUS material with $s_{uc} = 30$ kPa, $s_{ue}/s_{uc} = 0.6$, $s_{ue}/s_{uc} = 0.8$. As expected, both the strength and the stiffness in simple shear fall in between those of triaxial compression and extension.

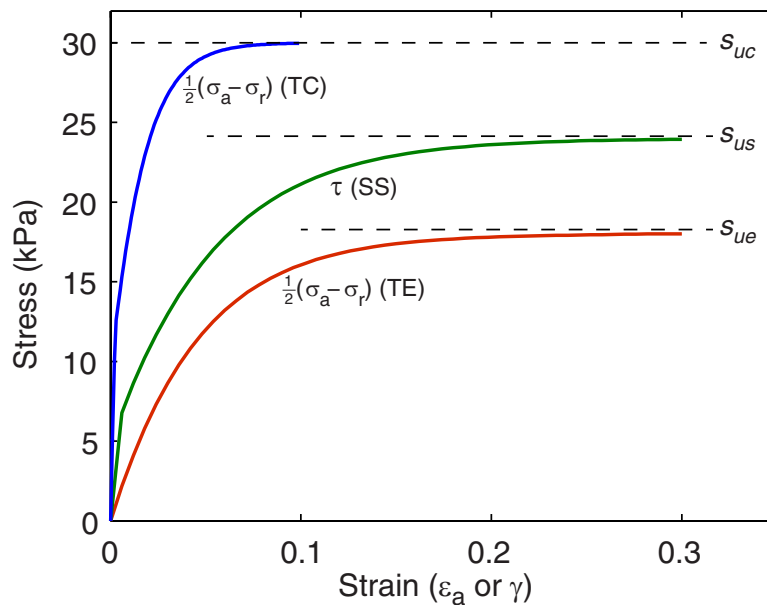


Figure 52.7: AUS elemental tests for triaxial compression (TC), triaxial extension (TE) and simple shear (SS).

53 FOUNDATION ON MARGINALLY STABLE SLOPE

The following example concerns the stability of a foundation on top of a slope as shown in Figure 53.1. The foundation is subjected to a load of 500 kN/m². The slope comprises sand with a constant-volume friction angle of 35°.

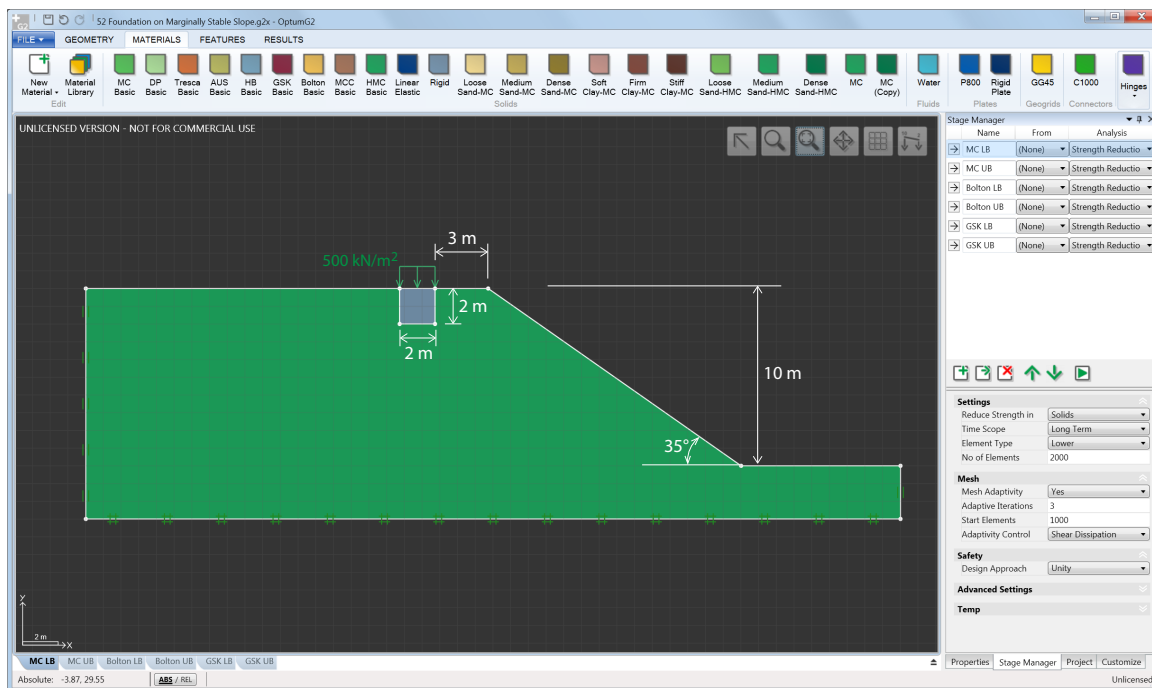


Figure 53.1: Foundation on top of marginally stable slope.

As the inclination of the slope equals the constant-volume friction angle, the use of this friction angle in the Mohr-Coulomb model will result in a factor of safety of at most 1, regardless of the load acting on the foundation and regardless of the distance of the foundation to the crest of the slope. This somewhat paradoxical situation could be remedied by basing the analysis on a more representative friction angle than the constant-volume angle. It is well known that the friction angle is quite pressure sensitive such that smaller pressures imply higher friction angles. At the face of the slope, therefore, it is entirely reasonable to assume a friction angle substantially higher than the constant-volume angle. In other parts of the problem, however, this angle may not be acceptable. Underneath the foundation, for example, the pressure is of order 0.5 MPa. At this level of pressure, the friction angle would have decreased significantly from the kind of values that can be attained at very low pressures.

The most rational approach is therefore to base the analysis on a model that explicitly takes the pressure dependence of the friction angle into account. OPTUM G2 offers two possibilities in this regard: the Bolton model and the GSK model, both of which are described in the Materials Manual.

The Bolton model makes use of a friction angle given by

$$\phi_B = \phi_{cv} + bI_R \tag{53.1}$$

where ϕ_{cv} is the constant-volume friction angle, b is a model parameter and I_R is the relative dilatancy. The latter quantity is defined by Bolton (1986) as:

$$I_R = I_D(Q - \ln p) - R \tag{53.2}$$

where I_D is the relative density, p is the mean stress, and Q and R and model parameters. As suggested by Bolton (1986) I_R is limited by:

$$0 \leq I_R \leq 4 \quad (53.3)$$

The friction angle therefore varies between:

$$\phi_{cv} \leq \phi_B \leq \phi_{cv} + 4m \quad (53.4)$$

The GSK model does not make reference to a pressure dependent friction angle in the same way as Bolton's model but instead three parameters, ϕ_1 , ϕ_2 and c as shown in Figure 53.2. It is seen that ϕ_1 and ϕ_2 correspond to Bolton's $\phi_{cv} + 4b$ and ϕ_{cv} respectively while c may be regarded as a fitting parameter.

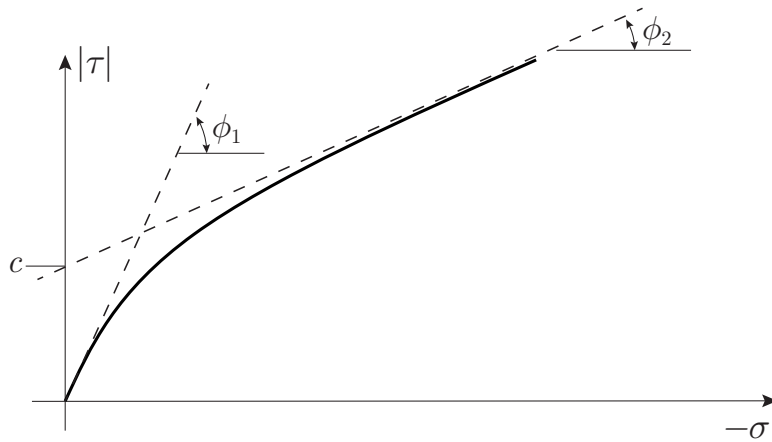


Figure 53.2: GSK failure envelope.

In the following, the sand is assumed to follow the behaviour measured by Ahmed (1972) for which the GSK model has been fitted with the following parameters (see the Materials Manual):

$$\phi_1 = 52^\circ, \quad \phi_2 = 35^\circ, \quad c = 25 \text{ kPa} \quad (53.5)$$

The Bolton parameters are:

$$\phi_{cv} = 35^\circ, \quad I_D = 0.72, \quad Q = 10, \quad R = 1, \quad b = 5 \quad (53.6)$$

Using Strength Reduction analysis with 2,000 Lower and Upper bound elements, the following factors of safety are computed:

Bolton	:	FS = 1.39 ± 0.04	
GSK	:	FS = 1.39 ± 0.03	
Mohr-Coulomb, $\phi = 35^\circ$:	FS = 1.00 ± 0.00	(53.7)
Mohr-Coulomb, $\phi = 52^\circ$:	FS = 1.83 ± 0.00	
Mohr-Coulomb, $\phi = 55^\circ$:	FS = 2.04 ± 0.00	

The results of the GSK and Bolton models are in excellent agreement and appear to be more reasonable than the results obtained with Mohr-Coulomb model which all predict a shallow failure at the slope face. In contrast, both the Bolton and GSK models predict the type of failures shown in Figure 53.3.

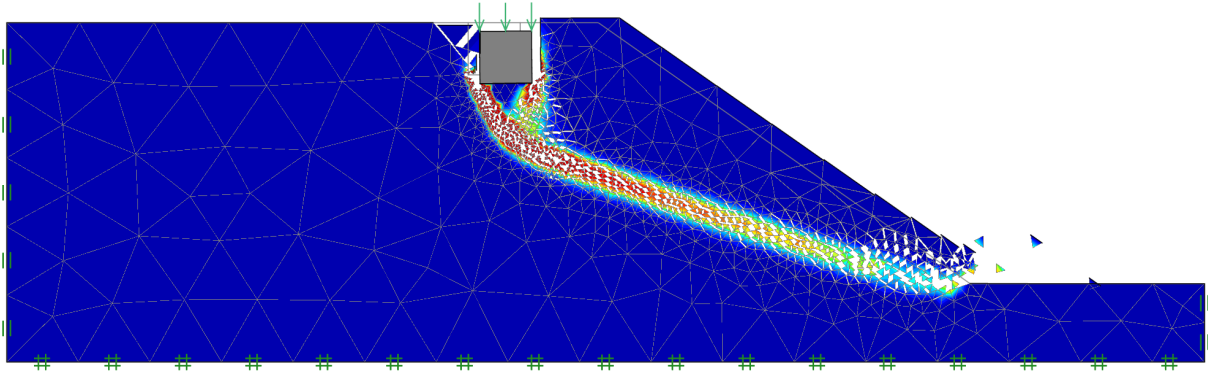


Figure 53.3: Failure mode for Bolton material. The failure mode for the GSK material is very similar.

54 DESIGN OF ANCHORED SHEET PILE WALL

The following example considers the design of an anchored sheet pile walls as shown in Figure 54.1. The wall supports an 8 m excavation in a medium dense sand with a characteristic friction angle of $\phi = 35^\circ$.

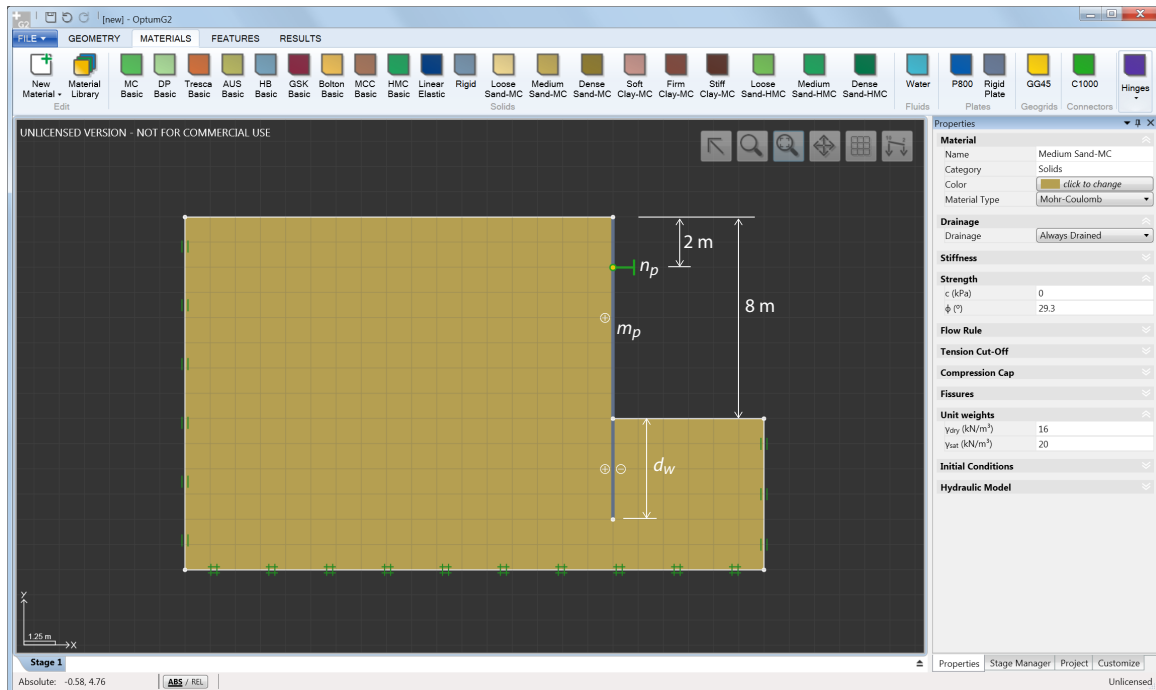


Figure 54.1: Anchored sheet pile wall.

The design parameters to be determined are:

- The embedment depth of the wall, d_w .
- The yield moment of the wall, m_p .
- The anchor strength, n_p .

In principle, the location and inclination of the anchor could also be considered design variables. However, in the following example, it will be assumed that the anchor is located 2 m below ground level as shown in Figure 54.1.

Most traditional design methods determine one unique set of these three parameters. In reality, however, there is an infinite number of combinations of d_w , m_p and n_p that lead to a safe design. For example, if the embedment depth is increased, the anchor strength can be decreased. Similarly, though less obvious, for a given depth, there is an infinite number of combinations of m_p and n_p that lead to a safe design. In other words, increasing the yield moment of the wall will lead to smaller required anchor strength and vice versa (within certain limits). The situation is sketched in Figure 54.2.

For a given embedment depth, say $d_{w,2}$ as shown in Figure 54.2, there is a unique n_p – m_p curve separating safe designs from unsafe ones. All points on or above this curve imply a safe design. Typically, the n_p – m_p curves are such that there is a lower limit on the yield moment. To this limiting

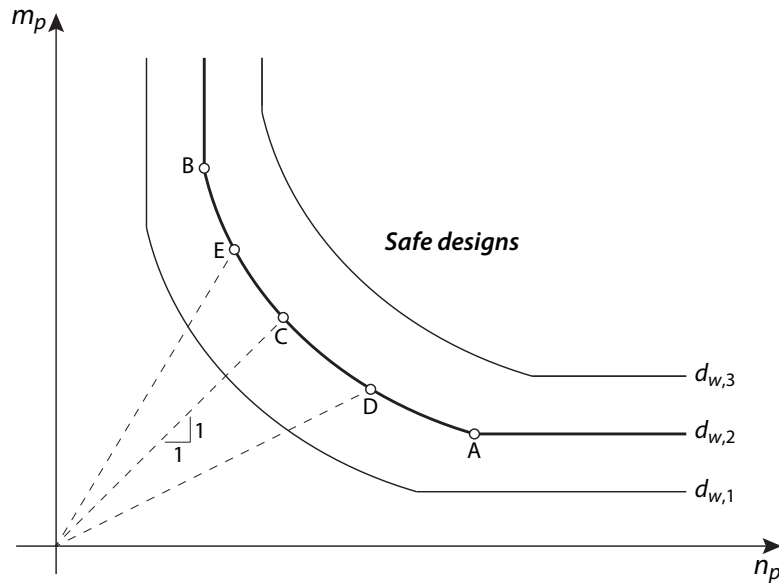


Figure 54.2: n_p – m_p curves for anchored sheet pile wall at different depths $d_{w,1}$, $d_{w,2}$ and $d_{w,3}$.

value corresponds an anchor force. This limit (n_p, m_p) combination corresponds to point A in Figure 54.2. Similarly, there is often a lower limit on the necessary anchor strength to which corresponds a particular yield moment (point B). These points, along with a selected number of intermediate points (C, D, E) defining the curve can be determined with OPTUM G2 as outlined in the following. The procedure involves four distinct steps:

1. Determine the minimum allowable embedment depth, d_w .
2. Determine the minimum wall yield moment (point A).
3. Determine the minimum anchor strength (point B).
4. Determine additional (n_p, m_p) corresponding to points C, D, E, etc as desired.

In the following where the friction angle is the only soil strength parameter, a partial factor of 1.25 is used such that the design friction angle is

$$\phi_d = \arctan[(\tan 35^\circ)/1.25] = 29.3^\circ \tag{54.1}$$

This friction angle is used in all calculations. Using Strength Reduction analysis with Reduce Strength in Solids, the aim is thus to obtain a strength reduction factor equal to 1. Conversely, when using the Reduce Strength in Structs option, the strength of the structural elements should be divided by the strength reduction factor to obtain an appropriate design.

Furthermore, to ensure safe designs, all calculations make use of Lower bound elements (2,000 elements and 3 adaptivity steps). Improvements on the results thus obtained can be achieved by increasing the number of elements and the proximity of the results to the exact solution can be gauged by using Upper bound elements.

Step 1: minimum embedment depth

To determine the minimum depth possible – disregarding any limitations the wall and anchor strength may impose – the wall is modeled as being rigid and the anchor is represented by a horizontal Plate BC. Successive Strength Reduction analyses are then performed until a strength reduction factor reasonably close to 1 is obtained. For the present example, a wall depth of $d_w = 1.5$ m gives a strength reduction factor of 1.00. The associated failure mechanism, which involves a rigid rotation of the wall about the anchor, is shown in Figure 54.3.

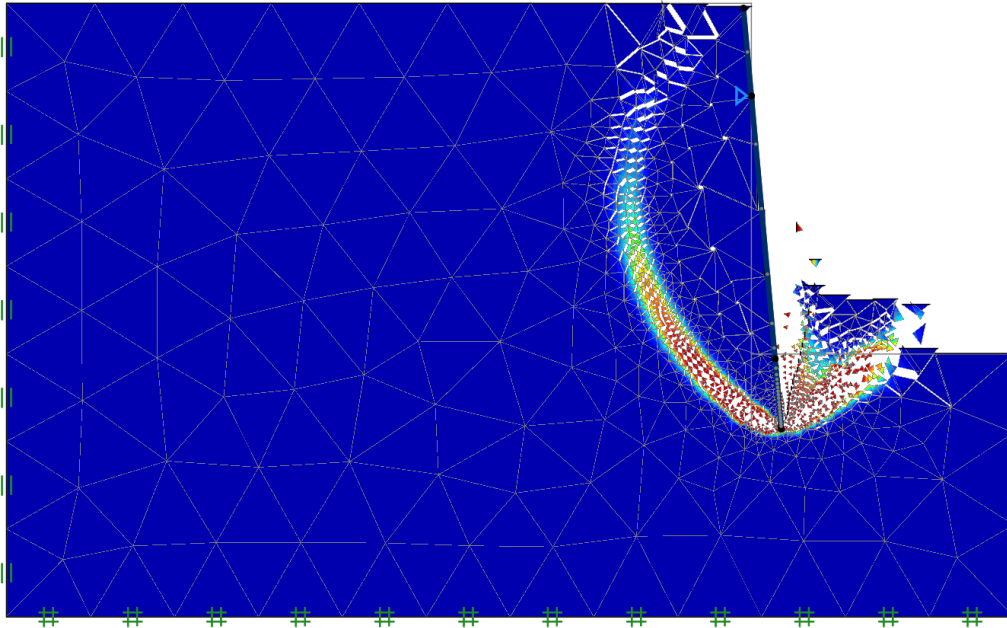


Figure 54.3: Failure mechanism for minimum wall depth calculation.

To give an indication of the necessary yield moment and anchor strength for this mode of failure, the maximum bending moment and the horizontal reaction at the Plate BC may be recorded. They are $m = 140$ kNm/m and $n = 226$ kN/m respectively. Yield moments and anchor strength equal to these values would give a safe, though most likely, not optimal design.

Step 2: minimum yield moment

Assuming a wall depth of $d_w = 2$ m (slightly larger than the minimum possible), the next task is to determine the minimum yield moment of the wall. This is done by assigning a regular Plate element to the wall while the anchor still is modeled using a Plate BC. A Strength Reduction analysis with Reduce Strength in Strucls is then carried out and the resulting maximum moment of the wall and the vertical reaction of the support are recorded. These are $m = 78$ kNm/m and $n = 183$ kN/m respectively. The failure mechanism is shown in Figure 54.4. It is seen that the mechanism involves a yield hinge in the wall.

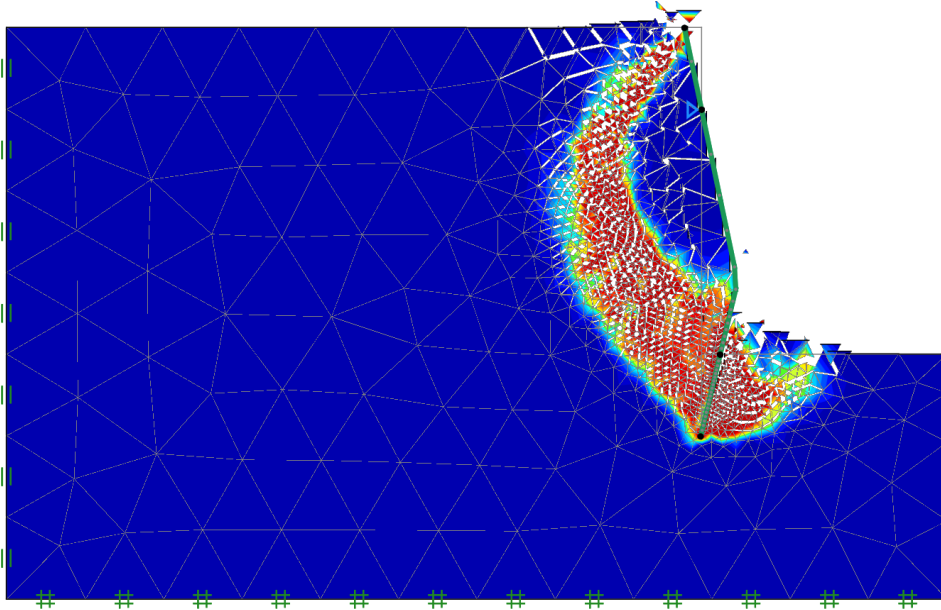


Figure 54.4: Failure mechanism for minimum yield moment calculation.

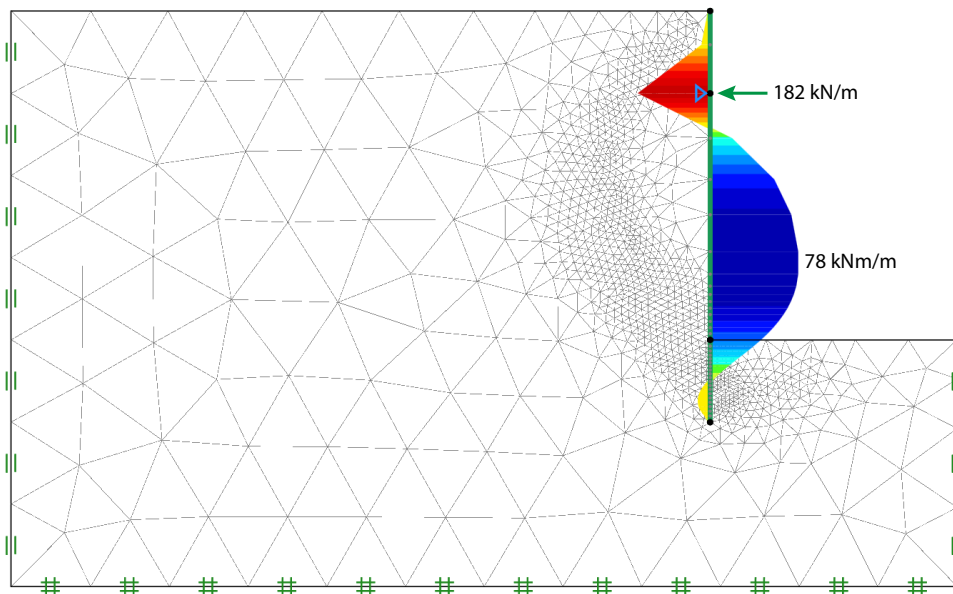


Figure 54.5: Bending moment and anchor force for minimum yield moment calculation.

Step 3: minimum anchor strength

Next, the minimum anchor strength is determined without considerations for limitations imposed by the wall strength. This is again done by a Strength Reduction analysis with Reduce Strength in Strucls, this time with a Fixed End Anchor of finite strength and a Rigid Plate for the wall. Again, the maximum moment and anchor forces are recorded. They are $m = 157 \text{ kNm/m}$ and $n = 80 \text{ kN/m}$ respectively.

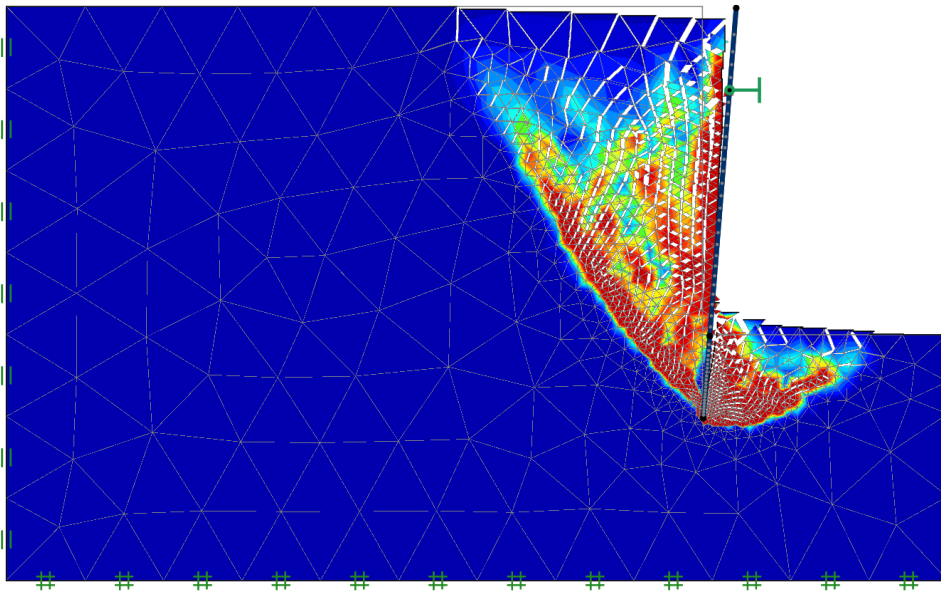


Figure 54.6: Failure mechanism for minimum anchor strength.

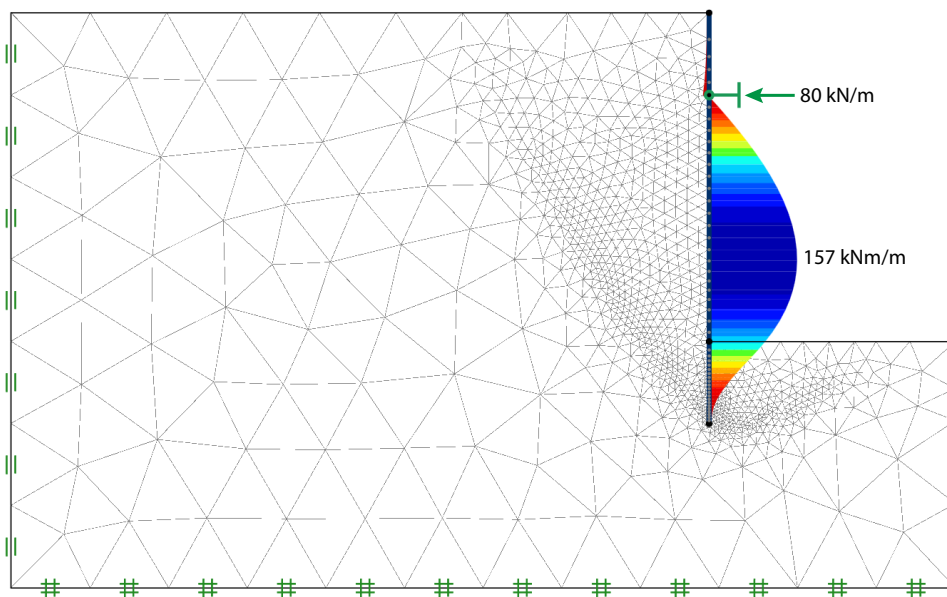


Figure 54.7: Bending moment and anchor force for minimum anchor strength calculation.

Step 4: combined yield moment and anchor strength

We now have two designs that each are “optimal” – one with a minimum yield moment and the other with a minimum anchor strength. Further designs, i.e. points on the n_p - m_p curve, can be obtained by using a wall and an anchor with a finite strength. For example, a Strength Reduction analysis assuming a wall yield moment of $m_p = 100$ kNm/m and a anchor strength of $n_p = 100$ kN/m will result in the point labeled C in Figure 54.2. That is, the yield moment and anchor strength are both factored and as they have identical values, the factored values will also be identical. Such a calculation leads to a yield moment of $m_p = 107$ kNm/m and an anchor strength of $n_p = 107$ kN/m. From Figure 54.8 we see that the associated failure mode involves simultaneous failure of the anchor and the wall.

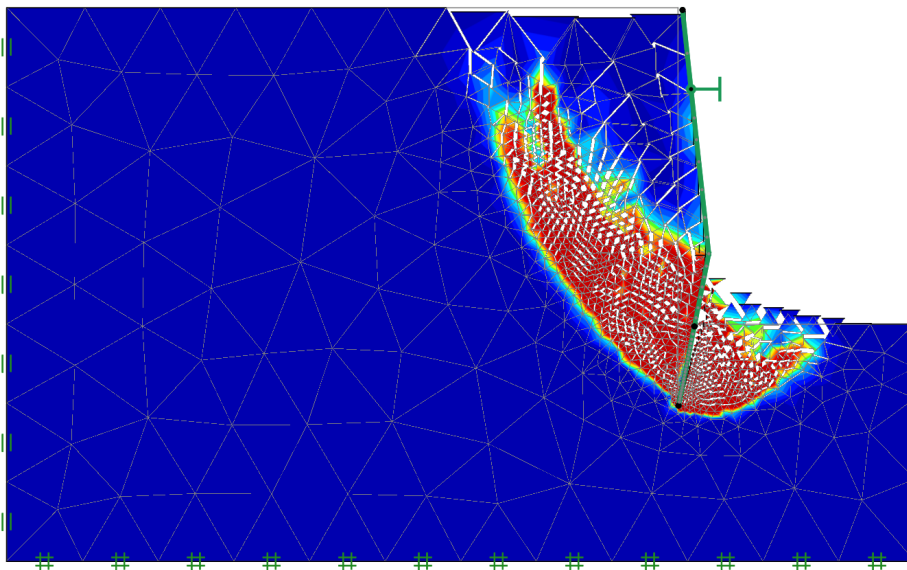


Figure 54.8: Failure mechanism for point C.

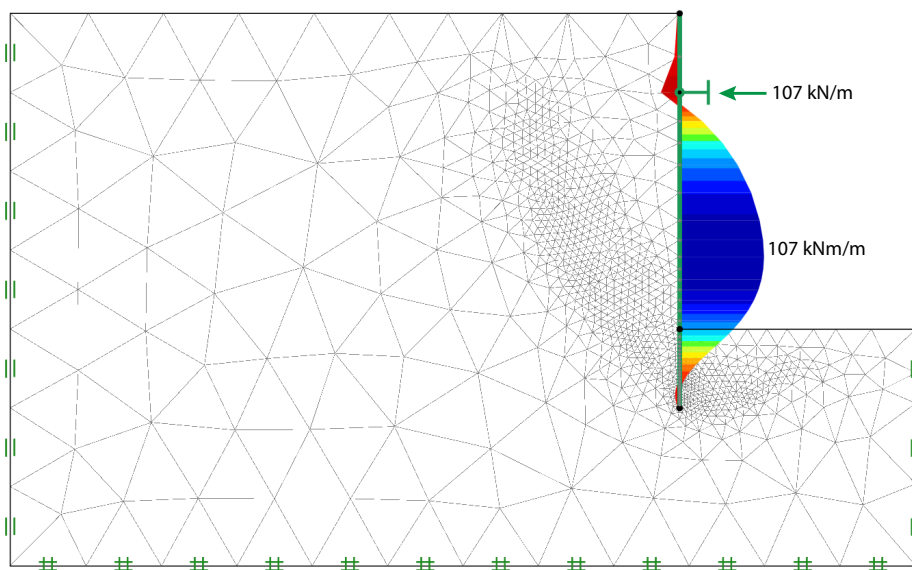


Figure 54.9: Bending moment and anchor force for point C.

Further points on the n_p-m_p , corresponding roughly to points D and E in Figure 54.2 can be obtained by using walls and anchors of different strength. For example, using $n_p = 100$ and $m_p = 65$ gives a point approximately midway between A and C, while $n_p = 100$ and $m_p = 140$ gives a point approximately midway between B and C.

The final n_p-m_p curve is shown in Figure 54.10. Also shown are upper bound results for all five points computed using 2,000 Upper elements with three adaptivity steps. We see that these are in reasonably good agreement with the lower bound results although some slight gains could be expected from increasing the number of elements in the lower bound analyses.

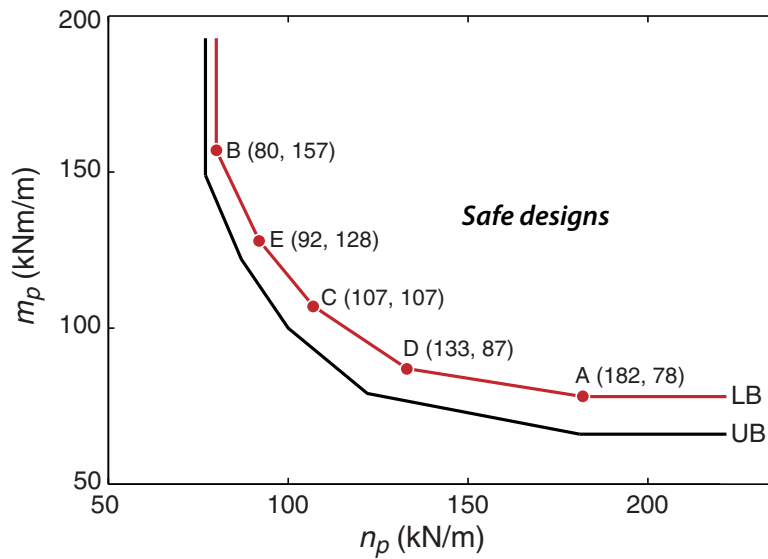


Figure 54.10: n_p-m_p curve for anchored sheet pile wall with $d_w = 2$ m.

Regarding the kinematics of each possible design, the n_p-m_p curve may be regarded as a yield surface with the relative amounts of wall bending and anchor point displacements at failure following

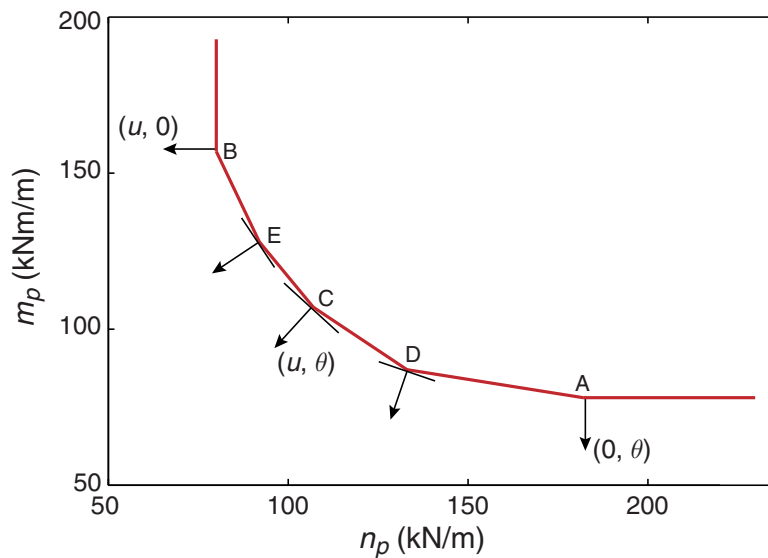


Figure 54.11: n_p-m_p curve and associated flow rule.

the associated flow rule. This is illustrated in Figure 54.11 where each vector normal to the n_p - m_p curve represents the relative magnitude of the anchor point displacement, u , and yield hinge rotation, θ , at failure. Thus, at point A, the u component is zero and the failure mode involves only wall bending while the anchor point remains fixed (see Figure 54.4). Similarly, for point B, $\theta = 0$ and the failure is by way of anchor point displacement without any deformation of the wall (see Figure 54.6). For point C, both u and θ are non-zero corresponding to the failure mechanism shown in Figure 54.8. Finally, the failure mechanisms corresponding to points D and E are shown in the Figures below. As expected, the failure mode at point D is dominated by wall bending while the one at point E involves a greater amount of anchor point displacement.

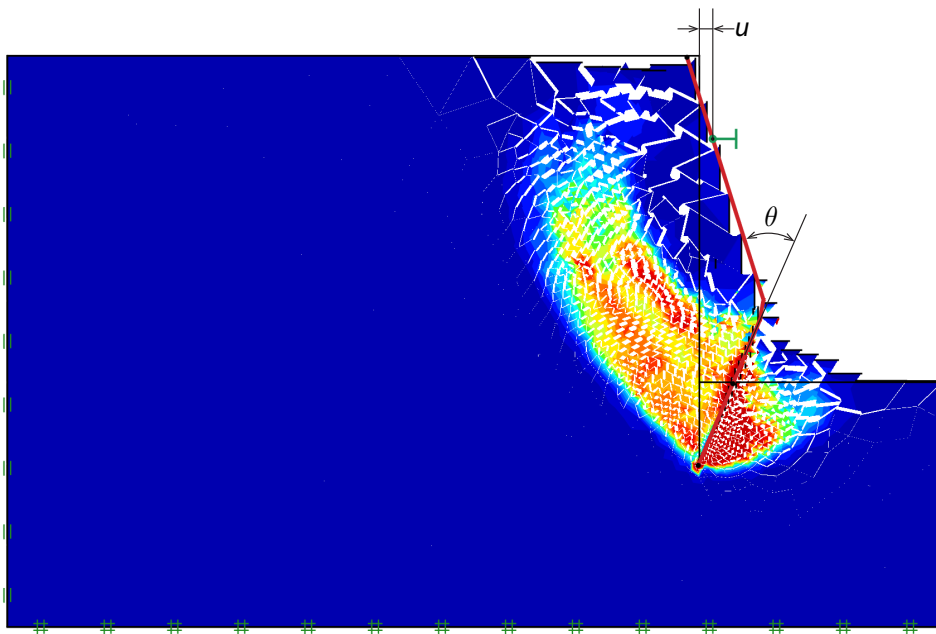


Figure 54.12: Failure mechanism for point D.

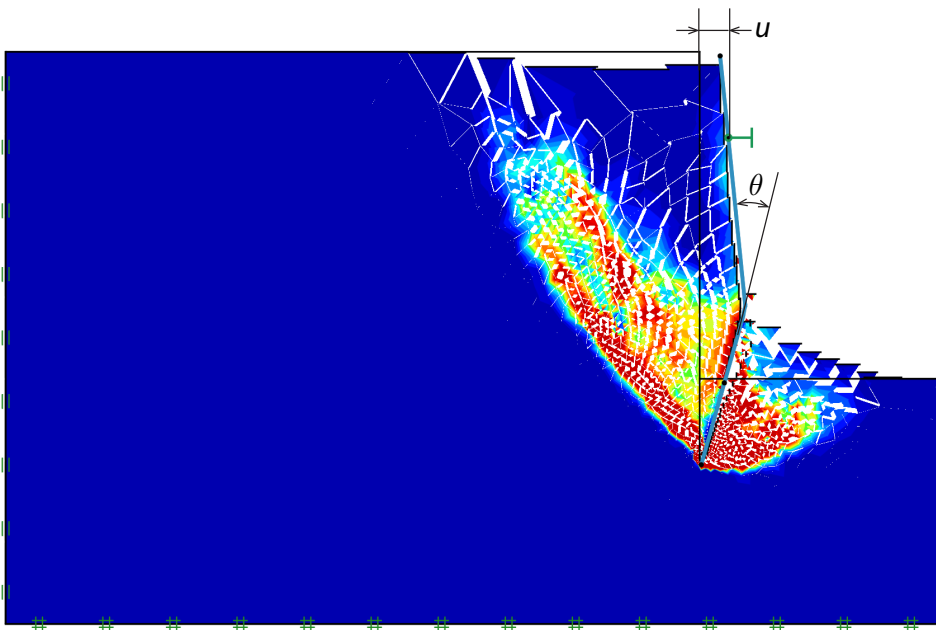


Figure 54.13: Failure mechanism for point E.

54.1 Serviceability limit state

Finally, it should be verified that the selected design satisfies the serviceability requirements. In the following, all five designs, A–E, are considered in this regard. The characteristic friction angle, $\phi = 35^\circ$, is now used. Furthermore, the flow rule is assumed nonassociated with a dilation angle of $\psi = 5^\circ$. For each design, the anchor stiffness and wall bending stiffness are taken as

$$EA = 500 \times n_p \text{ [kN/m]}$$

$$EI = 100 \times m_p \text{ [kNm}^2\text{/m]}$$
(54.2)

The simulations proceed by way of an initial stress stage and four excavation stages each removing 2 m of soil in front of the wall (see Figure 54.14). The anchor is inserted at the beginning of the third excavation stage, i.e. at the excavation depth of 4 m.

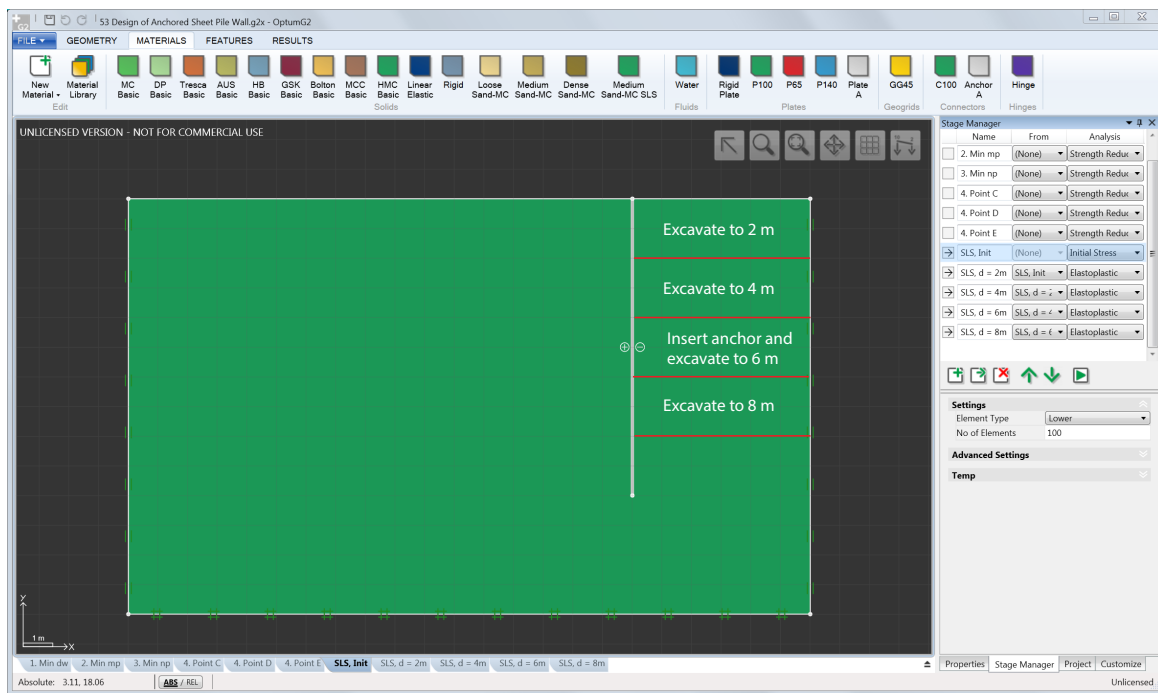


Figure 54.14: Excavation stages for SLS analysis.

Selected results of the analyses are shown in Table 54.1. The displacements, u_x , refer to the wall displacements. It should be noted that the maximum displacements and wall bending moments

Design	n_p (kN/m)	m_p (kNm/m)	n_{max}/n_p	m_{max}/m_p	$u_{x,max}$ (cm)	n_{final}/n_p	m_{final}/m_p	$u_{x,final}$ (cm)
A	182	78	0.59	0.69	7.8	0.59	0.52	5.3
B	80	157	1.00	0.36	4.8	1.00	0.36	4.8
C	107	107	0.97	0.50	5.8	0.97	0.36	3.8
D	133	87	0.78	0.62	7.0	0.78	0.46	4.7
E	92	128	1.00	0.42	5.1	1.00	0.34	4.3

Table 54.1: Selected results for SLS analysis of sheet pile designs.

are not necessarily encountered at the final state but rather at the last stage before the anchor is inserted. Concerning the wall bending moments, we see that these in all cases are well below the plastic moments. The anchors forces, on the other hand, are for Designs B and E at yield and for Design C very close to yield. While this in principle is quite legitimate (and actually leads to smaller overall wall displacements than for Designs A and D), relying on yielding in the anchor does require that the anchor has the necessary ductility to sustain the accompanying plastic strains.

The evolution of deformations for Design A are shown in the figure below.

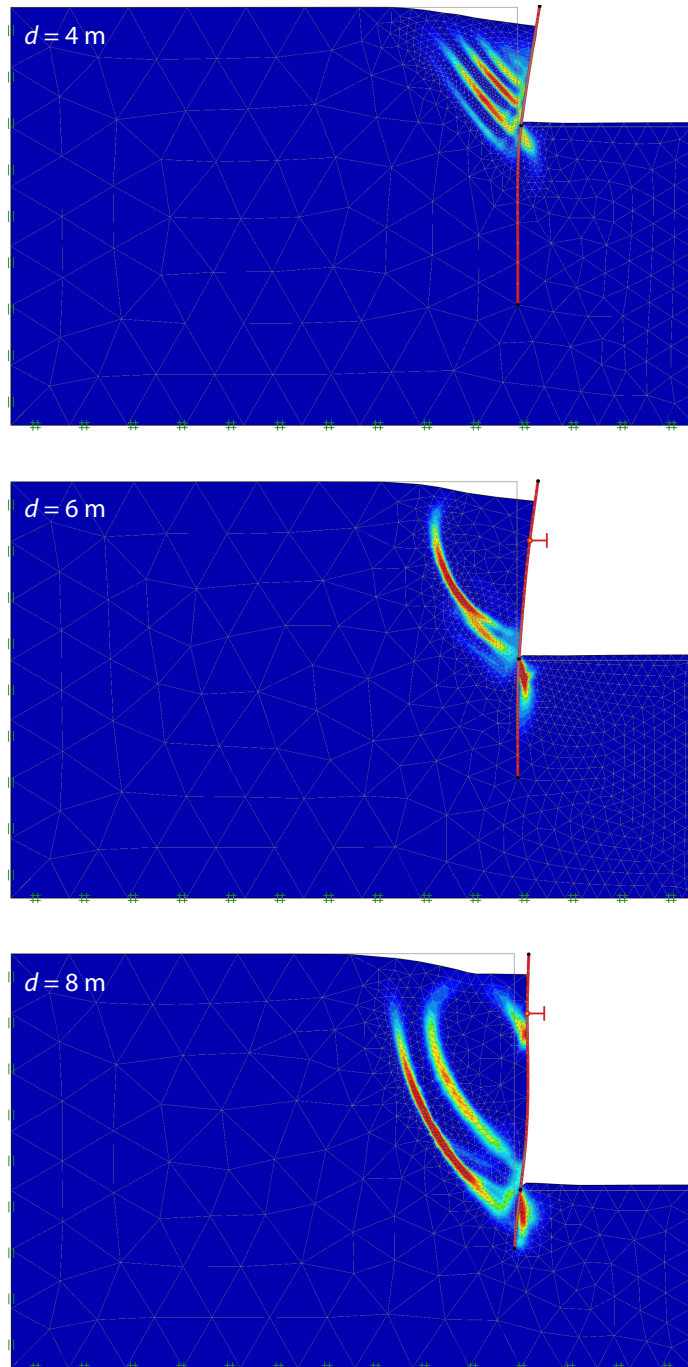


Figure 54.15: Evolution of deformations for Design A (scaled by a factor of 10).

55 PULL-OUT CAPACITY OF HELICAL ANCHOR IN CLAY

This example considers the pull-out of a helical anchor as shown in Figure 55.1. The anchor is modeled using Plate elements in axisymmetry as shown in the figure. The anchor is embedded a distance H from the upper anchor plate and the spacing between the plates is given by S . All anchor plates have diameter D . All soil-plate interfaces are assumed to be ‘smooth’ but able to sustain tension. This is achieved by setting the interface Reduction Factor to zero (see below). A range of alternative interface conditions are discussed in detail in Example 27.

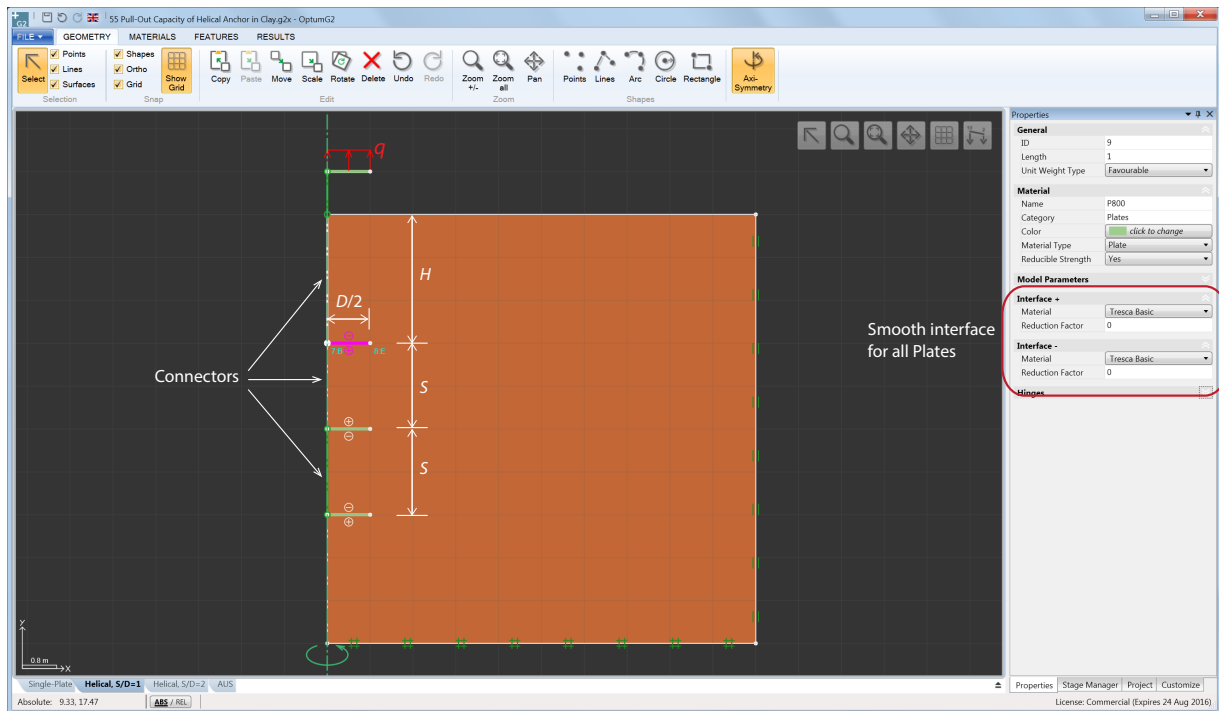


Figure 55.1: Helical anchor.

The soil is of the Tresca type with a constant shear strength, s_u . Assuming that both the soil and the anchor are weightless, the pull-out capacity may be expressed as:

$$\frac{Q}{\pi(D/2)^2} = s_u N_c \quad (55.1)$$

where Q is the total pull-out force and N_c is the pull-out capacity factor. This example deals with the determination of N_c .

55.1 Single-plate anchor

An anchor with a single plate embedded at a distance H from the ground surface is first considered. For such an anchor, N_c increases with depth until a certain depth where the failure mechanism becomes independent of the depth. At this point and for all greater embedment depths, N_c is given by (Martin and Randolph 2001):

$$N_c = 3 + 3\pi \simeq 12.42 \quad (55.2)$$

The computed variation of N_c with normalized depth H/D is shown in Figure 55.2. These results are based on upper and lower bound limit analyses using 10,000 elements and 3 adaptivity steps. It

is seen that the solution for a sufficiently high value of H/D is in excellent agreement with the exact solution of Martin and Randolph (2001).

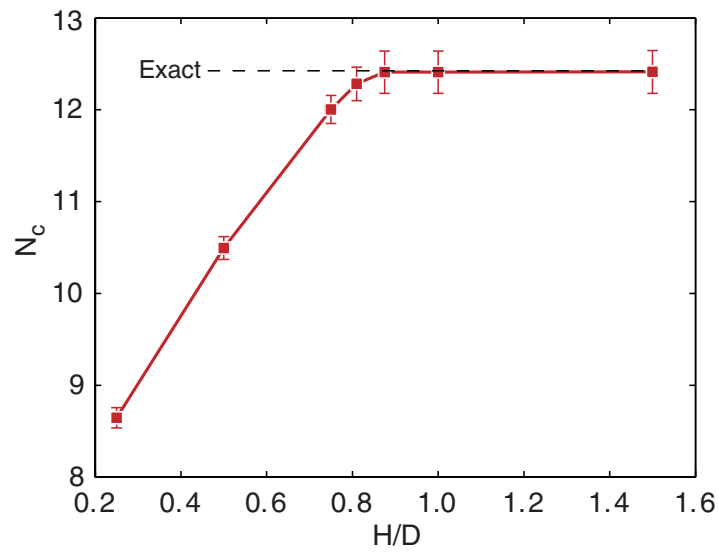


Figure 55.2: Variation of pull-out capacity factor with depth (mean values between upper and lower bounds with error bars indicating worst case error).

The transition from a global to a local failure mechanism is illustrated in the figure below.

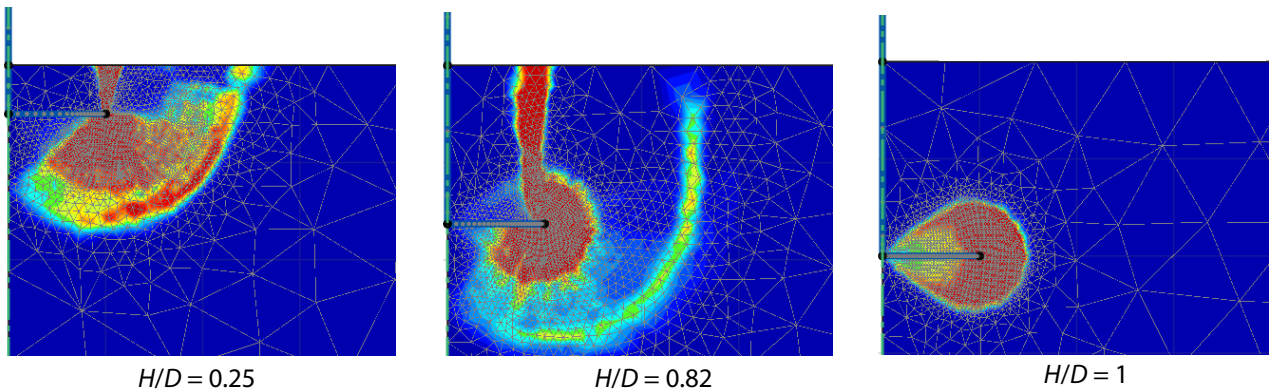


Figure 55.3: Transition from global (shallow) to local (deep) failure mechanism.

55.2 Multi-plate anchor

Next, the case of an anchor with three plates as shown in Figure 55.1 is considered. The behaviour in terms of embedment depth is here qualitatively the same as for a single-plate anchor: for small embedment depths the failure mechanism will be of the global type that reaches the ground surface and for sufficiently large embedment depths the mechanism will be local with a corresponding stationary value of N_c .

Moreover, the spacing between the plates influences both the shallow and the deep behaviour. For sufficiently small values of S/D , there will be a significant interaction between the plates while for

larger S/D , the plates will essentially behave independently. For the stationary value of N_c attained at large H/D , Merifield (2010) has proposed the following expression:

$$N_c = \begin{cases} 3 + 3\pi + (n - 1) \frac{5\pi S}{2D} & \text{for } S/D \leq \left(\frac{S}{D}\right)_{cr} \\ n(3 + 3\pi) & \text{for } S/D > \left(\frac{S}{D}\right)_{cr} \end{cases} \quad (55.3)$$

where n is the number of anchor plates ($n = 3$ in the present example). The critical value of the spacing ratio S/D signifies a switch between the range where the anchor behaves as an ‘effective’ single-plate anchor and that where the anchor plates act independently corresponding to n single-plate anchors. The critical spacing ratio is given by

$$\left(\frac{S}{D}\right)_{cr} = \frac{6 + 6\pi}{5\pi} \simeq 1.58 \quad (55.4)$$

Figure 55.4 shows the pull-out capacity of two helical anchors with $S/D = 1$ and $S/D = 2$. Merifield’s expressions for N_c at large H/D are in good agreement with the computed results in both cases.

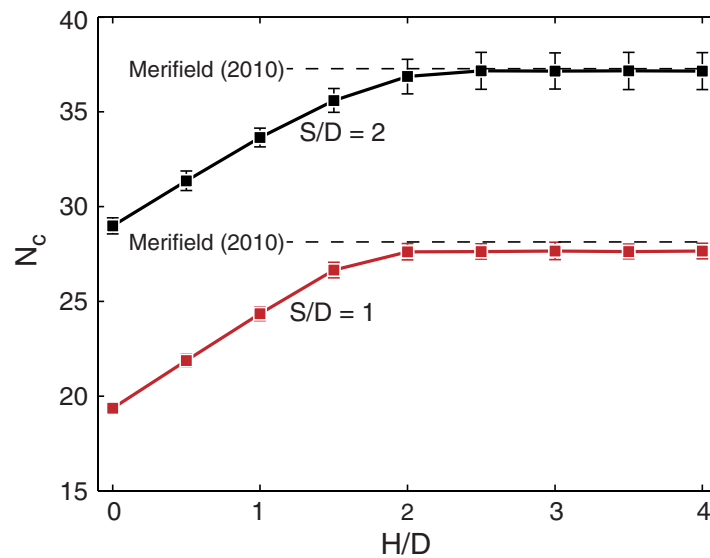


Figure 55.4: Pull-out capacity as function of embedment for helical anchors.

The failure mechanisms for $H/D = 4$ are shown in Figure 55.5. For $S/D = 1$ (below the critical ratio), the anchor behaves as a single effective anchor while $S/D = 2$ (above the critical ratio) implies a situation where the three plates act as three individual single-plate anchors in which cases the pull-out capacity is three times that of a single-plate anchor.

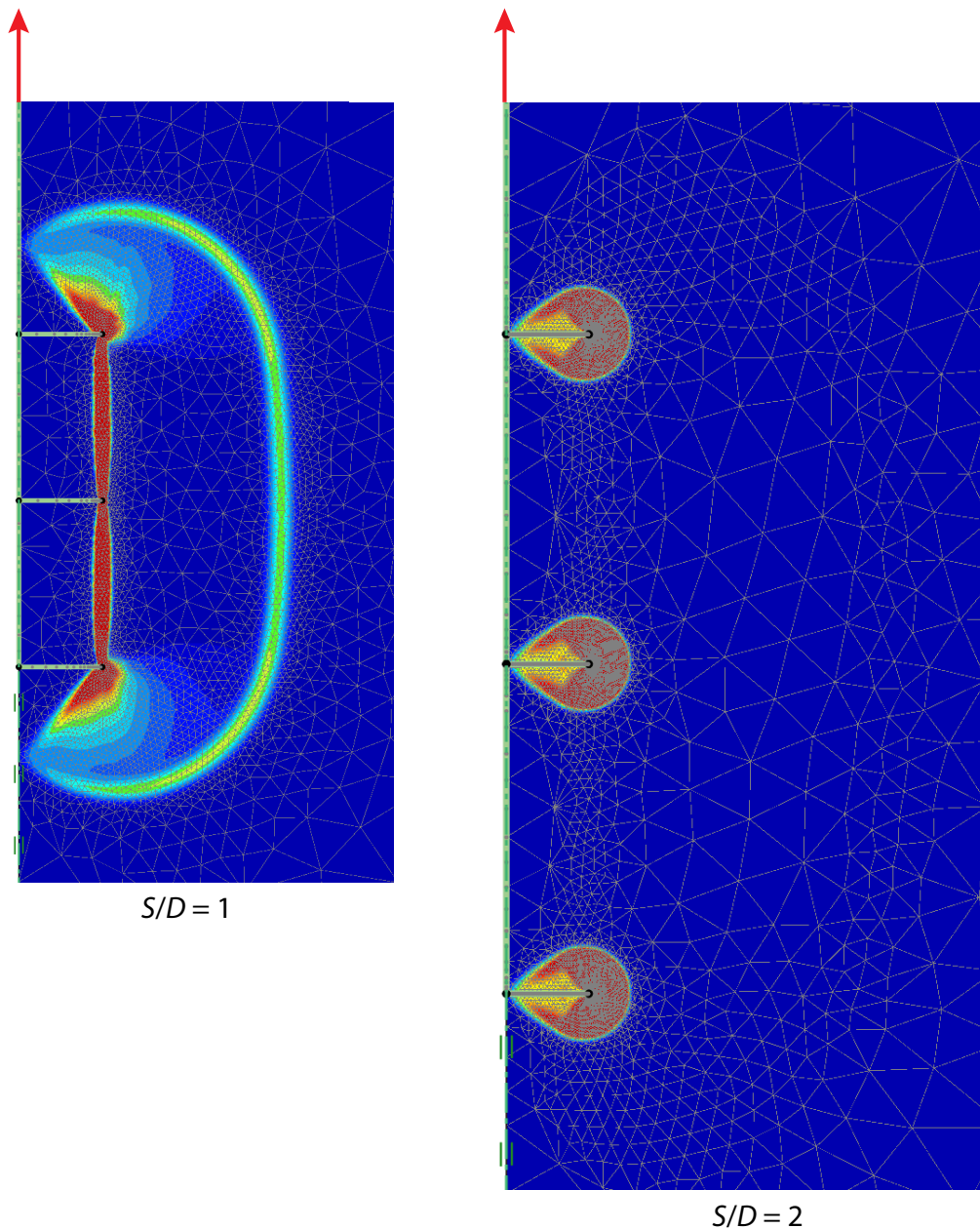


Figure 55.5: Deep failure mechanisms for helical anchors with $S/D = 1$ and $S/D = 2$.

55.3 AUS analysis

In the present example, the anchor plates are assumed smooth in the sense that there is no transfer of shear between the plates and the soil. However, normal stresses, including tensile stresses, can still be transferred. This means that the soil at the top of the plates will be in compression while the bottom will be in extension (see Figure 55.6). This in turn means that any differences between the undrained shear strength in compression and extension may have a relatively marked effect on the pull-out capacity. As discussed in the Materials Manual, differences between the two shear strengths is the norm rather than the exception and it is therefore of interest to examine this effect on overall pull-out capacity of the anchors.

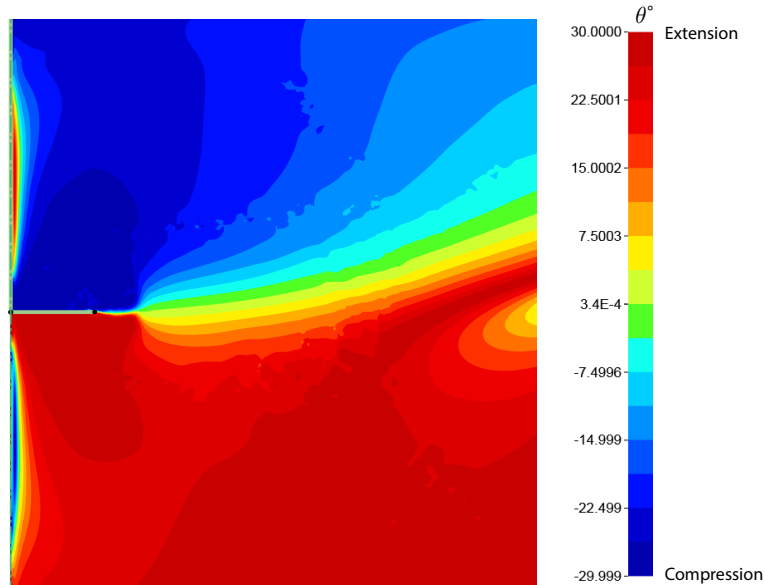


Figure 55.6: Variation of Lode angle θ in the vicinity anchor plate (single-plate anchor). $\theta = -30^\circ$ corresponds to compression and $\theta = +30^\circ$ to extension.

The relevant analysis may be carried out using the AUS model which takes the undrained shear strengths in compression and extension as input (and, optionally, also the strength in direct simple shear). In the following, the isotropic version of the model is used to analyze the single-plate anchor for a value of H/D corresponding to deep failure. This version of the model operates with the strengths in compression and extension, s_{uc} and s_{ue} respectively. The pull-out capacity factor N_c as function of s_{ue}/s_{uc} is shown in Figure 55.7. It is seen that the s_{ue}/s_{uc} ratio has a rather significant effect with N_c increasing some 50% between $s_{ue}/s_{uc} = 0.5$ and $s_{ue}/s_{uc} = 1$.

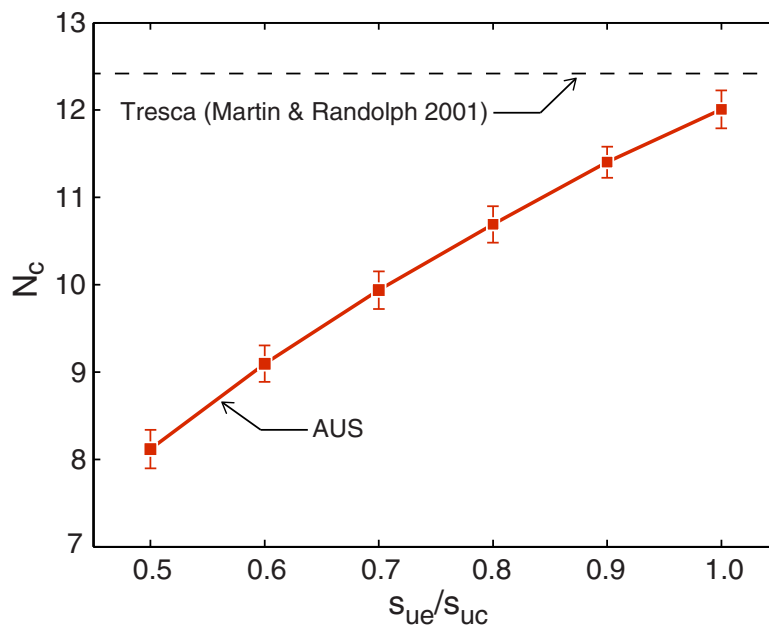


Figure 55.7: Pull-out capacity factor N_c corresponding to deep failure as function of undrained shear strength ratio s_{ue}/s_{uc} .

It is also noted that the solution for $s_{ue}/s_{uc} = 1$ is slightly below that of Martin and Randolph (2001). This is due to the effect of nonassociativity: while the AUS failure surface does reduce to the Tresca surface for $s_{ue}/s_{uc} = 1$, the flow rule is that of von Mises. Hence, a slight decrease in N_c results, from about 12.4 in the case where Tresca is used as failure surface and flow rule to about 12.0 for the AUS model.

56 PULL-OUT CAPACITY OF ANNULAR ANCHOR IN SAND

The following example is inspired by the work of Dyson and Rognon (2014) who fabricated and tested plate anchors with a fractal geometry similar to that of tree roots. Some examples of anchor plates considered by Dyson and Rognon are shown in Figure 56.1. Remarkably, the pull-out capacity is influenced only relatively little by the area of the plate. That is, the plate on the right in Figure 56.1 has a pull-out capacity comparable to the standard circular plate shown on the left.



Figure 56.1: Standard circular and fractal anchor plates (after Dyson and Rognon 2014).

In the following, the pull-out capacity of an anchor in the form of an annular ring as shown in Figure 56.2 is examined. In practice, it is clear that a system is required to transfer the force from the center to the annular ring (for example in for the form of the spokes indicated in Figure 56.2). In the following, this system is ignored and only the annular ring is considered in an axisymmetry model as shown below. Note that a Connector is used to apply force to the anchor. While this arrangement is not strictly necessary in this case (a force could have been applied directly to the anchor) it may be used for anchors comprising multiple concentric annular rings.

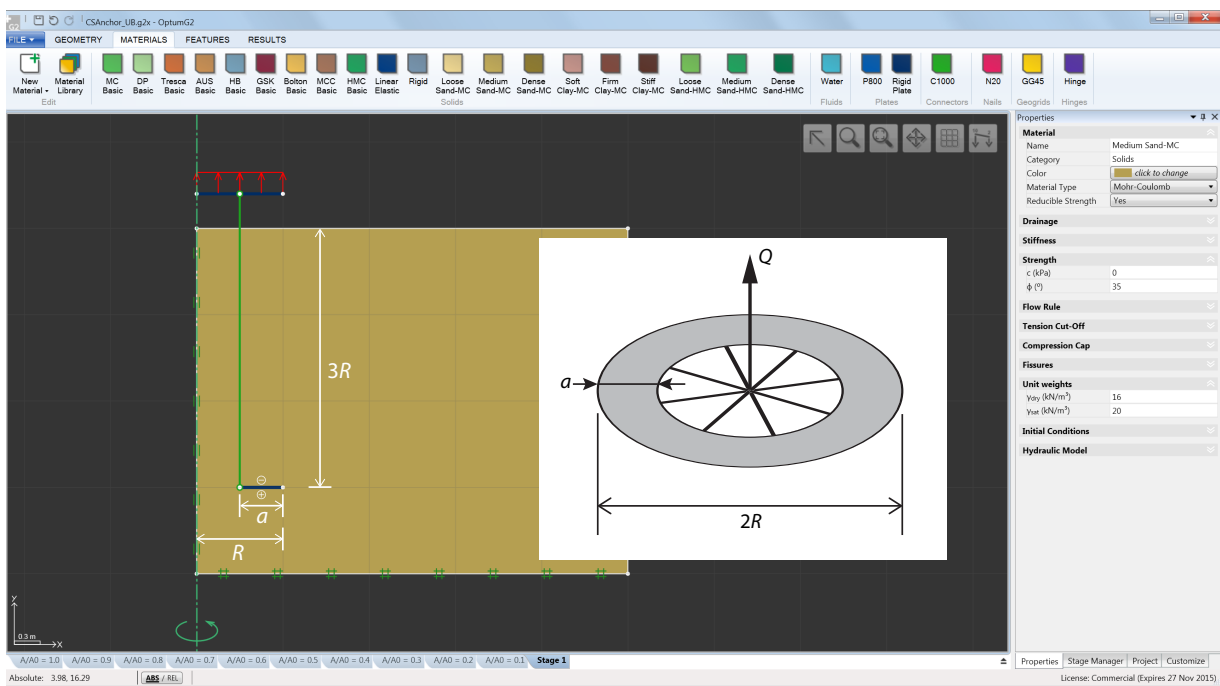


Figure 56.2: Annular ring anchor.

The soil is the default Medium Sand-MC material and the analyses are conducted using Limit Analysis with 5,000 Upper and Lower bound elements with 3 adaptivity iterations. The results in terms of the relative force versus the relative anchor plate area are shown in Figure 56.3. The quantities on the axes are:

Q_0 = Pull-out force for a full circular anchor plate ($a = R$).

Q = Pull-out force for an annular ring of width $0 < a < R$.

A_0 = Area of full circular anchor plate = πR^2 .

A = Area of annular ring = $\pi[R^2 - (R - a)^2]$.

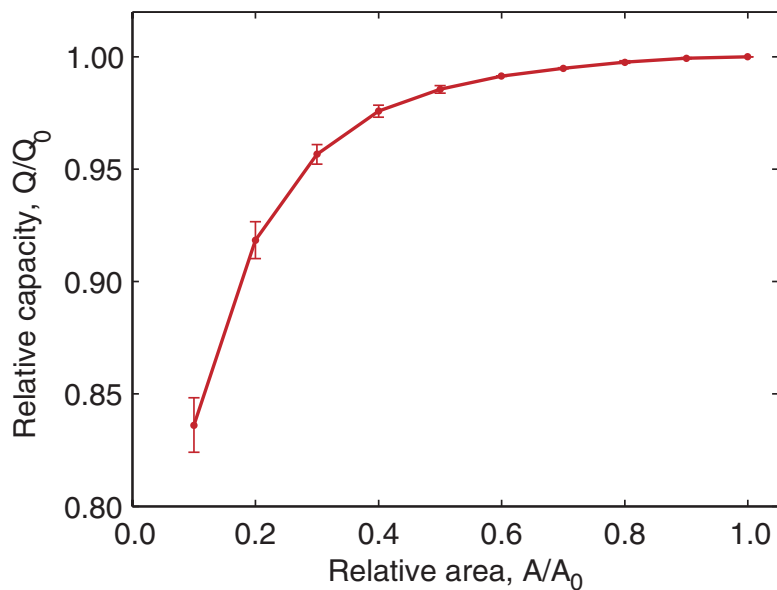


Figure 56.3: Relative pull-out capacity versus relative area with error bars indicating the worst case error between the upper and lower bound solutions.

We observe that the area of the anchor plate has a remarkably small effect on the pull-out capacity. Decreasing it by half has only negligible effect and decreasing it by a factor of 10 leads to less than a 20% reduction in pull-out force. These results echo the experimental findings of Dyson and Rognon (2014).

Collapse mechanism for selected A/A_0 are shown in Figure 56.4. These reflect the bearing capacities shown in Figure 56.3. That is, the effects of decreasing the area of the annular ring are very limited.

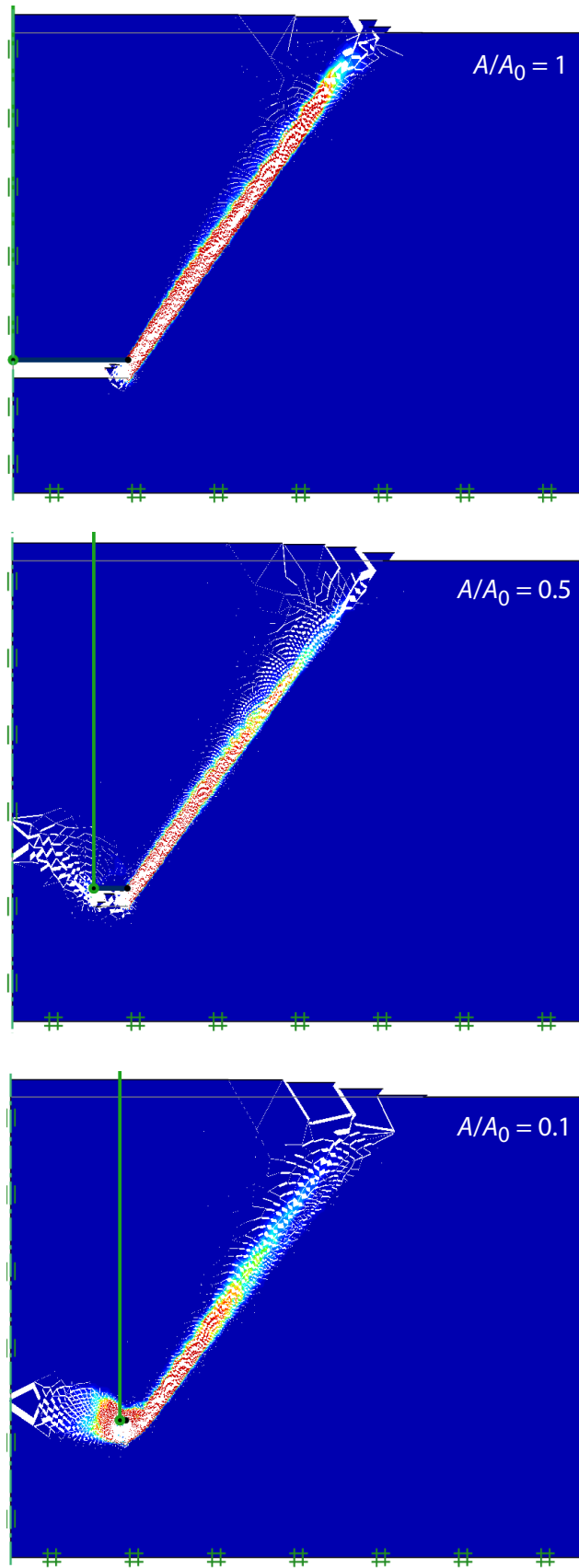


Figure 56.4: Collapse mechanisms for $A/A_0 = 1, 0.5$ and 0.1 .

57 STOCHASTIC ANALYSIS – INTRODUCTORY EXAMPLE

The following example introduces the possibilities for stochastic analysis available in OPTUM G2, in particular the concept of random field modeling of the spatial variability of material parameters. For that purpose, the problem of a strip footing on a Tresca material with a specified random variation of the undrained shear strength is considered (see Figure 57.1). The load acting on the footing is $q = 249 \text{ kN/m}^2$, leading to a deterministic factor of safety of $FS = 5.14s_u/q = 1.65$ for $s_u = 80 \text{ kPa}$.

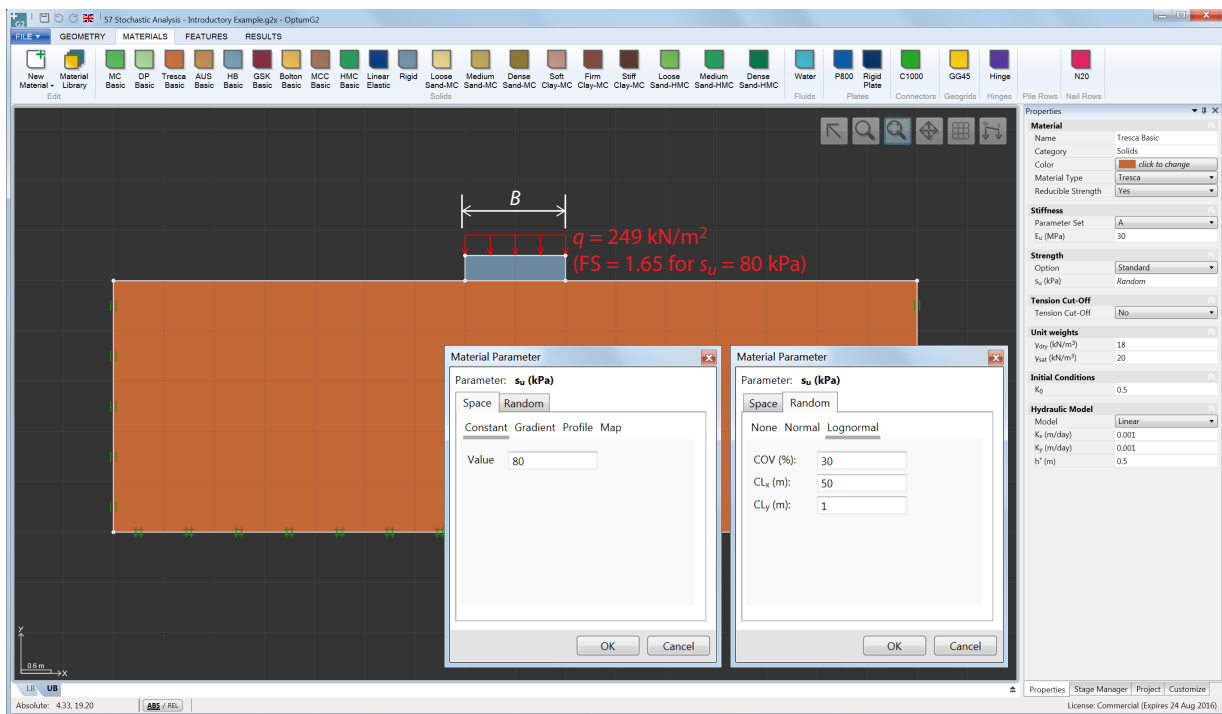


Figure 57.1: Strip footing on clay with random undrained shear strength.

57.1 Variability of material parameters

Natural soils display a considerable amount of variability, the origins of which can be traced to a variety of processes at a range of length scales. This variability can be taken into account in a number of ways. The simplest is to assume that a given parameter of interest, the undrained shear strength for example, follows a probability distribution given by a mean value and standard deviation. The variability of such parameters is often modeled using the lognormal distribution:

$$f(x; \mu, \sigma) = \frac{1}{x\sigma\sqrt{2\pi}} \exp\left[-\frac{(\ln x - \mu)^2}{2\sigma^2}\right], \quad x > 0 \quad (57.1)$$

where f is the probability distribution function for the parameter x and μ and σ are model parameters which are related to the mean and standard deviation by

$$\text{Mean} = \exp\left(\mu + \frac{\sigma^2}{2}\right) \quad (57.2)$$

$$\text{Std} = \text{Mean} \times \text{COV}/100\% = \exp(2\mu + \sigma^2)[\exp(\sigma^2) - 1] \quad (57.3)$$

with $\text{COV} = \text{Std}/\text{Mean} \times 100\%$ being the coefficient of variation. The cumulative distribution function is given by

$$F(x; \sigma, \mu) = \frac{1}{2} \text{erfc} \left(-\frac{\ln x - \mu}{\sigma \sqrt{2}} \right) \quad (57.4)$$

where erfc is the complementary error function.

An example of a lognormally distributed undrained shear strength with a mean value of 80 kPa and a COV of 30% is shown in Figure 57.2.

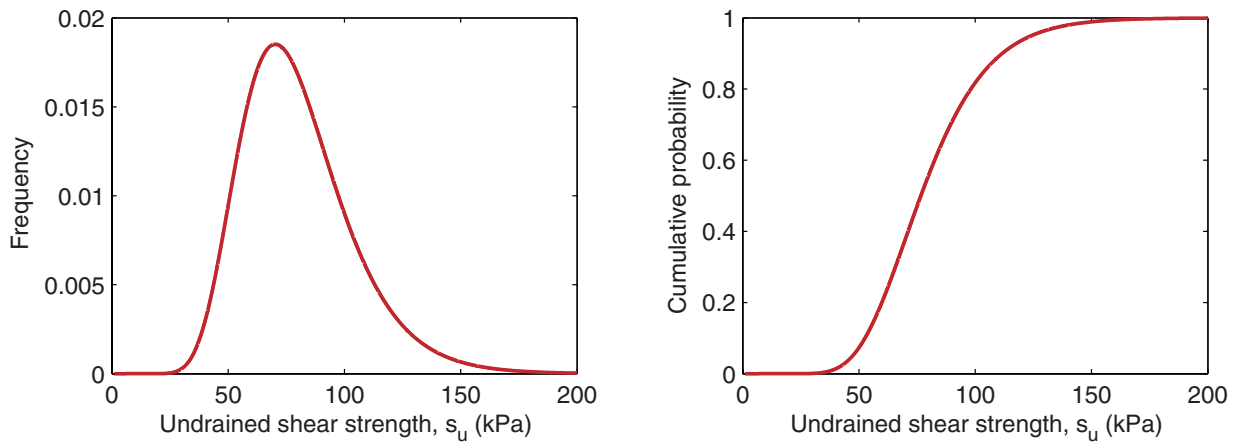


Figure 57.2: Lognormal distribution of undrained shear strength.

Next, to account for this kind of variability when determining the factor of safety for the problem shown in Figure 57.1, a series Monte Carlo simulations with s_u chosen according to the given probability distribution could be performed. Since the factor of safety is proportional to s_u , the probability distribution of the factor of safety follows the same distribution as s_u , i.e. a lognormal distribution with parameters $\mu = 1.65$ and $\sigma = \mu \times \text{COV}/100\% = 0.495$. This is shown in Figure 57.3 where a total of 1,000 Monte Carlo simulations have been performed. The finite element calculations are carried out using 1,000 upper and lower bound finite elements with 3 adaptivity iterations. The results reported in Figure 57.3 are based on the mean value between the upper and lower bounds for each run.

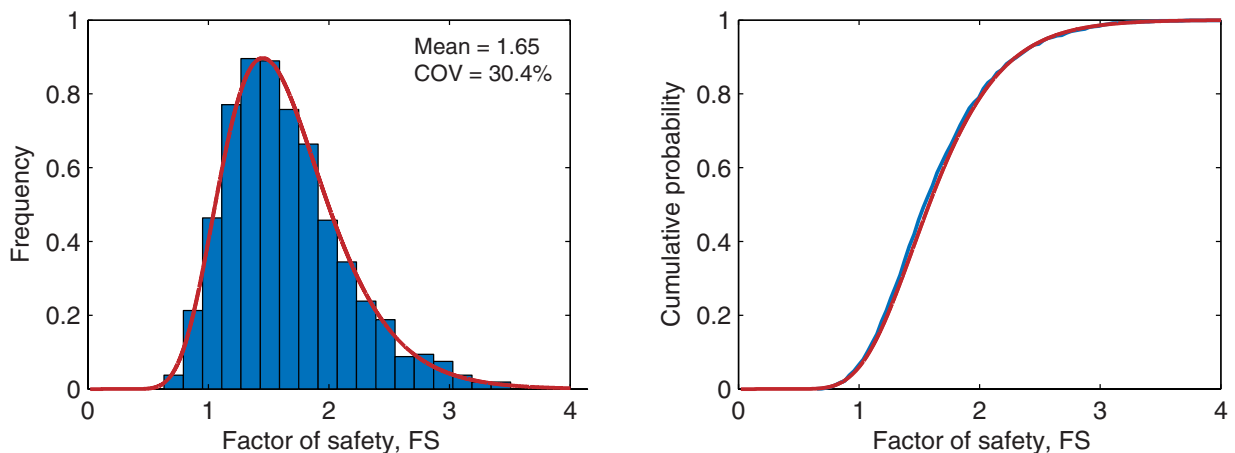


Figure 57.3: Probability distributions of factor of safety. The red curves are lognormal distributions with $\mu = 1.65$ and $\sigma = 0.495$ corresponding to the assumed variability of s_u .

57.2 Random fields

While the approach outlined above to some extent accounts for the variability of soil strength, it is not realistic to assume a constant value of the undrained shear strength throughout the domain, albeit that it varies from run to run.

The random fields concept provides a means of generating more realistic spatial distributions of the material parameters. A probability distribution is still assumed to account for the inherent variability following the previous section. In addition, vertical and horizontal correlation lengths are introduced, the idea being that a value of a material parameter measured at one point will have some correlation to the value measured at an adjacent point – depending on how far apart the two points are (vertically and horizontally). The correlation length describes the distance over which the the measured values will tend to be significantly correlated. A large correlation length will thus imply a smoothly varying field while a smaller value will imply a more ragged field. At the extreme ends of the spectrum, an infinite correlation length corresponds to the situation considered in the previous section (the value at a given point will be perfectly correlated, i.e. identical to the value at every other point) while a correlation length tending to zero implies no correlation at all (the value at each point in the domain follows an independent probability distribution). Some examples of random fields for undrained shear strength are shown in Figure 57.4. In all cases, the mean value is 80 kPa and the coefficient of variation is 30%.

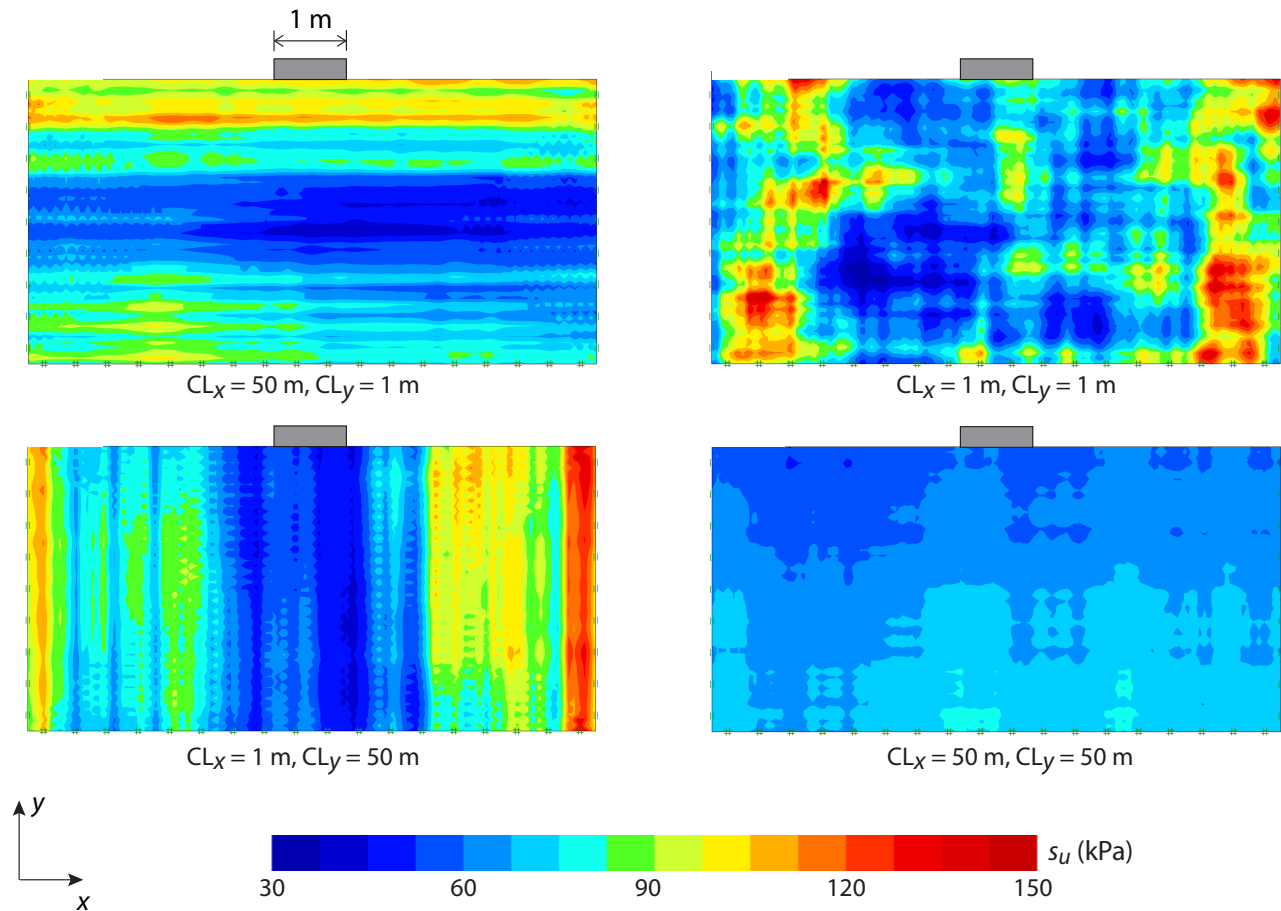


Figure 57.4: Random fields of undrained shear strength.

To generate a random field of a given material parameter, four input parameters are required:

1. The mean value of the parameter.
2. The coefficient of variation of the parameter, COV (%).
3. The horizontal correlation length of the parameter, CL_x (m).
4. The vertical correlation length, CL_y (m).

These parameters are defined through the spatial variation dialog as shown in Figure 57.1.

Regarding the exact value of the parameters, the three latter are the most uncertain ones. Traditionally, little effort has been made to quantify these parameters although several site investigation methods, notably, cone penetration testing, does allow for at least rough estimates. What is certain, however, is that the vertical correlation length generally is significantly less than the horizontal correlation length. In their paper examining a wide variety of data, Phoon and Kulhawy (1999) found vertical and horizontal correlation lengths (or ‘scales of fluctuation’) for s_u of 0.8 to 6.1 m and 46 to 60 m respectively. An indication of what such correlation lengths imply for the distribution of undrained shear strength can be gauged from the top left image in Figure 57.4 where the vertical and horizontal correlation length are 1 m and 50 m respectively. Regarding the coefficient of variation for s_u , the available data display a significant scatter between approximately 10% and 60% and with a decreasing trend for increasing mean value of s_u (see Figure 57.5).

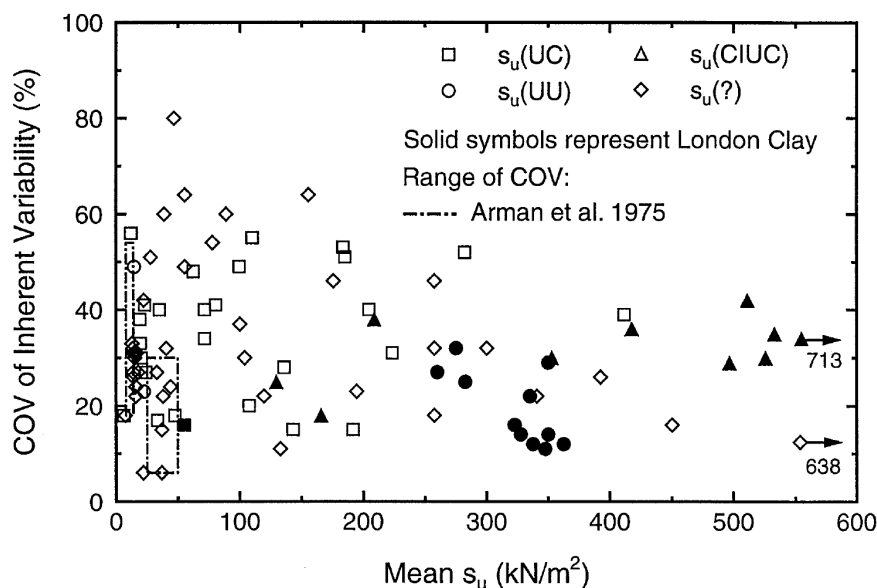


Figure 57.5: Coefficient of variation for s_u versus mean s_u (from Phoon and Kulhawy 1999).

On the basis of the guidelines provided by Phoon and Kulhawy (1999), the following parameters for s_u are used in the following:

- Mean value = 80 kPa
- Coefficient of variation, COV = 30%
- Horizontal correlation length, $CL_x = 50$ m
- Vertical correlation length, $CL_y = 1$ m

57.3 Deterministic analysis

A deterministic analysis with a constant $s_u = 80$ kPa throughout the domain is first carried out. This results in a factor of safety of 1.65 with the failure mechanism shown in Figure 57.6.

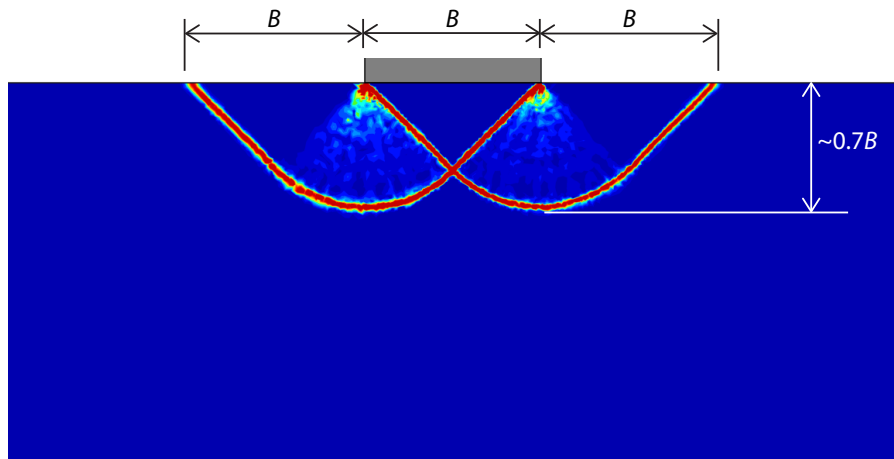


Figure 57.6: Failure mechanism for constant s_u .

The vertical extent of the failure mechanism is approximately $0.7B$. This quantity is of interest when gauging the influence of the vertical correlation length. For $B \ll CL_y$, the resulting probability distribution of FS would be expected to be of the same kind as the lognormal distribution accounting for the inherent variability of s_u . In other words, the variation of s_u implied by the random field does not come into effect as the failure is much shallower than the scale of this variation. Conversely, for $B \gg CL_y$ the failure mechanism covers all possible values of s_u generated by the random field and we should expect a probability distribution of FS corresponding to some characteristic average value and will little variation from run to run, i.e. with a small coefficient of variation.

57.4 Stochastic analysis

In the following, a stochastic analysis is conducted using the parameters mentioned above (mean $s_u = 80$ kPa, COV = 30%, $CL_x = 1$ m, $CL_y = 50$ m). Details regarding the appropriate analysis type, the necessary number of elements and the necessary number of Monte Carlo runs are discussed in further detail in Section 57.6.

The settings related to stochastic analysis can be specified under Project (see Figure 57.7).

Stochastic Parameters	
Monte-Carlo runs	1000
Seed	1
Expansion	Karhunen-Loeve
Terms in Expansion	1000

Figure 57.7: Settings for stochastic analysis.

The Seed (equal to 1 by default) is the seed used in the generation of the random fields. This quantity is incremented by 1 for each Monte Carlo run. As such, if the n 'th run is to be studied in

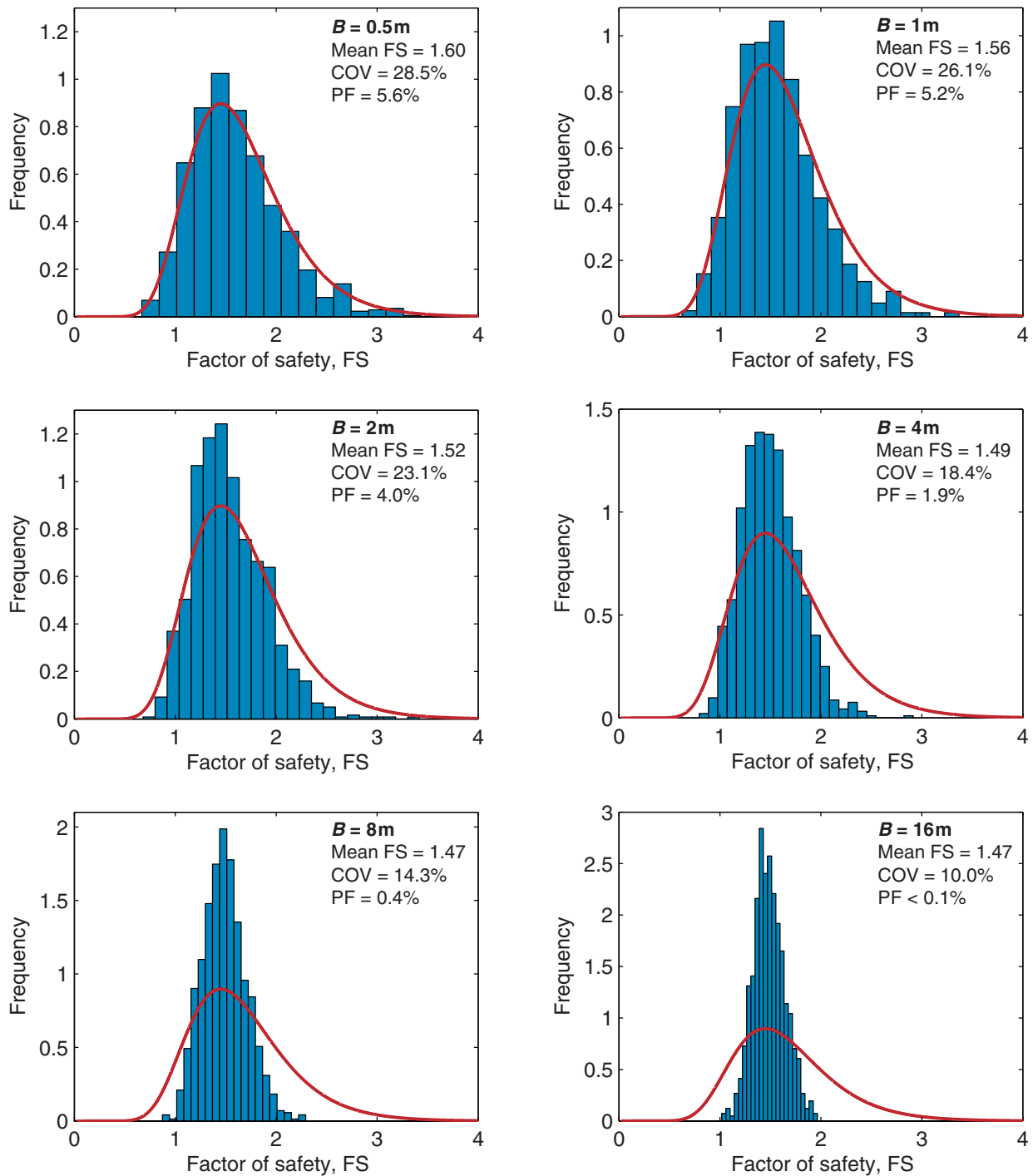


Figure 57.8: Probability distributions of factor of safety. The red curves correspond to an infinite correlation length (or an infinitesimal footing width). Shown in each figure are the mean factor of safety, its COV, and the probability of failure (PF) based on 1,000 runs.

more detail, the number of runs can be set to 1 and the Seed to n . This will be utilized in the following.

The results of the analysis in terms of probability distribution functions for a variety of footing widths are shown in Figure 57.8. The following trends are noted:

- For small footing widths, the probability distribution of the factor of safety approaches the

lognormal distribution corresponding to an infinite correlation length.

- As the footing width increases, the COV of the factor of safety decreases.
- The mean factor of safety increases with increasing footing width while the probability of failure decreases.

While the first two trends are expected, the last one is somewhat problem dependent. Indeed, it is not guaranteed, in general, that the mean factor of safety would decrease with increasing footing width (or for an increasing ratio between the characteristic system length and the correlation length).

57.5 Collapse mechanisms

The variability of the s_u distribution modeled by random fields gives rise to a variety of collapse mechanisms. A quick overview of the variability of these can be gauged by plotting the probability distribution function of the mobilized mass (available under XY Plots). An example, for $B = 2$ m, is shown in Figure 57.9.

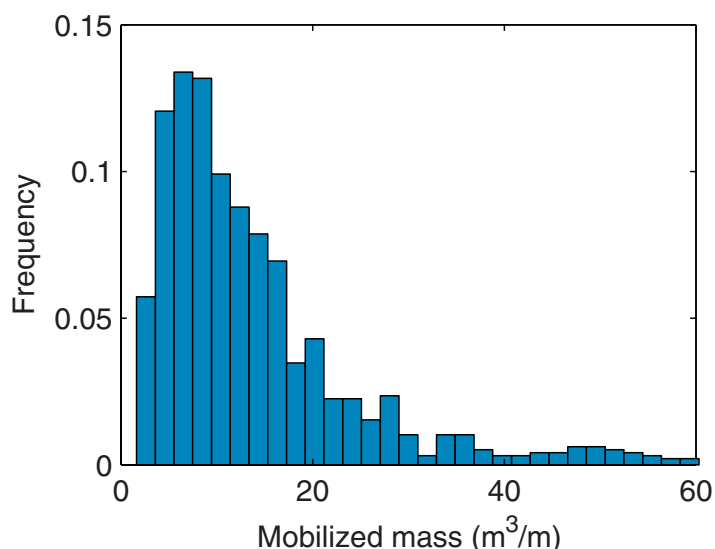


Figure 57.9: Probability distribution of mobilized mass (excluding footing) for $B = 2$ m.

To rerun particular Monte Carlo instances, the Seed should be set to the run number and the number of Monte Carlo runs should be set to 1 (see the previous section). Three examples are shown in Figure 57.10. These represent cases where:

- the mobilized mass is small as a result of a shallow weak layer overlying a strong layer.
- the mobilized mass is moderate as a result of a layer of moderate strength and depth overlying a strong layer.
- the mobilized mass is large as a result of a strong layer overlying a weak layer.

From Figure 57.9 we see that failure mechanisms similar to that of case (b) is more common than either the shallow or deep mechanism of cases (a) and (c) respectively. Furthermore, all the three mechanisms shown involve some amount of rotation resulting from the non-uniformity of the strength. This characteristic is more the rule than the exception.

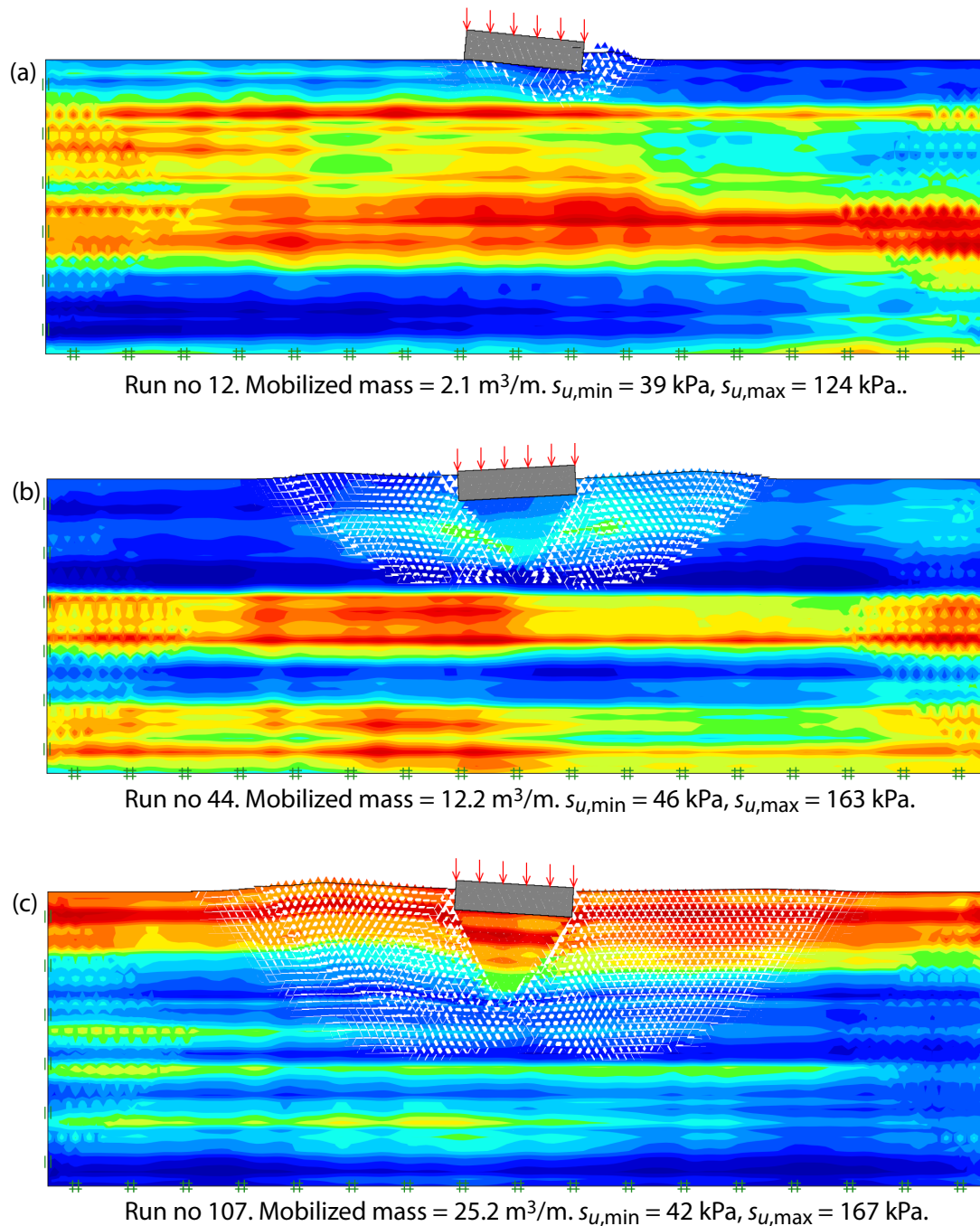


Figure 57.10: Selected collapse mechanisms with distribution of s_u for $B = 2 \text{ m}$ (mobilized mass excluding footing). Coloring represents the undrained shear strength varying between $s_{u,\min}$ (blue) and $s_{u,\max}$ (red).

57.6 Analysis type, number of elements and number of runs

57.6.1 Analysis type

For the present problem, the factor of safety is proportional to the undrained shear strength s_u as is the bearing capacity. As such, the factor of safety can either be determined directly from a Strength Reduction analysis or, alternatively, from a Limit Analysis with Multiplier = Load. Generally speaking,

Limit Analysis is somewhat faster than Strength reduction and is therefore preferred for the present stochastic analysis.

57.7 Number of elements

As for any deterministic analysis, the number of elements necessary to provide a sufficiently accurate solution is difficult to gauge a priori. However, as a rule of thumb, for limit analysis the mean value between the upper and lower bounds calculated using 1,000 elements with 3 adaptivity iterations usually provides a rather good estimate of the exact solution.

With the mean value given by

$$M = \frac{1}{2}(L + U) \tag{57.5}$$

where L and U are the upper and lower bounds, the relative error can be calculated by

$$\varepsilon = \frac{M - L}{M} = -\frac{M - U}{M} \tag{57.6}$$

such that it is guaranteed that the exact solution fall in the interval given by

$$E = M(1 \pm \varepsilon) \tag{57.7}$$

It should be noted here that ε is the worst case error. If the upper and lower bounds each contain errors of a similar magnitude (which is often the case), the mean value will be much close to the exact solution than implied by the error ε .

For $B = 2$, the worst case error ranges from 3% to 5% over 1,000 Monte Carlo runs using 1,000 elements and 3 adaptivity iterations. However, on comparing the mean value between the upper and lower bounds with the upper and lower bounds found using 10,000 elements it is found the actual error most likely is significantly smaller. This is illustrated in Figure 57.11 for the first 20 Monte Carlo runs. The worst case error between the upper and lower bounds using 10,000 elements is here around 1%. With the mean values for the 1,000 element case in all cases falling between these bounds, the actual error is most likely, on average, less than 1%.

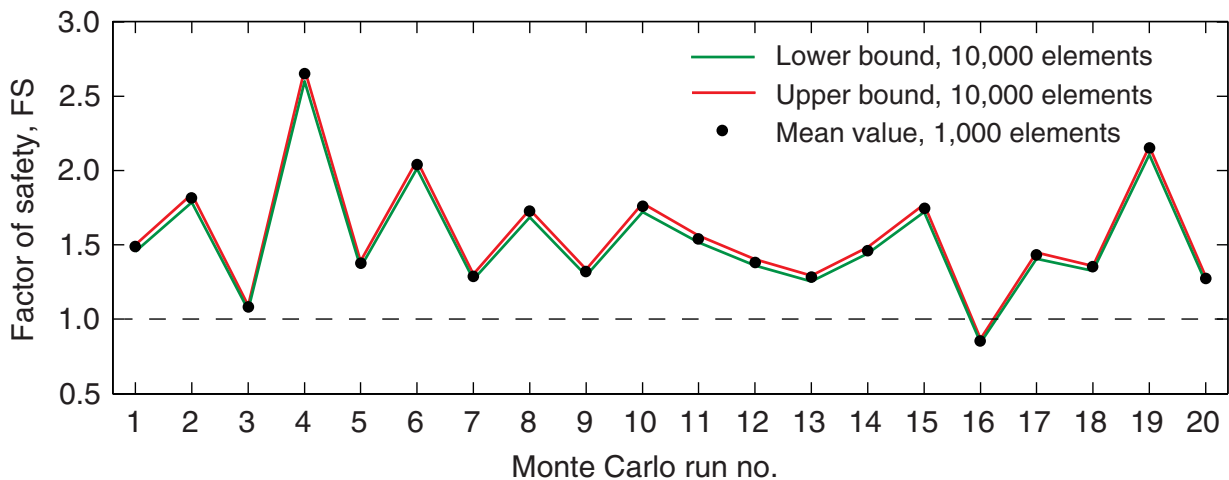


Figure 57.11: Factors of safety for the first 20 Monte Carlo runs using 1,000 and 10,000 elements ($B = 2m$).

57.8 Number of runs

As with the number of elements, the number of Monte Carlo runs necessary to extract key statistics (mean value, COV, etc) with reasonable confidence is to a certain extent problem dependent.

For the case of $B = 2$ m, the mean value and COV of the factor of safety versus run number are shown in Figure 57.12. In both cases, we see that what appears to be an acceptable degree of accuracy can be obtained with as little as 100-200 runs (as opposed to the 1,000 runs used for all problems in the present example). The probability of failure, on the other hand, requires somewhat more runs to be determined with the same degree of accuracy.

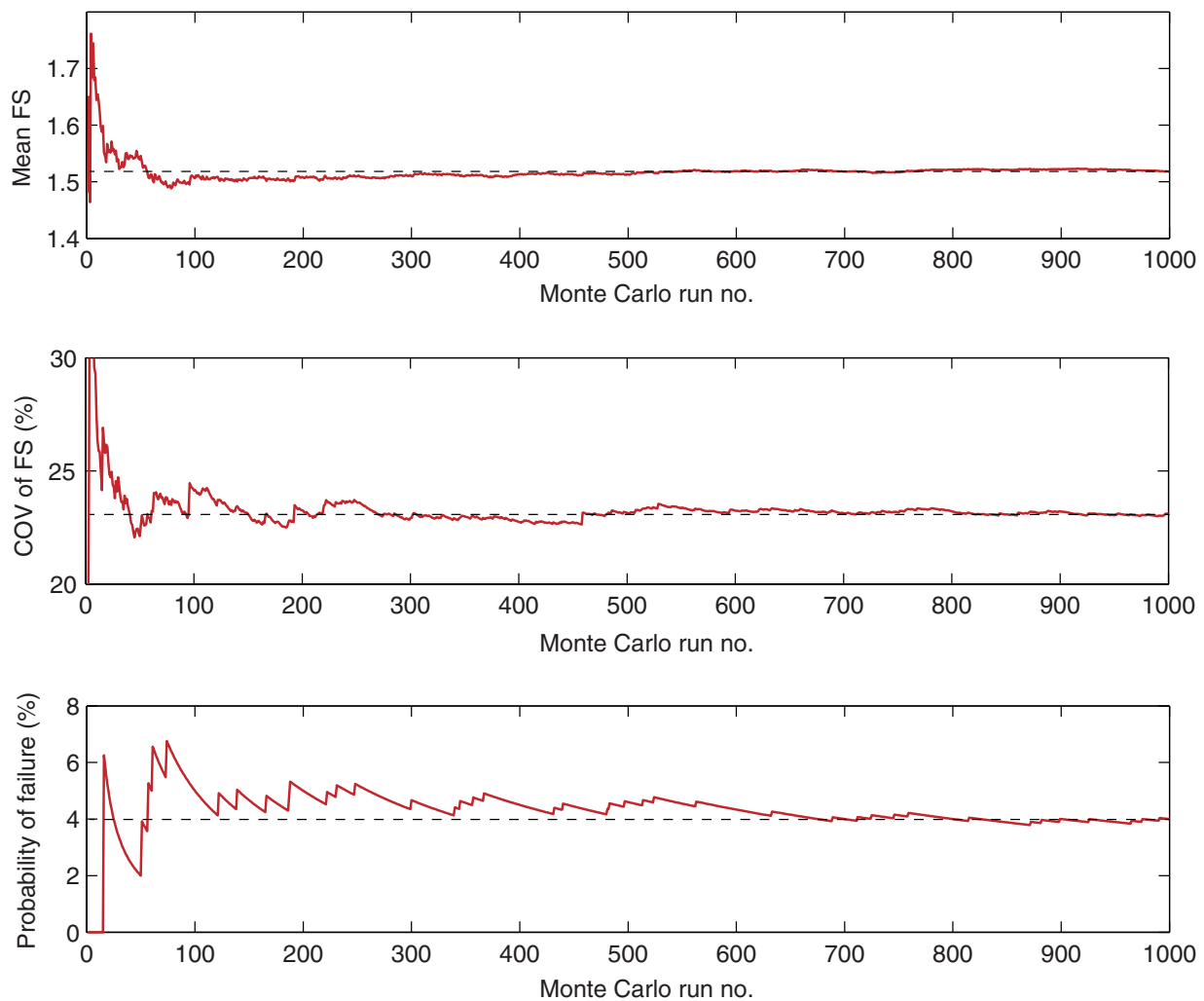


Figure 57.12: Key statistics versus Monte Carlo run number ($B = 2$ m).

58 STOCHASTIC FACTOR OF SAFETY ANALYSIS OF SLOPE IN CLAY

The following example considers the determination of the factor of safety for the slope shown in Figure 58.1. The material is Tresca and the undrained shear strength is modeled as a random field with a mean value of 70 kPa and a coefficient of variation of 30%, The vertical and horizontal correlation lengths are 2 m and 50 m respectively. These values of COV and correlation lengths correspond roughly to those indicated by Phoon and Kulhawy (1999) as being characteristic for undrained shear strength.

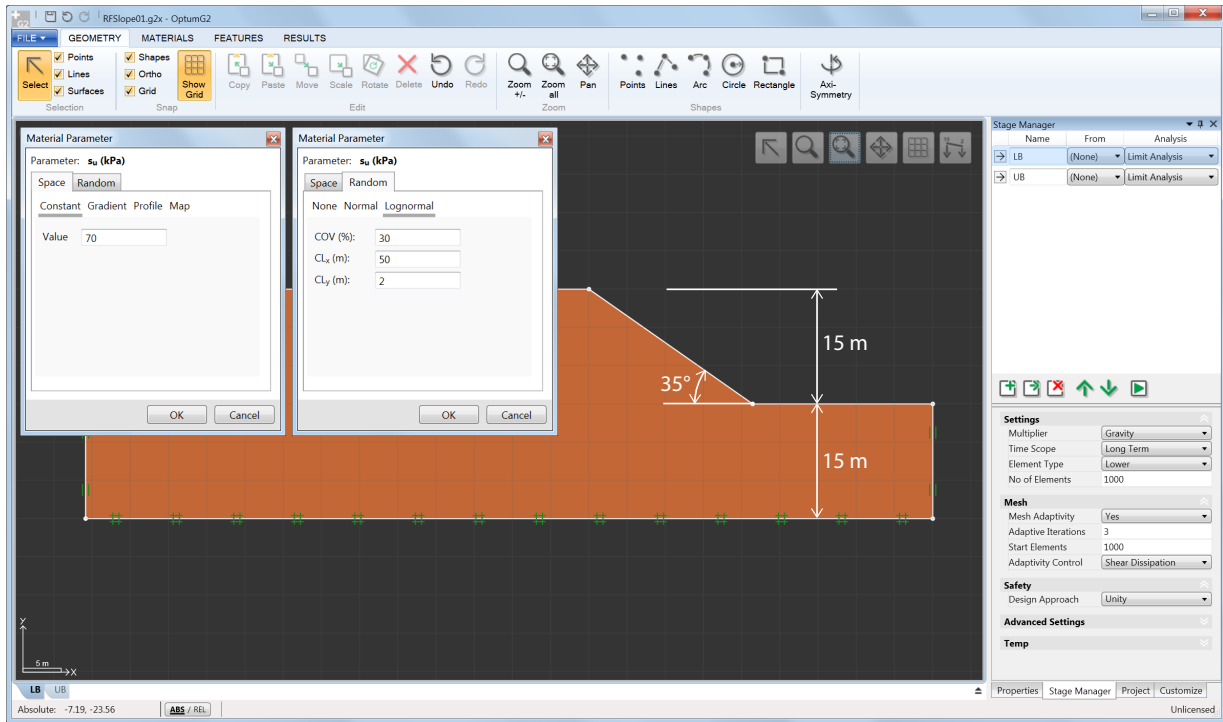


Figure 58.1: Slope in clay with random undrained shear strength.

Before the actual stochastic analysis proceeds, a standard deterministic analysis with $s_u = 70$ kPa is conducted for be used later for comparison purposes. The result of this analysis is a factor of safety given by:

$$FS = 1.45 \pm 0.01 \tag{58.1}$$

The collapse mechanism is shown in Figure 58.2.

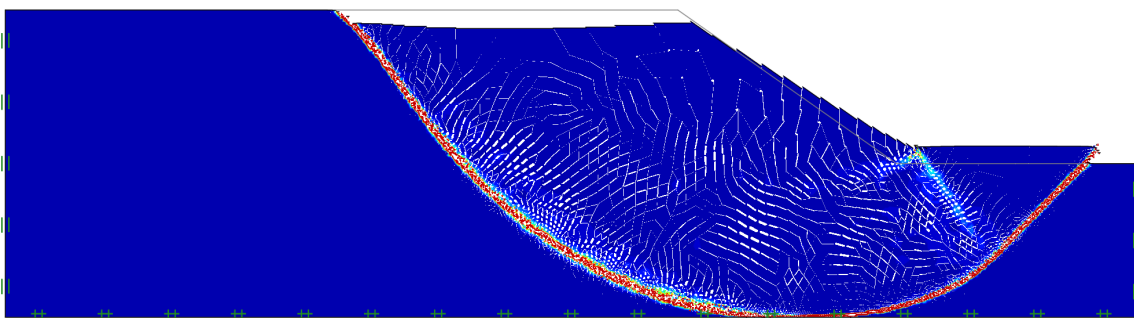


Figure 58.2: Collapse mechanism for deterministic analysis with constant $s_u = 70$ kPa.

As in the previous example, the factor of safety is determined by means of Limit Analysis (now with Multiplier = Gravity) using 1,000 upper and lower bound elements with 3 adaptivity iterations. The factors of safety reported in the following are the mean values between each upper and lower bound run. A total of 1,000 Monte Carlo runs are conducted.

The results in terms of probability distributions of the factor of safety are shown in Figure 58.3. Also shown are the distributions corresponding to infinite correlation lengths (mean value = 1.45 and standard deviation = $1.45 \times \text{COV}/100\% = 0.435$). Since the characteristic length scale of the failure mechanism is much larger than the vertical correlation length, the COV of the resulting factor of safety (10.3%) is significantly smaller than the inherent COV of the undrained shear strength (30%). The mean value is also somewhat smaller (1.29 vs 1.45) while the probability of failure is much less (0.3% vs 13.2%). These results follow the same trend as those of the previous example for a footing width much larger than the vertical correlation length.

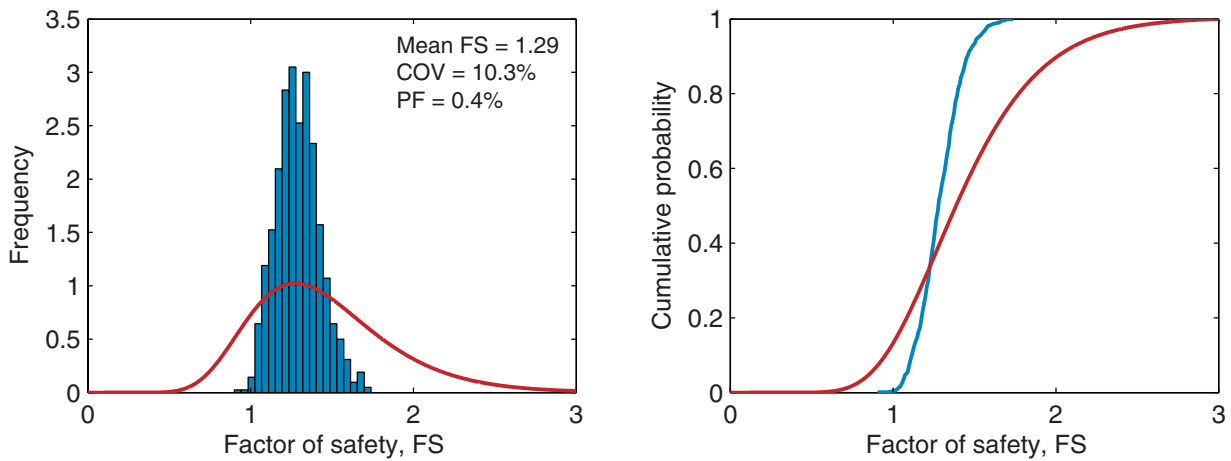


Figure 58.3: Probability functions for factor of safety. The red curves correspond to infinite correlation lengths.

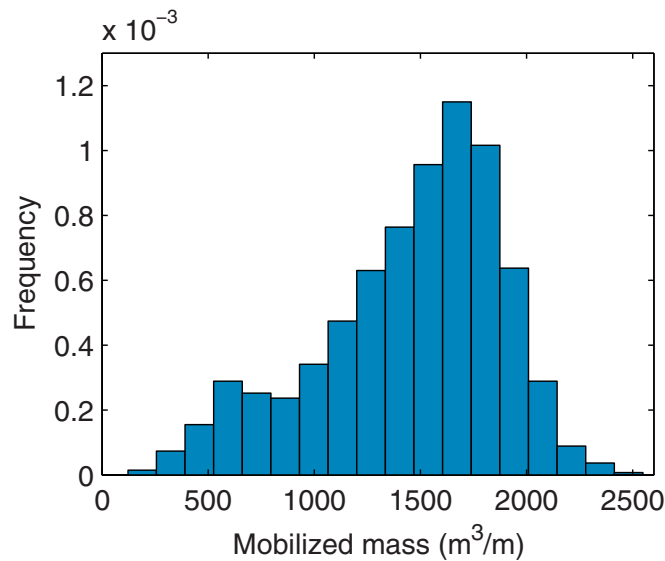


Figure 58.4: Probability distribution of mobilized mass.

The probability distribution of mobilized mass is shown in Figure 58.4. We see that the distributions tends to be somewhat bimodal with a peak around $600 \text{ m}^3/\text{m}$ and another one around $1,700 \text{ m}^3/\text{m}$. These two values represent two distinct families of failure mechanisms, the latter being deeper than the former. Examples are shown in Figure 58.5.

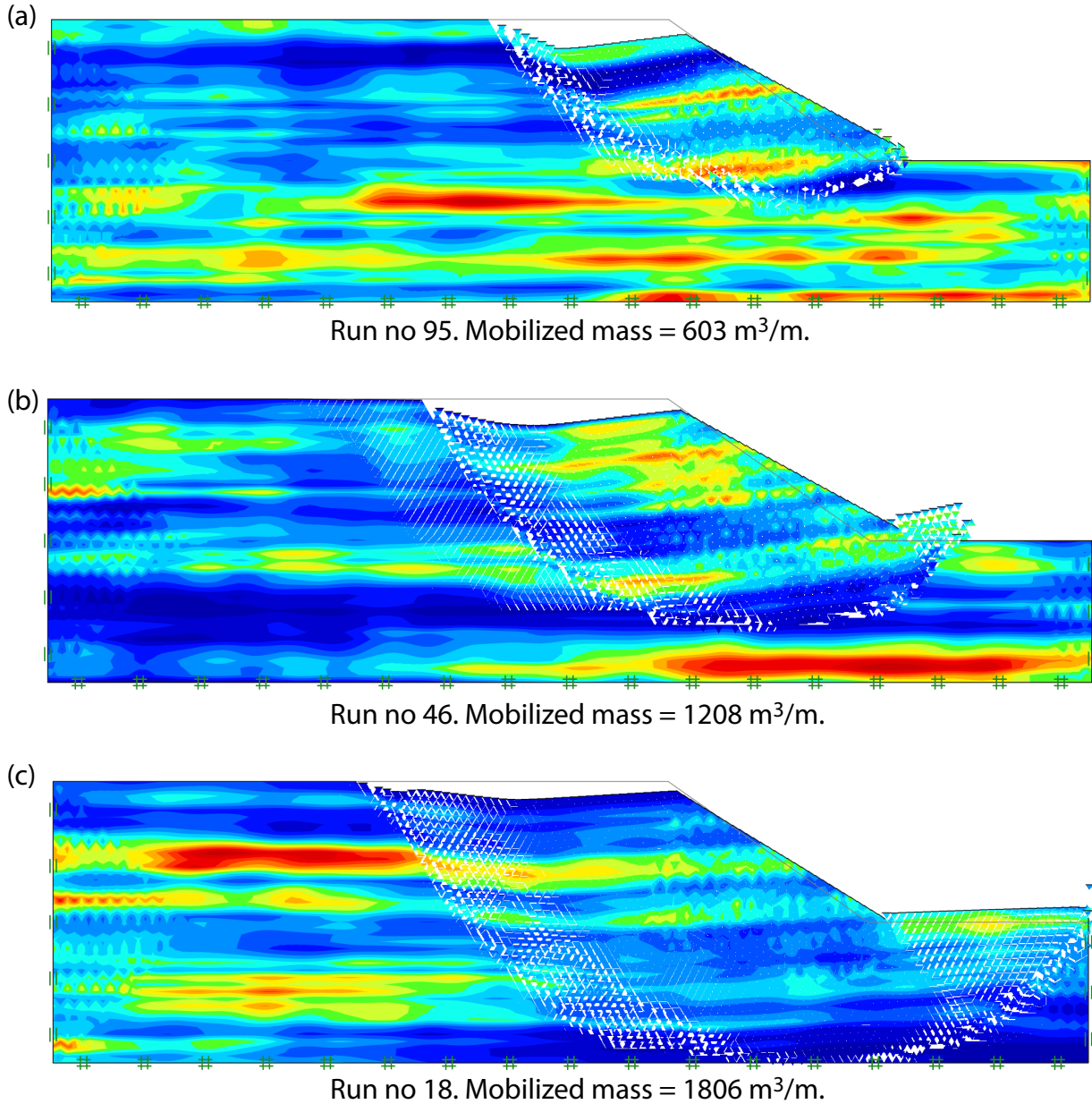


Figure 58.5: Examples of shallow (a), intermediate (b) and deep (c) failure mechanisms.

59 STOCHASTIC ANALYSIS OF FOOTING IN CLAY WITH DEPTH DEPENDENT STRENGTH

The following example involves the determination of the bearing capacity of a footing in a random field soil (see Figure 59.1). Undrained conditions are assumed and the Tresca model is used to model the soil. In contrast to the previous examples, the mean value of the undrained shear strength is not a constant but increases linearly with depth. An example of a random strength field using the parameters of Figure 59.1 is shown in Figure 59.3. We see that while there are significant strength fluctuations, especially vertically, the overall trend is a linear increase of strength with depth.

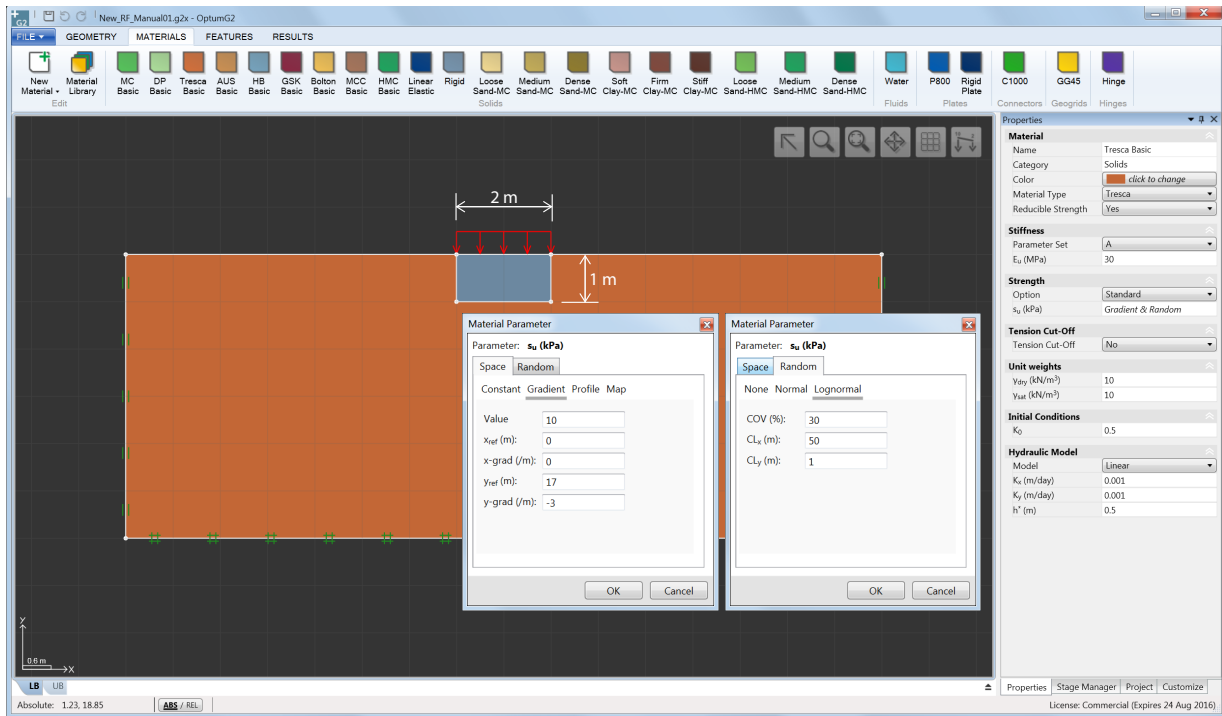


Figure 59.1: Footing in clay with strength increasing linearly with depth.

A standard deterministic analysis is first conducted, leading to a bearing capacity of $q_u = 93.0 \text{ kN/m}^2 \pm 1.3\%$. The associated collapse mechanism shown in Figure 59.2 is entirely dominated by vertical downwards movement, i.e. rotation is negligible.

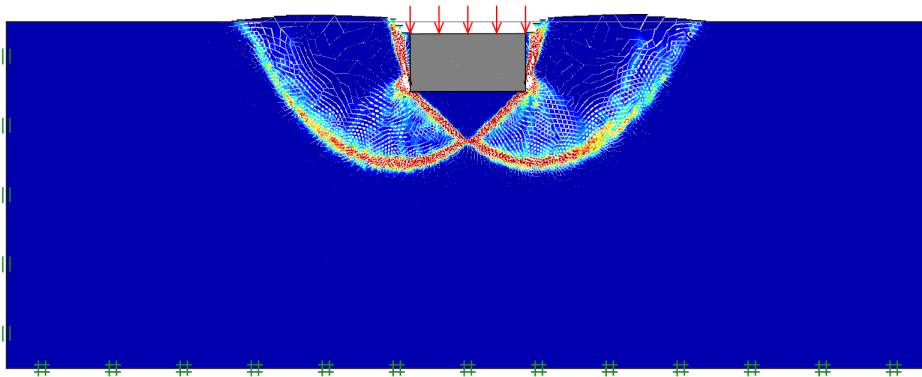


Figure 59.2: Collapse mechanism from deterministic analysis.

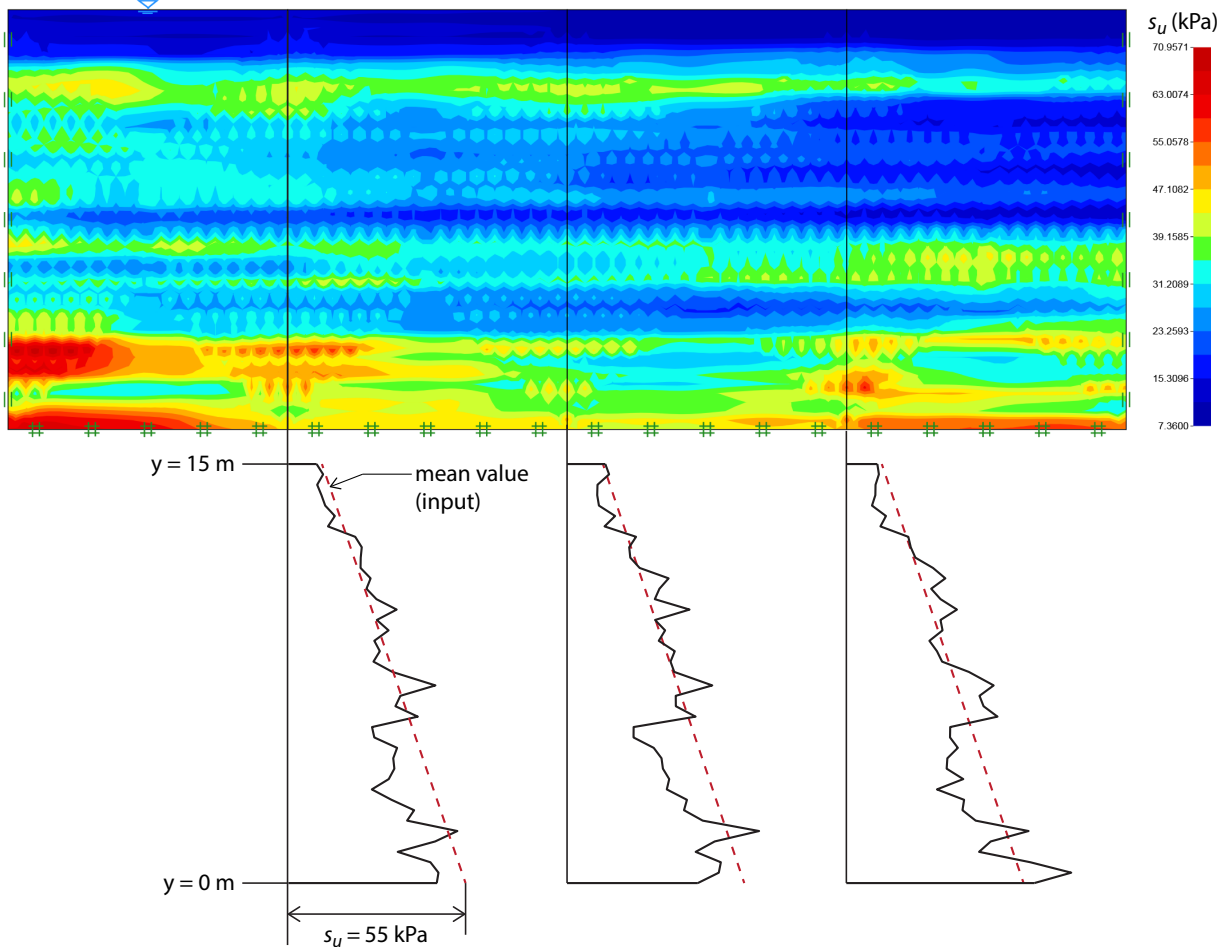


Figure 59.3: Random field with mean value of strength increasing linearly with depth.

Next, a stochastic analysis is performed using 1,000 Monte Carlo runs. The resulting statistics are shown in Figure 59.4. We see that the mean value of the bearing capacity is similar to that of the deterministic analysis while the coefficient of variation is somewhat smaller than that of the material,

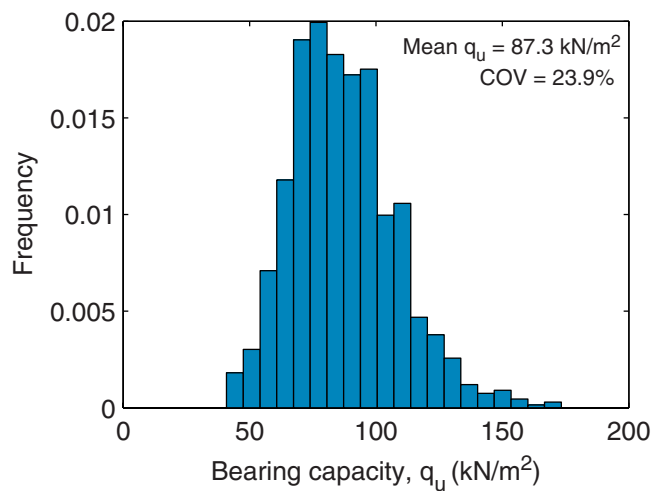


Figure 59.4: Probability distribution of bearing capacity.

echoing the findings of the previous examples.

Finally, three example of collapse mechanisms are shown in Figure 59.5. These all involve a significant rotation of the foundation, in contrast the mechanism of the deterministic analysis.

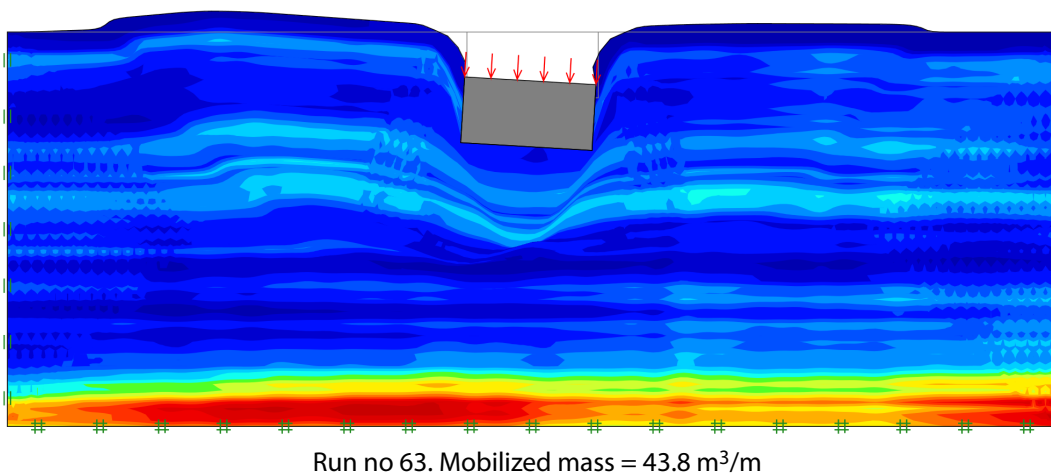
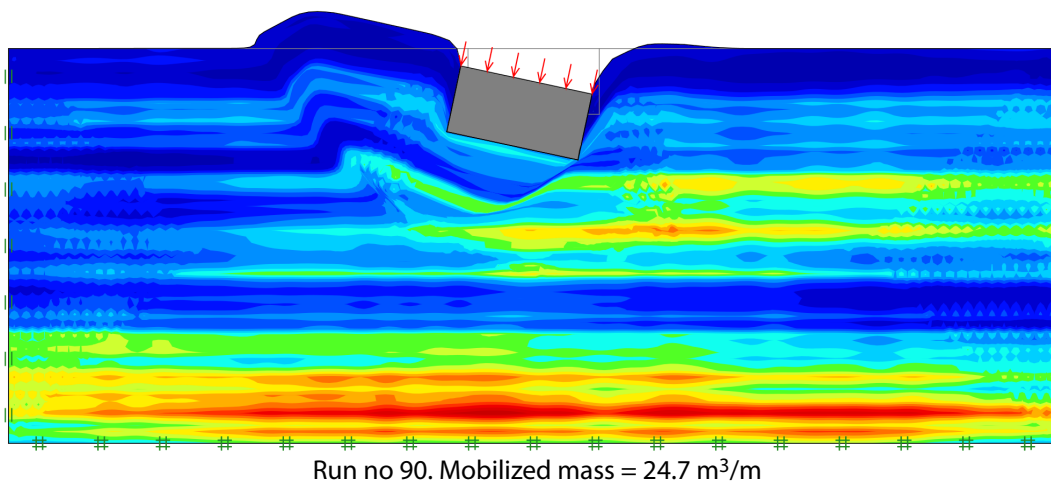
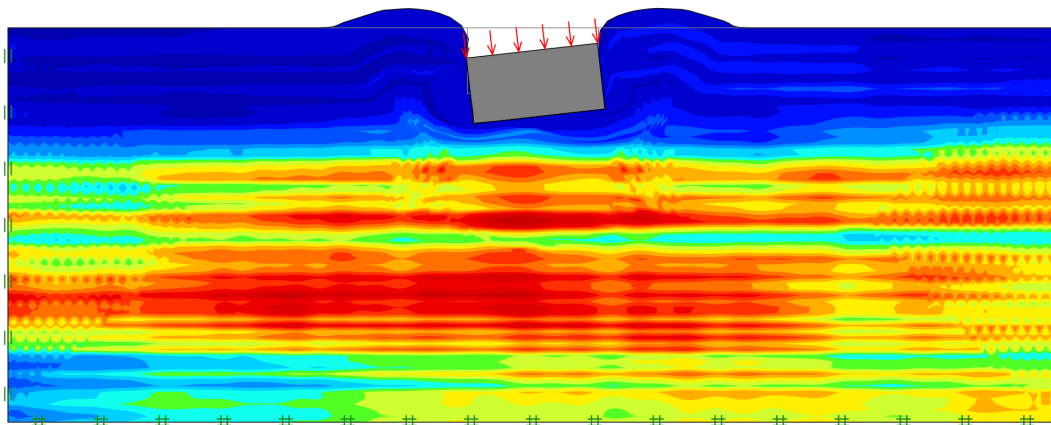


Figure 59.5: Collapse mechanisms from stochastic analysis.

60 STOCHASTIC ANALYSIS OF DEEP EXCAVATION

The stochastic capabilities of OPTUM G2 are not limited to bearing capacity and factor of safety analysis, but may be used in conjunction with any analysis type including Elastoplastic analysis. In the following this is utilized in connection with the analysis of an excavation supported by a cantilever sheet pile wall as shown in the figure below. The friction angle is modeled as a random field with a mean value of 35° , COV of 10%, vertical correlation length of 2 m and horizontal correlation length of 40 m. These values of COV and correlation lengths correspond roughly to those indicated by Phoon and Kulhawy (1999).

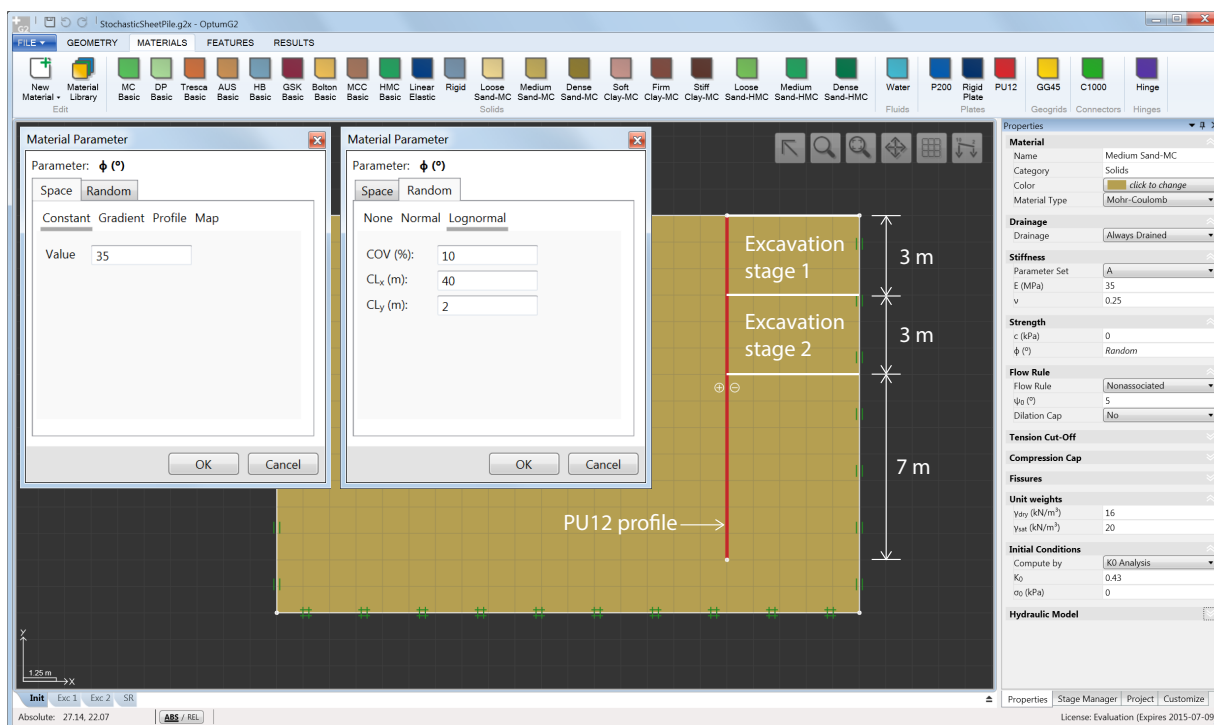


Figure 60.1: Excavation in sand with random field friction angle.

The analysis proceeds by way of four stages:

1. A stage to determine the initial stresses using the dedicated Initial Stress analysis type and with the sheet pile wall wished in place.
2. A first excavation stage to a depth of 3 m using Elastoplastic analysis.
3. A second excavation stage to a total depth of 6 m using Elastoplastic analysis.
4. A Strength Reduction stage to determine the factor of safety for a excavation depth of 6 m.

60.1 Deterministic analysis

For future reference, the analyses are first conducted using spatially constant friction angles of 25° , 30° , ..., 45° . The results in terms of the horizontal displacement of top the wall at an excavation depth of 6 m and the factor of safety at this depth are shown in Table 60.1.

Friction angle, ϕ ($^{\circ}$)	Displacement (cm)	Factor of Safety
25	33.2	1.03
30	17.5	1.28
35	10.2	1.55
40	6.8	1.85
45	4.0	2.21

Table 60.1: Displacement of top of wall and factor of safety as function of friction angle.

60.2 Stochastic analysis

For the stochastic analysis, the four stages defining the problem are processed in a Monte Carlo type manner using a total of 1,000 runs. Besides various global quantities (maximum displacement, factor of safety, etc), the displacements at the top of the wall are also monitored. This requires that a Result Point be introduced at that point.

The probability distribution function (PDF) and the cumulative distribution function (CDF) for the friction angle for a mean value of 35° and a COV of 10% are shown in Figure 60.2. On closer inspection of the CDF, it may be observed that about 85% of all realizations fall in the relatively narrow interval of $30^{\circ} \leq \phi \leq 40^{\circ}$. Similarly, the probability of a friction angle in the range $35^{\circ} \pm 2^{\circ}$ is approximately 50%. In other words, the inherent variability of the friction angle is relatively moderate.

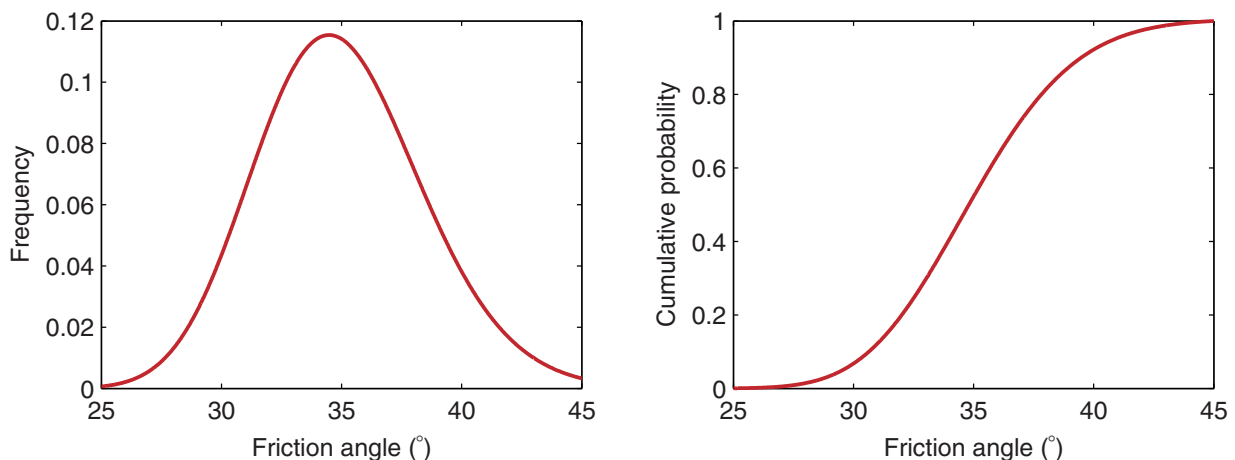


Figure 60.2: Probability functions for friction angle.

This variability nevertheless translates into significant variability in the final horizontal displacement of the wall at the last excavation step. This is shown in Figure 60.3.

The factor of safety for the second excavation stage (at a depth of 6 m) displays rather less variability, the COV being only 8%, i.e. similar to the input COV for the friction angle. This is shown in 60.4. It is noted that no failures are encountered in the course of the 1,000 Monte Carlo runs. In fact, the minimum factor of safety encountered is about $FS = 1.18$.

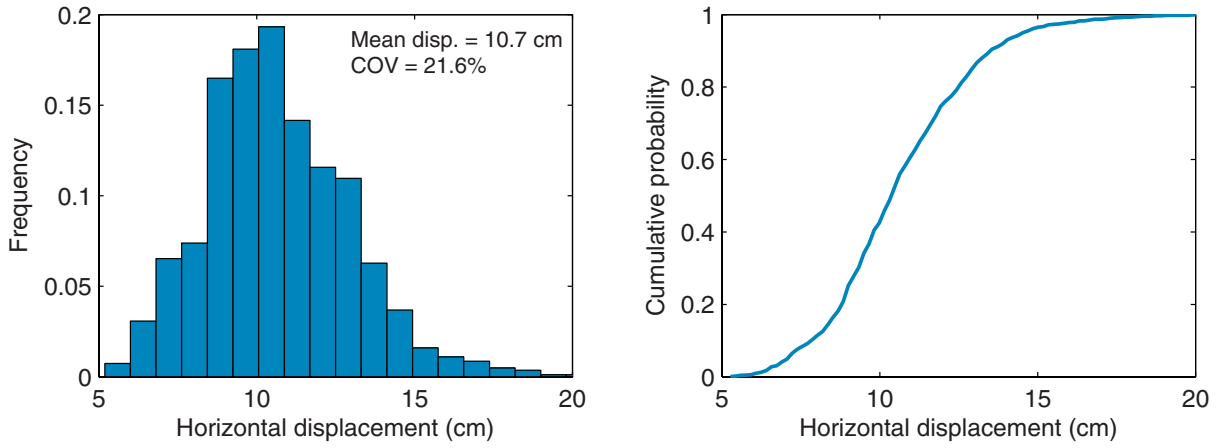


Figure 60.3: Probability functions for horizontal displacement of top of wall.

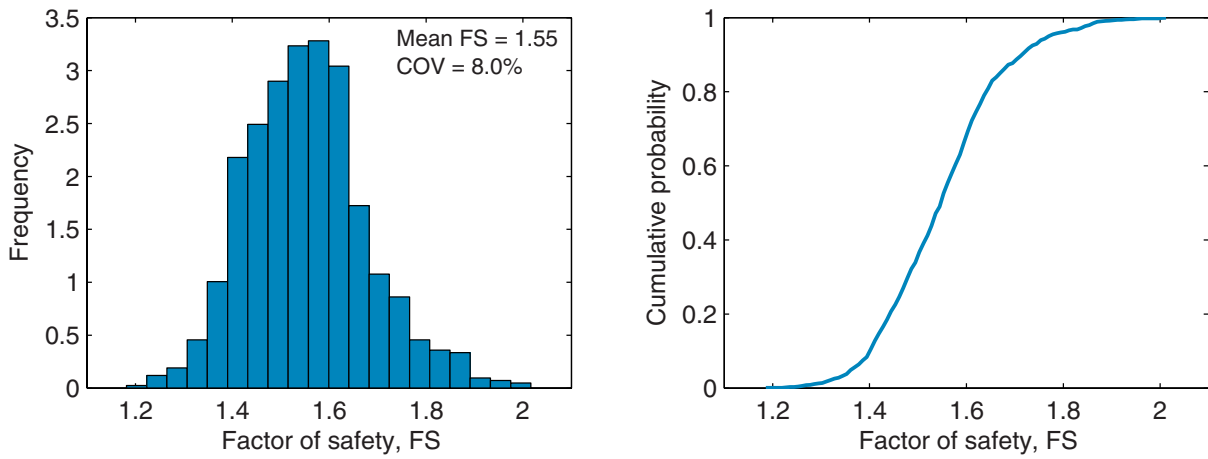


Figure 60.4: Probability functions for factor of safety.

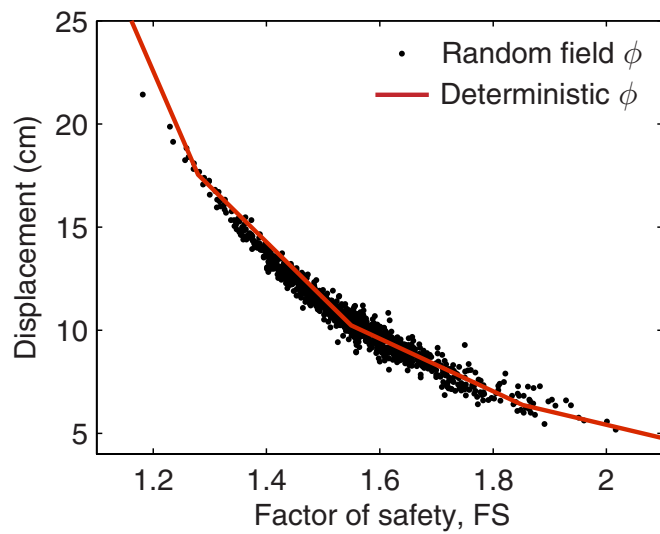


Figure 60.5: Factor of safety versus horizontal displacement of top of wall.

Finally, while the determination of the wall displacement and the factor of safety in principle comprise two separate analyses pertaining to the serviceability and ultimate limit states respectively, they can be correlated in the sense that a higher factor of safety generally implies a smaller wall displacement. Interestingly, the relation between wall displacement and factor of safety implied by the deterministic analysis summarized in Table 60.1 holds also, to a good approximation, in the random field case (see Figure 60.5).

61 EMBANKMENT CONSTRUCTION ON SOFT SOIL PRONE TO CREEP

The following example concerns the construction of an embankment on a soft clay prone to creep. The embankment, symmetric about the left vertical boundary as shown in Figure (61.1), is constructed in two stages, each adding 2 m of material to a 6 m layer of soft clay overlying a 4 m layer of medium sand. The fill and the sand are both modeled as Always Drained Mohr-Coulomb materials, i.e. they do not generate excess pore pressures. The clay is modeled as a Modified Cam Clay material which comes with the option of including creep. In the following, the effects of including more or less creep are examined, with and without drains placed underneath the embankment (see Figure 61.1). Four different values of the creep ratio are used: $\mu/\lambda = 0$ (no creep), 0.02, 0.05 and 0.1. This represents the range of ratios typically seen for inorganic soft clays (Mesri and Castro 1986).

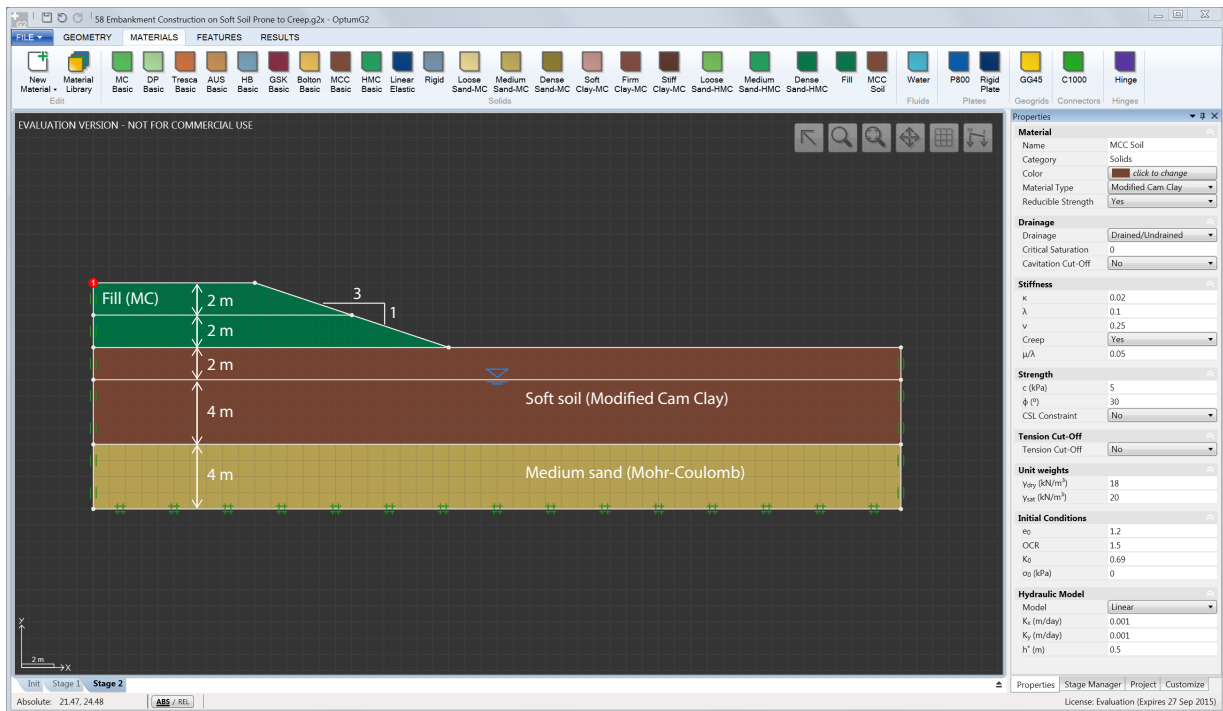


Figure 61.1: Embankment without drains.

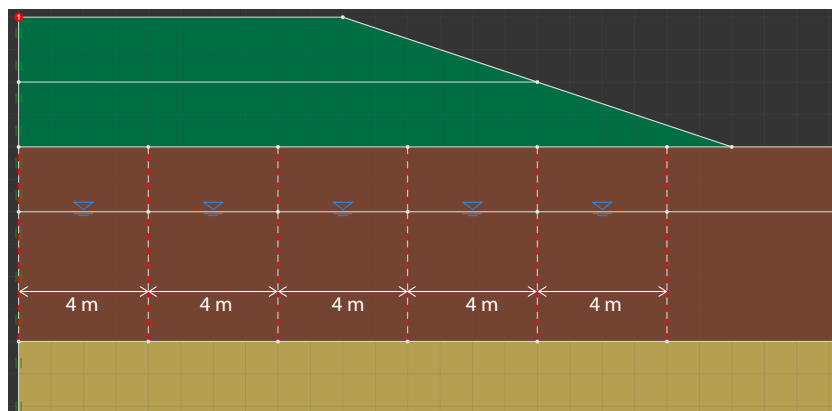


Figure 61.2: Embankment with drains modeled using the Fixed Excess Pressure tool from the Features ribbon

61.1 Without drains

For the analysis without drains, the vertical settlement versus time for the top central point of the embankment is shown in Figure 61.3.

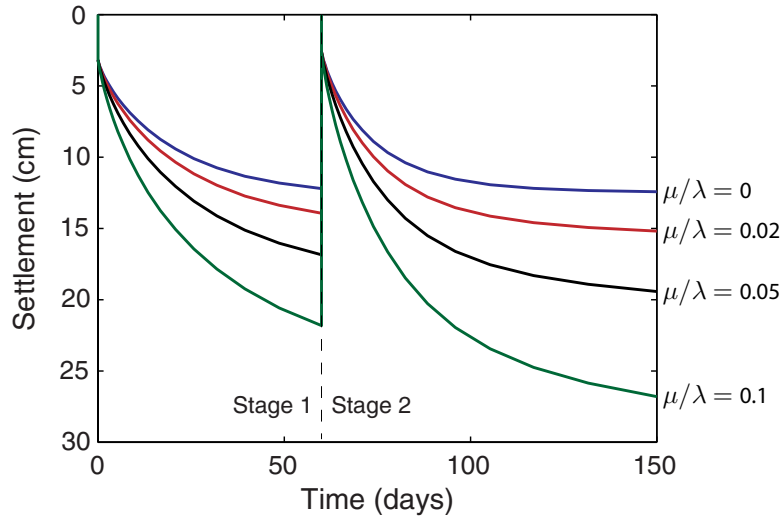


Figure 61.3: Vertical settlement of top central point of the embankment.

As expected, the settlements increase with increasing μ/λ and continue to increase past the primary consolidation settlement which, for $\mu/\lambda = 0$, attains its final maximum value after approximately 150 days.

61.2 With drains

Including drains and again running the analysis to a final time of 150 days makes the effects of creep more apparent. As shown in Figure 61.4, the material without creep comes to the end of primary consolidation relatively rapidly while in the case of $\mu/\lambda = 0.05$, the settlements continue beyond this time. In fact, in principle, the creep deformations continue indefinitely though at a still smaller rate

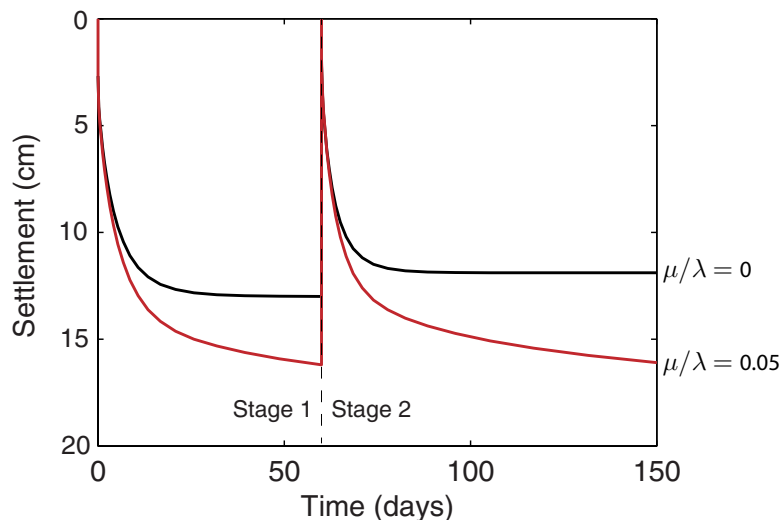


Figure 61.4: Vertical settlement of top central point of the embankment.

(see the Materials Manual for details).

The settlements in the two cases, at the end of each construction stage, are shown in Figure 61.5.

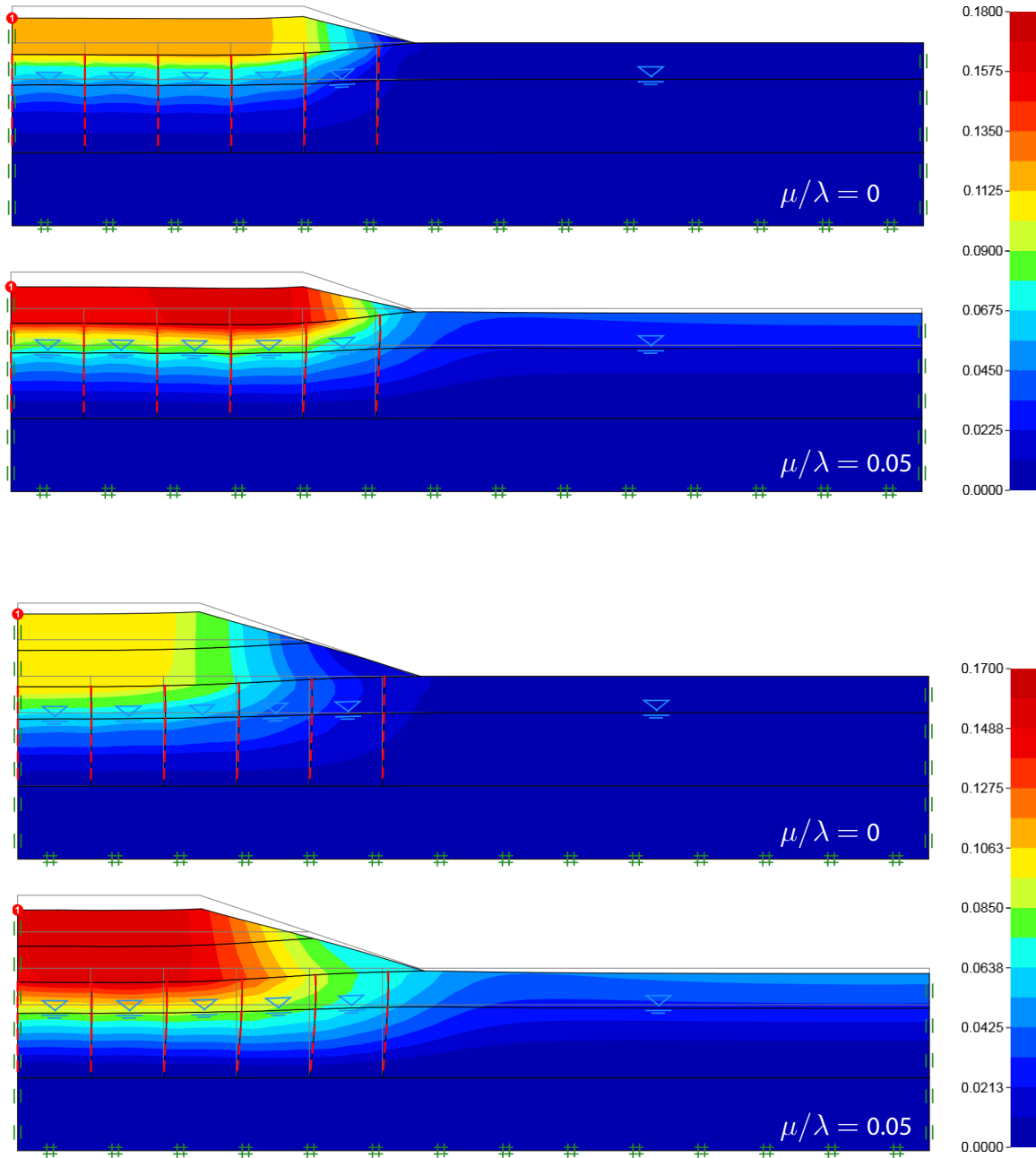


Figure 61.5: Stage displacements $|\Delta u|$ in cm (deformations scaled by a factor of 5).

62 ULS DESIGN OF CANTILEVER SHEET PILE WALL TO EUROCODE 7

The following example was dealt with as part of the *International Workshop on the Evaluation of Eurocode 7* held at Trinity College, Dublin in 2005. The data cited in the following are from the paper by Brian Simpson that formed part of the proceedings of this workshop. The problem concerns the design of a cantilever wall as shown in Figure 62.1. The wall is embedded in a sand with a unit weight of 20 kN/m^3 and a characteristic friction angle $\phi_k = 37^\circ$. On the left side of the wall, the groundwater table is located 1.5 m below ground level and on the right side it is located at the bottom of the excavation at 3 m below ground level. A variable surcharge load of 10 kN/m^2 acts on ground surface behind the wall. The wall is modeled as a Rigid Plate.

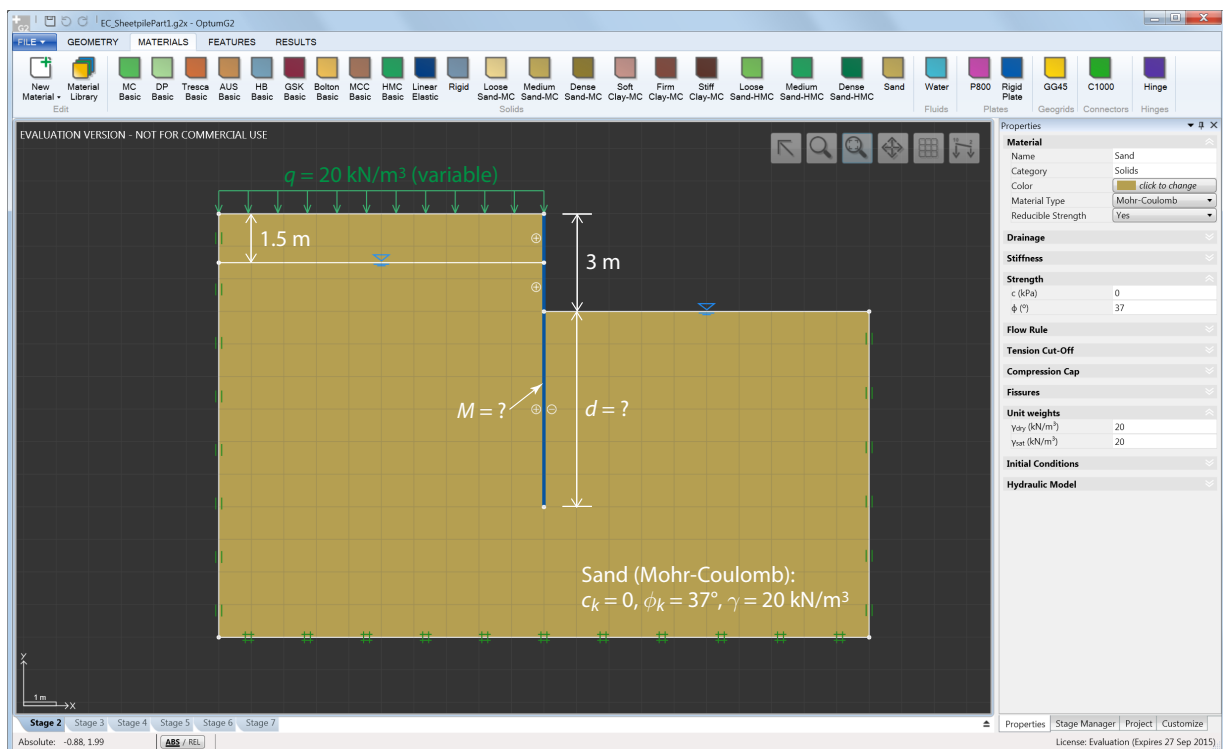


Figure 62.1: Cantilever sheet pile wall.

The quantities to be determined are:

- The embedment depth of the wall, d
- The design bending moment of the wall, M

In the following, this done in accordance with Design Approach 1 (DA1) of Eurocode 7 (EC7).

62.1 Partial factors

OPTUM G2 allows for automatic application of partial factors according to DA1 of EC7. The application of partial factor is relevant only with respect to the ultimate limit state. Hence, the option is only available for Limit Analysis and Strength Reduction analysis.

DA1 requires two separate calculations where two different sets of partial factors are applied to the soil strengths and/or external loads. These are referred to as DA1 Combination 1 (DA1/1) and DA1

Combination 2 (DA1/2). For a given stage, the set of partial factors to be applied is selected under Safety in the Stage Manager (see Figure 62.2).

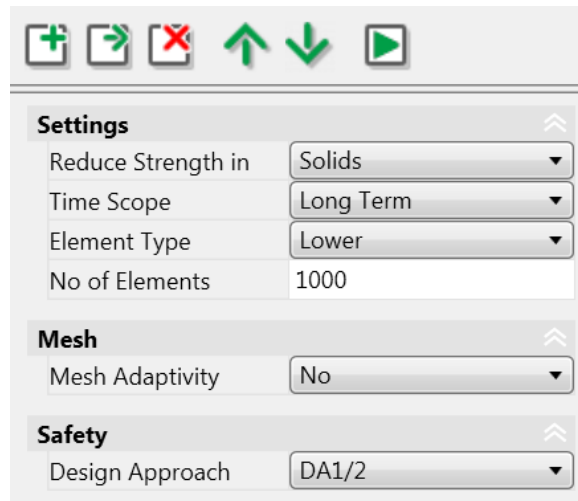


Figure 62.2: DA1/2 selected under Safety in the Stage Manager.

The partial factors associated with the various design approaches can be viewed by opening the Design Approaches dialog under the Project tab (see Figure 62.3). The sets Unity (applying a partial factor of 1 to all quantities), DA1/1 and DA1/2 are hard coded and cannot be edited, in contrast to the user sets User 1–4.

	Unity	DA1/1	DA1/2	User 1	User 2	User 3	User 4
Unit Weight - Unfavourable:							
Permanent	1	1.35	1	1	1	1	1
Unit Weight - Favourable:							
Permanent	1	1	1	1	1	1	1
Loads - Unfavourable:							
Permanent	1	1.35	1	1	1	1	1
Variable	1	1.5	1.3	1	1	1	1
Accidental	1	1	1	1	1	1	1
Loads - Favourable:							
Permanent	1	1	1	1	1	1	1
Variable	1	0	0	1	1	1	1
Accidental	1	0	0	1	1	1	1
Materials:							
c	1	1	1.25	1	1	1	1
ϕ	1	1	1.25	1	1	1	1
s_u (Tresca)	1	1	1.4	1	1	1	1

Figure 62.3: Design Approach table (open under Safety in Project).

62.2 Loads

Besides magnitude and direction, all loads are defined by a Load Type (Favourable/Unfavourable) and a Load Category (Permanent/Variable/Accidental). These settings are shown for the surcharge

load in Figure 62.4. Clearly, for this problem the surcharge is Unfavorable (works to destabilize the wall) and as it is classified as being Variable, the partial factors that are applied automatically are 1.5 for 1.5 DA1/1 and 1.3 for DA1/2 (see Figure 62.3).

Fixed Distributed Load	
Option	Fixed
Side	Left
Coordinate System	Local
Begin X (kN/m ²)	0
Begin Y (kN/m ²)	-10
End X (kN/m ²)	0
End Y (kN/m ²)	-10
Load Type	Unfavourable
Load Category	Variable

Figure 62.4: Settings for surcharge load behind wall.

The soil unit weight may be characterized analogously. For the present problem, the Load Category is Permanent meaning that the partial factor for DA1/2 is 1 regardless of whether it is deemed Favourable or Unfavourable. For DA1/1, the partial factor is 1.35 if it is deemed Unfavorable and 1 if it is deemed Favourable. One could argue for both classifications: on one hand, the soil weight has an obvious destabilizing effect on top part of the wall. On the other hand, the higher the stress level is on the lower part of the wall, the higher the shear strength, and thereby the resistance to failure, will be. However, for the present problem DA1/2 is the critical combination, regardless what is assumed with respect to the soil unit weight. This is usually the case for problems of this type.

62.3 Soil-wall interface strengths

According to EN1997-1, 9.5.1(6), the design interface friction angle, δ_d , between ground and steel sheet piling should not exceed $2/3\phi_d$ which is the value adopted in the following. The reduction factor of $2/3$ is most easily applied by selecting the Plate and applying the reduction factor as shown in Figure 62.5.

Interface +	
Material	Medium Sand-MC
Reduction Factor, r	0.6667
Interface -	
Material	Medium Sand-MC
Reduction Factor, r	0.6667

Figure 62.5: Application of soil-wall interface reduction factor.

62.4 Overdig

According to EN1997-1, 9.3.2.2(2), an overdig of 10% of the excavation depth (though not exceeding 0.5 m) should be accommodated. In other words, the wall should be designed for an excavation

depth of $3 \times 1.1 = 3.3$ m rather than the 3 m indicated in Figure 62.1.

62.5 Analysis

The minimum allowable embedment depth is found using Strength Reduction analysis. DA1/2 is chosen as the Design Approach under Safety in the Stage Manager (see Figure 62.2). In this way, the loads and soil strengths are first factored. The factored soil strength is then reduced to attain a state of collapse. The resulting strength reduction factor (SRF) reported by OPTUM G2 is calculated as:

$$\text{SRF} = \frac{\tan \phi_d}{\tan \phi_{\text{red}}} \quad (62.1)$$

where $\tan \phi_{\text{red}}$ is the reduced friction angle implying collapse and $\tan \phi_d$ is the design strength (calculated automatically on the basis of the characteristic strength and the relevant partial factor). As such, the aim of the analysis is to adjust the wall depth until a value of $\text{SRF} = 1$ is attained.

The wall depth is determined by trial and error, i.e. by first assuming a depth and then adjusting it according to the value of the strength reduction factor (increasing it for $\text{SRF} < 1$ and decreasing it for $\text{SRF} > 1$). For the present example, assuming $D = 5$ m and using 1,000 Lower bound elements with 3 adaptivity iterations results in

$$\text{SRF}_{LB} = 1.02 \quad (d = 5 \text{ m}) \quad (62.2)$$

This may well be deemed to be sufficiently close to 1 to not warrant any further adjustment of the wall depth. That the lower bound is close to the exact solution can be verified by subsequently running an upper bound analysis (Element Type = Upper). This results in

$$\text{SRF}_{UB} = 1.06 \quad (d = 5 \text{ m}) \quad (62.3)$$

In other words, the exact strength reduction factor is

$$\text{SRF} = 1.04 \pm 0.02 \quad (d = 5 \text{ m}) \quad (62.4)$$

This value suggests that a slight improvement is still possible. Subsequent analyses, using 10,000 elements, show that the embedment depth in fact can be reduced to $D = 4.9$ m. The collapse mechanism for this case is shown in Figure 62.6 along with the moment distribution in the wall. The maximum moment is found to be $M = 176$ kNm/m.

In conclusion, the design according to EC7 Design Approach 1 results in:

- Embedment depth of the wall of $d = 4.9$ m
- Design bending moment of the wall of $M = 176$ kNm/m

62.6 Workshop solutions

As part of the *International Workshop on the Evaluation of Eurocode 7* held at Trinity College, Dublin in 2005 from which this example originates, the participants were asked to submit solutions to the problem. These are shown in Figure 62.7. A variety of codes were used, as were the two other design approaches of Eurocode 7. The solutions based of DA1 are indicated by circled 1-symbols. A fairly good agreement between these solutions and the present one are observed.

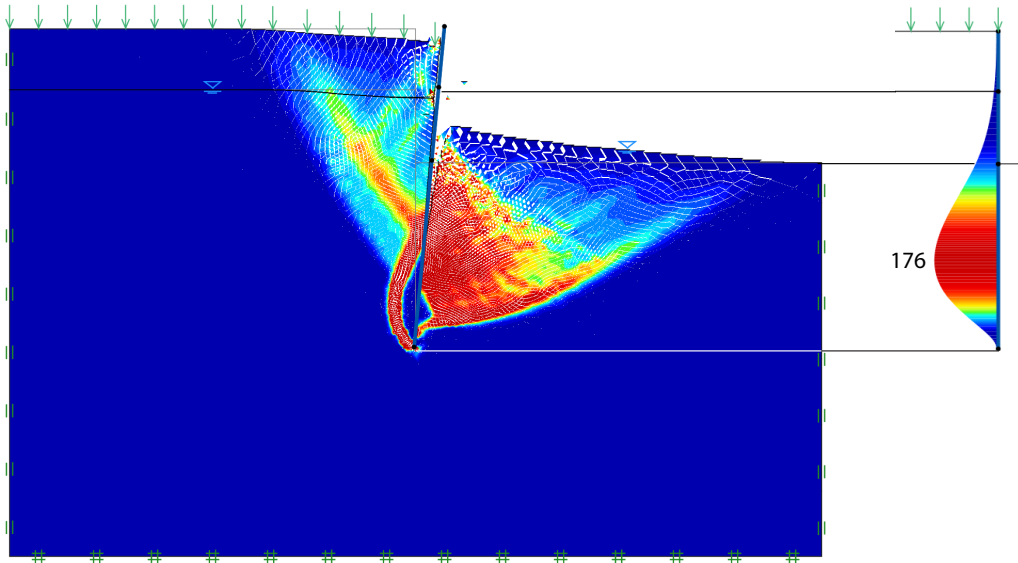


Figure 62.6: Collapse mechanism for $D = 4.9$ m using 10,000 Lower bound elements (right) and moment distribution in the wall (left).

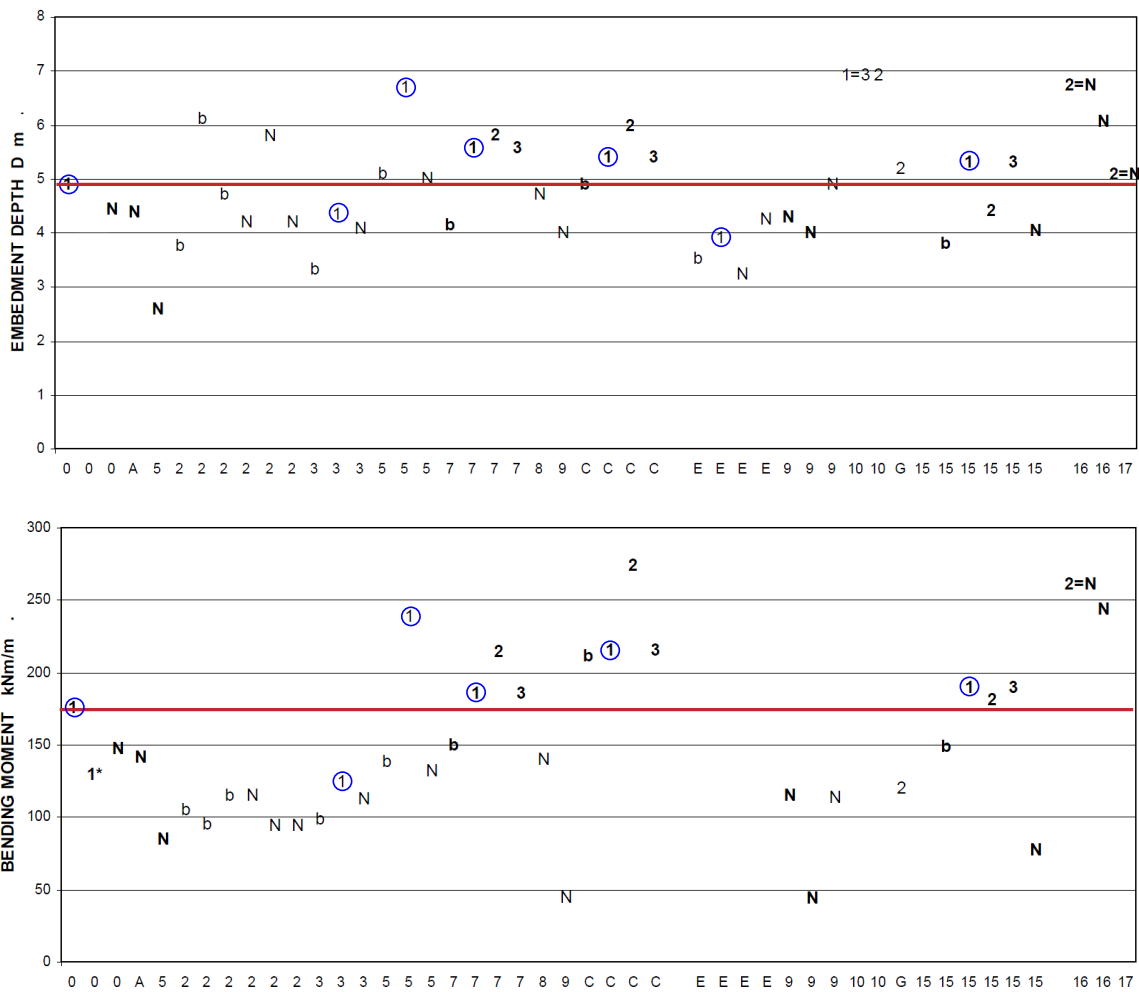


Figure 62.7: Workshop solutions (participant IDs on the horizontal axis) with the present OPTUM G2 solution shown in red. The circled 1-symbols indicate use of EC7 Design Approach 1.

62.7 Stochastic analysis

While the above design complies with the specifications of EC7, it is of interest to examine its sensitivity to the main uncertainty, namely the variability of the soil strength. Such an analysis can be carried out using the Random Field functionality of OPTUM G2. This type of analysis is discussed in detail in Sections 57-60.

In the following, the aim is to compute statistics (mean value, standard deviation, etc) for the ‘factor of safety’ which is defined as the strength reduction factor with respect to the characteristic friction angle

$$FS = \frac{\tan \phi_k}{\tan \phi_{red}} \tag{62.5}$$

where ϕ_{red} is the reduced angle implying a state of collapse. In addition, the variable surcharge load is factored by 1.3 consistent with the partial factor of DA1/2. Setting the Design Approach in the Stage Manager to Unity (all partial factors equal to 1), will then result in a factor of safety of $FS = 1.25$ in the deterministic case, i.e. with $\phi = \phi_k = 37^\circ$ throughout.

Following the guidelines of Phoon and Kulhawy (1999) the following random field parameters are used for the friction angle:

$$\begin{aligned} \text{Mean} &= 37^\circ \\ \text{COV} &= 10\% \\ \text{CL}_x &= 40 \text{ m} \\ \text{CL}_y &= 2 \text{ m} \end{aligned} \tag{62.6}$$

An example of a random field of ϕ generated on the basis of these parameters is shown in Figure 62.8.

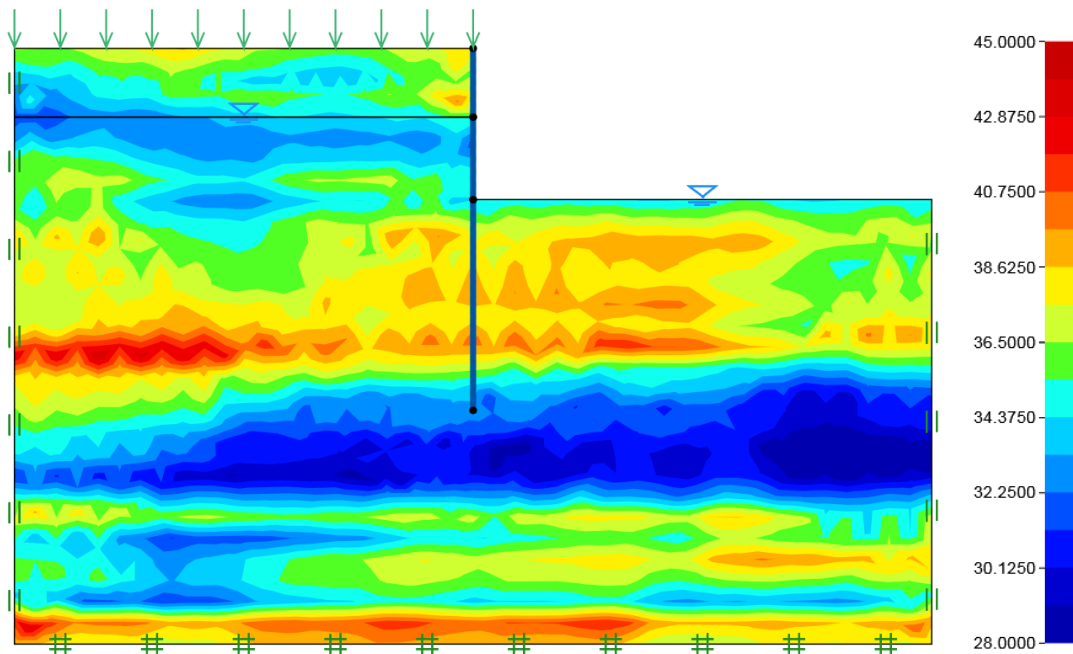


Figure 62.8: Random field of friction angle with Mean = 37°, COV = 10%, $CL_x = 40 \text{ m}$, $CL_y = 2 \text{ m}$.

The resulting probability and cumulative density functions are shown in Figure 62.9. These have been computed on the basis of 1,000 Monte Carlo simulations. Upper and lower bound analysis

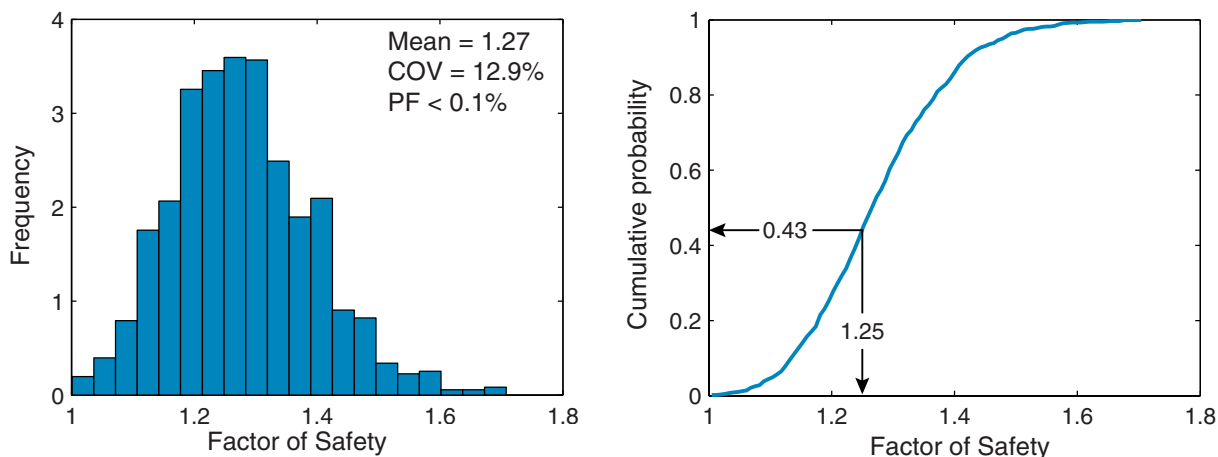


Figure 62.9: PDF (left) and CDF (right) for cantilever sheet pile wall.

were conducted, each with 1,000 elements and 3 adaptivity iterations. The values shown in the figure are the mean values between these (which come with a worst case error of about ± 0.03). We see that the output mean and COV correspond roughly to the input, though they are slightly more favorable, i.e. a mean FS of 1.27 versus a value of 1.25 in the deterministic case. In the course of the 1,000 Monte Carlo simulations, no instances of $FS < 1$ were recorded. Hence, we can conclude (somewhat loosely) that the probability of failure is less than 0.1%.

63 ULS DESIGN OF ANCHORED SHEET PILE WALL TO EUROCODE 7

The following example is from the same workshop as the example of the previous section. The soil is sand with a characteristic friction angle of $\phi_k = 35^\circ$ and unit weights of 18 kN/m^2 and 20 kN/m^2 above and below the ground water table respectively. The difference in water level between the left and right hand sides of the wall (resulting from a tidal lag) gives rise to seepage that is resolved automatically by OPTUM G2 as part of the mechanical calculations. A variable surcharge load of 10 kN/m^2 acts on ground surface behind the wall.

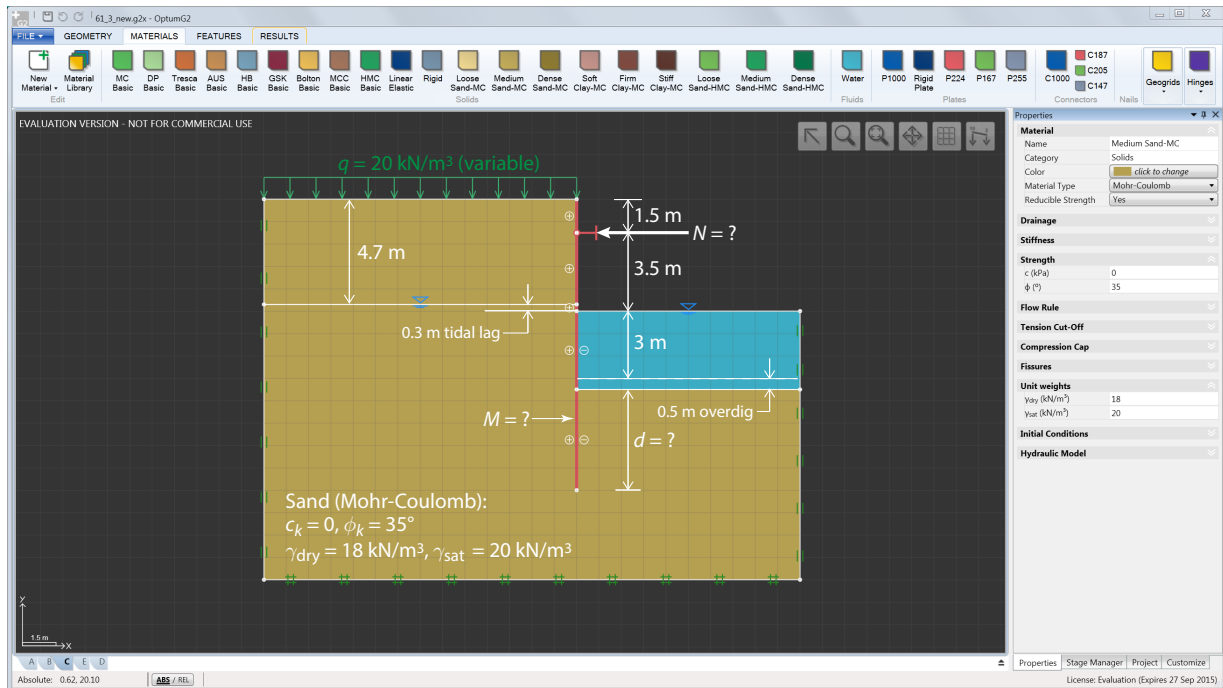


Figure 63.1: Anchored sheet pile wall.

The problem involves three design variables:

- The embedment depth of the wall, d
- The design bending moment of the wall, M
- The design anchor force, N

As discussed in the paper of Simpson, this situation offers numerous possible designs. Generally speaking, for a given admissible wall depth, there is an infinite number of combinations of design bending moment and anchor force that satisfy the relevant conditions at the ultimate limit state (equilibrium, yield conditions, etc). In the following, a general procedure for generating admissible combinations of moment and anchor force for a given wall depth is described. In all cases, Design Approach 1 Combination 2 (DA1/2) of Eurocode 7 (EC7) is used (this being the more critical of the two combinations).

63.1 Partial factors

The application of partial factors is described in detail in the previous example.

63.2 Loads

As in the previous example, the variable surcharge is recognized as being Unfavourable. All other loads are categorized as Favourable, meaning that a partial factor of 1 will be applied.

63.3 Soil-wall interface strengths

As in the previous example, an interface friction angle of $\delta = 2/3\phi$ is used between the soil and the wall.

63.4 Overdig

According to EN1997-1, 9.3.2.2(2), the excavation should be extended by 10% of the distance from the lowest anchor to the bottom of the excavation, though not exceeding 0.5 m. For the present problem, the distance between the anchor and the bottom of the excavation is 6.5 m and hence the excavation is extended by 0.5 m as indicated in Figure 63.1.

63.5 Analysis

As in the previous example, the analyses are based on Strength Reduction. However, in contrast to the previous example where the soil strengths were reduced to induce a state of collapse, the strength of the structural elements (wall and anchor) are now reduced. This requires that Reduce Strength is set to Structs under Settings in the Stage Manager (see Figure 63.2).

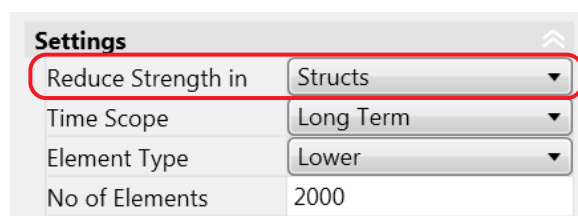


Figure 63.2: Reduce Strength in Structs option for Strength Reduction analysis.

The analyses are carried out by first estimating a wall embedment depth that, for sufficiently large, wall yield moment and anchor strengths will be admissible. This depth is taken as 5 m. For this depth, there exists an infinite number of combinations of wall yield moment and anchor strength leading to a design that satisfies the conditions of the ultimate limit state. For example, for a large wall yield moment, the necessary anchor force can be reduced and vice versa. To determine a representative range of possible solutions, the following approach is employed:

1. The anchor is first modeled as a rigid support (Plate BC) while the wall is ascribed a finite yield moment. A Strength Reduction analysis with Reduce Strength in Structs is then performed. The resulting moment and anchor force correspond to point A in Figure 63.3.
2. Next, the wall is modeled as Rigid while a Fixed End Anchor of finite strength is used to model the anchor. The resulting moment and anchor correspond to point B in Figure 63.3.
3. The next point on the curve, point C, is found by using both wall and anchor of finite strength. The yield moment and anchor strengths are taken as the average of those of points A and B.

4. Further points may be generated in the same way by using appropriate yield moments and anchor strengths, e.g. point D (average of A and C) and point E (average of A and B).

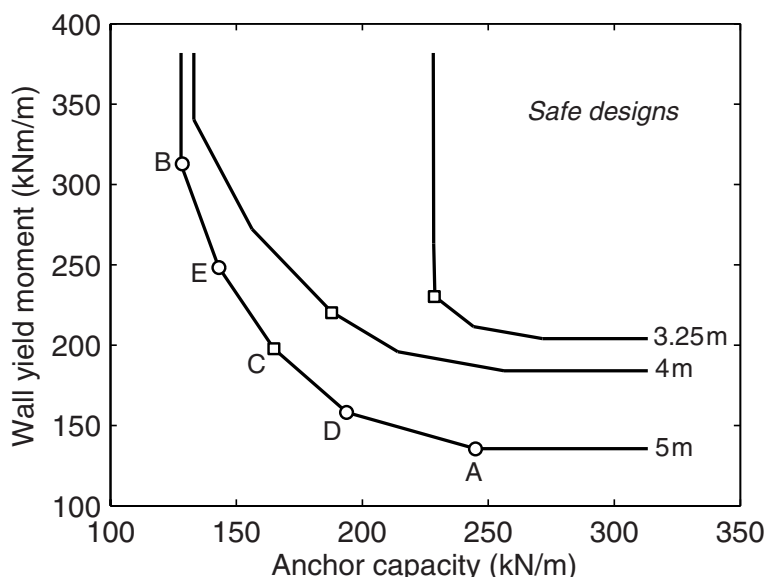


Figure 63.3: Yield envelopes for walls with embedment depths of $d = 3.25, 4$ and 5 m.

The resulting yield envelope, along with those for $d = 4$ m and $d = 3.25$ m, are shown in Figure 63.3. The depth of 3.25 m is close to the minimum attainable. For this depth, the yield envelope is close to a shape which effectively means that the yield moment and anchor strength are limited independently of each other.

The collapse mechanism corresponding to points A, B and C are shown in Figure 63.4. While points A and B involve only wall and anchor failure respectively, point C involves a combination of the two.

63.6 Workshop solutions

As part of the workshop of which this problem was considered, the participants were asked to submit solutions to the problem. These are shown in Figure 63.5 together with the present solutions corresponding to point C in Figure 63.3 (for depths of 3.25 m and 4 m the point is indicated by a square).

A variety of codes were used, as were the two other design approaches of Eurocode 7. The solutions based on DA1 are indicated by circled 1-symbols. A fairly good agreement between these solutions and the present one is observed. It is noted, though, that the present anchor forces generally tend to be somewhat larger than those submitted to the workshop. As discussed by Simpson, a number of common hand calculation methods underestimate the anchor forces significantly. This is a particular concern when there is risk of brittle rupture in the anchors of struts. In this regard, it is noted that the anchor forces obtained with OPTUM G2 rely on the basic assumption of ductile plasticity. Under this assumption, which is common to all methods in practical use, the anchor forces determined using Lower bound elements are 'safe' (and if a sufficient number of elements is used, close to the exact ones). In other words, unlike a range of commonly used hand calculation methods (many of which have been automated in the form of specialized software applications), there is no systematic underestimate of the anchor forces.

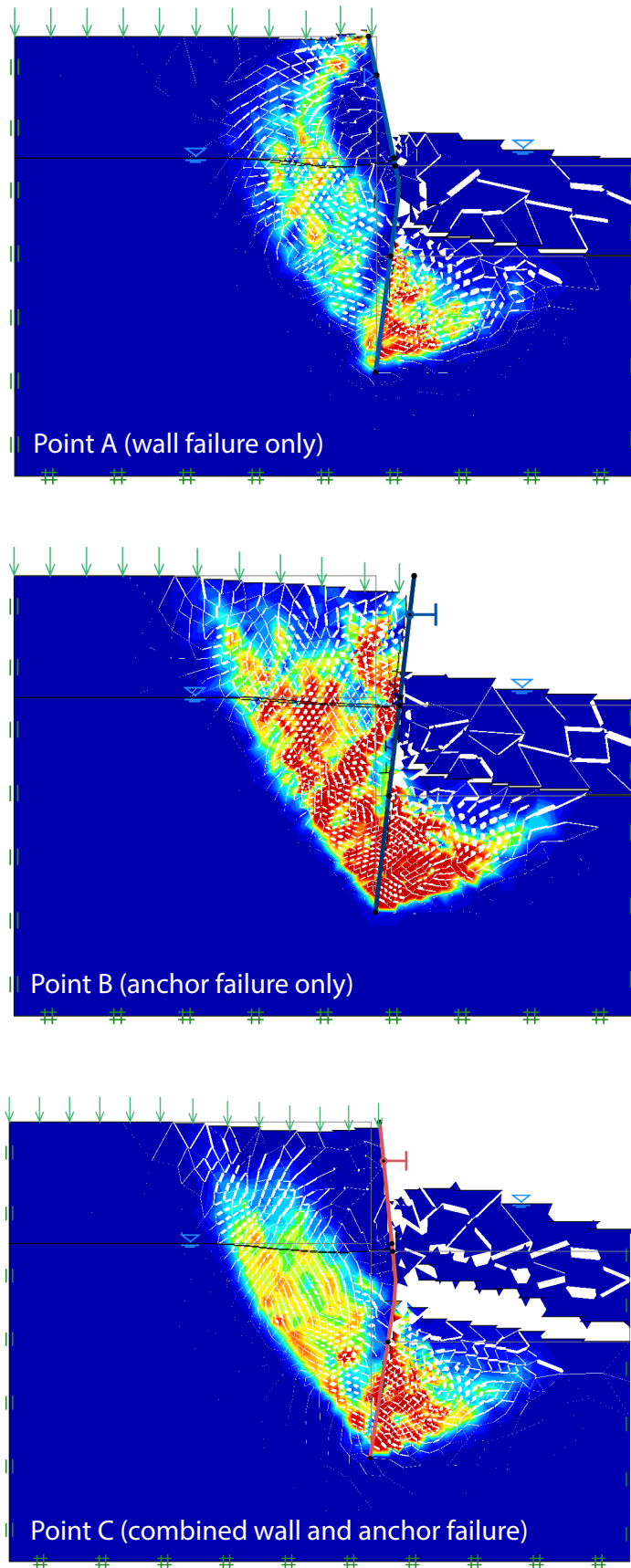


Figure 63.4: Collapse mechanism for points A, B and C.

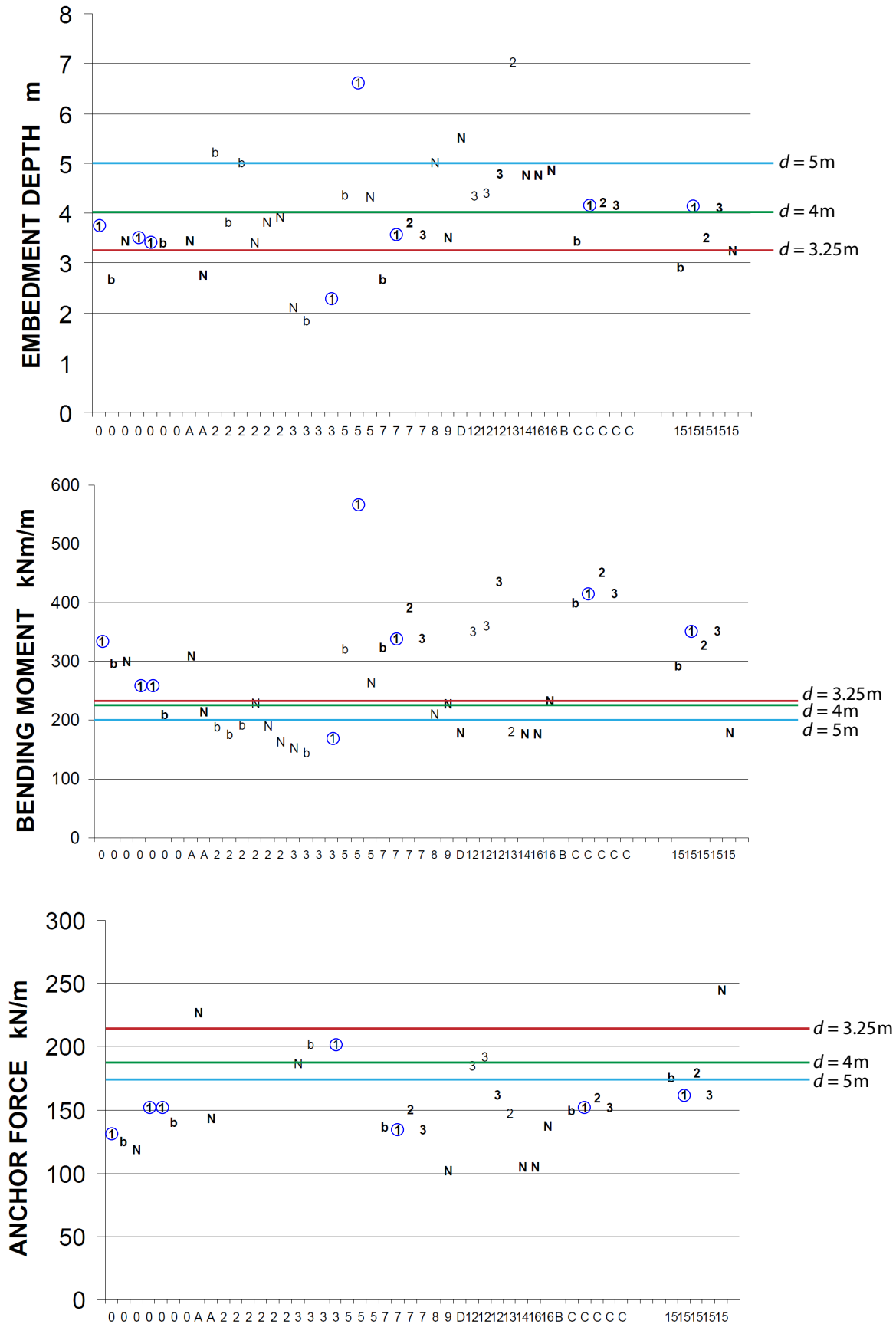


Figure 63.5: Workshop solutions (participant IDs on the horizontal axis) with the present OPTUM G2 solution shown in red. The circled 1-symbols indicate use of EC7 Design Approach 1.

63.7 Sensitivity analysis

For a given design, the ‘factor of safety’ may be defined as the partial factor applied to the soil strength, in the present case $FS = 1.25$. For a given embedment depth, an infinite number of designs, given by a combination of wall yield moment and anchor capacity, are possible. These all imply a factor of safety equal to 1.25. As such, it could be argued that these designs are equally apt and that economical considerations alone would distinguish one from another. That is, with reference to Figure 63.3, in some cases Design A (small moment, large anchor force) might be preferred over Design B (large moment, small anchor force) or an intermediate solution such as Design C might be the economically most favorable.

Besides economy, however, there is another consideration, namely the safety – or sensitivity – of a given design to the wall moment and anchor capacity. As a measure of this safety, the following quantities are introduced:

$$FS_M = \frac{M}{M_{red}} \quad \text{and} \quad FS_N = \frac{N}{N_{red}} \quad (63.1)$$

where M_{red} is the wall yield moment implying collapse, with all other quantities held constant, and N_{red} is the anchor capacity implying collapse with all other quantities held constant. The two new factors of safety, FS_M and FS_N can be visualized by determining the full yield moment–anchor capacity curves for different soil partial coefficients (or conventional factors of safety, FS). This family of curves is shown in Figure 63.6 for an embedment depth of 4 m.

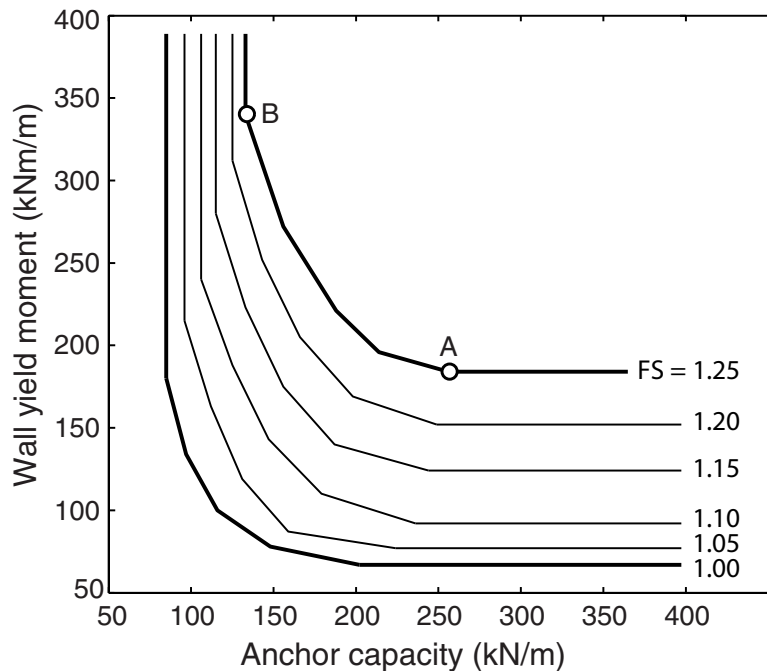


Figure 63.6: Yield envelopes for wall with $d = 4$ m.

We here see than Design A appears to have a significantly smaller safety with respect to the anchor capacity than Design B. The actual numbers are:

$$\begin{aligned} FS_N &= 3.01 \quad \text{for Design A} \\ FS_N &= 1.57 \quad \text{for Design B} \end{aligned} \quad (63.2)$$

On the other hand, both designs appear to have a relatively large safety with respect to the wall yield moment:

$$\begin{aligned}FS_M &= 2.75 \quad \text{for Design A} \\FS_M &= 3.86 \quad \text{for Design B}\end{aligned}\tag{63.3}$$

This sensitivity to particularly the anchor capacity may enter into the considerations when deciding on a suitable design, especially in cases where the plastic ductility of the anchor is questionable.

64 REINFORCED SOIL RETAINING WALL

The following example deals with a reinforced soil retaining wall as shown in Figure 64.1. The soil reinforcement is modeled using Geogrids with a strength of 45 kN/m and is clamped between the blocks comprising the wall. The interface friction angle between the blocks and the geogrid is 25°. For the soil-geogrid interface, a reduction factor of $r = 0.85$ is used.

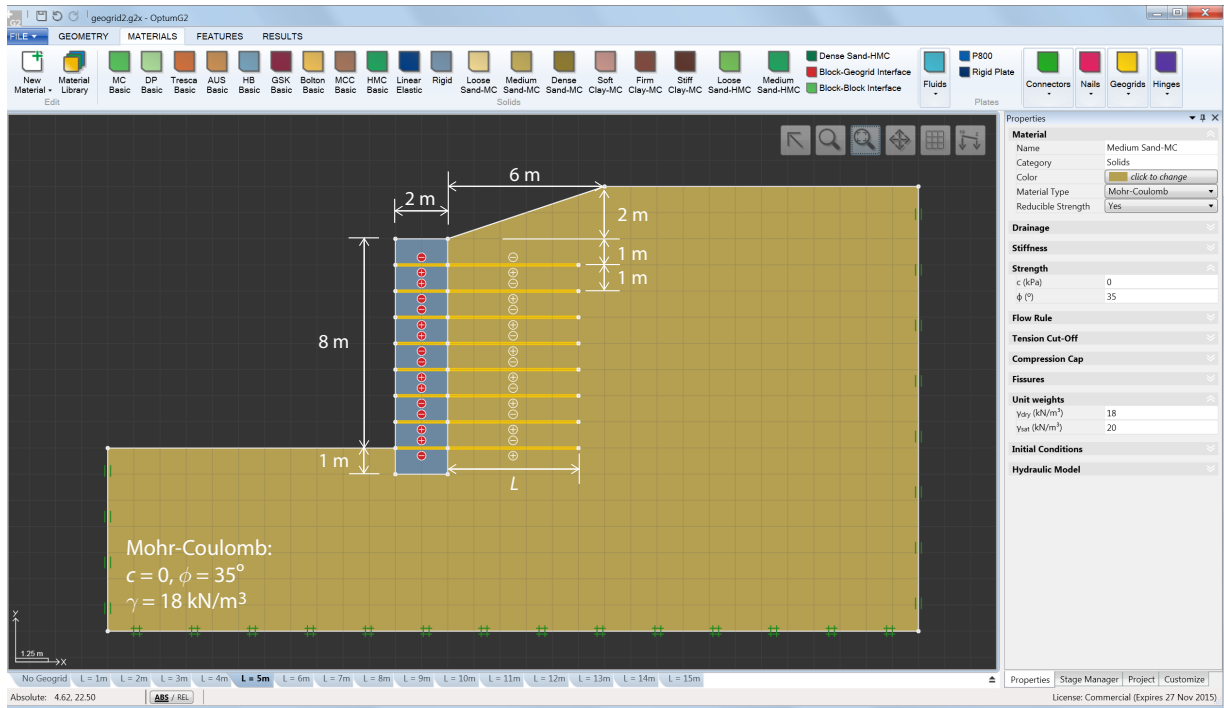


Figure 64.1: Reinforced soil retaining wall.

Two cases are considered: the standard static one as shown in Figure 64.1 and a case with seismic coefficient equal to $k = g_h/g_v = 0.1$, $g_v = 9.8 \text{ m/s}^2$ and g_h being the vertical and horizontal accelerations respectively.

Strength Reduction analysis is used to determine the factor of safety as function of the geogrid length, L . In all cases, 10,000 upper and lower bound elements are used with 3 adaptivity iterations. In the seismic case, Fixed Body accelerations are applied (see Figure 64.2).

Fixed Body Load	
Option	Fixed
Units	Acceleration
X (x g)	-0.1
Y (x g)	0
Load Type	Unfavourable
Load Category	Variable

Figure 64.2: Application of fixed horizontal accelerations. The two last categories (Load Type and Load Category) are related to the application of partial factors and are not relevant to the present analysis.

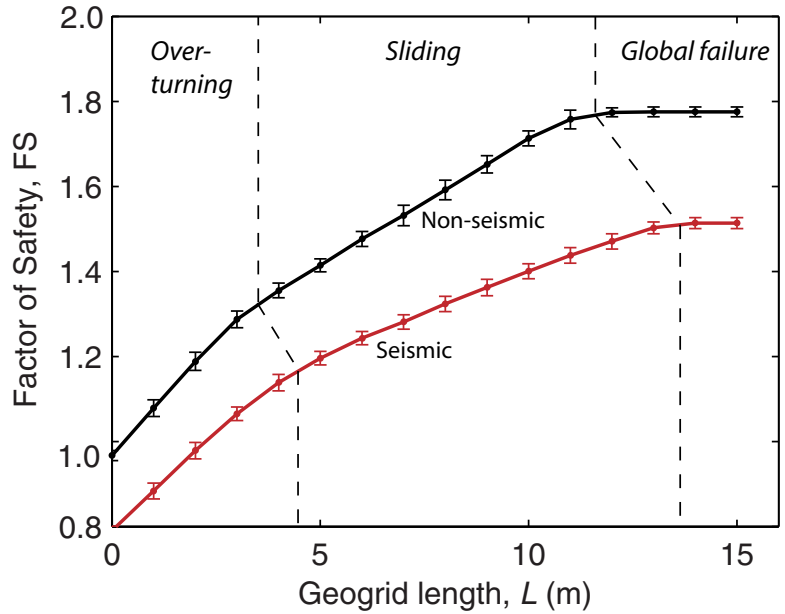


Figure 64.3: Factor of safety versus geogrid length with error bars indicating the worst case error between upper and lower bound solutions.

The results in terms of factor of safety versus geogrid length are shown in Figure 64.3. For both the seismic and non-seismic cases, three distinct regimes are observed. For small geogrid lengths, the mode of failure is overturning of the wall. For intermediate lengths, the failure is dominated by horizontal sliding of the wall. And for large enough lengths, the failure is via a global instability. At this point, further increase of the geogrid length has no influence on the factor of safety. Examples of the three types of failure modes are shown in Figure 64.4.

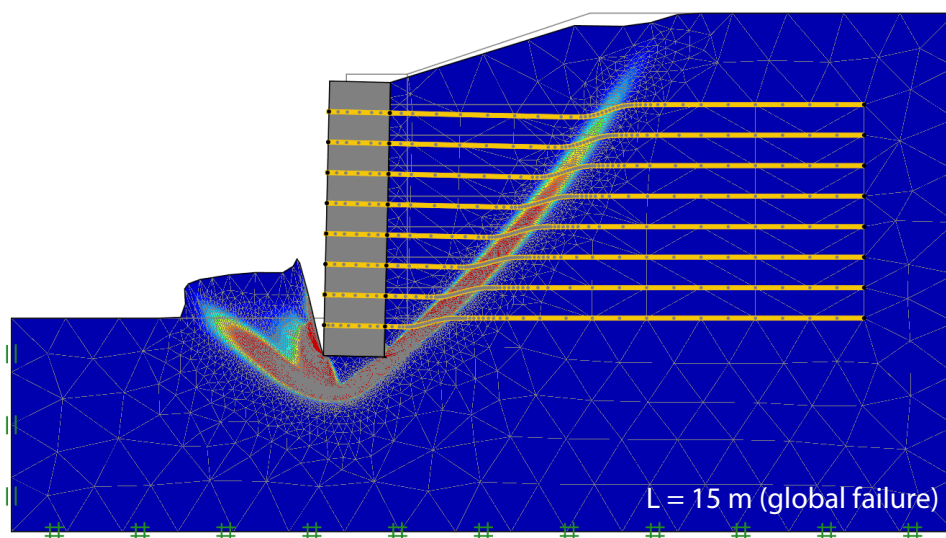
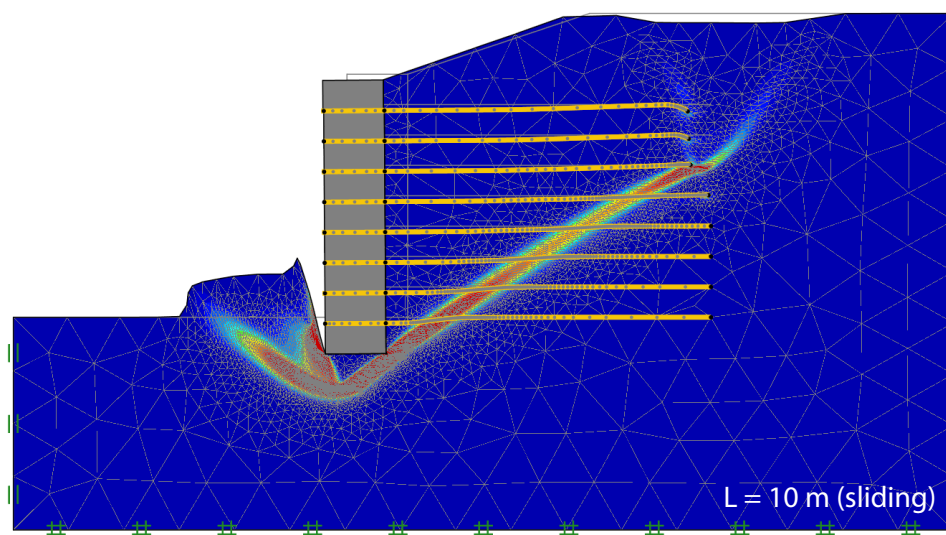
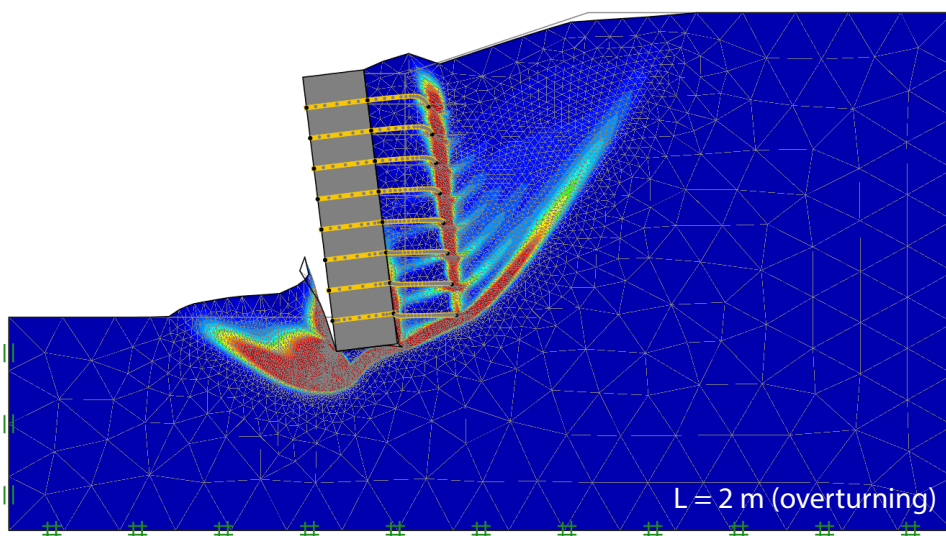


Figure 64.4: Reinforced soil retaining wall (non-seismic case).

65 MODELING PLATES AND SHELLS USING SOLIDS

In some cases, it is necessary to model walls, foundations and similar structures using solid finite element rather than Plate elements. At the same time, however, the sectional forces (moment bending moments and normal and shear forces) are often needed. In OPTUM G2, these may be inferred using the Result Section tool. This feature, which can be applied to Lines, may be thought of as a kind of “virtual plate” – on the basis of the stresses in the solid elements, sectional forces (normal force, bending moment, etc) are calculated as shown in Figure 65.2.

The following examples demonstrate the use of the Result Section tool on three problems with known analytical solutions (see Figure 65.1). The solutions (see Timoshenko and Woinowsky-Krieger 1959) all rely on the assumption that the thickness t is negligible in comparison to the other dimensions (length, height, out-of-plane width).

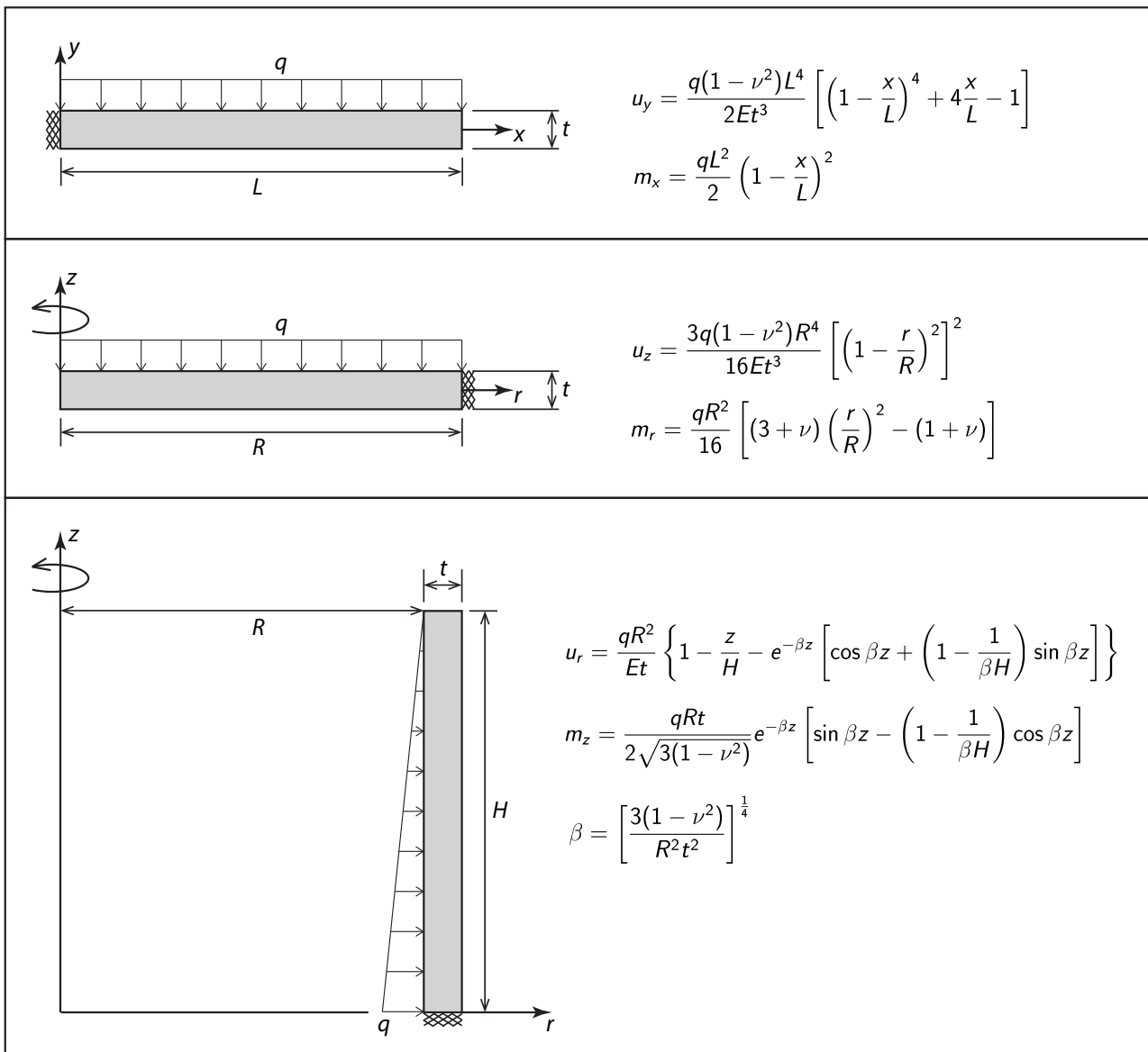


Figure 65.1: Test problems: cantilever plate (top), clamped circular plate (center), and clamped cylindrical tank (bottom).

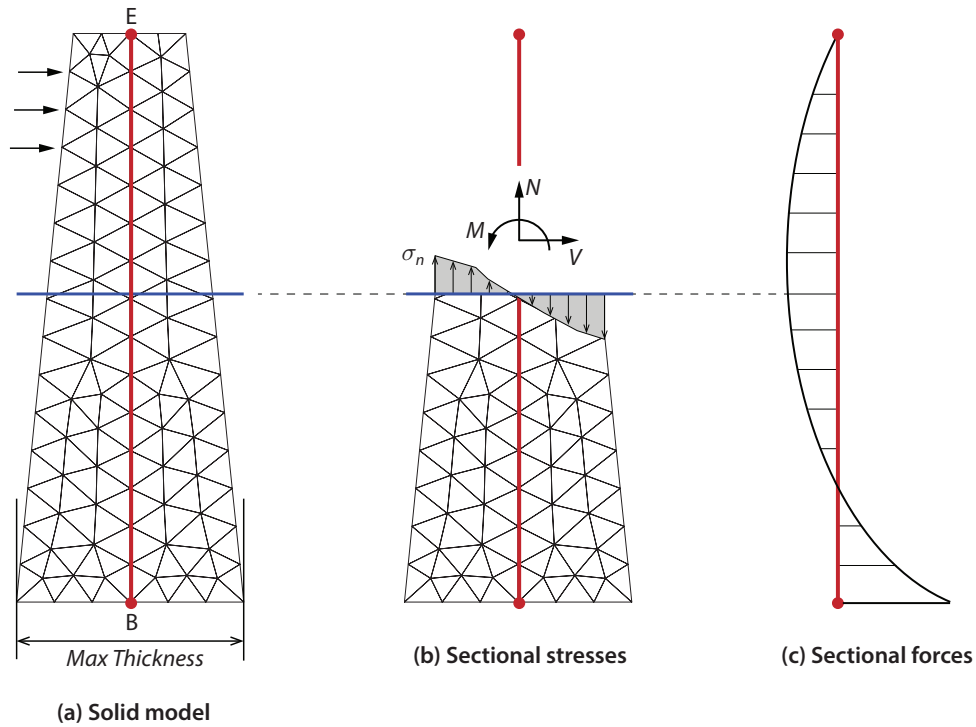


Figure 65.2: Extraction of sectional forces from solid model.

To extract the relevant sectional forces, the Result Section is applied in the center of cross section as shown in Figure 65.3 for the circular plate.

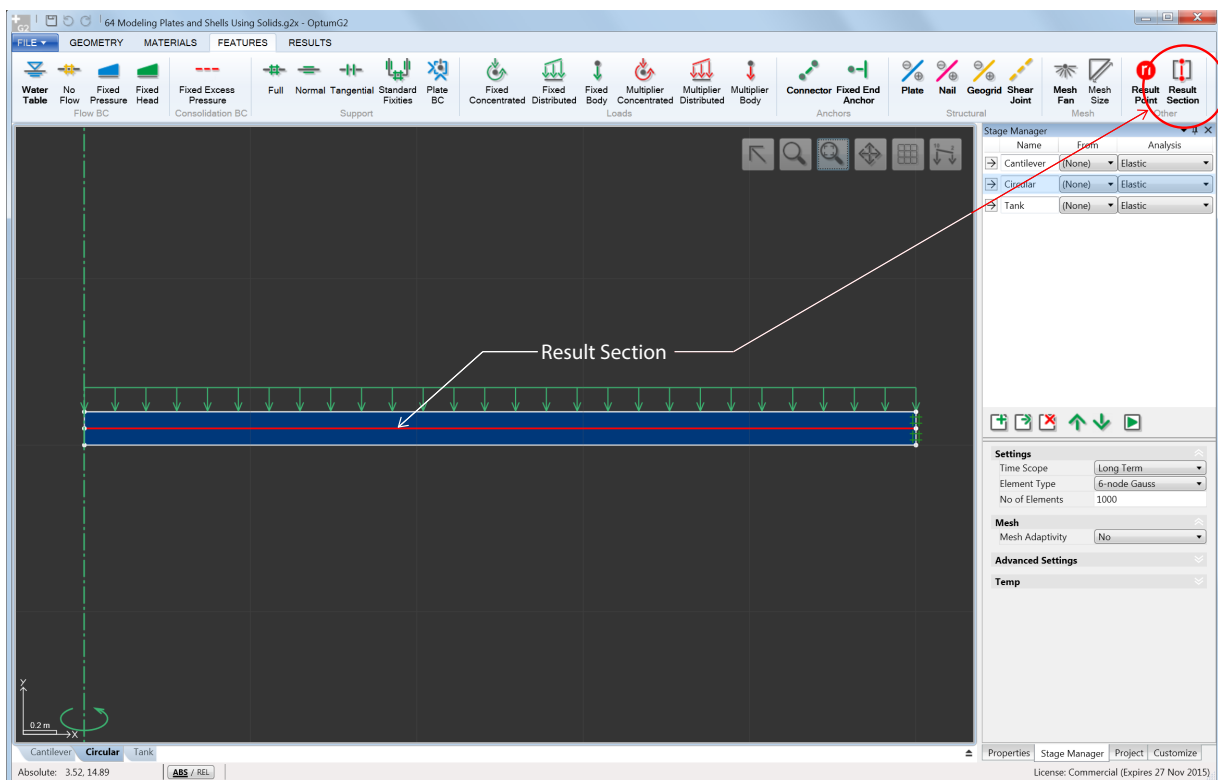


Figure 65.3: Result Section applied to circular plate.

The data used for the three test problems are given in Table 65.1

	Cantilever Plate	Circular Plate	Cylindrical Tank
E (MPa)	30,000	30,000	4.0606
ν	0.25	0.25	0.25
t (m)	0.2	0.2	0.2
L (m)	10	-	-
R (m)	-	5	5
H (m)	-	-	5
q (kN/m ²)	-17.067	-2184.5	50

Table 65.1: Data for test problems.

The results of the analyses are shown in Figure 65.4-5. We see that the agreement between the analytical and numerical solutions in all three cases is very good. For the cylindrical tank the deviation is mainly due to the fact that the thickness of the cross section (which in the analytical solution is assumed infinitesimal) influences the geometry of the problem, i.e. in the numerical solution the distance from the symmetry axis to the center line is $R + \frac{1}{2}t$ rather than R as in the analytical solution.

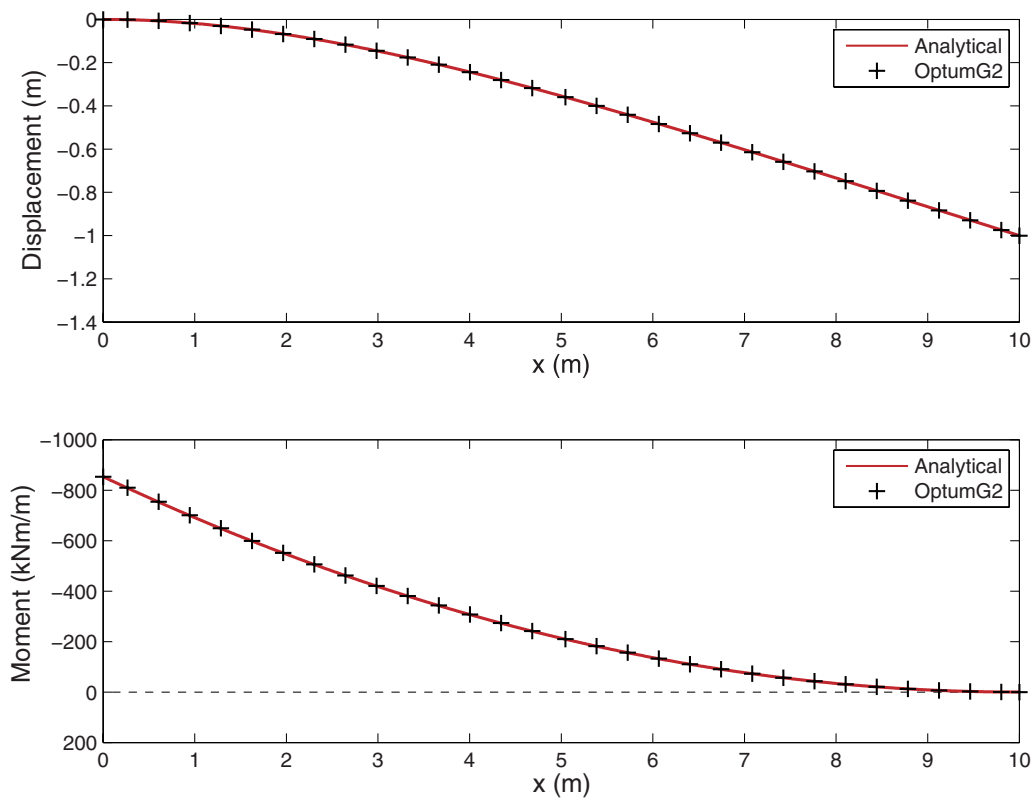


Figure 65.4: Cantilever plate: displacements and bending moments.

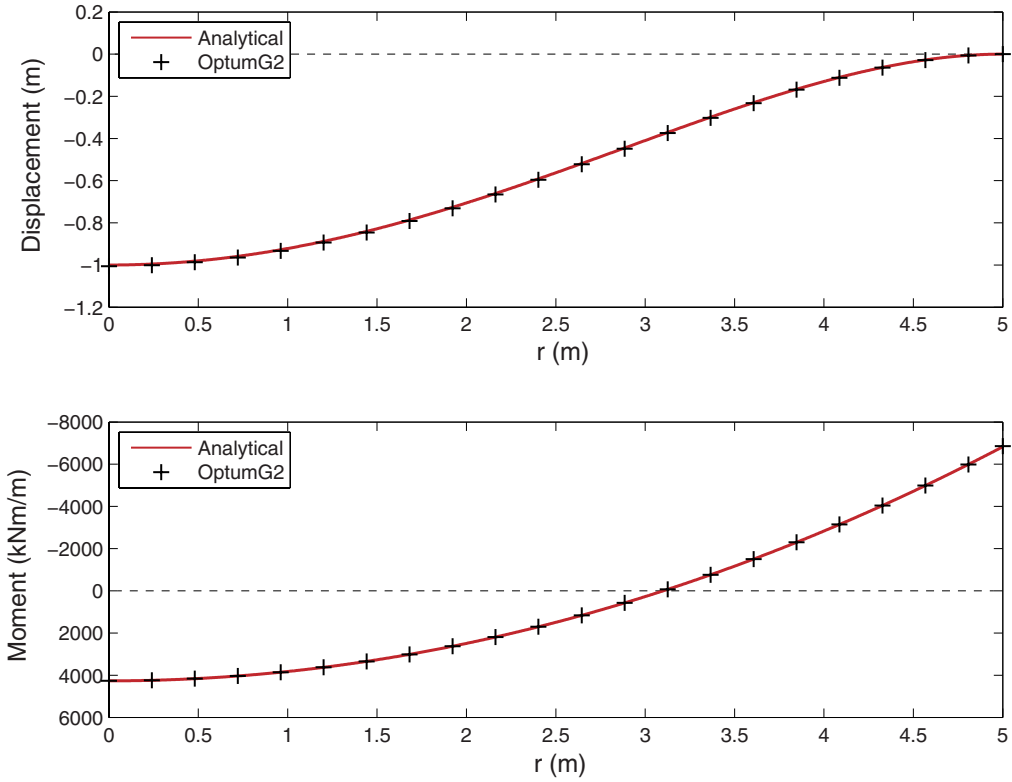


Figure 65.5: Circular plate: displacements and bending moments.

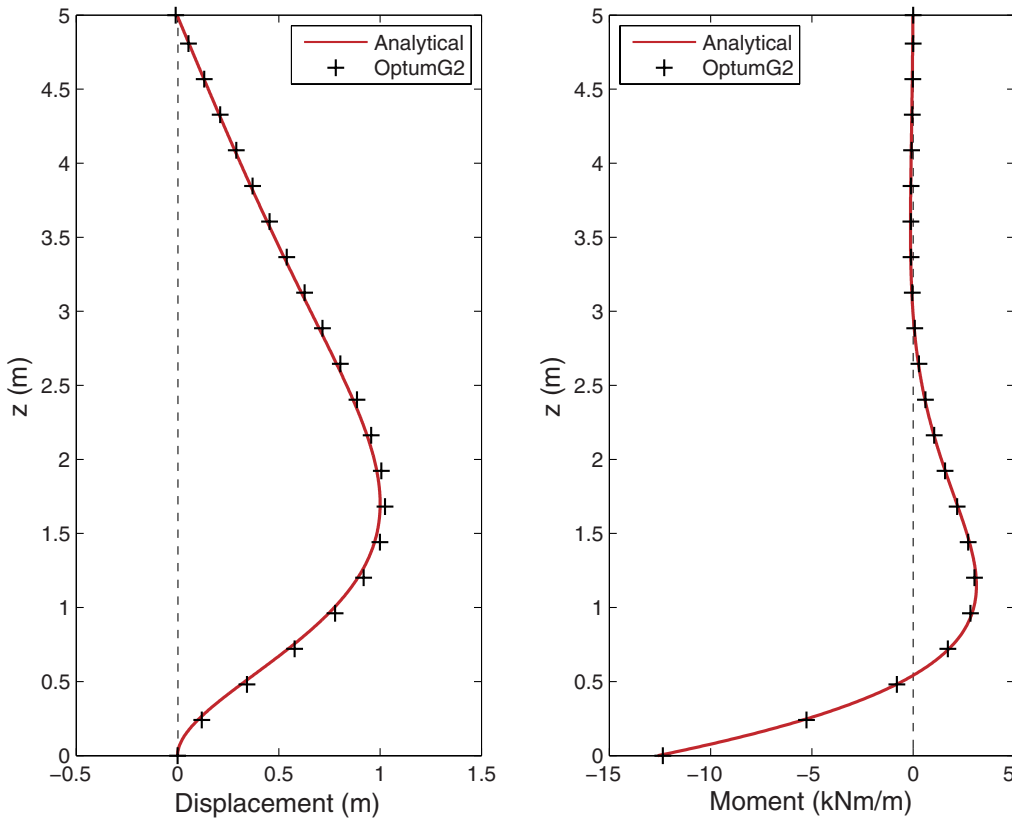


Figure 65.6: Cylindrical tank: displacements and bending moments.

66 BEARING CAPACITY OF FOOTING IN UNSATURATED SLOPE

The following example considers the effect soil suction on the long term bearing capacity of a footing in a slope as shown in Figure 66.1. The location of the water tables imply a seepage from left to right and a unsaturated zone above the phreatic surface (which is to be determined as part of the calculation). The soil is the default Firm Clay-MC materials ($c = 10\text{ kPa}$, $\phi = 22^\circ$). The van Genuchten hydraulic model with parameters $n = 0.9$ and $n = 1.5$ is used. To examine the effects of including soil suction in the calculations, the effective stress under Project is set to either Terzaghi or Bishop as shown in the bottom right corner in the figure below.

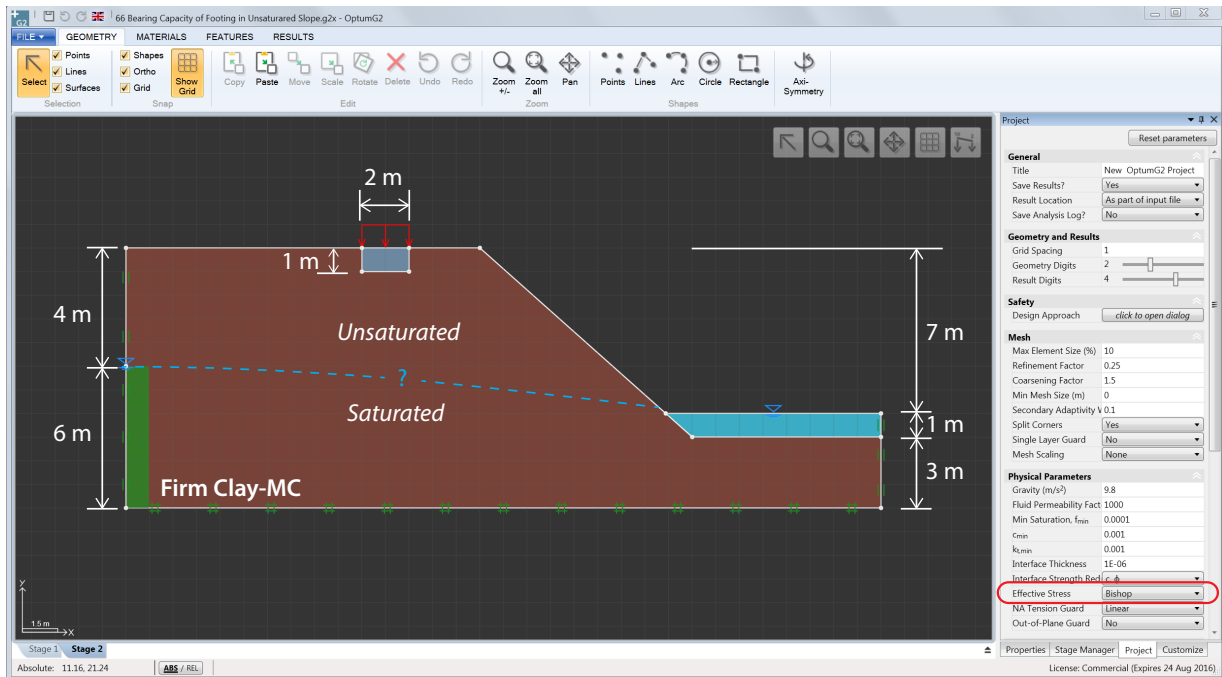


Figure 66.1: Footing in unsaturated slope.

With the Terzaghi option, the effective stress is given by

$$\sigma' = \sigma - \mathbf{m} \min(0, p_s) \quad (66.1)$$

where σ is the total stress and $\mathbf{m} = (1, 1, 1, 0, 0, 0)^T$. That is, soil suction ($p_s > 0$) is ignored.

With the Bishop option, the effective stress is given by:

$$\sigma' = \sigma - S_e \mathbf{m} p_s \quad (66.2)$$

where S_e is the effective saturation as defined in the van Genuchten model (see the Materials Manual). In this example, where the residual saturation is zero and the maximum saturation is 1, the effective saturation is equal to the usual saturation.

Considering now the Mohr-Coulomb failure model:

$$F = |\sigma_1 - \sigma_3| + (\sigma'_1 + \sigma'_3) \sin \phi - 2c \cos \phi \quad (66.3)$$

we have

$$F = |\sigma_1 - \sigma_3| + (\sigma_1 + \sigma_3) \sin \phi - 2c_{\text{eff}} \cos \phi \quad (66.4)$$

where

$$c_{\text{eff}} = c + S_e p_s \tan \phi \quad (66.5)$$

That is, for $p_s > 0$, the effect of suction can be thought of as an increase in soil cohesion of magnitude $S_e p_s \tan \phi$. In OPTUM G2, the quantity $S_e p_s$, for $p_s > 0$, is denoted the suction stress, σ_s , and is available under Results.

Running upper and lower bound limit analysis with 10,000 elements and 3 adaptivity iterations, the bearing capacity in the two cases are found to be:

$$\begin{aligned} \text{Terzaghi : } & q_u = 48.1, \text{ kN/m}^2 \pm 6.1\% \\ \text{Bishop : } & q_u = 87.9, \text{ kN/m}^2 \pm 3.5\% \end{aligned} \quad (66.6)$$

In other words, the effect of suction is an increase in bearing capacity by some 80%.

The distributions of the degree of saturation and the suction stress for the Bishop case are shown in the figures below.

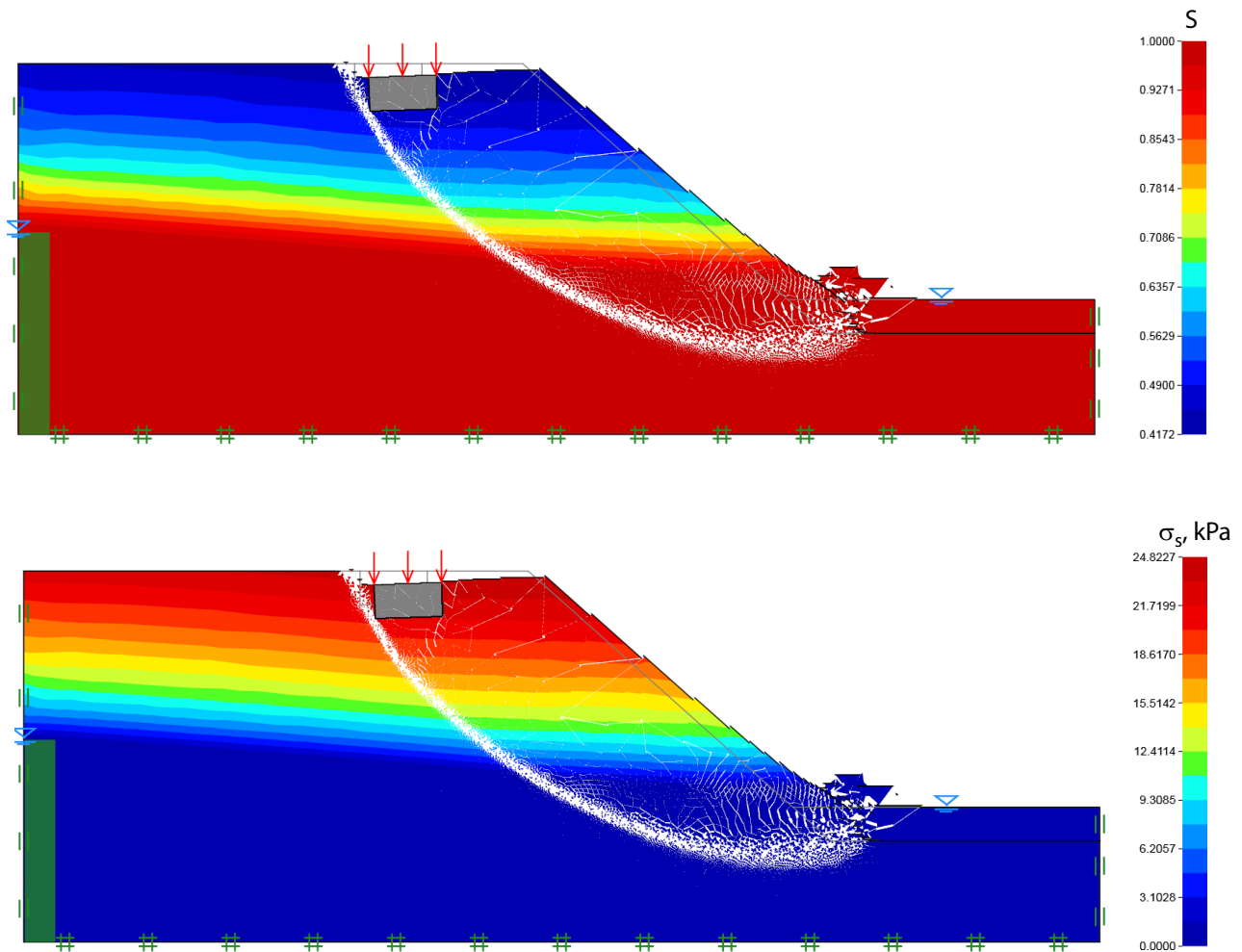


Figure 66.2: Degrees of saturation (top) and suction stress (bottom) with the displacements at collapse.

67 PILE ROWS – INTRODUCTORY EXAMPLE

The following example introduces the Pile Rows feature available in OPTUM G2. A single pile row as shown in Figure 67.1 is considered. The piles extend to a depth of 14 m through a 6 m layer of clay modeled as a Tresca material overlying a 12 m layer of sand modeled as a Mohr-Coulomb material. The piles are of the Massive Circular type with a diameter of 0.5 m, unit weight of 25 kN/m³ and Young’s modulus of 20,000 MPa. The out-of-plane spacing is 2 m.

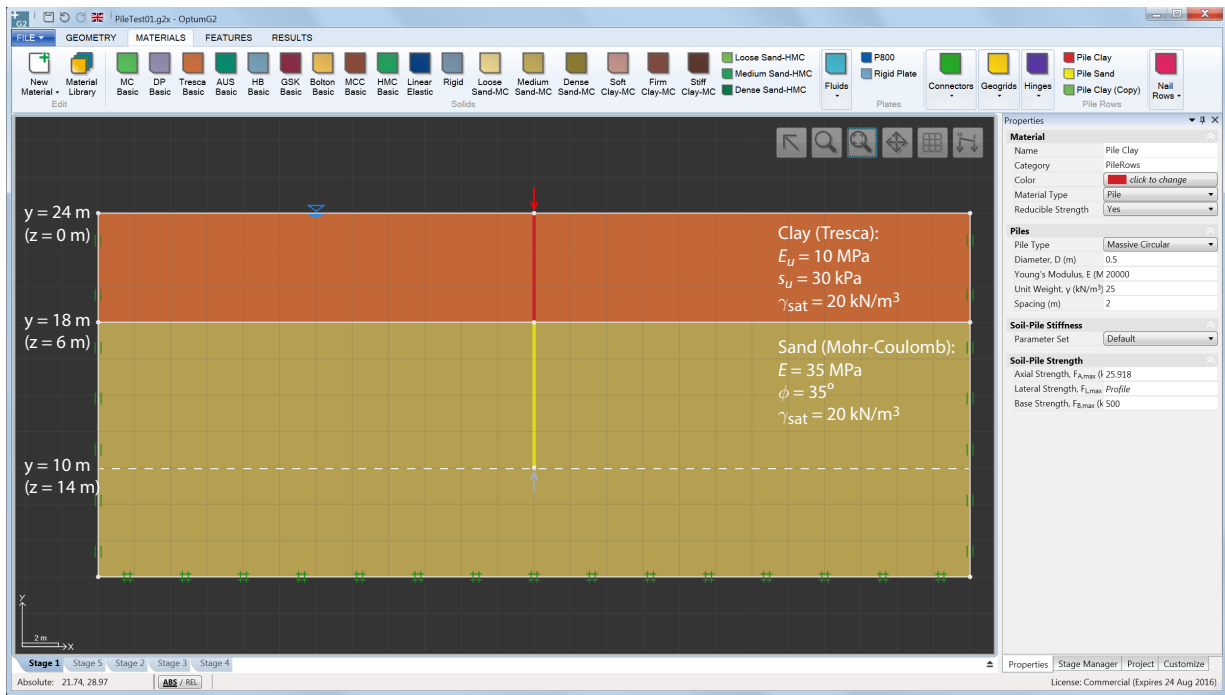


Figure 67.1: Deep foundation modeled using Pile Rows.

The soil-pile strength parameters are chosen on the basis of well known expressions summarized in Table 67.1. Since the piles traverse two soil layers, it is necessary to use two different pile row materials. The parameters are calculated as shown in the following.

Clay

For the clay layer, the axial skin strength is given by

$$\begin{aligned}
 F_{A,max} &= \alpha s_u \times P \\
 &= 0.55 \times 30 \times \pi \times 0.5 \\
 &= 25.9 \text{ kN/m}
 \end{aligned}
 \tag{67.1}$$

The lateral strength varies from

$$\begin{aligned}
 F_{L,max} &= [3 + \sigma'_v/s_u + Jz/D] \times s_u \times D \\
 &= [3 + 0/s_u + J \times 0/D] \times 30 \times 0.5 \\
 &= 45 \text{ kN/m at } y = 24 \text{ m (} z = 0 \text{ m)}
 \end{aligned}
 \tag{67.2}$$

Soil Type	Axial Strength	Factors	Reference
Clay	$F_{A,\max} = \alpha s_u \times P$	$\alpha = \min \{0.55, 0.70 - s_u/1000\}$	O'N & R (1999)
Sand	$F_{A,\max} = K_0 \sigma'_v \tan \delta \times P$	$\delta = \text{soil-pile interface friction angle}$ $K_0 = \text{earth pressure coefficient}$	API (2000)
Soil Type	Base Strength	Factors	Reference
Clay	$F_{B,\max} = N_c s_u \times A$	$N_c = 9$	API (2000)
Sand or clay	$F_{B,\max} = N_q \sigma'_v \times A$	$N_q = (\tan \phi + \sqrt{1 + \tan^2 \phi})^2 \exp(2\Psi \tan \phi)$ $\Psi = 1 \text{ (loose/soft soils) to } 1.8 \text{ (dense/hard soils)}$	Janbu (1976)
Soil Type	Lateral Strength	Factors	Reference
Clay	$F_{L,\max} = \alpha_L s_u \times D$	$\alpha_L = \min(3 + \sigma'_v/s_u + Jz/D, 9)$ $J = 0.25 \text{ to } 0.5 \text{ (empirical constant)}$	API (2000)
Sand	$F_{L,\max} = \beta_L \sigma'_v \times D$	$\beta_L = \min(C_1 z/D + C_2, C_3)$ $C_1 = \exp(-2.5 \tan^2 \phi + 6.9 \tan \phi - 2.5)$ $C_2 = \exp(-1.6 \tan^2 \phi + 4.1 \tan \phi - 0.84)$ $C_3 = \exp(-2.0 \tan^2 \phi + 7.9 \tan \phi - 0.58)$	API (2000)

Table 67.1: Sample of expressions for axial, base and lateral soil-pile strengths. D = pile diameter, P = pile perimeter, A = pile cross sectional area, z = depth from surface, σ'_v = vertical effective stress (positive in compression). Expressions for factors C_1 , C_2 , C_3 are fits to curves in Figure 6.8.6-1 of API (2000).

to

$$\begin{aligned}
 F_{L,\max} &= [3 + \sigma'_v/s_u + Jz/D] \times s_u \times D \\
 &= [3 + (20 - 9.8) \times 6/30 + 0.25 \times 6/0.5] \times 30 \times 0.5 \\
 &= 120.6 \text{ kN/m at } y = 18 \text{ m (} z = 6 \text{ m)}
 \end{aligned} \tag{67.3}$$

where a value of $J = 0.25$ has been used.

Sand

For the sand layer, the axial skin strength varies from

$$\begin{aligned}
 F_{A,\max} &= K_0 \sigma'_v \tan \delta \times P \\
 &= 0.43 \times (20 - 9.8) \times 6 \times \tan(23.33^\circ) \times \pi \times 0.5 \\
 &= 17.8 \text{ kN/m at } y = 18 \text{ m (} z = 6 \text{ m)}
 \end{aligned} \tag{67.4}$$

to

$$\begin{aligned}
 F_{A,\max} &= K_0 \sigma'_v \tan \delta \times P \\
 &= 0.43 \times [(20 - 9.8) \times 6 + (20 - 9.8) \times 8] \times \tan(23.33^\circ) \times \pi \times 0.5 \\
 &= 41.6 \text{ kN/m at } y = 10 \text{ m (} z = 14 \text{ m)}
 \end{aligned} \tag{67.5}$$

where a soil-pile interface friction angle of $\delta = \frac{2}{3}\phi = 23.33^\circ$ has been used along with the earth pressure coefficient of $K_0 = 1 - \sin \phi = 0.43$ used for the Mohr-Coulomb material representing the sand layer.

The lateral strength varies from

$$\begin{aligned} F_{L,\max} &= C_3\sigma'_v \times D \\ &= 377 \times (20 - 9.8) \times 6 \times 0.5 \\ &= 1,623 \text{ kN/m at } y = 18 \text{ m } (z = 6 \text{ m}) \end{aligned} \tag{67.6}$$

to

$$\begin{aligned} F_{L,\max} &= C_3\sigma'_v \times D \\ &= 377 \times [(20 - 9.8) \times 6 + (20 - 9.8) \times 8] \times 0.5 \\ &= 3,787 \text{ kN/m at } y = 10 \text{ m } (z = 14 \text{ m}) \end{aligned} \tag{67.7}$$

Finally, the base strength is given by

$$\begin{aligned} F_{B,\max} &= [\tan \phi + \sqrt{1 + \tan^2 \phi}]^2 \exp(2\Psi \tan \phi) \sigma'_v \times A \\ &= 22.8 \times [(20 - 9.8) \times 6 + (20 - 9.8) \times 8] \times \pi \times D^2/4 \\ &= 638.9 \text{ kN} \end{aligned} \tag{67.8}$$

where a value of $\Psi = 1.3$ has been used.

The full set of soil-pile strengths is summarized in Figure 67.2.

y (m)	Material	$F_{A,\max}$ (kN/m)	$F_{L,\max}$ (kN/m)	$F_{B,\max}$ (kN)
24	Clay	25.9	45.0	-
18	Clay	25.9	120.6	-
18	Sand	17.8	1,623	-
10	Sand	41.6	3,787	638.9

Figure 67.2: Soil-pile strength parameters.

67.1 Limit analysis

To assess the ultimate strength of the pile row, three limit analyses involving vertical, horizontal and moment loading are considered. The results, obtained using 10,000 6-node Gauss elements, are shown in Figure 67.3. We see that for horizontal loading, there is a minimum of interaction between the piles and the soil at failure whereas the opposite is observed for the cases of vertical and moment loading.

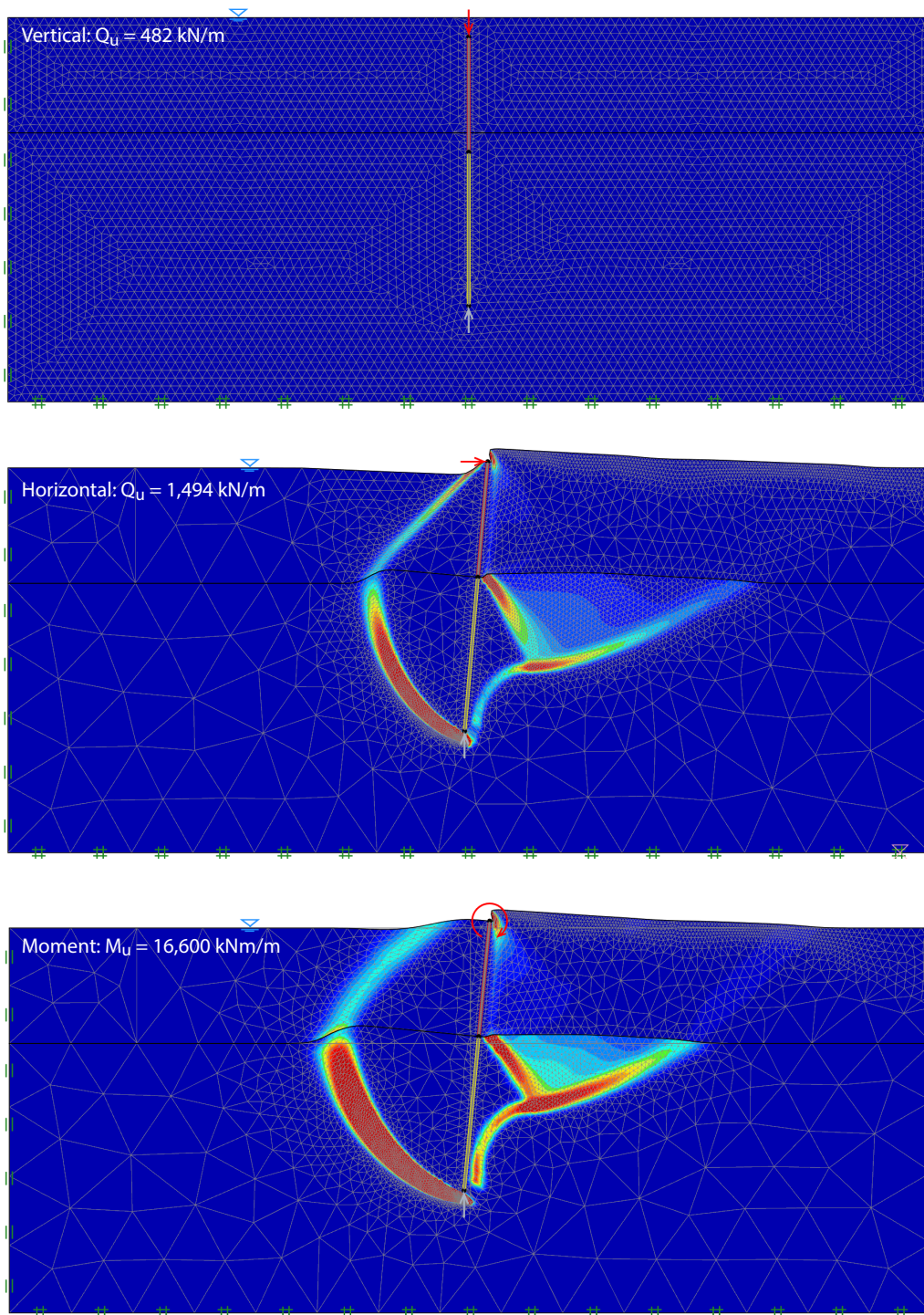


Figure 67.3: Pile row at failure in vertical (top), horizontal (center) and moment (bottom) loading with soil shear dissipation.

67.2 Elastoplastic analysis

For the cases of vertical and moment loading, the ultimate strength of the pile row is only mobilized at very large displacements. As such, the limit loads determined above are somewhat misleading. To obtain a meaningful assessment of the behaviour of the pile row, elastoplastic analyses with imposed displacement/rotation corresponding to the three load cases are conducted. The results

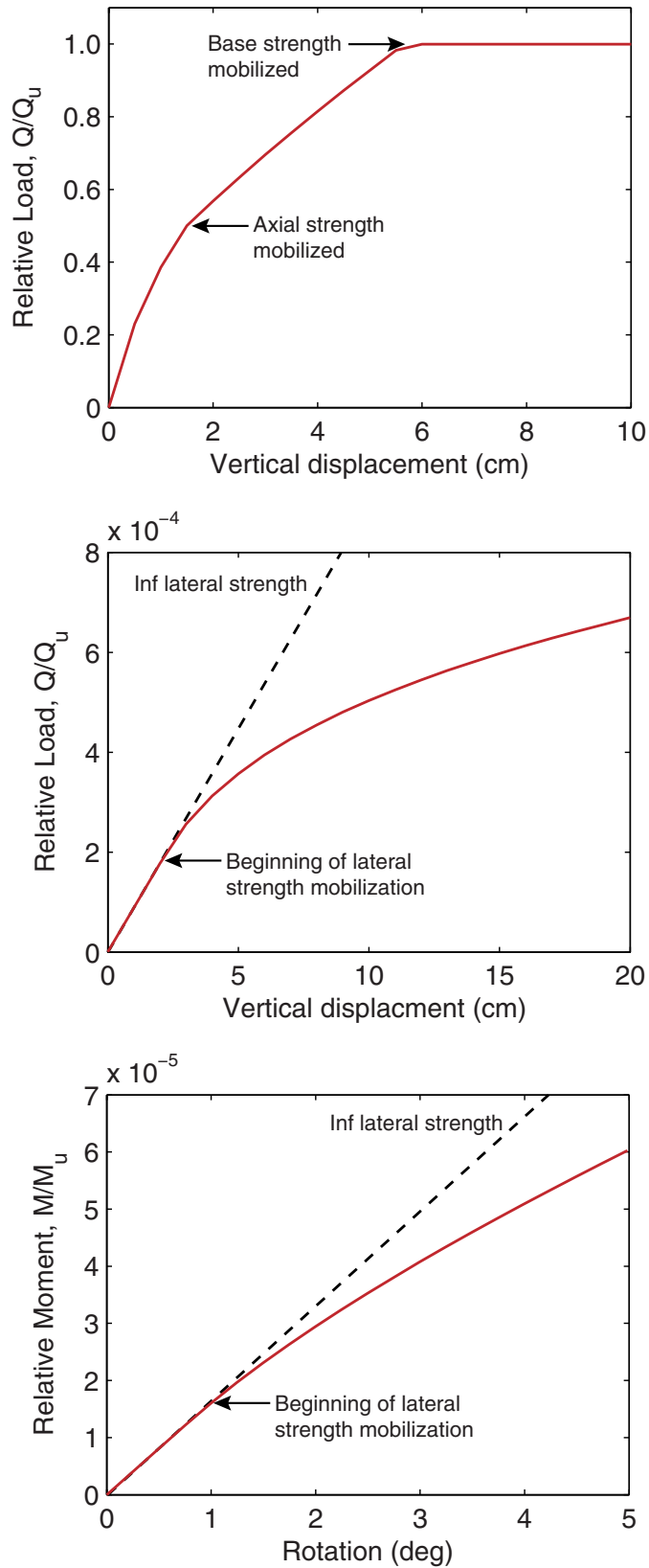


Figure 67.4: Load-displacement curves for vertical (top), horizontal (center) and moment (bottom) loading. The loads are normalized by the limit loads.

in terms of load-displacement curves are shown in Figure 67.4. For the horizontal case, the initial nonlinearity is due to the axial skin strength gradually becoming mobilized along the pile while failure takes place once the base strength is reached. For the vertical and rotational loading cases, the deviation from linear elastic behaviour is due to the lateral capacity of the clay layer gradually being mobilized. Without a lateral strength limitation, the curves indicated by dashed lines would result. The ultimate strength is reached once the lateral strength of the sand layer is fully mobilized and this occurs only at very large displacements. The gradual mobilization of the lateral strength in the vertical loading case is illustrated in Figure 67.5.

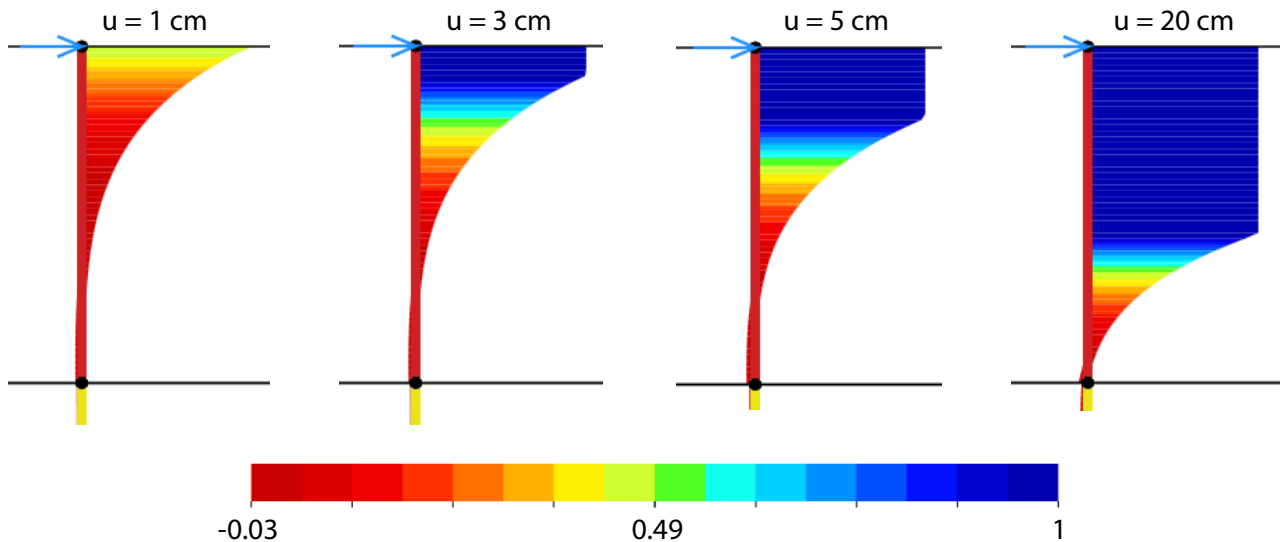


Figure 67.5: Relative lateral spring forces for different pile tip displacements showing a gradual mobilization of the lateral strength in the clay layer.

The soil and pile row deformations corresponding to the maximum imposed displacement/rotation are shown in Figure 67.6. We see that the soil and the pile row interact somewhat although most of the deformation is taken by the pile. It is noted that the soil deformations represent the average out-of-plane deformation.

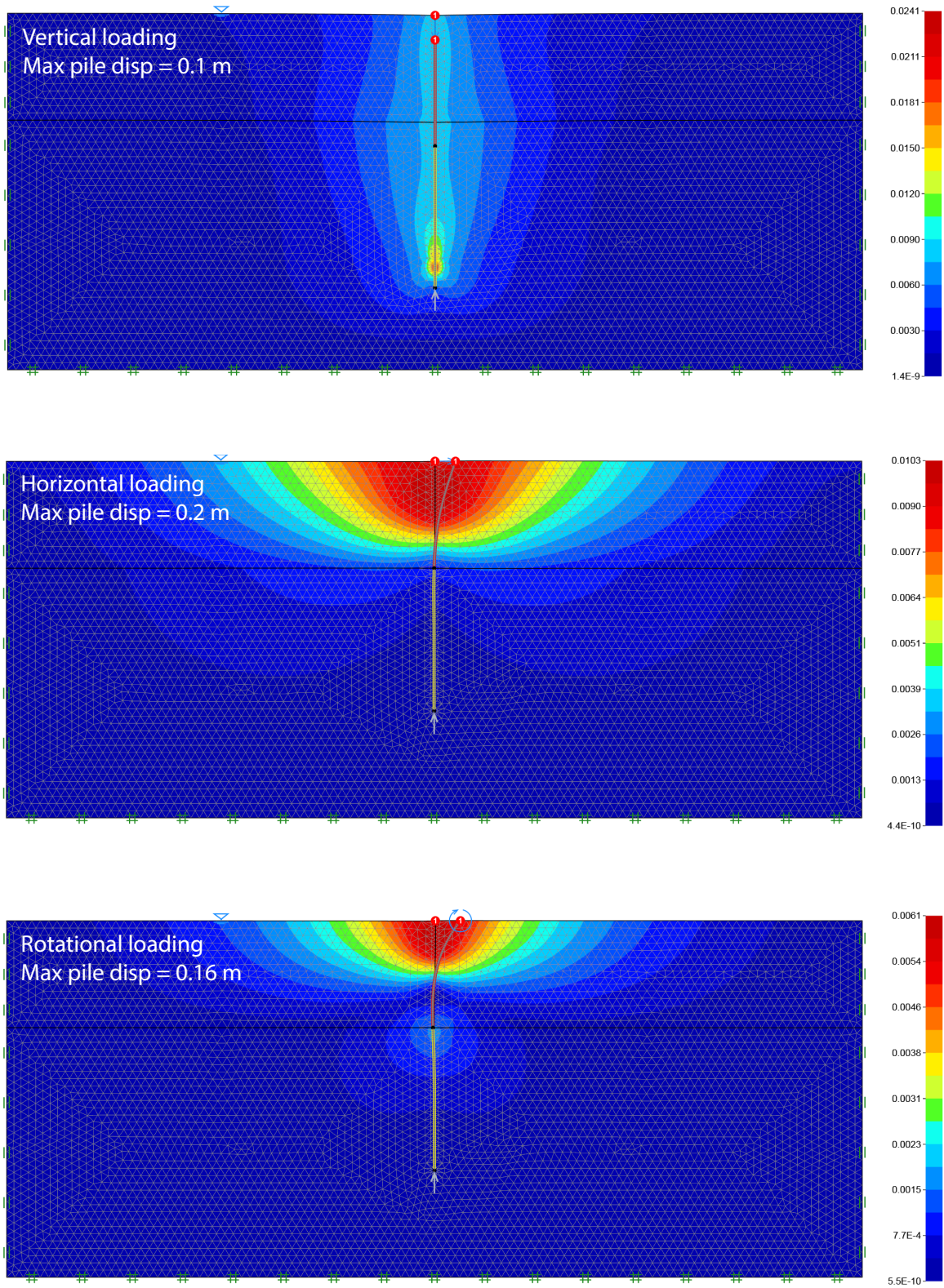


Figure 67.6: Pile row and soil deformations, $|u|$ (cm), at the final state of the loading corresponding to curves in Figure 67.4.

68 BRACED EXCAVATION

The following example concerns an excavation as indicated in Figure 68.1 (a). The excavation is 15 m deep and 30 m wide. The geometry is such that symmetry considerations cannot be utilized. The excavation is performed in a sequence of stages and struts are inserted at regularly intervals to eventually reach the final configuration shown in Figure 68.1 (b). The medium and dense sands

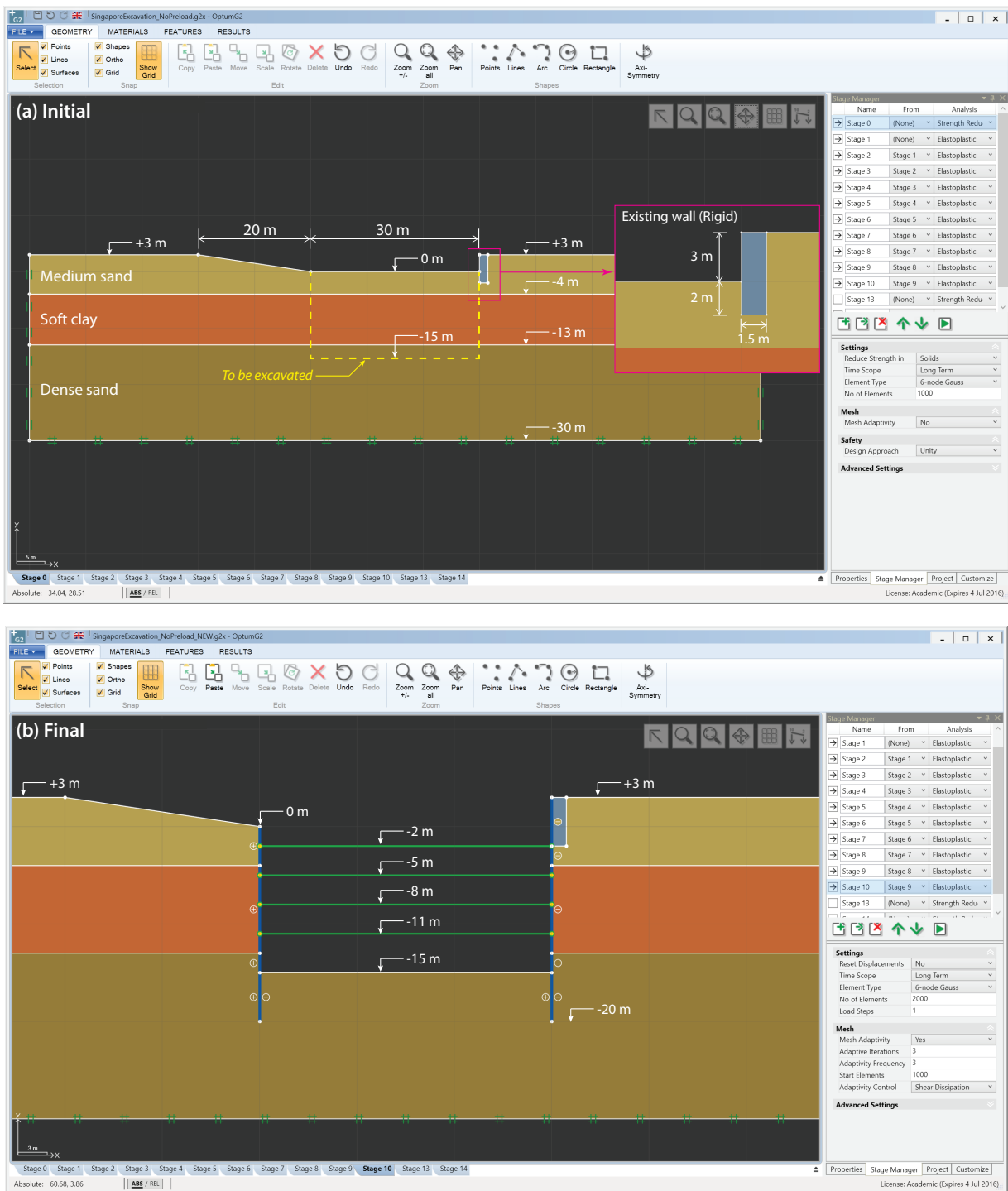


Figure 68.1: Initial (a) and final (b) configurations.

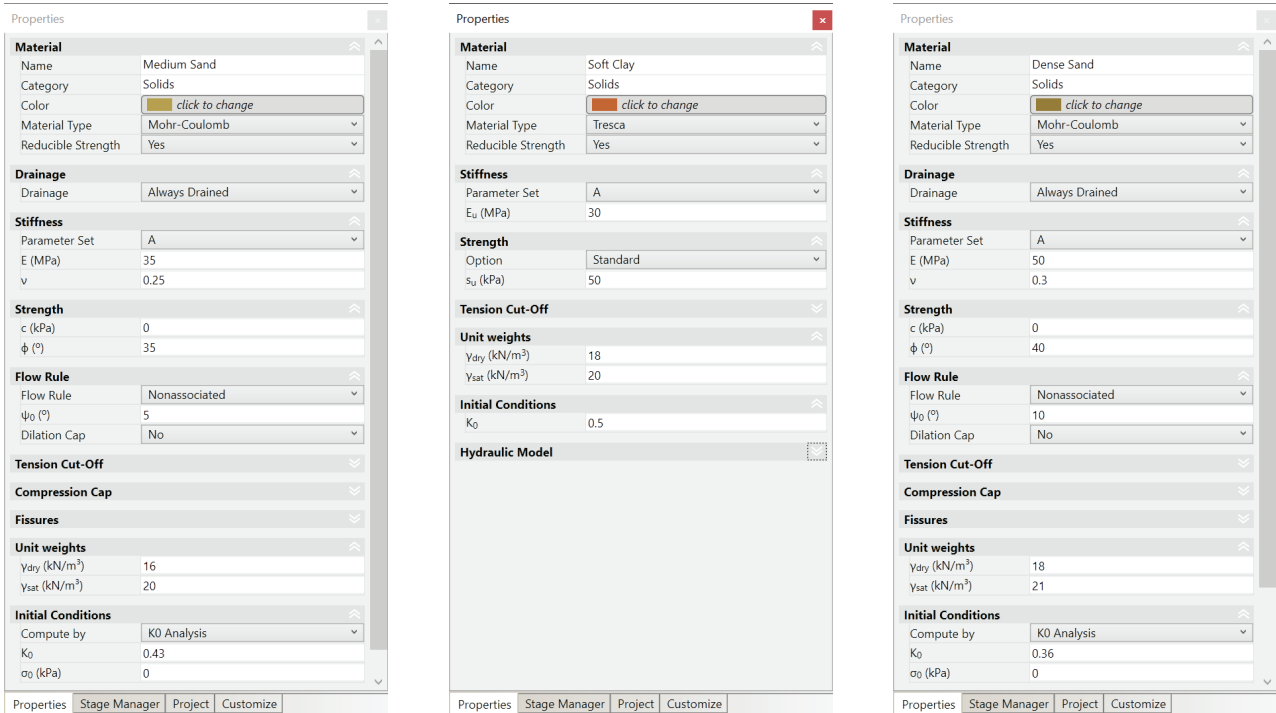


Figure 68.2: Soil materials.

are modelled as Mohr-Coulomb materials while the soft clay is modelled as a Tresca material. The parameters of the three materials are shown in Figure 68.2. The sheet piles are modelled as Plates while the struts are modelled using the Connector elements. The parameters of these elements are shown in Figure 68.3. Upon installation, the struts may or may not be preloaded. In the following both possibilities are investigated and the response of the system for each strategy are compared.

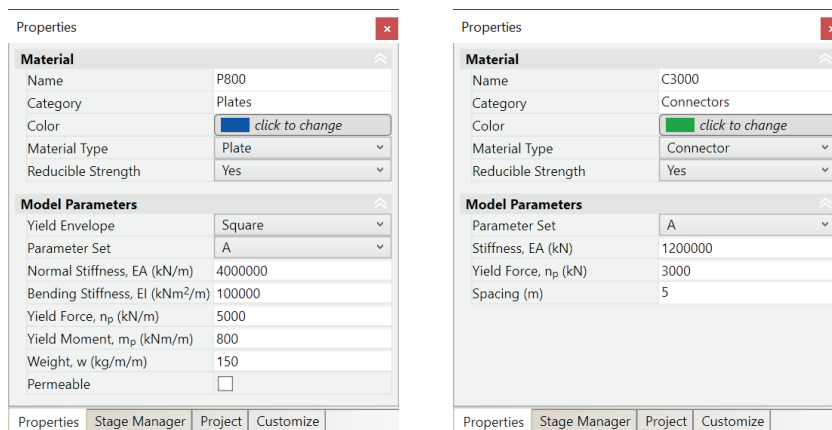


Figure 68.3: Sheet piles (Plates) and struts (Connectors).

68.1 Without preloading

We first consider the case where the struts are not preloaded. The program is summarized in Table 68.1. The first two stages (Stage 0 and 1) account for the initial stresses and the installation of the sheet piles respectively. The excavation then begins in intervals of 3 m, with a strut installed 1 m

above the current excavation level before each new excavation step. In the present analysis where no preloading is applied to the struts, the stages accounting only for the installation of the struts (Stages 3, 5, 7, 9) do not give rise to any deformations and could in principle have been combined with the subsequent excavation step, i.e. Stage 3 with Stage 4, Stage 5 with Stage 6, etc. However, for the sake of clarity, the installation of the struts have been performed in a separate stage.

Stage	Exc. level (m)	Action	Analysis Type
0	0.0	Initial stresses computed	Initial Stress
1	0.0	Sheet piles installed	Elastoplastic
2	-3.0	Excavation	Elastoplastic
3	-3.0	Strut installed at level -2 m	Elastoplastic
4	-6.0	Excavation	Elastoplastic
5	-6.0	Strut installed at level -5 m	Elastoplastic
6	-9.0	Excavation	Elastoplastic
7	-9.0	Strut installed at level -8 m	Elastoplastic
8	-12.0	Excavation	Elastoplastic
9	-12.0	Strut installed at level -11 m	Elastoplastic
10	-15.0	Excavation	Elastoplastic

Table 68.1: Definition of stages (without preloading).

68.2 With preloading

Next, we consider the case where the struts are preloaded. The program is shown in Table 68.2 and differs from the previous one only in that each of the struts are preloaded immediately upon installation, i.e. in Stages 3, 5, 7, and 9.

Stage	Exc. level (m)	Action	Analysis Type
0	0.0	Initial stresses computed	Initial Stress
1	0.0	Sheet piles installed	Elastoplastic
2	-3.0	Excavation	Elastoplastic
3	-3.0	Strut installed at level -2 m and preloaded to -2,000 kN	Elastoplastic
4	-6.0	Excavation	Elastoplastic
5	-6.0	Strut installed at level -5 m and preloaded to -1,500 kN	Elastoplastic
6	-9.0	Excavation	Elastoplastic
7	-9.0	Strut installed at level -8 m and preloaded to -2,000 kN	Elastoplastic
8	-12.0	Excavation	Elastoplastic
9	-12.0	Strut installed at level -11 m and preloaded to -2,000 kN	Elastoplastic
10	-15.0	Excavation	Elastoplastic

Table 68.2: Definition of stages (with preloading).

In OPTUM G2, preload (or prestress) is applied by selecting a Connector and then specifying “Apply Prestress = Yes” (see Figure 68.4). The application of preload should be seen as an action: the normal force in the Connector is set to the value specified. In this case, the relevant preloading will induce a state of compression in the struts, hence the negative value.

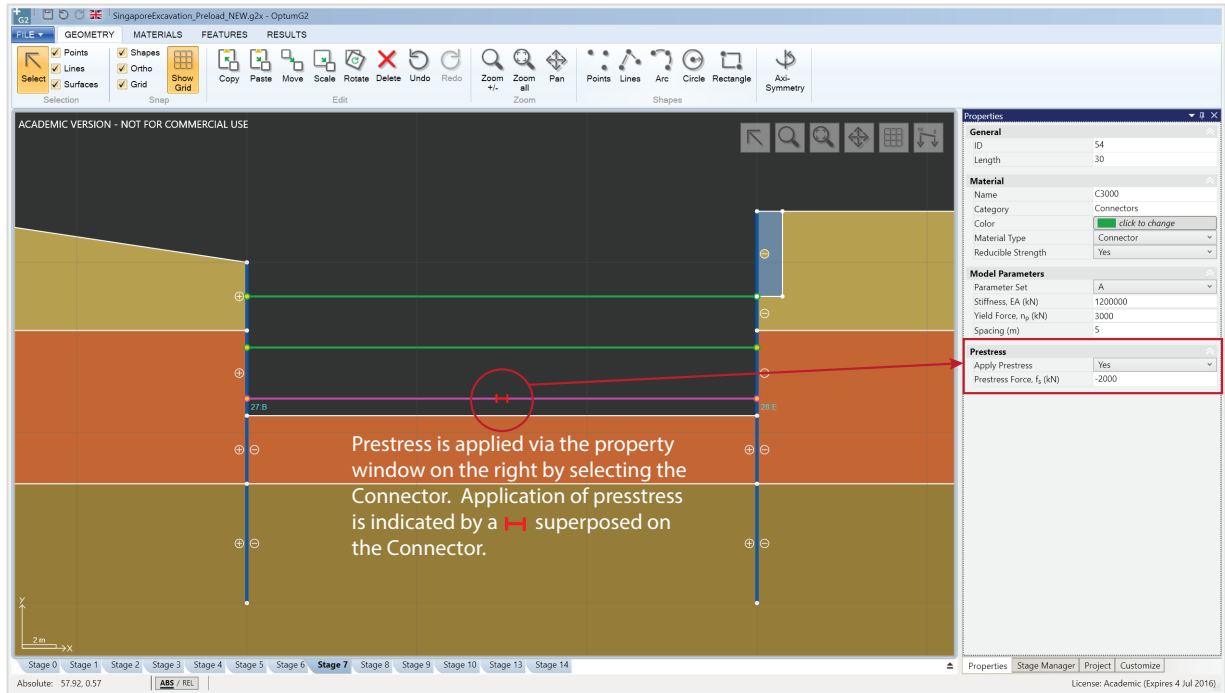


Figure 68.4: Application of preload in Stage 7.

68.3 Results

68.3.1 Factor of safety analysis

Before deformations are determined, a Strength Reduction analysis is conducted for each stage. The results, shown in Figure 68.5, reveal that the factor of safety remains above 1.9 throughout the excavation. It should be noted that preloading does not affect the factor of safety.

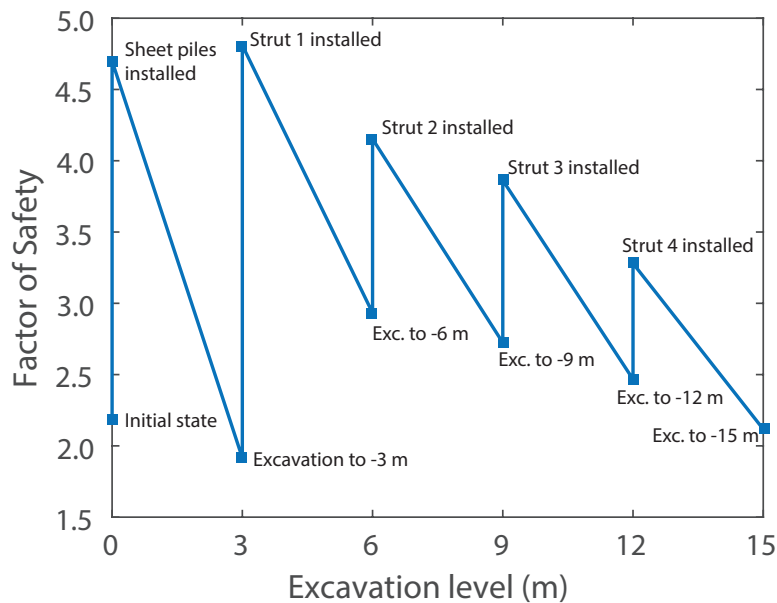


Figure 68.5: Factor of safety versus excavation level.

68.3.2 Displacements

With a reasonable level of safety against failure verified, the next step is to determine deformations according to the programs outlined in Tables 68.1-2.

The displacement fields at the final stage for the two cases – with and without preloading of the struts – are shown in Figure 68.6.

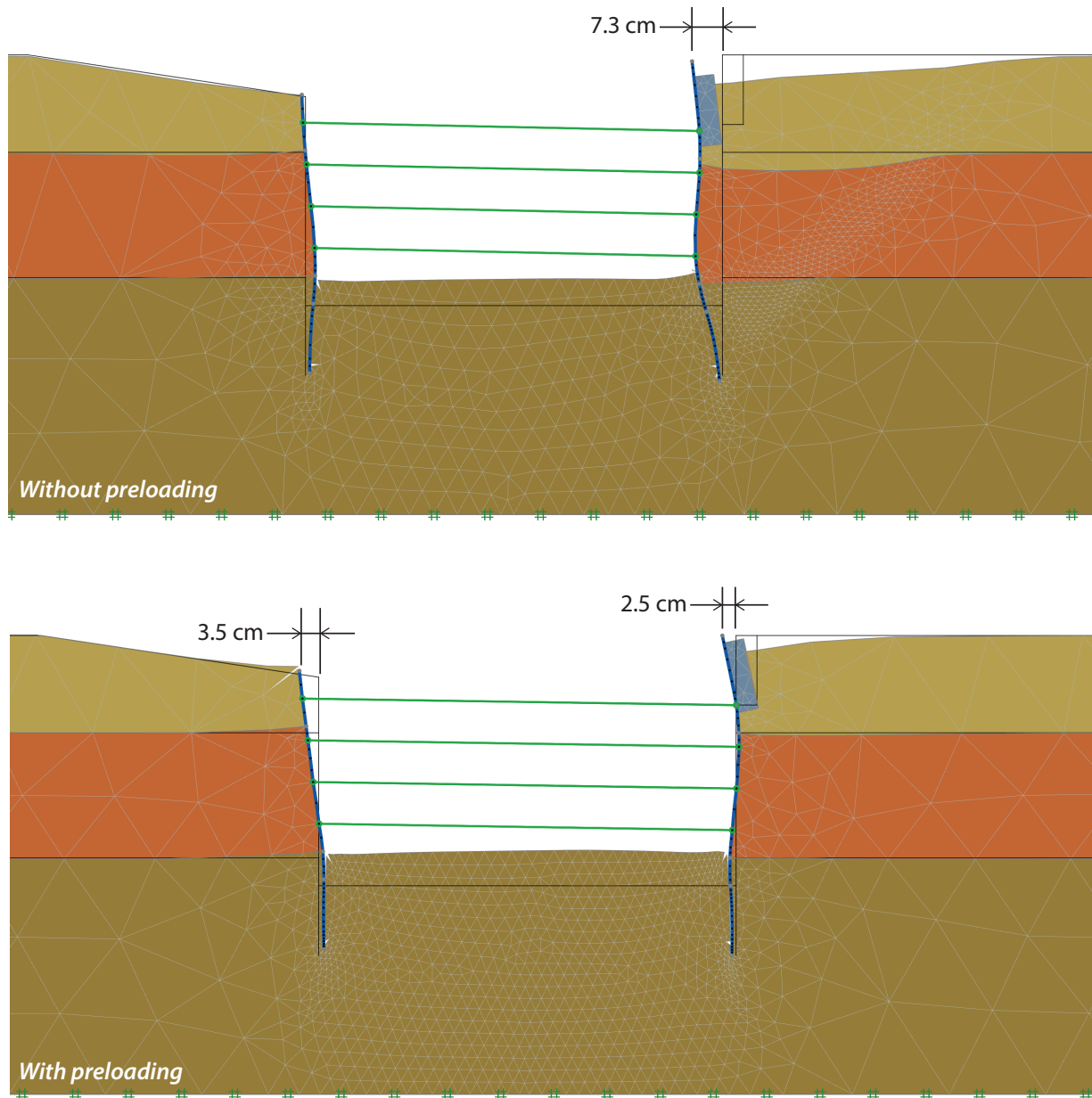


Figure 68.6: Final configurations without (top) and with (bottom) preloading of struts.

The horizontal displacements of the top of the left and right sheet piles are plotted in Figure 68.7. The effects of preloading are apparent: with preloading the displacement of the right pile is reduced significantly, though at the expense of displacing the left pile away from the excavation.

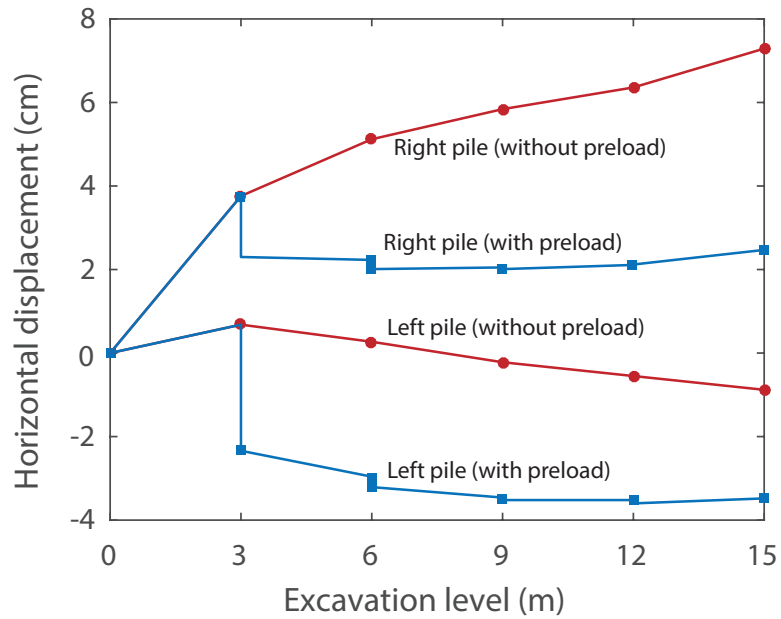


Figure 68.7: Horizontal displacement of top of sheet piles (positive into the excavation).

69 STABILITY OF EARTH DAM SUBJECTED TO SEEPAGE

The following example considers the stability of an earth dam as shown in Figure 69.1. The difference between the water table on the left and right-hand sides of the dam gives rise to a seepage from left to right of a magnitude depending on the water level D on the left-hand side. In the following, the full range of possible water depths from 0 to 20 m are considered. The geotechnical parameters for the materials involved are listed in Table 69.1.

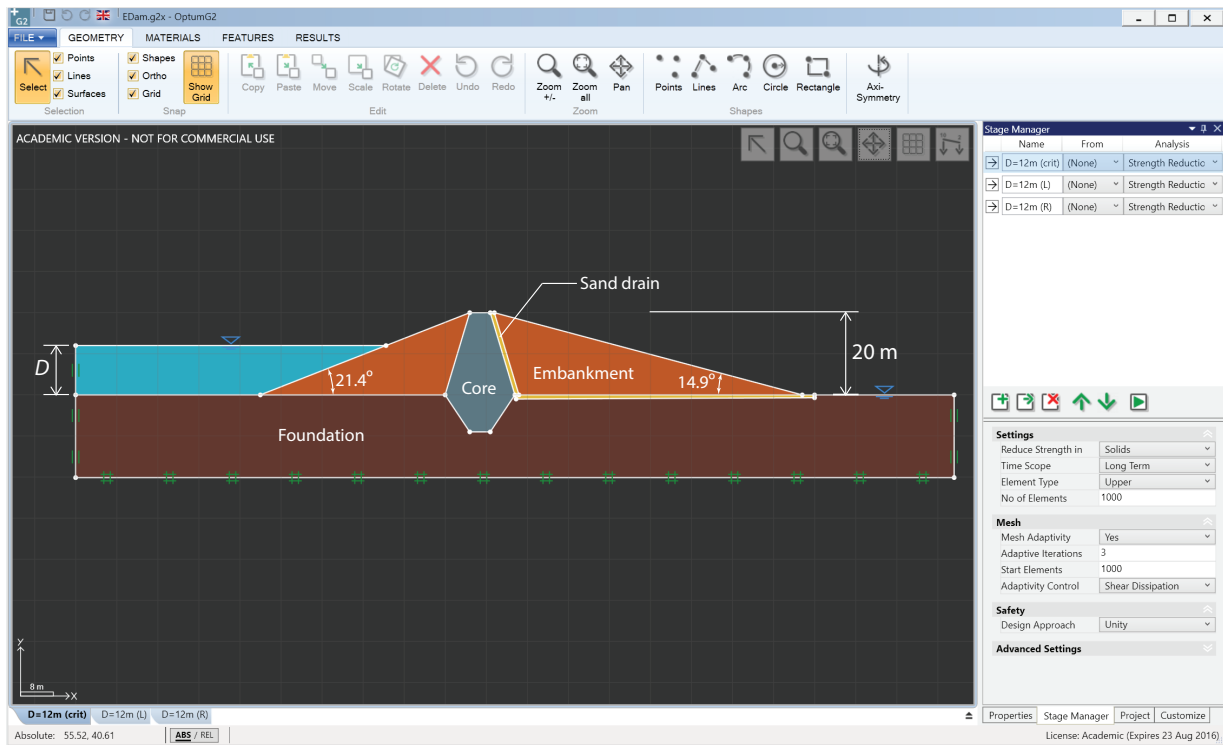


Figure 69.1: Earth dam. Please refer to the input file for precise dimensions.

	c (kPa)	ϕ ($^{\circ}$)	$K_x = K_y$ (m/day)
Foundation	20	32	10^{-1}
Embankment	10	30	10^{-1}
Core	10	30	10^{-5}
Sand drain	0	35	10^2

Table 69.1: Mohr-Coulomb strength parameters and hydraulic conductivities for earth dam materials.

69.1 Seepage

The seepage pattern through the dam is a function of the water level D on the left-hand side of the dam. The saturated and dry parts of the dam (separated by the phreatic surface) are shown in Figure 69.2 for different water levels. It is noted that the necessary seepage calculation is performed automatically as part of any mechanical analysis.

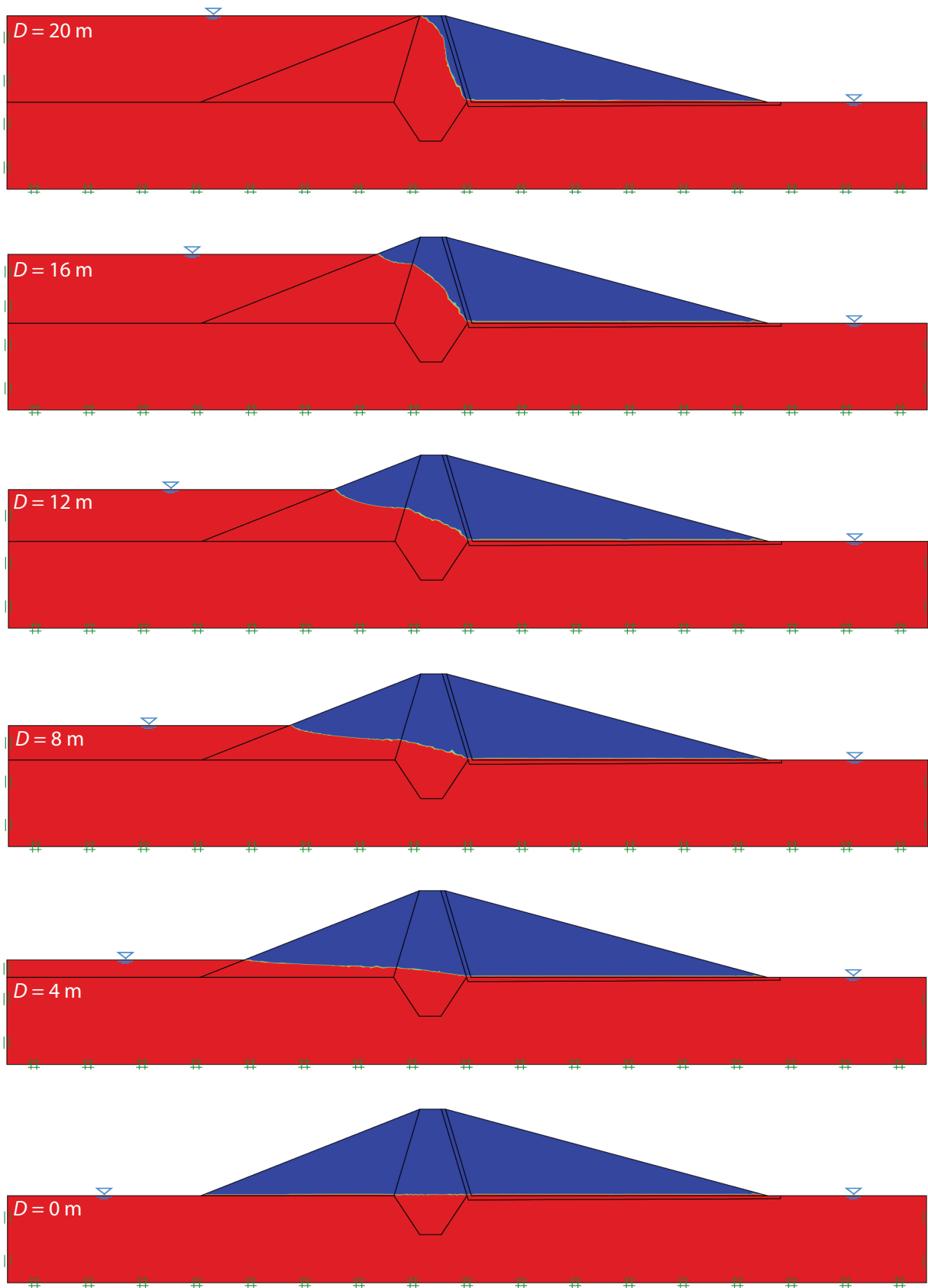


Figure 69.2: Degrees of saturation with red corresponding to $S = 1$ (fully saturated) and blue corresponding to $S = 0$ (dry).

69.2 Factor of safety

The factor of safety of the dam may be evaluated by means of Strength Reduction analysis. In this analysis a factor FS is calculated such that the reduced material strengths

$$c_{\text{red}} = \frac{c}{\text{FS}}, \quad \phi_{\text{red}} = \arctan\left(\frac{\tan \phi}{\text{FS}}\right) \quad (69.1)$$

imply a situation of impending collapse. The reduction factor FS is interpreted as the factor of safety.

The Strength Reduction analysis implemented in OPTUM G2 determines the critical, i.e. smallest, factor of safety among all possible modes of failure. In other words, it is not necessary to first postulate a mechanism of failure and then compute the corresponding factor of safety as is done with limit equilibrium methods.

In the present case, it is observed that the mode of failure is such that the right-hand side of the embankment fails for small water depths while the left-hand side fails for higher water depths. If the factor of safety is to be determined independently for failure on the right and left regardless of the water level, one can strengthen the side of the embankment that is assumed not to fail. For example, if the factor of safety for failure on the right is to be investigated, the left-hand side of the embankment is artificially strengthened by increasing the cohesion (which requires that a new material is defined, see input file). In this way the diagram shown Figure 69.3 can be constructed. We see that the failure is on the left for D less than about 16 m and otherwise on the right. Representative failure modes are shown in Figure 69.4.

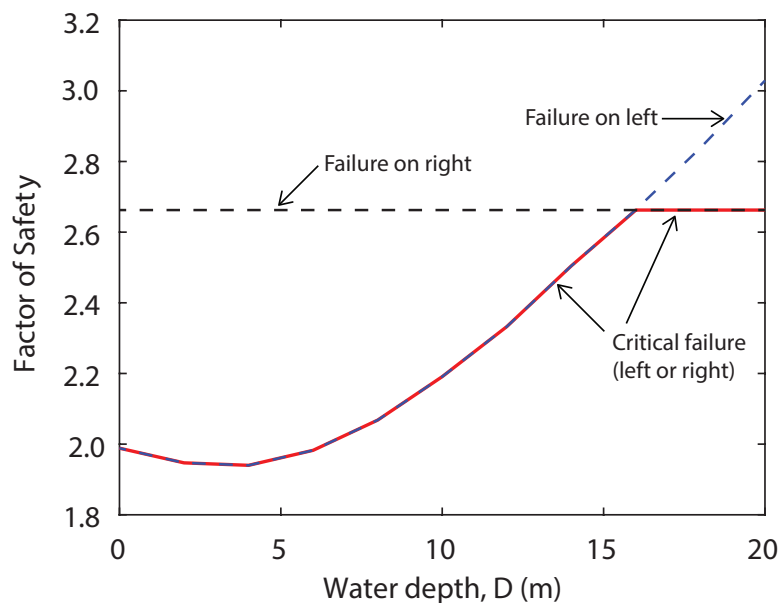


Figure 69.3: Factors of safety as function of water depth.

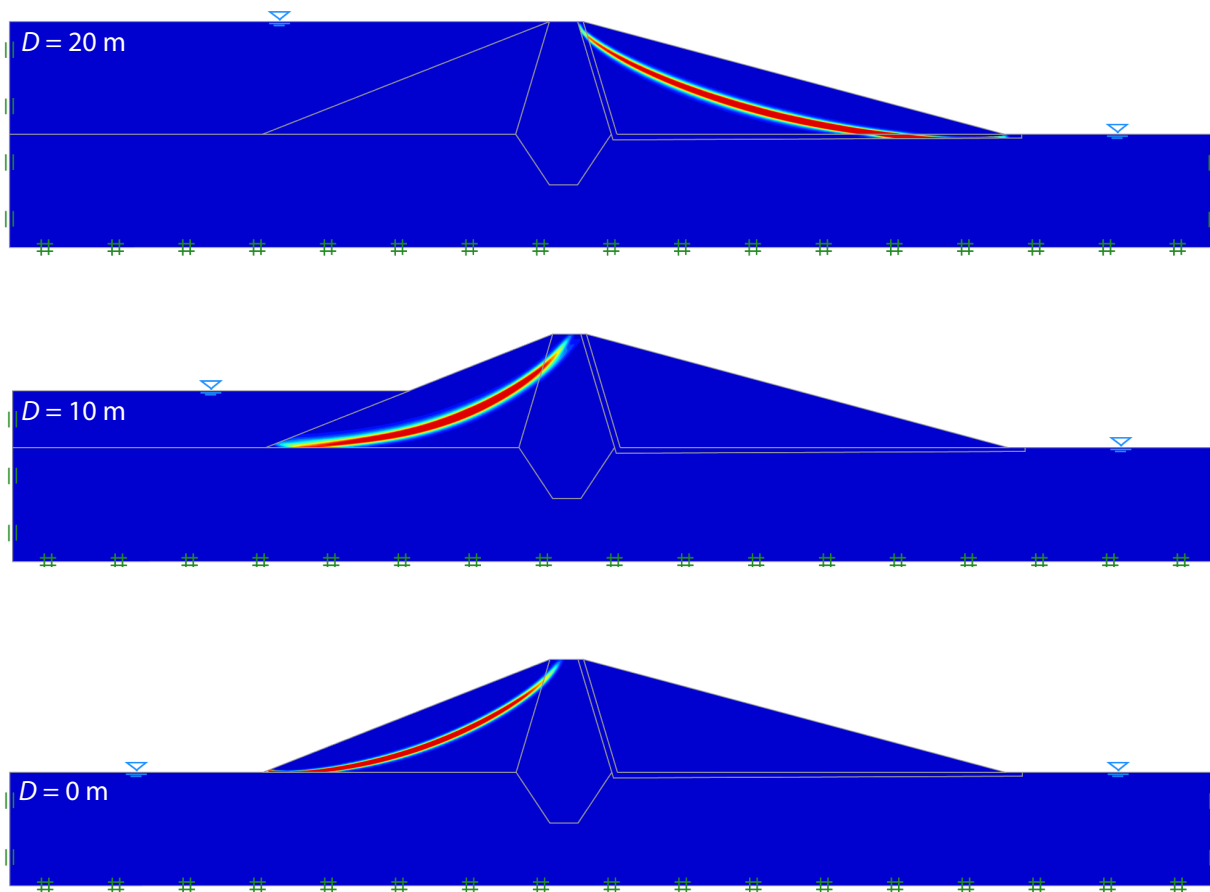


Figure 69.4: Slip lines (shear dissipation) for different water depths.

70 STABILITY OF CRACKED SLOPE

The following example concerns the slope shown in Figure 70.1. The slope comprises a Mohr-Coulomb material with $c = 10$ kPa and $\phi = 20^\circ$. The cracks, which extend to a depth of D_{crack} , are modeled as Shear Joints with $c = 0$ and $\phi = 15^\circ$.

In the following, the weakening of the slope as a result of the presence of these cracks is investigated. Two cases are considered: dry cracks and cracks filled with water. In the latter case it is assumed that the slope itself is impermeable so that the water pressures in the cracks act as additional driving forces. To model this situation, i.e. to preclude the water in the cracks from flowing into the slope, the slope material is chosen as being Non-Porous (setting under Drainage). The water in the cracks is assigned using the Water Table tool (select the relevant point and then the Water Table button in the Features ribbon. Alternatively, Fixed Pressures or Heads can be assigned to the Shear Joints).

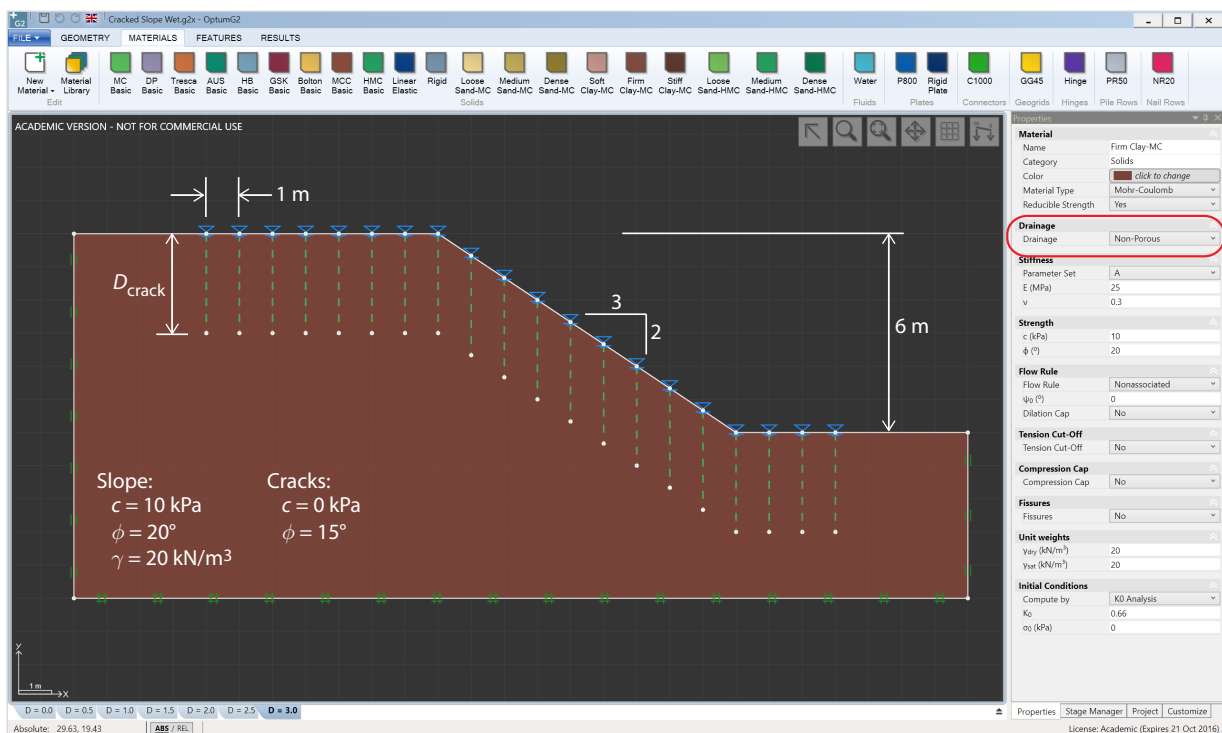


Figure 70.1: Cracked slope with cracks modeled as Shear Joints.

Strength Reduction analysis is used to determine the factor of safety as function of the crack depth. The results are shown in Figure 70.2. These results are computed on the basis of 2,000 elements with 3 adaptivity iterations. The results shown are the mean values between the upper and lower bounds for each case. The worst-case error (the relative error between the upper and lower bounds) is in all cases less than 3%. We see that the factor of safety drops markedly with the crack depth, especially in the case where the cracks are filled with water. Representative collapse mechanisms are shown in Figure 70.3.

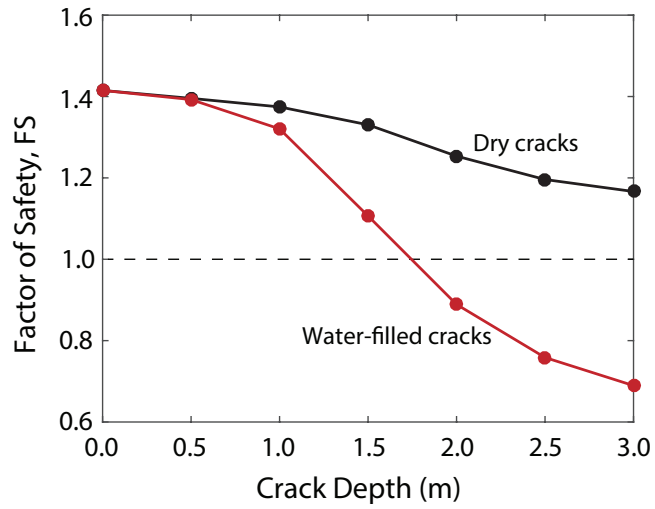


Figure 70.2: Factor of safety versus crack depth.

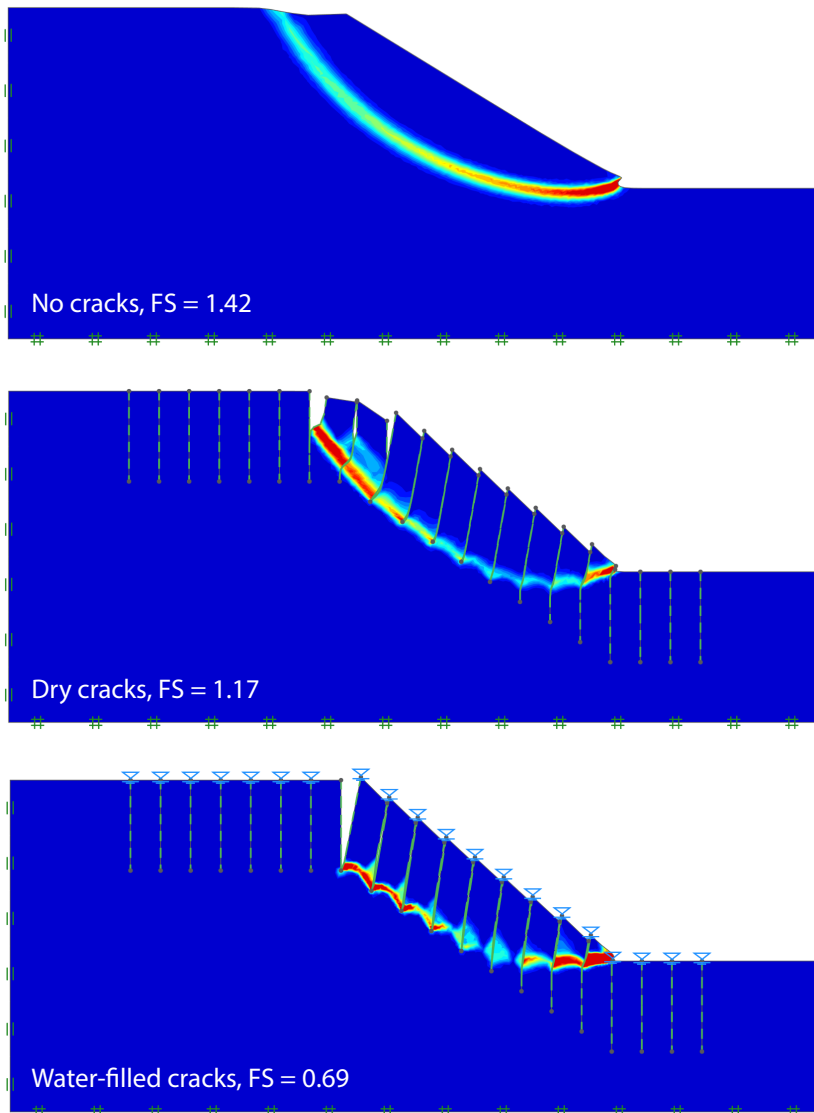


Figure 70.3: Collapse mechanisms. In the middle and lower figure the crack depth is 3 m.

References

- Ahmed, S. M. U. (1972). *A Study of the Influence of Confining Pressure on the Behaviour of Sands*. PhD thesis, McGill University, Montreal, Canada.
- Anastasopoulos, I., Gazetas, G., Bransby, M. F., Davies, M. C. R., and Nahas, A. E. (2007). Fault rupture propagation through sand: Finite-element analysis and validation through centrifuge experiments. *Journal of Geotechnical and Geoenvironmental Engineering*, 133:943–958.
- Benz, T. (2007). *Small-Stain Stiffness of Soils and its Numerical Consequences*. PhD thesis, University of Stuttgart.
- Bolton, M. D. (1986). The strength and dilancy of sands. *Geotechnique*, 36:65–78.
- Cox, A. D., Eason, G., and Hopkins, H. G. (1961). Axially symmetric plastic deformation in soils. *Proceedings of the Royal Society A*, 254:1–45.
- Dyson, A. S. and Rognon, P. G. (2014). Pull-out capacity of tree root inspired anchors in shallow granular soils. *Geotechnique Letters*, 4:301–305.
- Gibson, R. E. (1967). Some results concerning displacements and stresses in a non-homogeneous elastic half-space. *Geotechnique*, 17:58–64.
- Gourvenec, S. M., Vulpe, C., and Murthy, T. G. (2014). A method for predicting the consolidated undrained bearing capacity of shallow foundations. *Geotechnique*, 64:215–225.
- Hoek, E. (2007). *Practical Rock Engineering*. Available at: <http://www.rocscience.com>.
- Karman, T. (1926). Über elastische Grenzzustände. In *Proc. 2nd Int. Conf. on Appl. Mech.*, pages 23–32.
- Kazemzadeh-Parsi, M. J. and Daneshmand, F. (2012). Unconfined seepage analysis in earth dams using smoothed fixedgrid finite element method. *International Journal Numerical and Analytical Methods in Geomechanics*, 36:780–797.
- Krabbenhoft, K., Karim, M. R., Lyamin, A. V., and Sloan, S. W. (2012). Associated computational plasticity schemes for nonassociated frictional materials. *International Journal for Numerical Methods in Engineering*, 89:1089–1117.
- Lehane, B. M. and Jardine, R. J. (2002). Effects of long-term preloading on the performance of a footing on clay. *Geotechnique*, 53:689–695.
- Loukidis, D., Bandini, P., and Salgado, R. (2003). Stability of seismically loaded slopes using limit analysis. *Geotechnique*, 53:463–479.
- Martin, C. M. (2005). Exact bearing capacity factors for strip footings - notes. <http://www.eng.ox.ac.uk/civil/people/cmm/download/ncnqngamma.pdf>.
- Martin, C. M. and Randolph, M. F. (2001). Applications of the lower and upper bound theorems of plasticity to collapse of circular foundations. In *Proc. 10th IACMAG, Tucson*, volume 2, pages 1539–1549.

- Merifield, R. S. (2010). Ultimate uplift capacity of multiplate helical type anchors in clay. *Journal of Geotechnical and Geoenvironmental Engineering*, 137(7):704–716.
- Merifield, R. S., Lyamin, A. V., and Sloan, S. W. (2006). Limit analysis solutions for the bearing capacity of rock masses using the generalised Hoek-Brown criterion. *International Journal of Rock Mechanics and Mining Sciences*, 43:920–937.
- Mesri, G. and Castro, A. (1986). C_α/C_c concept and K_0 during secondary compression. *Journal of Geotechnical Engineering*, 113:230–247.
- Phoon, K. K. and Kulhawy, F. H. (1999). Characterization of geotechnical variability. *Canadian Geotechnical Journal*, 36:612–624.
- Polubarinova-Kochina, P. Y. (1962). *Theory of Groundwater Movement*. Princeton University Press.
- Potts, D. M. and Zdravkovic, L. (2001). *Finite Elements Analysis in Geotechnical Engineering*. Thomas Telford.
- Serrano, A., Olalla, C., and Gonzalez, J. (2000). Ultimate bearing capacity of rock masses based on the modified Hoek-Brown criterion. *International Journal of Rock Mechanics and Mining Sciences*, 37:1013–1018.
- Sloan, S. W., Sheng, D., and Abbo, A. J. (2000). Accelerated initial stiffness schemes for elastoplasticity. *International Journal for Numerical and Analytical Methods in Geomechanics*, 24:579–599.
- Souloumiac, P., Krabbenhoft, K., Leroy, Y. M., and Maillot, B. (2010). Failure in accretionary wedges with the maximum strength theorem: numerical algorithm and 2D validation. *Computational Geosciences*, 14:793–811.
- Tefera, T. H., Nordal, S., Grande, L., Sandven, R., and Emdal, A. (2006). Ground settlement and wall deformation from a large scale model test on a single strutted sheet pile wall in sand. *International Journal of Physical Modelling in Geotechnics*, 2:1–13.
- Timoshenko, S. and Woinowsky-Krieger, S. (1959). *Theory of Plates and Shells*. McGraw-Hill.
- Vermeer, P. A., Moller, S. C., and Ruse, N. (2003). On the application of numerical analysis in tunnelling. In *Proc. 12th Asian Regional Conference on Soil Mechanics and Geotechnical Engineering (12 ARC)*, volume 2, pages 1539–1549.
- Won, J. Y. (2013). Anisotropic strength ratio and plasticity index of natural clays. In *Proceedings of the 18th International Conference on Soil Mechanics and Geotechnical Engineering, Paris*, pages 445–448.